2024 International Conference on Informatics Electrical and Electronics (ICIEE)

Conference Proceedings

Denpasar Bali, Indonesia
5-6 December 2024

PRIMAKARA UNIVERSITY

IEEE INDONESIA SECTION

Conference Proceedings

2024 International Conference on Informatics Electrical and Electronics (ICIEE)

Bali, Indonesia

5 – 6 December 2024

Organizer:

Department of Electrical Engineering

Universitas Sultan Ageng Tirtayasa

Primakara University

Sponsor:

IEEE Indonesia Section

https://iciee.id/

Copyright

2024 International Conference on Informatics Electrical and Electronics (ICIEE) Proceedings

IEEE Catalog Number: CFP24W82-ART
ISBN: 979-8-3315-1921-6

Table of Contents

Welcome Message

Distinguished Guests, Respected Scholars, Esteemed Partners, and Participants,

It is with immense honour and joy that I welcome you all to The 4th International Conference on Informatics, Electrical, and Electronics (ICIEE). This prestigious event, hosted in collaboration with Primakara University Bali, brings together some of the brightest minds in the fields of informatics, electrical engineering, and electronics from around the globe.

Our world today is experiencing a remarkable transformation driven by advances in technology, which have permeated every aspect of human life. The role of informatics, electrical, and electronics engineering has been pivotal in addressing global challenges, fostering innovation, and creating sustainable solutions for our shared future. ICIEE provides a vital platform for intellectual exchange, collaboration, and the dissemination of cutting-edge research that will undoubtedly shape our technological landscape. The 4th International Conference on Informatics Electrical and Electronics (ICIEE) aims to bring together leading academician, scientist, researchers and engineers to exchange and share their experiences and research results on all aspects of smart technology toward smart energy.

This year, we are thrilled to host 32 outstanding submissions, reflecting the diversity and depth of research being conducted across the globe. These contributions span a wide array of topics, including renewable energy, smart grids, IoT, robotics, and next-generation communication systems, aligning with our theme: "Smart Technology Toward Smart Energy". We are privileged to have an impressive line-up of keynote speakers, panel discussions, and technical sessions that delve into the latest developments and future directions in our disciplines. I would like to extend a special and heartfelt welcome to our esteemed keynote speakers, whose ground breaking work continues to shape the future of our disciplines. It is our privilege to host Prof. Jun Kondoh from Shizuoka University Japan, Zulkifli Bin Zainal Abidin (Assoc. Prof. Dr) from International Islamic University Malaysia and Made Adi Paramartha Putra., PhD from Primakara University. Your insights will undoubtedly inspire meaningful discussions and drive further innovation in these critical fields.

I extend my heartfelt gratitude to our co-host, Primakara University - Bali, for their outstanding partnership in organizing this conference. Their commitment to academic excellence and innovation has greatly enriched this event. I also wish to thank our organizing committee, speakers, and participants for their invaluable contributions. Your presence here today signifies your dedication to advancing knowledge and collaboration across borders.

As we embark on this intellectual journey, I encourage you to actively engage, exchange ideas, and explore new horizons during this conference. Let us seize this opportunity to build networks, foster collaborations, and inspire future innovations.

Once again, welcome to ICIEE. I wish you a fruitful and rewarding conference experience. May your time here in Bali be as enriching and inspiring as the discussions we are about to embark upon.

Warm regards,

Dr. Eng. Rocky Alfanz., S.T., M.Sc
Chairperson Department of Electrical Engineering
Sultan Ageng Tirtayasa University

Welcome Message

INTERNATIONAL CONFERENCE ON INFORMATICS, ELECTRICAL AND ELECTRONICS (ICIEE 2024)

5th December 2024

Distinguished Guests:

1. Prof. Jun Kondoh - Shizuoka University Japan.
2. Assoc Prof Dr. Zulkifli Bin ZA - International Islamic University Malaysia
3. Rector Primakara University Bali Indonesia - Dr. I Made Artana, S.Kom., M.M
4. Vice Rector I Primakara University Bali Indonesia - Helmy Syakh Alam, S.T., S.Pd., M.Pd.
5. Vice Rector II Primakara University Bali Indonesia - I Made Sudama, S.E., M.M
6. Vice Rector III Primakara University Bali Indonesia - Putri Anugerah Cahya Dewi, M.Pd
7. Vice Rector IV Primakara University Bali Indonesia - I Gede Juliana Eka Putra, S.T., M.T
8. Dean of Information Technology and Design Faculty - Dr. Ni Made Satvika Iswari, S.T., M.T.
9. Dean of Economic and Business Faculty - Ketut Tri Budi Artani, S.E., M.Si., AK., CA., CSRA., CFM
10. Made Adi Pramartha Putra PhD. From Primakara University Bali Indonesia

Distinguished Guests, Esteemed Speakers, Honored Participants, and Respected Colleagues,

Good morning, and welcome to the "International Conference on Informatics Electrical and Electronics". As the Rector of Sultan Ageng Tirtayasa University, it is both an honor and a privilege to address you all at the opening of this remarkable international seminar.

Today's event holds a special significance, as it is the result of a collaborative effort between Universitas Sultan Ageng Tirtayasa and Primakara University, Bali. This partnership between our institutions reflects a shared commitment to advancing knowledge, fostering innovation, and strengthening academic and professional networks especially in the field of electrical engineering. Together, we are united in our mission to drive progress and inspire future breakthroughs that will benefit society.

This seminar serves as a platform to exchange knowledge, share innovative ideas, and discuss the latest advancements in the recent field of electrical engineering. Over the next few days,

we will explore a broad range of topics—from renewable energy and power systems to advanced electronics and smart technologies—that have the potential to reshape industries and improve lives.

In today's world, the challenges we face in energy sustainability, digital transformation, and technological advancement demand collaborative efforts and cutting-edge solutions. I believed that the insights shared by our esteemed speakers, along with the discussions and interactions during this seminar, will contribute meaningfully to these efforts. Thus, we have the opportunity to foster innovation that can address global challenges and promote a more sustainable and connected future. This goal is in line to our institution mission to contribute to the society by promoting eco-innovation and sustainable research and academic activity.

I would like to express my sincere gratitude to the organizing committee and all our partners. Organizing an event of this scale requires particular planning, hard work, and an unwavering commitment to excellence. Thank you for your dedication and for making this seminar possible.

As we embark on this journey of learning and collaboration, I encourage each of you to take full advantage of the opportunities this seminar provides. Engage actively in the sessions, ask questions, exchange perspectives, and build connections that will strengthen our global network of professionals and academics in electrical engineering.

Finally, welcome to this collaborative international seminar. I wish you all a productive and educational experience. May this event inspire new ideas, spark meaningful collaborations, and pave the way for future achievements in electrical engineering.

Thank you.

Prof. Dr. Ir. H. Fatah Sulaiman, ST., MT.
Rector of Universitas Sultan Ageng Tirtayasa

Welcome Message
by the Rector of Universitas Primakara

International Conference on Informatics, Electrical, and Electronics (ICIEE) 4th, 2024

Distinguished Guests,
Esteemed Speakers and Experts,
Fellow Academicians and Researchers,
Ladies and Gentlemen,

On behalf of Universitas Primakara, it is my utmost pleasure to welcome all of you to the 4th International Conference on Informatics, Electrical, and Electronics (ICIEE) 2024. It is a great honor for Universitas Primakara to serve as the *Co-Host* for this prestigious event, held in collaboration with our esteemed partner, Universitas Sultan Ageng Tirtayasa, the *Host* of this year's conference.

The theme for this year, *"Synergy of New Tech Frontiers: AI, Cybersecurity, 5G/6G, Renewables, IoT, and Climate Resilience for Tomorrow Challenges,"* is both timely and critical. We are standing at the crossroads of transformative advancements in technology and mounting global challenges. This theme underscores the need for a collaborative approach to harness the potential of emerging technologies while ensuring sustainability and resilience in our systems.

I am confident that this conference will serve as an invaluable platform for sharing insights, presenting cutting-edge research, and fostering collaborations that will shape the future of technology and its applications in addressing global issues. It is through gatherings like this that we can collectively innovate and contribute to a better tomorrow.

To our distinguished speakers and participants, thank you for sharing your expertise and contributing to the intellectual discourse of this conference. To Universitas Sultan Ageng Tirtayasa, thank you for leading this remarkable initiative and for entrusting Universitas Primakara as your partner in this endeavor.

I encourage all participants to make the most of this opportunity to exchange knowledge and build networks that extend beyond the conference. Let us move forward with a shared commitment to synergy and innovation, not only for the academic community but also for the benefit of society at large.

Once again, welcome to the 4th ICIEE 2024. May this conference be a resounding success and a meaningful milestone for us all.

Thank you, and I wish you fruitful discussions and an enjoyable conference.

Warm regards,

Dr. I Made Artana, S.Kom., M.M.
Rector, Universitas Primakara

Organizing Committee

GENERAL CHAIR
Dr. Eng. Rocky Alfanz, M.Sc. (UNTIRTA)

TECHNICAL PROGRAM CHAIR
Dr. Ni Made Satvika Iswari, S.T., M.T. (Primakara University)

PUBLICATION CHAIR
Imamul Muttakin Ph.D. (UNTIRTA)

TREASURER
Nengah Widya Utami, M.Kom. (Primakara University)
Felycia, M.T.((UNTIRTA)
Ni Nyoman Ayu Nirmala Putra Putra, S.E. (Primakara University)
I Gst Ayu Agung Dina Purnama Dewi, S.Tr.Akt. (Primakara University)

SECRETARY
Fadil Muhammad, M.T.(UNTIRTA)
Naufal Franata, M.T. (UNTIRTA)
Ni Kadek Sri Mas Dwayani (Primakara University)

LOCAL PROGRAM
Ceri Ahendyarti, M.Eng. (UNTIRTA)
Masjudin, M.Eng. (UNTIRTA)
Prof. Dr. Alimuddin, S.T., M.M., M.T. (UNTIRTA)
Dr. Ir. Wahyuni Martiningsih, M.T. (UNTIRTA)
Dr. Romi Wiryadinata, M.Eng. (UNTIRTA)
Dr. Irma Saraswati, S.Si., M.T. (UNTIRTA)
Rian Fahrizal, S.T., M.Eng. (UNTIRTA)
Heri Haryanto, S.T., M.T. (UNTIRTA)
HM. Hartono, S.T., M.T. (UNTIRTA)
H. Alief Maulana, S.T., M.T. (UNTIRTA)
Dr. Eng Teguh Firmansyah, S.T., M.T. (UNTIRTA)
Dina Estining Tyas Lufianawati, S.T., M.T. (UNTIRTA)
I Gede Juliana Eka Putra, S.T., M.T. (Primakara University)
I Nyoman Yudi Anggara Wijaya, S.Kom., M.T. (Primakara University)
I Gst. Agung Pramesti Dwi Putri, S.E., M.Si. (Primakara University)
A.A. Istri Ita Paramitha, S.Pd., M.Kom. (Primakara University)
Ni Putu Anik Mentayani, S.Kom. (Primakara University)

MEDIA
Adi Nugraha, M.T. (UNTIRTA)
Ahmad Ramadhani, M.T. (UNTIRTA)
Ratu Verlaili Erlindriyani, M.T. (UNTIRTA)
Muchtar Ali Setyo Yudono, M.T. (UNTIRTA)
I G A Pt Wina Pertiwi Putri Wardani, S.Sn., M.Ds (Primakara University)
I Gede Agus Widarsana, S.M. (Primakara University)
I Putu Maesa Pradita, S.Ds. (Primakara University)

Scientific Committee

Prof. Altyeb Altaher Taha	King Abdul Azis University, Saudi Arabia
Prof. Andi Adriansyah	Universitas Mercu Buana, Indonesia
Prof. A. N. Afandi	Universitas Negeri Malang, Indonesia
Prof. Bambang Sujanarko	Universitas Jember, Indonesia
Prof. Chii-Wann Lin	National Taiwan University, Taiwan
Prof. Dadang Gunawan	Universitas Indonesia, Indonesia
Prof. Didik Notosudjono	Universitas Pakuan, Indonesia
Prof. Elhadj Dogheche	Université Polytechnique Hauts-de-France, France
Prof. Hadi Suyono	Universitas Brawijaya, Indonesia
Prof. Josaphat Tetuko Sri Sumantyo	Chiba University, Japan
Prof. Jun Kondoh	Shizuoka University, Japan
Prof. Poki Chen	National Taiwan University of Science and Technology, Taiwan
Prof. Rosni Abdullah	Universiti Sains Malaysia, Malaysia
Prof. Sunny Joseph Kalayathankal	Jyothi Engineering College, India
Prof. Sunarno	Universitas Gadjah Mada, Indonesia
Prof. Syamsir Abduh	Institut Teknologi PLN, Indonesia
Prof. Taufik	California Polytechnic State University, USA
Prof. Tofael Ahamed	Tsukuba University, Japan
Prof. Wahyu Widada	BRIN, Indonesia
Dr. Ali Abdulrazzaq Khudher	University of Mosul, Iraq
Dr. Awf Abdulrahman Ramadhan	Duhok Polytechnic University, Iraq
Dr. Leau Yu Beng	Universiti Malaysia Sabah, Malaysia
Dr. Marlin Ramadhan Baidillah	BRIN, Indonesia
Dr. Muhammad Awais Sattar	Riphah International University Lahore, Pakistan
Dr. M. V. Reddy	Nouveau Monde Graphite, Canada
Dr. Panji Nursetia Darma	North Carolina State University, USA
Dr. Raja Kumar Murugesan	Taylor's University, Malaysia
Dr. Shafiq Ul Rehman	Kingdom University, Bahrain
Dr. Zulkifli Bin Zainal Abidin	International Islamic University Malaysia, Malaysia

Keynote Speaker

"Surface Acoustic Wave Sensors for Liquid Environment"

Prof. Jun Kondoh
(Shizuoka University, Japan)

Acoustic wave devices are indispensable as duplexers and filters in smartphones and other electronic devices. A surface acoustic wave (SAW) is a wave whose energy propagates along an elastic surface. The SAW were mathematically discovered by Lord Rayleigh in 1885. In 1965, White et al. reported that SAWs can be generated and received electrically by fabricating an interdigital transducer on a piezoelectric crystal surface. Since then, research and development on electronic device applications of SAWs have become active. SAWs can also be applied to sensors. The first SAW sensors were temperature and strain sensors. In 1987, Moriizumi et al. found that shear horizontal-SAW (SH-SAW) propagates at the interface between solid and liquid without attenuation. In other words, a liquid-phase sensor is realized by SH-SAW device. The velocity and amplitude of the SH-SAW depend on the physical properties of the liquid, such as viscosity, conductivity, and dielectric constant. SH-SAW sensors are also used in biosensors to measure immunoreaction. In this lecture, an overview of SAW will be presented first. Next, sensor applications of SAW devices, especially liquid-phase sensors using SH-SAWs, will be presented.

Jun Kondoh was born in Shiga, Japan in 1967. He received his B.E., M.S., and Dr. Eng. degrees in opto-electric and mechanical engineering from Shizuoka University in 1990, 1992, and 1995, respectively. From April 1993 to March 1997, he was a research fellow of the Japan Society for the Promotion of Science. In 1996, he was a guest scientist at Karlsruhe Research Center, Germany. In April 1997, he joined the Department of Systems Engineering, Shizuoka University as an associate professor and was promoted to an associate professor in 2003 and a professor in 2010. He received the IEC 1906 Award in 2020, the Best Paper Award at the 16th International Conference on Quality in Research, the Best paper Award of Japanese Journal Applied Physics, the Special Issue of Ultrasonic Electronics in 2016, and so on. His research interests include sensors and actuators using surface waves, interdigital electrode-type sensors, and machine learning. He is a member of the Acoustic Society of Japan, Japan Society of Applied Physics, IEEJ, the Institute of Electronics, Information and Communication Engineers (IEICE), and IEEE.

Keynote Speaker

"Developing Industry-Ready Talent for Robotics"

Zulkifli Bin Zainal Abidin

(Assoc. Prof. Eur. Ing. Ir. Ts. Gs. Inv. Dr.)
(International Islamic University Malaysia, Malaysia)

The rapid advancement of robotics technologies has led to an increasing demand for skilled professionals across various industries, including manufacturing, healthcare, and logistics. This keynote presentation will explore the evolving applications of robotics, from its historical role in automation to its future potential in areas such as AI integration and human-robot collaboration. It will highlight the gap between industry job requirements and the skills taught in educational institutions, emphasizing the need for closer collaboration between academia and industry to ensure the development of talent that meets current and future market demands. The presentation will also outline the essential skills expected from robotics professionals, including technical competencies in programming, engineering, and data analysis, as well as soft skills such as problem-solving and communication. A proposed talent development program will be introduced, focusing on a comprehensive, hands-on approach that aligns educational frameworks with industry needs, equipping graduates with the practical experience and interdisciplinary knowledge required to thrive in the rapidly changing robotics landscape.

Zulkifli Zainal Abidin, a roboticist, earned his B.Eng in Computer and Information Engineering from IIUM in 2003 and his MSc and Ph.D in Electrical & Electronics (Robotics) from USM, Penang, in 2007 and 2013, respectively. He joined IIUM's Mechatronics Engineering Department, where he continues to serve as a faculty member. Zulkifli collaborates extensively with industries and government agencies, including CREST, Delloyd R&D, Petronas, Hydrokinetic Technologies, Altus O&G, and many more. He is the director and co-founder of the Center for Unmanned Technologies (CUTe), part of the Industry@University program by MITI/KPT. Zulkifli has secured over RM7 million in research funding and signed more than 10 Research Agreements. He holds professional statuses such as PEng (Ir.) BEM, EUR ING, Gs. IGRSM, INV. IFIA, and Ts. MBOT. He is a Chartered Engineer (C.Eng) with the Engineering Council UK (IMarEST) and an executive committee member of IEEE Ocean Engineering Society and SAE International Malaysia. Certified as an HRDF Trainer & Instructor, Zulkifli actively publishes, reviews, and serves on editorial boards for academic journals. His research focuses on developing robotic platforms for underwater, ground, and space operations, along with new sensing devices and intelligent control algorithms. Outside academia, he is a dedicated off-road adventure motorcycle trainer.

KEYNOTE SPEAKER

"Transforming AI with Decentralized and Privacy-Preserving Solutions"

Made Adi Paramartha Putra, S.T., M.T., PhD

(Primakara University, Indonesia)

The presentation introduces Federated Learning (FL) as a groundbreaking method for implementing decentralized AI. It starts by reviewing traditional machine learning (ML) and its key applications, including image recognition, recommendation systems, and anomaly detection. It also highlights the drawbacks of centralized ML systems, such as concerns over data privacy, dependence on extensive labelled datasets, and centralized data processing, which hinder scalability and security.

FL is proposed as a solution to address these limitations, offering a decentralized approach that enables model training directly on devices while safeguarding user privacy. The speaker explores FL's potential across various domains, including healthcare, smart homes, and electric vehicles. Additionally, the presentation examines optimization strategies, particularly the TSFed framework, which integrates client selection, localized optimization, and blockchain-encrypted model updates to boost efficiency and security. The concluding remarks emphasize FL's transformative role in AI and advocate for its integration into a wide range of intelligent systems.

Dr. Putra is currently a full-time lecturer in Informatics Engineering at Primakara University, Bali, Indonesia, and has served as the Director of Postgraduate Studies since 2024. Previously, he was the Head Researcher at the Networked System Laboratory, Kumoh National Institute of Technology, from 2021 to 2023. Dr. Putra has published extensively in high-impact journals such as IEEE Sensors Journal, Internet of Things Journal, and IEEE Access. His notable works include research on federated learning, blockchain-based secure systems, and data-efficient architectures for industrial IoT applications.

In addition to his academic achievements, Dr. Putra has served as a reviewer for several prestigious journals, including IEEE Access, IEEE Journal, and IEEE Transactions on Communications. His professional experience is complemented by numerous awards and accolades, such as the Best Paper Award at the KICS Fall Conference (2021) and the first prize in the Road Damage Detection Competition hosted by the Indonesian Ministry of Public Affairs (2023).

Variable Speed Drive Inverter Design On B40 Biodiesel Circulation Pump Using Solar Panels at PLTD Tanjung Aru

Idham Nuryadi
PLN Nusantara Power UP Kaltimra
PT PLN Nusantara Power
Jakarta, Indonesia
idham.nuryani@pln.co.id

Pawenary
Faculty of Electricity and Renewable Energy
PLN Institute of Technology
Jakarta, Indonesia
pawenary@itpln.ac.id

Soetjipto Soewono
Faculty of Electricity and Renewable Energy
PLN Institute of Technology
Jakarta, Indonesia
soetjipto@itpln.ac.id

***Abstract*—the use of Biofuel (BBN) and its mixture with a content of 35% is planned to be increased to a maximum of 40%. The biodiesel handling system, namely blending in tanks with the use of circulation pumps, affects the level of homogeneity of mixing. The advantage of the inverter is that it can increase efficiency by allowing the motor to be operated at the ideal speed for each load condition. The need for solar PV as a replacement for the energy supply of motor operation with a capacity of 7.5 kW for the circulation pump of the B40 biodiesel fuel storage tank, namely 12 Modules with data on Direct Normal Irradiance 3,547 kWh/m2/day. The optimal parameters of the inverter mi = 1 and fc = 5 KHz with the results of Irms pump motor performance 12.2 Ampere, Vrms 413.9 Volts, System Input Power 7.19 kWh, THDi 2.4%, Pout 6.57, kW input power and Motor Efficiency 91.40%.**

***Index Terms*—Biodiesel, inverter, Solar Panel, Variable Speed Drive**

I. Introduction

One of the government's concrete steps is the Decree of the Minister of Energy and Mineral Resources Number 1.K/EK.01/MEM. E/2023 has stipulated the use of Biofuel (BBN) and its mixture with a content of 35% in all sectors of diesel engine users and is further planned to increase the mixture content to a maximum of 40% [1]. One of the biodiesel handling systems is blending in tanks with the help of the use of circulation pumps so that it affects the level of homogeneity of mixing [1]. A circulation pump is an electric motor equipment that moves the pump so that the fluid can flow [2].

The current condition of PLTD Tanjung operations is an isolated grid system with an operating duration of 16 hours per day with a time range of 17:00 to 09:00 WITA with an output voltage of 380 Volt directly supplied to customers, so it needs other environmentally friendly alternative energy. The condition of the storage tank level at PLTD Tanjung Aru is always changing to fuel consumption, of course, operational control is needed that can adjust the B40 fuel circulation process.

979-8-3315-1921-6/24/$31.00 ©2024 IEEE

The advantage of the inverter is that it can increase efficiency by allowing the motor to be operated at the ideal speed for each load condition [3]. The modulation index (ma) and carrier frequency (fc) are two important parameters that have a significant influence on the output characteristics of the inverter, especially to control electric motors [4].

This reason is the reference that the use of solar panel energy in the inverter as a speed regulator for the pump motor is the choice for operating the blending in tank method on B40 fuel while still looking at the efficiency value and total harmonic distortion in the motor as a circulation pump driver according to IEEE standards

II. Literature Review

A. Biodiesel Fatty Acid Methyl Ester (FAME)

Biodiesel is in the form of fatty acid methyl esters made from vegetable/animal oils that meet the required quality standards. Pure biodiesel (B100) and its mixture with diesel oil (BXX) can be used as fuel for diesel generation engines. In general, the characteristics of biodiesel are that it has a higher setana number than diesel oil so that the combustion emissions produced are more environmentally friendly than diesel fuel oil [5].

The execution of this basic mixing technique is that biodiesel must be sprayed on top of the fossil diesel layer that has been loaded into the tank. This mixing method is carried out with the help of a circulation pump or called sequential in-tank blending [6].

B. Solar Power Plant

Solar power builders are plants that convert sunlight energy into electrical energy. This conversion occurs in solar panels made up of solar cells. The working principle of solar cells is based on the photovoltaic effect, which is by causing potential differences at the junction of electromagnetic radiation where electrons are transmitted because the semiconductor material

absorbs light at frequencies above the material threshold frequency. The energy of light is called a photon. Solar panels or photovoltaics are the main components in the solar PV system. Photovoltaic cells are semiconductor devices that convert light energy into electricity. Once light falls on these cells under reverse bias conditions, these cells begin to generate electricity. In the planning of solar power generated in the fulfillment of energy needs, the formula under Array Area Calculation can be calculated using the following formula [7] [8].

$$\text{PV Array Area} = \frac{EL}{G_{av} \times \eta_{PV} \times FKT \times \eta_{out}} \quad [\text{m}^2] \quad (1)$$

Where:

- EL = Electrical Energy [kWh/day]
- G_{av} = Irradiance [kWh/m^2/day]
- PV Array Area = Surface Area of solar panel [m^2]
- FKT = Temperature Correction Factor [%]
- η_{PV} = Solar Panel Efficiency [%]
- η_{out} = Output efficiency [%]

The following formula can be used to find out the amount of power generated by solar PV can be determined based on the area of the array [8].

$$P_{\text{(watt peak)}} = \text{Luas Array} \times \text{PSI} \times \eta_{PV} \quad (2)$$

Where:

- PV Array Area = Surface Area of solar panel [m^2]
- PSI = Peak Solar Insolation 1,000 W/m^2
- η_{PV} = Solar Panel Efficiency [%]
- P (Watt Peak) = Power generated [Watt peak]

In addition, the number of solar panels needed can be determined depending on the amount of power to be generated (watt peak) using the formula [9]:

$$\text{Number of solar panels} = \frac{P_{\text{(watt peak)}}}{P_{\text{Maks}}} \quad [\text{Unit}] \quad (3)$$

Where:

- $P_{\text{watt peak}}$ = Generated power [Wp]
- P_{Maks} = Power Output Maximum [Watts]

C. DC/AC Inveter Variable Speed Drive

Variable Speed drive is a device that regulates the speed of the motor according to the needs of the load by changing the frequency value of the motor [10]. The three-level NPC-MLI is shown in Figure 1. The three feet of the inverter share a common dc bus, which is divided by two capacitors into three levels. The voltage in each switching device is limited to V/2 through the clamping diode and the voltage in each capacitor is Vdc/2 [11]. The switching operation is described as follows: Status 1 means the switch ON, and 0 means the switch is OFF. Each phase has two pairs of complementary switches so turning on one of the switches requires the other switch to be turned off [12]. .

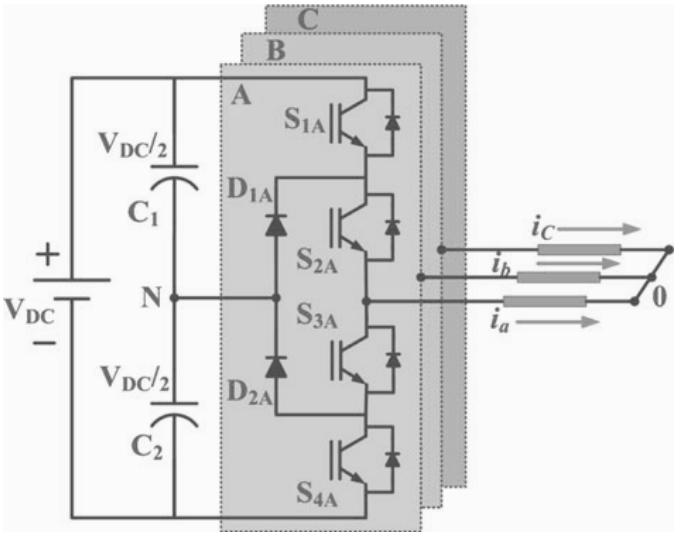

Fig. 1. Three-level Neutral point clamped topology

Pulse Width Modulation (PWM): The triangular wave will be modulated by the sinusoidal control signal by comparing the two waves, resulting in a variable ignition pulse width. The frequency of the triangular wave is the ignition frequency f_{tri} or called carrier frequency, while the sinusoidal signal is used to regulate the width of the IGBT ignition pulse and has a frequency of f_{control} or also called modulation frequency. This modulation frequency is the basic frequency of the inverter output voltage [13].

The modulation comparison (modulation index) of amplitude is defined as follows:

$$m_i = \frac{\sqrt{3} V_{\text{ref}}}{V_d} \quad (4)$$

Information:

- m_i = Amplitude modulation index
- V_{ref} = Amplitude of the control signal sinusoidal (Volts)
- V_d = Triangular signal amplitude (Volts)

$$f_{\text{tri}} = m_f \times f_{\text{control}} \quad (5)$$

Information:

- m_f = Frequency modulation index
- f_{tri} = Carrier frequency
- f_{control} = Modulation frequency

The maximum voltage between line to line (rms) generated by Space Vector Modulation (SVM) is defined as follows:

$$V_{\text{max SVM}} = \sqrt{3} \left(\frac{V_{\text{ref max}}}{\sqrt{2}} \right) = 0.7071\, V_d \quad (6)$$

D. Induction Motor

Induction motors in general that are often used are three-phase and single-phase induction motors. Three-phase induction motors are widely used in the industrial world with large capacity and are operated on three-phase systems [14]. Centrifugal pumps are pumping that work by using mechanical energy from outside the pump in the form of an electric motor which is then used to rotate the impeller. The speed of the motor according to the change in frequency is theoretically written in the following equation [15]:

$$N_r = \frac{120 \cdot f}{p} \tag{7}$$

Information:

- N_r = Motor rotation speed (rpm)
- f = Frequency (Hertz)
- p = Number of Poles

1) **Efficiency of Compressor Induction Motor**:

Efficiency is defined as the ratio between the output power and the input power. The efficiency value can be determined by the following equation [16]:

$$\eta = \frac{P_{\text{out}}}{P_{\text{in}}} \times 100\% \tag{8}$$

Where:

- η = Efficiency (%)
- P_{out} = Output power (Watts)
- P_{in} = Input power (Watts)

The values of P_{in} and P_{out} can be found through the equations below [16]:

$$P_{\text{in}} = V_L \times I_L \times \cos(\varphi) \tag{9}$$

$$P_{\text{out}} = T \times \omega \tag{10}$$

Where:

- V_L = Line Voltage (Volts)
- I_L = Line Current (Ampere)
- T = Load Torque (N-m)
- ω = Motor speed (rad/s)

III. Research Design

The concept analysis shows that the B40 fuel circulation operating system implemented at PLTD Tanjung Aru with solar heat source as energy supply and inverter for optimal operation control so that the goal of increasing the use of biodiesel (B40) in the power generation sector as an effort to reduce carbon emissions can run optimally. Based on this description, the research concept framework consists of two stages, namely:

- The modeling and simulation stage uses Simulink MATLAB software, at this stage it is carried out to determine the parameters that will be used for the modeling of an inverter equipped with a solar panel system as a support for plant operations in the work area at UP Kaltimra with PLTD Tanjung Aru as the first step in research design.
- The system testing stage is carried out by testing the performance of the VSD inverter design in generating output waves for the load of the pump electric motor with low THD values and inverter losses through the determination of the right modulation index and frequency variation.

In this study, the modeling of the SUNPOWER SPR-415E-WHT-D solar panel is shown in Fig. 2 below: .

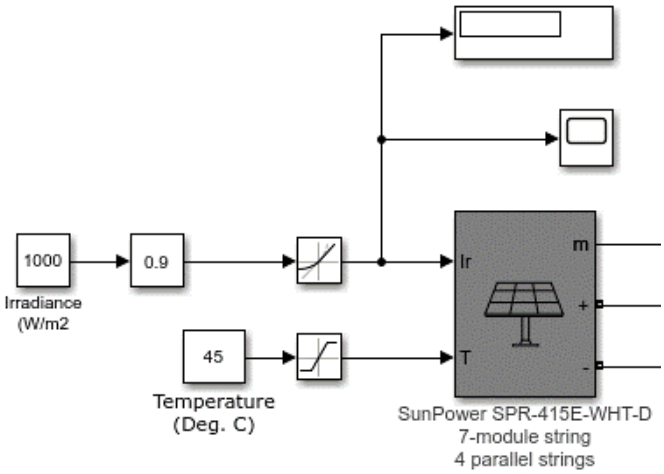

Fig. 2. PV Array Network on MATLAB Simulink

The pulse of the PWM generator is connected to each IGBT gate, in this design the generator output signal is separated by a demultiplexer bus to be separated between the phase A, phase B and Phase C inverter gate signals is shown in Fig. 3 below: .

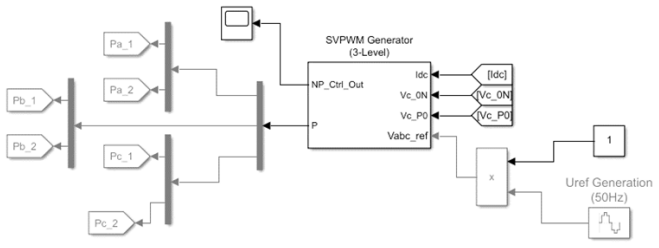

Fig. 3. PWM Modulator (3-Level) as a Gate Trigger on an Inverter

IV. Results and Analysis

A. VSD Inverter Testing in Applications at PLTD Tanjung Aru

PLTD Tanjung Aru, which is one of the plants in the UP Kaltimra work area, is planned for the application of 40% biodiesel fuel (B40). The B40 handling procedure is that it needs circulation to keep the content always homogeneous. The application of a 3-phase motor is a circulation pump to drain the fluid contained in the storage tank. The pattern of operating the circulation system is every day for 1 hour, namely from 13.00 WITA to 14.00 WITA before being transferred to the daily tank before being sprayed to the combustion chamber using an injector pump.

B. Calculation of Solar Energy Potential at PLTD Tanjung Aru

This study shows that in the Tanjung Aru PLTD area, there is potential that can be studied for the use of solar panels. The selection of solar panels aims to provide benefits in the form of electricity cost savings and greenhouse gas emission reduction. Energy potential data in the form of ambient temperature and solar radiation at peak sunlight hours are obtained directly from visual crossing data and are shown in the following table [17]:

TABLE I
Irradiation Data at PLTD Tanjung Aru Area

Location	Direct Normal Irradiation (I_{DC}) (kWh/m^2/day)	**Temperature (°C)**	**Coordinate**
PLTD Tanjung Aru	23,547	2*26,80	-02°10'26" 116°35'12"

The data presented in table I, displays potential for electrical energy production from solar panels per kilowatt peak (kWp) at the location PLTD Tanjung Aru. The data was taken as a basis for the number of array panel needs so that solar PV can always provide energy to the. In this study, the SUNPOWER SPR-415E-WHT-D solar panel model was used as follows:

TABLE II
Specifications Of Sunpower SPR-415E-WHT-D Type Solar Panel Module

Module Power	414,801	Wp
V_{MPP}	72,9	V
I_{MPP}	5,69	A
V_{pv}	22,50	%
N Out	90	%
Gav	3,547	kWh/m^2/day
Temp	26,8	°C
PSI	1000	W/m^2

$$\text{PV Array Area} = \frac{EL}{G_{av} \times \eta_{PV} \times FKT \times \eta_{\text{out}}} \quad [\text{m}^2] \quad (11)$$

$$\text{PV Array Area} = [21.07\,\text{m}^2]$$

The amount of power generated by the solar power plant can be determined based on the data of the previous array area calculation:

$$P_{(\text{watt peak})} = \text{PV Array Area} \times \text{PSI} \times \eta_{PV} \quad [\text{Wattpeak}] \quad (12)$$

$$P_{(\text{watt peak})} = 4741.5\,[\text{Wattpeak}]$$

The calculation of the number of solar panels adjusting to the large demand of power to be generated is shown below:

$$\text{Number of solar panels} = \frac{P_{\text{watt peak}}}{P_{\text{Maks}}}\,[\text{Units}] \quad (13)$$

$$= 11,4\,[\text{Units}] \rightarrow 12\,\text{Units}$$

C. Performance of VSD Inverter with DC Current Energy Source from Solar PV

The effect of VSD inverter on solar panel systems with motor load of storage tank circulation pumps can be seen from the current waves produced. The corresponding waveform is sinusoidal, the output current of the VSD Inverter with a frequency variation of 50 Hz to 35 Hz can be seen in Fig. 4 below:

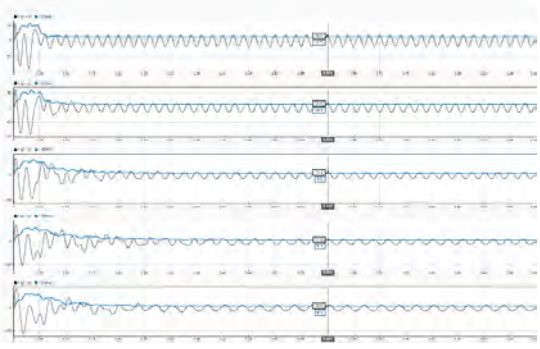

Fig. 4. Pump Motor Flow Chart Using VSD

The change in the output frequency of the VSD will affect the effective current at the output of the inverter connected to the pump motor as shown in:

$$T_n = \frac{7460\,\text{Watt}}{157.08\,\text{rad/s}} = 47.5\,\text{Nm}$$

The value of the k constant for variable load modeling is:

$$k = \frac{T_n}{\omega^2} = \frac{47.5\,\text{Nm}}{(157.08\,\text{rad/s})^2} = 1.92 \times 10^{-3}$$

TABLE III
MOTOR CURRENT VALUE DATA RELATIVE TO VSD FREQUENCY VARIATION

Frequency Output (Hz)					
Output	**50**	**45**	**40**	**35**	**30**
Current (A)	12,70	10,30	9,00	9,10	9,30
THD I (%)	2,2	2,8	3,5	4,6	3,9
Torque (Nm)	41,91	35,22	27,71	20,99	15,40
Speed (rad/s)	150,38	137,06	122,90	108,01	93,38

As shown in Table III, the current changes that occur are influenced by the operating speed of the motor, as we ll as the THD value. To view the voltage value Output Inverter VSDs with frequency variations of 50 Hz to 35 Hz can be seen in Fig. 5 below:

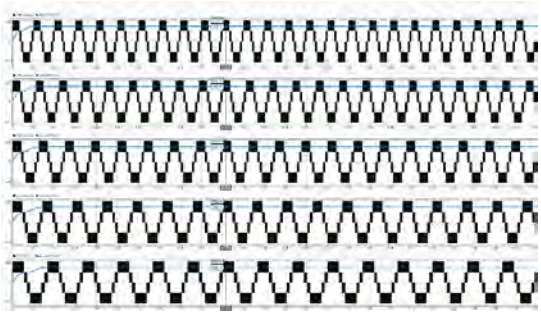

Fig. 5. Pump Motor Voltage Chart Using VSD

Frequency changes Output of VSD to voltage Inverter connected to the pump motor as shown in the following table:

TABLE IV
MOTOR VOLTAGE VALUE DATA ON VSD FREQUENCY VARIATION

Frequency Output (Hz)					
Output (Frequency (Hz))	**50**	**45**	**40**	**35**	**30**
Current (A)	12,70	10,30	9,00	9,10	9,30
THD I (%)	2,2	2,8	3,5	4,6	3,9
Torque (Nm)	41,91	35,22	27,71	20,99	15,40
Speed (rad/s)	150,38	137,06	122,90	108,01	93,38

As shown in Table IV, the change in effective voltage that occurs is not affected by the operating speed of the motor, nor is the THD value. This happens because in the simulation test, the output frequency variation of the modulation index and k values are kept constant. With these considerations, the Space Vector Pulse Width Modulation (SVPWM) type switching technique was chosen because it can make good use of all available DC voltages from Photovoltaic. In this study, data on the receipt of HSD fuel balance and the capacity of the Tanjung Aru PLTD tank level were used to determine the calculation of the tank level setpoint, the fuel receipt data is displayed in the following table:

TABLE V
TABLE OF RECEIPT AND USE OF HSD PLTD TANJUNG ARU

No	Date	Reception (Liters)	DO Number	Usage Per Day (Liters)	HSD balance (Liters)
1	06-Mar-24	10,000	8105646471	880	27,500
2	07-Mar-24			920	26,580
3	08-Mar-24			910	25,670
4	09-Mar-24			910	24,760
5	10-Mar-24			910	23,850
6	11-Mar-24			960	22,890
7	12-Mar-24			960	21,930
8	13-Mar-24			1,100	20,830
9	14-Mar-24			950	19,880
10	15-Mar-24			950	18,930
11	16-Mar-24			900	18,030
12	17-Mar-24			850	17,180
13	18-Mar-24			880	16,300
14	19-Mar-24			950	15,350
15	20-Mar-24			940	14,410
16	21-Mar-24	10,000	8105646472	940	23,180

The table above shows that the duration of fuel stock replenishment occurs with a duration of 15 days, the number of days is the duration of the time to use PV diesel energy consumption. From the table, the usage data is used as a conversion reference for the reduction of the level of the Tanjung Aru PLTD fuel storage tank, the conversion of the data is shown in the table below:

TABLE VI
TANK LEVEL CONVERSION DATA FOR *VSD* INVERTER OPERATION REFERENCE

Data	Value	Unit
Tank Maximum Capacity	22.074	Litre
Average Value of HSD Usage Per Day	950,67	Litre
Tank Height	3,060	Meter
Tank Drop Per Day	0,132	Meter
Energy Counting Duration Conversion Data		
Tank Drop Per 15 Days	1,977	Meter
Tank Level After Use	1,083	Meter
Data for Control Reference		
5 Intervals Per Setpoint	0,395	Meter

From the data of table VI, the setpoint interval is the tank level with a change value of every 0.395 meters. The operating data of the VSD solar panel inverter system adjusting the tank level is shown in the table below:

TABLE VII
Setpoint AND CONTROL LOGIC OF *VSD* INVERTER

***VSD* Input Frequency**	**Tank Level**	**Unit**	**Control Logic**	**Level Drop Duration**
30 Hz	1,48	meter	$x \leq 1.48$	3 Days
35 Hz	1,87	meter	$1.48 < x \leq 1.87$	3 Days
40 Hz	2,27	meter	$1.87 < x \leq 2.27$	3 Days
45 Hz	2,66	meter	$2.27 < x \leq 2.66$	3 Days
50 Hz	3,06	meter	$2.66 < x \leq 3.06$	3 Days

Implementation of control strategies Inverter the VSD for the circulation pump motor operation regulator is shown in the following table:

TABLE VIII
MOTOR *Output* DATA OF 3 PHASE CIRCULATION PUMP WITH *VSD* INVERTER CONTROL

Output	**Frequency Output**				
	50	**45**	**40**	**35**	**30**
Voltage (V)	413,9	414,2	413,9	413,9	414,0
THD V (%)	27,59	27,52	27,44	27,49	27,53
Current (A)	12,24	10,18	9,105	8,959	9,841
THD I (%)	2,44	2,93	3,73	3,94	3,96
Power Motor (kW)	6,986	5,083	3,716	2,633	1,768
Total Power (kW)	7,188	5,234	3,862	2,775	1,931
Motor Speed (rad/s)	151,40	137,30	123,40	109,10	93,47
Torque (Nm)	44,25	35,50	28,10	21,80	17,43
Power Out (mech)	6,699	4,874	3,468	2,378	1,629
Efficiency (%)	93,20	93,13	89,80	85,72	84,39

In the table above, variations are displayed Inverter Output for the load of the induction motor of the 3-phase circulation pump, the THD value at the frequency of 25Hz exceeds the standard limit of the IEEE519.

TABLE IX
ENERGY CONSUMPTION TO CONTROL *VSD* SOLAR PANEL INVERTER

***VSD* Input Frequency (Hz)**	**Tank Level (Meter)**	**Duration (Day)**	**Daily Electricity (kWh)**	**Total Losses (kW)**	**Total Energy (kWh)**
30	1,48	3	1,76	0,163	5,79
35	1,87	3	2,63	0,142	8,32
40	2,27	3	3,71	0,146	11,58
45	2,66	3	5,08	0,151	15,70
50	3,06	3	7,18	0,202	21,56

From table IX, it is shown that the total electrical energy requirement to operate the B40 biodiesel circulation pump motor with control Inverter VSD adjusts the tank level for 15 days requires 62.97 kWh of electrical energy. As for the control system Inverter without VSD control for 15 days, i.e. at full speed operation of 107.82 kWh. From this data, energy efficiency can be calculated with control Inverter VSD adjusted conditions by 41.6%. This data shows that the potential for operation control using VSD will be greater if Plant which is controlled is larger than the Tanjung Aru PLTD.

V. CONCLUSION

The need for solar PV as a replacement for the energy supply of motor operation with a capacity of 7.5 kW for the circulation pump of the B40 biodiesel fuel storage tank is 119 modules with a configuration of 8 series modules and 15 parallel modules. Data on March 27, 2023, at 13:00WITA-14:00WITA (Circulation Operating Hours), with an irradiance exposure of 172 W/ m2 of overcast weather conditions.

The optimal parameters to produce VSD inverter output on solar PV are a modulation index value of 1 and a carry frequency value of 5 KHz with the results of Irms pump motor performance of 12.2 Ampere, Vrms 413.9 Volts, System Input Power 7.19 kWh, Total Inverter Loss 0.20 kWh, THDi 2.4%, Pout 6.57, kW Input Power and Motor Efficiency 91.40%. VSD Inverter Performance has an output value that complies with IEEE standards for THD Maximum 5%.

REFERENCES

[1] S. Solistia Wirawan, M. Dewi Solikhah, and K. Amri, "General Guidelines for the Handling and Storage of Biofuels and Blends with a Maximum Content of 40% for Diesel Engines," 2023. [Online]. Available: www.ebtke.esdm.go.id

[2] Ubaedilah, "Analysis of the Needs of Pump Types and Specifications for Clean Water Supply in the 3-Story Canteen Building of PT Astra Daihatsu Motor," Oct. 2016.

[3] T. U. Syamsuri, H. Mukti, and R. Duanaputri, "Analysis of the Use of Variable Speed Drive (VSD) in Compressor Motors," *ELPOSYS: Jurnal Sistem Kelistrikan*, vol. 8, no. 3, 2021.

[4] H. Kubo and Y. Yamamoto, "Variable Carrier Frequency Mixed PWM Technique Based on Current Ripple Prediction for Reduced Switching Loss," 2014, p. 3370.

[5] B. Ali and A. Nugroho, "Analysis of Fuel Usage of High-Speed Diesel and Biodiesel (B30) on Fuel Consumption and Exhaust Emissions of Diesel Engines PLTD 1.4 MW," 2017.

[6] I. Tasić, R. Mićić, M. Tomić, A. Aleksić, and M. Simikić, "Storing, distribution and blending of biodiesel," 2020. [Online]. Available: http://www.cigrjournal.org

[7] B. N. Prashanth, R. Pramod, and G. B. Veeresh Kumar, "Design and Development of Hybrid Wind and Solar Energy System for Power Generation," 2018. [Online]. Available: www.sciencedirect.comwww.materialstoday.com/proceedings2214-7853

[8] T. Priyono, K. Hie Khwee, and J. Teknik Elektro, "Planning Study Of Solar Power Plant On Broiler Farm In Gang Karya Tani South Pontianak," 2015.

[9] T. Priyono, K. Hie Khwee, and Yandri, "Planning Study of Solar Power Plant on Broiler Farms in Gang Karya Tani South Pontianak," 2019.

[10] Mohsin and Abdulbaqi, *Analysis of an Irrigation Pump Driver Fed by Solar PV Panels (Part II)*. 2018.

[11] M. H. Rashid, *Power Electronics Handbook*, Third Edition. Elsevier, 2011.

[12] V. Jayakumar, B. Chokkalingam, and J. L. Munda, "Performance Analysis of Multi-Carrier PWM and Space Vector Modulation Techniques for Five-Phase Three-Level Neutral Point Clamped Inverter," *IEEE Access*, vol. 10, pp. 34883–34906, 2022, doi: 10.1109/ACCESS.2022.3162616.

[13] Muchlislah, "Simulation of Induction Motor Performance With PWM Inverter Supply," 2008.

[14] A. E. (Arthur E. Fitzgerald, C. Kingsley, and S. D. Umans, *Electric Machinery*. McGraw-Hill, 2003.
[15] M. Khusnul Munfiqoh and D. Aribowo, "Speed Control of Three-Phase Induction Motor Using Variable Frequency-Drive (VFD) to Detect Water Flow and Pressure in the Pumps Training System Module of PT. Festo Indonesia," *Jurnal Sains dan Teknologi (SAINTEK)*, vol. 1, no. 2, 2022.
[16] Angga Ghazali Rizal, "Calculation Method of Efficiency of Operating Induction Motor," 2011.
[17] Global Solar Atlas, "PV ELECTRICITY AND SOLAR RADIATION," https://globalsolaratlas.info/map (accessed Nov. 4, 2024).

Design and Development of a Voice-Assistant for the Mauritian Elderly

Yovesh Bhiwoo
Department of Mechanical and Production Engineering, Faculty of Engineering,
University of Mauritius
Réduit, Mauritius
yovesh.bhiwoo@gmail.com

Santaram Venkannah
Department of Mechanical and Production Engineering, Faculty of Engineering,
University of Mauritius
Réduit, Mauritius
sv@uom.ac.mu

Sabrina Ramsamy-Iranah
Academy of Design and Innovation
Ebene, Mauritius
director@adi.ac.mu

***Abstract*—For the last decennium, smart home systems have been integrated to provide a better living experience for the human's day-to-day activities using, smart sensors, smartphones, smart devices, and computers. Globally, interaction and communication with the existing voice assistants like Alexa®, Google Nest®, and Siri® are available only in English, German, French, Italian, Spanish, Portuguese, Japanese, and Hindi. In Mauritius, Amazon Alexa®, Google Nest®, and Siri® are available in English and French language which most people especially seniors have trouble using as they require more training to use these voice assistants. Despite all the impeccable technological advancement in the field of voice assistant, there is still a lack of age-related technology development that could cater to vulnerable people such as seniors and disabled people. Design considerations could include age-related design emphasising the section of the house where the seniors spend most of their time, which is the kitchen. Therefore, this paper presents the design and development of a voice control system named Eddy, devised to control any connected kitchen appliances using the Mauritian Creole language. The main objective of this conceptual design was to establish a voice recognition system that could be used by Mauritian seniors where executable voice commands are fed to an Arduino microcontroller and display the recent command using an LCD and voiceover feedback in Mauritian Creole language The smart system is comprised of an Arduino ATmega2560 microcontroller, TIP120 transistor, Micro SD card, I2C LCD 16x2 & 20x4, 8 Ohm speakers, 8-channel relay, EasyVR 3 voice recognition module, and Dupont wires.**

***Index Terms*—Home Automation System, IoT, Kitchen, Mauritius, Seniors, Smart Devices, Smart Technology**

I. Introduction

Technology [1] is the application of knowledge to achieve a task and a framework to comprehend and address a problem. Furthermore, it is stated that smart home technology is referred to as the integration of home-based technology [2] and services for a better living experience [3]. Commonly, smart homes are equipped with advanced automatic systems with various pre-programmed functions and tasks such as lighting [4], temperature control [5], multi-media, window and door operations [6], and many more. Furthermore, smart home has been a progressive hub for inclusive technology corporate like Amazon®, Google® and Apple®. By 2030, the global smart home market is anticipated to reach USD 537.01 Billion, with an annual growth rate of 27.07% from 2023-2030 [7]. The smart home systems in the market include smart rooms [8], energy-saving [9], security systems [10], home monitoring and controlling, and smart healthcare systems [11]. Usually, most smart home systems make use of wireless technology (WIFI and Bluetooth) as a means of communication between the controllers and the receivers. Where users can control any smart devices remotely via, smartphones, voice assistant devices, and computers [12]. Today, with the introduction of Google Home Nest® and Amazon Echo®, voice-controlled smart home systems have become the latest trend in this field [13]. These devices can be programmed to control several eligible smart devices using themselves as a home automation system [14]. These devices can be improved by the users by simply installing preferred "skills" (additional functionality developed by third-party vendors, in other settings more commonly called apps such as weather programs, maps, games, audio features, and many more) [15]. Additionally, the perk of using voice assistant devices is to decrease the use of smartphones, reduce one's walking fatigue, and control any connected smart devices via voice-over [9]. However, despite all the impeccable technological advancements in the field of voice assistant, there is still a lack of age-related technology development that could cater to vulnerable people such as seniors and disabled people. Design considerations could include age-related challenges, emphasizing a section of the house where the seniors spend most of their time, which is the kitchen, and the kitchen is known to be the most hazardous place in the house. Therefore, this paper aims to design and development of a smart kitchen voice assistant device (Eddy) which is devised to control any connected kitchen appliances using Mauritian Creole voice commands. The presented paper is organized as follows. Section II discusses the previous works related to smart home automation. Section III presents system design. Section IV provides the results and discussion of the system and section V provides the conclusion & highlights some future work.

979-8-3315-1921-6/24/$31.00 ©2024 IEEE

II. Literature Review

Azhiimah, et al. [16] reviewed papers based on voice recognition and Arduino-based work, to ascertain their commonalities and discrepancies. They found that to execute a voice command successfully, it is essential to use a voice recognition module, and the pre-eminent device to achieve this task would be the easy VR 3 commander, this device has a storage capacity of 256 recordings where 7 commands can be used simultaneously. Furthermore, Habiba, et al. [17] developed a system called a "third hand" which is an integrated system to facilitate older and disabled persons with a self-regulated system that is fully operational using voice commands and with a GPS tracking system that can determine the exact location of the concerned person while traveling alone. There are two core parts in the self-regulated system, namely the transmitter and the receiver. In this phase of the home automation system, 2 Arduino mega 2560 boards are used where one is connected to the transmitter and the other to the receiver. To allow data sharing between the transmitter and the receiver, a wireless connection is used, precisely 2 Bluetooth HC-05 modules are used in the 2 cores. To convert this system into a voice recognition system, an Easy VR voice recognition module is installed in the transmitter section. Furthermore, Dekate, et al. [18] proposed an adaptive smart system that used voice recognition software to operate, the voice recognition module in this proposed structure constantly waited for the wake word, and as soon as the wake word was heard, the system was ready to listen for the input command and compared it to the already stored information in the grammar library. Additionally, the system also provided voice history follow-ups, where it will identify the sequence of which the questions were asked and provide predictions upon future similar questions raised. Rani, et al. [19], designed a voice recognition system using human (natural) language to remove the tedious process of clicking through various application screens to control home appliances. They aimed to provide the easiest and most efficient way to interact with home appliances by simplifying voice commands in human (natural) language. Besides, Chowdhury & Sultana, [20], designed a voice recognition home base automation system that construed human voice commands (Bengali language) to control the electrical appliances wirelessly. Additionally, since the target audience was the disabled and the senior citizens of Bengali, Chowdhury & Sultana, [20] considered 6 different commands to control 3 individual home appliances that are connected to the design system. In this proposal, for safety reasons, the system will authorise only 4 people to communicate with it, where the command will be loaded via the easy VR voice recording device.

III. System Design

The main objective of this conceptual design (fig. 1) was to establish a voice recognition system (using the Mauritian Creole language) that could be used by Mauritian seniors where executable voice commands are fed to an Arduino microcontroller and display the recent command using an LCD and voiceover feedback in Mauritian Creole language (using pre-compiled of human-generated speech elements including syllables, words, and phrases). The smart system is comprised of an Arduino ATmega2560 microcontroller, TIP120 transistor, Micro SD card, I2C LCD 16x2 & 20x4, 8 Ohm speakers, 8-channel relay, EasyVR 3 voice recognition module, and Dupont wires. The 8-channel relay is used to link the non-smart appliances to the Arduino microcontroller, the EasyVR 3 voice recognition module is used to send voice commands to the Arduino, and the I2C LCD 16x2 & 20x4 are used to display the output result of each executable command given by the user, and the micro-SD card module is used to store the voiceover feedback that will be played through speakers. Additionally, the name for the smart voice assistant is Eddy, this name is chosen since it is widely known by the Mauritians. The Eddy voice assistant continuously waits for the wake word, for this instant, it is Eddy. As soon as the Eddy wake work is heard, the Eddy smart system will light blue, which will indicate that the system is active and will also display "Eddy pe acute" which means Eddy is listening, allowing enough time for the seniors to provide the second section of the command which is switching on/off of the connected devices. Upon switching on command, the Eddy smart system will light green, notifying the user that the system is waiting for a switching-on command, the system will also display "Ki up alime?" which means what to switch on in Mauritian Creole language. On the other hand, if the user gives a switch-off command, the smart system will light red, indicating to the user that the system is waiting for a switching-off command and will display "Ki up tengn?" which means what to switch off in Mauritian Creole language. Immediately when the second part of the command is heard, the voice recognition device will send the information to the microcontroller to process the information. This information will be compared to the human-generated library, and if a match is found, the associated execution will be carried out. Upon successful execution, the system will notify the current process via the LCD and voice feedback.

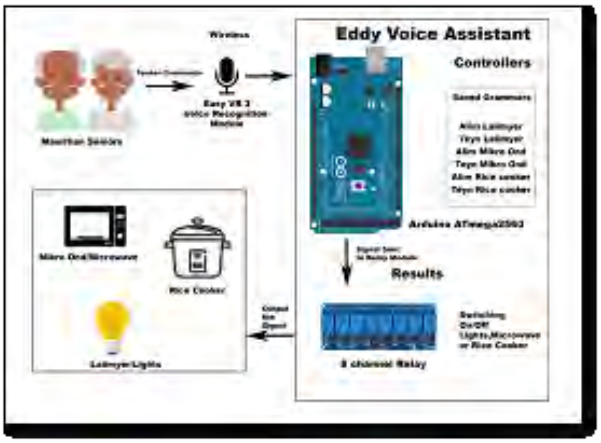

Fig. 1. The Conceptual Framework of the Voice Recognition System.

The Eddy smart system is designed to switch on/off the lights, the microwave, and the rice cooker using 6 pre-defined Mauritian grammars (the system has been trained using vr_sample_train on Arduino IDE). Table I shows the name under which the commands are saved in the Arduino library.The second column shows the command names in the Mauritian language (Mauritian Creole dictionary Carpooran, 2011) and the third column shows the English version.

TABLE I
THE VOICE COMMANDS IN MAURITIAN CREOLE AND ENGLISH LANGUAGE

Number	Command Name in Mauritian Language	Meaning
1	Alim Lalimier	Switch on the Lights
2	Tengn Lalimier	Switch off the Lights
3	Alim Mikro ond	Switch on the Microwave
4	Tengn Mikro ond	Switch off the Microwave
5	Alim Rice Cooker	Switch on the Rice-Cooker
6	Tengn Rice Cooker	Switch off the Rice-Cooker

A. Switching on/off the lights/microwave/rice cooker

As soon as the system has identified the switching on command of a connected appliance, the Arduino will process the following (fig. 2); It will first notify the user that the Eddy smart system is waiting for a switching on command For example, if the user says lights, the system will send the corresponding signal to the relay, where the PIN 7 on the Arduino microcontroller is identified as lights and connected to PIN 7 on the 8-channel relay. The microcontroller will send 5 V power to the relay, creating a full circuit and eventually switching on the lights. Similarly, to switch on the other 2 devices the user will have to repeat the same procedure with different end commands.

On the other hand, if the user wants to switch off any of the connected devices, the user must provide the switching off command (fig. 3). If the system detects the switching off command, the system will light red, indicating to the user that the system is waiting for a switching off command and is currently waiting for the last part of the command. For example, if the user says lights, a 0 V signal will be sent to the relay PIN 7 to open the circuit creating an incomplete circuit. Once the lights are switched off, the system will notify the user via the LCD “lalimier finn tengn” which means the lights are switched off in Mauritian Creole language as well as providing voice-over feedback. Hereafter, the system will go back to idle mode and will wait for the next command.

```
     if(EDDY){
    if(buf[1] == 1){
      lcd.clear();
      Serial.println("ALIM"); // Switch ON
      lcd.print("Ki");  // What to
      lcd.setCursor(0,1);
      lcd.print("Pu Alime ?"); // Switch ON ?
      ALIM = true;
      TENGN = false;
      myVR.clear();
      myVR.load(uint8_t (3)); // unit8_t is Connected to Lights
      myVR.load(uint8_t (4)); // unit8_t is Connected to Microwave
      myVR.load(uint8_t (5)); // unit8_t is Connected to Rice Cooker
    }
if(ALIM){
    if(buf[1] == 3){
      digitalWrite(Lalimier, LOW);
      Serial.println("Lalimier Finn Alime"); // Lights are Switched ON
      lcd.clear();
      lcd.print("Lalimier"); // Lights
      lcd.setCursor(0,1);
      lcd.print("Finn Alime"); // Are Switched ON
      tmrpcm.setVolume(5);
      tmrpcm.play("52.wav"); // Playing Voice Over
myVR.clear();
    }
```

Fig. 2. The Codes Written in Arduino IDE to Switch on the Lights.

```
if(EDDY){
  if(buf[1] == 2){
      Serial.println("TENGN"); // Switch OFF
      lcd.clear();
      lcd.print("Ki"); // What to
      lcd.setCursor(0,1);
      lcd.print("Pu Tengn ?"); // Switch OFF ?
      TENGN = true;
      ALIM = false;
      myVR.clear();
      myVR.load(uint8_t (3)); // unit8_t is Connected to Lights
      myVR.load(uint8_t (4)); // unit8_t is Connected to Microwave
      myVR.load(uint8_t (5)); // unit8_t is Connected to Rice Cooker
    }
    if(TENGN){
      if(buf[1] == 3){
        digitalWrite(Lalimier, HIGH); // Lights
        Serial.println("Lalimier Finn Tengn"); //Lights are Switched OFF
         lcd.clear();
        lcd.print("Lalimier"); // Lights
      lcd.setCursor(0,1);
      lcd.print("Finn Tengn"); // Are Switched OFF
      tmrpcm.setVolume(5);
      tmrpcm.play("53.wav"); // Playing Voice Over
  myVR.clear();
      }
}
```

Fig. 3. The Codes Written in Arduino IDE to Switch off the Lights.

IV. RESULT AND DISCUSSION

This section of the research shows the results obtained from the different tests carried out by 10 participants 6 females and 4 males. The test was carried out, to obtain the accurateness, adeptness, and preciseness of the Arduino-based Eddy smart system and its mobile application where further refinement could be done upon the results obtained. Several tests like switching on/off the kitchen appliances via Mauritian Creole voice command assessment were carried out. All the assessments were carried out in 10 trials each to ensure that the system is effective and understandable where good communication could be established between the user and the Eddy smart system. Additionally, all the recordings were

carried out in a silent environment around 0 – 70 dB (the sound level was recorded using a sound level meter)

A. Eddy Wake Word Assessment

All the participants were called into the kitchen to test the sensitivity of the microphone and the accuracy of the recorded data added to the Eddy smart system's library from a distance of 1-5 metres from the microphone. The participants had to say "Eddy" the wake word, to grab the attention of the system, and normally if the user has successfully awoken the system, the user shall say the next part of the request for example "Alim lalimier" which means switch on the lights. Figure 4 shows, Eddy the smart system with a green light on, which means Eddy is listening as soon as the wake word is heard. Following this, the user has 30 seconds to give the second part of the command, and after that, the Eddy system will go back to sleep mode until another wake-word request is heard. This sleep mode is added in case the user, unintentionally woke the system. Additionally, the Eddy system works as such, the user will have to say the wake word, then wait for one second then say the following command either switch on or switch off, "alim" or "tengn", then the user will have to wait for another one second then the user can say which device to switch on or off. If the user says the sentence in one go, the Eddy system will be unable to achieve what the user requested. This time delay is added so that there is better communication between the user and the system by providing enough time for the users to formulate their requests.

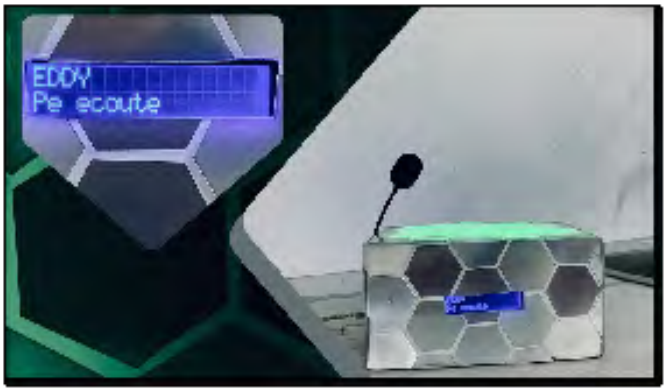

Fig. 4. Eddy Smart System in Listening Mode.

During this assessment participants were requested to wake the Eddy system in a silent environment (0-70 dB), 64% of the participants successfully woke the Eddy system from a range of 1-5 metres away from the microphone. However, 36% of the participants were unable to achieve the given assessment due to the users being unable to pronounce the wake word properly or speaking too fast as well as the difference in pitch and tone resulting in no detection by the Eddy system. Additionally, another assessment was carried out where participants were requested to wake the Eddy system in a noisy environment (70 –90 dB), only 44% of the participants were able to wake up the Eddy smart system in the noisy environment (including background noise around 77-88 dB and fan noise around 73-83 dB) while 56% of the participants failed to achieve the same. This was due to the different signals the Eddy system is receiving thus, making it difficult to decipher the wake word. During the training voice training/recording session of the Eddy session, it was carried out in a silent environment, thus, when in a noisy background, the system has difficulties hearing the wake word.

B. Switching on/off Indicator

During this assessment the participants were asked to pronounce the word "alim" which means switch on, this is the second phase of any command that the Eddy system waits for after hearing the wake word. Figure 5 shows the Eddy system detected the "alim" word. Additionally, after the system has detected the word "alim", it will light up blue indicating the "alim" word is heard. Also, it will display "ki pu alime" which means what to switch on. On average, 56% of the participants were able to successfully call the "Alim" command during their 3 given assessments while 44% failed to achieve same due to the noisy background, different pitch and loudness, making the Eddy system difficult to understand the command.

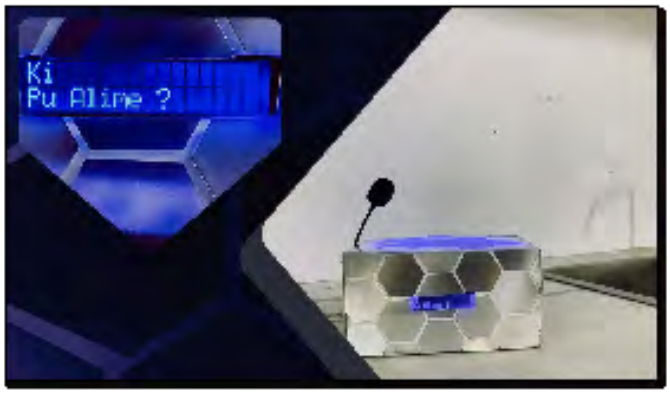

Fig. 5. Eddy System Detected the "Alim" Command.

On the other hand, after the Eddy system is awakened and the next detected word is "tengn", which means switch off a red light will be switched as an indicator to notify the user that the command "tengn" is heard and is waiting on the next command in the line (fig 6). Meanwhile, the Eddy system will display "Ki pu tengn" which means what to switch off in the Mauritian Creole language. On average 58% of the participants were able to call the given command "tengn" while 42% of the participants failed to achieve same during their 3 assessments. This was due to the system was unable to detect the command due to convolutional noise and different pitch and distance from which the user is standing from the microphone.

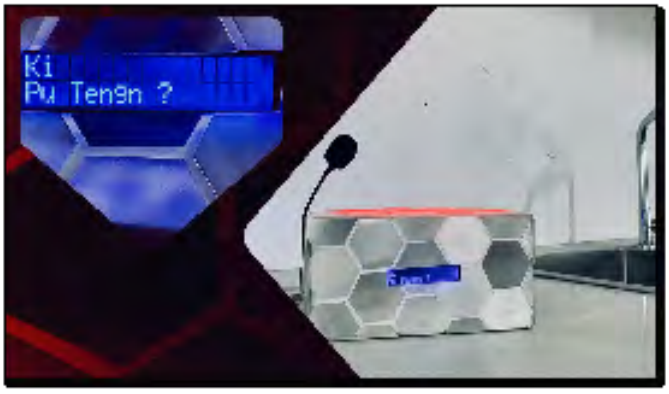

Fig. 6. Eddy System Detected the “Tengn” Command.

C. Switching on/off the lights via voice command assessment

During this assessment, the participants were requested to switch on/off the lights using the proper voice command. The assessment was carried out in three sections, where assessment 1 shows the participants at one meter away from the microphone, assessment 2 the participants were at the same distance but in a noisy background, and assessment 3 the participants were at different distances from the microphone. During assessment 1, 73 % of the participants were able to switch on/off the lights using the voice command “Eddy, Alim Lalimier” and” Eddy, Tengn Lalimier”. The low percentage success of this assessment was due to the system adapting to the user’s voice (pitch, loudness, and tone). On the other hand, 27 % of the participants (10 trials each) failed to use the commands due to the inability to wake the system using the wake word & having trouble understanding the command and talking too fast creating confusion in the Eddy system. During assessment 2, only 44% of the participants successfully switched on/off the lights using voice commands while 56% failed to achieve the same. This was due to the inability to carefully pronounce the command properly, high voice pitch creating confusion in the Eddy system, talking too fast right after waking Eddy thus, it was unable to understand the command properly, and the participants tended to create their command line that does not exist in the Eddy library, therefore, leaving the system confused after waking up. In assessment 3, participants 1 & 2 were asked to stand at two meters from the microphone, participants 3 & 4 at three meters, participants 5 & 6 at 4 four meters, participants 7 & 8 at five meters, and participants 9 & 10 at six meters. Each of them was asked to carry out the same assessment, which was to switch on/off the lights using the provided voice command. 61% of the participants successfully achieved the tasks while 39% of the participants were unable to achieve the same, this was due to participants 5,7,9 and 10 being too far away from the microphone, therefore, it was troublesome for the Eddy smart system to identify properly the voice command.

D. Switching on/off the microwave via voice command assessment

During this assessment, the participants were requested to switch on/off the microwave using the provided voice command. The assessment was executed in three sections, where assessment 1 shows the participants at one meter away from the microphone, in assessment 2 the participants were at the same distance but in a noisy background, and assessment 3 the participants were at different distances from the microphone. During assessment 1, the participants were asked to switch on/off the microwave using the following commands “Eddy, Alim Mikro Ond”, “Eddy, Tengn Mikro Ond”. Since the command was in the participant’s native language, 77% of them were able to achieve the assessment during their given trials whereas 23% of the participants failed to achieve the same, this was due to the participants being unable to pronounce the mikro-ond word properly thus, leading to error command request. During assessment 2, only 40% of the participants achieved the given commands while 60% failed to achieve the same. This was due to, the noisy interference (conversational background noise around 77-88 dB) creating confusion after waking the system, participants were using their command request, and participants number 5 and 7 were wrongly pronouncing the word “mikro-ond word”. In assessment 3, participants 1 & 2 were asked to stand at two meters from the microphone, participants 3 & 4 at three meters, participants 5 & 6 at four meters, participants 7 & 8 at five meters, and participants 9 & 10 at six meters. 67% of the participants were able to switch on/off the microwave properly using the voice command whereas 33% of the participants were unable to achieve the same due to nonlinear distortion. Participants 7,8,9 and 10 had difficulties waking the system and using the proper command line due to the distance constraint.

E. Switching on/off the rice cooker via voice command assessment

The participants were requested to switch on/off the rice cooker using the Mauritian Creole voice command. The assessment was executed in three assessments, where assessment 1 shows the participants at 1 meter away from the microphone, in assessment 2 the participants were at the same distance but in a noisy background, and assessment 3 the participants were at different distances from the microphone. During assessment 1, 86% of the participants were able to switch on/off the rice cooker properly respective to their given trials, the reason behind such great success was due to the familiarity with the wording, “Eddy, Alim Rice Cooker”, “Eddy, Tengn Rice Cooker”. Although 14% of the participants failed to achieve the same task due to convolutional noise (77-88 dB) & mispronunciation of the wake word, and participant number 4 was speaking fast, right after waking up Eddy, where there should have been 1-second intermediate leading to an unresponsive command request. The same task was carried out in a noisy background to see whether the system was able to understand

the participants in assessment 2. 43% of the participants were able to achieve the voice command requests in their respective trials and 47% of the participants were unable to achieve the same. However, since the EasyVR 3 is trained to work in a quiet environment (0 – 70 dB) and the library recorded was in a quiet space, the noisy background situation (80 - 90 dB) created confusion in the Eddy system leading to an error command request. In assessment 3 participants 1 & 2 were asked to stand at two meters from the microphone, participants 3 & 4 at three meters, participants 5 & 6 at four meters, participants 7 & 8 at five meters, and participants 9 & 10 at six meters. 65% of the participants successfully achieved the given voice commands and 35% of the participants failed to achieve the same due to nonlinear distortion. Participants number 8 and 10 had worries waking the system respective to the distance they were from the microphone.

F. The second phase of the voice command assessments

During the previous assessment sessions of the switching on/off of the connected devices using Mauritian Creole language voice commands in the particular 3 conditions (silent environment 0 – 70 dB, noisy environment 70 – 90 dB, and several distances from the microphone 2 – 6 m). The following issues were acknowledged that contributed to a low percentage of success that need to be addressed subsequently:

- Participants were speaking too fast one trial after another.
- Participants creating their voice command lines.
- Conversational noise around 77–88 dB.
- Fan noise around 73–83 dB.
- Background noise around 80–90 dB.
- Voice not detected due to distance constraint.

Therefore, the following solutions were adopted to address the above-mentioned issues:

- Re-training of the Eddy smart system while the participants speak faster than the previous recording and adding a voice-over feedback reply after each spoken word so that the participants will be aware of when to speak another part of the command.
- Practicing the given Mauritian Creole voice command using the EasyVR 3 training system.
- Recording the participants' voice command in various environment settings, including background noise ranging from 70–90 dB, so that the system can detect the voice of the participants irrespective of the level of background noise.
- Participants were requested to re-record their voice commands at several distances (1–6 m) from the microphone for the system to detect their voice regardless of the distance they stand.

Following the adjustments and re-recording sessions, the participants were requested to test the system once again with the new amended version of the voice commands. Table II shows the average success rate percentage (silent environment, noisy environment, and different distances from the microphone) obtained from each voice command provided by the Eddy smart system. The amended voice commands brought empirical changes to the results where most of the assessments reached a 100% success rate and the system's voice sensitivity was significantly enhanced. Furthermore, the voice-over feedback during each spoken word contributed immensely to the understanding of the participants to speak one word at a given time, leading to executable voice commands. The additional voice practices have also contributed to this success rate due to the participants were pronouncing each word carefully and precisely. Additionally, since each of the commands was recorded in a noisy background as well (70 -90 dB) this has led to a more comprehensive system, where the system can understand the participants irrespective of any background noise generated. Also, the recording of the participants at several distances has led to a higher success rate due to the system is now able to identify the participants' voices and the intended command

TABLE II
INITIAL AND SUBSEQUENT SUCCESS RATE PERCENTAGE OF MAURITIAN CREOLE VOICE COMMANDS

No.	Voice Command Name (Mauritian Language)	Initial Success Rate (%)	Subsequent Success Rate (%)
1	Alim Lalimier	57	100
2	Tengn Lalimier	61	100
3	Alim Mikro_ond	60	99
4	Tengn Mikro_ond	63	100
5	Alim Rice Cooker	65	100
6	Tengn Rice Cooker	65	100

Besides, to determine whether the Eddy smart system using is more adaptable to the Mauritian seniors, the ten participants were requested to perform the same tasks using English voice commands, spoken to the Amazon Alexa® and the Google Nest® voice assistants. Table III shows the success rate percentage using Amazon Alexa® and Google Nest® voice assistants. The results provided empirical evidence that the participants were more comfortable with the Mauritian Creole voice assistant setting than the English version. This shows that the Eddy system will be more convenient to use compared to Amazon Alexa® and Google Nest®. Given that the participants are more comfortable around their native language, this resulted in a better comprehension between the participants and the Eddy system.

Another assessment was carried out to test whether the Eddy system is more convenient to use compared to Amazon Alexa® and Google Nest®. this assessment was carried out to perform the same task as in the previous section, only this time it was in the French language, where the participants were requested to speak the given commands in French language.

Table IV provides empirical evidence that the participants were more comfortable with the Mauritian Creole language as the success rate for this French voice command assessment is relatively low compared to the Mauritian Creole voice command assessment. This also deduced that the participants would choose to control their kitchen appliances using Mau-

TABLE III
VOICE COMMANDS IN ENGLISH LANGUAGE USING THE AMAZON ALEXA® AND GOOGLE NEST® VOICE ASSISTANT

Voice Command Names	**Success Rate Percentage Using Alexa (%)**	**Average Success Rate Percentage Using Google Nest (%)**
Switch on the Lights	30	30
Switch off the Lights	32	31
Switch on the Microwave	35	36
Switch off the Microwave	32	35
Switch on the Rice Cooker	37	38
Switch off the Rice Cooker	35	37

ritian voice commands rather than English or French voice commands.

TABLE IV
VOICE COMMANDS IN FRENCH LANGUAGE USING THE AMAZON ALEXA® AND GOOGLE NEST® VOICE ASSISTANT

Voice Command names	Average success rate average percentage using Alexa® (%)	**Average success rate percentage using Google Nest® (%)**
Switch on the lights	38	39
Switch off the lights	35	38
Switch on the microwave	37	35
Switch off the microwave	37	37
Switch on the rice cooker	40	39
Switch off the rice cooker	39	39

V. CONCLUSION

Through the contemporary development of technology in smart devices, they can offer a broad spectrum of assistance to people specially seniors and disabled people if designed according to the user's necessities. In Mauritius, there have been no such age-related smart device developments that are engineered to work hand-in-hand with the seniors' activities of daily living. This paper has presented the design and development of a smart voice assistant (Eddy) that uses the Mauritian Creole language for communication. The Eddy system provided the control of any connected kitchen appliances using Mauritian Creole voice commands. In addition, the Eddy smart system was tested by 10 participants whereby, results have shown its level of adaptation, effectiveness & practicability of the system. Furthermore, to validate the system's operability, it was tested against the existing voice assistants Amazon Alexa® and Google Nest®. Where the tests comprised of the switching on/off of connected devices using English and French language. Conclusively, the success rate was low compared to the success rate of the Eddy system thus, showing that the Mauritian seniors are more comfortable around a device that comprehends the Mauritian Creole language. However, the Eddy system has room for improvement and if enhanced, it can help the seniors immeasurably during their time in the kitchen. The Eddy system provided only display feedback for each spoken/detected word, to ensure that the seniors are well aware of the recent command detection, sound feedback could be added. In this manner, even if the user is far away from Eddy, the user will still be apprised of the recent voice command detection. Another improvement of the system, it could also provide the switch on/off the devices using a mobile application, where users could use their smartphones or tablets to switch on/off the connected appliance remotely, providing more possibilities for seniors to control their devices.

REFERENCES

[1] S. J. Czaja, W. R. Boot, N. Charness and W. A. Rogers, Designing for Older Adults, 3rd ed., Boca Raton London New York : CRC Taylor & Francis, 2019.

[2] A. Raza, M. H. Baloch, S. Hussain, M. Z. Malik, I. Ali, S. A. Ali, D. Kumar and A. Ali, "A Home Automation Through Android Mobile App By Using Arduino UNO," in 23rd International Multitopic Conference (INMIC), Bahawalpur, Pakistan, 2020.

[3] A. Van Berlo, "Smart home technology," Have older people paved the way? Gerontechnology, pp. 77-87, 2002.

[4] D. Ioannidi, A. Stavridakis, M. Antona and C. Stephanidis, "Improving Stress Management and Sleep Hygiene in Intelligent Homes," Sensors, vol. 21, no. 2398, pp. 1-37, 2021.

[5] Z. Yang, "A Framework for Evaluating the Safety of Health Monitoring Systems in the Home Environment," IEEE Access, vol. 12, pp. 1146-1162, 2024.

[6] Y.-H. Lin, H.-S. Tang, T.-Y. Shen And C.-H. Hsia, "A Smart Home Energy Management System Utilizing Neurocomputing-Based Time-Series Load Modeling and Forecasting Facilitated by Energy Decomposition for Smart Home Automation," IEEE Access, vol. 10, pp. 116747-116765, 2022.

[7] G. Shinde, "Global Smart Home Market Size, Share, Trend and Forecast 2021-2030," Spherical Insights LLP, Pune, India, 2024.

[8] M. Ghafurian, K. Wang, I. Dhode, M. Kapoor, P. P. Morita And K. Dautenhahn, "Smart Home Devices for Supporting Older Adults: A Systematic Review," IEEE Access , vol. 11, pp. 47137-47158, 2023.

[9] S. Baker and W. Xiang, "Artificial Intelligence of Things for Smarter Healthcare: A Survey of Advancements, Challenges, and Opportunities," IEEE Communications Surveys & Tutorials, vol. 25, no. 2, pp. 1261-1293, 2023.

[10] A. Ghorayeb, R. Comber and R. Gooberman-Hill, "Older Adults' Perspectives of Smart Home Technology: Are We Developing the Technology That Older People Want?," Internation Journal of Human-Computer Studies, pp. 1-21, 2020.

[11] P.Mtshali and F.Khubisa,"A Smart Home Appliance Control System for Physically Disabled People," in 2019 Conference on Information Communications Technology and Society (ICTAS), Durban, South Africa, 2019, IEEE, pp.1-5.

[12] M. R. Lima, T. Su, M. Jouaiti, M. Wairagkar, P. Malhotra, E. Soreq, P. Barnaghi and R. Vaidyanathan, "Discovering Behavioral Patterns Using Conversational Technology for In-Home Health and Well-Being Monitoring," IEEE Internet of Things Journal, vol. 10, no. 21, pp. 18537-18552, 2023.

[13] N. Sarwar, I. S. Bajwa, M. Z. Hussain, M. Ibrahim And K. Saleem, "IoT Network Anomaly Detection in Smart Homes Using Machine Learning," IEEE Access, vol. 11, pp. 119462-119480, 2023.

[14] J. Aldahmashi and X. MA, "Real-Time Energy Management in Smart Homes Through Deep Reinforcement Learning," IEEEAccess, vol. 12, pp. 43155-43172, 2024.

[15] C. Dongarsane, C. Salim, D. M. Rajendra and K. A. Dilip, "Ubiquitous Home Control And Monitoring System Using Internet Of Things," International Research Journal of Engineering and Technology, vol. 3, no. 2, pp. 1091-1096, 2016.

[16] A. N. Azhiimah, K. Khotimah, M. S. Sumbawati and A. B. Santosa, "Automatic Control Based on Voice Commands and Arduino," in International Joint Conference on Science and Engineering (IJCSE 2020), Indonesia, 2020.

[17] U. Habiba, G. K. Dey, F. Ahmed and K. T. Ahmmed, "3rd Hand: A Device to Support Elderly and Disabled Person," in 2nd International Conference on Electrical Information and Communication Technology (EICT), Bangladesh, 2015.

[18] A. Dekate, C. Kulkarni and R. Killedar, ”Study of Voice Controlled Personal Assistant Device,” International Journal of Computer Trends and Technology (IJCTT), vol. 42, no. 1, pp. 42-46, 2016.
[19] P. J. Rani, J. Bakthakumar, K. Praveen , K. Praveen and S. Kumar, ”Voice Controlled Home Automation System Using Natural Language Processing (Nlp) And Internet Of Things (Iot),” India, 2017.
[20] M. A. H. Chowdhury and J. Sultana, ”Bangla Voice Recognition Based Home Automation for Elderly and Disabled Patient,” International Research Journal of Engineering and Technology (IRJET), vol. 5, no. 9, pp. 559-564, 2018.

The Effect of Data Balancing on Performance of Support Vector Machine and Random Forest Classification for Typhonium Flagelliforme Lodd Dataset

Iwan Binanto
Informatics, Sanata Dharma University
Yogyakarta, Indonesia
iwan@usd.ac.id

Bernadetha Mega Devina Ayuningtyas
Informatics, Sanata Dharma University
Yogyakarta, Indonesia
detha00mega@gmail.com

Nesti Fronika Sianipar
Biotechnology Departement,
Faculty of Engineering, Bina Nusantara University
Research Center Food Biotechnology,
Bina Nusantara University,
Jakarta, Indonesia
nsianipar@binus.edu

***Abstract*—This study investigates the effects of data balancing on Support Vector Machine and Random Forest classification. Unbalanced Typhonium Flagelliforme Lodd plant data were used in this study which balanced by SMOTE, then classifying with Random Forest and Support Vector Machine by sigmoid and RBF kernels on both imbalanced and balanced data. Support Vector Machine struggled to identify the minority class in both scenarios with precision, recall, and F1-score were poor, but accuracy was good. On balanced data, however, Random Forest performed somewhat worse in terms of performance indicators, but still did a great job of identifying the minority class. Meanwhile it had little effect on Support Vector Machine. We conclude that Random Forest performs better when classifying unbalanced data, particularly when identifying minority class despite concerns about overfitting. Meanwhile, Support Vector Machines is not suitable for classification on this dataset.**

***Index Terms*—Imbalanced Data, Support Vector Machine, Random Forest, SMOTE, Typhonium Flagelliforme Lodd plant data**

I. Introduction

Imbalanced data is a significant challenge in machine learning, affecting classification training and potentially leading to biased results towards the majority class [1], [2]. *Typhonium Flagelliforme Lodd* plant data is imbalanced data that has been extensively researched by [3], [4], [5], [6]. Figure 1 illustrates that the majority class has 663228 data points, whilst the minority class has just 9830 data points.

Support Vector Machines (SVM) and Random Forest (RF) are widely used classification algorithms for dealing with imbalanced data, focusing on finding the optimal separating hyperplane and do classifications or predictions [7], although they usually struggled with imbalanced data. Additionally, the SMOTE is a widely used method that generates syntethic data points to balance the dataset, improving model performance on minority classes.

979-8-3315-1921-6/24/$31.00 ©2024 IEEE

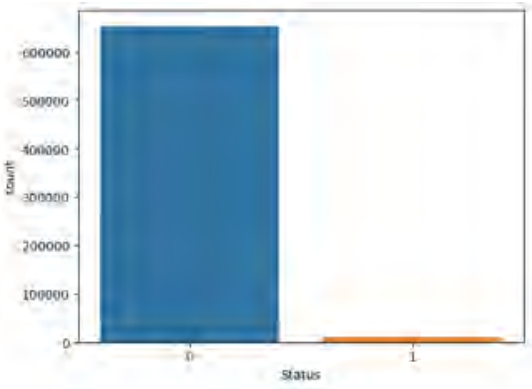

Fig. 1. The Typhonium Flagelliforme Lodd imbalanced dataset.

SMOTE approach is frequently used to deal with imbalanced data in order to have balanced data so that the classification results would be better [8], [9], [10].

II. Literatur Review

Support Vector Machine is a powerful classification algorithm for handling high-dimensional, non-linear data, offering advantages like large feature handling, non-linear decision boundaries, and preventing overfitting [7]. However it has disadvantages, like long computational time and performance can be influenced by parameter settings [11].

Random Forest is an ensemble algorithm that uses decision trees to enhance classification accuracy, efficiently handling large datasets with features, and preventing overfitting [12]. However, it requires long computational time and is less accurate for complex text classification [11].

SMOTE is a method used to address imbalanced data by generating synthetic samples from minority classes. It reduces overfitting by increasing the number of samples in the minority class, replicates existing samples, and increases classification accuracy [13], [14], [15]. However, it may be less efficient on datasets with many features and its computing time can be influenced by the algorithm used to find nearest neighbors [13].

III. Methodology

The research method for assessing the impact of data balancing using SMOTE on Support Vector Machine and Random Forest classification for unbalanced data is shown in Figure 2.

The first step is to load the dataset as shown in Figure 3 and then perform preprocessing by deleting the columns "NamaSenyawa" and "RumusSenyawa" as the columns are object-type. After that, the Support Vector Machine methods (RBF and sigmoid kernels) and Random Forest methods are classifying for imbalanced data, then compared to balancing data using the SMOTE method, and then classifying with the same method, and the results are compared and evaluated. The diagram of balanced data is shown in Figure 4

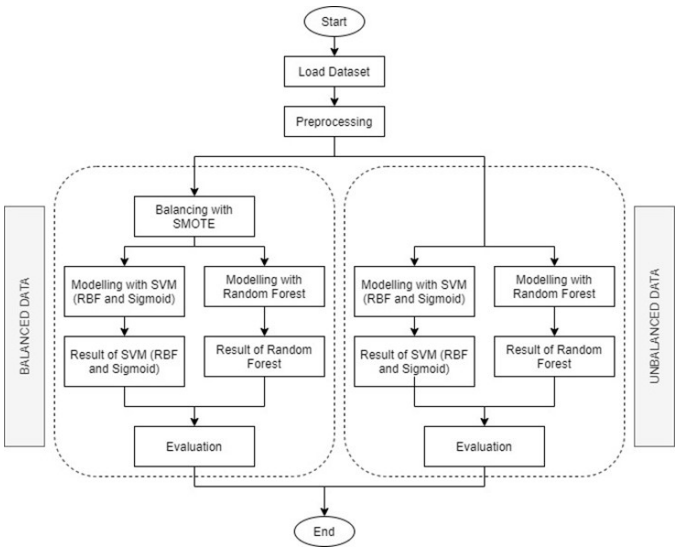

Fig. 2. Research Method

	Retention Time	Intensity	m/z	Real_m/z	NamaSenyawa	RumusSenyawa	Status
0	5.022	281952	60.057205	60.03236	Urea	CH4N2O	0
1	5.022	198032	60.246964	60.03236	Urea	CH4N2O	0
2	5.022	43064	66.886519	67.04220	Pyrrol	C4H5N	0
3	5.022	63172	67.268036	67.04220	Pyrrol	C4H5N	0
4	5.022	57852	68.280075	68.03745	Imidazole	C3H4N2	0
...	...	...	...	...	...	...	...
663223	2401.000	456	1188.677734	1188.42798	Man2Xyl/ManGlcNAcFucGlcNAc	C45H76N2O34	0
663224	2401.000	191	1191.460938	1191.38086	Foetoside C	C58H94O25	0
663225	2401.000	191	1193.358398	1193.40686	Man6GlcNAc-I	C44H75NO36	0
663226	2401.000	191	1195.192871	1195.35303	Furostane base -2H + O-Hex, O-Hex-dHex-dHex-dHex	C57H94O26	0
663227	2401.000	419	1196.572266	1196.35303	Furostane base -2H + O-Hex, O-Hex-dHex-dHex-dHex	C57H94O26	0

663228 rows × 7 columns

Fig. 3. The Typhonium Flagelliforme Lodd complete dataset [16], [17]

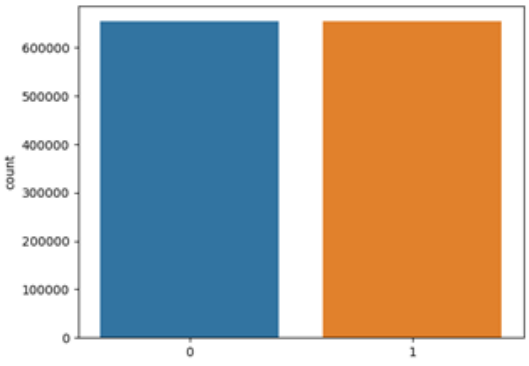

Fig. 4. The Typhonium Flagelliforme Lodd balanced dataset by SMOTE

In Figure 4 default parameters are used for both Support Vector Machine and Random Forest. It is for evaluating the default parameters too, is it good enough or not in this case.

IV. Results and Discussions

Support Vector Machine (SVM) with Sigmoid and RBF kernels perform poorly in identifying minority classes on imbalanced and balanced data. High accuracy doesn't always translate to good model performance, as Precision, Recall, and F1-Score are very low especially on RBF kernel.

TABLE I
Result Of Classification Of Support Vector Machine and Random Forest

	Imbalanced Data			Balanced Data		
	SVM		RF	SVM		RF
	RBF	Sigmoid		RBF	Sigmoid	
Accuracy	0.985	0.970	0.993	0.985	0.970	0.992
Precision	0.0	0.013	0.926	0.0	0.013	0.901
Recall	0.0	0.013	0.607	0.0	0.013	0.580
F1-Score	0.0	0.013	0.733	0.0	0.013	0.706
Time (minutes)	8.456	49.817	3.8958	9.605	49.796	4.888

Support Vector Machine performed poorly or failed in identifying the minority class, achieving high accuracy but very low precision, recall, and F1-score. Random Forest excelled at identifying the minority class, even with a slight decrease in performance metrics on balanced data.

Random Forest (RF), on the other hand, is superior in identifying minority classes, despite a slight decline in Precision, Recall, and F1-Score on balanced data. Random Forest does not perform better when the dataset is balanced using SMOTE. Its accuracy, precision, and recall are lower compared to the imbalanced data. This provides evidence that balancing data using SMOTE in this case is not suitable for Random Forest, let alone Support Vector Machine.

V. Conclusions

The study examined the impact of SMOTE data balancing on the performance of Support Vector Machine and Random Forest for imbalanced data classification. It used imbalanced Typhonium Flagelliforme Lodd plant data. Data balancing

using SMOTE significantly improved Random Forest's computational efficiency, but had minimal impact on Support Vector Machine's effectiveness. In conclusions, Random Forest is a more suitable classification algorithm for imbalanced data, especially when identifying the minority class although there are concerns about overfitting. The characteristics of the Typhonium Flagelliforme Lodd data is not suitable for classification using Support Vector Machine especially Sigmoid kernel, because both imbalanced and balanced data yield poor results, including long execution times.

Since Support Vector Machine and Random Forest perform differently with SMOTE, it would be useful to explore other balancing techniques or further tuning of these models.

ACKNOWLEDGMENT

Thank you to Dr. Nesti Fronika Sianipar, S.P., M.Si. for providing the raw data of Typhonium Flagelliforme Lodd to use in this research

REFERENCES

[1] P. Vuttipittayamongkol, E. Elyan, and A. Petrovski, "On the class overlap problem in imbalanced data classification," *Knowledge-Based Systems,* vol. 212, p. 106631, Jan. 2021, doi: 10.1016/j.knosys.2020.106631.

[2] D. Dablain, B. Krawczyk, and N. V. Chawla, "DeepSMOTE: Fusing Deep Learning and SMOTE for Imbalanced Data," *IEEE Trans. Neural Netw. Learning Syst.,* vol. 34, no. 9, pp. 6390–6404, Sep. 2023, doi: 10.1109/TNNLS.2021.3136503.

[3] G. A. Batan, M. J. Keytimu, F. L. Katumbo, I. Binanto, and N. F. Sianipar, "Penerapan Metode Random Forest, Gaussian NB, Dan KNN Terhadap Data Unbalance dan Data Balance Menggunakan Random Over Sampling Untuk Klasifikasi Senyawa Keladi Tikus".

[4] I. Binanto, N. F. Sianipar, F. Dea, M. N. Primadani, and T. W. Kartikasari, "Klasifikasi Senyawa Keladi Tikus Menggunakan Algoritma KNN, Gaussian Naïve Bayes dengan Menerapkan Imbalance Data Borderline SMOTE," *SNST*, vol. 13, no. 1, p. 377, Nov. 2023, doi: 10.36499/psnst.v13i1.9005.

[5] E. Tangkelobo, W. Mayaut, H. Listanto, I. Binanto, and N. F. Sianipar, "Perbandingan Algoritma Klasifikasi Random Forest, Gaussian Naive Bayes, dan K-Nearest untuk Data Tidak Seimbang dan Data yang diseimbangkan dengan metode Random Undersampling pada dataset LCMS Tanaman Keladi Tikus".

[6] A. P. Monika, F. E. P. Risti, I. Binanto, and N. F. Sianipar, "Perbandingan Algoritma Klasifikasi Random Forest, Gaussian Naive Bayes, dan KNearest Neighbor untuk Data Tidak Seimbang dan Data yang diseimbangkan dengan Metode Adaptive Synthetic pada Dataset LCMS Tanaman Keladi Tikus".

[7] Z. Rustam, E. Sudarsono, and D. Sarwinda, "Random-Forest (RF) and Support Vector Machine (Support Vector Machine) Implementation for Analysis of Gene Expression Data in Chronic Kidney Disease (CKD)," *IOP Conf. Ser.: Mater*. Sci. Eng., vol. 546, no. 5, p. 052066, Jun. 2019, doi: 10.1088/1757-899X/546/5/052066.

[8] L. Qadrini, "Handling Unbalanced Data With Smote Adaboost," Mantik, vol. 6, no. 36, pp. 2332-2336, August 2022, doi: 10.35335/mantik.v6i2.2597.

[9] A. Anggrawan, H. Hairani, and C. Satria, "Improving Support Vector Machine Classification Performance on Unbalanced Student Graduation Time Data Using SMOTE," *IJIET*, vol. 13, no. 2, pp. 289–295, 2023, doi: 10.18178/ijiet.2023.13.2.1806.

[10] B. Prasetiyo, Alamsyah, M. A. Muslim, and N. Baroroh, "Evaluation performance recall and F2 score of credit card fraud detection unbalanced dataset using SMOTE oversampling technique," *J. Phys.: Conf. Ser*., vol. 1918, no. 4, p. 042002, Jun. 2021, doi: 10.1088/1742-6596/1918/4/042002.

[11] L. Arnroth and J. Fiddler Dennis, 'Supervised Learning Techniques: A comparison of the Random Forest and the Support Vector Machine', Dissertation, 2016.L. Arnroth and J. Fiddler Dennis, 'Supervised Learning Techniques: A comparison of the Random Forest and the Support Vector Machine', Dissertation, 2016.

[12] D. Ramayanti, "Comparison of Random Forest and Support Vector Machine for Indonesian Tweet Complaint Classification," *IJSRCSEIT*, pp. 202–207, Dec. 2019, doi: 10.32628/CSEIT195628

[13] S. Sreejith, H. Khanna Nehemiah, and A. Kannan, "Clinical data classification using an enhanced SMOTE and chaotic evolutionary feature selection," *Computers in Biology and Medicine*, vol. 126, p. 103991, Nov. 2020, doi: 10.1016/j.compbiomed.2020.103991.

[14] M. Zhang and J. Yang, "SMOTE algorithm applying imbalanced data in higher education," in *Proceedings of the 2nd Information Technology and Mechatronics Engineering Conference (ITOEC 2016TOEC 2016)*, Chongqing, China: Atlantis Press, 2016. doi: 10.2991/itoec-16.2016.33.

[15] R. K. Tripathi, L. Raja, A. Kumar, P. Dadheech, A. Kumar, and M. N. Nachappa, "A Cluster Based Classification for Imbalanced Data Using SMOTE," *IOP Conf. Ser.: Mater. Sci. Eng.*, vol. 1099, no. 1, p. 012080, Mar. 2021, doi: 10.1088/1757-899X/1099/1/012080.

[16] Binanto, I., Warnars, H. L. H. S., Sianipar, N. F., & Budiharto, W. Anticancer Compound Identification Model of Rodent Tuber's Liquid Chromatography-Mass Spectrometry Data. *ICIC Express Letters, 16*(1), pp. 9–16, January 2022, https://doi.org/10.24507/icicel.16.01.9

[17] Binanto, I., Warnars, H. L. H. S., Sianipar, N. F., & Budiharto, W. Webscraping Data Labeling System on Liquid Chromatography-Mass Spectrometry of Rodent Tuber for Efficiency of Supervised Learning Preprocessing. *ICIC Express Letters, Part B: Applications, 13*(1), pp. 107–114, January 2022, https://doi.org/10.24507/icicelb.13.01.107.

Exploring the Ethical Landscape: Safeguarding Data Privacy in the Realm of Virtual Reality

Leandro Satyawira Tionanda
Computer Science Department, School of Computer Science
Bina Nusantara University
Jakarta, Indonesia
leandro.tionanda@binus.ac.id

Bun Jak Sin
Computer Science Department, School of Computer Science
Bina Nusantara University
Jakarta, Indonesia
bun.sin@binus.ac.id

Said Achmad
Computer Science Department, School of Computer Science
Bina Nusantara University
Jakarta, Indonesia
said.achmad@binus.edu

Rhio Sutoyo
Computer Science Department, School of Computer Science
Bina Nusantara University
Jakarta, Indonesia
rsutoyo@binus.edu

***Abstract*—As VR becomes more immersive and widespread, the fact that it collects vast amounts of personal and sensitive data from users, have raised concerns about how this information is managed and protected. This paper delves into the complex landscape of VR, focusing on the collection, management, and protection of user data. Through a systematic literature review using the PRISMA framework filtered by inclusion and exclusion criteria which are based on our research questions, this research identifies key privacy concerns, evaluates current security measures, and examines the ethical implications of VR usage. Our findings reveal several critical issues: the potential for misuse of personal data, insufficient transparency in data handling practices, and the lack of robust security protocols to safeguard user information. We also explore the ethical dimensions of VR, such as the potential for manipulation of user behavior and the responsibilities of VR companies to protect user welfare. To address these challenges, we recommend the development of comprehensive privacy policies, implementation of more advanced security measures, and establishment of clear ethical guidelines. Additionally, it is essential for VR companies to prioritize privacy and ethic in their products. By prioritizing these aspects, VR industry can create a safer and more trustworthy virtual environment for users which would in turn ensure a secure and ethical future for this technology. This paper aims to provide insights and practical recommendations for policymakers, developers, and researchers, encouraging a collaborative effort to enhance data privacy and ethical standards in the rapidly evolving field of Virtual Reality.**

Keywords— Virtual Reality, Data Privacy, Ethical Considerations, Data Security

I. Introduction

VR (Virtual Reality) technology offers immersive experiences through visual, haptic, and auditory stimulation, aiming to transport users into virtual worlds. Although VR headsets have been around since the 1960s, these technologies are becoming more prevalent across several industries, including education, gaming, and healthcare [1]. The VR market has rapidly grown, with revenue expected to reach 100 billion dollars in the next five years [2].

The utilization of Virtual Reality (VR) has experienced a consistent rise in popularity, especially in recent times. One noteworthy application of VR involves combining its educational and gaming potential, resulting in educational games proven to maintain or even improve student's academic performance [3]. According to Oberlo's data, there has been an increase in the percentage of US consumers engaging with VR, rising from 16% in 2019 to 19% in 2020. Projections suggest a sustained growth trajectory, with the VR market anticipated to witness an annual compound growth rate of 18% by 2028, as outlined by Grand View Research. Additionally, Valuates Reports predicts a substantial expansion in the global VR market, estimating its size to soar to US$ 26860 million by 2027, a significant jump from the US$ 7719.6 million recorded in 2020 [2].

However, the existence of VR systems is a double-edged sword. While they can bring value to certain industries and aspects of human life, they can also collect sensitive data such as facial movements and infrared images, raising privacy concerns [4] [5]. By its very nature, Virtual Reality (VR) technology can gather extensive non-verbal data, including user movements, biometric information, and usage patterns. Online data collection of consumer behavior has occurred for more than two decades, and it is highly likely to continue and expand in virtual and augmented reality advertising [6].

VR devices are outfitted with various sensors that capture both explicit user input and non-verbal cues, which are then utilized by the VR engine to construct the virtual environment in response to user actions. Non-verbal data is particularly revealing and can serve various purposes, from personalized advertising to assessing user performance levels. However, the lack of transparency regarding data management and machine

979-8-3315-1921-6/24/$31.00 ©2024 IEEE

learning algorithms, coupled with prolonged personal usage, may enable companies to deduce user preferences and predict their behavioral patterns [4] [2].

Additionally, VR introduces the possibility of virtual crimes, which previous research has shown to evoke strong emotional reactions akin to real-world crimes. Given the consistent and significant expansion of VR technology and its widespread integration, it is crucial to scrutinize any potential privacy and security implications that may arise from its use [2] [5].

Ignorance of these emerging security risks would greatly dampen users' enthusiasm for using VR apps and purchasing VR devices as well as VR services [7]. Privacy and autonomy concerns can arise from various factors. Privacy faces various threats, including informational privacy, physical privacy, and associational privacy, each further subdivided. Conversely, autonomy contends with threats to freedom, knowledge, and authenticity. [8]. Furthermore, safeguarding our personal information from virtual reality (VR), which continuously collects biometric data such as eye and facial features, presents additional challenges [4].

This research will thoroughly examine how VR data collection threatens user anonymity, such as our identity and private data. This research will use a detailed method called Systematic Literature Review (SLR) alongside the Preferred Reporting Items for Systematic Reviews and Meta-Analyses (PRISMA) framework to make sure this research covers all the existing research transparently. This research will also look into ways to keep our data safe and discuss the ethical implications of VR data use. This research aims to discover how VR companies manage our personal info. Ultimately, this research aims to help consumers understand how their privacy and security are handled in VR.

II. Related Works

Previous research has explored basic ideas important to our study. For example, research exploring the uses of VR to raise privacy awareness of the users [3]. Despite its benefits, VR presents significant risks, particularly concerning privacy, which can be categorized into data collection, physical harm, and manipulation of immersive experiences. This is because VR Systems collects extensive and various data from its users, even when it supposedly has been turned off. The data collected includes haptic, audio, camera inputs, and sensitive data, including facial movements and infrared images. It can also collect data about user's behavior and preferences. This raises significant concerns about the potential misuse of the data collected. [4] [6].

A. Privacy Policies

Although privacy policies that were supposed to be the "contract" for user to agree to data collection exists, it have been proved to be nothing but a sham for some companies [7].In a research done by Guo et al. in 2024, they found that out of 224 apps, 56 of them contain contradictory statements in their privacy policies, and only 38 of them fully complied with GDPR (General Data Protection Regulation) [7].

Although privacy policies are intended to safeguard user data, inconsistencies and non-compliance with regulations remain very concerning. This issue brings privacy and security concerns, which include informational privacy (protection against third-party access to personal data), physical privacy (protection against sensory access to user's body and actions), and associational privacy (protection against access to data about user's social interactions) [8].

B. Authenticity Problem & How To Address It

VR also introduces the challenge of verifying user authenticity, ensuring that the individual logged into the VR system is the rightful user. Failure to establish such authenticity can lead to issues like identity theft and defamation. Currently, the security measures surrounding user authenticity in VR are largely inadequate, making it relatively easy for hackers to gain unauthorized access to a user's VR account and impersonate them. This could result in the misuse of the user's account to carry out malicious activities aimed at damaging their reputation [2] [8].

This issue can be addressed through the implementation of more advanced authentication methods. Companies commonly utilize techniques such as token-based, knowledge-based, and biometric authentication. However, relying solely on these methods may not provide sufficient security. Token-based authentication, for instance, can be vulnerable if a hacker gains access to the user's email, which is often relatively straightforward. While knowledge-based and biometric authentication offers more robust security measures, they still have their limitations [1].

Because of this, more advanced authentication methods such as Oculock (an authentication method that uses the eyeball, eyelids, nerves around the eye, extraocular muscles, cells, etc. This method have a 3.55% and 4.97% error rate) and RubikAuth (an authentication method that uses a 9-digit pin overlay on a multicolored cube for input. Tests showed a 98.52% failure rate for attacks, proving its effectiveness against real-world threats) would be a better method for VR companies to use so they can ensure user's authenticity [9].

C. Challenges in VR: Autonomy, Anonymity, & Crime

Autonomy in VR faces threats from filter bubbles, gatekeeping, addiction, manipulative game/apps, and governmental regulations, potentially limiting users' freedom of speech and autonomy [2] [8]. Anonymity concerns also arise because VR motion data can uniquely identify users without explicit actions. Additionally, an adversary can reconstruct text typed by another user by observing their avatar movements, further eroding user anonymity [10]. A study has proven that this can be done with an accuracy of 87.5% [2].

Another important concern is the rise of new crimes in VR. As technology progresses, VR opens up opportunities for illegal activities. This means that rules and regulations for VR need to stay updated and firm. This is because even existing crimes like bullying can happen more easily through VR. [2] [5].

Despite all of these issues, there are still users who aren't aware of these privacy issues or health issues that can be caused by the immersive experience of VR, such as nausea and mental health problems [11]. That's where we can utilize VR to increase their privacy awareness so they can know the issues surrounding this tech. An escape room VR game that incorporates these problems [3] [12] is a great way to increase user's privacy and security awareness. VR may have all of these negative issues, but it also positively impacts some parts of human lives.

III. Methodology

This study employed a Systematic Literature Review (SLR) approach utilizing the PRISMA Flowchart Diagram to visualize the available records or papers for referencing purposes. The diagram precisely illustrates the number of records filtered during the process and the final count of records used as reference papers. Our research focuses on various topics related to privacy, security, ethics, virtual reality, biometrics, protection, and policies.

A search boundary was established to accomplish a systematic literature review with PRISMA. The flow of PRISMA used in this study is shown in fig 1 The rules for this research include the databases, search terms, and the range of publication years. The full boundary and criteria used to decide on the papers can be seen below in table I.

Firstly, this research utilized various databases, including Google Scholar, ResearchGate, and IEEE. The search keywords encompassed topics related to privacy, security, ethics, virtual reality, biometrics, protection, and policies. From these searches, 487 journal articles were retrieved. Secondly, this research involved eliminating duplicate articles found in different databases.

Each article was manually verified to ensure full-text availability and was written in English for an international audience. As a result, the initial pool of articles was reduced to 57.

After delineating our search boundaries, the research constructed a flowchart diagram for the PRISMA methodology. The inclusion criteria for the PRISMA method were research articles written between 2015 and 2023. This was to made sure that the articles we use for our paper are up to date and still relevant.

Certain related papers gathered from the database search, such as duplicates, outdated journals, and journals without full-text availability, were filtered and excluded from this process so we can ensure compliance with copyright law and data relevance. As these criteria were made based on our research questions, they allowed us to answer our research questions with the most relevant, current data, supported by clear, evidence-based analysis.

The final step involved reading all the filtered articles to select the most suitable papers from the eligibility steps. Ultimately, this research identified 30 final papers that were used as references. These systematic reviews will assist the authors in conducting research about privacy and security in virtual reality and the ethics applied in VR.

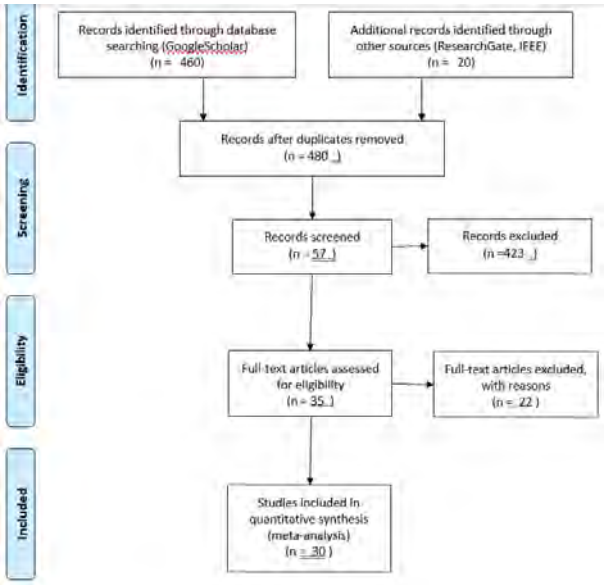

Fig. 1. PRISMA Flow

TABLE I
Inclusion and Exclusion Criteria

Criteria	
Inclusion	I1 Articles are written in English
	I2 Articles published from 2015 - 2024
	I3 Articles are related to privacy and ethic in virtual reality
	I4 Articles are related to method on how to protect virtual reality hardware
Exclusion	E1 Articles not related to virtual reality in privacy and ethic problems
	E2 Articles published before 2015
	E3 Articles with no full-text permission

IV. Results and Discussion

A. *RQ 1: How VR data collection poses a threat to user's anonymity?*

The collection and use of identity and privacy information by VR companies is a complex issue, especially when considering the potential risks to users' autonomy and privacy [4] [5] [6]. This particularly concerns children, who are the most vulnerable [13].

Parents often underestimate how much VR companies collect and infer data, leading to a false sense of security. This gap in understanding can result in children inadvertently disclosing sensitive information in immersive environments [13].

One significant area of concern is the use of eye-tracking technology. While it enhances VR experiences by analyzing visual attention and cognition, it also captures unique iris and gaze patterns through near-infrared cameras. These patterns are highly individualistic, posing a risk to users' biometric identity and privacies [4] [14] [15].

Similarly, head and hand motion data present another layer of risk. Studies have shown that users can be uniquely identified with high accuracy using just their motion data [2] [10] [16] [17]. This capability raises significant privacy concerns as tracked datasets could be exploited to violate user privacy through inferencing, physical harm, and manipulation of immersive experiences [2] [4] [18] [17]. This becomes even more alarming in scenarios where consent is not adequately obtained, as was the case with Fortnite, which faced legal consequences for such practices [18].

Moreover, the transmission of VR data over networks adds another dimension of risk. Unauthorized interception of this data could lead to severe breaches of user anonymity and identity security [2] [8] [19]. While these technologies offer highly personalized experiences, the inherent requirement for access to personal data compromises user anonymity and poses significant privacy risks [20].

In summary, while VR technologies have the potential to provide deeply personalized and immersive experiences, the associated risks to user privacy and autonomy, which are shown in table II, cannot be overlooked. It is crucial for VR companies to implement robust data protection measures and ensure transparent consent practices to safeguard users' sensitive information [2] [5].

TABLE II
THREATS POSED BY VR DATA COLLECTION

User Threat by Data Collection in Virtual Reality	Number of Papers	Study Identifier
Autonomy	3	[2] [8] [13]
Anonimity	7	[2] [8] [10] [14] [15] [19] [20]
User Profiling	6	[2] [13] [10] [16] [17] [18]

*B. **RQ 2:How do we protect VR devices that generate personal data, such as eye tracking, facial, hand, and body recognition technologies?***

VR devices generate a significant amount of personal data to enhance user experience and immersion [4] [5] [14] [15]. However, the extensive collection and transmission of this data to companies have raised substantial privacy and security concerns [4] [5] [6] [14] [15] [21]. Researches have highlighted these issues and proposed various solutions to mitigate the risks associated with VR data handling [1] [9] [20] [22] [23] [24] [25] [26] [27].

One primary recommendation is data encryption in transit and at rest. Encrypting data ensures that the information remains inaccessible to unauthorized parties even if intercepted. This approach provides a foundational level of security crucial for protecting personal information as it travels across networks [20].

An improved CSWC-SVM algorithm has been suggested to further enhance cyberattack detection. This algorithm boasts short processing times, high recognition accuracy, low false positive rates, and reliable classification accuracy under varying conditions. Implementing such sophisticated algorithms can significantly bolster the detection and prevention of cyber threats in VR environments [23].

Traditional authentication methods like PINs and passwords can be adapted into more complex forms to improve security in VR systems. For instance, RubikAuth and OcuLock offer advanced authentication by leveraging more intricate patterns and human visual system behaviors. These methods enhance security and provide a more seamless user experience [9] [22].

GaitLock, an authentication system that uses onboard IMU sensors, is another innovative solution. It detects intruders, prevents outlier attacks, and recognizes different legitimate users, thereby supporting personalized services while ensuring security. Such systems add a layer of protection by utilizing unique biometric and behavioral patterns [24].

Additionally, watermarking techniques like the Watermarking Blind Algorithm can embed biometric information invisibly into an avatar's face. This information can later be extracted and compared to ensure user authenticity [25]. Besides that, the Input Protection Method also perturbs or abstracts sensitive input information, preventing privacy breaches [26].

These proposed solutions are highlighted in table III and are a multifaceted approach for enhancing VR security and privacy. VR companies can significantly mitigate privacy risks by adopting advanced encryption, sophisticated authentication methods, and innovative detection algorithms. However, it is crucial for users to stay informed about data collection practices by carefully reading privacy policies before using VR devices [27]. Ultimately, VR companies are responsible for implementing these robust security measures as it is crucial to protect their users' data and maintain trust [2] [5].

TABLE III
METHOD TO PROTECT VIRTUAL REALITY HARDWARE

Protection of Virtual Hardware Device	Number of Papers	Study Identifier
Authentication	4	[9] [22] [24] [25]
Algorithm	3	[23] [25] [26]
Data Encryption	2	[20] [26]

*C. **RQ 3: How are ethics and privacy policies applied in Virtual Reality ?***

Ethics and privacy in Virtual Reality (VR) are very important and need careful attention to keep users safe. In social VR research, rules protect participants' well-being, get informed consent, and respect their rights. These basic principles help maintain ethical standards and protect people in virtual settings [28].

Major concerns in VR research include possible changes in thinking, emotions, and behavior due to virtual experiences. Users might see themselves and act differently because of their avatars, which can have lasting effects even after they leave the virtual world [2] [5] [29]. Using too much VR can also cause problems, like disorienting or becoming too dependent on virtual spaces [11]. These issues highlight the need for careful management and ethical oversight in VR research and use.

Privacy is a big concern in VR, especially with sharing personal data with third parties and accessing negative or mature content [4] [5] [6]. The risk of harm from too much use or exposure to inappropriate content means strong protective measures are necessary [2] [5]. Unfortunately, despite privacy policies intended to safeguard user data, many companies have proven these policies ineffective. Inconsistencies and non-compliance with regulations are common, which is very concerning [7].

In summary, the ethical considerations and privacy policies in VR research and use must be strict to protect users from various risks. That is because ethics and privacy policies in VR should be applied by focusing on protecting user well-being, ensuring informed consent, and adhering to principles that focus on respecting user's rights, as these are the main points of ethics in virtual reality, as shown in table . The goal should be to minimize harm, educate everyone involved, and safeguard personal data to create a safe and ethical VR space [30].

TABLE IV
ETHIC IN VIRTUAL REALITY

Protection of Virtual Hardware Device	Number of Papers	Study Identifier
Welfare and Consent	3	[2] [5] [7] [28]
Concern towards customers	7	[2] [5] [11] [25] [26] [28] [29]
Principles	1	[30]

V. CONCLUSIONS AND FUTURE WORKS

Exploring data privacy and ethics in Virtual Reality (VR) reveals significant challenges and opportunities. While VR offers exciting experiences, it poses serious user privacy and security risks. A systematic literature review using the PRISMA framework found that many VR companies have weak privacy policies and often fail to comply with regulations. To address these issues, robust security systems and comprehensive ethical guidelines are essential, focusing on user consent, transparency, and accountability. Future efforts should prioritize these measures to safeguard user data and ensure responsible data handling.

Building trust with users is crucial for the growth of VR technologies. VR companies must enhance their data privacy practices through regular audits, advanced encryption methods, and transparent data usage. Educating users about privacy risks is also essential, as it creates the need for user-friendly tools and resources. The VR industry can foster a safer and more trustworthy environment by increasing user awareness and promoting best practices.

Future work should focus on creating better security systems such as encrypted data transmission protocol and clear ethical guidelines to protect users. They also should look to how privacy issues in virtual reality change over time and include ideas from different fields to better understand and tackle these challenges. This is because addressing these challenges is vital for the sustainable development of VR, which would ensure a secure and ethical future for this technology. By prioritizing privacy and ethics, VR industry can grow responsibly and build a foundation for lasting user trust and widespread use across the world.

ACKNOWLEDGMENT

The CRediT author's statement as follows,
Leandro Satyawira Tionanda: Conceptualization, Formal analysis, Writing - Original Draft.
Bun Jak Sin: Conceptualization, Formal analysis, Writing - Original Draft.
Said Achmad: Methodology, Validation, Supervision, Project administration.
Rhio Sutoyo: Methodology, Validation, Supervision, Funding acquisition, Project administration.

REFERENCES

[1] N. Noah, S. Shearer, and S. Das, "Security and privacy evaluation of popular augmented and virtual reality technologies," in *Proceedings of the 2022 IEEE International Conference on Metrology for eXtended Reality, Artificial Intelligence, and Neural Engineering (IEEE MetroXRAINE 2022)*, 2022.

[2] A. Giaretta, "Security and privacy in virtual reality–a literature survey," *arXiv preprint arXiv:2205.00208*, 2022.

[3] S. N. Maragkoudaki and C. Kalloniatis, "Virtual reality as a mean for increasing privacy awareness: The escape room example," in *Proceedings of the 26th Pan-Hellenic Conference on Informatics*, 2022, pp. 261–266.

[4] D. Adams, A. Bah, C. Barwulor, N. Musaby, K. Pitkin, and E. M. Redmiles, "Ethics emerging: the story of privacy and security perceptions in virtual reality," in *Fourteenth Symposium on Usable Privacy and Security (SOUPS 2018)*, 2018, pp. 427–442.

[5] J. Jia and W. Chen, "The ethical dilemmas of virtual reality application in entertainment," in *2017 IEEE International Conference on Computational Science and Engineering (CSE) and IEEE International Conference on Embedded and Ubiquitous Computing (EUC)*, vol. 1, 2017, pp. 696–699.

[6] S. Blodgett-Ford and M. Supponen, "Data privacy legal issues in virtual and augmented reality advertising," in *Research handbook on the law of virtual and augmented reality*. Edward Elgar Publishing, 2018, pp. 471–512.

[7] H. Guo, H.-N. Dai, X. Luo, Z. Zheng, G. Xu, and F. He, "An empirical study on oculus virtual reality applications: Security and privacy perspectives," *arXiv preprint arXiv:2402.13815*, 2024.

[8] F. O'Brolcháin, T. Jacquemard, D. Monaghan, N. O'Connor, P. Novitzky, and B. Gordijn, "The convergence of virtual reality and social networks: threats to privacy and autonomy," *Science and engineering ethics*, vol. 22, pp. 1–29, 2016.

[9] K. Viswanathan and A. Yazdinejad, "Security considerations for virtual reality systems," *arXiv preprint arXiv:2201.02563*, 2022.

[10] Z. Yang, Z. Sarwar, I. Hwang, R. Bhaskar, B. Y. Zhao, and H. Zheng, "Can virtual reality protect users from keystroke inference attacks?" *arXiv preprint arXiv:2310.16191*, 2023.

[11] D. Adams, A. Bah, C. Barwulor, N. Musabay, K. Pitkin, and E. Redmiles, "Perceptions of the privacy and security of virtual reality," *iConference 2018 Proceedings*, 2018.

[12] V. Nair, G. M. Garrido, D. Song, and J. O'Brien, "Exploring the privacy risks of adversarial vr game design," *Proceedings on Privacy Enhancing Technologies*, 2023.

[13] J. Cao, A. Das, P. Emami-Naeini *et al.*, "Understanding parents' perceptions and practices toward children's security and privacy in virtual reality," *arXiv preprint arXiv:2403.06172*, 2024.

[14] B. John, S. Jörg, S. Koppal, and E. Jain, "The security-utility trade-off for iris authentication and eye animation for social virtual avatars," *IEEE transactions on visualization and computer graphics*, vol. 26, no. 5, pp. 1880–1890, 2020.

[15] E. Bozkir, S. Özdel, M. Wang, B. David-John, H. Gao, K. Butler, E. Jain, and E. Kasneci, "Eye-tracked virtual reality: A comprehensive survey on methods and privacy challenges," *arXiv preprint arXiv:2305.14080*, 2023.

[16] V. Nair, W. Guo, J. Mattern, R. Wang, J. F. O'Brien, L. Rosenberg, and D. Song, "Unique identification of 50,000+ virtual reality users from head & hand motion data." arxiv," 2023.

[17] M. Sabra, N. V. Sureshkanth, A. Sharma, A. Maiti, and M. Jadliwala, "Exploiting out-of-band motion sensor data to de-anonymize virtual reality users," *arXiv preprint arXiv:2301.09041*, 2023.

[18] A. Basu, M. J. M. Sunny, and J. S. N. Guthula, "Privacy concerns from variances in spatial navigability in vr," *arXiv preprint arXiv:2302.02525*, 2023.

[19] A. Gulhane, A. Vyas, R. Mitra, R. Oruche, G. Hoefer, S. Valluripally, P. Calyam, and K. A. Hoque, "Security, privacy and safety risk assessment for virtual reality learning environment applications," in *2019 16th IEEE Annual Consumer Communications & Networking Conference (CCNC)*. IEEE, 2019, pp. 1–9.

[20] Y. Gumbo, L. Zhao, X. Tian, Z. Li, and Y. Long, "A literature review on privacy and security in virtual reality and augmented reality," 2022.

[21] P. D. Patel and P. Trivedi, "A systematic literature review on virtual reality and augmented reality in terms of privacy, authorization and data-leaks," *arXiv preprint arXiv:2212.04621*, 2022.

[22] C. George, M. Khamis, E. von Zezschwitz, M. Burger, H. Schmidt, F. Alt, and H. Hussmann, "Seamless and secure vr: Adapting and evaluating established authentication systems for virtual reality." NDSS, 2017.

[23] Z. Lv, D. Chen, R. Lou, and H. Song, "Industrial security solution for virtual reality," *IEEE Internet of Things Journal*, vol. 8, no. 8, pp. 6273–6281, 2020.

[24] Y. Shen, H. Wen, C. Luo, W. Xu, T. Zhang, W. Hu, and D. Rus, "Gaitlock: Protect virtual and augmented reality headsets using gait," *IEEE Transactions on Dependable and Secure Computing*, vol. 16, no. 3, pp. 484–497, 2018.

[25] J. Lin and M. E. Latoschik, "Digital body, identity and privacy in social virtual reality: A systematic review," *Frontiers in Virtual Reality*, vol. 3, p. 974652, 2022.

[26] G. M. Garrido, V. Nair, and D. Song, "Sok: Data privacy in virtual reality," *arXiv preprint arXiv:2301.05940*, 2023.

[27] R. Trimananda, H. Le, H. Cui, J. T. Ho, A. Shuba, and A. Markopoulou, "{OVRseen}: Auditing network traffic and privacy policies in oculus {VR}," in *31st USENIX security symposium (USENIX security 22)*, 2022, pp. 3789–3806.

[28] D. Maloney, G. Freeman, and A. Robb, "Social virtual reality: ethical considerations and future directions for an emerging research space," in *2021 IEEE conference on virtual reality and 3D user interfaces abstracts and workshops (VRW)*. IEEE, 2021, pp. 271–277.

[29] J. Jia and W. Chen, "The ethical dilemmas of virtual reality application in entertainment," in *2017 IEEE International Conference on Computational Science and Engineering (CSE) and IEEE International Conference on Embedded and Ubiquitous Computing (EUC)*, vol. 1. IEEE, 2017, pp. 696–699.

[30] B. Kenwright, "Virtual reality: ethical challenges and dangers [opinion]," *IEEE Technology and Society Magazine*, vol. 37, no. 4, pp. 20–25, 2018.

The Impacts of Playing Video Game on Memory and Executive Control

Davin Antoni
Computer Science Department, School of Computer Science
Bina Nusantara University
Jakarta, Indonesia
davin.antoni@binus.ac.id

Richardo Antolin
Computer Science Department, School of Computer Science
Bina Nusantara University
Jakarta, Indonesia
richardo.antolin@binus.ac.id

Said Achmad
Computer Science Department, School of Computer Science
Bina Nusantara University
Jakarta, Indonesia
said.achmad@binus.edu

Rhio Sutoyo
Computer Science Department, School of Computer Science
Bina Nusantara University
Jakarta, Indonesia
rsutoyo@binus.edu

***Abstract*—Playing video games has become a widespread form of entertainment, raising questions about their impact on cognitive functions such as memory and executive control. While some studies suggest that video games can enhance cognitive abilities, others indicate potential drawbacks, such as mental fatigue. This study conducted a systematic literature review to understand the impacts of video games, finding mixed results. Previous research has shown improvements in cognitive functions and negative effects depending on the duration and type of video game. This research is crucial to maximising cognitive benefits from video games while minimizing adverse effects. The study investigates how playing video games can influence memory and executive control by reviewing 740 articles and selecting 30 for in-depth analysis. The results showed that some game genres, like action games can enhance visual attention and executive controls. Strategy games enhance critical thinking, planning, and working memory through complex decision-making involving resource management. Puzzle games, such as Tetris or Cut the Rope, enhance visual-spatial processing and problem-solving skills. The length of gameplay for ideal cognitive enhancement lasts from thirty minutes to an hour each day, avoiding negative effects brought on by longer play. This research highlights the potential for video games to be used as tools for cognitive enhancement across different age groups, emphasizing the need for balanced and well-designed gameplay experiences.**

Keywords— Game-based, Memory, Screen Time, Gamers

I. Introduction

Although video gaming is the most popular type of entertainment throughout the world, with the highest recorded use in this modern era, there is a great potential influence that is exerted on the brain, especially on memory and executive control. Contrastingly, there have been reports from other studies that video games enhance cognitive functions such as memory ability and executive control, with long sessions of video game usage causing mental fatigue, thereby reducing the performance of working memory. Many studies analyzing the impact of video games on memory and executive control reveal mixed results. Playing video games can sometimes improve cognitive functions such as memory abilities and executive control [1]–[4]. From a cognitive perspective, video games have the potential to influence various brain functions, including aspects of memory and executive control. However, prolonged video game sessions can also cause mental fatigue and hinder working memory performance [5]–[7]. Playing video games can benefit brain function and structure. This can influence the level of intelligence and increase the cognitive abilities possessed by humans [1], [2]. These advantages extend far beyond children and adolescents, encompassing adults, seniors, and even individuals diagnosed with dementia [8], [9]. Several papers are related to video game genres, including exergaming and non-action video games. Exergaming can positively affect children's inhibition control, working memory, and cognitive flexibility [3]. Non-action video games can improve attention and visuospatial working memory in young adults. However, the effectiveness is still unclear due to the lack of a passive non-intervention control group [10]. While video games offer a range of cognitive benefits, it's important to strike a balance. Excessive video game use, particularly when associated with addiction, can lead to a decline in cognitive abilities [7].

Previous research [1], [2], [5], [11] has not provided a clear understanding of the long-term effects of video games on memory and executive control. The studies so far conducted have not given any clear indication as to how video games, in particular, cause long-term impacts related to memory and executive control, or what genre and length of play is required to ensure the maximum cognitive benefit. Similarly, a gap exists in previous papers regarding the ideal video game genre and optimal play duration to maximize cognitive benefits. Therefore, further research is needed to understand the impact of playing video games on memory and executive control abilities. It is hoped that these video games can become a

979-8-3315-1921-6/24/$31.00 ©2024 IEEE

new means of improving a person's memory and executive control abilities.

This study used a systematic literature review (SLR) as a methodology to answer the research questions above. A systematic literature review aims to identify all research papers and publications related to a topic by following PRISMA guidelines, which provide an overview of the literature relevant to the research topic. Papers were searched through academic databases such as Google Scholar using relevant keywords. Filtering was done based on inclusion and exclusion criteria, such as papers written in English and related to video games. Then, each paper was analyzed to ensure its relevance to the research questions.

This study is organized as follows. Section II discussed related works on the impacts of playing video games on memory and executive control. Section III defined the methodology employed in this study. Section IV presented the result and discussion that related to the topic. Finally, section V summarized the conclusion of this study.

II. Related Works

Studies analyzing the impact of video games on memory and executive control reveal mixed results. Playing video games can sometimes improve cognitive functions such as memory abilities and executive power. However, prolonged video game sessions can also cause mental fatigue and hinder working memory performance [1]–[3], [11].

A. Memory and Executive Control

One type of memory is working memory. Working memory refers to a short-term memory process involved with online monitoring or control of information. Performance of task is influenced by working memory [12]. For instance, working memory is utilized for retaining and manipulating information on complex tasks, such as solving math problems, following instructions, remembering your grocery list while shopping, or engaging in conversations. It plays a crucial role in learning, reasoning, and making decisions effectively.

Executive controls are a set of cognitive skills required to plan, monitor, and control cognitive processes. The executive controls comprises three closely related but distinguishable component skills: updating, shifting, and inhibition [4]. For instance, the executive controls is used for planning your day, prioritizing tasks, managing time effectively, and making decisions that align with your long-term goals. It's essential for staying organized, achieving goals, and navigating daily challenges.

B. The Impacts of Playing Video Game on Memory and Executive Control

It has both positive and negative effects on the memory and executive control due to playing video games. On the negative side, longer hours of playing video games increased verbal and Stroop memory test errors, though they showed slightly better visual memory [5]. It also reduces performance in working memory and enhances heart rate while reducing relaxation during rest when video games are played compared to listening to music [6].

On the other hand, video games can have positive impacts too. Some studies investigated that there was an improvement in the number of correct answers of the PASAT test, response speed, maintaining attention, and decreased mental fatigues after playing video games [11]. Video games can also affect a person's brain function and structure that would increase a person's intelligence and cognitive abilities [1], [2].

C. Research Question

Here are the three research questions we have identified after reviewing the relevant literature:

- RQ 1: What are the impacts of playing video game on memory and executive control?
- RQ 2: What types of video games can improve memory and executive control?
- RQ 3: What are the ranges of duration used in the studies that showed the effects of playing video games?

III. Methodology

This study used a systematic literature review as a methodology. A systematic literature review identifies all research papers and other publications related to a topic according to PRISMA guidelines. The PRISMA guide provides an overview of the literature relevant to this research topic. The PRISMA flow diagram of this research is shown in fig. 1.

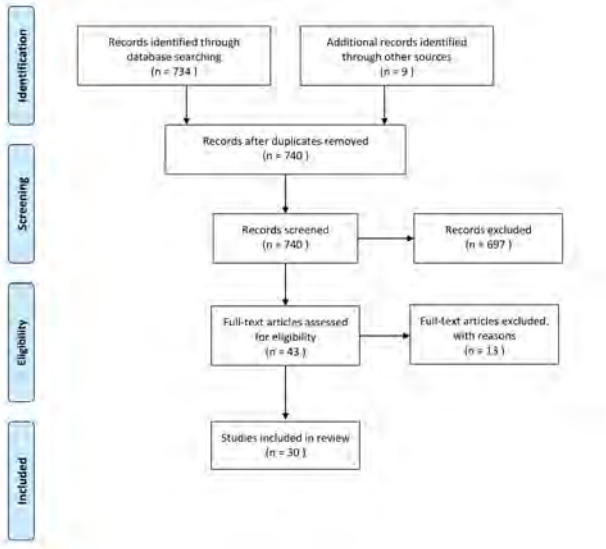

Fig. 1. PRISMA Flow Diagram

Identification involves specifying and searching for relevant keywords to the research question. Keywords used included 'video game', 'memory', and 'executive control' using available databases such as Google Scholar. A general search result of 740 articles resulted from a preliminary search. During the Screening stage, the titles and abstracts of the articles were reviewed to exclude those studies which did not comply exactly with the research objectives set out. This screening

isolated only the articles that more precisely corresponded to the focus of this study, hence further reducing the number of articles for review. The remaining articles then underwent a full-text review to determine whether they really met all the inclusion and exclusion criteria. Inclusion included articles in the English language, published between the years 2019-2024, and focused on video game activities involving memory and executive control, whereas non-qualifying articles were excluded from further analysis. Included, in the final stage, were 30 articles that passed every criterion. The inclusion and exclusion criteria to filter the paper are described in Table I. These were selected for in-depth analysis and comparison. These will comprehensively address the research questions regarding the effects of video games on memory and executive control.

After collecting relevant papers, the authors will read and analyze the collected documents to answer the research questions. This process involves understanding the paper's content and taking out important findings. Then, the authors can create meaningful conclusions that contribute to the overall understanding of the research topic.

TABLE I
INCLUSION AND EXCLUSION CRITERIA

Criteria		
Inclusion	I1	Papers related to video games
	I2	Papers related to memory and executive control
	I3	Papers published from 2019-2024
	I4	Papers are written in English
Exclusion	E1	Papers not related to video games
	E2	Papers not related to cognitive function
	E3	Papers published before 2019
	E4	Papers not available in full text

IV. RESULTS AND DISCUSSION

Section IV will answer the research questions by detailing the results obtained through the applied methodology. In this chapter, we will discuss in depth the impact of playing video games on memory and executive control abilities, the types of video games that can improve these abilities, and the ranges of duration used in the studies that showed the effects of playing games. These results will provide a more comprehensive insight into how interaction with video games may influence cognitive function and serve as a basis for recommendations regarding the use of video games in various fields.

A. RQ 1: What are the impacts of playing video game on memory and executive control

Based on the data gathered and analyzed, it can be concluded that video games can affect memory and executive control abilities. The most discussed ability, which is impacted by other works of literature, is improved executive control, such as memory, executive control, and problem-solving. It can also improve brain control and treatment potential and decrease cognitive performance. The effects of video games, summarized by the author, are shown in table II.

TABLE II
IMPACT VIDEO GAMES ON
MEMORY AND EXECUTIVE CONTROL

Impact of Video Games	**Number of Paper**	**Study Identifier**
Improved Executive Control	18	[2]–[5], [11], [13]–[16] [8], [17]–[24]
Improved Brain Function	4	[1], [10], [25], [26]
Treatment Potential	2	[9], [27]
Decreased Cognitive Performance	1	[6]

Several previous studies have stated that video games impact exectuive control. Well-designed video games present players with tasks and complex scenarios, fostering a problem-solving environment where they must develop solutions to conquer challenges and progress. Also, when playing Strategy, video games can train players in decision-making under uncertainty by requiring them to formulate plans based on limited information before attempting problem-solving actions [3]. Players then receive immediate feedback on the effectiveness of their plans, allowing for iterative refinement through trial-and-error learning. This continuous adaptation to increasingly complex scenarios fosters the development of critical thinking skills within a dynamic and challenging environment [16], [23].

Research suggests that certain types of video games, particularly action games and strategy games, may provide a workout for the brain's executive control system [1], [17], [25]. Previous research has shown that playing a physics-based puzzle game called Cut the Rope for 20 hours can improve higher-level thinking skills. [13].This and other studies suggest that video games could be a promising tool for training our brains [4], [26]. This new research is exciting because it shows that a simple handheld game can improve various skills involved in planning, focusing, and making decisions [19], [24], [28].

Playing video games can also improve brain function, especially in working memory, and impact a person's intelligence [2], [5], [29]. Video games can also improve response speed, ability to maintain attention, and decreased mental fatigue [10], [11]. Previous research suggests that well-designed video games, particularly action, strategy games, and puzzle games, can have a positive impact on working memory [21], [22]. Working memory involves holding and manipulating information in your mind for short periods. These games often require players to track multiple objects or pieces of information simultaneously and use that information to make decisions quickly [8], [15].

Based on previous studies, some have also investigated the the use of severe games in treatment is a promising area of research [14]. Several studies have explored the potential of serious games for dementia treatment and become an assessment tool for executive controls in older adults [9]. Because some games can be affected to improve memory and thinking performance, exercise social communication abilities and emotion control, and strengthen touching sense and hand flexibility [7], [27].

Playing video games during breaks can hurt working memory performance due to increased heart rate and decreased relaxation levels compared to listening to music. Specific executive control resources may be tired after gaming. So, based on the previous research paper, it is suggested that listening to music during breaks is more beneficial than playing games [6].

B. RQ 2: What types of video games can improve memory and executive control?

Based on the data gathered and analyzed, it can be concluded that several types of video games can improve people's memory and executive control. Different types of video games, including action, puzzle, and strategy games, significantly impact cognitive abilities such as memory, executive control, visual-spatial processing, problem-solving, and attention, with each genre offering unique benefits. The types of video games summarized by the author are shown in Table III.

TABLE III
TYPES OF VIDEO GAMES THAT IMPROVE MEMORY AND EXECUTIVE CONTROL

Types of Video Games	Number of Paper	Study Identifier
Action Games	9	[1], [5], [18], [22], [24] [13], [21], [25], [28]
Puzzle Games	5	[1], [2], [13], [15], [25]
Strategy Games	4	[1], [2], [16], [21]
Serious Games	4	[4], [19], [27], [29]
Brain-Training Games	3	[10], [25], [30]
Exergames	3	[3], [14], [15]
Sport Games	2	[11], [21]
Rhytm Dance Games	1	[1]
Motion Dance Games	1	[8]
Online Board Games	1	[15]

According to Table III, action games are the most frequently mentioned type of video game in the extracted data. Action video games have been a primary focus in studying the impact of playing video games on some cognitive abilities. Action game players outperform novices in visual attention tasks, and even non-gamers who train on these games show improvement [1], [5]. Long-term play of action video games leads to more significant improvements in cognitive skills related to the game compared to those assigned to control activities [18], [24]. Specifically, playing action-like video games enhances cognitive skills, particularly in attention and executive control, by training players to manage divided and focused attention under time pressure, especially in younger players [21], [24]. However, these effects can be less consistent and reliable in older individuals, as the complexity of the games may be too high for older players, restricting their performance to a lower, narrower range [13], [22]. First-person shooter games, such as Unreal Tournament or Medal of Honor, significantly enhance perceptual attention, with studies showing that individuals who played these games for extended periods performed better on perceptual attention tasks compared to those who played control games or no games [21], [25]. Additionally, Multiplayer Online Battle Arena (MOBA) games, such as League of Legends, can significantly impact various cognitive functions, including mental flexibility for adapting strategies, decision-making, working memory for tracking game elements and making informed decisions, and attentional control necessary for focusing on relevant information and reacting appropriately [28].

Then puzzle and strategy games are another type of video game often mentioned in the data gathered. Puzzle and strategy games require players to plan and execute steps to achieve a specific goal.

Playing puzzle games induces structural and functional alterations in the brain, including increased gray matter in the visual-spatial processing area and reduced activity in the frontal region, thereby stimulating visual-spatial processing and problem-solving abilities, ultimately enhancing overall cognitive function [1], [2], [13], [15]. These games significantly improve spatial reasoning skills, making them valuable tools for fostering spatial cognition in children. It is crucial for tasks requiring spatial awareness and problem-solving, contributing to their holistic cognitive development [15]. Additionally, puzzle games like Cut the Rope demonstrate substantial potential in enhancing executive control, such as strategizing, planning, and reframing. Unlike repetitive puzzle games, Cut the Rope's diverse and strategic gameplay yields more generalized cognitive benefits, making it particularly effective for populations requiring improvements in executive control, such as older people or individuals with ADHD, as it provides a non-violent and engaging alternative to action games [13]. Furthermore, playing spatial puzzle games like Tetris improves mental rotation abilities for two-dimensional shapes, although it doesn't show similar effects on other cognitive tasks [25].

Strategy video games engage the DLPFC, enhancing critical thinking and strategic planning abilities, while rhythm gaming influences visuospatial working memory, emotion, and attention areas [1]. These games improve memory by challenging players with complex strategies and strengthening executive control through efficient time allocation, prioritization, task management, and decision-making under pressure [2], [21]. Moreover, the unique challenges presented in strategy games, such as resourcefulness and teamwork in games like Dota 2, enhance problem-solving skills and communication abilities, making them engaging and beneficial for players of all levels [16], [21].

The types of video games mentioned above significantly impact memory and executive control. However, other types of games should not be ignored, as they may be helpful in certain situations.

C. RQ 3: What are the ranges of duration used in the studies that showed the effects of playing video games?

Based on the data gathered and analyzed, it can be concluded that several ranges of duration used in the studies show the positive impact of playing video games. Video game durations from less than 1 hour to 5 hours per day show varied cognitive benefits, with shorter durations generally

enhancing working memory, executive control, and attention, while longer durations can positively and negatively impact mental performance. The ranges of duration summarized by the author are shown in Table IV.

TABLE IV
RANGES OF DURATION THAT SHOWED THE BENEFIT OF PLAYING GAME

Ranges of Duration	Number of Paper	Study Identifier
Less than 1 hour/day	7	[1], [8], [14], [19] [10], [21], [22], [24]
1-2 hours/day	5	[4], [13], [18], [28], [30]
3-5 hours/day	2	[5], [26]

According to Table IV, less than 1 hour per day is among the shortest used in the studies as the training period. For instance, playing video games three times per week for 45 minutes each session (0.32 hours per day) enhances working memory and reasoning abilities in older adults [8], while 30-40 minutes of exergame training improves mental flexibility, problem-solving skills, and executive controls without adverse effects typically associated with longer gaming sessions [14]. Additionally, engaging in serious games for 30 to 45 minutes daily significantly enhances various cognitive functions crucial for memory and executive control, including working memory, attention, planning, and spatial skills [19]. Moreover, playing strategy games for 1–6 hours per week (0.14 to 0.86 hours per day) leads to better performance on perceptual attention tasks [21]. Finally, playing action-like video games for 20-60 minutes enhances cognitive skills, particularly attention, and executive control, by training players to manage divided and focused attention under time pressure [24].

Then, 1-2 hours per day is another range commonly used in the studies. Playing action video games for at least one hour per day has significant implications for cognitive development and skill enhancement [18], [28]. It can lead to measurable improvements in various cognitive domains, particularly in top-down attention and multitasking abilities. These gains are attributed to the regular engagement and focused practice that one hour per day ensures, providing sufficient time for the brain to adapt and improve its processing capabilities [18]. Additionally, playing serious games for 1.5 to 2 hours significantly improves executive control [4], while one hour of puzzle games boosts executive control [13].

Finally, 3-5 hours per day is the longest range used in the studies. Adolescents who spent between 3 and 4 hours per day playing video games showed both negative and positive impacts. For the negative consequences, there was a significant increase in total errors in cognitive tests like the Stroop Test and total interference in the California Verbal Learning Test. On the other hand, the positive impact was a slight improvement in visual memory results compared to the control group [5]. Playing games in virtual reality (VR) can also improve working memory (WM) performance and affective states of players [26].

Looking into the results of RQ1-RQ3, it can be observed that there are manifold various effects of playing video games on memory and executive control functions. In RQ1, the action and strategy game genres are found to improve executive skills such as decision-making and problem-solving. RQ2 provided results that included puzzle and strategy games, which are promising for the improvement of working memory and executive control. Regarding RQ3 on ideal playing duration, most gaming sessions done less than one hour daily had positive cognitive outcomes with no serious negative effects; longer may well impair cognitive performance.

One ongoing concern, however, is how excessively long gameplay durations may take away working memory performance and increase mental fatigue incrementally. Therefore, video games must be built with inbuilt time controls or intervals so that players can gain cognitive benefits without necessarily facing other detriments. More longitudinal studies are encouraged to explore the sustained impact of video gaming on cognitive functions. This might lead to wider insights and further optimize the cognitive benefits from video gaming in demographically different backgrounds.

Research findings from RQs 1 and 2 have shown that game genres such as action, strategy, and puzzle games are able to enhance cognitive skills including memory, executive control, and problem-solving. From the perspective of game developers, as indicated by RQ 2, it is worth developing games in such genres as action, puzzle, or strategy. Alternatively, developers can also develop video games targeting the improvement of cognitive skills, especially in children and adolescents. As for educators, teaching by means of video gaming is highly useful for working memory along with other cognitive skills. In such a case, with the integration of game elements, educators will be able to help students improve focus and problem-solving skills in a more fun and interactive manner.

Additionally, both game developers and educators have a very important role to play in ensuring that the video games are designed and played for optimal times (around 30 minutes to 1 hour) for maximum benefit while avoiding negative effects.

V. CONCLUSION

The research indicates that video games can significantly affect memory and executive control abilities. Most studies reviewed found that video games, especially action and strategy games, improve executive control by engaging players in complex problem-solving tasks that enhance critical thinking and decision-making skills. Additionally, video games can boost brain function, mainly working memory, by requiring players to handle multiple pieces of information simultaneously. Some studies also highlight the therapeutic potential of severe games in treating conditions like dementia and improving cognitive performance, social communication, emotional control, and motor skills. However, there are mixed findings: one study reported that playing video games during breaks can negatively affect working memory due to increased heart rate and reduced relaxation. At the same time, another found no significant cognitive benefits from short-term brain-training games. The duration of gameplay also matters, with shorter sessions (less

than one hour per day) generally showing positive cognitive impacts without the adverse effects associated with longer sessions. Overall, while video games can enhance specific mental abilities, the extent of their benefits depends on the type of game and the duration of play.

For future research, longitudinal studies are recommended to assess the long-term impact of video games on memory and executive control abilities, distinguishing between short-term and lasting cognitive effects. Investigating the optimal duration and frequency of gameplay for cognitive benefits and potential adverse effects would also be valuable. Furthermore, including a more diverse participant pool across various age groups, backgrounds, and gaming experiences could enhance the generalizability of the findings.

ACKNOWLEDGMENT

The CRediT author's statement as follows,
Davin Antoni: Conceptualization, Formal analysis, Writing - Original Draft.
Richardo Antolin: Conceptualization, Formal analysis, Writing - Original Draft.
Said Achmad: Methodology, Validation, Supervision, Project administration.
Rhio Sutoyo: Methodology, Validation, Supervision, Funding acquisition, Project administration.

REFERENCES

[1] D. Brilliant T, R. Nouchi, and R. Kawashima, "Does video gaming have impacts on the brain: Evidence from a systematic review," *Brain sciences*, vol. 9, no. 10, p. 251, 2019.

[2] C. Reynaldo, R. Christian, H. Hosea, and A. A. Gunawan, "Using video games to improve capabilities in decision making and cognitive skill: a literature review," *Procedia Computer Science*, vol. 179, pp. 211–221, 2021.

[3] J. Chen, X. Zhou, X. Wu, Z. Gao, and S. Ye, "Effects of exergaming on executive functions of children: a systematic review and meta-analysis from 2010 to 2023," *Archives of Public Health*, vol. 81, no. 1, p. 182, 2023.

[4] J. L. Plass, B. D. Homer, S. Pawar, C. Brenner, and A. P. MacNamara, "The effect of adaptive difficulty adjustment on the effectiveness of a game to develop executive function skills for learners of different ages," *Cognitive Development*, vol. 49, pp. 56–67, 2019.

[5] M. Özçetin, F. Gümüştaş, Y. Çağ, İ. Z. Gökbay, and A. Özmel, "The relationships between video game experience and cognitive abilities in adolescents," *Neuropsychiatric disease and treatment*, pp. 1171–1180, 2019.

[6] S. Liu, C. Kaufmann, C. Labadie, A. Ströhle, M. S. Kuschpel, M. Garbusow, R. Hummel, D. J. Schad, M. A. Rapp, A. Heinz *et al.*, "Short-term effects of video gaming on brain response during working memory performance," *PloS one*, vol. 14, no. 10, p. e0223666, 2019.

[7] Y. Farchakh, C. Haddad, H. Sacre, S. Obeid, P. Salameh, and S. Hallit, "Video gaming addiction and its association with memory, attention and learning skills in lebanese children," *Child and Adolescent Psychiatry and Mental Health*, vol. 14, pp. 1–11, 2020.

[8] X. Li, K. S. Niksirat, S. Chen, D. Weng, S. Sarcar, and X. Ren, "The impact of a multitasking-based virtual reality motion video game on the cognitive and physical abilities of older adults," *Sustainability*, vol. 12, no. 21, p. 9106, 2020.

[9] H. Ning, R. Li, X. Ye, Y. Zhang, and L. Liu, "A review on serious games for dementia care in ageing societies," *IEEE Journal of Translational Engineering in Health and Medicine*, vol. 8, pp. 1–11, 2020.

[10] E. Ruiz-Marquez, A. Prieto, J. Mayas, P. Toril, J. M. Reales, and S. Ballesteros, "Effects of nonaction videogames on attention and memory in young adults," *Games for Health Journal*, vol. 8, no. 6, pp. 414–422, 2019.

[11] H. Aliyari, H. Sahraei, M. Erfani, E. Tekieh, M. Salehi, M. Kazemi, M. R. Daliri, B. Minaei, H. Agaei, N. Sarahian *et al.*, "The impacts of video games on cognitive function and cortisol levels in young female volunteers," *J Exp Clin Neurosci*, vol. 6, no. 1, pp. 1–5, 2019.

[12] A. P. Shimamura, J. M. Berry, J. A. Mangels, C. L. Rusting, and P. J. Jurica, "Memory and cognitive abilities in university professors: Evidence for successful aging," *Psychological science*, vol. 6, no. 5, pp. 271–277, 1995.

[13] A. C. Oei and M. D. Patterson, "Playing a puzzle video game with changing requirements improves executive functions," *Computers in Human Behavior*, vol. 37, pp. 216–228, 2014.

[14] M. Adcock, M. Fankhauser, J. Post, K. Lutz, L. Zizlsperger, A. R. Luft, V. Guimarães, A. Schättin, and E. D. de Bruin, "Effects of an in-home multicomponent exergame training on physical functions, cognition, and brain volume of older adults: a randomized controlled trial," *Frontiers in medicine*, vol. 6, p. 321, 2020.

[15] V. Gashaj, L. C. Dapp, D. Trninic, and C. M. Roebers, "The effect of video games, exergames and board games on executive functions in kindergarten and 2nd grade: An explorative longitudinal study," *Trends in Neuroscience and Education*, vol. 25, p. 100162, 2021.

[16] A. Lie, A. Stephen, L. R. Supit, S. Achmad, and R. Sutoyo, "Using strategy video games to improve problem solving and communication skills: A systematic literature review," in *2022 4th International Conference on Cybernetics and Intelligent System (ICORIS)*. IEEE, 2022, pp. 1–5.

[17] K. Ryu, Y. Kim, J. Kim, and M. Woo, "False accusation of online games: Internet gaming can enhance the cognitive flexibility of adolescents," *Asian Journal of Sport and Exercise Psychology*, vol. 1, no. 2-3, pp. 116–121, 2021.

[18] B. Bediou, M. A. Rodgers, E. Tipton, R. E. Mayer, C. S. Green, and D. Bavelier, "Effects of action video game play on cognitive skills: A meta-analysis," 2023.

[19] S. Y. J. Lau, "A framework and serious game to support those with mild cognitive impairment," Ph.D. dissertation, Brunel University London, 2021.

[20] O. Holst, "Video game-based language learning and literacy a systematic review of the current state of research on video game-based learning and language learning," 2023.

[21] J. Parong, C. Holman, E. Cunningham, C. S. Green, and D. Bavelier, "Video games and higher cognition," in *Using cognitive and affective metrics in educational simulations and games*. Routledge, 2021, pp. 3–30.

[22] T. Ono, T. Sakurai, S. Kasuno, and T. Murai, "Novel 3-d action video game mechanics reveal differentiable cognitive constructs in young players, but not in old," *Scientific Reports*, vol. 12, no. 1, p. 11751, 2022.

[23] T. Thankachan, "Problem solving ability of secondary school students playing video games," *EDUCATIONAL EXTRACTS*, p. 111, 2019.

[24] A. Nguyen and D. Bavelier, "Play in video games," *Neuroscience & Biobehavioral Reviews*, p. 105386, 2023.

[25] R. E. Mayer, "Computer games in education," *Annual review of psychology*, vol. 70, pp. 531–549, 2019.

[26] D. Gabana Arellano, "Games 4 vrains: affective gaming for working memory training in virtual reality," Ph.D. dissertation, Queen Mary University of London, 2019.

[27] P. Wang, Y. Fang, J.-Y. Qi, and H.-J. Li, "Fisherman: A serious game for executive function assessment of older adults," *Assessment*, vol. 30, no. 5, pp. 1499–1513, 2023.

[28] C. Valls-Serrano, C. de Francisco, E. Caballero-López, and A. Caracuel, "Cognitive flexibility and decision making predicts expertise in the moba esport, league of legends," *SAGE Open*, vol. 12, no. 4, p. 21582440221142728, 2022.

[29] B. Babusiak, M. Hostovecky, M. Smondrk, and L. Huraj, "Spectral analysis of electroencephalographic data in serious games," *Applied Sciences*, vol. 11, no. 6, p. 2480, 2021.

[30] J. Parong and R. E. Mayer, "Cognitive consequences of playing brain-training games in immersive virtual reality," *Applied Cognitive Psychology*, vol. 34, no. 1, pp. 29–38, 2020.

Evaluation of Internet Connection Reconfiguration for Reliable Monitoring and Treatment of Toraja Lada Katokkon Smart Farming

Martina Pineng
Dept. of Electrical Engineering
Universitas Hasanuddin/Christian Indonesia Toraja University
Center of Excellence for Applied Intelligent Technologies (CEAIT)
Gowa, Indonesia
pinengm2od@student.unhas.ac.id
martinapineng@ukitoraja.ac.id

Elyas Palantei
Dept. of Electrical Engineering
Universitas Hasanuddin
Center of Excellence for Applied Intelligent Technologies (CEAIT)
Gowa, Indonesia
elyas_palantei@unhas.ac.id

Intan Sari Areni
Dept. of Electrical Engineering
Universitas Hasanuddin
Center of Excellence for Applied Intelligent Technologies (CEAIT)
Gowa, Indonesia
intan@unhas.ac.id

Wardi
Dept. of Electrical Engineering
Universitas Hasanuddin
Center of Excellence for Applied Intelligent Technologies (CEAIT)
Gowa, Indonesia
wardi@unhas.ac.id

***Abstract*—This study evaluates the internet transmission performance in smart farming in Lembang Madandan, Tana Toraja Regency, focusing on how router distance affects download speed, upload speed, and latency. The greenhouse cultivates Lada Katokkon plants, valuable yet sensitive to environmental conditions, necessitating IoT technology for monitoring and control. Data were collected at distances ranging from 1 to 20 meters under loaded and unloaded conditions. Results showed that the download speed fluctuated significantly with values ranging from 4.3 Mbps to 12 Mbps, upload speed varied between 1 Mbps and 3.1 Mbps, unloaded latency ranged from 0 ms to 49 ms, and loaded latency ranged from 304 ms to 995 ms. These variations indicate that distance significantly affects network performance. Optimizing device placement, adding access points, and using repeaters or extenders are recommended to improve signal strength and connection stability. Limitations include specific greenhouse conditions and measurement range. Further studies should explore other environmental factors and test network optimization strategies. Implementing these strategies is expected to enhance IoT system operation, boost productivity, and sustainability in smart agriculture, and ensure better management of Lada Katokkon plants.**

***Index Terms*—Internet of Things, smart farming, network performance, internet connectivity and data collection**

I. Introduction

Tana Toraja Regency, located in the highlands of South Sulawesi, Indonesia, is renowned for its rich cultural heritage and stunning landscapes, and it also holds significant agricultural potential. One of the standout agricultural products from this region is the unique Toraja chili, locally known as Lada Katokkon [1] [2]. This chili variety is highly valued for its distinctive flavor and high market value, making it an attractive crop for local farmers [3]. However, the cultivation of Lada Katokkon presents several challenges, primarily due to its susceptibility to pests and varying environmental conditions [4]. To mitigate these challenges and optimize crop yields, the integration of Internet of Things (IoT) technology into agricultural practices has become increasingly important [5] [6] [7].

979-8-3315-1921-6/24/$31.00 ©2024 IEEE

IoT technology, which involves using interconnected sensors and devices to collect and analyze data in real time, offers significant advantages for agriculture [8] [9] . In the context of Lada Katokkon cultivation, IoT can provide critical insights into various environmental parameters such as soil moisture, temperature, and humidity [10] [11]. Farmers can make informed decisions to enhance crop management, reduce the risk of pest infestations, and respond promptly to environmental changes by continuously monitoring these conditions. IoT in agriculture has improved efficiency, productivity, and sustainability [12]] . IoT systems typically comprise several layers: the physical layer (sensors and actuators), the network layer (communication protocols), the middleware layer (data processing), and the application layer (user interfaces and decision support systems). These layers work together to collect, transmit, and analyze data, providing actionable insights to farmers [9] [13].

Despite the clear benefits of IoT in agriculture, implementing this technology in Tana Toraja presents unique challenges. The region's mountainous terrain poses significant obstacles to establishing reliable internet connectivity, essential for the seamless operation of IoT systems. Poor connectivity can disrupt data transmission from sensors to central monitoring systems, leading to potential gaps in monitoring and delayed responses to environmental changes. Additionally, the cost of IoT infrastructure can be prohibitive for small-scale farmers. High-tech sensors, communication devices, and data processing systems require substantial investment, which may only be feasible for some regional farmers. Furthermore, the maintenance and technical know-how required to operate these systems effectively can hinder widespread adoption. A notable development in adopting IoT technology in Tana Toraja is the establishment of a smart greenhouse in Madandan Village, which employs IoT technology to oversee and regulate environmental conditions, ensuring ideal growth for Lada Katokkon. The implementation of the smart greenhouse has shown promising results in improving the yield and quality of Lada Katokkon, underscoring the potential of IoT to transform agricultural practices in challenging environments.

This study aims to evaluate the quality of the internet connection in the Smart Greenhouse used for cultivating Katokkon chili in Lembang Madandan to ensure sustainability and operational efficiency in environmental automation management. The urgency of this research lies in the need for a stable and reliable internet connection to support the operation of sensors and IoT devices that collect and transmit data in real-time, as well as execute automation commands for regulating temperature, humidity, and irrigation. By identifying the quality of the connection and the factors that hinder it, this study is expected to provide recommendations for connectivity improvements to enhance the effectiveness of control applications and the productivity of sustainable agricultural systems in the Smart Greenhouse.

II. Literature Review

A. IoT Applications in Smart Farming

The Internet of Things (IoT) refers to a network of interconnected physical devices that can collect and share data via the internet. In agriculture, IoT incorporates sensors, actuators, and other devices into farming systems to automate and improve the efficiency of various agricultural processes . [7] [14]. IoT sensors can monitor soil conditions, weather, humidity, and plant health, and can also automatically manage irrigation and fertilizer systems [15]. By using IoT, farmers can access real-time data from their fields and make more informed decisions based on the information obtained.

The implementation of IoT in agriculture encompasses a range of applications, including smart greenhouse systems, monitoring soil moisture and temperature, automating agricultural machinery, tracking livestock health, detecting plant diseases and pests, and overseeing grain storage conditions [16] [17]. The devices essential for IoT applications in agriculture consist of sensors, actuators, wireless networks, data storage and processing units, cameras, imaging systems, and GPS devices. This technology enables farmers to gather real-time information on weather conditions, soil moisture levels, plant diseases, and field pests [18].

IoT allows for the collection of real-time data to optimize agricultural processes. For example, soil moisture sensors can automatically manage irrigation, decreasing water usage and ensuring plants receive the correct amount of water, thereby enhancing resource use efficiency [19].

IoT allows for more precise monitoring and management of plant conditions. Farmers can take necessary actions to prevent diseases and pests and ensure plants grow under optimal conditions by obtaining accurate data about plant and environmental conditions. This action can improve the quality and quantity of crops [20].

IoT technology can support sustainable farming practices by optimizing natural resources such as water and energy. Using sensors to monitor and manage water and fertilizer usage can reduce the negative environmental impact and help maintain the agricultural ecosystem balance [21] .

B. Challenges in Implementing IoT in Smart Farming

Internet connectivity is essential for deploying IoT technology in agriculture, particularly within smart greenhouses. The main challenges faced in providing internet connectivity in rural areas include network infrastructure limitations, high costs for network installation, and energy limitations.

Network infrastructure must be improved in many rural areas to support IoT devices' connectivity due to the extended distance from urban centers, rugged terrain, and lack of investment in telecommunications infrastructure development. These limitations result in weak signals, low internet speeds, and poor reliability.

Installing network infrastructure in rural areas often requires very high costs. These costs include installing telecommunications towers, fiber optic cables, and other supporting devices. Additionally, operational costs to maintain the network running fast are also high. Solutions such as using LoRaWAN and satellite technology have been proposed to address this issue, but they also have limitations [22].

Previous research has examined different challenges and solutions related to IoT network performance in agricultural settings. IoT has been applied in various agricultural areas to boost efficiency and productivity through the automatic monitoring and control of environmental conditions. However, although there is extensive research on IoT applications in agriculture, comprehensive and specific network performance analysis in smart greenhouses still needs to be improved.

A relevant study [23] introduced a smart greenhouse system for chili cultivation using Raspberry Pi 3B technology and the MQTT protocol. This system allows real-time environmental

condition monitoring and automatic control through a mobile application. The study showed that using IoT technology can increase the efficiency of environmental management within the greenhouse.

Research developed an IoT-based smart greenhouse system using a combination of soil sensors, LDR sensors, fire sensors, and DHT11 to monitor and regulate environmental conditions to achieve optimal cultivation. This system demonstrates how integrating various sensor scans helps create ideal conditions for plant growth [24].

Additionally, a model utilizing IoT for monitoring plant growth in greenhouses was created. This model allows automatic monitoring and control using microcontrollers, sensors, fans, pumps, and appropriate network technology [25]. The study highlights the importance of accurate data for continuous plant growth monitoring, which can improve crop yields and reduce manual intervention.

The designed an environmental control system in a smart greenhouse using a Fuzzy Logic Controller for chili plants. This system regulates greenhouse air temperature, humidity, and soil moisture [26]. The study showed that a Fuzzy Logic Controller can quickly and efficiently achieve the desired environmental conditions.

A smart farming monitoring and automation system for chili plants was developed using IoT applications [10]. This system incorporates an Arduino microcontroller, soil moisture sensors, DHT11 for measuring air temperature and humidity, and ultrasonic sensors to measure plant height. It assists farmers in managing their farms more efficiently, enhancing both the quality and quantity of their harvests [27].

III. Smart Farming Network Configuration and Testing

This study evaluates the performance of the internet applied in smart farming located in Randanan Village, Tana Toraja Regency, by measuring upload speed, download speed, and latency.

A. IoT Network and Testing Purposes

The practical testing applies the quantitative methods. Quantitative methods are chosen because this study aims to measure and analyze numerical data generated from IoT devices installed throughout the smart farming network. Quantitative data is used to conduct statistical analysis that can clearly understand the relationship between the variables measured, such as internet speed, latency, and distance from the router. The experimental approach is chosen to control certain variables and observe their effects on other variables in controlled conditions. Using quantitative methods and an experimental approach, this research is expected to provide a clear and objective picture of the IoT network performance in the smart greenhouse and how distance affects that performance. This approach also allows researchers to identify and propose solutions that can be implemented to improve network performance in smart greenhouses in rural areas. The method of data collection in this study is as shown in Fig.1 below.

Fig. 1. Illustration of measuring internet speed in a smart greenhouse.

B. Population and Samples

The population in this research is all internet speed measurements conducted in the smart greenhouse in Lembang Madandan, Tana Toraja Regency as in Fig.2. These measurements encompass network performance parameters like download speed, upload speed, latency in both loaded and unloaded network conditions, and the distance from the router.

Fig. 2. Smart greenhouse

The study sample is taken from the population of internet speed measurements that have been conducted. This sample is chosen to accurately represent the smart greenhouse's internet network performance at various distances and conditions. The research sample includes:

- Measurements are taken at various distances from the router to see how distance affects network performance. The measured distances vary from one meter to several meters from the router.
- The download speed is evaluated at different distances to determine how quickly devices within the greenhouse can receive data. This download speed data determines whether the network can support high-bandwidth applications.
- Upload speed is measured to assess how quickly data can be sent from devices within the greenhouse to the server or cloud. That is important for real-time data transmission applications like live environmental monitoring.
- Loaded latency is measured to evaluate the delay time when the network is busy. That provides information about network performance under high load conditions, crucial to determining the network's reliability in intensive usage conditions.
- Unloaded latency is measured to determine the delay time under unloaded network conditions. Low latency is essential for applications that require quick responses, such as automatic control.

The sampling method used is stratified random sampling. This method takes measurements at various distance strata from the router (e.g., 1 meter, 2 meters, 3 meters, and etc) and under various network conditions (loaded and unloaded). Each distance stratum and network condition is represented in the sample to ensure that the collected data covers various operational conditions in the smart greenhouse.

The selection of internet speed measurements as samples is based on the importance of this parameter in assessing IoT network performance in smart greenhouses. Download speed, upload speed, and latency are key indicators of network performance and directly affect the effectiveness of smart greenhouse operations. By analyzing this data, the research can provide appropriate recommendations to improve network performance and ensure the network can support critical IoT applications in smart greenhouses.

C. Components Used

a) *WiFi Router*: A WiFi router is a device that enables various devices, such as computers, smartphones, and smart TVs, to connect to the internet wirelessly. Fig. 3 below shows the type of router used.

It operates by receiving data from the internet modem and distributing it to devices via radio signals. The latest technologies, like WiFi 6 and 6E, offer higher speeds and broader coverage. Modern routers also come with advanced security features and better network management controls.

Fig. 3. WiFi Router

b) *The fast.com Aplication:* Fast.com is an internet speed testing application developed by Netflix. It provides a simple and quick way to measure an internet connection speed, primarily focusing on download speeds, which are most relevant for streaming and consuming online content. The test works globally on any device with a web browser and is designed to be ad-free and straightforward. When the user clicks the "Show more info" button, Fast.com displays upload speeds and latency, offering a comprehensive view of your connection's performance. The following image, Fig.4, showcases the Fast.com application.

Fig. 4. WiFi Router

c) *Internet Service Provider (ISP):* In this study, internet service from Telkom Indonesia ISP was accessed using a Telkomsel card. Telkomsel was selected as the internet service provider because the mountainous terrain in Lembang Madandan results in intermittent internet access. In this area, only Telkomsel can offer internet connectivity, albeit not at an optimal level. Using a Telkomsel card enables researchers to access the internet more reliably and stably in an area difficult for other providers to reach. As a product of Telkom Indonesia, Telkomsel offers wide and robust network coverage, which is essential to support

research activities reliant on internet connectivity.

IV. Results and Discussion

After several measurements were conducted using the internet speed measurement application, a data summary was obtained, as shown in Table 1.

TABLE I
MEASUREMENTS RESULTS

Distance (m)	Download Speed (Mbps)	Upload Speed (Mbps)	Unloaded Latency (ms)	Loaded Latency (ms)
1	7.4	3	42	690
1	4.3	2.2	44	953
1	10	2.7	36	382
5	5	2.7	43	829
5	11	1.8	36	406
5	8.5	1.9	40	995
10	6.4	2	45	314
10	6.7	3.1	44	605
10	6.4	1.4	44	421
15	5	1.4	49	859
15	12	2	35	304
15	9.4	1.6	44	311
20	5.8	1	45	721
20	6.1	1.4	46	398
20	6.9	1.4	43	544

Based on the data analysis, the internet network performance in the smart farming set-up at Lembang Madandan, Tana Toraja Regency, shows a decline in download and upload speeds and an increase in latency as the distance from the router increases. The average download speed decreased from 7.4 Mbps at 1 meter to 5.0 Mbps at 5 meters, while the upload speed decreased from 3 Mbps to 1.4 Mbps. Unloaded latency increased from 36 ms to 49 ms, and loaded latency increased from 382 ms to 995 ms. This decline indicates that the distance from the router significantly impacts the network's ability to send and receive data quickly and efficiently. Implementing strategies such as adding access points, using repeaters or extenders, and optimizing the placement of network devices is expected to improve the internet network performance in the smart farming set-up. The average values of the internet speed measurements are shown in Table 2.

TABLE II
AVERAGE MEASUREMENTS RESULTS

Distance (m)	Average Download Speed (Mbps)	Average Upload Speed (Mbps)	Average Unloaded Latency (ms)	Average Loaded Latency (ms)
1	7.2	2.6	40.6	675
5	8.1	2.1	39.6	743.3
10	6.5	2.1	44	446.6
15	8.8	1.6	42.6	491.3
20	6.2	1.2	44.6	554.3

The table shows that the distance from the signal source affects network performance, with a decrease in upload speed and an increase in latency under load, while download speed and unloaded latency tend to remain stable with minor fluctuations, indicating that distance primarily impacts performance under heavier network conditions.

In this context, the decrease in internet network performance in the smart greenhouse becomes an issue that must be addressed promptly to ensure the optimal operation of the IoT system. The increasing distance from the router results in lower download and upload speeds and higher latency, which can hinder the performance of systems relying on stable and fast internet connectivity. So, several recommendations have been proposed.

First, adding access points can help extend the reach of the internet network signal. The internet signal can cover a wider area within the greenhouse by adding access points and maintaining stable download and upload speeds even at greater distances from the primary router. Additionally, using repeaters or extenders can also help strengthen the network signal in areas that are hard to reach by the router.

Second, optimizing the placement of network devices is crucial for enhancing Internet network performance. Strategically placing routers and access points can help ensure the internet signal spreads evenly throughout the greenhouse. Avoiding physical obstructions such as thick walls or metal equipment can also help reduce interference and improve network speeds.

Third, considering the upgrade of network infrastructure with advanced technologies like mesh networks or LoRa can provide a long-term solution to this issue. Mesh networks, for example, allow multiple network devices to work together to provide broader and stronger signal coverage. Meanwhile, LoRa technology, designed for long-distance communication with low power consumption, can be an effective alternative to support IoT systems in smart greenhouses.

Implementing these recommendations is expected to improve the internet network performance in the smart greenhouse in Lembang Madandan. The Internet network performance can be enhanced by adding access points, using repeaters or extenders, optimizing the placement of network devices, and upgrading infrastructure with advanced technologies. The scenario will support the optimal operation of the IoT system used in the smart greenhouse, ensuring that all devices can communicate smoothly and efficiently.

In a broader context, improving Internet network performance will also provide additional benefits such as increased productivity, operational efficiency, and cost savings. Stable and fast connectivity enables better management of smart greenhouses, from monitoring plant conditions to automatically controlling irrigation and lighting systems. Thus, investing in improving the internet network in smart greenhouses is a crucial step to support modern agriculture and sustainability.

Overall, enhancing the internet network performance in the smart greenhouse in Lembang Madandan, Tana Toraja Regency, is essential for supporting the optimal operation of the IoT system. Through the implementation of the mentioned recommendations, it is expected that internet connectivity can be improved, ensuring that the smart greenhouse can function with high efficiency and effectiveness.

The findings of this study show that the distance from the router significantly impacts the internet network performance in the smart greenhouse. Download and upload speeds decrease, while latency increases as the distance from the router increases. This condition indicates that the WiFi signal weakens and network efficiency decreases at longer distances. To address this issue, optimizing the placement of network equipment within the greenhouse can significantly improve performance.

One recommended strategy is to install additional access points at strategic locations within the greenhouse. Additional access points can strengthen the WiFi signal, ensuring that connected IoT devices can send and receive data at higher speeds and lower latency. Additionally, using repeaters or extenders can help extend the WiFi signal range, reducing areas with weak signals and improving connection stability.

However, this study has several limitations that need to be considered. Specific environmental conditions of the greenhouse, such as building structure, construction materials, and other environmental elements, can affect WiFi signal transmission. The limited measurement range, which only covers distances up to 5 meters from the router, may only partially reflect the dynamics of network performance throughout the greenhouse area. Further studies are needed to explore other environmental factors' effects and test network optimization strategies under various conditions and configurations.

Considering these limitations, the given recommendations remain relevant and can be implemented to improve the internet network performance in the smart greenhouse. Improved connectivity will support the optimal operation of the IoT system, ensuring that monitoring and controlling environmental conditions within the greenhouse can be done in real-time and efficiently. The results of this study provide a solid basis to further development in optimizing IoT networks in smart agricultural environments.

This research contributes to evaluating internet connection performance for IoT systems in Lada Katokkon smart farming in Tana Toraja, with several key points: (1) providing insights into the impact of distance on network performance (download speed, upload speed, and latency) in smart greenhouses, which can serve as a reference for IoT networks in other remote areas; (2) recommending network optimization strategies, such as adding access points, using repeaters, and optimizing device placement for stable connections and real-time plant monitoring; (3) supporting sustainable farming through precise environmental management, which can save resources and increase crop yields; and (4) offering essential baseline data for IoT technology development in smart agriculture, especially in areas with limited infrastructure.

V. Conclusion

This study evaluates the internet network performance in a smart greenhouse in Lembang Madandan, Tana Toraja Regency, focusing on how the distance from the router affects download speed, upload speed, and latency. The results show that distance significantly impacts network performance: download speed fluctuated between 4.3 Mbps and 12 Mbps, upload speed varied from 1 Mbps to 3.1 Mbps, unloaded latency ranged from 0 ms to 49 ms, and loaded latency ranged from 304 ms to 995 ms. These variations demonstrate that greater distances from the router correlate with decreased speeds and increased latency.

These findings confirm that optimizing network device placement, such as adding additional access points, can significantly improve network performance within the greenhouse. Strategies like using repeaters or extenders are also recommended to extend the WiFi signal range and improve connection stability.

Acknowledgment

We express our deepest gratitude to our supervisors at the Department of Electrical Engineering, Universitas Hasanuddin (UNHAS), who provided valuable guidance, support, and advice throughout this research. Their guidance greatly assisted in formulating the appropriate research methodology and provided in-depth insights that enhanced the quality of the research results. We also appreciate the encouragement and motivation they provided, enabling us to complete this research successfully. The support from all staff and lecturers at the Department of Electrical Engineering, UNHAS, is also highly appreciated. We would also like to express our sincere gratitude to the AI application as one of the tools that assisted us in composing this writing.

References

[1] R. Sjahril, M. Riadi, I. Ridwan, Kasmiati, I. Suryani, and A. R. Trisnawaty, "Kinship of katokkon chili (Capsicum chinense Jacq.) in Tana Toraja and North Toraja Regencies," *IOP Conf. Ser. Earth Environ. Sci.*, vol. 486, no. 1, 2020, doi: 10.1088/1755-1315/486/1/012101.

[2] Kaimuddin *et al.*, "Evaluation of CropSyst model in simulating the growth and production of Katokkon chili (Capsicum chinense Jacq)," *IOP Conf. Ser. Earth Environ. Sci.*, vol. 575, no. 1, 2020, doi: 10.1088/1755-1315/575/1/012115.

[3] Anggraheni, Yuliana, Fiqolbi, and Paradisa, "Effect of Organic Fertilizer Types and Varieties on Growth and Yield of Chili Pepper (Capsicum annum L.)," *Proj. Prod. Biomass Energy Mater. through Regen. Alang-alang (Imperata Cylind. Fields)*, vol. 7, pp. 173–181, 2019.

[4] A. S. Iryani and A. D. M. Bali, "Farmer Group of Cabe Bakul (Lada Katokkon) in Rantepao District, North Toraja Regency," *Mattawang J. Pengabdi. Masy.*, vol. 2, no. 1, pp. 27–35, 2021, doi: 10.35877/454ri.mattawang204.

[5] C. C. Sobin, "A Survey on Architecture, Protocols and Challenges in IoT, vol. 112, no. 3 *Springer US*, 2020.

[6] E. P. Yadav, E. A. Mittal, and H. Yadav, "IoT: Challenges and Issues in Indian Perspective," *Proc,-2018 3rd Int. Conf. Internet Things Smart Innov. Usages IoT-SIU*, pp. 1–5, 2018, doi: 10.1109/IoT-SIU.2018.8519869.

[7] A. K. Singh, K. Verma, and M. Raj, "IoT based Smart Agriculture System," *2021 5th Int. Conf. Inf. Syst. Comput. Networks (ISCON)*, pp. 2018–2021, 2021, doi: 10.1109/ISCON52037.2021.9702478.

[8] K. Gulati, R. S. Kumar Boddu, D. Kapila, S. L. Bangare, N. Chandnani, and G. Saravanan *et al.*, "A review paper on wireless sensor network techniques in Internet of Things (IoT)," *Mater. Today Proc.*, vol. 51, pp. 161–165, 2021, doi: 10.1016/j.matpr.2021.05.067.

[9] V. K. Quy *et al.*, "IoT-Enabled Smart Agriculture: Architecture, Applications, and Challenges," *Appl. Sci.*, vol. 12, no. 7, 2022, doi: 10.3390/app12073396.

[10] R. Sharma and P. Roy, "Methodology, Applications, and Challenges of IoT," pp. 502–507, 2020.

[11] I. S. Areni, A. Waridi, Indrabayu, C. Yohannes, A. Lawi, and A. Bustamin,, "IoT-Based of Automatic Electrical Appliance for Smart Home," *Int. J. Interact. Mob. Technol.*, vol. 14, no. 18, pp. 204–211, 2020, doi: 10.3991/ijim.v14i18.15649.

[12] H. Lee *et al.*, "Feasibility of Networking Technology for Smart Farm: LoRa vs APRS," *2020 Int. Conf. Omni-Layer Intell. Syst. (COINS)*, pp. 2–7, 2020, doi: 10.1109/COINS49042.2020.9191428.

[13] H. Muthukrishnan *et al.*, "Performance Analysis of Wi-Fi and LoRa Technology in Farm Monitoring System," *IOP Conf. Ser. Mater. Sci. Eng.*, vol. 1055, p. 012051, 2021, doi: 10.1088/1757-899x/1055/1/012051.

[14] F. Abou-Mehdi-Hassani *et al.*, "Design and Remote Monitoring of a Wireless-Controlled Smart Agricultural Greenhouse," *E3S Web Conf.*, vol. 469, 2023, doi: 10.1051/e3sconf/202346900038.

[15] I. Mat M. R. Mohd Kassim, A. N. Harun, and I. Mat Yusoff, "IoT in Precision Agriculture applications using Wireless Moisture Sensor Network," *ICOS 2016 - IEEE Conf. Open Syst.*, pp. 24–29, 2017, doi: 10.1109/ICOS.2016.7881983.

[16] A. S. Nechaev E. A. Ilina, and O. A. Morozevich, "Improving the process of growing crops through the use of smart greenhouses," *BIO Web Conf.*, vol. 71, 2023, doi: 10.1051/bioconf/20237102011.

[17] C. Bersani C. Ruggiero, R. Sacile, A. Soussi, and E. Zero, , "Internet of Things Approaches for Monitoring and Control of Smart Greenhouses in Industry 4.0," *Energies*, vol. 15, no. 10, 2022, doi: 10.3390/en15103834.

[18] P. Cihan, "IoT Technology in Smart Agriculture," *Int. Conf. Recent Acad. Stud.*, vol. 1, pp. 185–192, 2023, doi: 10.59287/icras.693.

[19] B. Parvez R. A. Haidri, and J. K. Verma, "IoT in Agriculture," *2020 Int. Conf. Comput. Perform. Eval. (ComPE)*, pp. 844–847, 2020, doi: 10.1109/ComPE49325.2020.9200035.

[20] S. R. Prathibha A. Hongal, and M. P. Jyothi, "IOT Based Monitoring System in Smart Agriculture," *2017 Int. Conf. Recent Adv. Electron. Commun. Technol. (ICRAECT)*, pp. 81–84, 2017, doi: 10.1109/ICRAECT.2017.52.

[21] M. S. Farooq S. Riaz, A. Abid, K. Abid, and M. A. Naeem, "A Survey on the Role of IoT in Agriculture for Smart Farming," *IEEE Access*, vol. 7, pp. 156237–156271, 2019, doi: 10.1109/ACCESS.2019.2949703.

[22] N. Islam M. M. Rashid, F. Pasandideh, B. Ray, S. Moore, and R. Kadel, "Applications and Communication Technologies for IoT in Smart Farming," *Sustain.*, vol. 13, no. 4, 2021, doi: 10.3390/su13041821.

[23] C. Maraveas, "AI in Smart Greenhouses: State of the Art," *Appl. Sci.*, vol. 13, no. 1, 2023, doi: 10.3390/app13010014.

[24] R. Medhe and S. Sarvankar, "IoT Based Smart Farming," *Int. J. Res. Appl. Sci. Eng. Technol.*, vol. 11, no. 6, 2023, doi: 10.22214/ijraset.2023.54057.

[25] A. Q. Mohabuth and D. Nem, "IoT-Based Model for Monitoring Plant Growth," *J. Inf. Syst. Informatics*, vol. 5, no. 2, 2023, doi: 10.51519/journalisi.v5i2.489.

[26] L. G. Hakim A. Sofwan, and A. Triwiyatno, "Smart Greenhouse Control using Fuzzy Logic," *Transient J. Ilm. Tek. Elektro*, vol. 9, no. 1, 2020, doi: 10.14710/transient.v9i1.46-55.

[27] N. Azman D. M. Ali, and Y. Yusuf, "Smart Agricultural Monitoring for Chili Plants using IoT," *J. Adv. Res. Appl. Sci. Eng. Technol.*, vol. 33, no. 1,pp. 53–66, 2023, doi: 10.37934/araset.33.1.5366.

Analysis Effect of FWHM on Efficiency and Power Quality in OWC using VLC

Arman Haditiansyah
Department of Electrical Engineering
Universitas Al Azhar Indonesia
Jakarta, Indonesia
armanhaditiansyah@gmail.com

Ary Syahriar
Department of Electrical Engineering
Universitas Al Azhar Indonesia
Jakarta, Indonesia
ary@uai.ac.id

Octarina Nur Samijayani
Department of Electrical Engineering
Universitas Al Azhar Indonesia
Jakarta, Indonesia
octarina.ns@uai.ac.id

Dwi Astharini
Department of Electrical Engineering
Universitas Al Azhar Indonesia
Jakarta, Indonesia
astharini@uai.ac.id

Faathir Alfath Risdarmawan
Department of Electrical Engineering
Universitas Al Azhar Indonesia
Jakarta, Indonesia
faathiralfath1303@gmail.com

Nida Salsabila
Department of Electrical Engineering
Universitas Al Azhar Indonesia
Jakarta, Indonesia
nidasalsabila423@gmail.com

***Abstract*—This study investigates the impact of Full Width at Half Maximum (FWHM) on the efficiency and power quality in Optical Wireless Communication (OWC) using Visible Light Communication (VLC). VLC, a subset of OWC, employs the visible light spectrum to transmit data and offers advantages such as broad spectrum availability, no electromagnetic interference, and enhanced security. The research emphasizes the importance of FWHM, a critical parameter defining the width of a light pulse or spectral line at half its maximum intensity, which directly influences the resolution and quality of data transmission. Narrowing the FWHM enhances VLC system performance by increasing data rates, reliability, and precision while minimizing signal interference. The study aims to optimize FWHM in VLC technology to achieve higher energy efficiency and better signal quality, crucial for practical applications in energy-sensitive environments. The findings highlight the significance of understanding and managing FWHM for the advancement and practical deployment of VLC systems.**

***Index Terms*—FWHM, OWC, VLC, Optic, Technology**

I. Introduction

The development of optical technology has significantly impacted various fields such as communications, medicine, photography, and astronomy. One of the most revolutionary applications is Optical Wireless Communication (OWC), which uses light as a transmission medium to wirelessly transmit information. OWC operates by converting electronic information signals into optical signals, which are then transmitted through the air and converted back into electronic signals at the receiver end [1]. This technology employs light sources like LEDs or lasers to generate optical signals that are modulated according to the transmitted data, traveling through either free space in Free Space Optical Communication (FSO) applications or indoor environments in Visible Light Communication (VLC) applications [2].

979-8-3315-1921-6/24/$31.00 ©2024 IEEE

VLC was an innovative technology that utilized the visible light spectrum to transmit data. In the rapidly evolving digital era, the demand for faster and more efficient data communication became increasingly urgent, and VLC emerged as a potential solution to meet these needs [3]. This technology employed light emitted from lighting devices such as Light Emitting Diode (LED) to send information. The primary advantage of VLC lay in its ability to combine lighting functions with data communication, thereby leveraging existing lighting infrastructure without the need for significant additional installations [4].

VLC operated by converting digital signals into variations in light intensity that were invisible to the human eye but could be received and interpreted by special detectors. These features made VLC particularly suitable for applications in sensitive environments like hospitals and airplanes, as well as for indoor use where high data speeds without interference were required [5]. As advanced LED technology continued to develop, the potential for VLC expanded [6]. Research and development in the field of VLC progressed, exploring applications across various sectors such as vehicle-to-vehicle communication for improved road safety, indoor navigation systems, and faster, more reliable internet connectivity in homes and offices [7].

Understanding light source characteristics is critical to optimizing the performance of VLC and other optical technologies, with a key parameter in this optimization being Full Width at Half Maximum (FWHM), which defines the width of a spectral line or light pulse at half its maximum intensity [8]. FWHM affects the resolution and quality of data transmission by indicating the spread of light, where a narrower FWHM indicates a more monochromatic light source, reducing signal interference and increasing the precision of data communication [9]. Historically, FWHM has been widely used across various disciplines to characterize the resolution of imaging systems, the bandwidth of optical filters,

and the performance of lasers and LEDs. In VLC, a deep understanding of FWHM enables engineers and researchers to design systems that achieve optimal performance, ensuring clear and efficient data transmission [10].

Efficiency in VLC and optical technology aims to maximize data transmission quality by managing FWHM in light sources. This parameter, defining the width of a light spectrum at half its maximum intensity, significantly affects system performance, including resolution, data transmission speed, and resilience against signal interference [11]. Narrowing the FWHM enhances VLC systems' capability to distinguish desired signals from environmental disturbances, thereby improving accuracy and reliability, even in challenging optical conditions [12]. Furthermore, optimizing FWHM promotes efficient energy usage by minimizing energy wastage outside the desired spectrum, critical for energy-sensitive applications like battery-powered devices. This approach not only enhances VLC system performance but also extends operational lifespan in energy-constrained environments, reinforcing the sustainability and practicality of these advanced communication technologies [13].

This research will discuss how FWHM affects efficiency and power quality in VLC. The study will explore the relationship between FWHM width and energy consumption, and its impact on the resulting power. Using light sources with a narrower FWHM is expected to reduce energy wasted outside the desired spectrum, thereby improving energy efficiency. The research will also examine how variations in FWHM affect the integrity and clarity of the VLC signal, crucial for practical applications like energy-sensitive environments and battery-operated devices. The main contribution of this research was to investigate the extent to which FWHM affected quality and power in VLC.

II. Methodology

A. Literature Review

VLC was part of OWC, OWC was a wireless communication system that utilized light as its transmission medium. In this context, VLC technology used the light spectrum with a wavelength range from 350 nm to 850 nm and a frequency range from 4.0×10^{14} Hz to 7.5×10^{14} Hz. LED (Light Emitting Diode) lights played a crucial role in VLC technology, functioning as the light source to transmit data from the transmitter to the receiver [14]. The communication principle in the VLC system included three main components. First, the LED, equipped with a signal processing unit, acted as the transmitter. Second, the transmission channel used air as the medium to convey the light. Third, on the receiving end, there was a photodetector that served as the light signal receiver [15]. Figure 1 showed the block diagram of the VLC system, where the electrical signal first entered the mapper system. Then, the mapped signal entered the LED, carrying the information signal and producing light, which was transmitted through the air channel.

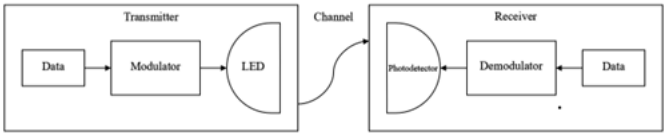

Fig. 1. Block Diagram of VLC.

VLC technology offers significant advantages for data communication applications by utilizing a broader light spectrum compared to traditional radio frequencies. This makes it ideal for high-speed and secure data transfer in environments like indoor settings or densely populated areas [16]. The information signal is transmitted via light through the air channel and received by a photodetector, which converts the light signal into an electrical signal. This electrical signal is then processed by the modulator unit, ensuring that the information from the transmitter is accurately decoded and received. As a result, the information received matches the original transmitted signal, maintaining the integrity and accuracy of the communication [17].

B. Mathematical Model

Because LEDs can be employed for various purposes such as illumination, data communication, indoor localization, and sensing, it is crucial to specify both light intensity and transmitted optical power [18]. Light intensity denotes the brightness of an LED and is characterized by the amount of light flux per solid angle, given as:

$$I = \frac{d\Phi}{d\Omega} \tag{1}$$

where Ω represents the spatial angle, and Φ denotes the luminous flux, which can be calculated from the energy flux Φ_e, as given by:

$$\Phi = K_m \int_{380}^{780} V(\lambda)\Phi_e(\lambda)\, d\lambda \tag{2}$$

Where $V(\lambda)$ represents the standard luminous curve, and K_m denotes the maximum visibility, which is approximately $\sim 683\,\text{lm/W}$ at a wavelength of 555 nm. The transmitted optical power P_t, indicating the total energy radiated from an LED, is given by:

$$P_t = K_m \int_{A_{\min}}^{A_{\max}} \int_0^{2\pi} \Phi_e\, d\theta\, d\lambda \tag{3}$$

Where $A_{\min}$ and $A_{\max}$ are determined from the PD's responsivity curve. Figure 2 illustrates a typical office environment equipped with LED-based lighting panels that offer wireless connectivity to users. In this setup, the primary transmission mode is Line-of-Sight (LOS). Assuming LEDs emit light in a Lambertian radiation pattern, the radiation intensity at a desk surface can be described as:

$$I(\varphi) = I(0)\frac{m_l + 1}{2\pi}\cos^{m_l}(\varphi) \tag{4}$$

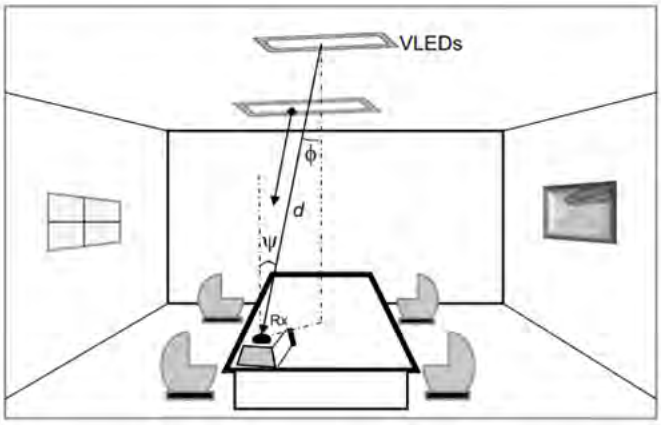

Fig. 2. Illumination by LED [19].

where φ represents the angle of irradiance relative to the axis normal to the transmitter surface, $I(0)$ denotes the central luminous intensity, and m_l signifies the Lambertian emission order, which quantifies the directivity of the light beam, defined as:

$$m_l = \frac{\ln(2)}{\ln\cos\left(\Phi_{1/2}\right)} \tag{5}$$

where $\Phi_{1/2}$ is the semi-angle at a half illuminance of an LED. For the LOS path, the horizontal illuminance/intensity at a point (x, y, z) and the received power at the receiver are given as:

$$I_{\text{hor}} = \frac{I(0)\cos^{m_1}(\varphi)}{d^2\cos(\Psi)} \tag{6}$$

$$P_r = P_t \frac{(m_l+1)A_{PD}}{2\pi d^2}\cos^{m_l}(\phi)T_s(\Psi)g(\Psi)\cos(\Psi) \quad 0 \le \Psi \le \Psi_{\text{con}} \tag{7}$$

Where Ψ is the angle of incidence relative to the axis normal to the receiver surface, $T_s(\Psi)$ is the filter transmission coefficient, $g(\Psi)$ and Ψ_{con} represent the concentrator gain and Field of View (FOV) respectively, and d is the distance between the LED and the photodetector surface area A_{PD}. The gain of the optical concentrator at the receiver is defined by:

$$g(\Psi) = \begin{cases} \frac{n_{\text{con}}^2}{\sin^2\Psi_{\text{con}}}, & 0 \le \Psi \le \Psi_{\text{con}} \\ 0, & 0 \ge \Psi_{\text{con}} \end{cases} \tag{8}$$

where n_{con}^2 is the refractive index of the optical concentrator [19].

C. VLC Parameters

Table I outlines the critical parameters necessary for modeling a typical room environment in a VLC system. These parameters include room dimensions, receiver characteristics, optical filter properties, and the specifications of a lens at the photodetector. Each factor significantly influences the overall performance and accuracy of the VLC system simulation, providing a thorough understanding of the system's operation under various conditions [20].

TABLE I
PARAMETERS SYSTEM

Parameter	Value
Room	
Size	$5 \times 5 \times 3\,\text{m}^3$
Reflection coefficient	0.8
Receiver	
Receive plane above the floor	0.85 m
Active area (A_{PD})	1 cm^2
Half-angle FOV	60°
Elevation	90°
Azimuth	0°
Δt	0.5 ns
Optical filter	
Gain	1
A lens at the PD	Refractive index 1.5

Table II provides an overview of parameters for two VLC light sources, including LED locations, FWHM, transmit power per LED, LED count per array, and center luminous intensity. These parameters are essential for modeling the system and assessing each source's performance. The study compared Source 1 and Source 2 to identify which offered better power and quality.

TABLE II
LED PARAMETERS

Parameter	Value
Source 1	
Location (4 LEDs)	(1.25, 1.25, 3) (1.25, 3.75, 3) (3.75, 1.25, 3) (3.75, 3.75, 3)
Location (1 LED)	(2.5, 2.5, 3)
FWHM	80°
Transmit power (per LED)	30 mW
Number of LEDs per array	70 × 70 (4900)
Center luminous intensity	300–910 lx
Source 2	
Location (4 LEDs)	(1.25, 1.25, 3) (1.25, 3.75, 3) (3.75, 1.25, 3) (3.75, 3.75, 3)
Location (1 LED)	(2.5, 2.5, 3)
FWHM	10°
Transmit power (per LED)	25 mW
Number of LEDs per array	65 × 65 (4225)
Center luminous intensity	300–910 lx

III. RESULT AND DISCUSSION

The simulation models optical-electrical parameters and room dimensions to analyze power distribution in a 5 × 5 × 3 m³ room, focusing on LED positions and the receiver plane. It calculates the distance, angle vectors, channel DC gain, and received power for Source One, adjusting the received power for symmetry and converting it to decibels (dBm). The results are then visualized with labeled axes and a colorbar, providing a clear representation of the power distribution. This

analysis highlights the crucial impact of LED layout, room size, and receiver specifications on the performance of the VLC system, offering insights into how these factors influence overall system efficiency and effectiveness.

A. Source 1

The FWHM is set to 80 degrees, determining the Lambertian order of emission. Each LED transmits 30 watts of optical power in a 70×70 array, providing significant total power. The photodetector's area is 1e-4 square meters for efficient light detection. The system includes an optical filter to improve the signal-to-noise ratio by passing specific wavelengths. The lens's refractive index focuses the incoming light, while the receiver's 70-degree FOV allows wide-angle light capture, increasing system robustness. The optical concentrator's gain, based on the refractive index and FOV, directs optical power onto the photodetector, ensuring efficient signal capture and processing.

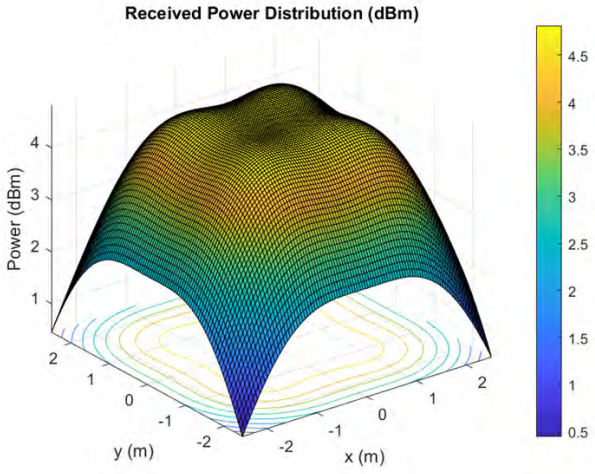

Fig. 3. Optical power distribution at the receiver plane for an 80° FWHM

Figure 3 illustrates the optical power distribution at the receiver plane for a LOS path, ignoring wall reflections. This figure shows an almost uniform power distribution at the center, with maximum and minimum power levels of 2.5 dBm and -2.5 dBm, respectively. Achieving this uniform distribution is heavily dependent on the half-angle of the light source. A smaller half-angle typically leads to a more focused light beam, resulting in higher power density at the center but less uniformity across the plane. Conversely, a larger half-angle can spread the light more evenly but may reduce the overall intensity. Therefore, selecting the appropriate half-angle is crucial for optimizing the power distribution to meet specific application requirements.

The system, with a total power output of 30 mW, produced a maximum power level of 4.814 dBm and a minimum power level of 0.441 dBm. In Figure 4, the yellow color represents the maximum output power captured by the receiver, while the blue color indicates the minimum output power. Each square in the figure corresponds to the power distribution values received

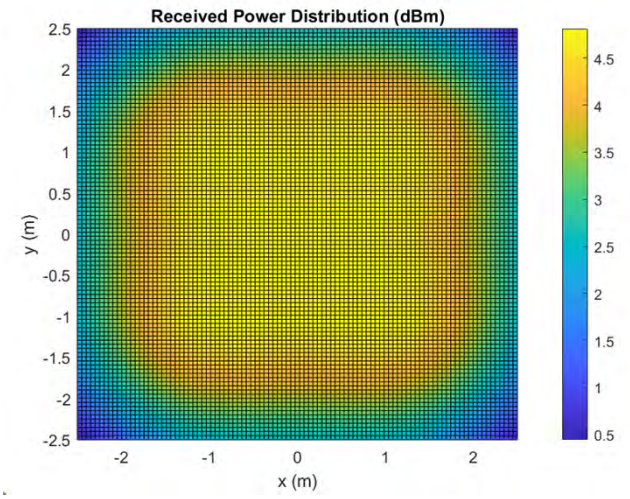

Fig. 4. Optical power distribution at the receiver plane for an 80° FWHM (looks flat)

by the receiver, offering a clear visual representation of the varying power levels across the system's output. This detailed mapping provides valuable insights into the distribution and reception of power, effectively highlighting areas of maximum and minimum reception.

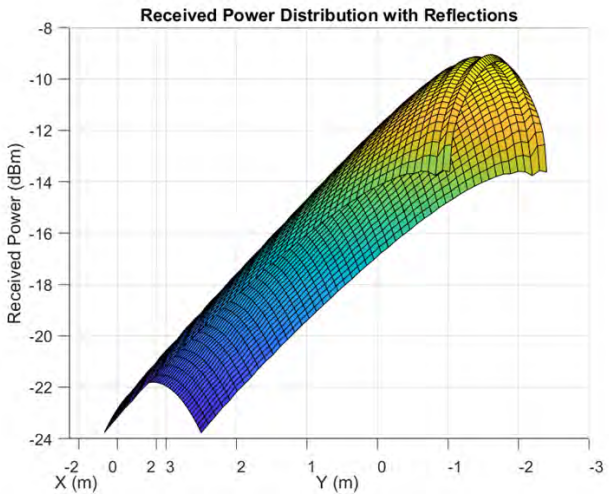

Fig. 5. Power distribution with reflections for 80° FWHM

The curve in Figure 5 illustrates that received power decreases as the distance from the receiver increases, a result of the spreading of light from the transmitter, which leads to reduced intensity at longer distances. The figure also shows peaks and valleys in the received power distribution, providing valuable insights into the locations of objects within the room. By analyzing these variations, we can estimate the positions of objects and assess the impact of light reflection on the power distribution. These curves, therefore, offer critical information not only about the indoor light distribution but also about the physical layout of the environment, facilitating the accurate identification and localization of objects within the space.

B. Source 2

The semi-angle at half power was set to 10 degrees, which determined the Lambertian emission order of the LED, dictating the spread of the light emitted. Each LED in this system was configured to transmit 25 watts of optical power, ensuring a robust light output. In this scenario, an LED array consisting of 65 × 65 LEDs was employed, significantly contributing to the total transmitted power, providing a substantial illumination area. Additionally, the gain value of the optical filter and the refractive index of the lens on the photodetector were meticulously determined to enhance system performance, optimizing the reception and conversion of the optical signal. The receiver's FOV was also a critical factor in this configuration, as it influenced the efficiency and accuracy with which the optical signal was received and processed. By carefully considering these parameters, the system was designed to achieve optimal performance in terms of signal quality and transmission efficiency.

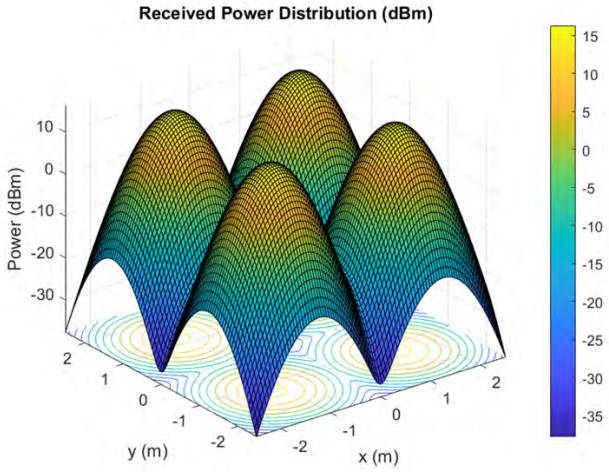

Fig. 6. Optical power distribution at the receiver plane for an 10° FWHM

Figure 6 shows a pattern of peaks and valleys in the received power distribution, indicating the presence of multiple LEDs arranged in an array. The highest power, approximately 15 dBm, is located near the LEDs, confirming their placement, while the power rapidly decreases with distance, dropping below -35 dBm due to attenuation. The 10-degree FWHM indicates a narrow, focused beam, which enhances point-to-point communication but limits coverage and necessitates precise receiver positioning. The low uniformity in the power distribution could impact communication quality, suggesting the need for careful LED placement. To achieve more even coverage, additional LEDs or diffusers may be required.

Figure 7 illustrates the received power distribution of a laser beam, showing a concentration at the center that decreases towards the edges, which is characteristic of its directional and coherent properties. With an estimated FWHM of approximately 0.8 meters, the laser beam demonstrates a narrow focus, making it highly suitable for VLC systems. This trade-

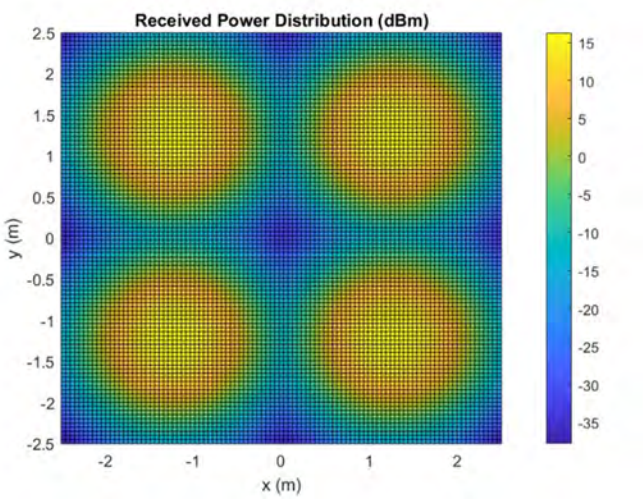

Fig. 7. Optical power distribution at the receiver plane for an 10° FWHM (looks flat)

off between extended range and reduced coverage highlights the importance of optimizing the FWHM for balancing performance and coverage in VLC applications.

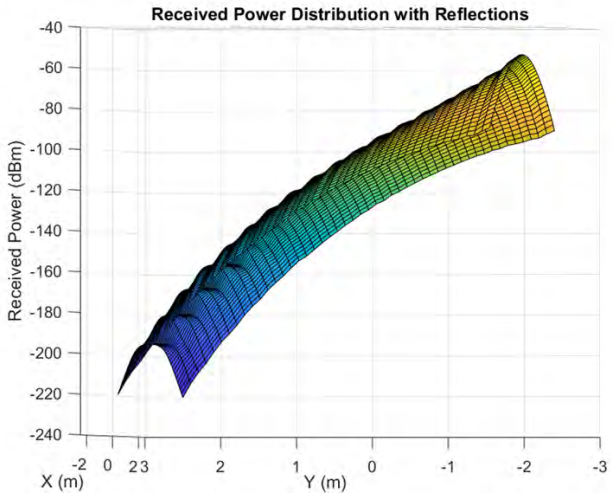

Fig. 8. Power distribution with reflections for 10° FWHM

Selecting the appropriate half-angle is essential for optimizing power distribution in wireless optical communication systems. Smaller half-angles are ideal for high-intensity, localized applications, as they focus the light in a narrow region. In contrast, larger half-angles provide more uniform coverage, spreading the light over a wider area. The receiver's FOV is equally important; with a narrow FWHM, the receiver must remain within the main lobe of the emitted light to avoid power loss. A 10-degree FWHM in a VLC system delivers a focused beam, making it suitable for high data rate applications, but it can limit uniform coverage. To improve coverage and ensure more consistent power distribution, adjustments such as modifying LED placement, adding more LEDs, or incorporating optical diffusers may be necessary.

These measures can help strike a balance between focusing power for high-speed communication and ensuring adequate coverage across the area.

C. Bit Error Rate

The data presented in Figure 9 offers a detailed comparison of Bit Error Rate (BER) values for Source 1 and Source 2 across varying Signal-to-Noise Ratio (SNR) levels, shedding light on the performance characteristics of both sources in a VLC system. At lower SNR values (from 0 dB to 6 dB), both sources exhibit a decrease in BER, indicating improved signal quality as the SNR increases. However, Source 1 starts with a higher BER of 0.4024 at 0 dB, which decreases to 0.3791 at 6 dB. In contrast, Source 2 demonstrates superior performance from the outset, with a lower BER of 0.2478 at 0 dB, dropping to 0.2443 at 6 dB. This suggests that Source 2 is inherently more efficient in maintaining signal integrity under low SNR conditions, possibly due to more advanced modulation techniques or better control of noise, providing a more stable and reliable signal in challenging environments.

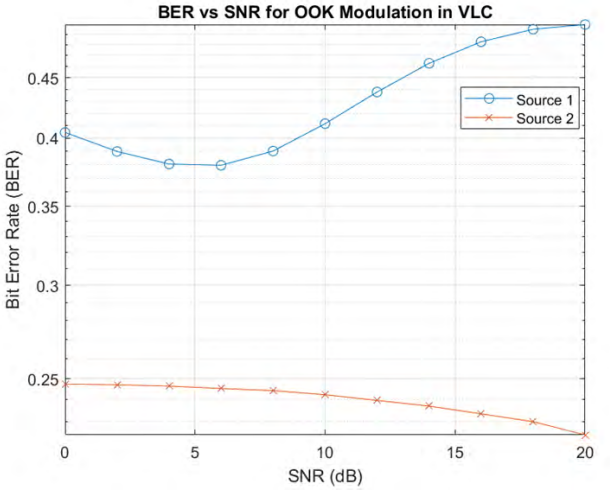

Fig. 9. BER at 80° and 10° FWHM

As the SNR increases further (from 8 dB to 14 dB), Source 1 begins to exhibit a noticeable increase in BER, rising from 0.3896 at 8 dB to 0.4623 at 14 dB. This upward trend in BER suggests that Source 1 is reaching a threshold where further increases in SNR do not lead to improvements in error rates. This may be due to system limitations such as non-linearities, interference, or the saturation of the receiver's ability to process higher SNR signals. In contrast, Source 2 continues to demonstrate a consistent improvement in signal quality within this range, with its BER decreasing from 0.2432 at 8 dB to 0.2368 at 14 dB. This steady decline reflects Source 2's superior performance and better error correction capabilities at higher SNR values, indicating its ability to maintain signal integrity even as the SNR increases.

At the highest SNR levels (from 16 dB to 20 dB), the performance difference between the two sources becomes even more evident. Source 1's BER continues to rise, reaching 0.4986 at 20 dB, which confirms that merely increasing the SNR does not improve its performance and may even introduce additional noise or errors into the system. On the other hand, Source 2's BER steadily decreases, dropping to 0.2225 at 20 dB, showcasing its ability to maintain optimal signal quality even with higher SNR values. This contrast highlights Source 2's superior efficiency and reliability in reducing error rates as the SNR increases.

TABLE III
COMPARISON DATA OF SNR VS BER

SNR (dB)	BER (Source 1)	BER (Source 2)
0.0000	0.4024	0.2478
2.0000	0.3889	0.2471
4.0000	0.3806	0.2454
6.0000	0.3791	0.2443
8.0000	0.3896	0.2432
10.0000	0.4105	0.2416
12.0000	0.4368	0.2393
14.0000	0.4623	0.2368
16.0000	0.4823	0.2332
18.0000	0.4941	0.2292
20.0000	0.4986	0.2225

Overall, as shown in Table III, Source 2 consistently outperforms Source 1 across all SNR levels, with lower BER values and a more stable decrease in errors as the SNR increases. This indicates that Source 2 is more reliable and efficient in maintaining high-quality signals within a VLC system, making it particularly well-suited for applications that require robust and reliable data transmission, such as high-speed internet or real-time communication in energy-sensitive environments. In contrast, Source 1 exhibits diminishing returns as the SNR increases, suggesting that further optimizations or advanced signal processing techniques may be needed to improve its performance, especially in scenarios where higher SNRs are common. Based on this analysis, Source 2 emerges as the preferred choice for systems where minimizing data errors is critical, making it the better option for enhancing VLC performance and ensuring efficient data transmission.

IV. CONCLUSION

This research examines the impact of FWHM on efficiency and signal quality in OWC systems using VLC The results emphasize the important role of FWHM in determining the performance of VLC, showing that a narrower FWHM increases data transmission speed, improves resolution, and increases resistance to signal interference, thereby significantly improving the accuracy and reliability of the communication system. In addition, FWHM optimization proves important for reducing energy wastage, which is an important factor for energy-sensitive applications such as battery-powered devices. This study emphasizes the need for balancing FWHM choices to achieve the desired balance between high intensity and uniform coverage, tailored to specific application requirements. By providing detailed insights into FWHM optimization, this study paves the way for designing more efficient and reliable VLC systems. Further studies are encouraged to delve deeper

into the interaction between FWHM and other parameters to further enhance the capabilities and applications of VLC technology.

V. Acknowledgment

This publication is supported by UAI research grant 2020-2024.

References

[1] S. M. Hameed, S. M. Abdulsatar, and A. A. Sabri, "BER Comparison and Enhancement of Different Optical OFDM for VLC," *Int. J. Intell. Eng. Syst.*, vol. 14, no. 4, pp. 326–336, 2021.

[2] F. Wang, F. Yang, J. Song, and Z. Han, "Access Frameworks and Application Scenarios for Hybrid VLC and RF Systems: State of the Art, Challenges, and Trends," *IEEE Commun. Mag.*, vol. 60, no. 3, pp. 55–61, 2022.

[3] M. Obeed, S. Member, A. M. Salhab, and S. Member, "On Optimizing VLC Networks for Downlink Multi-User Transmission: A Survey," pp. 1–27.

[4] S. Agha et al., "NOMA-Based VLC Systems: A Comprehensive Review," 2023.

[5] H. Abuella and S. Member, "Hybrid RF/VLC Systems: A Comprehensive Survey on Network Topologies, Performance Analyses, Applications, and Future Directions," *IEEE Access*, vol. 9, pp. 160402–160436, 2021.

[6] M. S. Mir, B. Majlesein, B. G. Guzman, J. Rufo, and D. Giustiniano, "LED-to-LED based VLC systems," pp. 1–6, 2021.

[7] A. R. Ndjiongue, T. M. N. Ngatched, O. A. Dobre, and H. Haas, "Towards the Use of Re-configurable Intelligent Surfaces in VLC Systems: Beam Steering," pp. 1–12.

[8] T. Khee and S. Boon, "3.8-Gbit/s visible light communication (VLC) based on 443-nm superluminescent diode and bit-loading discrete-multiple-tone (DMT) modulation scheme," no. Vlc, 2024.

[9] D. Version and G. Guzman, "Dowhuszko, Alexis; Genoves Guzman, Borja Closed form approximation of the actual spectral power emission of commercial color LEDs for VLC," 2022.

[10] A. Huang, C. W. Lee, and H. M. Liu, "Time to peak and full width at half maximum in MR perfusion: valuable indicators for monitoring moyamoya patients after revascularization," *Sci. Rep.*, pp. 1–11, 2021.

[11] S. I. Mushfique, A. Alsharoa, and M. Yuksel, "MirrorVLC: Optimal Mirror Placement for Multielement VLC Networks," *IEEE Trans. Wirel. Commun*., vol. 21, no. 11, pp. 10050–10064, 2022.

[12] B. L. Xu, Y. J. Li, W. L. Zhou, H. J. Zhan, J. Y. Lu, and Y. H. Tong, "Application of the Full-Width-at-Half-Maximum Image Segmentation Method to Analyse Retinal Vascular Changes in Patients with Diabetic Retinopathy," vol. 2022, 2022.

[13] B. Turan, O. Narmanlioglu, O. N. Koc, E. Kar, S. Coleri, and M. Uysal, "Measurement Based Non-Line-Of-Sight Vehicular Visible Light Communication Channel Characterization," *IEEE Trans. Veh. Technol*., pp. 1–6, 2022.

[14] G. S. Rao, "ROLE OF CONSERVATIVE LAWS IN IDENTIFYING THE COSMOS AS A SYSTEM OF SYMMETRICAL UNITY," no. 4, pp. 1–8, 2020.

[15] D. Milovancev, T. Jukic, N. Vokic, P. Brandl, B. Steindl, and H. Zimmermann, "VLC Using 800-μm Diameter APD Receiver Integrated in Standard 0.35-μm BiCMOS Technology," *IEEE Photonics J*., vol. 13, no. 1, 2021.

[16] S. N. Ismail and M. H. Salih, "A review of visible light communication (VLC) technology," *AIP Conf. Proc.*, vol. 2213, no. March, 2020.

[17] G. A. Mapunda, R. Ramogomana, L. Marata, B. Basutli, A. S. Khan, and J. M. Chuma, "Indoor Visible Light Communication: A Tutorial and Survey," *Wirel. Commun. Mob. Comput*., vol. 2020, 2020.

[18] M. M. Fouda, S. Hashima, S. Sakib, Z. M. Fadlullah, K. Hatano, and X. Shen, "Optimal Channel Selection in Hybrid RF/VLC Networks: A Multi-Armed Bandit Approach," *IEEE Trans*. Veh. Technol., vol. 71, no. 6, pp. 6853–6858, 2022.

[19] Z. Ghassemlooy, W. Popoola, and S. Rajbhandari, *Optical Wireless Communications*. 2019.

[20] F. Aghaei, H. B. Eldeeb, L. Bariah, S. Muhaidat, and M. Uysal, "Comparative Characterization of Indoor VLC and MMW Communications via Ray Tracing Simulations,*"IEEE Access*, vol. 11, no. August, pp. 90345–90357, 2023.

Optimization of LED Array and FOV Configurations for Indoor Visible Light Communication System

Faathir Alfath Risdarmawan
Dept. of Electrical Engineering
Universitas Al Azhar Indonesia
Jakarta, Indonesia
faathiralfath1303@gmail.com

Octarina Nur Samijayani
Dept. of Electrical Engineering
Universitas Al Azhar Indonesia
Jakarta, Indonesia
octarina.ns@uai.ac.id

Ary Syahriar
Dept. of Electrical Engineering
Universitas Al Azhar Indonesia
Jakarta, Indonesia
ary@uai.ac.id

Isma Artyani
Dept. of Electrical Engineering
Universitas Al Azhar Indonesia
Jakarta, Indonesia
ismartyani@gmail.com

Arman Haditiansyah
Dept. of Electrical Engineering
Universitas Al Azhar Indonesia
Jakarta, Indonesia
armanhaditiansyah@gmail.com

Nida Salsabila
Dept. of Electrical Engineering
Universitas Al Azhar Indonesia
Jakarta, Indonesia
nidasalsabila423@gmail.com

***Abstract*—This paper introduces a method of modeling indoor wireless optical communication channels using MATLAB software. The focus of the research is to simulate the characteristics of the communication system between the transmitter and receiver in an indoor environment using the line-of-sight (LOS) propagation principle. The simulation results include the received power distribution in various configurations of the number of LEDs and variations in the field of view (FOV) of the receiver. Simulations were performed with detailed optical parameter settings, resulting in visualization of the power distribution in graphs and tables. The main findings show that increasing the number of LEDs can improve the even power distribution and expand the communication coverage, while FOV variations affect the intensity and quality of the received signal. This research contributes to the optimization of Visible Light Communication (VLC) systems to improve the reliability and efficiency of indoor data transmission.**

***Index Terms*—FOV, OWC, VLC, Optic, Technology**

I. Introduction

The advent of Optical Wireless Communication (OWC) marks a significant milestone in the evolution of communication technologies. As the digital era demands ever-increasing data rates and secure communication channels, OWC has emerged as a vital technology, leveraging the unique properties of light to transmit data. Unlike traditional radio frequency (RF) communication systems, OWC offers the advantages of higher bandwidth, enhanced security, and immunity to electromagnetic interference. This rapid technological progress has paved the way for innovative applications and widespread adoption of OWC in various sectors [1].

OWC systems utilize light, typically in the visible, infrared, or ultraviolet spectrum, as a medium for data transmission. These systems can be broadly categorized into three types based on their operational spectrum and applications: Visible Light Communication (VLC), Infrared Communication, and Ultraviolet Communication. VLC uses the visible light spectrum (400-700 nm) and is particularly suitable for indoor environments where LED lighting can simultaneously provide. illumination and communication. Infrared communication, using wavelengths from 700 nm to 1 mm, is often employed in short-range, point-to-point applications such as remote controls. Ultraviolet communication, operating in the 10 nm to 400 nm range, is used in specialized applications requiring secure, non-line-of-sight (NLOS) communication [2].

The versatility of OWC systems allows for a wide range of applications, particularly in indoor environments where they support high-speed data transmission for WLANs, smart lighting, and device-to-device communication. Channel modelling is crucial for optimizing OWC systems, as it simulates the communication channel characteristics, accounting for factors like optical attenuation, noise, and environmental conditions. Indoor environments present unique challenges such as reflections, scattering, and absorption by walls and objects, necessitating accurate modelling [3].

Field of view (FOV) and optical power management are integral aspects in the deployment and operation of Visible Light Communication (VLC) systems within indoor environments. FOV defines the angular range within which VLC receivers can effectively receive optical signals from transmitters [4]. In indoor settings, where VLC systems are deployed alongside various light sources and obstacles, the FOV plays a crucial role in ensuring reliable communication links. A wider FOV allows receivers to capture signals over a broader area, accommodating movements and positional adjustments of devices without sacrificing connectivity [5]. However, the trade-off involves managing optical power levels to maintain signal integrity and avoid interference with neighbouring VLC systems or ambient light sources [6].

979-8-3315-1921-6/24/$31.00 ©2024 IEEE

Optical power management is equally critical as it directly impacts the signal strength and range of VLC systems. Balancing transmit power levels is essential to achieve optimal coverage while minimizing potential interference and ensuring efficient data transmission rates for WLANs, precise control of smart lighting systems, and seamless device-to-device communication [7]. Moreover, effective channel modelling, which considers factors like optical attenuation, noise characteristics, and environmental conditions specific to indoor spaces, is essential for accurately predicting signal propagation and optimizing VLC system performance [8]. Together, FOV and power management strategies enable VLC systems to overcome the challenges posed by indoor environments, such as reflections, scattering from surfaces, and absorption by walls and objects [9]. By fine-tuning FOV parameters and carefully managing optical power levels, VLC systems can maximize their reliability, adaptability, and effectiveness in supporting a wide array of indoor applications, ultimately enhancing user experience and operational efficiency in modern indoor communication infrastructures [10].

This paper aims to introduce a method for modelling optical wireless communication channels using MATLAB software. By employing a mathematical approach, the study allows for a thorough analysis of the performance of optical wireless communication systems. The primary focus is on modelling channels for indoor optical wireless communication scenarios. The paper will provide a detailed explanation of the MATLAB simulation results, analysing the application of mathematical model simulations in indoor conditions to understand channel modelling performance [11]. Additionally, relevant optical parameters will be presented in tabular form, serving as a basis for comparing system performance across various scenarios and conditions. This research aspires to contribute significantly to the development and deeper understanding of optical wireless communications [12].

II. Method

This research utilized laptop hardware components and MATLAB software, specifically employing the MATLAB programming language for mathematical modelling to achieve accurate simulation results with optical parameters tailored for indoor environments. The MATLAB simulation focused on detailed modelling and analysis of indoor optical wireless communication channels, providing comprehensive insights into their performance. In the methodology section, the study began by defining and exploring critical parameters such as field of view (FOV) and optical power within indoor Visible Light Communication (VLC) systems [13]. FOV, crucial for determining the angular range within which receivers effectively detect transmitted optical signals, was systematically varied and analyzed using MATLAB simulations. This investigation aimed to assess how different FOV settings impact signal coverage, reliability, and resilience against indoor environmental challenges like reflections and signal blockages caused by obstacles [14]. Additionally, the research methodically examined the management of optical power levels in VLC systems to optimize signal strength and integrity across varying distances within indoor environments [15]. This approach facilitated the evaluation of power efficiency and the determination of optimal settings to achieve robust data transmission rates essential for WLANs, smart lighting, and device-to-device communication [16].

A. Literature Review

In indoor optical wireless communication systems, LEDs are typically used as light sources, while photodetectors serve as receivers. The LED acts as the transmitter, and the photodetector captures the optical signal, forwarding it to the receiver. The photodetector is responsible for converting the incoming optical signal (whether analogue or digital) into an electrical signal, generally in the form of current or voltage [17].

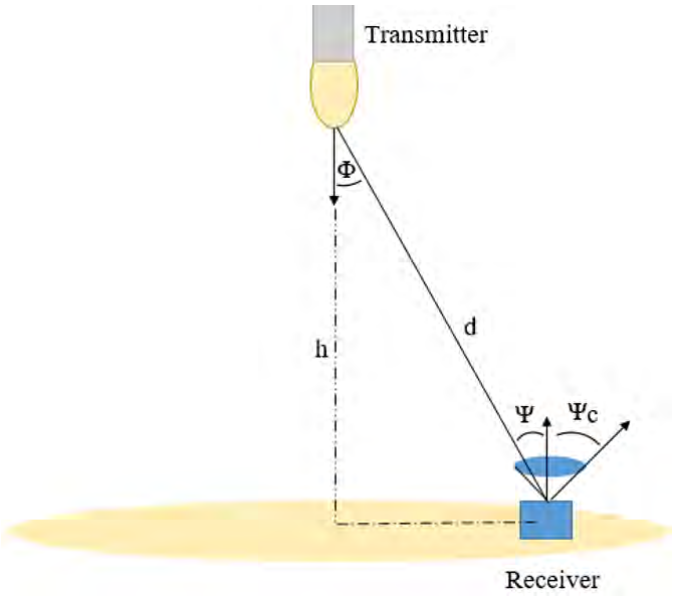

Fig. 1. Geometry of LOS and FOV Propagation Model [design and implementation]] [18].

Fig. 1 illustrates the geometry modelling of optical communication transmission paths utilizing the line of sight (LOS) and FOV methods. LOS represents a direct and unobstructed transmission path between the transmitter and receiver, indicating that the transmission path must remain free of obstacles to ensure linear propagation of optical signals.

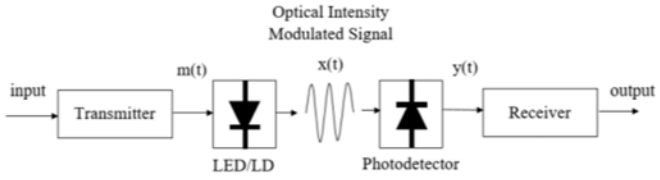

Fig. 2. Block diagram transmission.

Fig. 2 depicts the block diagram of a direct transmission line. Here, the transmitter emits an optical signal as modulated

light. This modulated signal travels linearly through the medium to the receiver, which uses a photodetector to capture it. The photodetector then converts the optical signal into an electrical signal for further data processing [19].

B. Mathematical Model

To accurately characterize and optimize the performance of indoor optical wireless communication (OWC) systems, it is essential to develop a robust mathematical model. This model will account for the unique propagation characteristics and challenges encountered in indoor environments, including reflections, scattering, and absorption by walls and objects.

A mathematical approach to measuring LOS propagation uses the Lambertian model,

$$H_A = \frac{(m+1)A_{\text{det}}\cos(\Phi_A)^{(m+1)}}{2\pi d^2} \tag{1}$$

Where H_A is the channel gain for the light source based on the Lambertian model, m is the Lambertian order of emission with $m = \frac{-\ln(2)}{\ln\cos\Phi_{1/2}}$ and $\cos\Phi_{1/2}$ is the semi-angle at half power. $\cos\Phi_A$ is the angle between the straight line from the light source to the receiving point and the normal to the receiving plane with $\cos\Phi_A = \frac{h}{d}$, Ψ_c : Reception angle (Field of View, FOV) This is the maximum viewing angle of the receiver.

$$d = \sqrt{(X_r - X_t)^2 + (Y_r - Y_t)^2 + h^2} \tag{2}$$

D is the distance from the light source to the receiving point that can be positioned in the vector plane. Where XR and YR are the positions on the receiving plane, XT and YT are the light source positions on the emitting plane, and h is the distance between the transmitting plane and the receiving plane.

$$P_{rec} = P_{total}.H_A.T_sG_{con} \tag{3}$$

Where P_{rec} is the power received at the receiver from the light source, P_{total} is the optical power emitted by the source, T_s is the optical filter gain, and G_{con} is the gain of the optical concentrator with $G_{con} = \frac{n}{\sin\theta_r}$, n is the refractive index and θ_r is the angle field of view of the receiver [20].

C. parameters of the system

Table I presents the details of the simulated space used in this study to analyze the Visible Light Communication (VLC) system in the context of indoor Optical Wireless Communication (OWC). With room dimensions of 5 x 5 x 3 cubic meters, this study sets the distance between the source and receiver planes at 2.15 meters, as well as the position of the transmitter placed at coordinate (0,0). These parameters were designed to simulate realistic environmental conditions, allowing for an accurate evaluation of the effects of LED and angle-of-view (FOV) variations on signal receivability in the specified room configuration [21].

TABLE I
ROOM SPACE SIMULATIONS

No	Space Simulation	
1	Room dimension	$5 \times 5 \times 3\,\text{m}^3$
2	Distance between source and receiver plane	$2.15\,\text{m}$
3	Transmitter position	$(0, 0)$

Table II provides details of the optical parameters used in the simulation of the Visible Light Communication (VLC) system for this study. These parameters include a transmitter semi-power angle of 70 degrees, an emitted optical power of 20 dBm, and a detector physical area of 0.0001 square meters. In addition, the table also lists the optical filter gain value of 1, the refractive index of 1.5, and the receiver field of view of 60 degrees. Each of these parameters plays an important role in determining the efficiency and performance of the VLC system, so a thorough understanding of these parameters is crucial for analysis and optimization in OWC applications.

TABLE II
OPTICS PARAMETER

No	Optics Parameter	Value
1	semi-angle	$70°$
2	Total	640 dBm
3	Detector	(0.0001)
4	Gain of	1
5	Refractive	1.5
6	Angle field	$20°, 40°, 60°, 80°$

The combination of information from Tabel I and Tabel II provides a comprehensive overview of the settings and parameters used in the simulation of the Visible Light Communication (VLC) system for indoor Optical Wireless Communication (OWC) applications. Table I specifies the dimensions of the simulation room which include a room size of $5\times5\times3\,\text{m}^3$, a distance between the source and receiver of 2.15 meters, and a transmitter position located at coordinate (0,0). Meanwhile, Table II details key optical parameters such as a transmitter semi-power angle of 70 degrees, a transmission optical power of 640 dBm, a detector physical area of 0.0001 square meters, an optical filter gain of 1, a refractive index of 1.5, and a receiver viewing angle of 60 degrees. The combined data allows for an in-depth evaluation of how the room configuration and optical parameters affect the performance of a VLC system, especially in terms of signal-receiving power and communication efficiency in an indoor environment.

III. RESULT AND DISCUSSION

The simulation models optical-electrical parameters and room dimensions to analyze the distribution of received power within a 5m x 5m x 3m room. It begins by defining these parameters and mapping LED positions using a mesh grid, with the receiver plane gridded for detailed analysis. For Source One, the simulation calculates the distance and angle vectors to the receiver plane, and the channel DC gain, then computes the received power considering transmitted power, channel gain, optical filter gain, and optical concentrator gain,

setting it to zero for angles beyond the FOV. The received power is mirrored across various axes for symmetry, converted into decibels (dBm), and visualized with labelled axes and a color bar. This provides insights into the VLC system's effectiveness and efficiency, highlighting the importance of factors like LED layout, room size, and receiver specifications for optimal performance.

A. Variation in the number of LEDs

Variations in the number of LEDs in indoor VLC systems significantly influence their performance and coverage capabilities. The number of LEDs determines how effectively the system can illuminate spaces and transmit data, impacting signal distribution and intensity. This exploration is crucial for optimizing VLC systems to meet specific indoor communication needs, such as ensuring robust WLAN connectivity, precise smart lighting control, and seamless device-to-device communication. Understanding these variations is essential for designing efficient VLC infrastructures that meet the demands of modern indoor wireless communication requirements. Furthermore, optimizing the number of LEDs can enhance energy efficiency and reduce operational costs by minimizing power.

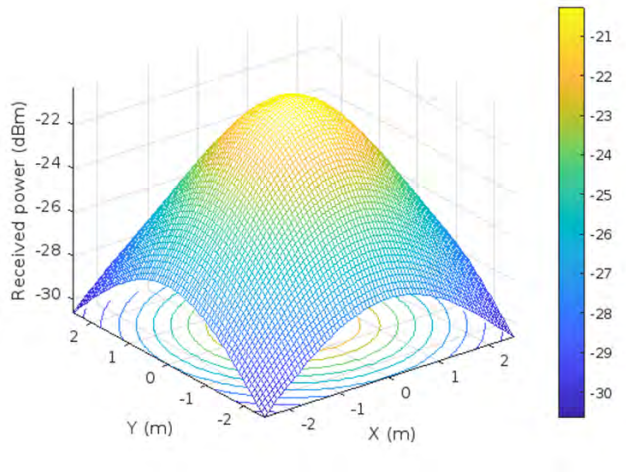

Fig. 3. Received Power with one LED.

Figure 3 describes the optical receiving power distribution showing that the highest receiving power is around the LED and decreases gradually with distance, indicating that the LED emits light directionally with the highest intensity in the direct beam direction. The communication range of indoor VLC with a single LED can be estimated from the optical receiving power which is still above -30 to -40 dBm at a distance of about 2 m from the LED and its maximum power at -21 dBm indicating that the communication range can reach about 2 m. In addition, the optical received power distribution also shows the influence of reflections from walls and other surfaces in the room, which can be seen from the interference pattern in the graph. The effect of these reflections can increase the optical receiving power in some locations but can also decrease it in other locations.

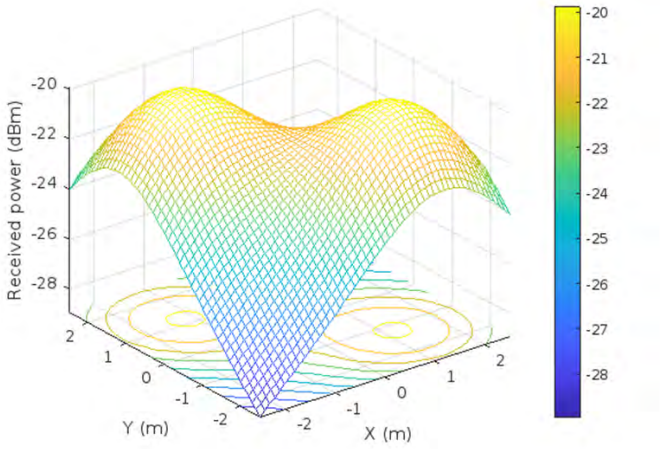

Fig. 4. Received Power with two LED.

Figure 4 describes the optical received power distribution showing that the highest received power is in the vicinity of the LED and decreases gradually with distance, indicating that the LED emits light directionally with the highest intensity in the direct beam direction. The communication range of indoor VLC with 2 LEDs can be estimated from the optical receiving power, which remains above -28 dBm at a distance of about 2 meters from the LEDs, with a maximum power of -20 dBm, indicating that the communication range can reach about 2 meters. In addition, the optical received power distribution also shows the influence of reflections from walls and other surfaces in the room, evident from the interference pattern in the graph. These reflections can increase the optical receiving power in some locations but can also decrease it in others, causing variations in signal strength throughout the area. The presence of reflective surfaces plays a crucial role in determining the quality and consistency of the signal, affecting both the reliability and efficiency of data transmission. Compared to the image of the indoor VLC with 1 LED, this image shows that the optical received power distribution with 2 LEDs is more even, which indicates that 2 LEDs can increase the coverage area of the indoor VLC communication. The use of multiple LEDs not only enhances coverage but also reduces the likelihood of dead zones, providing more stable and comprehensive communication capabilities across the indoor environment. This setup demonstrates the potential for scalable and adaptable VLC systems that can be tailored to specific spatial configurations and communication needs.

Figure 5 describes the optical received power distribution showing that the highest received power is in the vicinity of the LEDs and decreases with distance, indicating a directional beam of LED light with the highest intensity in the direct direction. The communication range of indoor VLC with 3 LEDs can reach about 2 metres, as seen from the optical receiving power that is still above -26 dBm at that distance and the maximum power generated is -18 dBm. The effect of

reflections from walls and other surfaces causes interference patterns, which can increase or decrease the optical receiving power in some locations. Compared to 1 and 2 LEDs, the use of 3 LEDs results in more even power distribution and wider communication coverage, improving the performance of indoor VLC systems.

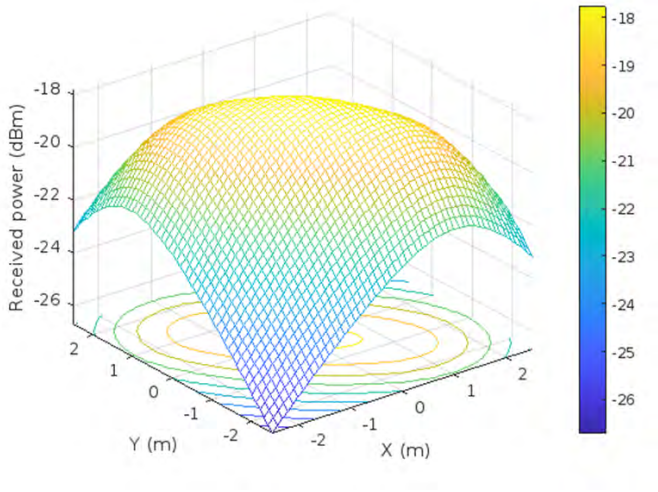

Fig. 5. Received Power with three LED.

The yellow area indicates the maximum optical power that is transmitted and then distributed throughout the room with the beam angle limit extending until the blue area indicates the lowest optical power obtained by the receiver. As the distance between the transmitter and receiver gets closer, the optical signal does not need to travel such a long distance, minimizing the signal attenuation due to the long distance. However, too close a distance between the transmitter and receiver can cause signal saturation. Saturation occurs when the signal power received by the receiver is too high, causing distortion and reducing signal quality.

B. Variation of FOV (Field of View) Values

The setting and optimization of optical parameters a crucial aspect in the design of visible light-based communication (VLC) systems. One of the parameters that greatly affects the performance of these systems is the Field of View (FOV) of the receiver. The FOV determines how wide the viewing angle of the receiver is in capturing the optical signal emitted by the LED. Variations in the FOV can significantly affect the received power intensity and the quality of the received signal. Therefore, it is important to understand how FOV changes affect the performance of VLC communication systems in various scenarios. This study aims to explore the impact of FOV variations on the system performance, by measuring the received power and other parameters for various receiver viewpoints.

From Figure 6 The optical received power distribution shows that the highest intensity is focused around the LED and decreases with distance, indicating a directional beam from the LED. The indoor VLC communication range using 1 LED and

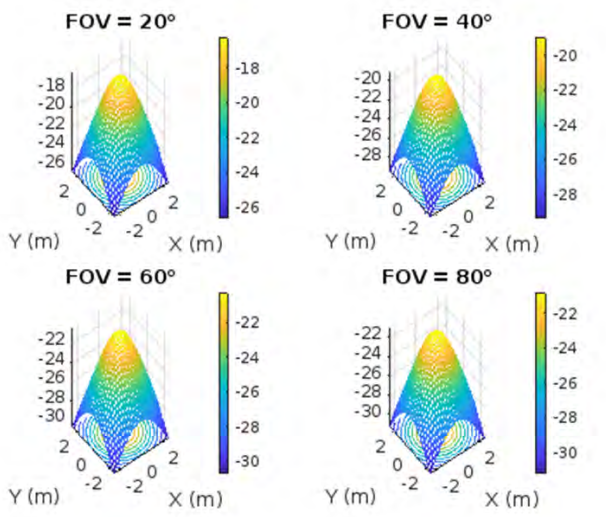

Fig. 6. FOV value with one LED.

various FOV values varies, with the widest range at 20° FOV and the smallest at 80° FOV. A smaller FOV results in a more focused distribution of received power, while a larger FOV results in a more dispersed distribution. The distribution pattern of optical receiving power in visible light communication (VLC) systems also reflects the influence of reflections from walls and other surfaces, which can increase or decrease the optical receiving power at certain locations. These variations affect the quality and stability of indoor VLC signals, as reflections can cause complex interference depending on their position and angle. In some cases, reflections can enhance the signal, while in others, they can lead to undesirable signal cancellation. The application of more than one LED can expand the communication coverage area and improve the reliability of the VLC system in the face of challenges from indoor environments full of reflections and shadows. Thus, optimizing optical receiving power distribution and handling reflections are key to improving the efficiency and performance of indoor VLC communications. This involves strategies such as strategic placement of LEDs, using signal coding techniques to mitigate interference effects, and designing room layouts that account for reflective factors. This approach can help maximize data transmission and ensure a more stable and reliable connection under various environmental conditions.

From Figure 7, the highest optical received power distribution is focused around the LED and decreases gradually with distance, indicating a directional beam with the highest intensity directly from the direction of the LED. This pattern reflects the inherent nature of LED emissions, where the majority of the light is concentrated in the forward direction. The concentrated power near the LED ensures strong signal transmission nearby, making it crucial for applications requiring high precision and intensity.

The indoor VLC communication range using 2 LEDs and varying FOV values shows variation, with the widest range

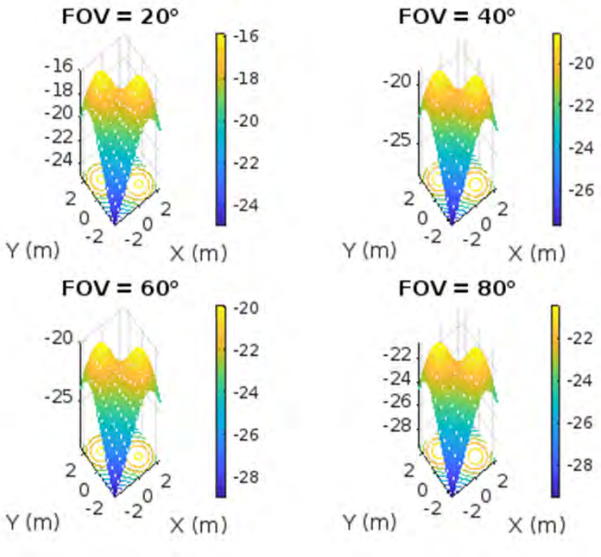

Fig. 7. FOV value with two LED.

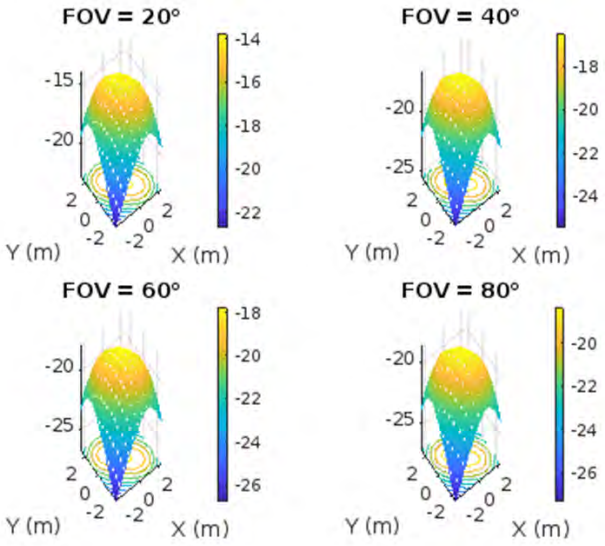

Fig. 8. FOV value with three LED.

at 20° FOV and the narrowest at 80° FOV. Different FOV values result in different received power distribution patterns, where a smaller FOV (20°) results in a more concentrated distribution, while a larger FOV (80°) results in a more dispersed distribution. This variation in distribution patterns highlights the importance of selecting appropriate FOV settings based on specific communication needs. A narrower FOV is advantageous for focused communication in specific areas, while a wider FOV can cover larger spaces with a more diffuse signal, balancing the trade-offs between range and intensity.

Reflection effects from walls and other surfaces create interference patterns that may increase or decrease the receiving power at some locations. Compared to using 1 LED, the received power distribution with 2 LEDs is more even and has a wider communication range, increasing the coverage area of indoor VLC communications. The presence of multiple LEDs also mitigates shadowing effects and provides more robust coverage in complex indoor environments. As such, this technology offers flexibility in setting up lighting patterns and receiving power distribution to optimize communication performance in indoor VLC applications. The adaptability of VLC systems to different spatial configurations and lighting requirements makes them a versatile option for modern wireless communication.

Figure 8 explains that the highest optical received power distribution is around the LED and decreases with distance, indicating a directional beam of light with the highest intensity in the direct direction. The communication range of an indoor VLC with 3 LEDs varies depending on the FOV value; an FOV of 20° results in the widest communication range, while an FOV of 80° is the narrowest. A small FOV (20°) results in a more concentrated distribution of received power, while a large FOV (80°) is more dispersed. The effect of reflections from walls and other surfaces is seen in the interference patterns that can increase or decrease the optical receiving power at various locations. Compared to 1 and 2 LEDs, the optical receiving power distribution with 3 LEDs is more even, has a wider range, and higher receiving power, indicating better communication coverage and superior performance. The optical receiving power values from the images range from -30 dBm to -40 dBm, with the highest values observed at 20° FOV and proximity to the LEDs, while the minimum values show no significant disturbances affecting the amplitude after the filtering process. Additionally, the frequency of the signal appears constant over the displayed time range, indicating no significant frequency changes due to the filtering process. The smooth signal curve, free from significant noise, demonstrates that the filter has effectively attenuated any potential noise in the original signal.

Indoor Visible Light Communication (VLC) systems use LEDs for both illumination and data transmission, with performance influenced by the number of LEDs and the receiver's Field of View (FOV). The number of LEDs affects light distribution and signal strength, while the FOV impacts the angle at which the receiver detects the light. Analyzing how power received varies with FOV for different LED configurations is essential for optimizing VLC system design. The graph above shows this relationship for three different LED setups (LED1, LED2, and LED3).

Figure 9 shows the relationship between Field of View (FOV) and Power received in an indoor Visible Light Communication (VLC) system with a varying number of LEDs. The graph shows three different LEDs (LED1, LED2, and LED3) with their measured power receive values at various FOV values (20, 40, 60, and 80 degrees). In general, the receiving power decreases as the FOV increases for all three LEDs. LED1 has the lowest receiving power among the three LEDs, while LED3 has a relatively higher receiving power at almost

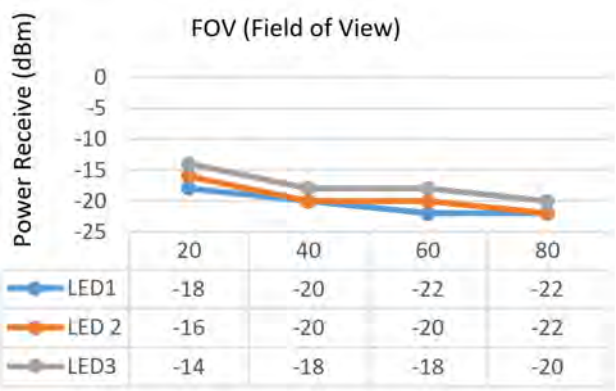

Fig. 9. Received power from varyi.ng the number of LEDs and FOV values.

all FOV values. This shows that larger viewing angles tend to reduce the received signal intensity, which could be due to the wider dispersion of light and reduced signal concentration at larger angles. Variations in the number of LEDs and their optical characteristics, such as light intensity and angle of spread, greatly affect the performance of the VLC system in terms of power reception, with LED3 performing better than LED1 and LED2 under the conditions tested.

IV. Conclusion

This paper examines indoor wireless optical communication channel models using MATLAB, focusing on Lambertian models to predict the performance of Optical Wireless Communication (OWC) systems. OWC technology, particularly Visible Light Communication (VLC), offers advantages over radio frequency (RF) systems such as higher bandwidth, better security, and immunity to electromagnetic interference, making it particularly suitable for indoor applications. By utilizing LEDs as light emitters, VLC enables the use of existing light sources in the room for both communication and illumination. Simulation results show that increasing the number of LEDs and varying the receiver's angle of view (FOV) have a significant impact on the received power distribution and communication coverage; the more LEDs used, the more even the power distribution and the wider the communication coverage, while varying the FOV affects signal intensity and quality. In a VLC system, FOV variation allows adjustment of the reception range to ensure communication reliability over a large area and reduce the area without signal. Thus, modeling indoor OWC channels using MATLAB provides valuable insights for VLC system optimization, highlighting the importance of optical parameter settings in improving the performance and effectiveness of light-based communications in indoor environments, while opening up opportunities for further innovation in this field.

References

[1] H. Haas, J. Elmirghani, I. White, and H. Haas, "Optical wireless communication Subject Areas: Author for correspondence," 2020.

[2] I. B. Djordjevic, Advanced Optical and Wireless Communications Systems: Second Edition. 2022.

[3] A. Al-Kinani, C. X. Wang, L. Zhou, and W. Zhang, "Optical wireless communication channel measurements and models," IEEE Commun. Surv. Tutorials, vol. 20, no. 3, pp. 1939–1962, 2018, doi: 10.1109/COMST.2018.2838096.

[4] A. Singh, A. Srivastava, and V. A. Bohara, "Optimum LED semiangle and the receiver FOV selection for Indoor VLC System with Human Blockages," pp. 1–7.

[5] A. Singh, A. Srivastava, V. A. Bohara, and A. K. Jagadeesan, "Performance of Indoor VLC System under Random Placement of LEDs with Nonimaging and Imaging Receiver," IEEE Syst. J., vol. 16, no. 1, pp. 868–879, 2022, doi: 10.1109/JSYST.2020.3019823.

[6] A. G. A. Al-Sakkaf and M. Morales-Cespedes, "Interference Management for VLC Indoor Systems Based on Overlapping Field-of-View Angle Diversity Receivers," IEEE Access, vol. 12, no. April, pp. 51431–51449, 2024, doi: 10.1109/ACCESS.2024.3381968.

[7] S. M. El-Garhy, H. Fayed, and M. H. Aly, "Power distribution and BER in indoor VLC with PPM based modulation schemes: a comparative study," Opt. Quantum Electron., vol. 51, no. 8, 2019, doi: 10.1007/s11082-019-1970-1.

[8] F. Miramirkhani and M. Uysal, Channel modelling for indoor visible light communications, vol. 378, no. 2169. 2020.

[9] D. N. Anwar, A. Srivastava, and V. A. Bohara, "Adaptive channel estimation in VLC for dynamic indoor environment," Int. Conf. Transparent Opt. Networks, vol. 2019-July, no. 0, pp. 1–5, 2019, doi: 10.1109/ICTON.2019.8840284.

[10] I. Abdalla, M. B. Rahaim, and T. D. C. Little, "Interference Mitigation through User Association and Receiver Field of View Optimization in a Multi-User Indoor Hybrid RF/VLC Illuminance-Constrained Network," IEEE Access, vol. 8, pp. 228779–228797, 2020, doi: 10.1109/ACCESS.2020.3045929.

[11] A. M. Ramirez-Aguilera, J. M. Luna-Rivera, V. Guerra, J. Rabadan, R. Perez-Jimenez, and F. J. Lopez-Hernandez, "A Review of Indoor Channel Modeling Techniques for Visible Light Communications," Proc. - 2018 10th IEEE Latin-American Conf. Commun. LATINCOM 2018, pp. 1–6, 2018, doi: 10.1109/LATINCOM.2018.8613205.

[12] A. Kumar and S. K. Ghorai, "Performance of MIMO-VLC System for Different Radiation Patterns of LED in Indoor Optical Wireless Communication System," Int. Symp. Adv. Networks Telecommun. Syst. ANTS, vol. 2019-December, pp. 2–6, 2019, doi: 10.1109/ANTS47819.2019.9118062.

[13] S. Chatterjee and B. Roy, "Design, development and practical realization of a VLC supportive indoor lighting system," Light Eng., vol. 28, no. 3, pp. 87–97, 2020, doi: 10.33383/2019-048.

[14] I. Abdalla, M. Rahaim, and T. Little, "Impact of Receiver FOV and Orientation on Dense Optical Networks," Proc. - IEEE Glob. Commun. Conf. GLOBECOM, pp. 1–6, 2018, doi: 10.1109/GLOCOM.2018.8647842.

[15] D. T. Nguyen, S. Park, Y. Chae, and Y. Park, "VLC/OCC Hybrid Optical Wireless Systems for Versatile Indoor Applications," IEEE Access, vol. 7, pp. 22371–22376, 2019, doi: 10.1109/ACCESS.2019.2898423.

[16] Y. Wang et al., "Impact of LED transmitters' radiation pattern on received power distribution in a generalized indoor VLC system," Opt. Express, vol. 25, no. 19, p. 22805, 2017, doi: 10.1364/oe.25.022805.

[17] O. Alsulami, A. T. Hussein, M. T. Alresheedi, and J. M. H. Elmirghani, "Optical Wireless Communication Systems, A Survey," pp. 1–22, 2018.

[18] Z. Ghassemlooy, W. Popoola, and S. Rajbhandari, Optical Wireless Communications. 2019.

[19] C. Jenila and R. K. Jeyachitra, "Green indoor optical wireless communication systems: Pathway towards pervasive deployment," Digit. Commun. Networks, vol. 7, no. 3, pp. 410–444, 2021, doi: 10.1016/j.dcan.2020.09.004.

[20] K. Wang, Indoor Infrared Optical Wireless Communications Systems and Integration. Taylor & Francis Group, LLC, 2020.

[21] K. Wang, T. Song, S. Kandeepan, H. Li, and K. Alameh, "Indoor optical wireless communication system with continuous and simultaneous positioning," Opt. Express, vol. 29, no. 3, p. 4582, 2021, doi: 10.1364/oe.409395.

Effect of Temperature Using Silica, POF, and Fluoride Glasses Materials in Optical Fiber on Refractive Index and Attenuation

Nida Salsabila
Dept. Electrical Engineering
University of Al-Azhar Indonesia
Jakarta, Indonesia
nidasalsabila423@gmail.com

Ary Syahriar
Dept. Electrical Engineering
University of Al-Azhar Indonesia
Jakarta, Indonesia
ary@uai.ac.id

Octarina Nur Samijayani
Dept. Electrical Engineering
University of Al-Azhar Indonesia
Jakarta, Indonesia
octarina.nur@uai.ac.id

Ivan Adhi Pramana
Dept. Electrical Engineering
University of Al-Azhar Indonesia
Jakarta, Indonesia
ivanadhiprmna@gmail.com

Arman Haditiansyah
Dept. Electrical Engineering
University of Al-Azhar Indonesia
Jakarta, Indonesia
armanhaditiansyah@gmail.com

Faathir Alfath Risdarmawan
Dept. Electrical Engineering
University of Al-Azhar Indonesia
Jakarta, Indonesia
faathiralfath1303@gmail.com

***Abstract*—This paper explores the effect of temperature on the refractive index and attenuation of various types of optical fibers, including Silica, POF (Polymer Optical Fiber), and Fluoride Glasses, at wavelengths of 850 nm, 1310 nm, and 1550 nm. Measurements were taken over a temperature range of 0°C to 300°C to understand how temperature variations affect the optical properties of each material. The results show that an increase in temperature leads to a small but consistent decrease in refractive index across all fiber optic types. Attenuation also increases with temperature, with a more significant increase in POF compared to Silica and Fluoride Glasses. These findings are important for optical applications where temperature stability is an important factor.**

***Index Terms*—Optical Fiber, Refractive Index, Attenuation, Temperature Effect, Silica, POF (Polymer Optical Fiber), Fluoride Glasses.**

I. Introduction

Optical fiber is a very important technology in modern communications, especially in high-speed data transmission. Optical fiber consists of a core that has a high refractive index, flanked by a protective layer (cladding) that has a lower refractive index. This structure allows light to propagate in the core by means of perfect reflection, so that light does not escape from the optical fiber [1].

The refractive index of a material greatly affects the refraction and reflection of light in an optical fiber. A high refractive index in the core allows light to propagate with high speed and stable intensity. This is very important in maintaining the quality of the signal transmitted through the optical fiber. Meanwhile, attenuation is a decrease in the intensity of the light signal propagating in the optical fiber [2]. Attenuation can be caused by several factors, such as absorption, scattering, and radiation loss. Low attenuation is essential to maintain signal quality and ensure that data can be received with high accuracy [3]. Refractive index and attenuation are very important in the design and use of optical fibers because they have a direct effect on data transmission performance. A high refractive index allows light to propagate with high efficiency, while low attenuation ensures that the signal does not lose intensity significantly during the journey [4].

979-8-3315-1921-6/24/$31.00 ©2024 IEEE

The effect of the variable temperature degree will affect the thermal expansion value of the optical component material, which affects the shape coefficient and position coefficient. While the shape coefficient depends on the value of the radius of curvature for the surface of the optical component and the position coefficient depends on the distance value of the object & image [5].

The change in the value of shape coefficient and position coefficient will be transferred indirectly to the focal length value as any change in the refractive index of the optical component material will change the value of shape coefficient and position coefficient. Therefore, the focal length can be calculated

from the following equation :

$$f = \frac{K}{n-1} \tag{1}$$

While K is geometric constant, any variable in refractive index will be a variable in focal length, so any variable in temperature it will be a variable in refractive index, therefore,

$$\frac{\partial f}{\partial n} = \frac{K}{(n-1)^2} \tag{2}$$

Ultimately, any change in the focal length value will be a change in the shape of the focal point which will cause defocus or a distorted image, while the change in focal length, as follows:

$$\Delta f = \frac{\Delta n K}{(n-1)^2} \tag{3}$$

The materials used in optical fibers to calculate the refractive index and tentation due to temperature changes are silica (silicone dioxide) and POF (polymer optical fiber), which Silica has a relatively small thermo-optical coefficient, about $-1 \times 10^{-5}/^{\circ}\mathrm{C}$. This means that the change in refractive index with temperature change is minimal. The refractive index in silica decreases slightly with increasing temperature, but this change is very small and insignificant in many practical applications, because of this very small change silica is the first choice in terms of applications that require high stability. Silica has a very low attenuation, about $0.2\,\mathrm{dB/km}$ at the communication wavelength (1550 nm), this attenuation increases slightly with increasing temperature due to slightly higher Rayleigh scattering [6]. Silica-based optical fiber technology is becoming popular in many industries because it can be used for communication on Earth and in space, as well as for measuring strain, temperature, and pressure [7].

Whereas POF usually uses Polymethyl Methacrylate (PMMA) or other polymeric materials as the core. POF has a larger thermo-optical coefficient, about $-3 \times 10^{-4}/^{\circ}\mathrm{C}$. The change in refractive index with temperature is more significant than that of silica. This means that the refractive index of POF decreases faster as the temperature increases, which can affect the quality of light transmission in the fiber. POF has higher attenuation, often around $1\,\mathrm{dB/km}$ or more at communication wavelengths. A rise in temperature can cause a greater increase in attenuation compared to silica, partly due to increased scattering and absorption [8] [9].

Then the refractive index of fluoride glasses is influenced by temperature. As the temperature increments, the molecular structure of the material can experience thermal extension, which in turn can change the density and interactions between molecules inside the material. Temperature coefficient of refractive index for fluoride glasses, the refractive index ordinarily includes a negative value, which suggests that the refractive index decreases as the temperature increases. Although the value of this coefficient can change depending on the particular composition of the fluoride glass utilized, the values are generally within the range of -1×10^{-5} to -3×10^{-5} per $^{\circ}\mathrm{C}$. Whereas the attenuation in fluoride glasses is low, especially within the infrared extend. The low scattering permits for high speed information transmission without significant signal distortion [10].

II. Methodology

A. The Importance of Temperature Effect and The Matlab Simulation

This research is important because by understanding the effect of temperature on refractive index and attenuation, fiber optic manufacturers can select or develop more stable materials for applications that require high reliability, such as telecommunications or temperature sensors. Three fiber optic materials that are already widely used in the industry, namely silica, fluoride glasses and POF, were compared[5]. Furthermore, the simulation-based approach allows the optical characteristics of the three materials to be studied without the need for direct experiments, which are more expensive, and these simulations also provide preliminary data that can form the basis for further testing, making it more efficient in terms of time and cost [9]. The results of this study are also useful for industries that require fiber stability in environments with high temperature fluctuations, such as oil and gas and medical. This information will also help optimize the performance of fiber optic sensors in harsh environments [13].

This research uses MATLAB simulation by creating a simulation model in MATLAB using optical parameters (such as refractive index and initial attenuation) and relevant gradients of change (such as change with temperature and wavelength). Then calculate and analyze the data by specifying the desired temperature range (0°C to 300°C) and wavelength. Simulate the changes in refractive index and attenuation at various temperatures and wavelengths for each fiber material (silica, POF, and fluoride) [14].

B. Materials of Fiber Optic

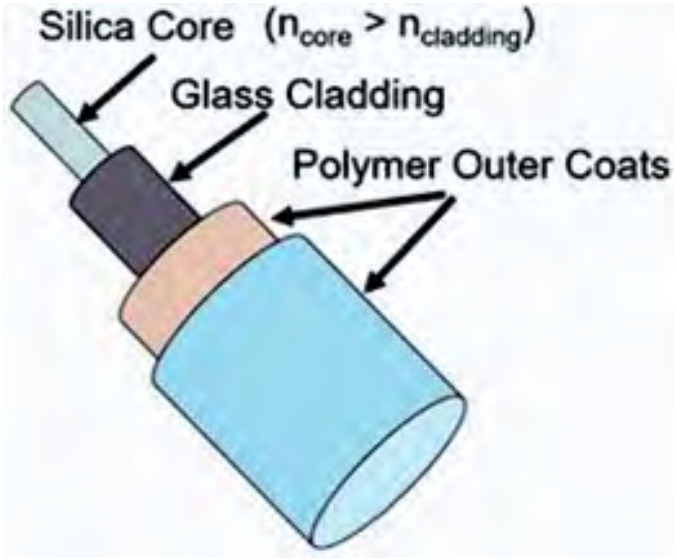

Fig. 1. Silica Fiber Optic

Figure 1 is fiber optic of silica that a special type of tube made of different layers. The inside layer (Silica Core) is like a path for light to travel through and is made of a material called silica. The middle layer (Glass Cladding) is like a shield that helps keep the light inside the tube. The outside layer (Polymer Outer Coats) is like a protective jacket that keeps the tube safe from getting damaged.

Figure 2 shows POF optical fiber consisting of a single-core sheath which is a single protective layer that protects the plastic optical fiber to keep it safe and stable. POF Fiber is the inside of this cable made of plastic optical fibers that can transmit data using light. The outer sheath is the outer layer of this cable protecting all parts of the cable from

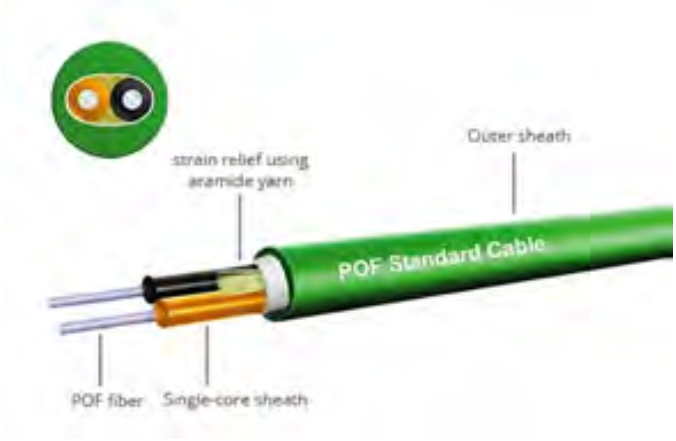

Fig. 2. POF Fiber Optic [11]

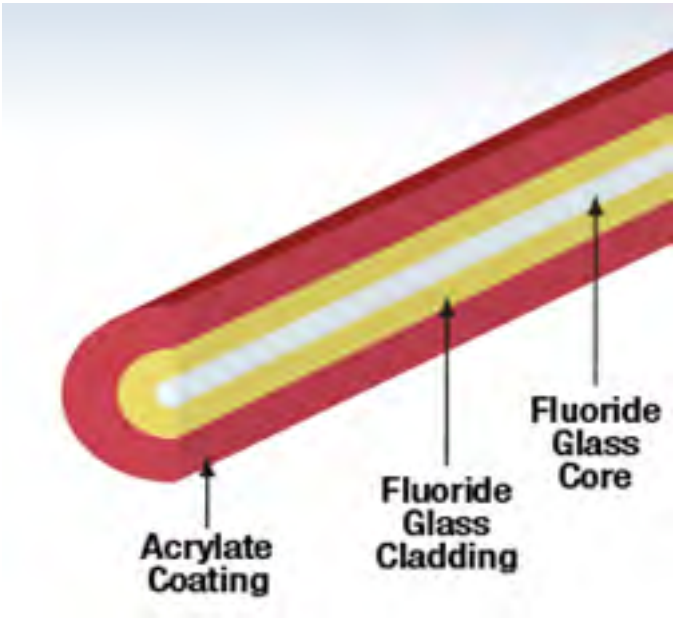

Fig. 3. Fluoride Glasses Fiber Optic [12]

physical damage, moisture, and other environmental factors. Strain relief using aramid yarn is an aramid rope used to provide additional strength to the cable and prevent damage due to pressure or pulling [15].

Figure 3. shows a fluoride glass optical fiber consisting of a Fluoride Glass Core: This is the centerpiece of an optical fiber made of fluoride glass. The core is the main medium for transmitting light, where optical signals pass through this core: This covering layer is also made of fluoride glass, which has a lower refractive index than the core. Its job is to keep light inside the core by reflecting light back into the core through a phenomenon called total internal reflection. An acrylate coating is like a protective outer layer made of a special material called acrylate. Its main task is to keep the optical fiber safe from damage [16].

C. Parameters of Refractive Index Based on Wavelength

The index of refraction of silica and fluoride glasses can be calculated using the Sell Meier Equation, which is a very accurate mathematical model for calculating the index of refraction of a material based on the wavelength of light. And this one is mathematical equation of sell Meier :

$$n^2(\lambda) = 1 + \sum_{i=1}^{3} \frac{B_i \lambda^2}{\lambda^2 - C_i} \tag{4}$$

$n(\lambda)$ is the refractive index at wavelength λ, B_i and C_i are Sellmeier constants for a particular material. λ is the wavelength of light in micrometers (μm). While the refractive index of POF can be calculated using Cauchy's Equation, which is an empirical model to describe how the refractive index of optical materials changes with wavelength. And here is the equation of Cauchy's:

$$n(\lambda) = A + \frac{B}{\lambda^2} + \frac{C}{\lambda^4} \tag{5}$$

$n(\lambda)$ is the refractive index at wavelength λ. A, B, and C are constants corresponding to the material used. λ is the wavelength of light in micrometers (μm).

TABLE I
PARAMETERS OF REFRACTIVE INDEX

Material	Equation	Constant	Value
Silica	Sell Meier Equation	B_1	0.6961663
		B_2	0.4079426
		B_3	0.8974794
		C_1	0.0684043^2
		C_2	0.1162414^2
		C_3	9.896161^2
POF (PMMA)	Cauchy's Equation	A	1.489
		B	0.005
		C	0
Fluoride Glasses (ZBLAN)	Sell Meier Equation	B_1	0.40351
		B_2	0.37825
		B_3	2.1161
		C_1	0.01913^2
		C_2	0.0464^2
		C_3	102

From the table parameters and every equation of Sell Meier and Cauchy we get the result refractive index vs wavelength in every material

TABLE II
RESULT OF REFRACTIVE INDEX VS WAVELENGTH

Wavelength (nm)	Refractive Index Silica	Refractive Index POF	Refractive Index Fluoride Glasses
650	1.4534	1.4961	1.3425
850	1.452	1.4934	1.34
1310	1.4479	1.4903	1.3368
1550	1.444	1.4891	1.3345
2000	1.4415	1.4883	1.331

The refractive index of Silica shows a slight decrease with increasing wavelength. This indicates that Silica has a relatively stable refractive index in the wavelength range tested

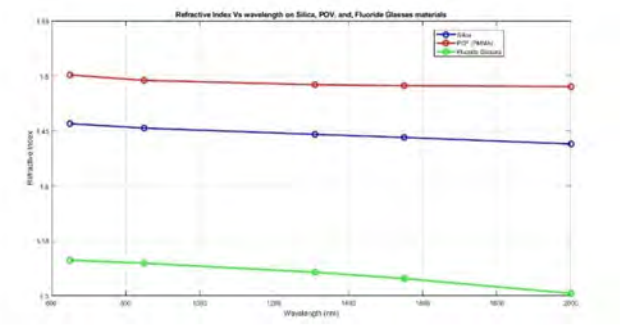

Fig. 4. Refractive index Vs Wavelength

(600-2000 nm) [11]. POF has an almost constant refractive index with a slight decrease. This indicates that POF is less sensitive to wavelength changes compared to Silica and Fluoride Glasses. Fluoride Glasses showed a more significant decrease in refractive index with increasing wavelength, indicating that this material is more sensitive to wavelength changes.

D. Parameters of Attenuation Based on Wavelength

Attenuation in fiber optics is the reduction of light signal power as it propagates through the fiber and is usually measured in dB/km (decibels per kilometer) [19]. Here's the mathematical equation for calculating attenuation:

$$\alpha = \frac{10}{L} \log_{10} \left(\frac{P_{\text{in}}}{P_{\text{out}}} \right) \tag{1}$$

α is the attenuation in dB/km, L is the length of the fiber in kilometers (km), P_{in} is the optical power going into the fiber, and P_{out} is the optical power exiting the fiber after a distance of L. So that from the equation we get the graphic bellows:

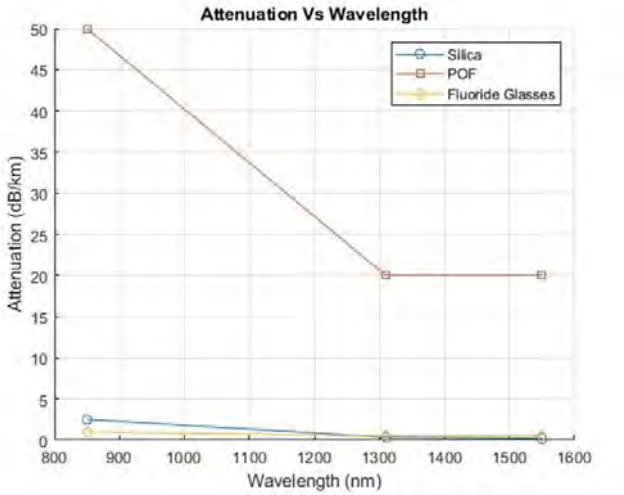

Fig. 5. Attenuation Vs Wavelength

Silica is the most efficient fiber optic material with the lowest attenuation over the entire wavelength range shown.

TABLE III
RESULT OF REFRACTIVE INDEX VS ATTENUATION

Materials	Wavelength (nm)	Attenuation (dB/km)
Silica	850	2.5
	1310	0.35
	1550	0.2
POF	850	50
	1310	20
	1550	20
Fluoride Glasses	850	1
	1310	0.5
	1550	0.5

POF (Plastic Optical Fiber) has much higher attenuation, especially at shorter wavelengths, but decreases with increasing wavelength. Fluoride Glasses perform well, with very low attenuation, close to that of Silica.

E. Parameter of Temperature

Temperature parameters for different types of materials, namely Silica, POF (Plastic Optical Fiber), and Fluoride Glasses. Divided into 3 temperature categories: 0-100°C, 101-200°C, and 201-300°C. This division is necessary to analyze in more detail the response or change in optical characteristics of each material at a certain temperature. The materials show heat different temperature ranges, which may have an effect on their light transmission properties or material stability in optical applications. This is useful for understanding how each material may perform at different temperatures, for example, in fiber optic applications in environments with high temperature fluctuations.

To find the effect of temperature on refractive index and attenuation on silica, POF, and fluoride glasses materials, there are 3 parameters: first parameter is from 0-100°C, and then from 100-200°C, and the last one from 200-300°C. And this one is the mathematical equation how to find refractive index based on temperature effect and wavelength:

$$n(T, \lambda) = n_0 + \frac{dn}{dT} \times T + \frac{dn}{d\lambda}(\lambda - \lambda_0) \tag{2}$$

Where n_0 is the initial refractive index. $\frac{dn}{dT}$ is the rate of change of refractive index with temperature. T is the temperature change from the reference temperature. $\frac{dn}{d\lambda}$ is the rate of change of refractive index with wavelength. λ_0 is the reference wavelength. And then this one is the mathematical equation on how to find attenuation based on temperature effect and wavelength:

$$A(T, \lambda) = A_0 + \frac{dA}{dT} \times T + \frac{dA}{d\lambda}(\lambda - \lambda_0) \tag{3}$$

A_0 is the initial attenuation. $\frac{dA}{dT}$ is the rate of change of attenuation with temperature. T is the temperature change from the reference temperature. $\frac{dA}{d\lambda}$ is the rate of change of attenuation with wavelength. λ_0 is the reference wavelength.

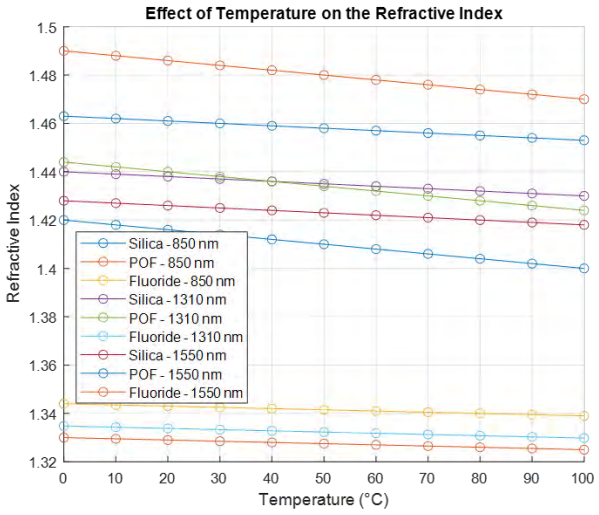

Fig. 6. A Graph of Temperature Effect 0-100°C on the Refractive Index

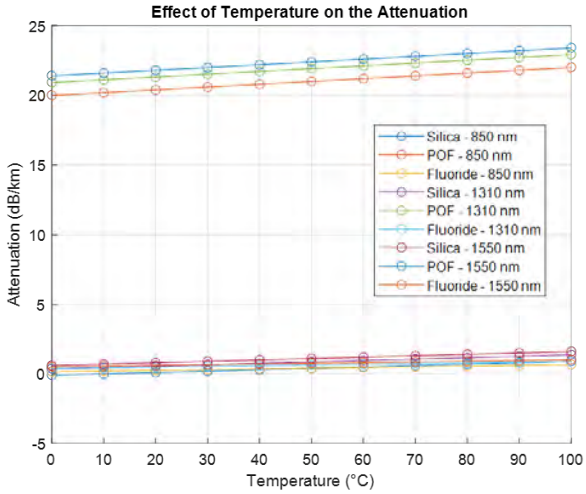

Fig. 7. A Graph of Temperature Effect 0-100°C on the Attenuation

III. Result and Discussion

A. *Effect of Temperature on Refractive Index and Attenuation on Temperature 0-100°C*

Fig. 6 show at temperatures 0-100°C, at a wavelength of 850 nm silica material with a refractive index of 1.463 to 1.453, then in POF material 1.49 to 1.47, in Fluoride glasses material 1.344 to 1.339 while at a wavelength of 1310nm silica material from 1.44 to 1.43, POF material from 1.444 to 1.424, and flouride glasses material from 1.3348 to 1. 3298 then at a wavelength of 1550 in silica material from 1.428 to 1.418, in POF material from 1.42 to 1.4. from the above data it can be concluded that from temperature 0-100°C the refractive index decreases and also the longer the wavelength the lower the refractive index but at wavelengths of 1310 and 1550 the decrease in refractive index is not too significant.

Fig. 7 shows while the effect temperature on 0-100°C the attenuation on silica increased, at a wavelength of 850nm from -0.11 to 0.89, then on POF material from 20db/km - 22db/km, and on fluoride glasses material from 0.15db/km - 0.65db/km. Then at wavelength 1310 the attenuation of the silica material from 0.35 to 1.35, the POF material from 20.92db/km - 22.92db/km, and the fluoride glasses material from 0.38db/km - 0.88db/km while at wavelength 1550 the attenuation of the silica material from 0. 59db/km - 1.59db/km, POF material from 21.4db/km - 23.4db/km, and Fluoride glasses material from 0.5db/km - 1db/km so that the longer the wavelength, the temperature effect that affects the attenuation will increase.

B. *Effect of Temperature on Refractive Index and Attenuation in Temperature 100-200°C*

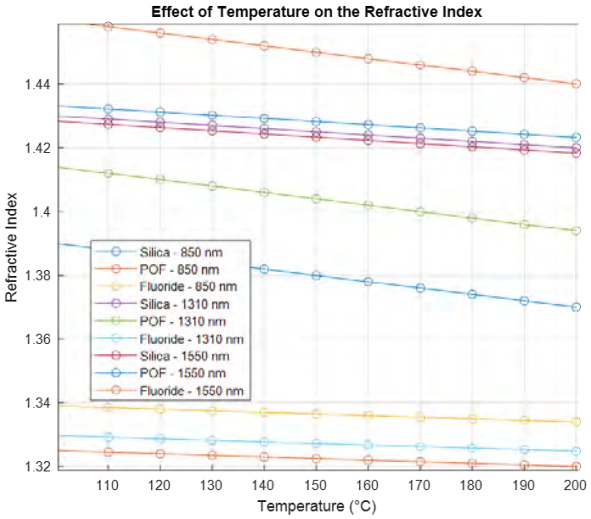

Fig. 8. A Graph of Temperature Effect on the Refractive Index 100-200°C

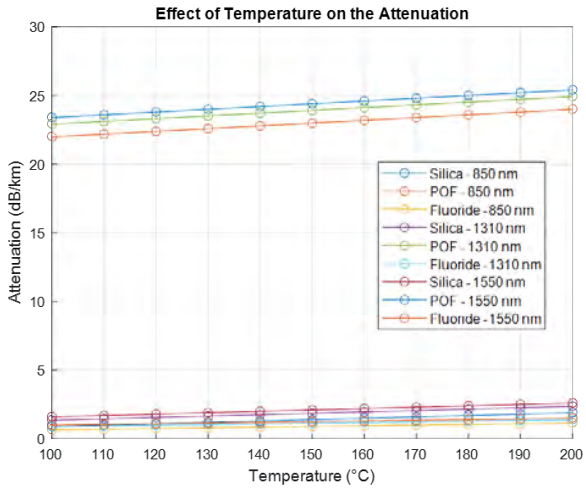

Fig. 9. A Graph of Temperature Effect 100-200°C on the Attenuation

Fig. 8 shows at a temperature of 100-200 °C, the effect of temperature on refractive index decreased in silica material, at a wavelength of 850nm from 1.4332 - 1.4232, in POF material from 1.46 - 1.44, and in fluoride glasses material from 1.339 - 1. 334, while at a wavelength of 1310nm, silica material from 1.43 - 1.42, POF material from 1.414 - 1.394, and fluoride glasses material from 1.3298 - 1.3248, then at a wavelength of 1550nm silica from 1.4283 - 1.4183, POF material from 1.39 - 1.37, and fluoride glasses material from 1.325 - 1.32.

Fig. 9 show while the effect of temperature 100-200 °C on attenuation increases, at a wavelength of 850nm silica material from 0.89db/km - 1.89 dB/km, POF material from 22db/km - 24db/km, and fluoride glasses material from 0.65db/km - 1.15db/km, then at a wavelength of 1310nm silica material from 1. 35db/km - 2.35db/km, POF material from 22.92db/km - 24.92db/km, and fluoride glasses material from 0.88db/km - 1.38db/km, then at a wavelength of 1550nm silica material from 1.59db/km - 2.59db/km, POF material from 23.4db/km - 25.4db/km and fluoride glasses material from 1db/km - 1.5db/km

C. Effect of Temperature on Refractive Index and Attenuation in Temperature 200-300°C

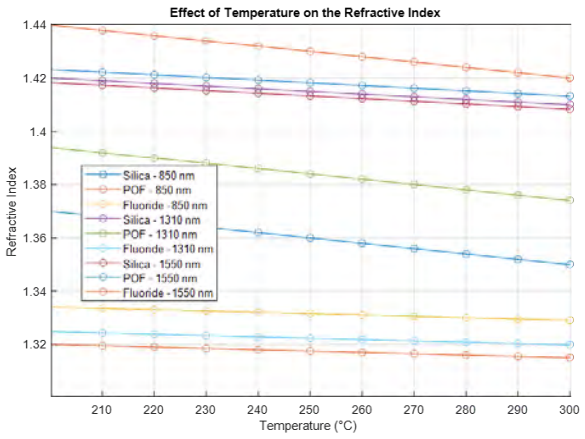

Fig. 10. AA Graph of Temperature Effect on the Refractive Index 200-300°C

Fig. 10 show at temperatures 200-300°C, the effect of temperature on refractive index decreased, at a wavelength of 850nm, silica material from 1.4232 - 1.4132, POF material from 1.44 - 1.42, and fluoride glasses material from 1.334 - 1.329, then at a wavelength of 1310nm silica material from 1. 42 - 1.41, POF material from 1.394 - 1.374, and fluoride glasses material from 1.3248 - 1.3198, then at a wavelength of 1550nm silica material from 1.4183 - 1.4083, POF material from 1.37 - 1.34, and fluoride glasses material from 1.32 - 1.315.

Fig. 11 show while the effect of temperatures 200-300°C on attenuation increases, at a wavelength of 850nm the silica material from 1.89db/km - 2.89db/km, POF material from 24db/km - 26db/km, and fluoride glasses material from 1.15db/km - 1.65db/km, then at a wavelength of 1310nm from

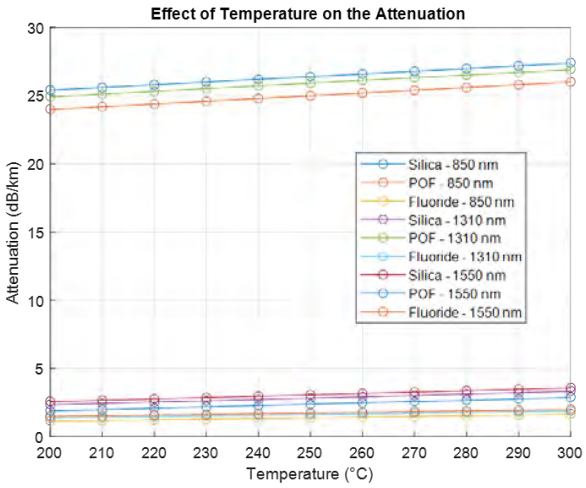

Fig. 11. A Graph of Temperature Effect 200-300°C on the Attenuation

0.35db/km - 1.35db/km, POF material from 24.92db/km - 26.92db/km, and fluoride glasses material from 1.38db/km - 1.88db/km. At the wavelength of 1550nm, the silica material was 2.59db/km - 3.59db/km, the POF material was 25.4db/km - 27.4db/km, and the fluoride glasses material was 1.5db/km - 2db/km.

IV. Conclusions

The refractive index of all types of optical fibers tested shows a decrease as the temperature increases. This decrease is relatively small, especially in Silica and Fluoride Glasses, which show good thermal stability. POF, although also stable, shows slightly more variation with temperature compared to Silica. Meanwhile, the attenuation increases with temperature at all wavelengths tested. This increase is greater in POF compared to Silica and Fluoride Glasses. Silica exhibits the least attenuation and is stable, making it a better choice for applications where signal loss must be minimized. Silica and Fluoride Glasses materials are recommended for applications that require high temperature stability, while POF may be more suitable for applications that are more tolerant of temperature variations. The use of the right material under different thermal conditions is critical to ensure optimal performance of the fiber optic.

References

[1] H. Tanyildizi, "Effect of temperature, carbon fibers, and silica fume on the mechanical properties of lightweight concretes," *Xinxing Tan Cailiao/ New Carbon Materials*, vol. 23, no. 4, pp. 339–344, 2008, doi: 10.1016/s1872-5805(09)60005-6.

[2] T. E. Tabaru, "The Temperature Effect on U and Coil Shaped POF Sensors to Detect Refractive Index Change," *Fiber and Integrated Optics*, vol. 40, no. 1, pp. 48–69, 2021, doi: 10.1080/01468030.2021.1904059.

[3] A. Morana *et al.*, "Operating Temperature Range of Phosphorous-Doped Optical Fiber Dosimeters Exploiting Infrared Radiation-Induced Attenuation," *IEEE Trans Nucl Sci*, vol. 68, no. 5, pp. 906–912, May 2021, doi: 10.1109/TNS.2021.3053164.

[4] K. J. Kaltenecker, E. J. R. Kelleher, B. Zhou, and P. U. Jepsen, "Attenuation of THz Beams: A 'How to' Tutorial," Springer New York LLC, Aug. 15, 2019, doi: 10.1007/s10762-019-00608-x.

[5] A. A. Mohammed and G. A. Qasmarrogy, "Thermal effect on the optical signal of fiber optics networks," *International Review of Applied Sciences and Engineering*, vol. 13, no. 2, pp. 164–173, Aug. 2022, doi: 10.1556/1848.2021.00328.

[6] H. Tanyildizi, "Effect of temperature, carbon fibers, and silica fume on the mechanical properties of lightweight concretes," *Xinxing Tan Cailiao/ New Carbon Materials*, vol. 23, no. 4, pp. 339–344, 2008, doi: 10.1016/s1872-5805(09)60005-6.

[7] A. Morana *et al.*, "Operating Temperature Range of Phosphorous-Doped Optical Fiber Dosimeters Exploiting Infrared Radiation-Induced Attenuation," *IEEE Trans Nucl Sci*, vol. 68, no. 5, pp. 906–912, May 2021, doi: 10.1109/TNS.2021.3053164.

[8] F. Sequeira, N. Cennamo, A. Rudnitskaya, R. Nogueira, L. Zeni, and L. Bilro, "D-shaped POF sensors for refractive index sensing—the importance of surface roughness," *Sensors (Switzerland)*, vol. 19, no. 11, Jun. 2019, doi: 10.3390/s19112476.

[9] F. Sequeira, N. Cennamo, A. Rudnitskaya, R. Nogueira, L. Zeni, and L. Bilro, "D-shaped POF sensors for refractive index sensing—the importance of surface roughness," *Sensors (Switzerland)*, vol. 19, no. 11, Jun. 2019, doi: 10.3390/s19112476.

[10] A. M. Alatwi and A. N. Zaki Rashed, "Conventional doped silica/fluoride glass fibers for low loss and minimum dispersion effects," *Indonesian Journal of Electrical Engineering and Computer Science*, vol. 21, no. 1, pp. 287–295, Jan. 2021, doi: 10.11591/ijeecs.v21.i1.pp287-295.

[11] Fernxu, "Plastic Optical Fiber vs. Glass Optical Fiber," Medium.com. [Online]. Available: https://medium.com/@fernxu123/plastic-optical-fiber-vs-glass-optical-fiber-b4591bf4f6b.

[12] "Fluoride Glass Optical Fiber,"Thorlabs.com. [Online]. Available: https://www.thorlabs.com/newgrouppage9.cfm?objectgroup$_id = 7062$.

[13] A. Guttilla, "Study of combined effects of radiation and temperature on silica-based material and optical fibers." [Online]. Available: https://theses.hal.science/tel-03377158.

[14] L. N. Binh, *Guided Wave Photonics Fundamentals and Applications with MATLAB®*.

[15] U. O. Uyor, A. P. I. Popoola, O. M. Popoola, and V. S. Aigbodion, "Polymeric cladding materials under high temperature from optical fibre perspective: a review," Springer, Apr. 01, 2020, doi: 10.1007/s00289-019-02830-y.

[16] J. Lee, Y. Ososkov, S. Cozic, A. Pastre, R. Bernard, and S. D. Jackson, "Metal-coated fluoride glass fiber," *Opt Mater Express*, vol. 13, no. 7, p. 2101, Jul. 2023, doi: 10.1364/ome.493834.

[17] J.-hui Chen, Y.-feng Xiong, F. Xu, and Y.-qing Lu, "Silica optical fiber integrated with two-dimensional materials: towards opto-electro-mechanical technology," Springer Nature, Dec. 01, 2021, doi: 10.1038/s41377-021-00520-x.

[18] N. A. Kudryashov, "Highly Dispersive Optical Solitons of an Equation with Arbitrary Refractive Index," *Regular and Chaotic Dynamics*, vol. 25, no. 2, 2020.

[19] A. N. Z. Rashed et al., "Multi-mode step graded index fibers performance parameters (attenuation/dispersion/mode field) measurements by using OptiFiber simulation," *Journal of Optical Communications*, 2022, doi: 10.1515/joc-2022-0217.

[20] K. J. Kaltenecker, E. J. R. Kelleher, B. Zhou, and P. U. Jepsen, "Attenuation of THz Beams: A 'How to' Tutorial," Springer New York LLC, Aug. 15, 2019, doi: 10.1007/s10762-019-00608-x.

[21] F. Zhou, H. Su, H. E. Joe, and M. B. G. Jun, "Temperature insensitive fiber optical refractive index probe with large dynamic range at 1,550 nm," *Sens Actuators A Phys*, vol. 312, Sep. 2020, doi: 10.1016/j.sna.2020.112102.

Design and Construction of a Temperature Monitoring System for Photovoltaic based on ESP32 Microcontroller

Kholistianingsih
Electrical Engineering
Universitas Wijayakusuma
Purwokerto, Indonesia
kholistianingsih@unwiku.ac.id

Isra' Nuur Darmawan
Electrical Engineering
Universitas Wijayakusuma
Purwokerto, Indonesia
isra.nuur.darmawan@unwiku.ac.id

Rahardian Luthfi Prasetyo
Electrical Engineering
Universitas Wijayakusuma
Purwokerto, Indonesia
rahardian@unwiku.ac.id

Ryan Aditya Fiana
Electrical Engineering
Universitas Wijayakusuma
Purwokerto, Indonesia
ryan.aditya.fiana@unwiku.ac.id

***Abstract*—Solar energy is a major source of energy for humans. This energy is derived from solar radiation using photovoltaic (PV) systems, which convert thermal energy into electrical energy. In this regard, PV panel technology has made rapid progress in addressing electricity demands in homes, businesses, and industries. Although solar panels are successful at generating power from sunshine, their efficiency can be influenced by operational temperature, which is heavily influenced by ambient temperature. To monitor the temperature of solar panels, the author created a tool that is incorporated into the Android mobile platform. This tool includes three types of sensors: DHT11 for external temperature, DS18B20 for solar panel temperature, and PZEM-017 for voltage, current, and power on the panel. This study found that the DHT11 sensor is 0.65% accurate, the DS18B20 sensor is 0.12% accurate, and the PZEM-017 sensor has a voltage reading error of 0.20%, a current reading error of 0.65%, and a power reading error of 0.65%. In addition, the monitoring system is designed to send real-time notifications when the panel temperature hits 50. The biggest temperature increases from 11.00 to 12.30 is shown in the 7-day test data, with a decrease in power proportional to the increase in temperature. These findings are verified by test graphs that show the trends.**

***Index Terms*—Solar panel, panel temperature, temperature sensor, monitoring, photovoltaic**

I. Introduction

Energy is one of humanity's most basic requirements. Solar energy is obtained by transforming the heat energy emitted by the sun through certain equipment into various resources. A.C. Becquerel devised the technique for utilizing solar energy in 1839. He utilized silicon crystals to transform solar radiation into electrical energy [1]. With the advancement of PV (Photovoltaic) panel technology, electricity sources for houses, offices, and industry, among others, have advanced more quickly. PV panels have the advantage of being ecologically friendly and widely available in practically every part of the world. The essential component of PV panels is photovoltaic cells, which convert photon energy in sunlight into electrical energy [2]. Solar panels convert photon energy from the sun into electrical energy and are always directly exposed to the elements [2]. One issue that might affect the performance of a solar panel module is its temperature. Meanwhile, the temperature of the solar panel is influenced by the temperature of its surroundings.Solar panels are built of crystalline silicon, hence the higher the temperature, the poorer the performance. The goals for designing this tool include:

1) Create a prototype tool and application that detects temperature spikes on solar panels.
2) Test the equipment, specifically sensor and delay testing.
3) Understand the relationship between time and temperature rise.

979-8-3315-1921-6/24/$31.00 ©2024 IEEE

II. Theoretical Background

A. Literature Review

The study titled "Using the ESP32 Microcontroller Data Processing" Discusses the ESP32 microcontroller's development experience and provides a complete picture of future data processing platform enhancements [9]. The study, titled "IoT-based Temperature Increase Monitoring System in Transformers," employs ESP32 as a controller to monitor temperature increases in transformers to maintain transformer performance and prevent overheating.

The research titled "IoT-Based Environmental Temperature and Humidity Monitoring System and Solar Electricity" uses the DH11 sensor to remotely monitor environmental conditions to help determine the scenario and conditions that arise [14].

The study is titled ”Early Warning System for Flood Danger in Irrigation Areas”. Discussing the usage of the modular editor in the monitoring system built in this study, it was successful in sending notifications or warning messages to users via Android devices [5].

Studies titled ”Monitoring Water Chiller Temperature using an Android Platform Based on IoT (Internet of Things)”. Discusses Kodular as an application that may be used to show the temperature read by the sensor as well as provide notifications based on changes in the sensor’s temperature state [11].

B. Internet of Things (IoT)

The utilization of the Internet of Things (IoT) provides significant benefits for the advancement of social life and civilization. The Internet of Things (IoT) is a network of computers and other gadgets that may be managed remotely over the internet. The usage of IoT promotes the development of concepts for large-scale data storage (big data) and integrated data storage media (data centers) that can be accessed remotely [21].

C. Solar Panel

Solar panels are semiconductor components that transform light wave energy from the sun into electricity. Solar cells capture sunlight from semiconductor cells and turn it into electricity. Conventional solar cells operate on the p-n junction principle, which distinguishes between p-type and n-type semiconductors. The structure of this semiconductor is composed of many atomic bonds made up of electrons, which are the main building blocks.

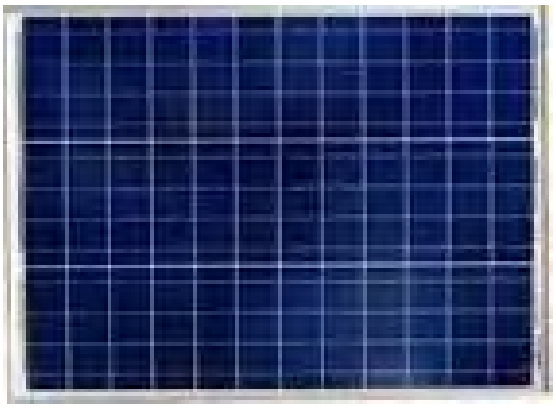

Fig. 1. Polycrystalline Panel

D. Microcontroller

A microcontroller is an electronic component shown on a physical microcontroller, which is an electronic component combined with one another to perform the function of controlling and controlling a specific job or work in a specified manner. A microcontroller is a single-chip computer that uses a microprocessor as its processing brain (E-Book).

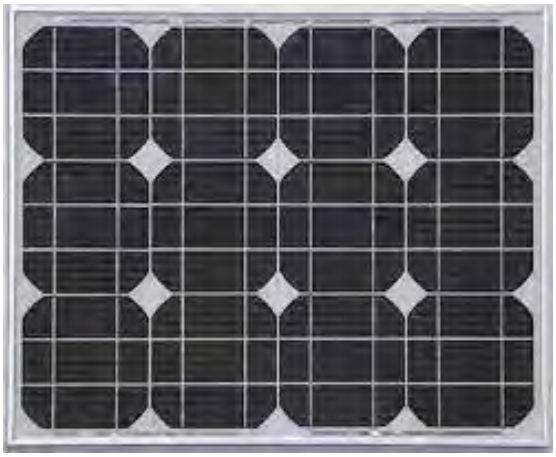

Fig. 2. Monocrystalline Panel

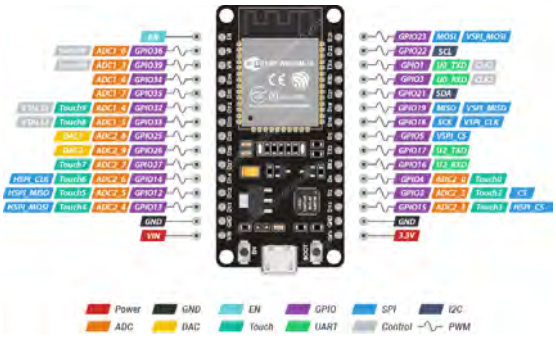

Fig. 3. ESP32 Microcontroller

In this research paper, the microcontroller utilized is the ESP32, a robust and versatile module known for its dual-core processor and Wi-Fi/Bluetooth connectivity. Manufactured by Ekspresif Systems, the ESP32 is powered by a 32-bit LX6 microprocessor that can reach clock speeds of up to 240 MHz, making it suitable for high-performance IoT applications. It comes with up to 520 KB of SRAM, supports various communication protocols (UART, SPI, I2C, and CAN), and includes a range of digital and analog GPIO pins. The ESP32 also integrates built-in sensors, such as a hall effect sensor and temperature sensor, providing enhanced functionality for real-time data monitoring and control in embedded systems. With low power modes and extensive peripheral support, it is an ideal choice for IoT projects requiring efficient wireless communication and processing capabilities.

E. DS18B20 Sensor

The DS18B20 sensor detects room temperature from -55°C to 125°C with an accuracy of ±0.5°C from -10°C to +85°C and a resolution of 9-12 bits. If many sensors are linked in simultaneously, the data from the output can be read using a single data cable or (one-wire) [28].

F. DHT11 Sensor

The DHT11 sensor is a basic, ultra-low-cost digital sensor used for measuring temperature and humidity. It combines a

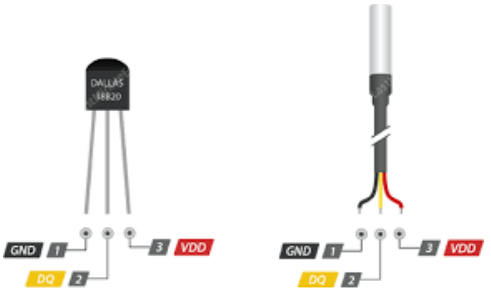

Fig. 4. DS18B20 Sensor

capacitive humidity sensor and a thermistor to measure the surrounding air, providing a digital signal on the data pin without requiring additional components. With a temperature measurement range of 0–50°C and an accuracy of ±2°C, and a humidity range of 20–80% RH with an accuracy of ±5% RH, the DHT11 is suitable for simple environmental monitoring applications. The sensor operates at a voltage range of 3.3V to 5.5V, making it compatible with most microcontrollers. Although it has a slower response time and limited precision compared to more advanced sensors, the DHT11 is widely used in IoT projects due to its affordability, ease of use, and compatibility with Arduino, ESP32, and other popular development boards. [16].

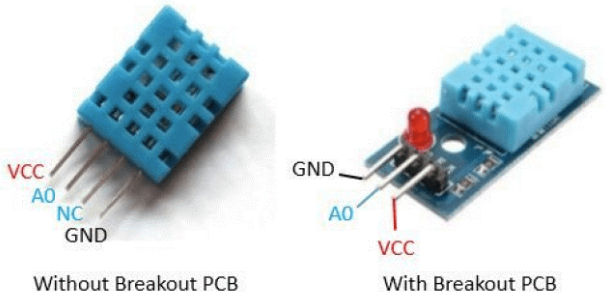

Fig. 5. DHT11 Sensor

G. PZEM-017 Sensor

The PZEM-017 sensor is intended to monitor voltage, current, and power. This sensor can measure DC power up to 300VDC and an external shunt current of 50A to 300A.

H. LCD 12C

LCD (Liquid Crystal Display) is a type of electronic device that uses CMOS logic technology to reflect or transmit light via a front-light or back-light source. LCDs serve as data processors, displaying characters, letters, numbers, and images. LCDs are made up of many layers of clear glass crystals and transparent indium oxide electrodes. This layer has seven segments and is positioned on the rear glass.

The LCD's memory comprises of 9,920 bits CGROM, 64 bytes CGRAM, and 80x8 bits DDRAM. LCDs come in two

Fig. 6. PZEM-017 Sensor

shapes and sizes: 20x4 and 16x2, which means the maximum number of characters per line is 20 or 16, and the maximum number of lines is 4 or 2. The LCD module comes with memory [33].

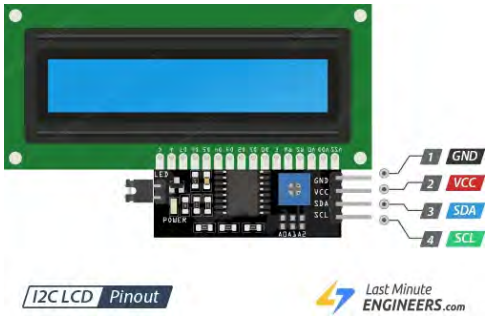

Fig. 7. LCD 12C

I. Arduino IDE

Arduino IDE (Integrated Development Environment) is software that allows you to develop, edit, and upload program code to a microcontroller board. The Arduino IDE software is written in the JAVA programming language and includes a C/C++ library to facilitate input and output operations. This software can be used to program a variety of boards, including the Arduino Nano, Arduino Leonardo, Mappi32, NodeMCU, and others. The program code used by Arduino is known as the Arduino "sketch" or Arduino source code, with the file source code extension "uno" [34].

J. Kodular Editor

Kodular Builder is a web-based open-source platform that allows you to easily and quickly construct numerous sorts of Android applications without requiring any programming skills. Kodular employs a visual block programming approach, which allows apps to be created without the need for code or scripts. Visual block programming involves manipulating,

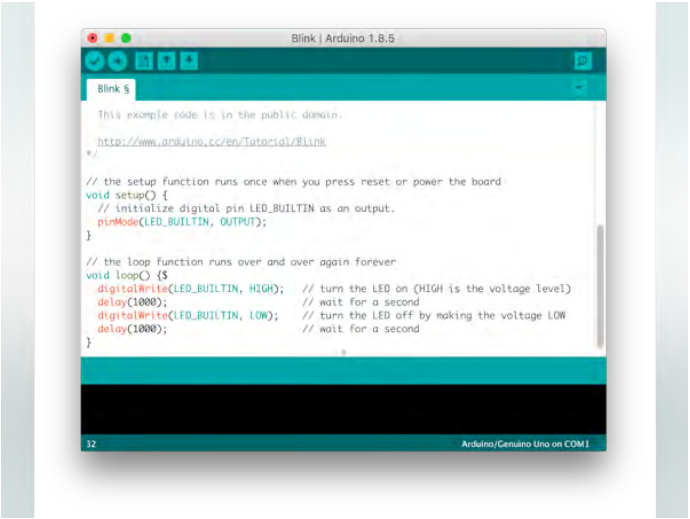

Fig. 8. Arduino IDE

arranging, or dragging-and-dropping blocks that serve as command symbols for certain tasks while developing Android applications [34].

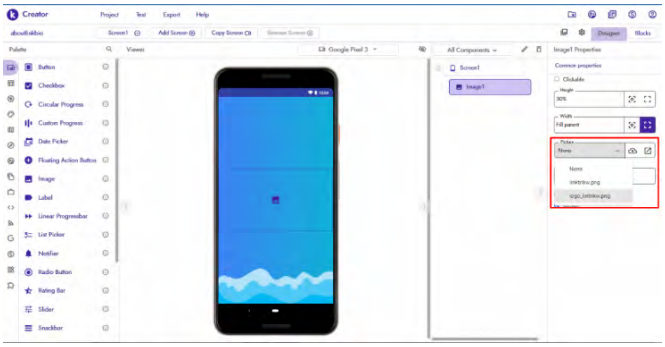

Fig. 9. Kodular Editor

III. Methodology

A. Research Stages

This final assignment is implemented in steps that are completed progressively and in a systematic order. The flow of research into the design and development of temperature monitoring in photovoltaics.

B. System Planning

Making hardware must adhere to the plans that have been made. This design's tools and materials include hardware, software, and other supporting components.

C. Flowchart System

The system flowchart below is used before proceeding to the next stage and to describe the stages before creating the system circuit. This flowchart describes the system workflow.

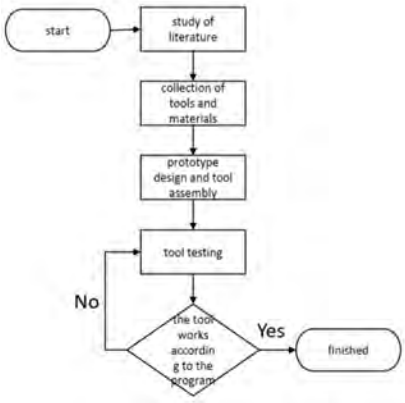

Fig. 10. Flowchart

TABLE I
Tools and Materials

No	Name	Total
1	Laptop	1
2	Solder	1
3	Analog Multimeter	1
4	PCB Drill and Drill Bit	1
5	Tinol (Tin Solder)	as necessary
6	Simple PCB	1
7	Male-to-female cable	4
8	Female-to-female cable	5
9	Male-to-male cable	5
10	Box 12cm x 5cm	1
11	ESP32	1
12	DS18B20 temperature sensor	1
13	DHT11 sensor	1
14	Modul DC step-down	1
15	LCD 12C 20x4	1
16	PZEM-017	1
17	Serial to RS485	1

D. Schematic Series

The wiring on tools is tailored to the requirements for input, processing, and output. The circuit's inputs are the DS18B20 temperature sensor, DHT1, and PZEM-017, the processor is Esp32, and the output is an LCD.

IV. Tool Design

The design stage involves determining the intended shape of the tool

A. Software Design

The software design procedure is conducted to create an overview of the appearance of the program.

V. Result and Discussion

The Temperature Monitoring System Design Tool for Photovoltaics is tested every 15 minutes from 08.00 in the morning to 16.00 in the afternoon. Sample data is collected for each

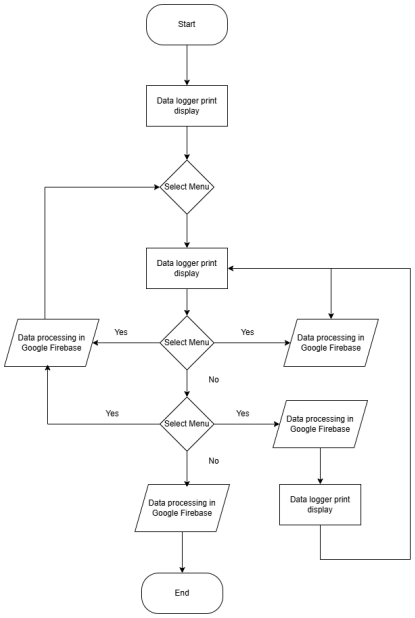

Fig. 11. Flowchart System

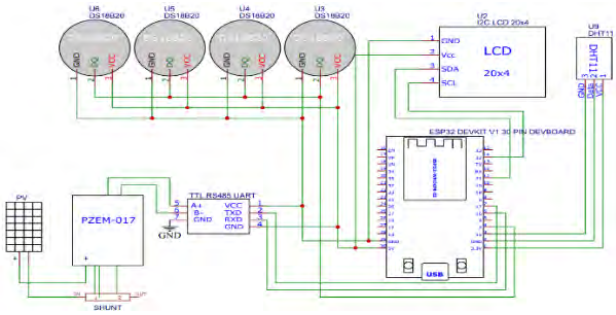

Fig. 12. Schematic Series

variable, including PV temperature, environmental temperature, humidity, voltage, current, power, and light intensity. This test was repeated 30 times for data collection, with the following findings.

The average error for the four DS18B20 sensors was calculated using the following formula:

$$\text{Average of Error } (\%) = \frac{n(\text{Error S1 + S2 + S3 + S4}\%)}{n(\text{total sensor})}$$

$$= \frac{0.49}{4}$$

$$= 0.12\% \quad (1)$$

Error testing on the DHT11 sensor can be described as follows,Temperature Reading Error (%) in testing using a single data sample can be expressed as follows:

$$\text{Error } (\%) = \frac{\text{Hygrometer} - \text{DHT11 temperature reading}}{\text{Hygrometer}} \times 100 \quad (2)$$

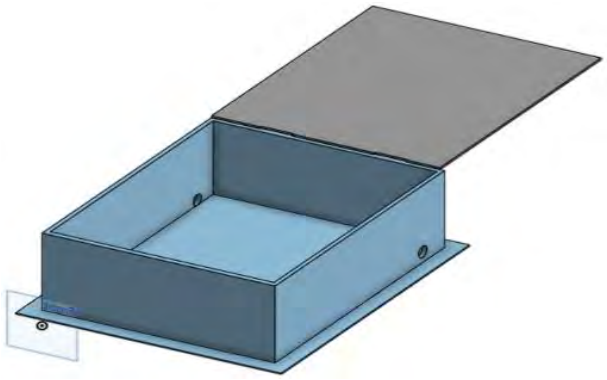

Fig. 13. Tool Design

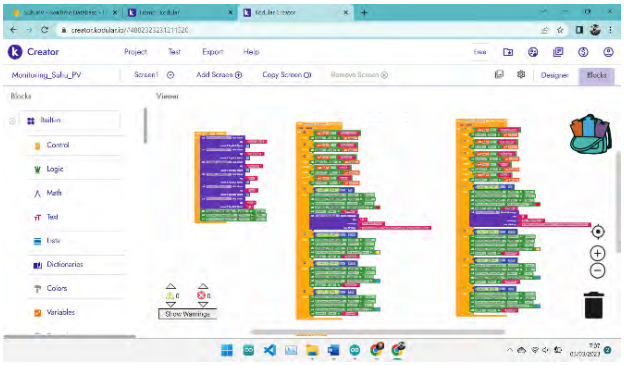

Fig. 14. Software Design

TABLE II
SENSOR TESTING 1 DS18B20

Testing	DS18B20 Sensor Temperature (°C)	DS18B20 Termometer Temperature (°C)	Error (%)
1	35.31	35.4	0.25
2	35.31	35.4	0.25
3	35.44	35.4	0.11
4	35.48	35.5	0.05
5	35.49	35.5	0.02
6	35.56	35.6	0.11
7	35.63	35.6	0.08
8	35.69	35.7	0.02
9	35.81	35.8	0.02
10	35.93	35.8	0.36
Average			**0.09**

TABLE III
SENSOR TESTING 2 DS18B20

Testing	DS18B20 Sensor Temperature (°C)	DS18B20 Termometer Temperature (°C)	Error (%)
1	35.44	35.5	0.16
2	35.48	35.5	0.05
3	35.56	35.6	0.11
4	35.63	35.6	0.08
5	35.69	35.7	0.02
6	35.81	35.8	0.02
7	35.88	35.9	0.05
8	35.94	35.9	0.11
9	36.00	36.1	0.27
Average			**0.13**

Fig. 15. Application Design

TABLE IV
SENSOR TESTING 3 DS18B20

Testing	DS18B20 Sensor Temperature (°C)	DS18B20 Termometer Temperature (°C)	Error (%)
1	35.63	35.7	0.19
2	35.63	35.7	0.19
3	35.63	35.7	0.19
4	35.75	35.8	0.13
5	35.81	35.8	0.02
6	35.81	35.8	0.02
7	35.88	35.9	0.05
8	35.88	35.9	0.05
9	35.94	35.9	0.05
10	35.94	36.9	0.10
Average			**0.10**

TABLE V
SENSOR TESTING 4 DS18B20

Testing	DS18B20 Sensor Temperature (°C)	DS18B20 Termometer Temperature (°C)	Error (%)
1	35.69	35.6	0.25
2	35.75	35.8	0.13
3	35.75	35.8	0.13
4	35.88	35.9	0.05
5	35.94	35.9	0.11
6	35.94	35.9	0.11
7	35.94	36.0	0.16
8	35.94	36.0	0.16
9	36.0	36.1	0.27
10	36.02	36.1	0.49
Average			**0.17**

$$\text{Error\%} = \frac{29.30 - 29.20}{29.30} \times 100 = 0.34\% \quad (3)$$

The Humidity Reading Error (%) in testing using one data sample can be calculated as follows:

$$\text{Error } (\%) = \frac{\text{Hygrometer} - \text{DHT11 humidity reading}}{\text{Hygrometer}} \times 100 \quad (3)$$

$$\text{Error\%} = \frac{70 - 69}{70} \times 100 = 1.42\% \quad (5)$$

Average temperature reading error:

$$\text{Error } (\%) = \frac{n(\text{Error\%})}{n(\text{Testing})} \quad (4)$$

$$\text{Error\%} = \frac{6.5}{10} = 0.65\% \quad (6)$$

Average humidity reading error:

$$\text{Error } (\%) = \frac{n(\text{Error\%})}{n(\text{Testing})} \quad (5)$$

$$\text{Error\%} = \frac{14.72}{10} = 1.47\% \quad (7)$$

TABLE VI
SENSOR TESTING PZEM-017

Test	Manual Measurement			Results			Error		
	V	A	W	V	A	W	V	A	W
1	57.7	2.1	124.05	57.84	2.1	124.30	0.2	0.46	0.2
2	57.7	2.1	122.90	57.81	2.1	123.10	0.1	0.46	0.1
3	57.8	2.1	122.53	57.81	2.1	123.00	0.0	0.47	0.4
4	57.8	2.1	121.74	57.81	2.1	123.10	0.0	0.47	1.1
5	57.8	2.1	121.91	57.82	2.1	123.10	0.0	0.47	1.0
6	57.8	2.1	121.53	57.82	2.1	123.00	0.0	0.47	0.7
7	57.8	2.1	122.12	57.82	2.1	123.10	0.0	0.47	0.8
8	57.8	2.1	121.77	57.82	2.1	123.00	0.0	0.47	0.4
9	57.8	2.1	121.74	57.82	2.1	123.10	0.0	0.47	1.1
10	57.8	2.1	121.95	57.82	2.1	123.10	0.0	0.94	0.4
Average	–	–	–	–	–	–	**0.2**	**0.65**	**0.5**

Notes: V = Voltage; A = Electric Current/Ampere; W = Power/Watt
Source: Personal Documentation

Based on the findings of the PZEM-017 sensor test, an error on the sensor was calculated using the following formula: The Voltage Reading Error (%) in the test utilizing one of the data samples can be expressed as follows:

$$Error(\%) = \frac{\text{Manual Measurement} - \text{Sensor Reading}}{\text{Manual Measurement}} \times 100 \quad (8)$$

$$Error(\%) = \frac{57.7 - 57.84}{57.7} \times 100 = 0.24\% \quad (9)$$

The current reading error (%) in testing with one of the data samples might be expressed as follows:

$$Error(\%) = \frac{\text{Manual Measurement} - \text{Sensor Reading}}{\text{Manual Measurement}} \times 100 \quad (10)$$

$$Error(\%) = \frac{2.15 - 2.14}{2.15} \times 100 = 0.46\% \quad (11)$$

The Power Reading Error (%) in testing using one of the data samples can be expressed as follows:

$$Error(\%) = \frac{\text{Manual Measurement} - \text{Sensor Reading}}{\text{Manual Measurement}} \times 100 \quad (12)$$

$$Error(\%) = \frac{124.05 - 124.30}{124.05} \times 100 = 0.20\% \quad (13)$$

The average error on the PZEM 017 sensor can be calculated using the following formula:

The average voltage error is calculated using the formula below.

$$\text{Average of Error } (\%) = \frac{n(\text{Error}\%)}{n(\text{Testing})} = \frac{2.03}{10} = 0.20\% \quad (14)$$

The average of current error is calculated using the formula below.

$$\text{Average of Error } (\%) = \frac{n(\text{Error}\%)}{n(\text{Testing})} = \frac{6.5}{10} = 0.65\% \quad (15)$$

The average of power error is calculated using the formula below.

$$\text{Average of Error } (\%) = \frac{n(\text{Error}\%)}{n(\text{Testing})} = \frac{6.5}{10} = 0.65\% \quad (16)$$

Once all sensors have been tested, a delay test is performed between hardware and software. This test is used to determine how responsive the application produced with the Kodular editor is. For the delay test, 20 attempts were done to measure the delay time with a timer

TABLE VII
DELAY TESTING

Testing	Delay (second) Hardware	Delay (second) Application	Delay Deviation
1	14.30	14.23	0.07
2	14.38	14.31	0.07
3	14.08	14.00	0.08
4	14.26	14.21	0.05
5	14.25	14.20	0.05
6	14.13	14.02	0.10
7	15.37	15.27	0.10
8	14.20	14.12	0.08
9	13.96	13.80	0.16
10	14.11	13.97	0.13
11	14.10	13.81	0.15
12	13.93	13.72	0.21
13	14.10	13.80	0.19
14	13.94	13.87	0.07
Average			**0.11**

The test results show that the application's reaction has an average delay difference (seconds) of 0.11 seconds across 20 trials, indicating that the application's response is excellent.

On the second day, the highest temperature increase on the panel was at 10.45 WIB and 11.50 WIB, with the panel temperature reaching 50.45 °C and 50.38 °C, with an increase in light intensity of 107,700 Lux and 106,100 Lux, with an environmental temperature of 35.00 °C and 34.80°C, respectively, and an environmental humidity of 46%. The power generated was 107.9 W and 110.50 W.

On the third day, the highest temperature increase on the panel was at 11.00 WIB, with the panel temperature reaching 54.30 °C and an increase in light intensity of 110,600 Lux. The environmental temperature was 33.40 °C, the humidity was 48%, and the power generated was 100.60 W.

TABLE VIII
STUDY MIDDLE PANEL DAY 1

No	Time	Temperature PV (°C)	Temperature Env (°C)	Hum (%)	V	A	W	Lux
1	08.30	37.07	29.50	67.00	55.93	2.24	125.20	85,700
2	08.45	39.30	31.90	65.00	56.94	2.21	125.40	89,500
3	09.00	41.15	31.90	62.00	57.90	2.18	125.40	95,000
4	09.15	44.16	34.80	58.00	57.98	2.15	125.40	99,500
5	09.30	46.34	36.00	55.00	58.10	2.13	125.30	97,500
6	09.45	46.93	34.50	52.00	57.90	2.08	125.20	104,700
7	10.00	47.30	34.50	50.00	57.80	2.07	125.20	100,600
8	10.15	47.96	34.50	49.00	57.70	2.08	125.20	100,800
9	10.30	48.27	34.50	48.00	57.60	2.10	125.20	97,500
10	10.45	48.32	34.50	47.00	57.50	2.11	125.10	93,500
11	11.00	50.05	34.80	46.00	57.40	2.11	125.10	92,200
12	11.15	51.52	36.00	45.00	57.20	2.11	125.00	89,500
13	11.30	52.25	37.80	44.00	57.10	2.10	125.00	86,700
14	11.45	51.99	39.10	44.00	57.00	2.10	125.00	84,200
15	12.00	50.67	40.30	45.00	57.10	2.10	125.10	79,200
16	12.15	48.42	41.90	46.00	57.20	2.12	125.20	75,700
17	12.30	46.19	44.10	48.00	57.30	2.15	125.20	71,500
18	12.45	44.15	45.60	50.00	57.60	2.18	125.30	69,800
19	13.00	43.45	49.00	51.00	57.70	2.19	125.30	66,900
20	13.15	45.95	49.80	53.00	57.70	2.20	125.40	63,000
21	13.30	45.40	50.30	55.00	57.80	2.20	125.40	60,000
22	13.45	44.40	50.30	57.00	57.70	2.19	125.30	58,700
23	14.00	43.34	50.00	58.00	57.50	2.17	125.20	56,400
24	14.15	42.93	49.50	59.00	57.40	2.14	125.10	54,200
25	14.30	41.69	49.10	60.00	57.30	2.10	125.00	52,100
26	14.45	39.69	49.10	62.00	57.30	2.06	125.00	50,400
27	15.00	37.90	49.60	63.00	57.20	2.00	125.00	47,800
28	15.15	36.60	49.80	65.00	56.80	1.90	125.00	46,000
29	15.30	35.03	49.60	63.00	56.60	1.85	124.90	45,400
30	15.45	33.60	49.30	61.00	56.50	1.80	124.90	45,400

TABLE IX
STUDY MIDDLE PANEL DAY 2

No	Time	Temperature PV (°C)	Temperature Env (°C)	Hum (%)	V	A	W	Lux
1	08.30	39.63	30.20	67.00	55.89	2.22	124.00	78,500
2	08.45	40.78	30.70	69.00	56.08	2.21	124.40	89,200
3	09.00	42.35	30.60	66.00	56.28	2.18	124.50	89,100
4	09.15	45.02	32.20	56.00	57.21	2.01	115.00	89,100
5	09.30	45.92	33.20	51.00	58.09	1.87	67.90	94,000
6	10.00	46.16	33.40	50.00	58.64	1.89	110.80	103,300
7	10.15	46.92	34.00	50.00	58.55	1.83	107.10	100,500
8	10.30	47.38	34.00	50.00	58.45	1.80	101.50	100,500
9	10.45	50.35	35.00	51.00	58.47	1.89	115.00	106,500
10	11.00	48.69	32.20	47.00	58.39	1.98	115.60	109,600
11	11.15	50.87	33.00	48.00	58.21	1.90	115.00	106,100
12	11.30	48.83	31.90	53.00	58.51	1.94	115.00	109,600
13	11.45	48.75	32.20	48.00	58.24	1.97	115.00	109,500
14	12.00	48.92	32.20	47.00	58.40	1.97	115.00	109,900
15	12.15	48.86	32.50	47.00	58.39	1.94	115.80	104,700
16	12.30	46.50	33.20	47.00	58.39	1.94	115.00	100,700
17	12.45	48.23	32.60	47.00	58.24	1.90	110.60	100,700
18	13.00	47.97	32.20	48.00	58.24	1.89	110.00	100,700
19	13.15	47.34	32.40	47.00	58.28	1.91	111.30	96,100
20	13.30	45.50	34.00	48.00	58.43	1.93	112.70	105,100
21	13.45	45.15	34.50	47.00	58.42	1.89	110.90	98,900
22	14.00	44.14	34.50	47.00	58.24	1.89	110.00	84,800
23	14.15	42.53	34.50	48.00	56.80	2.00	113.60	78,500
24	14.30	39.53	34.50	48.00	55.49	2.04	113.10	68,500
25	14.45	38.48	33.00	50.00	54.39	2.06	110.30	63,000
26	15.00	39.70	33.20	50.00	55.49	2.04	113.10	68,500
27	15.15	40.30	33.50	50.00	56.80	1.97	110.00	62,000
28	15.30	39.69	32.50	50.00	55.19	1.80	101.80	60,800
29	15.45	35.53	32.48	53.00	49.70	1.97	90.50	46,400
30	15.45	35.53	32.48	53.00	49.70	1.97	90.50	46,400

TABLE X
STUDY MIDDLE PANEL DAY 3

No	Time	Temperature PV (°C)	Temperature Env (°C)	Hum (%)	V	A	W	Lux
1	08.30	44.66	31.40	66.00	57.11	1.82	103.90	71,900
2	08.45	45.67	31.30	65.00	57.35	1.82	104.10	79,100
3	09.00	46.20	34.70	50.00	58.08	1.84	107.00	87,500
4	09.15	45.56	34.70	51.00	57.89	1.80	104.80	87,900
5	09.30	45.73	33.50	52.00	58.12	1.78	103.60	89,700
6	09.45	46.71	33.20	53.00	58.39	1.77	103.60	95,800
7	10.00	46.61	33.30	54.00	58.37	1.76	102.60	100,100
8	10.15	50.55	33.20	48.00	57.93	1.79	103.60	100,900
9	10.30	50.40	32.30	49.00	57.99	1.80	104.00	105,500
10	10.45	50.23	32.30	48.00	58.05	1.80	104.50	109,100
11	11.00	52.23	33.40	47.00	58.03	1.78	103.40	109,900
12	11.15	53.00	33.50	45.00	57.99	1.78	103.00	110,000
13	11.30	53.39	33.60	44.00	57.96	1.78	102.70	110,500
14	11.45	53.64	34.50	45.00	57.95	1.77	102.50	110,000
15	12.00	53.42	34.40	47.00	57.96	1.78	102.90	109,000
16	12.15	52.80	34.50	48.00	57.98	1.79	103.60	108,100
17	12.30	50.38	34.50	50.00	57.94	1.80	104.20	107,000
18	12.45	49.97	34.40	51.00	57.94	1.80	104.00	105,800
19	13.00	49.77	34.30	50.00	57.93	1.79	103.60	104,800
20	13.15	49.45	33.60	51.00	57.92	1.80	103.00	102,500
21	13.30	48.63	33.50	51.00	57.90	1.81	103.80	99,800
22	13.45	47.24	33.60	52.00	57.85	1.80	103.50	97,500
23	14.00	46.50	34.50	53.00	57.91	1.81	104.60	95,800
24	14.15	45.59	34.50	54.00	57.95	1.82	105.40	91,000
25	14.30	45.38	34.70	54.00	57.86	1.80	103.80	89,000
26	14.45	45.14	34.60	54.00	57.94	1.79	103.40	85,800
27	15.00	44.53	33.50	54.00	57.94	1.80	103.50	79,900
28	15.15	43.94	33.30	55.00	57.94	1.81	103.70	77,000
29	15.30	43.59	32.50	56.00	57.95	1.93	103.00	74,900
30	15.45	35.53	32.48	53.00	49.70	1.97	90.50	54,100

TABLE XI
STUDY MIDDLE PANEL DAY 4

No	Time	Temperature PV (°C)	Temperature Env (°C)	Hum (%)	V	A	W	Lux
1	08.30	43.30	32.20	60.00	58.02	1.80	104.40	86,400
2	08.45	43.64	32.50	60.00	58.17	1.80	104.50	88,600
3	09.00	45.53	33.80	50.00	58.21	1.80	104.60	97,000
4	09.15	44.92	34.10	50.00	57.99	1.79	104.20	97,500
5	09.30	45.35	34.20	50.00	58.07	1.78	103.50	97,500
6	09.45	46.53	32.90	49.00	58.05	1.80	104.30	94,300
7	10.00	49.12	32.90	49.00	58.10	1.80	104.90	105,700
8	10.15	50.51	32.50	47.00	58.04	1.78	103.40	105,700
9	10.30	51.32	32.90	46.00	57.99	1.78	103.10	105,800
10	10.45	52.50	34.10	46.00	57.80	1.78	103.00	105,800
11	11.00	51.98	33.60	45.00	57.80	1.77	102.50	110,100
12	11.15	52.44	34.80	45.00	57.83	1.78	103.00	110,000
13	11.30	52.45	34.30	45.00	57.81	1.79	103.50	110,000
14	11.45	51.07	33.40	46.00	57.84	1.78	103.10	108,500
15	12.00	51.09	33.50	46.00	57.83	1.79	103.40	108,100
16	12.15	50.68	33.60	46.00	57.82	1.79	103.30	107,500
17	12.30	49.52	33.40	46.00	57.83	1.79	103.40	106,800
18	12.45	48.90	34.00	47.00	57.85	1.79	103.60	106,000
19	13.00	47.97	34.50	48.00	57.83	1.80	103.40	106,500
20	13.15	47.32	34.20	48.00	57.87	1.81	104.30	102,500
21	13.30	47.53	34.40	50.00	57.89	1.79	103.80	101,900
22	13.45	46.50	33.40	50.00	57.83	1.80	103.50	100,200
23	14.00	45.44	33.30	50.00	57.81	1.79	103.10	98,500
24	14.15	44.33	34.40	50.00	57.89	1.80	103.50	96,800
25	14.30	43.50	34.10	50.00	57.90	1.80	103.60	93,500
26	14.45	43.30	33.40	49.00	57.86	1.79	103.40	92,500
27	15.00	42.99	33.20	49.00	57.84	1.80	103.50	88,200
28	15.15	42.74	33.40	50.00	57.94	1.79	103.00	86,300
29	15.30	41.66	32.50	50.00	57.92	1.80	103.30	84,100
30	15.45	34.66	31.60	49.00	56.50	1.80	101.90	54,100

TABLE XII
STUDY NORTH PANEL DAY 5

No	Time	Temperature PV (°C)	Temperature Env (°C)	Hum (%)	V	A	W	Lux
1	08.30	43.20	32.20	71.00	56.48	1.82	102.80	99,400
2	08.45	43.85	32.40	71.00	56.38	2.10	118.60	99,400
3	09.00	44.58	32.50	66.00	56.25	2.10	118.20	97,800
4	09.15	45.34	32.40	64.00	57.08	2.11	120.60	96,500
5	09.30	45.93	32.50	62.00	57.19	2.12	121.20	95,000
6	09.45	46.52	32.60	60.00	57.58	2.13	122.80	93,400
7	10.00	47.35	32.60	59.00	57.93	2.14	124.00	89,800
8	10.15	48.11	32.70	58.00	58.13	2.15	125.00	88,800
9	10.30	48.84	33.00	57.00	58.30	2.15	125.30	88,300
10	10.45	49.31	33.20	57.00	58.25	2.15	125.20	87,800
11	11.00	49.83	33.40	56.00	58.38	2.15	125.60	87,400
12	11.15	50.25	33.40	55.00	58.43	2.16	125.80	87,000
13	11.30	50.50	33.60	54.00	58.50	2.17	126.10	86,700
14	11.45	50.93	33.80	53.00	58.53	2.17	126.20	86,500
15	12.00	51.27	33.80	53.00	58.60	2.18	126.50	86,400
16	12.15	51.51	34.00	52.00	58.62	2.18	126.60	86,100
17	12.30	51.78	34.10	51.00	58.63	2.18	126.60	85,900
18	12.45	51.94	34.10	50.00	58.64	2.19	126.80	85,600
19	13.00	51.85	34.10	50.00	58.60	2.19	126.70	85,300
20	13.15	51.76	34.20	49.00	58.58	2.19	126.60	85,000
21	13.30	51.67	34.20	49.00	58.55	2.19	126.60	84,700
22	13.45	51.58	34.30	48.00	58.50	2.19	126.40	84,400
23	14.00	51.49	34.40	48.00	58.47	2.19	126.30	84,200
24	14.15	51.40	34.50	47.00	58.43	2.19	126.20	84,000
25	14.30	51.31	34.60	47.00	58.38	2.19	126.00	83,800
26	14.45	51.22	34.60	47.00	58.35	2.19	125.90	83,500
27	15.00	51.13	34.60	46.00	58.30	2.19	125.80	83,200
28	15.15	51.04	34.70	46.00	58.28	2.19	125.70	83,000
29	15.30	50.95	34.80	46.00	58.25	2.19	125.60	82,800
30	15.45	50.86	34.80	46.00	58.22	2.19	125.50	82,500

TABLE XIII
STUDY NORTH PANEL DAY 6

No	Time	Temperature PV (°C)	Temperature Env (°C)	Hum (%)	V	A	W	Lux
1	08.45	45.35	31.60	62.00	58.72	2.23	123.10	93,100
2	09.00	46.58	31.80	60.00	58.50	2.23	123.10	92,300
3	09.15	46.96	32.00	59.00	58.70	2.22	123.00	91,500
4	09.30	47.35	32.10	58.00	58.50	2.22	122.80	90,900
5	09.45	47.73	32.20	57.00	58.72	2.22	123.10	90,100
6	10.00	48.11	32.30	56.00	58.70	2.22	123.00	89,700
7	10.15	48.49	32.40	55.00	58.50	2.22	122.80	89,400
8	10.30	48.86	32.50	54.00	58.70	2.22	123.00	88,800
9	10.45	49.24	32.60	53.00	58.50	2.22	122.80	88,400
10	11.00	49.62	32.70	52.00	58.70	2.22	123.00	88,100
11	11.15	49.99	32.80	51.00	58.50	2.22	122.80	87,900
12	11.30	50.37	32.90	50.00	58.70	2.22	123.00	87,500
13	11.45	50.75	33.00	49.00	58.50	2.22	122.80	87,300
14	12.00	51.12	33.10	48.00	58.70	2.22	123.00	87,000
15	12.15	51.50	33.20	47.00	58.50	2.22	122.80	86,800
16	12.30	51.88	33.30	46.00	58.70	2.22	123.00	86,600
17	12.45	52.25	33.40	45.00	58.50	2.22	122.80	86,300
18	13.00	52.63	33.50	44.00	58.70	2.22	123.00	86,100
19	13.15	53.00	33.60	43.00	58.50	2.22	122.80	85,900
20	13.30	53.38	33.70	42.00	58.70	2.22	123.00	85,700
21	13.45	53.75	33.80	41.00	58.50	2.22	122.80	85,400
22	14.00	54.13	33.90	40.00	58.70	2.22	123.00	85,200
23	14.15	54.50	34.00	39.00	58.50	2.22	122.80	84,900
24	14.30	54.88	34.10	38.00	58.70	2.22	123.00	84,700
25	14.45	55.26	34.20	37.00	58.50	2.22	122.80	84,500
26	15.00	55.63	34.30	36.00	58.70	2.22	123.00	84,300
27	15.15	56.01	34.40	35.00	58.50	2.22	122.80	84,100
28	15.30	56.38	34.50	34.00	58.70	2.22	123.00	83,900
29	15.45	56.76	34.60	33.00	58.50	2.22	122.80	83,700
30	16.00	57.13	34.70	32.00	58.70	2.22	123.00	83,500

TABLE XIV
STUDY NORTH PANEL DAY 7

No	Time	Temperature PV (°C)	Temperature Env (°C)	Hum (%)	V	A	W	Lux
1	08.45	42.80	31.40	65.00	58.85	2.08	122.40	65,200
2	09.00	43.20	31.50	63.00	58.90	2.09	122.50	65,500
3	09.15	44.01	31.70	62.00	58.83	2.10	122.50	66,200
4	09.30	44.80	32.00	60.00	58.92	2.11	122.70	67,800
5	09.45	45.30	32.50	59.00	58.94	2.13	122.80	68,800
6	10.00	45.85	33.00	58.00	59.00	2.15	123.00	69,700
7	10.15	46.35	34.00	57.00	59.05	2.16	123.10	70,300
8	10.30	46.80	34.50	56.00	59.10	2.17	123.20	71,500
9	10.45	47.00	35.00	55.00	59.20	2.18	123.30	72,200
10	11.00	47.50	35.50	54.00	59.30	2.19	123.50	72,800
11	11.15	47.80	36.00	53.00	59.40	2.20	123.60	73,500
12	11.30	48.00	36.50	52.00	59.50	2.21	123.70	74,200
13	11.45	48.20	37.00	51.00	59.60	2.22	123.80	74,900
14	12.00	48.50	37.50	50.00	59.70	2.23	123.90	75,300
15	12.15	48.70	38.00	49.00	59.80	2.24	124.00	75,900
16	12.30	49.00	38.50	48.00	59.90	2.25	124.10	76,500
17	12.45	49.20	39.00	47.00	60.00	2.26	124.20	77,100
18	13.00	49.40	39.50	46.00	60.10	2.27	124.30	77,700
19	13.15	49.60	40.00	45.00	60.20	2.28	124.40	78,300
20	13.30	49.80	40.50	44.00	60.30	2.29	124.50	78,900
21	13.45	50.00	41.00	43.00	60.40	2.30	124.60	79,500
22	14.00	50.20	41.50	42.00	60.50	2.31	124.70	80,100
23	14.15	50.40	42.00	41.00	60.60	2.32	124.80	80,700
24	14.30	50.60	42.50	40.00	60.70	2.33	124.90	81,300
25	14.45	50.80	43.00	39.00	60.80	2.34	125.00	81,900
26	15.00	51.00	43.50	38.00	60.90	2.35	125.10	82,500
27	15.15	51.20	44.00	37.00	61.00	2.36	125.20	83,100
28	15.30	51.40	44.50	36.00	61.10	2.37	125.30	83,700
29	15.45	51.60	45.00	35.00	61.20	2.38	125.40	84,300
30	16.00	51.80	45.50	34.00	61.30	2.39	125.50	84,900

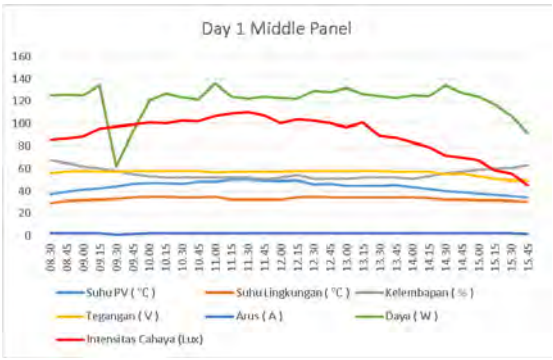

Fig. 16. Graph of Testing Day 1

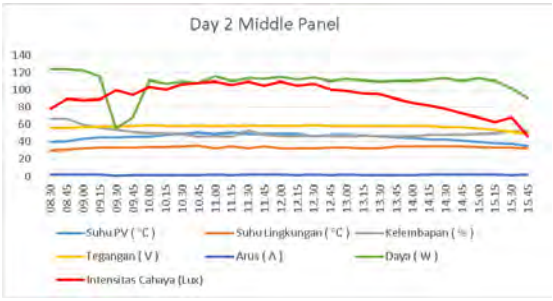

Fig. 17. Graph of Testing Day 2

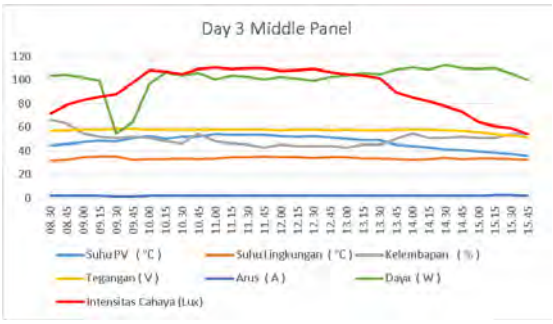

Fig. 18. Graph of Testing Day 3

On the fourth day, the highest temperature increase on the panel was at 11.15 WIB, with the panel temperature reaching 52.45 °C and an increase in light intensity of 111,500 Lux. The environmental temperature was 34.10 °C, humidity was 45%, and power generated was 104.40 W.

On the fifth day, the highest temperature increase on the panel was at 10.59 WIB, with the panel temperature reaching 52.31 °C and an increase in light intensity of 96,700 Lux. The environmental temperature reached 33.20 °C, humidity was 48%, and power generated was 123.60 W.

On the sixth day, the highest temperature increase on the panel was at 11.20 WIB, with the panel temperature reaching 54.30°C and an increase in light intensity of 112,100 Lux. The environmental temperature reached 34.50°C, humidity was 49%, and the power generated was 123.80 W.

On the seventh day, the panel temperature reached 57.16°C at 10:19 WIB, with an increase in light intensity of 104,500 Lux. The environmental temperature was 32.60°C, humidity was 47%, and power generated was 1114.20 W.

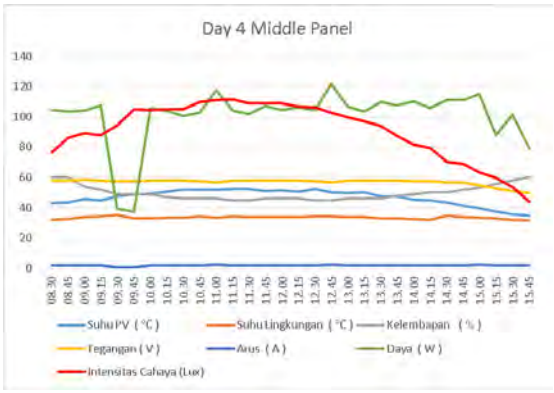

Fig. 19. Graph of Testing Day 4

In the data collected from days 1 to 4, an anomaly was observed due to factors beyond the author's control, resulting in a decrease in the recorded power values. These uncontrollable factors likely influenced the system's performance, leading to lower power measurements during this period.

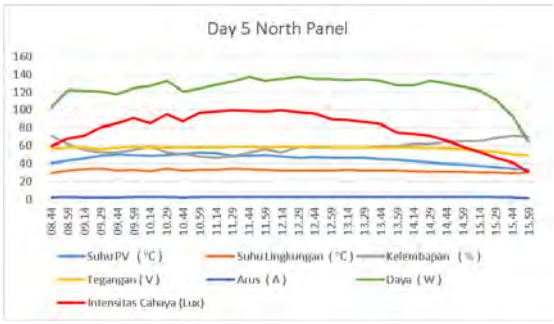

Fig. 20. Graph of Testing Day 5

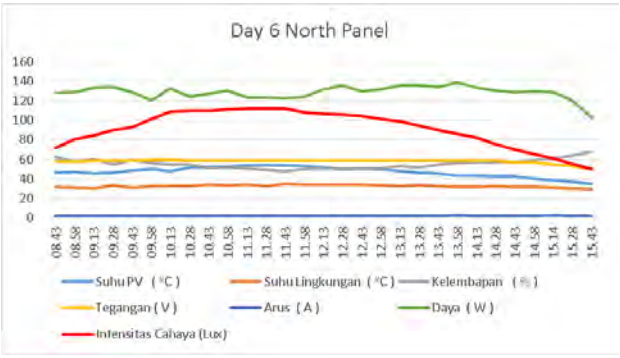

Fig. 21. Graph of Testing Day 6

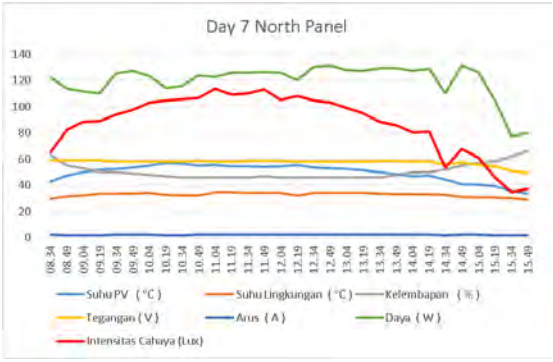

Fig. 22. Graph of Testing Day 7

The data collection reveals a noticeable decrease in the power output generated by the PV (photovoltaic) system as temperature rises. This drop in power output is primarily due to factors such as the temperature coefficient of the PV cells, which causes efficiency to decline as cell temperature increases. Higher temperatures can reduce the open-circuit voltage of the cells, directly impacting the overall power output. Additionally, elevated temperatures may increase the resistance within the PV system's internal circuitry, further lowering efficiency. These combined effects illustrate the sensitivity of PV systems to temperature fluctuations, which can lead to suboptimal performance in hotter conditions.

In the image description, the terms in Indonesian represent various measurement parameters: "Suhu PV" refers to "PV Temperature," "Tegangan" means "Voltage," "Intensitas Cahaya" translates to "Light Intensity," "Suhu Lingkungan" refers to "Ambient Temperature," "Arus" means "Current," "Kelembapan" translates to "Humidity," and "Daya" means "Power."

VI. Conclusion

Based on the findings of this study, the author can conclude:

1) The system for monitoring temperature on photovoltaics has been successfully created, using the DS18B20 sensor for heat sensors, the DHT11 sensor to determine the ambient temperature around the panel, the PZEM-017 sensor as a voltage, current, and power sensor, and the Kodular application to monitor the performance of photovoltaics. The percentage of component performance can be seen from the error generated for the DS18B20 sensor, which has an average error of 0.12
2) The system used in the "Design and Construction of a Temperature Monitoring System on Photovoltaics" can be employed, and the notification will switch on when the temperature on the panel hits 50 °C, providing real-time updates.
3) The average results of the 7-day test showed that the temperature increase on the PV occurred between 10:00 and 14:00, and the average highest temperature increase on the PV for 7 days was from 11:00 to 12:30, and when the temperature began to rise, the PV's power output decreased, as shown in the test graph.

References

[1] R. Yandri, "Prospek Pengembangan Energi Surya Untuk Kebutuhan Listrik Di Indonesia," *J. Ilmu Fis. Univ. Andalas*, vol. 4, no. 1, pp. 14–19, 2012, doi: 10.25077/jif.4.1.14-19.2012.

[2] S. Nahela, I. F. Faridyan, N. A. Rachman, A. Risdiyanto, and B. Susanto, "Analisa Unjuk Kerja Grid Tied Inverter Terhadap Pengaruh Radiasi Matahari dan Temperatur PV pada PLTS On Grid," *Elkha*, vol. 11, no. 2, pp. 60–65, 2019.

[3] A. Asrori and E. Yudiyanto, "Kajian Karakteristik Temperatur Permukaan Panel terhadap Performansi Instalasi Panel Surya Tipe Mono dan Polikristal," *FLYWHEEL J. Tek. Mesin Untirta*, vol. 1, no. 1, p. 68, 2019, doi: 10.36055/fwl.v1i1.7134.

[4] S. Sarna, Subhan, R. Murniati, and S. Nojeng, "Pengaruh Temperatur Permukaan Terhadap Efisiensi Konversi Fotovoltaik Tipe Monocrystalline Pada Daerah Tropis," *J. JMove*, vol. 3, pp. 24–30, 2021.

[5] A. Fauzan and L. Hayat, "11520-33322-1-Pb," vol. 3, no. 2, pp. 101–110, 2021.

[6] Y. Mukhammad and A. S. Hyperastuty, "Sensitivitas Sensor MLX90614 Sebagai Alat Pengukur Suhu Tubuh Tubuh Non-Contact Pada Manusia," *Indones. J. Prof. Nurs.*, vol. 1, no. 2, p. 51, 2021, doi: 10.30587/ijpn.v1i2.2339.

[7] W. P. A. Pamungkas, N. Kholis, Nurhayati, and F. Boskoro, "Sistem Control Dan Keamanan Smart Home Berbasis Google Firebase," *J. Tek. Elektro*, vol. 11, pp. 40–46, 2022.

[8] M. Srilatha, C. Abhinav, M. Balaram, and A. Sanjana, "System Using Internet of Things," no. Icicv, pp. 335–342, 2021.

[9] M. Babiuch, P. Foltynek, and P. Smutny, "Using the ESP32 microcontroller for data processing," *Proc. 2019 20th Int. Carpathian Control Conf. ICCC*, pp. 1–6, 2019, doi: 10.1109/CarpathianCC.2019.8765944.

[10] A. Nurbaeti, M. Kusumawardani, and H. Darmono, "Rancang Bangun Alat Pengering Biji Kopi Berbasis Internet of Things," *J. Jartel J. Jar. Telekomun.*, vol. 11, no. 2, pp. 74–80, 2021, doi: 10.33795/jartel.v11i2.60.

[11] J. Sistem, R. Jscr, and R. D. Pranata, "Monitoring Temperature Chiller Water Menggunakan Android Berbasis IoT (Internet of Things)," vol. 4, no. April, pp. 1–8, 2022.

[12] G. Jin, X. Zhang, W. Fan, Y. Liu, and P. He, "Design of non-contact infra-red thermometer based on the sensor of MLX90614," *Open Autom. Control Syst. J.*, vol. 7, no. 1, pp. 8–20, 2015, doi: 10.2174/1874444301507010008.

[13] W. G. Ariastina, "Suhu Bearing Motor Untuk Pompa," vol. 9, no. 2, pp. 20–29, 2022.

[14] A. H. Martin, H. Pranjoto, and R. S. Sitepu, "Sistem Monitoring Suhu Dan Kelembaban Lingkungan Berbasis IoT Dan Listrik Tenaga Surya," *Widya Tek.*, vol. 18, no. 2, pp. 71–76, 2019, doi: 10.33508/wt.v18i2.1918.

[15] K. P. Kartika Riyanti and Y. Prastyo, "Analisis Penggunaan Sensor Suhu Dan Kelembaban Untuk Monitoring Lingkungan Greenhouse Berbasis Arduino," *J. Ilm. Tek. Inform.*, vol. 16, no. 2, pp. 200–210, 2022.

[16] A. Y. Rangan, A. Yusnita, and M. Awaludin, "Sistem Monitoring berbasis Internet of Things pada Suhu dan Kelembaban Udara di Laboratorium Kimia XYZ," *J. E-Komtek*, vol. 4, no. 2, pp. 168–183, 2020, doi: 10.37339/ekomtek.v4i2.404.

[17] S. Samsurizal, A. Makkulau, and C. Christiono, "Analisis Pengaruh Sudut Kemiringan Terhadap Arus Keluaran Pada Photovoltaic Dengan Menggunakan Regretion Quadratic Method," *Energi & Kelistrikan*, vol. 10, no. 2, pp. 137–144, 2019, doi: 10.33322/energi.v10i2.286.

[18] A.- Alhaddad et al., "Perancangan Sistem Pendingin Photovoltaic dengan Memanfaatkan Kontroler Water Spray," *Elkha*, vol. 12, no. 2, p. 47, 2020, doi: 10.26418/elkha.v12i2.39647.

[19] D. Suryana, "Pengaruh Temperatur/Suhu Terhadap Tegangan Yang Dihasilkan Panel Surya Jenis Monokristalin (Studi Kasus: Baristand Industri Surabaya)," *J. Teknol. Proses dan Inov. Ind.*, vol. 1, no. 2, pp. 5–8, 2016, doi: 10.36048/jtpii.v1i2.1791.

[20] M. T. Afif and I. A. P. Pratiwi, "Analisis Perbandingan Baterai Lithium-Ion, Lithium-Polymer, Lead Acid dan Nickel-Metal Hydride pada Penggunaan Mobil Listrik - Review," *J. Rekayasa Mesin*, vol. 6, no. 2, pp. 95–99, 2015, doi: 10.21776/ub.jrm.2015.006.02.1.

[21] H. Apriyani, S. Sismadi, and S. Sefrika, “Penggunaan Internet of Things Dalam Pemasaran Produk Pertanian,” *J. Sist. Komput. Musirawas*, vol. 3, no. 2, p. 74, 2018, doi: 10.32767/jusikom.v3i2.367.
[22] O. K. Sulaiman and A. Widarma, “Sistem Internet of Things (IoT) Berbasis Cloud Computing Dalam Campus Area Network,” 2017, doi: 10.31227/osf.io/b6m79.
[23] A. Junaidi, “Internet of Things, Sejarah, Teknologi Dan Penerapannya: Review,” *J. Ilm. Teknol. Inf.*, vol. IV, no. 3, pp. 62–66, 2015.
[24] A. A. Rahim et al., “Pertanian Pintar menggunakan IoT,” vol. 3, no. 1, pp. 422–428, 2022.

Design and Construction of an IOT-based Electrical Energy Monitoring System using ESP32 at the Hybrid Power Plant on Baru Beach Pandansimo

Isra' Nuur Darmawan
Electrical Engineering
Universitas Wijayakusuma
Purwokerto, Indonesia
isra.nuur.darmawan@unwiku.ac.id

Kholistianingsih
Electrical Engineering
Universitas Wijayakusuma
Purwokerto, Indonesia

Rafi Dwi Waseso
Electrical Engineering
Universitas Wijayakusuma
Purwokerto, Indonesia

***Abstract*— Electricity is essential, and as technology and population grow, so does the demand for electrical energy. Renewable sources like solar and wind power are expanding rapidly, with monitoring systems vital for maximizing efficiency. Technological advancements allow energy monitoring to be accessed remotely via the Internet of Things and an Android app, eliminating manual field measurements. In this study, an energy monitoring system was implemented at the 5kW and 450W Hybrid Power Plant (HPP) at Baru Beach Pandansimo, using the ESP32 microcontroller to process measurements from Pzem 004T (AC voltage/current) and Pzem 017 (DC voltage/current) sensors. Data is sent to a cloud database and displayed on an Android app. The study found average error values for the Pzem 004T sensor: Active Power (2.57%), Frequency (0.004%), Current (2.4%), Energy (2.3%), Apparent Power (2.55%), Voltage (0.28%), and Power Factor (1.8%). For the Pzem 017 sensor, the highest error was 7.49% and the lowest 1.18% (voltage). Despite modest errors, the system is suitable for effective use in real-time energy monitoring.**

***Keywords*—Monitoring of energy, Pzem 004T sensor, Pzem 017 sensor, Internet of Things**

I. Introduction

Electricity is a basic necessity, vital for numerous applications across industries, offices, retail, public infrastructure, and households. As technology advances and populations grow, the demand for electrical energy rises correspondingly, leading to a significant reliance on renewable energy sources [1]. Renewable energy, seen as an environmentally sustainable approach to meeting human energy needs, is gaining widespread adoption. Solar and wind energy are two prominent renewable sources, with photovoltaic (PV) systems and wind turbines emerging as popular options for harnessing energy from sunlight and wind. Monitoring the performance and efficiency of these systems is essential to fully realize their potential [2]. Hybrid Power Plants (HPP), which combine renewable sources with grid or backup systems, are increasingly used to supply reliable power. In an HPP, the inverter is a key component, converting the DC energy generated by solar panels into usable AC electricity. However, any issues with the inverter, such as malfunctions or inefficiencies, can significantly impact the entire system's performance. This highlights the need for an advanced monitoring solution to track and promptly address any issues within the inverter, ensuring the HPP functions at peak efficiency [3]. With the rapid development of information technology, particularly in the field of the Internet of Things (IoT), monitoring systems can now deliver real-time data remotely and with minimal human intervention. IoT-based solutions provide valuable opportunities to monitor, control, and enhance renewable energy systems in a highly efficient manner [4]. This study proposes an innovative IoT-based energy monitoring system as a reliable and efficient solution for tracking HPP performance, implemented at Baru Beach HPP in Pandansimo. Utilizing the ESP32 microcontroller, this system collects data from Pzem 004T sensors for AC parameters (voltage, current) and Pzem 017 sensors for DC parameters. Data on input/output voltage, current, frequency, and conversion efficiency is transmitted to a cloud database, accessible remotely through an Android application. This approach reduces the need for on-site monitoring and provides users with real-time insights to optimize inverter performance, diagnose faults, and take corrective actions as needed. The primary contribution of this research lies in developing a comprehensive real-time monitoring solution that offers intuitive and accessible data for assessing HPP performance. The novelty of this work is its integration of IoT capabilities with traditional energy monitoring, enabling effective, mobile-enabled oversight of a hybrid renewable energy system. This system has the potential to improve overall energy efficiency by providing actionable information to users, making it an essential advancement for sustainable energy management.

979-8-3315-1921-6/24/$31.00 ©2024 IEEE

II. Theoretical Background

A. Literature Review

A study titled "Development of Sensor Nodes for Wireless Electrical Energy Monitoring in Buildings on the Samarinda State Polytechnic Campus with a Microcontroller Base via Android Smartphone as Information Media." This study makes use of an Arduino microcontroller, a PZEM 004t sensor, and a 20x4 LCD screen to display the sensor's data. The data

is then transmitted wirelessly to the gateway or sink using a LoRa radio wave transmitter. The research findings compare the measurement results obtained with the PZEM-004T sensor with the PQA measuring device. The variances are 0.291% for voltage, 2.634% for current, 2.421% for apparent power, 2.449% for active power, 6.505% for power factor, and 0.256% [5]. A study named "Design and Building of Electric Power Monitoring Systems in Boarding Rooms based on the Internet of Things (IoT)". The goal of this research is to create an electrical energy monitoring system with the aim that if there is a significant current surge and it is possible for a short circuit to occur, the microcontroller will order the buzzer to turn on and send a notification to the application to immediately disconnect the electrical circuit before a fire occurs. Excessive electricity consumption can be turned off from anywhere using the Android app [6]. The study is named Design and Development of an Electric Power Monitoring and Control System in Boarding Houses using Android-Based NodeMCU and Firebase. The sensor measurement findings have an accuracy error of ± 1.8% compared to a digital multimeter. The system application test results demonstrate that the application can monitor the power in each boarding room in real-time [7].

B. Electrical Energy Parameters

- Electrical Power

Electric power is defined as the rate at which electrical energy is delivered in a circuit. In AC power networks with sinusoidal waveforms, there are three types of power: active power, reactive power, and apparent power. In complex form, the multiplication of voltage (V) and current (I) yields V*I, also known as power or pseudo with the symbol S and is measured in Volt amperes (VA). The formula for active power, also known as real power, is S cos θ or VI* cos θ , represented by the sign P and measured in watts (W). Meanwhile, reactive power or imaginary power is formulated as S sin θ or VI* sin θ with the symbol Q, in units of reactive Volt Amperes (VAR). Electrical power is separated into three categories: active power, reactive power, and perceived power [6].

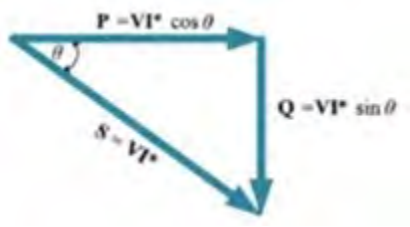

Fig. 2.1. Power Triangle

- Electrical Current

Electric current is the amount of charge that flows in a conductor in one second (coulombs per second), and it is measured in amperes (A). The following equation describes electric current:

$$I = \frac{Q}{t} \tag{1}$$

Description:
I = Electric Current in Ampere (A)
Q = Electric charge in coulomb (C)
t = Time in second (s)

- Voltage

Electric voltage is the size of the potential energy difference between two places, expressed in volts (V) [6]. Voltage can alternatively be expressed as joules per coulomb. Electric voltage can be written using the following equation:

$$V = \frac{E}{Q} \tag{2}$$

Description:
V = Voltage in Volt (V)
Q = Electric charge in couloumb (C)
E = Energy in joule (J)

- Electrical Energy

Electrical energy is the energy produced by electric charges (static) and the movement of electric charges (dynamic). Electrical energy units are typically given in WH (watt hour) or Kwh (Kilo watt hour), as 1 Wh = 3600 joule or 1 joule = 1 watt second. Thus, the electric energy formula can be expressed as the following equation:

$$W = V \times I \times T \tag{3}$$

Description:
W is the Electrical Energy in joules (J)
V is the Voltage in volts (V)
I is the Electric Current in amperes (A)
T is the Time in seconds (s)

- Frequency

Frequency is the number of waves produced in one second, represented by the Latin letter "f" and measured in Hertz (Hz). In international units (SI), Hz denotes a wave that occurs once per second. Frequency is a property of the voltage produced by a generator and its value fluctuates with time [6].

C. Internet of Things

The Internet of Things (IoT) is a technology that allows us to connect machines, equipment, and other physical items with network sensors and actuators to obtain and manage data without the need for two-way human intermediates [8]. The Internet of Things is a concept that uses the internet network to connect electronic equipment with humans, such as processing data collected from electronic equipment via a system-to-user interface. The Internet of Things is a system architecture made up of several devices, including software, hardware, and the web. An example of an Internet of Things application is in

the health sector, where sensors that can detect temperature, humidity, and air pressure are added or installed on tools used on patients, with a system that is integrated with IoT to make the doctor's job easier. In terms of evaluating, monitoring, and treating patients with records, the place where the Internet of Things will be installed has a reliable Internet connection [8].

D. Pzem 004T Sensor

The PZEM-004T is a sensor that measures rms voltage, rms current, and active power and may be connected to Arduino or other open-source platforms. This module is primarily used to measure AC voltage, current, active power, frequency, power factor, and active energy. The module lacks a display capability and data is read via the TTL interface. This module's TTL interface is a passive interface that requires an external 5V power source. When communicating, all four ports (5V, RX, TX, GND) must be connected; otherwise, the sensor will not communicate [9]. Figure 2.2 shows the layout of the PZEM 004T sensor.

E. Pzem 017 Sensor

The DC communication module, also known as PZEM-017, can measure dc power up to 300VDC and current in external and internal shunt installations ranging from 50 to 300 A DC. PZEM-017 is manufactured by Peacefair, a well-known Chinese company known for high-quality products at reasonable costs. Peacefair manufactures metering equipment. This module measures voltage, current, power, and energy. All PZEM Energy Meters are equipped with an inbuilt RS485 communication interface and employ the Modbus-RTU protocol, which is widely used in industrial devices [10]. Figure 2.3 shows the layout of the PZEM 017 sensor.

Fig. 2.2. PZEM 004T Sensor

F. NodeMCU ESP32

NodeMCU is an open-source Internet of things (IoT) platform and development kit that allows programmers to construct IoT product prototypes using the Lua programming language or by using Sketch with the Arduino IDE [11]. This kit's creation is based on the ESP8266 module, which

Fig. 2.3. PZEM 017 Sensor [3]

includes GPIO, PWM (Pulse Width Modulation), IIC, 1-Wire, and ADC (Analogue to Digital Converter) on a single board.

G. Kodular Editor

The process of developing an application for monitoring electrical energy uses Kodular, a web-based open-source platform. This platform allows you to easily and rapidly construct a variety of Android applications without needing to program in writing. This coder is built on visual block programming, which allows you to design programs without coding. Visual block programming is the process of designing Android applications by arranging, dragging, and dropping blocks that contain command symbols and specific event handler routines. Kodular allows users to easily construct applications using the block-type editor. No coding skills are necessary. The application may be run with the Material Design UI [12].

H. Google Firebase

Google Firebase is a Google service that may be accessed through the Firebase website. Firebase is used to help developers with the application development process. This service, known as BaaS (Back as a Service), is a solution provided by Google that attempts to make it easier for developers to conduct their work. Firebase can be used on a variety of platforms, including iOS, Android, and the web [13]. Firebase has numerous types/features, including:

1) Firebase Authentication
   It is one of the back-end services, with Android and iOS support, an easy-to-use SDK, and a ready-to-use interface. Firebase Authentication accepts authentication via phone numbers, passwords, and so on.
2) Firebase Real-Time Database
   It is a cloud-hosted database that stores and executes data in JSON format and synchronizes in real-time with each connected user. This solution can easily manage big databases.
3) Firebase Storage
   It is a service for storing many forms of material, including photographs, audio, and video. Firebase Storage allows you to easily upload and download data for applications.
4) Firebase Cloud Messaging
   It is a service that establishes a dependable and power-efficient link between servers and devices. It provides

free messaging and notification services for Android, iOS, and the Web.

I. LCD 12C 16x2

Liquid Crystal Display (LCD) is a form of display media that uses liquid crystals to create viewable images on the LCD. LCDs are created using Complementary Metal Oxide Semiconductor (CMOS) logic technology [14]. LCD consists of two parts: the main part, which is the backlight, and the liquid crystal part. LCD merely reflects and transmits light that passes through it; hence it requires a backlight (background light) for its light source [15].

J. Arduino IDE

When programming the ESP32 microcontroller, use the Arduino IDE to modify, create, and upload program code to the ESP32 board. The Arduino IDE is built on the JAVA programming language and includes a C/C++ library that simplifies input/output operations. Figure 2.13 shows the Arduino IDE software logo. This software is frequently used by programmers. This Arduino IDE software is suitable for programming a variety of boards, including the Arduino Nano, Arduino Genio, Mappi32, NodeMCU, and others [16]. The code used on Arduino is known as the Arduino ”sketch” or Arduino source code, with the file extension source code.

III. METHODOLOGY

This research, titled Design of an IoT-based electrical energy monitoring system utilizing ESP32 at the HPP Pantai Baru Pandansimo, follows a methodical technique carried out in multiple sections, including:

A. Research Flowchart

This research was conducted in stages, sequentially and systematically, utilizing a research approach that began with a literature review of existing references and the components required to develop an electrical energy monitoring system. The microcontroller utilized is an ESP32 NodeMCU, which includes programming tools and Google Firebase, an internet-connected real-time database. The sensors utilized in the construction of this system are current and voltage sensors that determine current, voltage, and power values from AC and DC sources, with Google Spreadsheet serving as a data logger for measurement results. Programming during the tool design stage is done with the Arduino IDE software, block code, and HTML. Figure 3.1 shows the research path for this research.

Fig. 3.1. Flowchart

B. Identification of Problems

Problem identification is commonly defined as the identification of several issues or problems that exist and the development of plans to address these difficulties. The challenge in this last assignment is to design a hardware and software system for monitoring electrical energy in hybrid power plants.

C. Analysis of Tools and Materials

The hardware development process must follow carefully designed plans to ensure a functional and reliable system. For more information, refer to Tables 3.1, 3.2, and 3.3, which detail the tools, components, and materials selected for this research. The following section provides a thorough justification for each component used, along with an explanation of the design and integration process to create a cohesive and reproducible methodology. The Pzem 004T sensor was chosen for measuring AC voltage and current due to its high accuracy, cost-effectiveness, and compatibility with the ESP32 microcontroller. This sensor is widely used in power monitoring projects and offers reliable measurement data essential for analyzing HPP performance. Similarly, the Pzem 017 sensor, specialized for DC measurements, was selected to monitor DC voltage and current from the PV panels. Its ability to capture precise readings ensures accurate data on solar power generation, which is critical for evaluating and optimizing the inverter's efficiency. The ESP32 microcontroller serves as the central processing unit, gathering data from each sensor and sending it to a cloud-based database. The ESP32 was selected due to its robust wireless capabilities, supporting both Wi-Fi and Bluetooth, which makes it ideal for IoT applications. Additionally, the ESP32's processing power enables real-time data handling and transmission to the Android application, providing immediate access to HPP performance metrics. This methodology integrates the hardware components with custom-designed software, ensuring seamless communication between the sensors, microcontroller, and Android interface.

The system's software is developed to process sensor data, perform necessary calculations, and display results in an accessible format for users. This cohesive flow between hardware and software components improves system reliability, making it easier to monitor and address HPP performance issues. In summary, each sensor and component was selected based on its specific capabilities, reliability, and suitability for the demands of the HPP monitoring system. The unified design and integration of hardware and software create a robust, reproducible methodology that can facilitate further research and improvements in IoT-based energy monitoring systems.

TABLE III.1
LIST OF TOOLS

No	Tools Name	Qty (pcs)
1	Multimeter (Multitester)	1
2	AC and DC Ampere Meter Tongs	1
3	Press Tongs	1
4	Tespen	1
5	Toolkit Set	1
6	Electric Drill	1
7	Cutting Grinder	1
8	Ruler	1
9	Marker Watermark	1
10	K3 Equipment Set	1
11	Laptop	1
12	Holso Drill Bit	1
13	Resibon (Cutting Grinding Bit)	1
14	Electric Drill Bit	1

TABLE III.2
LIST OF MATERIALS

No	Materials Name	Qty (pcs)
1	Male to Female Cable	as required
2	Female to Female Cable	as required
3	Male to Male Cable	1
4	Panel Box 40x30x12 cm	1
5	Power Supply 5 vdc	1
6	LCD 16x2 Yellow Green	2
7	USB Cable Type C	1
8	PZEM 004T Sensor	1
9	Relay 2 Channel 5 Volt	1
10	Selector	1
11	ESP32	2
12	Buzzer	1
13	LED	1
14	Terminal	1
15	PCB Board	50 cm^2
16	Screw Bolt	as required
17	NYAD Cable 1.5 & 2.5 mm	as required
18	MCB	1
19	Burn Glue	3
20	PZEM 017 Sensor	1
21	Panel Box 30x15x10	2
22	Skunk Cable	as required
23	Krustin Terminal 10 Holes	1
24	Timon	5
25	Ties Cable	as required

D. Block of Diagram Series

Block diagrams are used to simplify and explain the design of an electrical energy monitoring system, which is the fundamental blueprint of how the circuit operates. Figure 3.2 shows the block diagram.

TABLE III.3
LIST OF SOFTWARE

No	Software Name	Qty (pcs)
1	Arduino IDE	1
2	Google Firebase	1
3	Kodular	1
4	Google Spreadsheet	1
5	Canva	1
6	Proteus	1

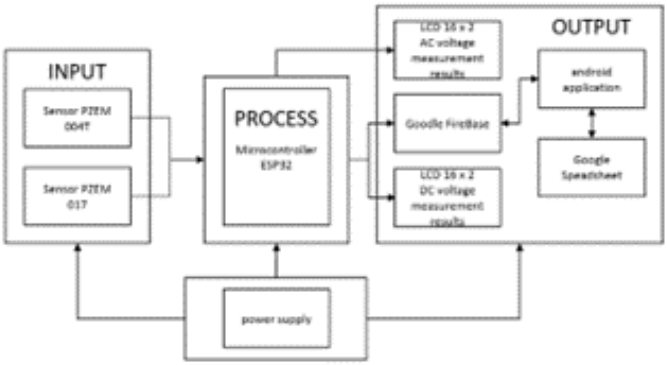

Fig. 3.2. Block of Diagram

E. Flowchart System

This flowchart explains how the system that will be built will employ an ESP32 microcontroller, a Pzem 004T sensor, and a Pzem 017 sensor to read AC and DC measurement values. Figure 3.3 depicts the following flowchart diagram: The software system design employs Kodular software and Google Firebase to handle measurement data, which is subsequently captured and saved in a data logger using Google Spreadsheet. For more information, see Figure 3.4.

F. Hardware Tool Design

Tool design is the first step in taking into account the potential risks. To make the tool production process easier, tool design must follow a proper methodology. The design of an IoT-based electrical energy monitoring tool uses an ESP32 microcontroller according to the input and output needs of each component. Hardware design is the process of creating tools that will eventually be utilized to read sensor input, process data, and generate output. This gadget will function once it is connected to an electrical power source. The stages will be explained below:

- Designing the Schematic of Wiring Series

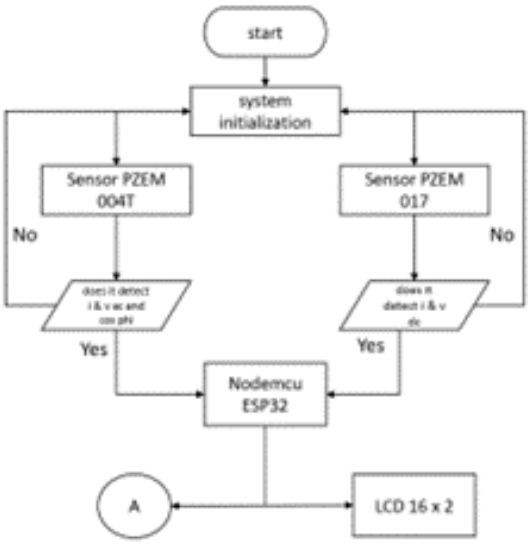

Fig. 3.3. Flowchart of Monitoring System

Fig. 3.4. Flowchart of IoT Software System

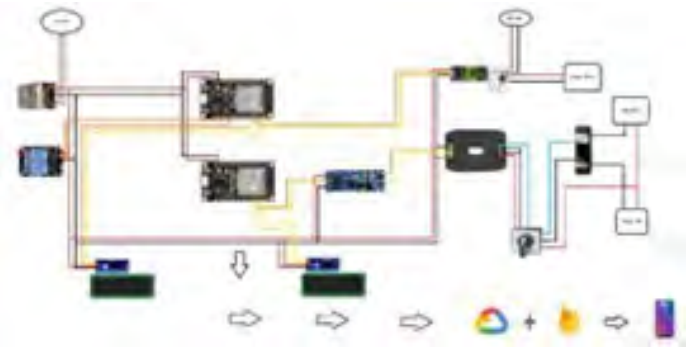

Fig. 3.5. Overall Schematic Wiring Series

- Tool Design

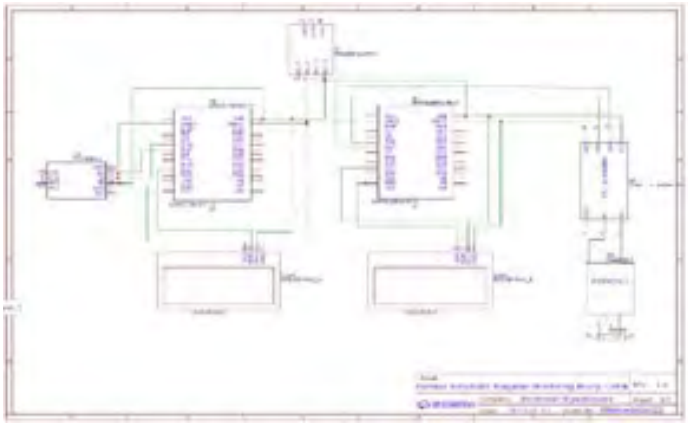

Fig. 3.6. Schematic Series of Electric Energy Monitoring

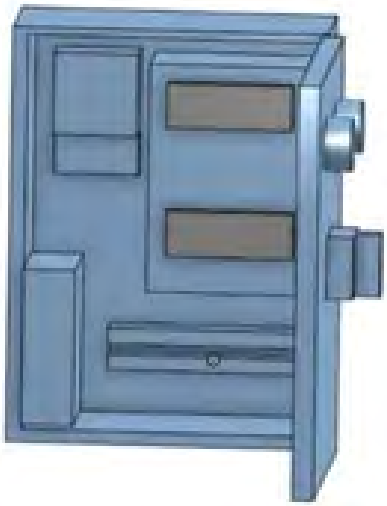

Fig. 3.7. Tool Design

- Component Assembly

Fig. 3.8. Installation of Box Components 1

Fig. 3.9. Installation of Box Components 2

- Mechanical Design Planning
  After the component assembly is completed, the monitoring equipment is mechanically manufactured in a panel box measuring 40x30x12 cm2. Mechanical manufacturing follows the guidelines. 3D design drawings have been created following the drawings. Figure 3.10 shows a picture of the mechanical installation.

Fig. 3.10. Installation of Mechanical Design

Fig. 3.11. Firebase Overview

- Software Tool Design
  Software design is the process of developing programs, databases, and Android application interfaces that will be used to supplement hardware. The program is created using Arduino software, which will then be used as instructions for the microcontroller to carry out tasks. Meanwhile, to create a database, use Google's NOSQL device, Google Firebase. Google Firebase provides the advantage of allowing this device to work in real-time without the need for additional supporting devices. Google Firebase is used to store temporary data before it is displayed in Android applications, as well as to serve as a bridge between Android applications and hardware. The Android application displays measurement results, saves them to a Google Spreadsheet, and prints measurement result logger data. Software development is divided into numerous parts, which include:

- Making Database The objective of constructing a database is to serve as a liaison, information medium, and controller. The database used is a Google Firebase service with real-time database capabilities. The Firebase database is used to store measurement results before they are displayed in the Android application interface, as seen in Figure 3.11.

- Designing Android Application The Android application design stage is completed using the Kodular Studio web service and the block code programming language. Canva software was used to create backdrop images for the application design.

Fig. 3.12. Application Overview

- Making a Spreadsheet of Data Logger
  The data logger design stage uses Google Spreadsheet technologies to store and record measurement data outcomes. To link Google Spreadsheet to the application, input or copy the spreadsheet URL and the URL of each column into the Android Application's block code program. Figure 3.13 shows an image of the data logger.

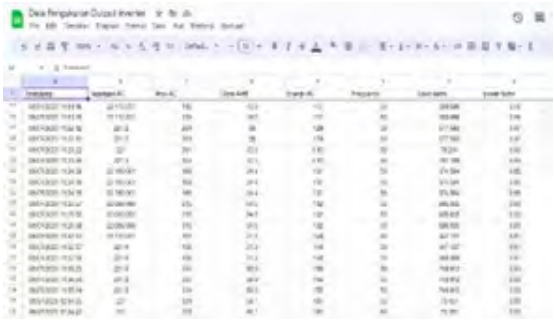

Fig. 3.13. Google Spreadsheet AC Voltage Data

- Making Program of Arduino IDE
  Program creation is the process of writing a program that will be executed by a microcontroller using Arduino IDE software. When you turn on the microcontroller, the program will run. The program is saved in the ESP32's EEPROM, thus it requires more than just writing a set of instructions. When writing a program, it is best to do so in detail because it is well known that when compiling a program, we must pay close attention to whether the program follows the correct logical rules. If the logic in the program is not correct, it will undoubtedly result in errors in the program output.

IV. Result and Discussion

This chapter discusses the results of the design, tool making, research and discussion, and testing carried out following the block diagram of the IoT-based Electrical Energy Monitoring System Design using ESP32 at the Baru Beach HPP Pandansimo. This includes testing of process blocks, input, output, power supply, delay sending data, comparing system performance on different objects, and comparing measurement results from this monitoring tool with existing tools at the test findings are intended to establish the extent to which this tool can perform effectively and efficiently.

A. Software Design Results

- The Android application is compatible with handsets from the lowest version, 5.0 (Lollipop), to the most recent version. The outcomes of developing this application can still be enhanced by adding more comprehensive features. If you want to add new features or screens, simply upgrade the Android program to the latest version.
- The outcomes of developing a database to serve as a bridge between the Android application and electrical energy monitoring gear. Using Google Firebase features to collect real-time measurement data from sensors, which is then shown in an Android app interface.
- The data displayed in the Android application is then recorded and saved in a Google Spreadsheet data logger, allowing us to save measurement data for the desired time. The data saved in Google Spreadsheet can then be downloaded using the Android app as a PDF file.

B. Hardware Design Results

Wiring, mechanical installation, and testing are all part of the hardware design results. Figure 4.1 shows the results of the hardware design.

Fig. 4.1. Electrical Energy Monitoring Tool

C. Tool Testing

The electrical energy monitoring tool was tested on three separate objects: the 450-watt HPP output on the coast, the 450-watt HPP output in the highlands, and the input output of the 5Kw HPP Inverter at Baru Beach Pandansimo. Figure 4.2 shows the following image of tool testing:

Fig. 4.2. Testing of Electrical Energy Monitoring Tools

D. IoT Testing

The tests in this section are designed to test data delivery (delay) and the Android application's ability to work properly with each button and data provided to Google Firebase. Pressing each button helps to test Android applications. Tables IV.1 and IV.2 present the test results.

TABLE IV.1
ANDROID APPLICATION TESTING

Name of Test	Type of Test	Expected Result	Test Result
Opening Application	Opening Application	The application login page appears	Success
Login to the login page	Pressing the login button	The main page appears	Success
Entering the settings page	Pressing the setting button	The settings page appears	Success
Entering the DC voltage monitoring page	Pressing the DC measurement button	The DC voltage monitoring page with its value appears	Success
Entering the AC voltage monitoring page	Pressing the AC measurement button	The AC voltage monitoring page with its value appears	Success
Entering the print data page	Pressing the print data button	The print page of AC and DC voltage data appears	Success
Logout from application	Pressing the exit button	Logout from application	Success
Saves the results of DC voltage measurements into spreadsheets	Pressing the save DC voltage button	Data is saved and recorded in Google Spreadsheet	Success
Saves the results of AC voltage measurements into spreadsheets	Pressing the save AC voltage button	Data is saved and recorded in Google Spreadsheet	Success
Download the results of AC/DC voltage measurement data from the spreadsheet	Pressing the AC/DC voltage download button	AC voltage measurement results data in Google Spreadsheet can be downloaded in PDF form	Success

TABLE IV.2
SOFTWARE DELAY TESTING

No	ESP32 to Firebase (s)	Firebase to Android App (s)	Android App to Spreadsheet (s)	ESP32 to LCD 16x2 (s)
1	3	5	2	6
2	2	6	2	8
3	3	6	1	6
4	3	7	2	7
5	2	5	2	6
6	4	6	1	6
7	4	6	2	6
8	3	5	2	8
9	2	6	2	8
10	2	6	2	7
Mean ($\bar{x}$)	**2.8**	**5.8**	**1.8**	**6.8**

Table IV.2 shows that delay testing is used to get response values for changes in reading in each software sector, from Google Firebase to Google Spreadsheet. The average data delivery values for each sector are shown below. According to the calculation of the fastest delivery value, data is sent from the Android application to Google Spreadsheet in 1.8 seconds, while the longest data transmission is from the ESP32 microcontroller to LCD16 x 2 in 6.8 seconds, sending from the ESP32 microcontroller to Firebase takes 2.8 seconds, and sending from Google Firebase to the Android application takes 5.8 seconds. The following is a bar table displaying average data delivery delays.

E. Testing of Overall System

1) Testing on 450-watt HPP output on the beach
This test was conducted to measure the usage of electrical energy in the 450-watt HPP while in coastal areas. The loads used were 14-watt LED lights, a 45-watt soldering iron, and a 15-watt mobile charger. This test is used to collect data from manual and sensor measurements, and the error value for each experiment is determined based on the results. Table 4.3 shows the following conclusions from computing the error value.

TABLE IV.3
CALCULATION OF ERROR VALUES

Calculation of Error Values%								
No	**V**	**I**	**S**	**P**	**Q**	**F**	**E**	**CosΘ**
1	0.09	5.00	4.95	1.42	5.11	0	1.70	0
2	0.09	6.13	6.22	6.53	16.32	0	6.78	0
3	0.05	1.94	1.98	1.19	11.67	0	0.13	0
4	0.09	1.94	1.98	1.19	11.67	0	0.13	0
5	0.09	6.13	6.22	6.53	16.32	0	6.78	0
$\bar{x}$	0.08	4.23	4.27	3.37	12.22	0	3.50	0

2) Testing on 450watt HPP output in the mountains
This test was performed to monitor the usage of electrical energy on a 450-watt HPP in a highland (hill) environment. Because the HPP produces very little energy, the load employed is merely a 17-watt LED bulb and a 10-watt mobile phone charger. This test is used to collect data from manual and sensor measurements, and the error value for each experiment is determined based on the results. Table IV.4 shows the following conclusions from computing the error value.

TABLE IV.4
CALCULATION OF ERROR VALUES

Calculation of Error Values%								
No	**V**	**I**	**S**	**P**	**Q**	**F**	**E**	**CosΘ**
1	0	1.54	1.53	3.34	1.42	3.58	0	0
2	0.14	2.31	2.18	3.96	2.03	4.33	0	0
3	0.14	0.83	0.68	1.58	0.55	1.11	0	0
4	0.14	1.54	1.66	0.28	1.82	3.05	0	0
5	0	2.31	2.30	4.05	2.13	3.58	0	0
$\bar{x}$	0.08	1.71	1.67	2.64	1.59	3.13	0	0

3) Testing on the input and output of the 5Kw HPP Inverter
The testing on the input and output items of the 5KW HPP inverter lasted 30 trials, with measurements being compared using a multi-tester or the existing measuring

instrument on the 5KW inverter with the electrical energy monitoring tool created by the designer. This test will yield 30 measurement results in the form of data from manual AC voltage measurements and the Pzem 004T sensor, as well as 30 measurement results from DC voltage measurements taken with the Pzem 017 sensor and manually. The data is then analyzed using the percentage error algorithm to determine the error value in the reading results. The error computation yielded the following results: Voltage test results for the Pzem 004T Sensor were obtained by measuring the inverter output voltage to calculate the correct error value for each test. Figure 4.3 shows the error results for the Pzem 004T sensor measurement data using the following formula:

$$\text{Error} = \frac{\text{SMR} - \text{MMR}}{\text{MMR}} \times 100 \tag{4}$$

SMR = Sensor measurement result
MMR = Manual measurement result

The average error findings from trial 1 to trial 30 are as follows:

$$\sum \%\text{Error} = \frac{\text{The number of error values for each trial}}{30} \tag{5}$$

$$\sum \%\text{VE} = \frac{8.41}{30} = 0.28\%$$

$$\sum \%\text{IE} = \frac{72}{30} = 2.4\%$$

$$\sum \%\text{SE} = \frac{76.6}{30} = 2.55\%$$

$$\sum \%\text{PE} = \frac{77.2}{30} = 2.57\%$$

$$\sum \%\text{QE} = \frac{76.6}{30} = 2.55\%$$

$$\sum \%\text{EE} = \frac{68.6}{30} = 2.3\%$$

$$\sum \%\text{FE} = \frac{0.12}{30} = 0.004\%$$

$$\sum \%\text{PFE} = \frac{54.9}{30} = 1.83\%$$

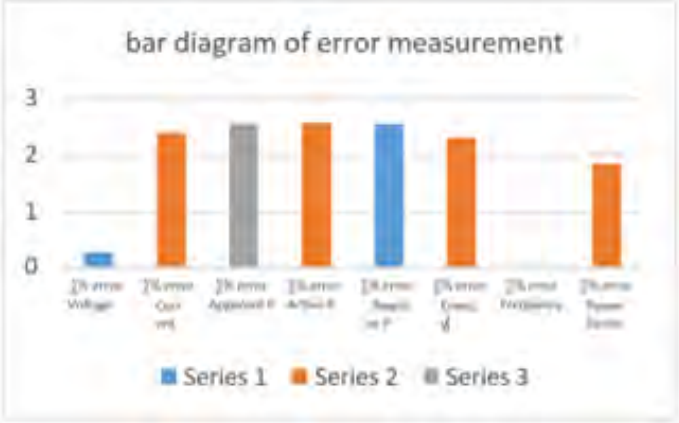

Fig. 4.3. Bar diagram of AC voltage error calculation results

The largest error value obtained from calculating the AC measurement error value is the Active Power error value of 2.57%, while the smallest error value is the Frequency value of 0.004%. The current error value is 2.4%, the energy error value is 2.3%, the apparent power error value is 2.55%, the voltage error value is 0.28%, and the power factor error value is 1.83%. Based on this error value, using the PZEM 004T sensor for AC measurements is still highly suggested to achieve a lower measurement error value, which may then be recalibrated until the same result is obtained.
The inverter input voltage was measured based on the results of voltage testing on the PZEM 017 Sensor to calculate the right error value for each test. Figure 4.4 shows the error results for the PZEM 017 sensor measurement data using the following formula:

$$\text{Error} = \frac{\text{SMR} - \text{MMR}}{\text{MMR}} \times 100 \tag{6}$$

SMR = Sensor measurement result
MMR = Manual measurement result

Based on the error calculation results for each trial from trial 1 to trial 30, the average error results are as follows:

$$\sum \%\text{VE} = \frac{35.4}{30} = 1.18\%$$

$$\sum \%\text{IE} = \frac{212.4}{30} = 6.87\%$$

$$\sum \%\text{WE} = \frac{224.8}{30} = 7.49\%$$

$$\sum \%\text{EE} = \frac{226}{30} = 7.4\%$$

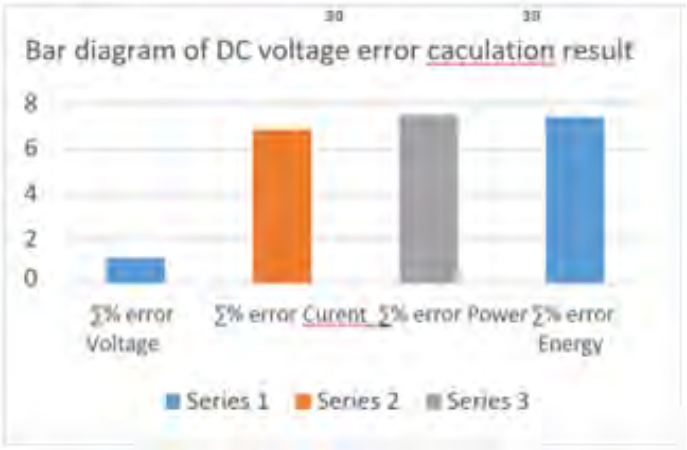

Fig. 4.4. Bar diagram of DC voltage error calculation results

measurement error value was the Power error value of 7.49%, while the smallest error value was the voltage value of 1.18%, the Current error value of 6.87%, and the Energy error value of 7.4%. Proper maintenance on schedule will limit downtime for the Hoover components itself.

V. Conclusion

After completing the design, construction, testing, and data collection stages, several key insights and implications emerge from this research:

1) The developed electrical energy monitoring tool, which includes the Nodemcu ESP32 microcontroller, Pzem 004T and Pzem 017 sensors, TTL RS485 Serial, relay, and power supply, is capable of accurately reading both DC and AC voltage and current measurements. Specifically, it can measure AC voltage from 80 to 260 volts at up to 100 amps and DC voltage from 0.05 to 300 volts at up to 50 amps. Operating at 220 volts with 0.04 amps of current, this tool consumes a minimal power of 8.8 watts, making it suitable for real-time monitoring applications.
2) Testing on three different objects revealed that the prototype performs reliably, with an acceptable percentage error below 8%. For the Pzem 004T sensor, the highest error rate was 2.57% for active power, while the lowest was 0.004% for frequency. Additional results showed current, energy, apparent power, voltage, and power factor errors at 2.4%, 2.%, 2.55%, 0.28%, and 1.83%, respectively. The Pzem 017 sensor showed a slightly higher error margin, with the largest error at 7.49% for power, while the lowest was 1.18% for voltage, followed by 6.87% for current and 7.4% for energy.

These findings indicate that this IoT-based monitoring system provides reliable, real-time performance data, making it a practical solution for optimizing energy efficiency in hybrid power plants. The insights gathered through this tool can assist operators in identifying and addressing inefficiencies or faults promptly. Furthermore, the system's high precision and low power consumption highlight its potential for broader applications in renewable energy monitoring and management, contributing to more sustainable energy practices.

There will be faults and shortcomings in developing and completing this research tool during the system design phase and the tool's making. To achieve more ideal results and rectify the flaws listed above, the following recommendations are required:

1) The application's appearance can be made more appealing and unique by including screens and other elements that allow users to utilize Android applications more conveniently and effectively.
2) To collect more data, do additional experiments on other things such as commercial buildings, Micro Hydro Power Plants, and so on.
3) Attempting to integrate the Android application with other devices so that it may be used in other monitoring tools such as PV temperature monitoring, humidity monitoring, and smart buildings.

References

[1] A. Nurrohim, "Pembangkit Listrik Tenaga Hibrid Sebagai Solusi Kelistrikan Di Daerah Terpencil," J. Sains dan Teknol. Indones., vol. 14, no. 2, pp. 96–103, 2013, doi: 10.29122/jsti.v14i2.911.

[2] Dyah Ayu Kartika Sari, Fransisco Danang Wijaya, and Husni Rois Ali, "Optimasi Sistem Pembangkit Listrik Tenaga Hybrid di Pulau Enggano," J. Nas. Tek. Elektro dan Teknol. Inf., vol. 11, no. 2, pp. 154–160, 2022, doi:10.22146/jnteti.v11i2.3849.

[3] D. Anggraini, "Analisis Potensi Angin Di Pantai Baru Pandansimo Kabupaten Bantul," *J. Tek. Nukl. dan Tek. Fis. UGM*, no. September, pp. 1–6, 2016. [Online]. Available: https://www.researchgate.net/profile/Dita_Anggraini4/publication/307973212_Analisis_Potensi_Angin_Di_Pantai_Baru_Pandansimo_Kabupaten_Bantul/links/57d4dfa208ae0c0081e6fd68/.pdf

[4] M. Naim and S. Wardoyo, "Rancangan Sistem Kelistrikan PLTS on Grid 1500 Watt Dengan Back Up Battery di Desa Timampu Kecamatan Towuti," *Din. J. Ilm. Tek. Mesin*, vol. 8, no. 2, pp. 11–17, 2017.

[5] Irawati, Sunardi, and A. Nurwanto, "Rancang bangun pembangkit listrik tenaga surya (PLTS) dengan sistem kontrol," *J. Elektro Inform. Swadharma*, vol. 03, no. 01, pp. 1–30, 2023.

[6] A. Ansori, B. Yunitasari, S. Soeryanto, and M. Muhaji, "Model Hybrid Pembangkit Listrik Di Pedesaan," Otopro, vol. 13, no. 2, p. 58, 2019, doi: 10.26740/otopro.v13n2.p58-62.

[7] R. M. AKBAR, "Studi Analisa Indeks Keandalan Menggunakan Analisa Perhitungan Eens (Expected Energy Not Supplied) Pada Pembangkit Listrik Tenaga Uap (Pltu) Pt. Pjb Up Gresik," Http://Eprints.Umm.Ac.Id/, vol. 1, no. 2, pp. 96–107, 2020, [Online]. Available: http://eprints.umm.ac.id/54456/

[8] U. Redo et al., "Kajian daya keluaran dari ketidakharmonisan modul fotovoltaik terhadap temperatur ruang dan intensitas cahaya matahari".

[9] S. Sudarti and F. A. Dani, "Potensi Pembangkit Listrik Tenaga Angin di Pantai Blimbingsari Kabupaten Banyuwangi," CIRCUIT J. Ilm. Pendidik. Tek. Elektro, vol. 5, no. 2, p. 93, 2021, doi: 10.22373/crc.v5i2.9565.

[10] A. Choudar, D. Boukhetala, S. Barkat, and J. M. Brucker, "A local energy management of a hybrid PVstorage based distributed generation for microgrids," Energy Convers. Manag., vol. 90, pp. 21–33, 2015, doi: 10.1016/j.enconman.2014.10.067.

[11] M. Azhar and D. A. Satriawan, "Implementasi Kebijakan Energi Baru dan Energi Terbarukan Dalam Rangka Ketahanan Energi Nasional," Adm. Law Gov. J., vol. 1, no. 4, pp. 398–412, 2018, doi: 10.14710/alj.v1i4.398-412.

[12] T. S. Hayu and R. H. Siregar, "Studi Potensi Pembangkit Listrik Tenaga Hybrid (Surya-Bayu) Di Banda Aceh Menggunakan Metode Jaringan Syaraf Tiruan," Kitektro, vol. 3, no. 1, pp. 9–16, 2018.

[13] T. Alamsyah, A. Hiendro, and Z. Abidin, “Analisis Potensi Energi Matahari Sebagai Pembangkit Listrik Tenaga Surya Menggunakan Panel Mono-Crystalline dan Poly-Crystalline Di Kota Pontianak dan Sekitarnya,” J. Tek. Elektron., p. 10, 2019.

[14] S. Rahmah Fitri *et al.*, ”Perbandingan Metoda Interpolasi Inverse Distance Weighted (IDW), Natural Neighbour, Dan Spline Untuk Perapatan Data Peta Potensi Energi Surya,” *Comparison of Inverse Distance Weighted (IDW), Natural Neighbour, and Spline Interpolation Methods for Downscaling*, vol. 13, no. 1, pp. 27–38, 2014. [Online]. Available: https://eosweb.larc.nasa.gov/project/sse/sse_ta

[15] K. A. H. Lakshika, M. A. K. S. Boralessa, M. K. Perera, D. P. Wadduwage, V. Saravanan, and K. T. M. U. Hemapala, ”Reconfigurable solar photovoltaic systems: A review,” *Heliyon*, vol. 6, no. 11, 2020. doi: 10.1016/j.heliyon.2020.e05530.

[16] S. D. Ahmed, F. S. M. Al-Ismail, M. Shafiullah, F. A. Al-Sulaiman, and I. M. El-Amin, ”Grid Integration Challenges of Wind Energy: A Review,” *IEEE Access*, vol. 8, pp. 10857–10878, 2020. doi: 10.1109/ACCESS.2020.2964896.

[17] F. M. Noman, G. A. Alkawsi, D. Abbas, A. A. Alkahtani, S. K. Tiong, and J. Ekanayake, “Comprehensive Review of Wind Energy in Malaysia: Past, Present, and Future Research Trends,” IEEE Access, vol. 8, pp. 124526–124543, 2020, doi: 10.1109/ACCESS.2020.3006134.

[18] R. Mardani, R. F. Gusa, A. Asmar, and W. Sunanda, “Pengaruh Sudut Kemiringan Terhadap Unjuk Kerja Panel Surya (Studi di Universitas Bangka Belitung),” Setrum Sist. Kendali-Tenaga-elektronikatelekomunikasi-komputer, vol. 11, no. 1,pp. 90–97, 2022, doi: 10.36055/setrum.v11i1.14579

Performance Analysis of Convolutional Neural Network Architecture in Batik Design Classification for Mobile Application

Alimuddin
Department of Electrical Engineering
Universitas Sultan Ageng Tirtayasa
Cilegon, Banten, Indonesia
email: alimuddin@untirta.ac.id

Ria Arafiyah
Computer Science
Faculty of Natural Science and Mathematics
Universitas Negeri Jakarta
Jakarta, Indonesia
email: riaarafiah@unj.ac.id

Irfansyah Nur Aviatna
Department of Electrical Engineering
Universitas Sultan Ageng Tirtayasa
Cilegon, Banten, Indonesia
email: 3332200056@untirta.ac.id

Mukhtar
Department of Statistics
Universitas Sultan Ageng Tirtayasa
Cilegon, Banten, Indonesia
email: mukhtar@untirta.ac.id

Heri Haryanto
Department of Electrical Engineering
Universitas Sultan Ageng Tirtayasa
Cilegon, Banten, Indonesia
email: heri.haryanto@ft-untirta.ac.id

Masjudin
Department of Electrical Engineering
Universitas Sultan Ageng Tirtayasa
Cilegon, Banten, Indonesia
email: masjudin@untirta.ac.id

***Abstract*—Indonesia, an archipelago rich in cultural heritage, is home to batik, a traditional textile art recognized by UNESCO. Batik is known for its distinctive and intricate patterns, which have evolved over time and remain an important part of Indonesian cultural identity. Batik's unique pattern characteristics and thousands of patterns make it an interesting subject to study. The purpose of this study is to analyze the performance of different artificial neural network architectures, such as MobileNet, MobileNetV2, MobileNetV3, EfficientNetV2, and ShuffleNetV2, with classifying batik designs for mobile applications. This study evaluated and compared how well each architecture does in classifying batik designs. Testing involves implementing and training artificial neural networks with a dataset of batik designs. The research compared five pre-trained CNN architectures: MobileNet, MobileNetV2, MobileNetV3, EfficientNetV2, and ShuffleNetV2 for classifying batik patterns. The EfficientNetV2 architecture outperformed others, achieving the highest validation accuracy of 85.93% and an F1-score of 86%. MobileNet architecture followed closely with 83.32% validation accuracy and an F1-score of 83%. The results underline the effectiveness of CNN-based transfer learning in cultural heritage preservation, offering a robust method for accurately classifying intricate batik patterns. It is hoped that this research will help in the development of effective and appropriate technologies for using artificial intelligence in the context of art and culture.**

***Index Terms*—Convolutional Neural Network, Batik Design, MobileNet, MobileNetV2, MobileNetV3, ShuffleNetV2, EfficientnetV2**

I. Introduction

Indonesia is renowned for being an archipelagic nation abundant in artistic and cultural diversity. One of Indonesia's renowned cultural legacies, which has endured for centuries as a distinctive aspect of the nation's identity, is batik, a form of textile art that has been acknowledged by UNESCO [1].

979-8-3315-1921-6/24/$31.00 ©2024 IEEE

Indonesian batik is rapidly developing, with more types and new patterns that are hard to distinguish. Batik's unique pattern characteristics and thousands of patterns make it interesting to study [2]. Batik techniques have been the subject of patent research since 1974 [3]. There are four different methods for making batik: written batik, stamped batik, printed batik, and combination batik. Visually, the texture of batik images is defined by (1) pattern repetition, (2) spatial distribution, and (3) color arrangement and intensity [4].

Batik patterns have been classified using artificial intelligence (AI) techniques like neural networks [5]. Education is just one of many areas that makes extensive use of artificial intelligence [24] [29]., ANFIS is a prediction method that combines the principles of artificial neural networks and fuzzy logic [22] [25] [26], Broiler chicken cultivation management [28], electricity load forecasting for the short term [23], optimization of power losses in the distribution network [27].

The significance of image classification in computer vision has experienced rapid growth, primarily due to its utilization in various applications such as object recognition, quality control, medical diagnosis, content-based image retrieval, and video analysis [6] [7] [8] [9]. Because Deep Convolutional Neural Networks (CNN) can learn high-level image representations, they have gained popularity as a solution to this issue [10].

CNN itself is often used in several studies such as image classification to detect welding defects [11], Remote Sensing [12], Classification of brain tumors [13], classification of plant diseases [14], breast cancer [15]. Nevertheless, this project recognizes batik designs using CNN.

This project tested a number of MobileNet convolutional neural network (CNN) architectures [16],, MobileNetV2 [17], MobileNetV3 [18], EfficientNetV2 [19], and ShuffleNetV2

[20], are purpose-built to perform computer vision tasks such as image classification and object detection. Apart from that, it is suitable for use on mobile devices because it has a lightweight architecture. The CNN model is used as transfer learning, which has been previously trained to perform image classification tasks. Later it can be adjusted to the project being worked on. The aim of using transfer learning is to increase accuracy during training.

II. Methods

A. Study of literature

The objective of the literature study is to examine the theories that underpin system planning and design. The literature review should cover topics such as machine learning, Convolutional Neural Network (CNN), different CNN architectures, various Python libraries used in computer vision, and Transfer learning.

B. Algorithm Design

Our algorithm design aims to organize the use of machine learning and transfer learning in the dataset training process so that we can get a model for sorting batik patterns into groups. Python is used in this project, along with libraries like Tensorflow, Keras, and Tf Hub. This picture shows the design of the model training algorithm.

Fig. 1. Research Flow Diagram.

Figure 3.1 above depicts the algorithm design for model training in machine learning. Datasets were initially collected from the Kaggle website and a variety of other sources. Following that, the dataset is divided into training and test sets. Both data sets were pre-processed, specifically by changing the pixel size to 224 x 224 pixels. Following that, before being trained in a machine learning architecture to determine weight and bias values, the training data is applied to the data augmentation step. This aims to reduce overfitting between training and test accuracy. Following that, an evaluation is performed using pre-processed test data. The evaluation will continue until the optimal weight and bias values are obtained. The final result is a machine learning model with the.h5 extension that can detect the given object.

C. Dataset Collection

This dataset was collected in two ways, namely by Web Scrapping and also through various sources such as Kaggle. The following is an image of the Kaggle display with the Google Colab display.

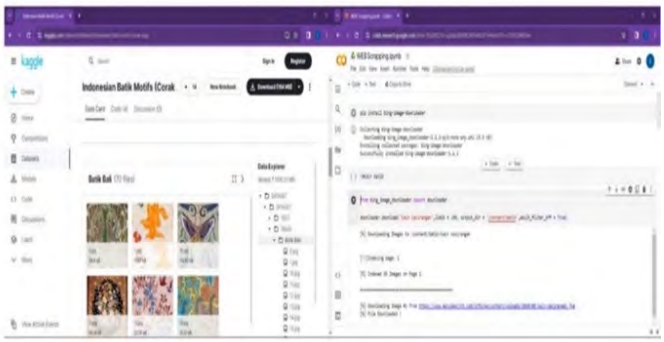

Fig. 2. Dataset collection sources

Figure 2 above shows the appearance of the Kaggle website and also the appearance of Google Colab which is used for web scrapping after the dataset has been successfully obtained. Next, the dataset that has been successfully downloaded is sorted and selected, because many classifications are not suitable, which can affect accuracy when training is carried out.

D. Convolutional Neural Network Architecture Design

For the design of this architecture, an initial choice was made to use a pre-trained CNN architecture that had undergone transfer learning. The architectures considered for transfer learning included MobileNet, MobileNetV2, MobileNetV3, EfficientNetV2, and ShuffleNetV2. Subsequently, a custom-built architecture is employed, featuring an output layer that aligns with the number of classes or designs to be predicted.

The function to lessen overfitting during training is shown in Figure 3's Dropout section. Beneath it is a Dense layer with units of 150 that has been adjusted to ReLU activation. Subsequently, the output layer, also known as the bottom Dense Layer, activates Softmax and sets the layer's units value to 104. There are units in the output layer that represent the number of trained classes.

Dropout 0.6: Regularization technique to prevent overfitting during training by randomly deactivating a subset of neurons in the layer. During training, a fraction (e.g., 20%-50%) of the neurons are randomly selected and set to zero for each forward pass.

This forces the network to learn robust features by not relying on specific neurons. At inference time, all neurons are

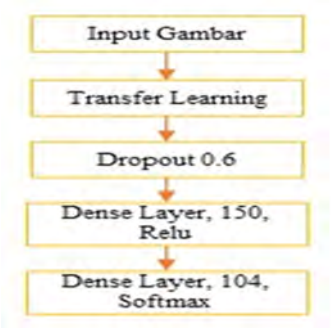

Fig. 3. Incremental architecture

active, but their weights are scaled down proportionally to the dropout rate to maintain consistency.

Dense Layer 150: Connects every neuron from the current layer to every neuron in the next layer, enabling the network to learn global patterns. Computes weighted sums of inputs followed by a non-linear activation function (like ReLU or Sigmoid) to introduce non-linearity. Often used at the final stages of a neural network to map learned features to specific output predictions (e.g., class probabilities).

Softmax Activation: Converts raw logits (real-valued outputs) from the final dense layer into probabilities for classification tasks. Exponentiates each logit to make all values positive. Normalizes these exponentiated values by dividing by their sum, ensuring the output lies between 0 and 1 and sums to 1.

1) MobileNetV1: MobileNetV1 is a lightweight neural network architecture designed specifically for mobile and embedded vision applications. It introduces an innovative concept called **depthwise separable convolutions,** which factorizes a standard convolution into two separate layers: depthwise convolution (spatial filtering) and pointwise convolution (channel-wise combination). This design significantly reduces the computational complexity and model size while maintaining high performance on tasks like image classification, object detection, and more [18].

2) MobileNetV2: MobileNetV2 is particularly notable for its ability to perform well on modern benchmarks like ImageNet while being compact and efficient. MobileNetV2 is a deep learning architecture designed for resource-constrained environments such as mobile and embedded devices. It builds upon the strengths of its predecessor, MobileNetV1, and introduces two major innovations: 1) **Inverted Residuals:** This structure connects thin bottleneck layers directly, allowing the network to use fewer parameters while maintaining performance. The expansion phase increases the number of channels before applying lightweight convolutions, and 2) **Linear Bottlenecks:** Non-linearities are removed in narrow layers to preserve the representational power of the network. This improves efficiency without sacrificing accuracy [19].

3) MobileNetV3: MobileNetV3 is a family of efficient neural network architectures designed for mobile and resource-constrained devices. It is developed through a combination of hardware-aware neural architecture search (NAS) and the NetAdapt algorithm, coupled with advancements in network design [18].

4) EfficientNetV2: EfficientNetV2 is a family of convolutional networks designed for faster training and better parameter efficiency. It achieves significant improvements in both training speed and model size through the combination of training-aware Neural Architecture Search (NAS) and a novel scaling method [19].

5) ShuffleNetV2: ShuffleNet V2 is an efficient neural network architecture designed to optimize performance for mobile and resource-constrained devices. The architecture was developed based on the principle that computational efficiency should go beyond FLOPs (floating-point operations) and consider real-world performance factors, such as memory access cost and platform characteristics [19].

E. Training Dataset

Dataset training is one of the most important parts of this research, because the results of this training will produce a model that is able to classify objects which in this research are able to detect batik designs. The dataset training process can be seen in Figure 3.1, where after the training data has been subjected to pre-processing, it then enters the training stage. In this training stage, the transfer learning method uses MobileNet, MobileNetV2, MobileNetV3, EfficientNetV2, and ShuffleNetV2. After that I used the Dropout layer to reduce overfitting and also the Dense layer and also softmax as output layers which have been adjusted to the specified number of classes.

F. Testing

At this stage, the prediction results from the previously created model are tested. The goal is to determine whether the model is suitable for use. Figure 3.1 shows the testing flow during the evaluation stage. This test determines the model's accuracy in predicting the class or design based on the input entered. To measure or evaluate a model's performance, parameters such as accuracy, precision, recall, and F1-score are required. The equations for these parameters are as follows:

$$\text{Accuracy} = \frac{Tp + Tn}{Tp + Tn + Fp + Fn} \tag{1}$$

$$\text{Precision} = \frac{Tp}{Tp + Fp} \tag{2}$$

$$\text{Recall} = \frac{Tp}{Tp + Fn} \tag{3}$$

$$F1\text{-score} = 2 \cdot \frac{\text{Precision} \cdot \text{Recall}}{\text{Precision} + \text{Recall}} \tag{4}$$

True positive (Tp) refers to a test result that correctly identifies someone as positive when they are. True negative (Tn) refers to a test result that correctly identifies a person as negative when they are actually negative. False positive (Fp) refers to a test result that incorrectly identifies a person as

positive when they are actually negative. False negative (Fn) refers to a test result that incorrectly identifies a person as negative when they are actually positive [21].

III. Results and Discussion

A. Dataset Preparation Stage

Following the successful collection of the dataset from multiple sources. This dataset uses a variety of pre-processing and augmentation methods, including resize, flip horizontal, flip vertical, rotation, brightness, noise, crop, and blur.

1) Resize : After applying the resizing process, all images are changed to a size of 224 x 224 pixels, this size is chosen so that it is consistent with the model architecture used and does not take too long training time, because the larger the pixel size of an image, the longer the training process will take because the model which is formed increasingly complex with a greater number of parameters. The following is a comparison of the images after applying the resize:

Fig. 4. Image after applying resize

In the image above you can see that the image is losing pixels or data from the image itself so it looks blurrier.

2) Flip : The images in the dataset are transformed by being flipped horizontally as well as vertically. This aims to enable the model to recognize objects from different viewpoints and also increase the sensitivity of the model in horizontal and vertical variations. The following is an image where Rotation is applied. The following is a comparison of the images after applying the flip in Figure 5.

3) Rotation : The images in the dataset are transformed by being flipped horizontally as well as vertically. This aims to enable the model to recognize objects from different viewpoints and also increase the sensitivity of the model in horizontal and vertical variations. The following is an image where Rotation is applied in Figure 6.

Fig. 5. Image after applying Horizontal and Vertical Flip

Fig. 6. Image after rotation is applied

4) Noise : A noise filter is implemented on the images in the training data. White spots are present in images that employ the applied noise feature. Because of inadequate lighting or inadequate camera quality, images may contain noise. The objective of this feature is to enhance the model's ability to identify objects that exhibit these disorders. The image below is an example of noise application in Figure 7.

5) Brigtness: The images in the training data are given brightness settings. This seeks to allow the model to identify objects or images varying in lighting level. Here is a picture illustrating application of brightness in Figure 8.

6) Crop: The training data contains cropped images. The objective of this is to guarantee that the model can concentrate more on identifying the design of the desired object. Due to the presence of a combination of batik designs in certain batiks. The subsequent example is a cropped image in Figure 9.

7) Blur: The training data contains cropped images. The objective of this is to guarantee that the model can concentrate more on identifying the design of the desired object. Due to the presence of a combination of batik designs in certain batiks. The subsequent example is a cropped image in Figure 10.

Fig. 7. Image after applying noise

Fig. 8. Image after applying Brightness

Fig. 9. Image after Crop is applied

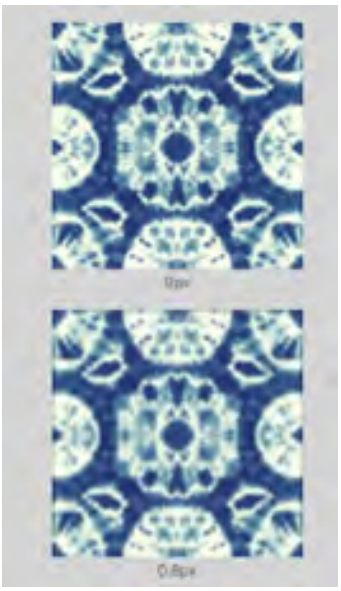

Fig. 10. Image after applying Blur

B. Artificial Neural Network Architecture Analysis

This section examines each architecture's application of the machine learning process to a dataset of batik design objects or classes. The parameters used in this study are training accuracy, validation accuracy, precision, recall, F1-score, and number of parameters.

1) Analysis of MobileNet Architecture Results: In research using the MobileNet architecture, results can be seen using a confusion matrix to find out the values of Accuracy, Precision, Recall and also F1-score by using several functions such as Accuracy score, Precision score, Recall score, F1-score, and classification report which are functions from a library in Python called Sklearn. The following is a table of results from experiments that use parameters such as Accuracy, Precision, and Recall, and F1-score.

TABLE I
PERFORMANCE OF THE MOBILENET ARCHITECTURE

Total Parameter	Training Accuracy	Validation Accuracy	Precision	Recall	F1-score
3.398.318	94,24	83,32	86	83	83

Based on table 1 above, the total parameters of the MobileNet architecture are 3,398,318. Results were obtained with a validation accuracy of 83.32% and an F1-score value was achieved which is the balance value of Precision and Recall of 83%. Apart from that, it also displays a visualization of the performance of training per epoch using a Python library called matplotlib as shown in the image below.

In Figure 11 above is a comparison of training loss and

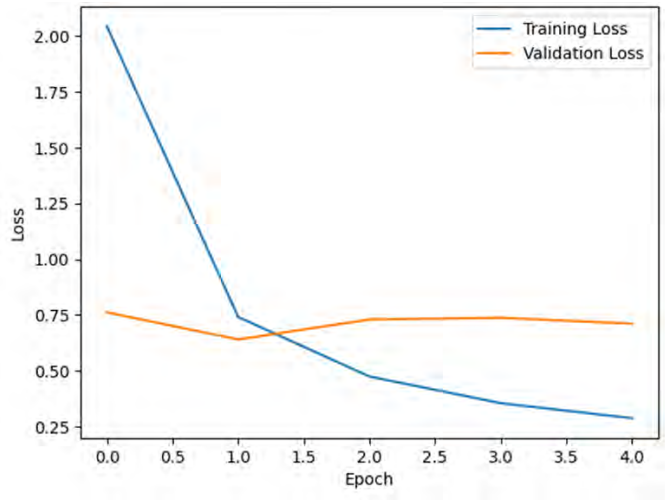

Fig. 11. Loss graph in the MobileNet Architecture Training Process

validation loss per epoch in the MobileNet Architecture. It can be seen that in the second epoch the validation loss shows that there is no decrease in the amount of loss. So the training process on the MobileNet architecture stops at the fourth epoch because programming uses the EarlyStopping callback feature, where the training process will stop when there is no decrease in the amount of loss for several epochs. In programming, the patience argument is set to a value of 3, which regulates the number of limits in the training process when there is no reduction in the number of losses. If for 3 epochs there is no decrease in the amount of loss, then the training process will be stopped.

Fig. 12. Confusion Matrix Results for MobileNet Architecture

Following a series of observations during the training process. Subsequently, we evaluate the outcomes of the model classification for each classification. We employ one of the Sklearn library's functions, confusion matrix, in the image above. Tabular representations of the confusion matrix are available. The objective of this function is to compare the model's predictions with the actual situation. In the example image above, the Betawi Batik class successfully classified 32 objects. However, there was a classification error in the Javanese Barong Batik class once and in the Ayam Pelung Batik class twice, which was considered to be the Betawi Batik class. The classes in the image above are restricted to a maximum of 10 classes due to the fact that the results of the confusion matrix will be difficult to discern if the entire class is displayed.

2) Analysis of Results from the MobileNetV2 Architecture: When conducting research with the MobileNetV2 architecture, one can analyze the results using a confusion matrix to determine the values of Accuracy, Precision, Recall, and F1-score. These metrics can be calculated using various functions such as Accuracy score, Precision score, Recall score, F1-score, and the classification report function provided by the sklearn library in Python. Below is a table displaying the outcomes of experiments utilizing parameters such as Accuracy, Precision, Recall, and F1-score.

TABLE II
PERFORMANCE OF THE MOBILENET ARCHITECTURE

Total Parameter	Trainig Accuracy (%)	Validation Accuracy (%)	Precision (%)	Recall (%)	F1-score (%)
3.398.318	94,24	83,32	86	83	83

Based on table 2 above, with a total parameter of 3,706,269, results were obtained with validation accuracy of 82.04% and an F1-score value was achieved which is the balance value of Precision and Recall of 78%, which has smaller results than the previous version. namely MobileNet. Apart from that, it also displays a visualization of the performance of training per epoch using a library from Python called Matplotlib as shown in the image below.

In Figure 13 below is a comparison of training loss with validation loss for each epoch on the MobileNetV2 architecture. It can be seen that in the third epoch validation loss shows that there is no decrease in the amount of loss. So the training process on the MobileNetV2 architecture stops at the sixth epoch because the programming process uses the EarlyStopping callback feature, where the training process will stop when there is no decrease in the number of losses for several epochs. In programming, the patience argument is set to a value of 3, which regulates the number of limits in the training process when there is no reduction in the number of losses. If for 3 epochs there is no decrease in the amount of loss, then the training process will be stopped.

In figure 14 After observations were made in the training process. Next, we observe the results of the model classification for each class. One of the functions in the Sklearn library called confusion matrix is used. The confusion matrix is presented in tabular form. This function aims to compare model predictions with the actual situation. As in the example

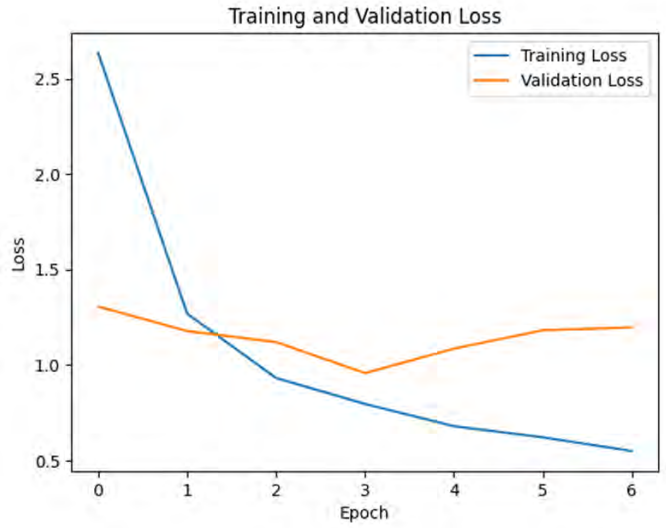

Fig. 13. Loss graph in the MobileNetV2 Architecture Training Process

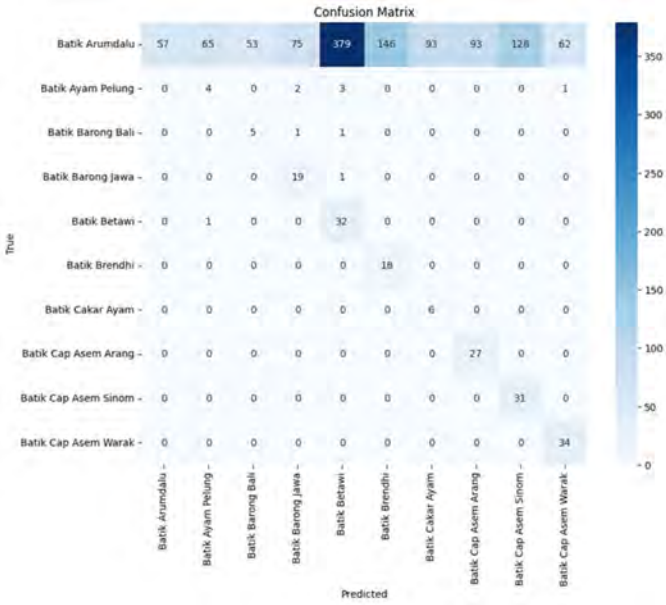

Fig. 14. Confusion Matrix Results for MobileNetV2 Architecture

in Figure 14 above, the Betawi Batik class succeeded in classifying 32 objects correctly, and there was an error in classification in the Javanese Barong Batik class 1 time, Balinese Barong Batik 1 time, and Pelung Chicken Batik 3 times which were considered as classes. Betawi Batik. In the picture above the classes are limited to 10 classes, because the results of the confusion matrix will be difficult to see if all classes are displayed.

3) Results Analysis of MobileNetV3 Architecture: Results of research employing the MobileNetV3 architecture can be observed using a confusion matrix to ascertain the values of Accuracy, Precision, Recall and also F1-score by using several functions such Accuracy score, Precision score, Recall score, F1 score, and classification report which is a function from a library in Python called Sklear. The results of tests employing accuracy, precision, recall, and F1-score are compiled in a table here.

TABLE III
PERFORMANCE OF THE MOBILENET ARCHITECTURE

Total Parameter	Trainig Accuracy (%)	Validation Accuracy (%)	Precision (%)	Recall (%)	F1-score (%)
5.674.717	89,21	79,65	81	80	78

Based on table 4.3 above, with a total parameter of 5,674,717, results were obtained with a validation accuracy of 79.65% and an F1-score value of 81%, representing the balance of Precision and Recall. Despite having a higher F1-score value than the MobileNetV2 version, it is still several percentage points lower than the MobileNet version. Aside from that, it shows a visualization of training performance per epoch using the Python library matplotlib, as shown in the image below.

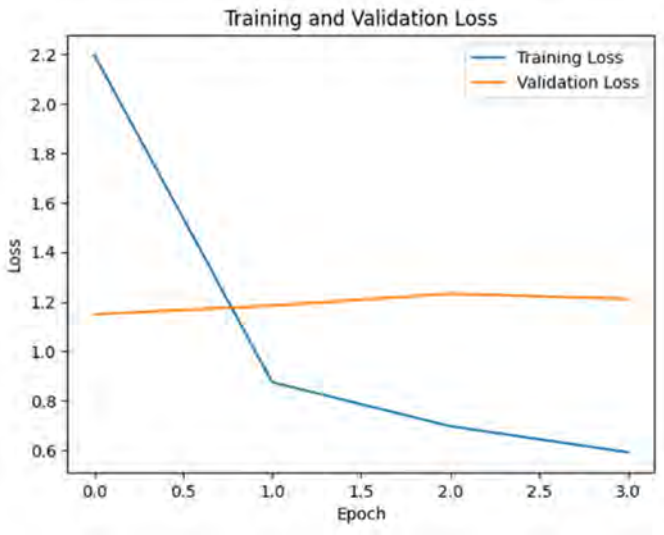

Fig. 15. The MobileNetV3 Architecture Training Process's Loss Graph

Figure 15 shows a comparison of training loss to validation loss per epoch on the MobileNetV3 architecture. It is clear that after the first epoch, the validation loss remains constant. So, the training process on the MobileNetV3 architecture ends at the third epoch because the programming process employs the EarlyStopping callback feature, which causes the training process to stop when the number of losses does not decrease over several epochs. In programming, the patience argument is set to 3 to control the number of limits in the training process when the number of losses does not decrease. If the amount of loss does not decrease after three epochs, the training process will be stopped.

Following a series of observations during the training process. Subsequently, we evaluate the outcomes of the model classification for each classification. The Sklearn library em-

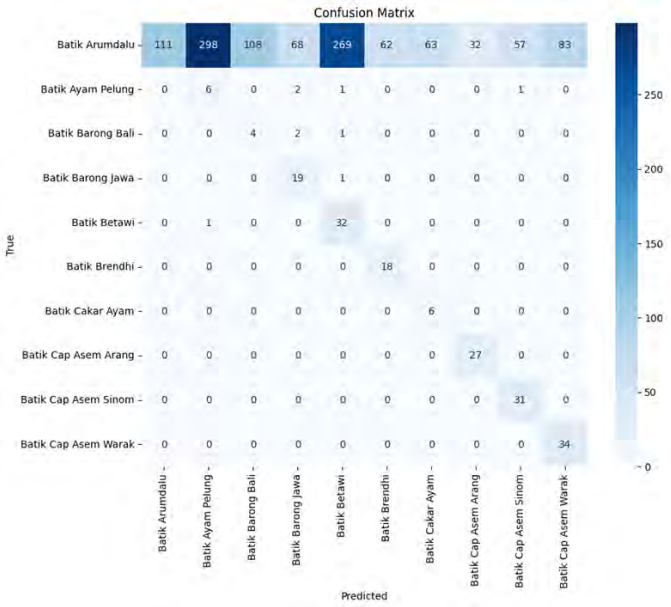

Fig. 16. Confusion Matrix Results for MobileNetV3 Architecture

ploys a function known as the confusion matrix. Tabular representations of the confusion matrix are available. The objective of this function is to compare the model's predictions with the actual situation. As illustrated in Figure 16, the Betawi Batik class successfully classified 32 objects. However, there was an error in classification in the Javanese Barong Batik class, Balinese Barong Batik class, and Pelung Chicken Batik class, which were all considered classes. Betawi Batik. The classes in the image above are restricted to a maximum of 10 classes due to the fact that the results of the confusion matrix will be difficult to discern if the entire class is displayed.

4) Analysis of Results from the EfficientNetV2 Architecture: Research employing the EfficientNetV2 architecture shows results using a confusion matrix employing several functions from one of the libraries in Python called sklearn: Accuracy score, Precision score, Recall score, F1 score, and classification report. Results from studies employing parameters including Accuracy, Precision, Recall, and F1-score are compiled here.

TABLE IV
PERFORMANCE OF THE MOBILENET ARCHITECTURE

Total Parameter	Trainig Accuracy (%)	Validation Accuracy (%)	Precision (%)	Recall (%)	F1-score (%)
7.366.166	97,35	85,93	87	86	86

Based on table 4 above, with a total parameter of 7,366,166, results were obtained with a validation accuracy of 85.93% and an F1-score value of 86%, representing the balance of Precision and Recall. So far, the EfficientNetV2 architecture has the highest F1-score among the previous architectures: MobileNet, MobileNetV2, and MobileNetV3. Aside from that, it displays a visualization of the training performance for each epoch using the Python library matplotlib, as shown in the image below.

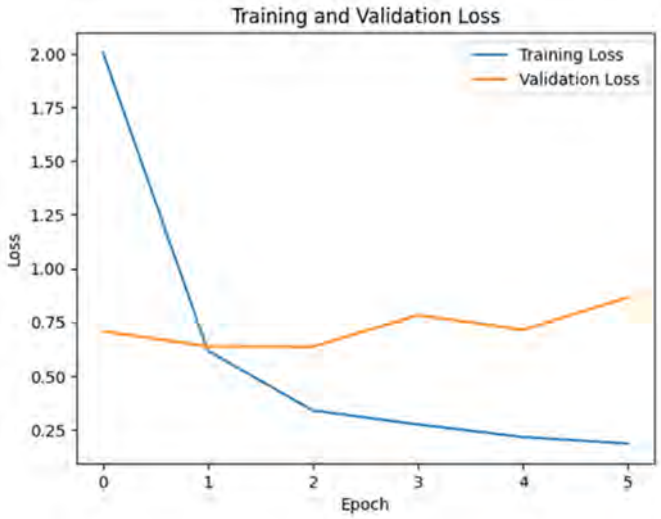

Fig. 17. Loss graph in the EfficientNetV2 Architecture Training Process

The diagram in Figure 17 illustrates the training loss and validation loss per epoch for the EfficientNetV2 Architecture. It is evident that the validation loss does not decrease after the second epoch. The training process of the EfficientNetV2 architecture is halted at the 6th epoch due to the implementation of the EarlyStopping callback feature. This feature terminates the training process if there is no reduction in the loss function for a consecutive number of epochs. In programming, the patience argument is assigned a value of 3, which controls the number of iterations in the training process where there is no decrease in the loss function. The training process will be terminated if there is no reduction in the loss for 3 consecutive epochs.

In Figure 18 following the completion of observations during the training process. Subsequently, we analyze the outcomes of the model's classification for every individual class. The Sklearn library includes a function called confusion matrix that is utilized. The confusion matrix is displayed in a tabular format. The purpose of this function is to juxtapose model predictions with the real-life circumstances. In the given example shown in Figure 18, the Betawi Batik class accurately classified 32 objects, while the Balinese Barong Batik class had one classification error, and the Ayam Pelung Batik class also had one misclassification, which was mistakenly identified as the Betawi Batik class. The number of classes in the picture is restricted to 10 in order to enhance the visibility of the confusion matrix results. Displaying all classes would make it challenging to perceive the results effectively.

5) ShuffleNet V2 Architectural Result Analysis: In research on the performance of the ShuffleNetV2 architecture, results can be seen using a confusion matrix to find out the values of Accuracy, Precision, Recall, and F1-score by using several functions such as Accuracy score, Precision score, Recall score, F1 score, and classification report from a Python library

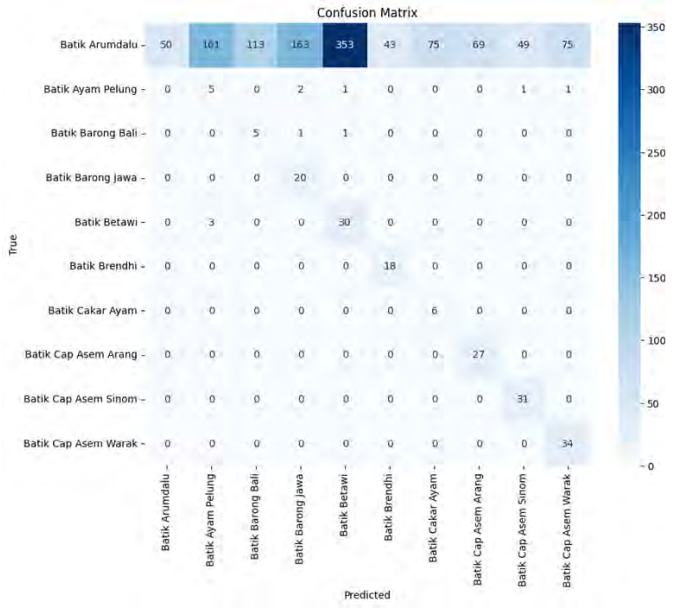

Fig. 18. EfficientNetV2 Architecture Confusion Matrix Results

called Sklearn. The table below shows the results of experiments using parameters such as accuracy, precision, recall, and F1-score.

TABLE V
PERFORMANCE OF THE MOBILENET ARCHITECTURE

Total Parameter	Trainig Accuracy (%)	Validation Accuracy (%)	Precision (%)	Recall (%)	F1-score (%)
1.423.058	77,17	78,76	79	79	77

Based on table 5 above and a total parameter of 1,423,058, results were obtained with a validation accuracy of 78.76% and an F1-score value of 77%, which represents the balance of Precision and Recall. Compared to previous architectures, the ShuffleNetV2 architecture has the fewest parameters, but an F1-score value that is nearly identical to MobileNetV2, which has 3,706,269 parameters and an F1-score value of 78%. Aside from that, it shows a visualization of training performance per epoch using the Python library matplotlib, as shown in the image below.

Figure 19 below shows a comparison of the ShuffleNetV2 architecture's training and validation losses for each epoch. It is evident that there has been no decline in the number of validation losses following the 28th epoch. Because the programming process makes use of the EarlyStopping callback feature, which causes the training process to end when there is no decrease in the number of losses for multiple epochs, the training process on the ShuffleNetV2 architecture ends at the 29th epoch. When there is no decrease in the number of losses, the number of limits in the training process is controlled by the patience argument in programming, which has a value of 3. The training process will end after three epochs if there is no decrease in the loss amount.

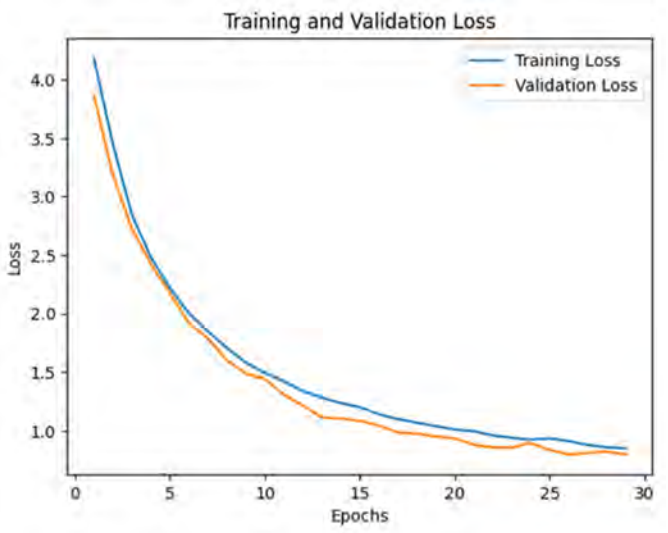

Fig. 19. displays the graph of losses during the training process of the ShuffleNetV2 architecture.

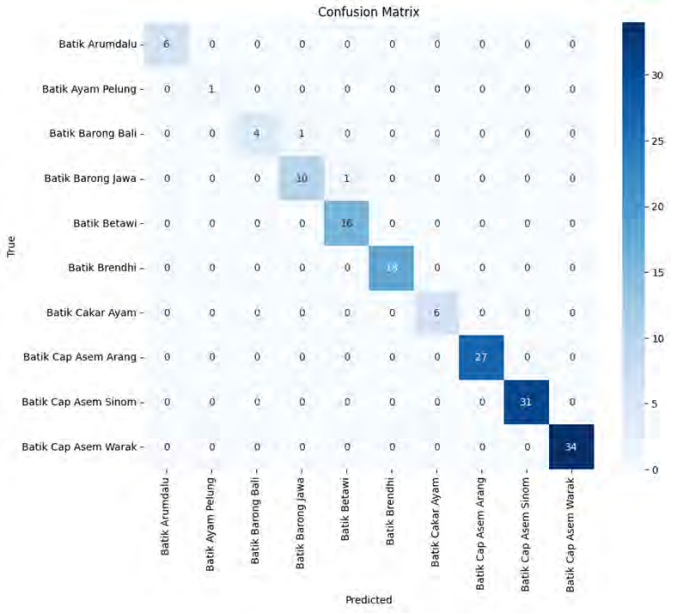

Fig. 20. ShuffleNetV2 Architecture Confusion Matrix Results

Following the completion of observations during the training process. Subsequently, we analyze the outcomes of the model's classification for every individual class. The Sklearn library includes a function called confusion matrix, which is utilized. The confusion matrix is displayed in a tabular format. The purpose of this function is to assess the concordance between model predictions and real-world observations. In the aforementioned example depicted in image 20, the Betawi Batik class achieved a successful classification of 16 objects, with only one instance of misclassification occurring in the Javanese Barong Batik class, which was mistakenly identified as the Betawi Batik class. The number of classes in the picture is restricted to 10 in order to enhance the visibility of the

confusion matrix results. Displaying the entire class would make it challenging to discern the results.

6) Comparative Study of Every Architectural Performance Quality: This section compares the performance of each architecture in performing image classification by comparing the F1-score value and validation accuracy of all architectures. This comparison can be seen in figure 21 below:

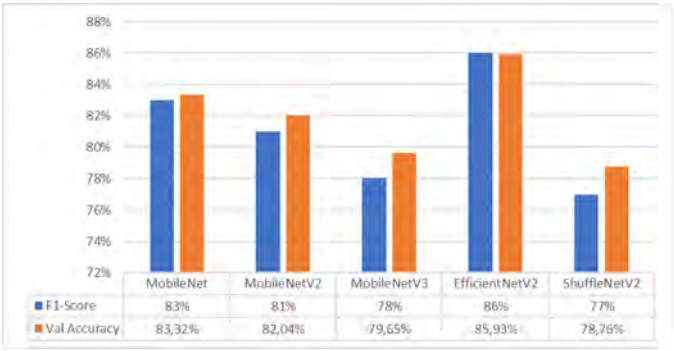

Fig. 21. Performance Comparison on Each Architecture

Figure 21 above shows that the EfficientNetV2 architecture, with a validation accuracy value of 85.93% and an F1-score value of 86%, has the best performance in terms of validation accuracy and the highest F1-score value. MobileNet, MobileNetV2, MobileNetV3, and ShuffleNetV2 came next, with an F1-score value of 77% and an accuracy validation value of 78.76%. Next, contrast all of each architecture's parameters, as displayed in the following image:

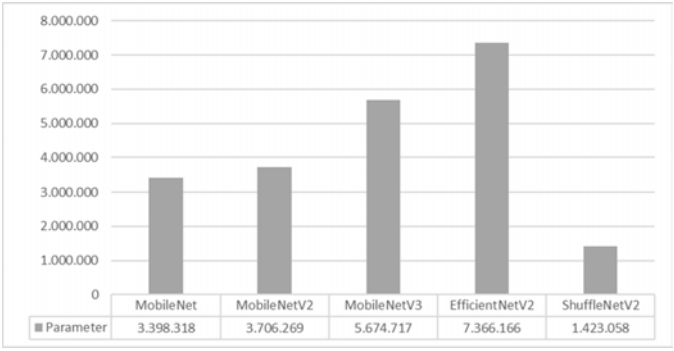

Fig. 22. Comparative Analysis of Every Architectural Parameter

Based on Figure 22 above, it can be seen that EfficientNetV2 has the highest parameters of 7,366,166, followed by MobileNetV3 with 5,674,717, MobileNetV2 with 3,706,209, MobileNet with 3,398,318, then the smallest is the ShuffleNetV2 architecture with total parameters. 1,423,058. From Figure 21 and Figure 22, when compared, the total parameters do not affect performance in image classification. Even though the MobileNet architecture has a total of 3,398,318 parameters which is smaller than MobileNetV2 which has a total of 3,706,269 parameters and MobileNetV3 which has a total of 5,674,268 parameters, the performance of the MobileNet architecture is better in terms of F1-score, namely 83% and validation accuracy is 83.32% compared to MobileNetV2 which has an F1-score value of 81% and validation accuracy of 82.04% and MobileNetV3 which has an F1-score value of 78% and validation accuracy of 79.65%.

IV. Conclusions

Based on the results of previous research that has been discussed, the following are the conclusions that have been obtained:

1. The characteristics of numerous Convolutional Neural Network (CNN) models, including MobileNet, MobileNetV2, MobileNetV3, EfficientNetV2, and ShuffleNetV2, are particularly well-suited for mobile device implementation due to their relatively low number of parameters.

2. The Convolutional Neural Network (CNN) method utilizing the EfficientNetV2 architecture demonstrates superior performance. It achieves a training accuracy of 97.35%, a validation accuracy of 85.93%, a precision value of 87%, a recall value of 86%, and an F1-score value of 86%. The model has a total of 7,366,166 parameters.

3. The performance of an object classification model is not directly correlated with the number of parameters it has. This demonstrates that models with fewer parameters can attain an equivalent or even superior level of accuracy compared to models with a greater number of parameters.

4. Each model has different performance in classifying batik designs or certain classes.

The following recommendation can be made as a result of the research that has been conducted:

1. Future research can compare the performance of batik design classification between datasets with image augmentation processes and datasets without image augmentation.

2. Subsequent studies can conduct a comparative examination of alternative architectures, such as SqueezeNet, GhostNet, CondenseNet, and others, in order to ascertain the performance and efficiency of each architecture in the classification of batik designs on mobile devices.

References

[1] Minarno A. E., M. C. Mustaqim, Y. Azhar, W. A. Kusuma, Y. Munarko, "Deep Convolutional Generative Adversarial Network Application in Batik Pattern Generator," in 9th International Conference on Information and Communication Technology (ICoICT), Yogyakarta, 2021.

[2] Minarno A. E., Y. Azhar, F. D. S. Sumadi, Y. Munarko, "A Robust Batik Image Classification using Multi Texton Co-Occurrence Descriptor and Support Vector Machine," in 2020 3rd International Conference on Intelligent Autonomous Systems (ICoIAS), Singapore, 2020.

[3] Bartleson F. E., "TOTEM NAME BATIK KIT". United States of America Patent 3,840,113, 8 Oktober 1974.

[4] Wibawa A. D., E. A. Wicaksono, S. D. Suryani, R. Rumadi, "Javanese Batik Image Classification using Self-Organizing Map," in International Conference on Computer Science, Information Technology and Engineering (ICCoSITE), Jakarta, 2023.

[5] Abdurrahman M., N. H. Shabrina, D. K. Halim, "Generative Adversarial Network Implementation for Batik Design Synthesis," in 5th International Conference on New Media Studies (CONMEDIA), Bali, 2019.

[6] Das R., S. De, S. Bhattacharyya, J. Platos, V. Snasel, A. E. Hassanien, "Data Augmentation and Feature Fusion for Melanoma Detection with Content Based Image Classification," in The International Conference on Advanced Machine Learning Technologies and Applications (AMLTA2019), 2020.

[7] Dewan J. H., S. D. Thepade, "How Scopus is Shaping the Research Publications of Feature Fusion-Based Image Retrieval," *Library Philosophy and Practice (e-journal)*, pp. 2-15, 2021.

[8] Das R., S. Thepade, S. Ghosh, "Novel feature extraction technique for content-based image recognition with query classification," *International Journal of Computational Vision and Robotics*, vol. 7, no. 1/2, p. 123, 2017.

[9] Dewan J. H., S. D. Thepade, "Image Retrieval using Weighted Fusion of GLCM and TSBTC Features," in 2021 6th International Conference for Convergence in Technology (I2CT), Maharashtra, 2021.

[10] Dewan J. H., R. Das, S. D. Thepade, H. Jadhav, N. Narsale, A. Mhasawade, S. Nambiar, "Image Classification by Transfer Learning using Pre-Trained CNN Models," in 2023 International Conference on Recent Advances in Electrical, Electronics, Ubiquitous Communication, and Computational Intelligence (RAEEUCCI), Chennai, 2023.

[11] Pan H., Z. Pang, Y. Wang, Y. Wang, L. Chen, "A New Image Recognition and Classification Method Combining Transfer Learning Algorithm and MobileNet Model for Welding Defects," *IEEE Access*, vol. 8, pp. 119951-119960, 2020.

[12] Huang X., "High Resolution Remote Sensing Image Classification Based on Deep Transfer Learning and Multi Feature Network," *IEEE Access*, vol. 11, pp. 110075-110085, 2023.

[13] Asif S., W. Yi, Q. U. Ain, J. Hou, T. Yi, J. Si, "Improving Effectiveness of Different Deep Transfer Learning-Based Models for Detecting Brain Tumors From MR Images," *IEEE Access*, vol. 10, pp. 34716-34730, 2022.

[14] Rani K. P. A., S. Gowrishankar, "Pathogen-Based Classification of Plant Diseases: A Deep Transfer Learning Approach for Intelligent Support Systems," *IEEE Access*, vol. 11, pp. 64476-64493, 2023.

[15] "Photoacoustic Image Classification and Segmentation of Breast Cancer: A Feasibility Study," *IEEE Access*, vol. 7, pp. 5457-5466, 2019.

[16] Velasco J., C. Pascion, J. W. Alberio, J. Apuang, J. Cruz, M. A. Gomez, B. Molina, L. Tuala, A. Thio-ac, R. J. Jorda, "A Smartphone-Based Skin Disease Classification Using MobileNet CNN," *International Journal of Advanced Trends in Computer Science and Engineering*, vol. 8, no. 5, pp. 2632-2637, 2019.

[17] Sugiarto D., J. Siswantoro, M. F. Naufal, B. Idrus, "Mobile Application for Medicinal Plants Recognition from Leaf Image Using Convolutional Neural Network," *Indonesian Journal of Information Systems (IJIS)*, vol. 5, no. 2, pp. 43-56, 2023.

[18] Howard A., M. Sandler, G. Chu, L.-C. Chen, M. T. Bo Chen, W. Wang, Y. Zhu, R. Pang, V. Vasudevan, Q. V. Le, H. Adam, "Searching for MobileNetV3," 20 November 2019. [Online]. Available: https://arxiv.org/abs/1905.02244v5. [Accessed 1 Februari 2024].

[19] Tan M., Q. V. Le, "EfficientNetV2: Smaller Models and Faster Training," 23 Juni 2021. [Online]. Available: https://arxiv.org/abs/2104.00298. [Accessed 2 Februari 2024].

[20] Ma N., X. Zhang, H.-T. Zheng, J. Sun, "ShuffleNet V2: Practical Guidelines for Efficient CNN Architecture Design," in *Computer Vision – ECCV 2018*, 2018.

[21] Hunt J. S., C. Cock, E. L. Symonds, "A True Positive and a False Negative? The Dilemma of Negative Colonoscopy After a Positive Fecal Occult Blood Test," *Digestive Diseases and Sciences*, vol. 67, no. 5, p. 1843–1849, 2022.

[22] Arafiyah R., Alimuddin, "Prediction of Price of Local Fruits in Jakarta With ANFIS (Adaptive Neuro Fuzzy System Inference)," in *AFITA 2010 International Conference, The Quality Information for Competitive Agricultural Based Production System and Commerce*, 2010.

[23] Handayani I., Alimuddin, Suhendar, "Peramalan Beban Tenaga Listrik Jangka Pendek Menggunakan Metode Jaringan Syaraf Tiruan," *SETRUM*, vol. 1, no. 1, pp. 35-40, 2012.

[24] Nopriadi, Alimuddin, F. Amhar, A. Sujarwo, Suswanta, F. Lukman, Y. Wibisono, K. Sadik, A. Kurniawan, E. Permana, S. Sutardi, A. Setiawan, A. D. Sutrisno, F. Menne, Y. T. Utomo, *ChatGPT untuk Pendidikan: Literasi Artificial Intelligence untuk Dosen dan Guru*, Bandung: CV. Media Sains Indonesia, 2023.

[25] Alimuddin, *Teori dan Aplikasi Dasar Sistem Kendali Cerdas*, Serang: UNTIRTA PRESS, 2020.

[26] Alimuddin, K. B. Seminar, I. D. M. Subratas, N. Nomura, Sumiati, "Temperature Control System in Closed House for Broilers Based on ANFIS," *TELKOMNIKA*, vol. 10, no. 1, pp. 75-82, 2012.

[27] Alimuddin, A. Bima, Herudin, S. Wardoyo, R. Munarto, "Optimasi Rugi-Rugi Daya Jaringan Distribusi dengan Menggunakan Jaringan Syaraf Tiruan," in *Seminar Nasional Teknik Ketenagalistrikan dan Teknologi Informasi (SNTKTI)*,

[28] Alimuddin, K. B. Seminar, I. M. Setiawan, Sumiati, "Critical Information Design for House Broilers Used by Artificial Neural Network," in *AFITA 2010 International Conference, The Quality Information for Competitive Agricultural Based Production System and Commerce*, 2010.

[29] Alimuddin, R. Arafiyah, "KONSEP MACHINE LEARNING," in *TRANSFORMASI DIGITAL (Pengantar Literasi Digital Untuk Mahasiswa)*, Nusa Tenggara Barat, Seval Literendo Kreasi, 2024, pp. 103–126.

Prediction of Diabetes Using the Decision Tree Algorithm Based on the Streamlit Web

Alief Maulana
Department of Electrical Engineering
Universitas Sultan Ageng Tirtayasa
Cilegon, Indonesia
aliefftuntirta@gmail.com

Muhamad Yusup
Department of Electrical Engineering
Universitas Sultan Ageng Tirtayasa
Cilegon, Indonesia
2001muhamadyusup@gmail.com

***Abstract*—Diabetes mellitus is a chronic disease that occurs either when the body cannot use the insulin produced by the pancreas or when the pancreas does not produce enough insulin. Diabetes mellitus can cause damage to various body systems such as failure of various organs such as eyes, kidneys, nerves, heart and blood vessels. The purpose of this research is to create a web-based diabetes disease prediction system using the machine learning algorithm method, namely Decision Tree Classifier. With various steps carried out, namely data collection, data preprocessing, machine learning model building with the Decision Tree algorithm, model evaluation and model implementation using the web. The results showed that the developed model was able to detect the risk of diabetes with 95% accuracy, 98% precision, 75% recall for the minority class, and 97% F1-score.**

***Index Terms*—Diabetes, machine learning, decision tree**

I. Introduction

Diabetes is still a global concern today, because the disease is a serious health problem that causes morbidity and mortality in various parts of the world, especially in developing countries including Indonesia. The World Health Organization (WHO) says that diabetes is a chronic disease that occurs either when the body cannot use the insulin produced by the pancreas or when the pancreas does not produce sufficient amounts of insulin [1].The International Diabetes Federation (IDF) reports that in 2021 there are approximately 537 million adults (20-79 years) living with diabetes and the total number of people living with diabetes is projected to increase to 643 million in 2030 and 783 million in 2045 [2].

Based on the explanation above, of course, early detection of diabetes is very important to do, it aims to reduce the increasing number of people with diabetes. Early detection can be done by experts and also by developing a diabetes prediction system by utilizing various methods, one of which is by utilizing information from data on people with diabetes by involving computational processes, machine learning, statistical techniques, classification, clustering and pattern discovery [3].

Machine Learning is one of the branches of Artificial Intelligence, especially those that study how computers are able to learn from data to improve their intelligence [4]. Machine learning can be defined as the application of computer and mathematical algorithms adopted by learning from data and generating future predictions [5] [6].Each machine learning algorithm has its own advantages and disadvantages, which are usually influenced by the characteristics of the dataset, the purpose of the analysis, and the level of complexity of the problem to be solved. Certain algorithms may be more suitable for datasets with large amounts of data or when there is class imbalance, while other algorithms are superior in handling data that has many features or requires clear interpretation [7].

Decision Tree algorithm is one of the widely used techniques in machine learning and data mining for classification and regression tasks. It works by dividing a dataset into smaller subsets based on selected features, until the subset reaches a minimum size or cannot be divided anymore. Decision trees are effective in handling complex and non-linear data and are easy to understand.

Based on this background, this research makes a diabetes prediction system using machine learning methods with the web-based Decision Tree algorithm using Streamlit which is useful for predicting whether someone is predicted to have diabetes or not.

II. Previous Work

This research was conducted based on previous studies, both from the theoretical basis, methods or research techniques used. Here are some previous studies that became the foundation of this research:

The first study, examined the classification of people with diabetes using the Decision Tree C4.5 algorithm. As for the results of this study, the model obtained an accuracy of 97.12% precision of 93.02% and recall of 100% [8]. The second study examined the prediction of diabetes mellitus using the Decision Tree C4.5 algorithm using RapidMiner software. The results of this study showed that the model obtained an accuracy of 91.82% [9]. The third study examined the detection of diabetes mellitus using the Decision Tree algorithm C4.5 architecture model, while the result was that the model got an accuracy value of 96% [10]. The fourth study examined classification modeling to determine diabetes with causal factors using Decision Tree C4.5 in women, the test results obtained an accuracy of 76.67%, precision of 72% and recall of 41.67%. [11].

979-8-3315-1921-6/24/$31.00 ©2024 IEEE

III. Methodology

This research is carried out in several stages, namely searching for diabetes medical data, data processing, dividing data into training data and test data, building models with the Decision Tree algorithm, evaluating models using confusion matrix and implementing models in web form using Streamlit. The stages carried out in this study are described as in Figure 1 below:

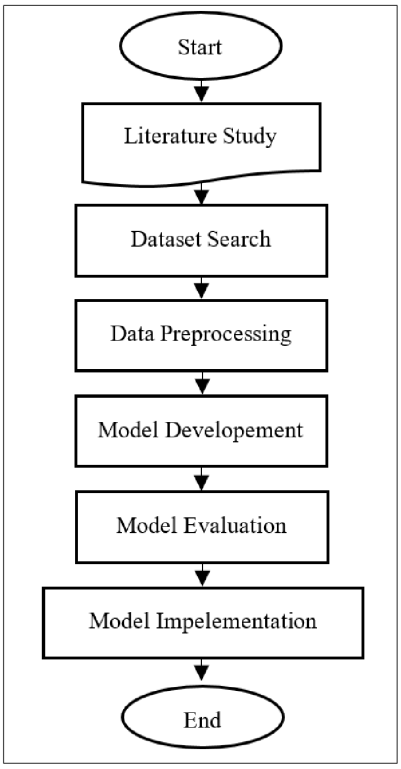

Fig. 1. Research Flow Chart

A. Research Data

The data used in this study was obtained from https://www.kaggle.com/datasets/iammustafatz/diabetes-prediction-dataset. This data is the medical and demographic data of the patient, along with the patient's diabetes status both positive and negative. The data is 100,000 patient data including 9 variables such as age, gender, body mass index (BMI), history of hypertension, history of heart disease, smoking history, HbA1c levels, and blood glucose levels and diabetes status.

B. Preprocessing Data

In the data pre-processing stage, the data will be cleaned from empty or missing values so that the data used for the model building process is clean and improves the quality of the data used for good model building. Furthermore, mapping is also carried out so that data that has categorical values can be converted into numerical data so that the data can be processed and read during model building, and also the data standardization process to avoid bias caused by different feature scales. At this stage, the diabetes dataset will be split into 70:30 in two parts using `train_test_split` from scikit-learn, namely the training dataset (`train`) of 70% and the test dataset (`test`) of 30%. The training data split will be used to build patterns or models, while the test dataset split will be used to test the models.

	B	C	D	E	F	G	H	I
1	age	hypertension	heart_disease	smoking_history	bmi	HbA1c_level	blood_glucose_level	diabetes
27	30.00.00	0	0	never	33.76	06.01	126	0
28	67.00.00	0	1	not current	27.32.00	06.05	200	1
29	40.00.00	0	0	former	27.85	05.08	80	0
30	45.00.00	1	0	never	26.47.00	04.00	158	0
31	43.00.00	0	0	never	26.08.00	06.01	155	0
32	53.00.00	0	0	No Info	31.75	04.00	200	0
33	50.00.00	0	0	No Info	25.15.00	04.00	145	0
34	41.00.00	0	0	current	22.01	06.02	126	0
35	20.00	0	0	never	22.19	03.05	100	0
36	76.00.00	0	0	never	23.55	05.00	85	0
37	05.00	0	0	No Info	15.01	05.08	85	0
38	15.00	0	0	No Info	0,927777778	04.05	130	0
39	26.00.00	0	0	never	21.22	06.06	200	0
40	50.00.00	1	0	current	27.32.00	05.07	260	1
41	34.00.00	0	0	never	56.43.00	06.02	200	0
42	73.00.00	0	0	former	25.91	09.00	160	1

Fig. 2. Variable Dataset

C. Model Developement

After the dataset is divided into training data and test data, the next is the construction of a prediction classification model using the decision tree algorithm from scikit learn, the decision tree has the ability to handle data with non-linear interdependent features. Data is built using training data. After the model is trained, the next step is to test the model using the training data.

D. Model Evaluation

After the model is built, the results of the model testing will be evaluated using the confusion matrix from the confusion matrix, then the classification report values such as accuracy, precision, recall and F1-Score will be obtained.

E. Model Implementation

The next step is to save the model and build an interface that can be used by users to predict diabetes using the modeling, the construction of this modeling interface using streamlit, streamlit has a simple appearance and is also easy to use in integrating pyhton and has the ability to visualize data in real-time.

IV. Result and Analysis

A. Machine Learning Model Building Results

The results of building a machine learning model with the Decision Tree algorithm can be seen from the evaluation results of the model. There are evaluation results in this study using confusion matrix and also classification reports such as accuracy, precision, recall and F1-Score. The confusion matrix

generated in the model that has been built is as shown below:

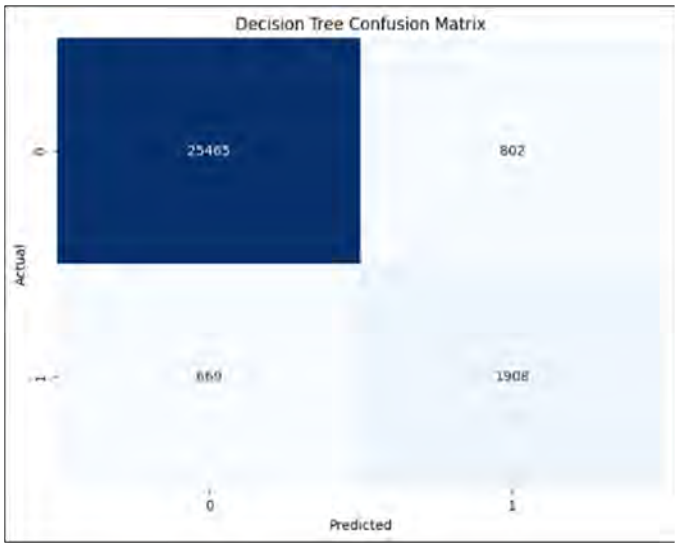

Fig. 3. Confusion Matrix

In the figure above, it can be seen that the model successfully predicted 25,465 negative data accurately (TN) and the model successfully predicted 1,908 positive data accurately (TP). However, the model incorrectly predicts 802 data as positive when it should be negative (FP), and the model also incorrectly predicts 669 data as negative when it should be positive (FN). Based on the confusion matrices above, it can be used to calculate several performance matrices such as accuracy, precision, recall and F1-Score using existing equations. The results of the performance matrix are as follows:

Classification Report:

	precision	recall	f1-score	support
0	0.97	0.97	0.97	26267
1	0.70	0.74	0.72	2577
accuracy			0.95	28844
macro avg	0.84	0.85	0.85	28844
weighted avg	0.95	0.95	0.95	28844

Fig. 4. Classification Report

The figure above shows that the model has a good accuracy of 95%, meaning that the model successfully predicts 95% of all data. Then also in the negative class of diabetes (0) the model managed to get a precision value of 97%, which means 97% of class 0 predictions are truly negative. Only 3% of class 0 predictions are wrong (False Positive), then the model also managed to get a recall value of 97% which indicates that 97% of negative data was successfully detected correctly as negative. Only 3% of negative cases were missed (False Negative) and also the model managed to get an F1-Score value of 97% which is a combination of precision and recall. This value shows that the model has a very good balance in predicting class 0.

Furthermore, in the positive class of diabetes (1) the model managed to get a precision value of 70% which means 70% of class 1 predictions are really positive, while the other 30% are False Positive (wrong prediction as positive). Furthermore, the model managed to get a recall value of 74% which indicates that 74% of all positive data were correctly detected as positive. However, there are 26% positive cases that were missed (False Negative). Furthermore, the model managed to get an F1-Score value of 72%, which shows its performance is slightly lower compared to class 0, because the precision and recall for this class are lower.

In the classification report, there is also a Macro Average which gives an overview of the average performance of the model equally between class 0 and class 1, without considering the imbalance in the amount of data for each class. The model gets 84% average precision from both classes, 85% average recall from both classes, and 85% average f1-score from both classes. In addition, there is also a Weighted Average, which is a weighted average that considers the proportion of each class in the dataset where the model gets a Precision, Recall, and F1-Score value of

B. Model Implementation Result

In order to make it easier for users to interact with the diabetes prediction model that has been developed, the web interface is made using Streamlit. This web application consists of several menus that can help and facilitate users in predicting diabetes, there are 5 menus designed to facilitate the prediction of diabetes, namely the Dashboard menu which is the main menu of this web application, the BMI calculation menu to make it easier for users if they do not know their body mass index, the multiple predict menu that can predict faster because it can predict a lot of data in csv form, the history menu that can help to track and review the prediction history that has been done by users and the About menu that provides information about this diabetes prediction web application.

The Dashboard menu is the core feature of this web application, which is designed to facilitate live diabetes prediction using the trained Decision Tree model. In this menu, users are presented with a simple yet comprehensive interface, where they are asked to enter various relevant health parameters, including age, hypertension, heart disease, smoking history, BMI, and blood glucose level.

Each of these parameters is taken from the data collected during the evaluation process, and the user is asked to fill them in the form provided. Once all the parameters are inputted, the user can click on the prediction button to get the analysis results instantly. The results will display the possibility of whether the user has diabetes or not based on the data that has been entered. The implementation of this Dashboard feature not only provides convenience in obtaining prediction results quickly and accurately, but also offers a user-friendly interface, making it easy to assess individual health without the need for in-depth technical skills. With this feature, the app provides

Fig. 5. Menu Dashboard

easy and efficient access for users to monitor their diabetes risk, while allowing them to make better health decisions based on the prediction results presented in real-time.

Fig. 6. Menu BMI

The BMI menu is an important feature in the app that allows users to easily calculate their Body Mass Index (BMI). Users are invited to enter their weight and height data into the form provided.

Fig. 7. Menu Multipe Predict

The Multiple Predict menu is a powerful feature in the app designed to handle diabetes prediction quickly and accurately. This feature is particularly useful in clinical or research contexts where data analysis for large groups is required. Through this interface, users can upload a CSV file containing health parameter data for multiple individuals at once, including information such as age, hypertension, heart disease, smoking history, BMI, and blood glucose levels. Once the file is uploaded, the app will automatically process each line of data and provide diabetes prediction results for each individual listed in the file.

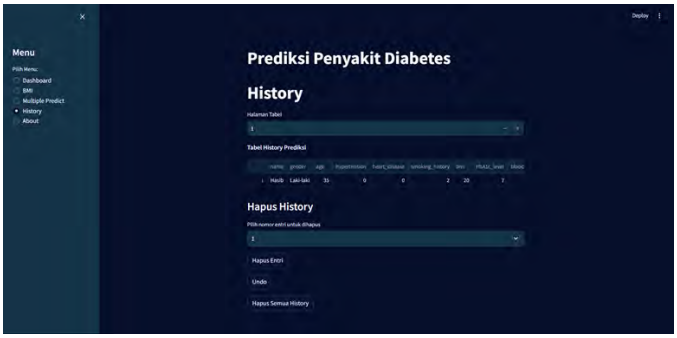

Fig. 8. Menu History

The History menu in the application serves as an important tool for tracking and reviewing the history of predictions that have been made by the user. This feature allows users to see a list of all the predictions that have been made, which are stored systematically in an easy-to-read table.

V. Conclusion

Based on the results of the research and analysis that has been carried out, the conclusions of this study are as follows:

1) In this study, a Decision Tree model has been successfully built for diabetes prediction. This process involves data preprocessing, division of datasets into training data and test data, model building, model evaluation and model implementation.
2) The evaluation results show that the Decision Tree model has good performance with accuracy reaching 95%. Evaluation metrics such as precision, recall, and f1-score also show that this model is able to predict diabetes effectively.
3) The interactive web interface built using Streamlit allows users to interact with the diabetes prediction model easily and intuitively. Features such as Dashboard, BMI, Multiple Predict, History, and About provide various tools and information that are useful for users in managing and monitoring health.

References

[1] T. A. Sholikah, R. P. Febrinasari, and D. N. Pakha, "Edukasi Penyakit Diabetes Melitus dan Cara Pemeriksaan Glukosa Darah Secara Mandiri," 2021.

[2] H. Sun et al, "IDF diabetes Atlas: Global, regional and country-level diabetes prevalence estimates for 2021 and projections for 2045," *Diabetes Res Clin Pract*, vol. 183, no. 109119, Dec. 2021.

[3] M. Komi, J. Li, Y. Zhai, and X. Zhang, "Application of data mining methods in diabetes prediction," *2017 2nd International Conference on Image, Vision and Computing (ICIVC)*, pp. 1006–1010, 2017, [Online]. Available: https://api.semanticscholar.org/CorpusID:37768095

[4] T. Wahyono, U. Kristen, and S. Wacana, "Fundamental of Python for Machine Learning: Dasar-Dasar Pemrograman Python untuk Machine Learning dan Kecerdasan Buatan," 2018. [Online]. Available: https://www.researchgate.net/publication/330441937

[5]]. Available: https://www.researchgate.net/publication/330441937 [5] J. Homepage, A. Roihan, P. Abas Sunarya, and A. S. Rafika, "IJCIT (Indonesian Journal on Computer and Information Technology) Pemanfaatan Machine Learning dalam Berbagai Bidang: Review paper," 2019.

[6] M. Arief Rahman, “Implementasi Machine Learning pada Application Programming Interface untuk Klasifikasi Komentar Cyberbullying,” UIN Syarif Hidayatullah, Jakarta, 2023.
[7] E. Alpaydin, *Introduction To Machine Learning Fourth Edition*. Cambridge, Massachusetts: MIT Press, 2020.
[8] F. M. Hana, “Klasifikasi Penderita Penyakit Diabetes menggunakan Algoritma Decision Tree C4.5,” *Jurnal SIstem Komputer dan Kecerdasan Buatan*, vol. 4, no. 1, pp. 32–39, Sep. 2020.
[9] Fitriyani and R. A. Siallagan, “Prediksi Penyakit Diabetes Melitus Menggunakan Algoritma C4.5,” *Jurnal Responsif*, vol. 3, no. 1, pp. 44–52, Feb. 2021.
[10] A. Afifuddin and L. Hakim, “Deteksi Penyakit Diabetes Mellitus Menggunakan Algoritma Decision Tree Model Arsitektur C4.5,” *Jurnal Krisnadana*, vol. 3, no. 1, pp. 25–33, Sep. 2023.
[11] N. N. Habibah, A. Nazir, I. Iskandar, F. Syafria, L. Oktaviana, and I. Syurfi, “Pemodelan Klasifikasi untuk Menentukan Penyakit Diabetes dengan Faktor Penyebab Menggunakan Decision Tree C4.5 pada Wanita,” *Jurnal Sistem Komputer dan Informatika (JSON)*, vol. 4, no. 4, pp. 654–661, Jun. 2023.

Analysis of Coil Effect and Number of Turns For Power Generation in Compact Disc Solar Cell

Hartono
Dept. of Electrical Engineering
Universitas Sultan Ageng Tirtayasa
Cilegon, Indonesia
hartono@untirta.ac.id

Edra Tri Adinata
Dept. of Electrical Engineering
Universitas Sultan Ageng Tirtayasa
Cilegon, Indonesia
3332190078@untirta.ac.id

Dina Estining Tyas Lufianawati
Dept. of Electrical Engineering
Universitas Sultan Ageng Tirtayasa
Cilegon, Indonesia
dina.lufianawati@untirta.ac.id

Felycia
Dept. of Electrical Engineering
Universitas Sultan Ageng Tirtayasa
Cilegon, Indonesia
felycia@untirta.ac.id

Yusraini Muharni
Dept. of Industrial Engineering
Universitas Sultan Ageng Tirtayasa
Cilegon, Indonesia
yusraini@untirta.ac.id

Irma Saraswati
Dept. of Electrical Engineering
Universitas Sultan Ageng Tirtayasa
Cilegon, Indonesia
irma.saraswati@untirta.ac.id

***Abstract*—A compact disc can be made to function like a solar cell because a piece of a compact disc that is wired can generate electricity. This process occurs due to the photoelectric or photovoltaic effect. When sunlight strikes an object that is sensitive to light, that object can generate voltage. There are several factors that influence the generated voltage, namely the number of turns, the Zener diode, and the intensity of light received. This research is conducted to analyze the impact of the number of turns on a compact disc. This study is an implementational research where it will create, modify, and analyze the impact of light intensity on the compact disc, thus this research will use experimental methods. The data was obtained by creating and measuring a device. The results indicate that the compact disc experiences an increase in voltage generated with the addition of the number of turns and the Zener diode used; furthermore, light intensity also plays an important role in the voltage produced. The best compact disc is type 1, type 3 at the peak point with a sunlight intensity of 94,400 Lux, producing a voltage of 2.4 volts. This type features an axial winding with 60 turns and 5 Zener diodes. A simple solar power system was created using this type 1, type 3, generating a power output of 1.3 W for series connection and 0.7 W for parallel connection, with an efficiency of 5.7**

***Index Terms*—Solar cell, compact disc, wiring, Zener.**

I. Introduction

Solar cells are a good alternative energy because of the use of sunlight using solar panels. Solar panels are an important component in PLTS where the sunlight received undergoes the phenomenon of energy conversion from light to electricity. Solar panels are also known as photovoltaic cells which mean ”light-electric” [1]. The principle of operation of these solar cells is called a photo-voltaic effect where a solar cell exposed to sunlight changes the energy of the sun to create a current flowing on two layers that have opposite charges. To ensure the provision of clean and environmentally friendly electricity using solar power, it is necessary to analyze the various failures associated with photovoltaic systems that can result in energy deficits and system damage and can cause fire hazards that are often difficult to avoid [2].

979-8-3315-1921-6/24/$31.00 ©2024 IEEE

The use of solar energy as a solar cell today can be made using a Compact disc, a compact disc that is treated to generate electrical voltage. This can happen because of the photovoltaic effect when a solar cell is exposed to sunlight and radiates an object that has a level of sensitivity to light then objects can generate electric voltage Under clear weather conditions, the earth’s surface receives about 1000 watts of solar thermal energy per square meter [3]. So that the modified compact disc is placed in an open place and there is enough sunlight Compact disc can receive light from the sun to be converted into electricity. By using the Compact disc as a solar panel, the cost of using it is not too expensive because it takes advantage of the used Compact disk so the cost is not very expensive. For now, the Compact disc has begun not to be much used by the public because of its estimated size and small storage size. So most people prefer flash disc because of its small size so it’s easy to store and put in a pants pocket as well as large file storage capacity. The impact of a lot of compact disks being discarded and adding to garbage pollution, is why compact disc recycling is one way to deal with the problem. Solar Photovoltaic Devices, and Photo-Electrochemical Cells both these techniques they use sunlight without generating by-products or risk of pollution [4]. [5].

This research will focus on the solar panels of the Compact disc as an affordable and environmentally-friendly alternative energy source, where several variable modifications will be made to the compact disc with different methods of treatment both in the type of wire, the number of curtains and the method used [6]. It aims to find out the effect of the curtain and the amount of curtain to generate power on the Solar panel of this Compact disk, so that later it will be known the impact of modifying the quantity of curtail in the solar cell of this compact disk. The curtain amount is influential because it follows Michael Faraday’s law in his theory where in a curve

that causes changes in magnetic fluxes or commonly called electromagnetic induction where if the magnetic field when the value of the flux changes can produce electric current [7]. [8]. In addition, there is also Ohm's law, which says that the electric current in a closed circuit is directly relative to the voltage and vice versa relative to the impedance [8].. This research is influenced by weather because data collection is done by sunning the panel in the sunshine so the intensity of solar radiation the panel receives will vary all the time [9].

At the time the panel is sunny the panel will experience a phenomenon of energy change from light to electricity where this is called photovoltaic [10]. It can generate electricity due to the photoelectric effect, where a metal or copper plate exposed to light/light will release electrons [11].. In this phase of the process, the testing and measurement is done using a multimeter that is already arranged based on the guidelines from the electrical engineering books and electronics of instruments [12]. And for the measuring angle is 00 so that all the panels of this Compact disc will receive the same intensity of solar radiation, although the same voltage will also be different depending on the type and type of panel [13]. This photovoltaic effect can produce electric energy constantly will produce energy ranging from 0.5 volts up to 600 mV [13] [14]. The data will then be collected twice on each type and type of solar cell where 2 each is made as a comparison and as the accuracy of every type and its type then will be compared its values according to the measurement tolerance guidelines, so that the result will be accurate data and can be analyzed well [15]. The purpose of analyzing the data obtained is to know the impact of the change of the curve and the amount of curvature on the voltage generated by the solar cell of the compact disc.

II. Research Methods

This research is an implemented research where this research will make and modify its own compact disc solar panel so that this research will use the experimental method. The stages of this research can be seen in Figure 1 below:

The research process is carried out through several stages as follows:

- Identification the problem, purpose and limitation of the problem, done by discussing and looking for references that have the same topic.
- Making solar panels using compact disc.
- Data collection, data is obtained by directly measuring the compact disc solar cell by drying it, data collection is carried out starting from 9 am to 3 pm.
- Data evaluation, the data is evaluated whether the data obtained is sufficient and good.
- Data analysis, the data obtained if it is deemed sufficient and good then it is analyzed
- The results can be drawn conclusions and opinions about the data obtained so that the research can be said to be finis.

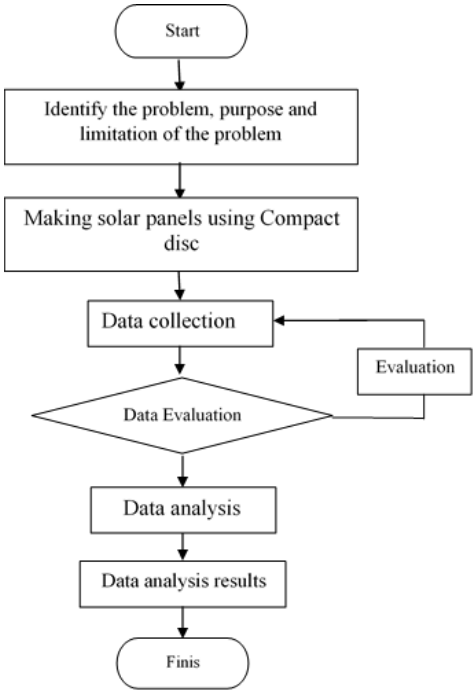

Fig. 1. Research Flowchart

A. *Faraday's law*

Using solar energy using Compact disc to generate electricity. It could happen because of the photovoltaic effect. The principle of photovoltaic operation is that if the bias of light uses an object with a high light sensitivity then the object can generate a voltage. The way it works is a compact disc placed in an open place that has enough sunlight, then it will generate electricity. For the output voltage itself depends on the intensity of sunlight or weather. When the weather is bright, the voltage will be higher than in fog or fog weather. The number of curves can also be influenced according to Michael Faraday in the theory where the curve can cause changes in magnetic flow or commonly called electromagnetic induction where if the magnetic field that when the flow value changes can produce electric current [7]

$$B = \frac{\mu_0 N I}{2r} \tag{1}$$

Where:

B = Magnetic field magnitude
μ_0 = Vacuum space permeability $(4\pi \times 10^{-7}$ T.m/A$)$
I = Electrical current (A)
N = Number of cubes (units of length (cm))
r = Sinusoidal length (cm)

The amount of buckle has a direct influence on the voltage generated in a system where the number of bucks determines the ratio of voltage between the input bucket and the output bucket. Where the conclusion is the amount of packaging also affects the voltage generated. When a current flows through an

inductor, a magnetic field generated by a change in the current that flows, according to Faraday's law, a larger amount of wire can produce a higher voltage. As for the component used, it consists of a modified compact disk as shown in Figure 2:

Fig. 2. Solar Cell Compact Disc

The compact disc from the compact disc in Figure 2 is made using easy-to-reach materials, as well as a fairly easy tool making process, and pollution-free. Here is the stage of making a compact disc solar panel based on the refraction of research similar to the title potential of used compact disc pieces as alternative solar panels.

B. *Photovoltaic efficiency*

Photovoltaic efficiency refers to the power of a solar panel or solar cell to convert sunlight into electricity. It is a key parameter in evaluating the performance of a PV system. Phovoltaic effectiveness is measured as the percentage of the sunlight that affects the solar panel converted to power.

$$Efisiency\ fotovoltaik(\eta) = \frac{Maximum\ output\ power}{The\ power\ of\ sunlight\ received} \quad (2)$$

Where the maximum output power is the maximum electrical power (W). And the sunlight power received is the the amount of light falling on the surface area of the solar panel (W/m2).

C. *Electrical measurement tolerance*

Electrical measurement tolerance refers to how close the electrical measuring result is to the actual value of the measured parameter. Electricity is a vital element in many applications, including industry, engineering, and everyday life, so tolerance in electrical measurement is crucial. Too much tolerance can lead to significant errors in calculation and decision-making; too little tolerance will be difficult or expensive to. Tolerances for electrical measurements are usually determined by standards and technical specifications issued by relevant standardized bodies and regulatory authorities such as the International Electro technical Commission (IEC), the American National Standards Institute (ANSI), or other national standards. These standards specify tolerances for various types of electrical, voltage, current, power, etc. Measurement of voltage in electrical power systems, tolerance is usually expressed as a percentage of the nominal voltage value. If the electrical device has a voltage measurement tolerance of ±5%, the measured voltage value must be in the range of 95% to 105% of the actual identifying voltage. Understanding the tolerances of electrical measurement ensures that the electrical system operates accurately [15].

III. Result and Discussion

The results and discussion where the results are the data obtained during the research and the discussion is an analysis of the data obtained and then analysis in order to obtain conclusions and results from this study.

A. *Measurement Result*

The research data is obtained from the results of measurements made directly on the device made by using a digital MultiMate at the specified time, namely from 9 am to 3 pm. Data is taken from different compact disc where there are 3 types of compact disc, each of which has 3 different types of coils and each type is also made 2 pieces for proof or clarification of the voltage produced. The following are the data obtained from this research.

- Compact Disc Type 1

Compact disc type 1 is a winding or axial coil type compact disc where in this type the supreme wire is wrapped around a compact disc (CD).

Fig. 3. Compact disc type 1

In Figure 3 there are 3 types of compact disc with different numbers of windings or coils, where each is made 2 for comparison. The 3 types consist of 20 turns with 3 Zener diodes, 80 turns with 3 Zener diodes and 60 turns with 5 Zener diodes.

TABLE I
MEASUREMENT DATA

Type	Compact disc Voltage CD 1 (V)	Compact disc Voltage CD 2 (V)	Time	Light Intensity (Lux)
1-1	0.73	0.81	09.00	16280
	0.92	0.92	10.00	26250
	1.2	1.2	11.00	68250
	1.4	1.4	12.00	72750
	1.4	1.4	13.00	94400
	1.5	1.5	14.00	94400
	1.2	1.1	15.00	60390
1-2	0.74	0.93	09.00	16280
	1.1	1.2	10.00	26250
	1.4	1.4	11.00	68250
	1.5	1.5	12.00	70820
	1.5	1.5	13.00	72750
	1.5	1.5	14.00	94400
	1.2	1.3	15.00	60390
1-3	0.98	1	09.00	16280
	1.2	1.2	10.00	26250
	1.5	1.5	11.00	68250
	1.6	1.6	12.00	70820
	1.8	1.8	13.00	72750
	2.3	2.4	14.00	94400
	1.5	1.5	15.00	60390

From the data in Table I section 1-1, a graph is made to see the development of voltage measurements that take place at each time, this graph aims to facilitate analysis. The following is a picture of the graph in Figure 4 below:

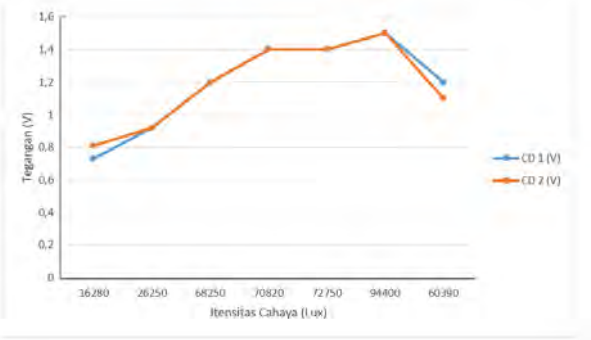

Fig. 4. Graphic data Type 1-1

In Figure 4, there are 2 graphs where Figure 4 is a graph of the measurement data done. In Figure 4, the graph data above shows that the voltage data is increasing as the light intensity received by the compact disc on Compact disc 1 and Compact disk 2, where Compact Disc 1 is better than Compact Disk 2, where compact disk 1 is stable and produces a voltage of 0.70 to 1.5 volts and compact disc 2 produces only 0.56 volts to 1,5 volts, although both are the same but the results are slightly different, from the data table 1 and also the graphic image on Figure 4. There are several factors causing the difference in voltage among them is the condition of compact solar disc disturbed which causes measurements or calibration error of measuring instruments. But despite the difference, the data is still in good shape given that the measurement tolerance is not too great. So the result is still said to be good, because it is still within a value not far from the measuring tolerance value of +5%.

Table I section 1-2 data is made graph to see the development of voltage measurements that take place at each time, this graph aims to facilitate analysis. The following is a picture of the graph in Figure 5 below:

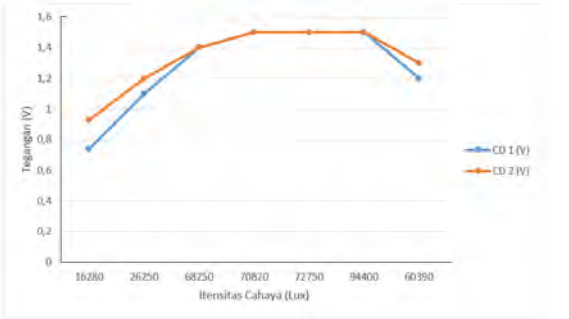

Fig. 5. Graphic data Type 1-2

In Figure 5, there are 2 graphs where Figure 5 is a graph of compact disc measurement data. In Fig. 5, it can be seen that the voltage data is still not very different from the type 1 compact disc, where the tension is stable at 1.4 volts and peaked to 1.5 volts due to the increased sunlight intensity of 94400 Lux for Compact disc 1 and Compact disk 2, although there is still a small difference due to compact disc compact disc condition interrupted by sending, measuring errors or calibration of measuring instruments. But the data can still be said to be good and still within the measurement tolerance.

Table I section 1-3 data is made graph to see the development of voltage measurements that take place at each time, this graph aims to facilitate analysis. The following is a picture of the graph in Figure 6 below:

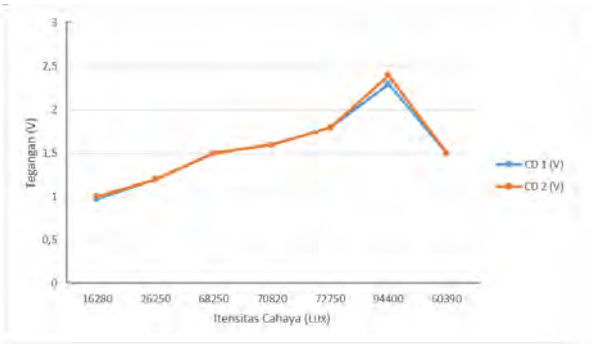

Fig. 6. Graphic data Type 1-3

In Figure 6, there are 2 graphic images where Figure 6 is a measurement data graph. As for the data obtained on Compact

disc 1 and 2, there are still the same differences as in type 1 and type 2 compact disc due to a number of factors, such as disturbed or dispatched compact disc conditions that cause measurement or calibration errors of measuring instruments. But it's still said good to refer to measurement tolerance. In Figure 6 and Table 1, we can see that the voltage generated by compact disc is increasing compared to type 1 and type 2, where the voltage reaches 2.4 volts on the Compact disc 2. It is concluded that the increase in the amount of splashes affects the tension generated according to the law of Faraday, although the increase is not large enough as in type 3, so it can be inferred that the increased amount of flushes must be accompanied by the number of diodes as well as a large sunlight intensity of 94400 Lux.

- Compact disc Type 2

Compact disc type 2 is a radial coil or coil type compact disc where in this type the supreme wire is placed on a compact disc (CD).

Fig. 7. Compact disc type 2.

In Figure 7 There are 3 types of compact disc with different numbers of windings or coils, where each is made 2 for comparison, namely 10 windings with 3 Zener diodes, 13 windings with 4 Zener diodes and 10 windings with 5 Zener diodes.

data graph. Where in Table II and Figure 8 the voltage data produced by compact disc 1 and 2 are not as good as before, both CD 1 and CD 2 data. The voltage produced is also slightly superior to type 1 type 1 and 2, where voltage steps at the figure of 1.5 volts.

In Figure 9 there are 2 graphs where Figure 49 is a measurement data graph. In Table II and Figure 9 it can be seen that compact disks 1 and 2 both before and after coating produce a good voltage so that they are still in the

TABLE II
MEASUREMENT DATA

Type	Compact disc Voltage CD 1 (V)	Compact disc Voltage CD 2 (V)	Time	Light Intensity (Lux)
2-1	0.62	0.71	09.00	16280
	1.1	0.98	10.00	26250
	1.6	1.3	11.00	68250
	1.3	1.4	12.00	72750
	1.4	1.5	13.00	94400
	1.5	1.5	14.00	94400
	1.3	1.3	15.00	60390
2-2	0.78	0.82	09.00	16280
	1.3	1.3	10.00	26250
	1.4	1.4	11.00	68250
	1.6	1.6	12.00	70820
	1.7	1.7	13.00	72750
	1.8	1.8	14.00	94400
	1.3	1.3	15.00	60390
2-3	1	0.93	09.00	16280
	1.2	1.2	10.00	26250
	1.6	1.6	11.00	68250
	1.7	1.7	12.00	70820
	1.9	1.8	13.00	72750
	2.2	2.2	14.00	94400
	1.5	1.5	15.00	60390

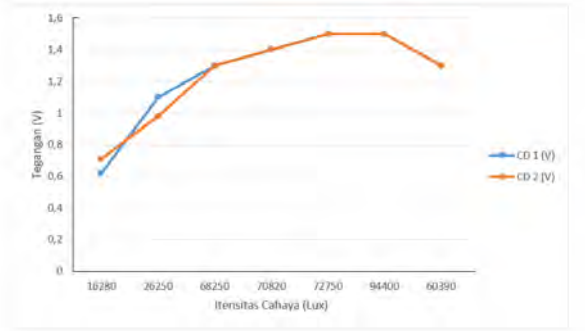

Fig. 8. Graphic data Type 2-1

measurement tolerances, and for the data the voltage increases as the intensity of light, the number of blisters and diodes in the compact disc increases.

In Figure 10 there are 2 Graphics where Fig. 10 is a diagram of measurement data. In Table II and Figure 10 it can be seen that compact disc 1 and 2 are still fairly tight, referring to the measurement tolerances, and the voltage data has improved even better than the type 2 compact disc type 2, and can be concluded for the result that as the light intensity increases, the number of blisters and diodes then the tension will increase.

- Compact disc type 3

Compact disc type 3 is a winding or axial coil type compact disc, different from type 1, in this type the supreme wire

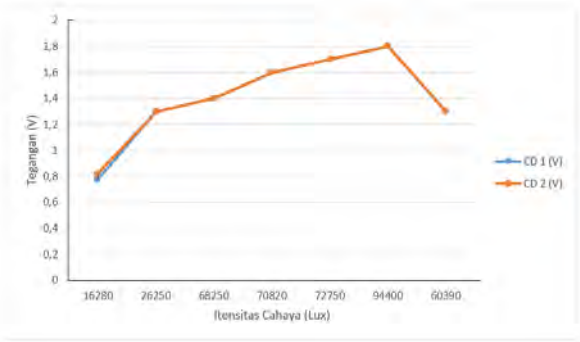

Fig. 9. Graphic data Type 2-2

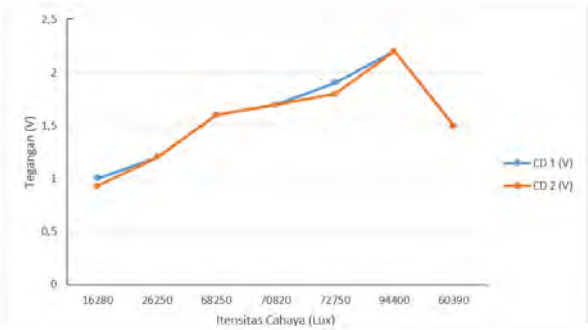

Fig. 10. Graphic data Type 2-3

is placed on a CD (compact disc). The modification is also different where only the addition of the winding does not occur with the diode.

In Figure 11 there are 3 types of compact disc with different numbers of windings or coils, where each is made 2 for comparison, namely 5 windings with 4 Zener diodes, 7 windings with 4 Zener diodes and 10 windings with 4 Zener diodes.

In Figure 12 there are 2 Graphics where Fig. 12 is a measurement data graph. In Table III and Figure 12 we can see compact disc data 1 and 2 very well, and for the voltage not as much as type 1 - 2 and type 2 - 1, 2 and 3 where this just strengthens the theory of the law of faraday and ohm where with the addition of the number of brakes as well as the intensity of light and also diodes then the generated voltage will be bigger and bigger, where in this type there is a great decrease in the amount of bridges so that the tension is not big.

In Figure 13, there are 2 graphic images where Figure 13 is a measurement data graph. In Table III and Figure 13, compact disc voltage data 1 and 2 both prior to coating and after well-fitting refer to the measurement tolerance, and the voltage also increases as the amount of light intensity and the number of flashes adds, this reinforces the conclusion that as the quantity of flashing adds then the tension will increase and greatly influenced by the amount and the intensity of light received by the compact disc.

Fig. 11. Compact disc type 3

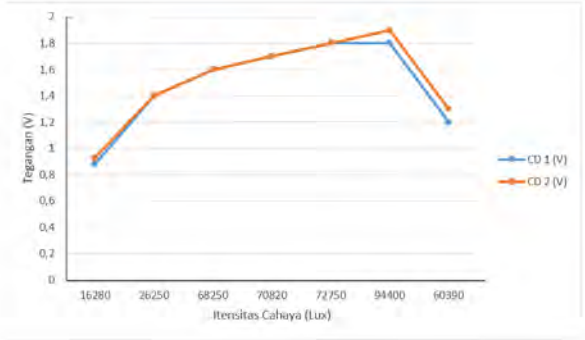

Fig. 12. Compact disc type 3-1

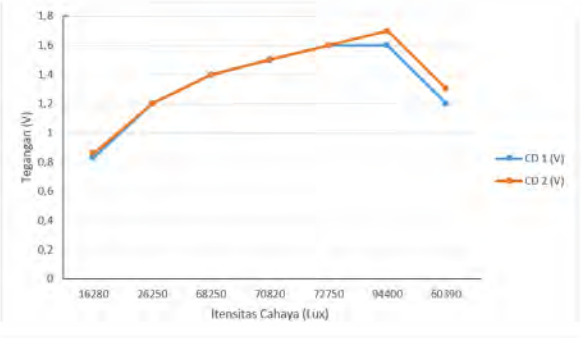

Fig. 13. Compact disc type 3-2

TABLE III
MEASUREMENT DATA

Type	Compact disc Voltage CD 1 (V)	Compact disc Voltage CD 2 (V)	Time	Light Intensity (Lux)
3-1	0.88	0.93	09.00	16280
	1.4	1.4	10.00	26250
	1.6	1.6	11.00	68250
	1.7	1.7	12.00	72750
	1.8	1.8	13.00	94400
	1.8	1.9	14.00	94400
	1.2	1.3	15.00	60390
3-2	0.83	0.86	09.00	16280
	1.2	1.2	10.00	26250
	1.4	1.4	11.00	68250
	1.5	1.5	12.00	70820
	1.6	1.6	13.00	72750
	1.6	1.7	14.00	94400
	1.2	1.3	15.00	60390
3-3	0.88	0.93	09.00	16280
	1.4	1.4	10.00	26250
	1.6	1.6	11.00	68250
	1.7	1.7	12.00	70820
	1.8	1.8	13.00	72750
	1.8	1.9	14.00	94400
	1.2	1.3	15.00	60390

Fig. 14. Compact disc type 3-2

In Figure 14, there are 2 graphic images where Figure 14 summarizes a graphic image of the measurement data on type 3 compact disc. In Table III and Figure14, compact disc voltage data 1 and 2 are said to refer both to the measuring tolerances, and the voltage values are increased even more than type 1 and 2, with the addition of the intensity of light and curvature and reinforcing the theory of Faraday's law of influence on the increasing voltage.

B. Simple solar power plant

After making many diverse compact disc that aim to find the best one to make a simple solar power plant that will produce electrical power. As for finding out the best compact disc, the highest voltage data has been made at 14.00 from each type and type in Table IV.

TABLE IV
HIGHEST MEASUREMENT DATA

Type I			Type II			Type III		
1-1	*1-1*	*1-1*	*1-1*	*1-2*	*1-2*	*1-1*	*1-1*	*1-2*
1.5 V	1.5 V	2.4 V	1.5 V	1.8 V	2.2 V	1.6 V	1.7 V	1.9 V

Based on table IV above, it can be seen that the best is type 1 type 3 with 2.3 volts where this type is an axial winding type with 60 turns and 5 Zener diodes, then 8 compact disc are made, each of which is divided into 13 to make 2 types of relationships, namely series and parallel, for a simple solar power plant circuit in Figure 15.

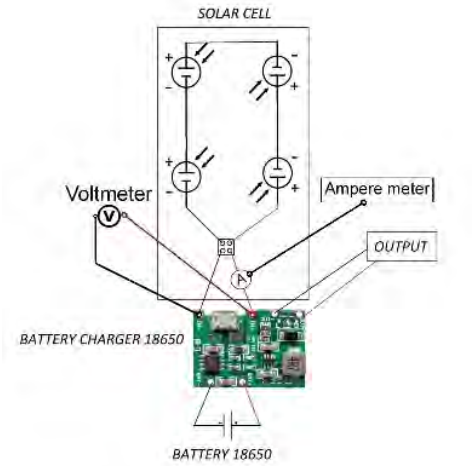

Fig. 15. Simple solar power plant

In Figure 4 is a simple solar power plant circuit that is made into 2 where one is connected in series and the other is connected in parallel as in Figure 16:

Fig. 16. (a) Parallel circuit (b) Series circuit

After being made, it was tested by drying it in the hot sun at the peak temperature at 14:00 pm. The following are the results of the data obtained:

No.	Parallel circuits		Series circuits		Light intensity
	Voltage (V)	Current (I)	Voltage (V)	Current (I)	**(LUX)**
1	2.2	0.36	10.3	0.13	94400
2	0.7 W		1.3 W		

In the table V data above, it can be concluded that the power generated is better in series than parallel, where the voltage value in series is greater than parallel but the current is greater than parallel. The efficiency value of the compact disc is:

Photovoltaic efficiency can be calculated mathematically as follows:

$$\textit{Efisiency fotovoltaik} = \frac{\textit{Maximum output power}}{\textit{The power of sunlight received}} \quad (3)$$

Where the maximum output power is the maximum electrical power (W). And the received sunlight power is the sunlight power that falls on solar panel surface area (W/m²). It is known that the electric power generated is 0.7 W for parallel connection and 1.3 W for series connection. To calculate the efficiency, the value of the received sunlight power is the sunlight power that falls on the surface area of the solar panel (W/m²). To find the received sunlight power a relationship equation as follows:

$$\cos\theta = \sin(\alpha - \beta) + \cos\delta \cdot \cos(\alpha - \beta) \cdot \cos\omega \quad (4)$$

Where:
θ = Angle of the incident ray to the surface normal line
δ = Angle of declination
α = Latitude of the tool position
β = Angular slope of surface and tool
ω = Time angle

When the result of multiplying the solar intensity received by the earth with the cosine of the angle of the incident rays, the amount of energy rate received by a surface on earth with a square area can be written with the equation.

$$\frac{q}{A} = G_r \cos\theta \quad (5)$$

Where:

q : Energy rate (W)
A : Unit area on the field (m^2)
G_T : Solar light intensity received by the earth's surface (W/m^2)
θ : Angle of incident ray

Thus

1.
$$\frac{q}{A} = G_T \cos\theta$$
$$\frac{1.3}{576\,\mathrm{m}^2} = G_T \cos 0$$
$$G_T = \frac{1.3}{576\,\mathrm{cm}^2} \cdot \cos 0$$
$$G_T = \frac{1.3}{5.76\,\mathrm{m}^2} \cdot \cos 0$$
$$G_T = 0.225\,\mathrm{W/m}^2$$
$$= 5.7\%$$
$$\textit{Efficiency}(\eta) = \frac{\textit{Maximum output power}}{\textit{Received sunlight power}} = \frac{1.3\,W}{0.225\,W/m^2}$$
$$= 5.7\%$$

2.
$$\frac{q}{A} = G_T \cos\theta$$
$$\frac{0.7}{576\,\mathrm{m}^2} = G_T \cos 0$$
$$G_T = \frac{0.7}{576\,\mathrm{cm}^2} \cdot \cos 0$$
$$G_T = \frac{0.7}{5.76\,\mathrm{m}^2} \cdot \cos 0$$
$$G_T == 0.121\,\mathrm{W/m}^2$$
$$\textit{Efficiency}(\eta) = \frac{\textit{Maximum output power}}{\textit{Received sunlight power}} = \frac{0.7\,W}{0.121\,W/m^2}$$
$$= 5.7\%$$

The efficiency value obtained is quite low because Compact disc solar cells do not produce as much power as solar cells in general and it can be concluded that solar cells from Compact discs cannot be used as alternative energy but can be used as a learning medium about the photoelectric effect that is good and easy to make at low cost.

IV. Conclusion

Compact disc compact disc are made based on the type of winding, namely axial or radial as we as the number of turns and zener diodes. The resulting voltage varies, in Table V the best obtained is type 1 type 3 with 2.4 volts axial winding type with 60 turns and 5 zener diodes. In Table I to Table II the number of turns and diodes is added and the resulting voltage increases, and in Table III only the number of turns is added, the result is that the voltage has increased so that it can be concluded that the more turns the voltage will increase. The potential of compact disc compact disc is quite good with an efficiency of 5.7% and in terms of cost and how to make compact disc from compact disc which are quite easy and good as an alternative learning media about photoelectricity that is cheap and easy to make. My recommendation is not to use ordinary solder because too high a temperature can damage the diode part so that the compact disc will not work properly. However, ordinary solder can also be used by using a special soldering gel so as not to damage the diode part. and there is still a possibility that the type of compact disc is one of the parameters that have an impact on the power generated.

References

[1] H. Auliya, N. Widyowati, and A. K. Haqiqi, "Potensi Keping Dvd Bekas Sebagai Panel Surya Alternatif," Konstan - J. Fis. Dan Pendidik. Fis., vol. 4, no. 2, pp. 131–138, 2019, doi: 10.20414/konstan.v4i2.44.

[2] R. Prasanna, C. Karthik, S. Chowdhury, and B. Khan, "Comprehensive Review on Modelling, Estimation, and Types of Faults in Solar Photovoltaic System," Int. J. Photoenergy, vol. 2022, 2022, doi: 10.1155/2022/3053317.

[3] S. A. Pakpahan, "Pemanfaatan Energi Matahari menggunakan CDROM dan Dioda Zener," Progr. Stud. Tek. Elektro Univ. Muhammadiyah Sumatera Utara, pp. 1–68, 2018.

[4] R. Sianipar, M. Y. Puriza, and W. Sunanda, "Pembangkit Listrik Tenaga Surya Rooftop Untuk Perumahan di Pulau Bangka," J. Ilm. Pendidik. Tek. Elektro, Vol.7, No.1, vol. 7, no. 1, pp. 37–44, 2023.

[5] M. Ibrahim and R. Sbeah, "Recycling of Waste CdS Film Solar Cells by Different Depositions," An-Najah Natl. Univ., 2017.

[6] M. Moshinsky, "Sumber Eenergi Listrik Menggunakan Panel Surya Dengan KASET CD Bekas," Fak. Mat. Ilmu Pengetah. Alam, vol. 13, no. 1, pp. 104–116, 2018.

[7] F. E. SILVANUS P. THOMPSON, D.Sc, Michael Faraday His Life and Work, THE OENTUR. London, Paris, New York: CASSELL and COMPANY, 1901. [Online]. Available: https://ia600205.us.archive.org/10/items/cu31924015746096/cu31924015746096.pdf

[8] D. W. Andini, H. Saputro, W. S. Ratri, and A. Sudigdo, "Simple Solar Panel (PASUSS) From Used DVD (Digital Versatile Disc) As Insect Repellent on Agricultural Land," InCoTES, no. November, pp. 150–155, 2022.

[9] M. H. Sigit Sukmajati, "Perancangan Dan Analisis Pembangkit Listrik Tenaga Surya Kapasitas 10 Mw on Grid Di Yogyakarta," Jur. Tek. Elektro, Sekol. Tinggi Tek. PLN, vol. 7, no. JURNAL ENERGI & KELISTRIKAN VOL. 7 NO. 1, JANUARI-MEI 2015, p. 49, 2015.

[10] I. W. Hendrik Kurniawan, Ahmad Izzuddin, "Perbandingan Tegangan Keluaran Sel Surya Berbahan Dioda Zener Dengan Sel Surya Tipe Monokristal Berukuran 118x63mm," J. Energy, vol. 10, no. 2, pp. 92–100, 2022.

[11] M. Iqbal Firmansyah, B. Suprianto, and J. Unit Three Kartini, "Kombinasi CDROM dan Dioda Zener Sebagai Suplai Energi Listrik Untuk LED 1,5 Volt," J. Tek. Elektro, vol. 11, no. 1, pp. 146–154, 2022.

[12] F. Maulana and A. Sutiagad, Teknik Kelistrikan Dan Elektronika Instrumentasi, Buku 1. Jakarta: KEMDIKBUD, 2013. [Online]. Available: https://repositori.kemdikbud.go.id/9537 /1/TEKNIK-KELISTRIKAN-DAN-ELEKTRONIKA-INSTRUMENTASIBUKU-2.pdf

[13] D. F. Alifyanti, J. M. Tambunan, S. Plnj. Jurusan Teknik Elektro, and J. co. Jurusan Teknik Elektro, STT PLNJakarta, "Pengaturan Tegangan Pembangkit Listrik Tenaga Surya(PLTS) 1000 WATT," J. Kaji. Tek. Elektro, vol. 1, no. 1, pp. 79–95, 2019.

[14] EBTKE, "Kebijakan, Regulasi dan Inisiatif Pengembangan Energi Surya di Indonesia Akselerasi pengembangan PLTS di Indonesia untuk mencapai 6,5 GW di tahun 2025," Kementrian ESDM, p. 4, 2018, [Online]. Available: https://iesr.or.id/wp-content/uploads/2019/10/2019-10-10-Bahan-Paparan-Akselerasi-PLTS-Mencapai-65-GW-pada-2025-IESR.pdf

[15] J. G. Webster, Electrical Measurement, Signal Processing, and Displays, no. September. 2004.

[16] R. Rusman, "Pengaruh Variasi Beban Terhadap Efisiensi Solar Cell Dengan Kapasitas 50 Wp," Turbo J. Progr. Stud. Tek. Mesin, vol. 4, no. 2, 2017, doi: 10.24127/trb.v4i2.75.

[17] T. T. Gusman, R. Novri, H. R. Husal, and D. A. Lubis, "Pengembangan Alat Pembangkit Listrik Tenaga Surya Dengan DVD Bekas Sebagai Alternatif Panel Surya Menggunakan Metode QFD Fase TALENTA Conference Series Pengembangan Alat Pembangkit Listrik Tenaga Surya Dengan DVD Bekas Sebagai Alternatif Panel Surya Mengg," Talent. Confernce Ser. energy Eng., vol. 5, no. 2, 2022, doi: 10.32734/ee.v5i2.1577.

[18] B. A. Ahmed, I. H. Shallal, and F. I. Mustafa Al-Attar, "Physical properties of CdS/CdTe/CIGS thin films for solar cell application," J. Phys. Conf. Ser., vol. 1032, no. 1, 2018, doi: 10.1088/1742-6596/1032/1/012022.

[19] R. T. Rw and S. Agung, "PERANCANGAN PEMBANGKIT LISTRIK TENAGA SURYA DENGAN DAYA 50 WATT MENGGUNAKAN COMPACT DISC BEKAS," J. Kaji. Tek. Mesin, 2022.

[20] Z. Fang, X. C. Wang, H. C. Wu, and C. Z. Zhao, "Achievements and challenges of CdS/CdTe solar cells," Int. J. Photoenergy, vol. 2011, no. 1, 2011, doi: 10.1155/2011/297350.

[21] M. Atowar Rahman, "Enhancing the photovoltaic performance of Cd-free Cu2ZnSnS4 heterojunction solar cells using SnS HTL and TiO2 ETL," Sol. Energy, vol. 215, no. December 2020, pp. 64–76, 2021, doi: 10.1016/j.solener.2020.12.020.

[22] K. L. Kennerud, "Analysis of Performance Degradation in CDS Solar Cells," IEEE Trans. Aerosp. Electron. Syst., vol. AES-5, no. 6, pp. 912–917, 1969, doi: 10.1109/TAES.1969.309966.

[23] S. M. Seck, E. N. Ndiaye, M. Fall, and S. Charvet, "Study of Efficiencies CdTe/CdS Photovoltaic Solar Cell According to Electrical Properties by Scaps Simulation," Nat. Resour., vol. 11, no. 04, pp. 147–155, 2020, doi: 10.4236/nr.2020.114009.

[24] D. B. Li et al., "20%-efficient polycrystalline Cd(Se,Te) thin-film solar cells with compositional gradient near the front junction," Nat. Commun., vol. 13, no. 1, pp. 1–8, 2022, doi: 10.1038/s41467-022-35442-8.

[25] P. D. Rizaldi, "PEMODELAN SEL SURYA FILM TIPIS ZnO/CdS/CdTe MENGGUNAKAN AFORS-HET: PENGARUH KETEBALAN CdS DAN TEMPERATUR DEVAIS TERHADAP PERFORMANSI SEL SURYA JUDUL," UNNES, 2018, [Online]. Available: http://lib.unnes.ac.id/37648/1/4211 414030.pdf

Enhancing Performance of Sigmoid implementation in FPGA using Approximate computing

Rohan Murmu
Department of Information Technology
ABV-Indian Institute of
Information Technology and Management
Gwalior, (M.P.), India

Mahua Bhattacharya
Department of Information Technology
ABV-Indian Institute of
Information Technology and Management
mb@iiitm.ac.in

Somesh Kumar, *IEEE Senior Member*
Department of Electrical and Electronics Engineering
ABV-Indian Institute of
Information Technology and Management
somesh@iiitm.ac.in

***Abstract*—This paper explores an efficient implementation of the sigmoid function on Field-Programmable Gate Arrays (FPGAs) through Piecewise Linear Approximation (PLAN). Recognizing the high computational demands of exact sigmoid calculations, we propose a methodology that leverages Approximate Computing techniques to enhance performance. By strategically reducing precision, our approach significantly speeds up computations while maintaining acceptable accuracy levels, thus optimizing resource usage. This trade-off is particularly advantageous in scenarios demanding high-speed data processing and low power consumption. We demonstrate the feasibility and benefits of our method with empirical results, suggesting its practicality for real-time applications in neural networks and machine learning.**

***Index Terms*—Sigmoid Activation function, FPGA, Approximate Computing**

I. Introduction

The landscape of artificial intelligence and machine learning has witnessed unparalleled growth in innovation and demand. As these fields advance, there is an increasing need for specialized hardware to accelerate complex neural network computations. Very-Large-Scale Integration (VLSI) provides a crucial platform for designing and optimizing hardware tailored to specific computational requirements [1][2].

This paper investigates the integration of the sigmoid activation function, a vital component in neural networks, on a FPGA using VLSI design principles. The Sigmoid function introduces non-linearity to neural network layers, enabling the capture of complex data relationships. By implementing the Sigmoid function on an FPGA using VLSI methodologies, this research aims to harness the parallel processing capabilities of FPGAs to expedite inference and training tasks [3].

The integration of the sigmoid function in FPGA through approximate computing represents a novel approach to enhancing computational efficiency. This technique involves strategic reductions in computational precision, which, while slightly decreasing accuracy, substantially optimizes power consumption and resource utilization within FPGA environments. By simplifying the calculations involved in the sigmoid function, the system demands less power and fewer resources, making it highly suitable for applications where these factors are constrained. Potential applications of this technology include embedded systems in portable medical devices, where long battery life is crucial, and real-time processing systems in IoT devices, where efficiency is prioritized over perfect accuracy.

To ensure a clear understanding of this research, we will go through the sigmoid activation function and its approximation techniques and also learn about approximate computing. We will also discuss the methodology that explain the specific methods used in this study, including how the sigmoid function was designed and implemented in FPGA using approximate computing. The results section will show the findings, highlighting the performance improvements achieved with the proposed approach. We will also examine these results, comparing them with existing methods and noting the significance of the improvements.

II. Sigmoid Activation function and its approximation techniques

The sigmoid function is a mathematical function that produces an "S"-shaped curve. It is widely used in various fields, particularly in artificial neural networks, to introduce non-linearity into the model by mapping real-valued numbers into the range between 0 and 1. This bounded output makes the sigmoid function ideal for tasks like binary classification, where it can represent probabilities. The classic equation of sigmoid can be defined Eq.(2) [3].

$$f(x,k,b,T,c) = k + \frac{c}{1+be^{Tx}}, \forall x \in R \tag{1}$$

979-8-3315-1921-6/24/$31.00 ©2024 IEEE

where $k \in R, b \in R^+, T, c \in R \setminus \{0\}, R$ - the set of real numbers $(-\infty, +\infty), R^+$ - the set of real positive numbers $(0, +\infty), R\{0\}$ - The set of real numbers except zero point $(-\infty, 0)$ and $(0, +\infty)$

- Classical sigmoid function ($k = 0, c = b = 1, T = -1$)

$$f(x) = \frac{1}{1 + e^{-x}} \tag{2}$$

- Thermodynamic-like function ($k = 0, c = b = 1, T = -1/T'$)

$$t(x, T) = \frac{1}{1 + e^{-x/T}} \tag{3}$$

- Hyberbolic Tangent ($k = 1, c = b = -2, T = 2$)

$$h(x) = \frac{e^x - e^{-x}}{e^x + e^{-x}} \tag{4}$$

There are different ways of approximating a sigmoid function which includes LUT [4], Taylor transformation, Piecewise Linear Approximation (PLAN). Some research suggest their own approximation techniques which focuses on more accuracy. A novel approach of approximating and implementing non-linear functions by utilizting logarithmic function and implementing Taylor series Expansion [5]. A proposed a method combination of second order nonlinear function (SONF) and the differential lookup table (dLUT) [6]. A unique approach called Chebyshev's polynomial approximation [7].

For simplification, we will make use of the basic technique for approximating a non-linear function which is Piecewise Linear Approximation (PLAN).

A. Piecewise linear approximation of the sigmoid function (PLAN approximation)

This method involves in spliting the function into several linear or non-linear segment. For example, PLAN approximation for sigmoid in the range of -5 to 5, we might split this range into several intervals, let's say we divide at (-5, -2, 0, 2, 5), the slope between the each consecutive points using the Eq. $f(x) = mx + c$, as we observe in the Fig.(1).

In this paper, the following Eq.(5) is used for the approximation using PLAN [4],

$$f(x) = \begin{cases} 1 & 5.0 \leq |x| \\ 0.03125 * |x| + 0.84375 & 2.375 \leq |x| < 5.0 \\ 0.125 * |x| + 0.625 & 1.0 \leq |x| < 2.375 \\ 0.25 * |x| + 0.5 & 0 \leq x < 1.0 \end{cases} \tag{5}$$

For reducing the complexity we converted into integer by multiplying its terms without the variable $|x|$ by 2^{10} [8], as given in Eq.(6).

$$f(x) = \begin{cases} 1024 & 5120 \leq |x| \\ 2^{-5} * |x| + 864 & 2432 \leq |x| < 5120 \\ 2^{-3} * |x| + 640 & 1024 \leq |x| < 2432 \\ 2^{-2} * |x| + 512 & 0 \leq x < 1024 \end{cases} \tag{6}$$

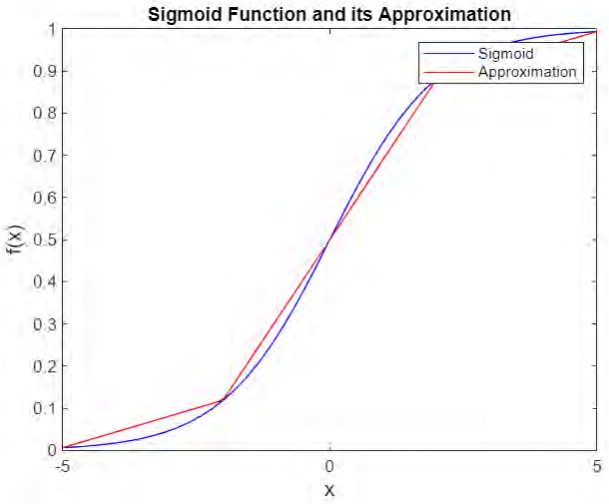

Fig. 1. Comparision between PLAN and Sigmoid Function

III. Approximate Computing for Optimiztion

Approximate Computing is an emerging research area that focuses on optimizing computational efficiency by intentionally reducing precision. This technique is particularly valuable in scenarios where absolute accuracy is less crucial. By allowing slight inaccuracies in calculations, systems can achieve substantial improvements in speed and power consumption. This approach is well-suited for applications like multimedia processing, machine learning, and sensor data analysis, where minor errors are tolerable in return for enhanced performance and reduced resource usage. The main advantages of approximate computing include lowered computational demands and improved efficiency, especially in environments with limited resources [9].

A. Approximate Adder

Although the operation of an adding cell is relatively straightforward, the frequency with which it is used means that the electrical performance of a Full Adder is crucial for system efficiency. Full adders are designed with three inputs , two operand bits (A and B) and a carry-in (Cin), and they produce two outputs and its given with the Eq.(7) and Eq.(8).

$$S = A \oplus B \oplus Cin \tag{7}$$

$$Cout = (A \cdot B) + (A \oplus B) \cdot Cin \tag{8}$$

This is where the concept of Approximate adders comes into play. Approximate adders are used to improve power efficiency and computational speed by simplifying the arithmetic operations, but at the cost of some accuracy [10]. In many real-world applications, such as video processing and machine learning, the slight loss in precision due to approximate computing does not substantially affect the final outcome but does allow for a

reduction in power consumption and faster processing speeds [11].

An approximate adder modifies the arithmetic operations by altering how the least significant bit (LSB) and, sometimes, the most significant bit (MSB) are processed, aiming to simplify the computations [12]. The carry output $Cout$ (Eq. (9)) is calculated as the logical AND of A and B, ignoring the carry-in which simplifies the logic and reduces the hardware needed as shown in the Fig. (2).

$$Cout = (A\&B) \tag{9}$$

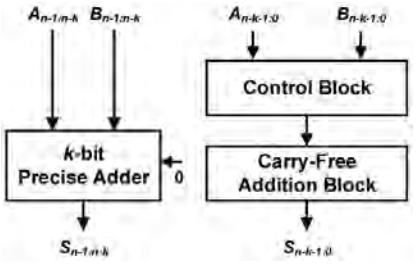

Fig. 2. Approximate Adder Structure

IV. Implementation of Sigmoid function in FPGA

The implementation of the sigmoid function has been carried out in Xilinx Vivado 2023.2 which uses the board XC7K70TFBV676-1 for FPGA and Verilog is used for HDL(Hardware Descriptive Language).

For implementation of the Eq.(6) in verilog requires multiplier which has long latency and large complexity. Since we reduced the complexity of Eq.(5) by multiplying the integers with 2^{10}, we can use shift operators (<<) which usually means x << n effectively multiplies x by 2^n, while x >> n divides x by 2^n. Therefore instead using the multiplier, we use the right shift >>. We get the Eq.(10).

$$f(x) = \begin{cases} 1024 & 5120 \leq |x| \\ |x|>>5 + 864 & 2432 \leq |x| < 5120 \\ |x|>>3 + 640 & 1024 \leq |x| < 2432 \\ |x|>>2 + 512 & 0 \leq x < 1024 \end{cases} \tag{10}$$

Now since we are implementing approximate computing, we would not use (+) operator, instead we create a module of approximate adder and the implement it on the Eq.(10). In our case, we have taken 6-bit LSB (Least Significant Bits) which didn't go proper addition without carry and can be implemented by XOR operator and the rest bits go through normal full adder addition. Based on all variables and function, we formed the pseudo code as given in the Algo.(1).

V. Results Analysis and Performance Bench marking

In our study on the implementation of the sigmoid function in FPGAs using approximate computing, we conduct key analyses to evaluate the effectiveness and trade-offs of this approach. To simply understand, the flow chart is given in the Fig.(3) based on workflow of the approach.

Algorithm 1 Sigmoid implementation using Approximate Computing

procedure PLAN(x, f_x)
  $x\_abs \leftarrow |x|$
  if $x < 0$ **then**
    $x\_abs \leftarrow -x$
  else
    $x\_abs \leftarrow x$
  end if
  if $x\_abs \geq 5120$ **then**
    $f\_x \leftarrow 1024$
  else if $2432 \leq x\_abs \leq 5120$ **then**
    $adder\_a \leftarrow x\_abs >> 5$
    $adder\_b \leftarrow 864$
    $f\_x \leftarrow approx\_adder(adder\_a, adder\_b)$
  else if $1024 \leq x\_abs \leq 2432$ **then**
    $adder\_a \leftarrow x\_abs >> 3$
    $adder\_b \leftarrow 640$
    $f\_x \leftarrow approx\_adder(adder\_a, adder\_b)$
  else
    $adder\_a \leftarrow x\_abs >> 2$
    $adder\_b \leftarrow 512$
    $f\_x \leftarrow approx\_adder(adder\_a, adder\_b)$
  end if
  return f_x
end procedure

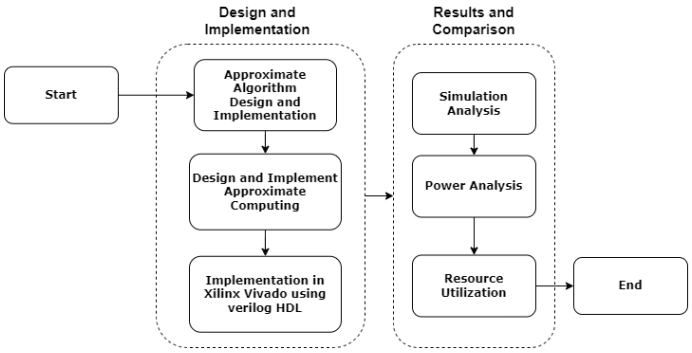

Fig. 3. Flow diagram of desing, implementing the sigmoid function and conducting analyses.

A. Error analysis

For estimation of the error of approximation the maximum and average errors are used. The average absolute error and the maximum absolute error of the function f(x) are calculated by the Eq.(11) and Eq.(12) [3].

$$\varepsilon(avg) = \frac{\sum |f'(xi) - f(xi)|}{Np} \tag{11}$$

$$\varepsilon(max) = max(f'(xi) - f(xi)), i = 0, ...Np \quad (12)$$

For our FPGA implementation of the sigmoid function using approximate computing, we utilized Xilinx Vivado for synthesis, simulation, and power and resource analysis. Vivado's comprehensive tools allowed us to model and test our design meticulously, providing detailed reports on power consumption and resource utilization. This enabled us to optimize our design effectively, balancing accuracy with efficiency, and ensuring optimal performance within the FPGA's constraints.

B. RTL View of implemented function

RTL (Register-Transfer Level) view as given in Fig.(4) shows a module named approx_plan_v1_0, which is responsible for the PLAN approximation of a sigmoid function using approximate adder. This module has an input port x[15:0], which is a 16-bit signal representing the input value to the sigmoid approximation function. The output port is labeled f_x[15:0], which is also a 16-bit signal representing the approximated output value of the sigmoid function. This high-level view abstracts the internal complexity of the sigmoid approximation, focusing on the module's interface and how it interacts with other components in the design.

Fig. 4. RTL view of implemented module

C. Simulation Results

We initiated testing with an initial input number of 1728 and gradually raised it to 2240, allowing us to assess the effectiveness of our approximation across a variety of numbers. Between each increment, we implemented a brief delay of 10 nanoseconds to ensure the stability and accuracy of the output we obtained. We compared simulations with and without approximate adder, and we achieved two in the simulations results.

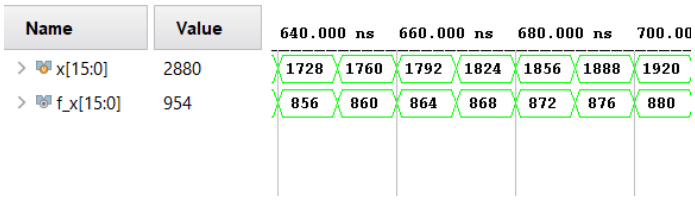

Fig. 5. Time charts of the module of the sigmoid function calculation using PLAN without approximate adder

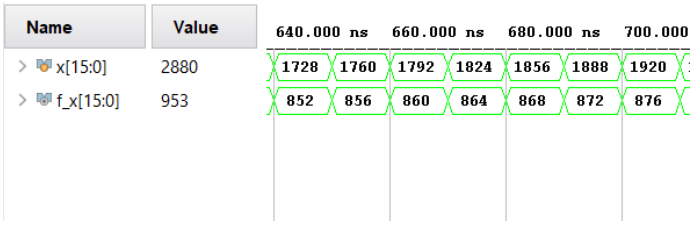

Fig. 6. Time charts of the module of the sigmoid function calculation using PLAN with approximate adder

As we observed that in the Fig.(5) and Fig.(6), a fragment with input values ranging from 1728 to 1920, For example, the value of the input signal $x = 1760$ corresponds to the value of the signal $f_x = 2^{-3} * 1760 + 640$ (as given in Eq.(6)) which is equal to 860. So Fig.(5) shows accurate results but there is 0.24% error in Fig.(6) because of approximate adder implementation.

D. Power Analysis

We did the power analysis on implementation of Xilinx Vivado for both types of designs and we achieved the following results. We can observe that Fig.(7) and Fig.(8) there is difference between the Total on-chip power. We can observe the Dynamic and Static power deflection, which is approximately 14.60% reduction in power usage.

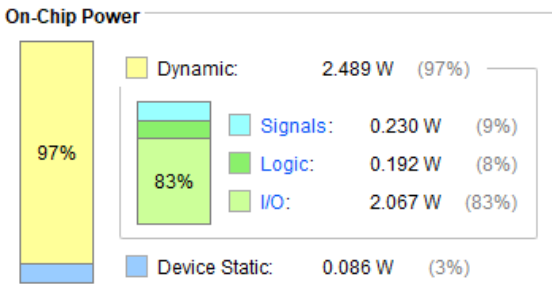

Fig. 7. Power analysis of PLAN without approximate adder

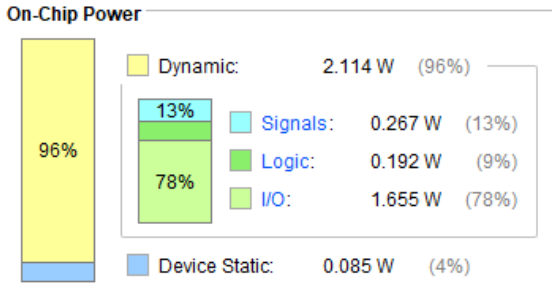

Fig. 8. Power analysis of PLAN with approximate adder

E. Resource Utilization and Accuracy Comparision

We tested the resource utilization as well as average absolute error and the maximum absolute error on both designs with

and without approximate adder, we can observe in the Table (I) the resources utilized.

TABLE I
RESOURCE UTILIZATION COMPARISION BETWEEN PLAN VS PLAN WITH APPROXIMATE ADDER

	PLAN	**new PLAN**	**% Change**
Slice LUTs (41000)	53	50	5.66
Slice (10250)	16	16	No change
LUT as Logic (41000)	53	50	5.66
Bonded IOB(300)	32	32	No change
$\varepsilon(avg)$	0.02408	0.02414	0.24
$\varepsilon(max)$	0.0408	0.0409	0.24

VI. CONCLUSION

Our research on implementing the sigmoid function in FPGAs using approximate computing has shown great potential for improving efficiency. By reducing precision in calculations, we managed to lower power use and better utilize resources without significantly affecting accuracy. We used Xilinx Vivado to thoroughly analyze our design, allowing us to see the trade-offs and benefits clearly. Our findings prove that this method works well in situations where small errors are acceptable if they lead to faster performance and less power consumption. This study adds to the existing knowledge on approximate computing and opens up new possibilities for its use in embedded systems and other areas.

REFERENCES

[1] V. A. Sumayyabeevi, J. J. Poovely, N. Aswathy and S. Chinnu, "A New Hardware Architecture for FPGA Implementation of Feed Forward Neural Networks," 2021 2nd International Conference on Advances in Computing, Communication, Embedded and Secure Systems (ACCESS), Ernakulam, India, 2021, pp. 107-111, doi: 10.1109/ACCESS51619.2021.9563342.

[2] S. S. Lingala, S. Bedekar, P. Tyagi, P. Saha and P. Shahane, "FPGA Based Implementation of Neural Network," 2022 International Conference on Advances in Computing, Communication and Applied Informatics (ACCAI), Chennai, India, 2022, pp. 1-5, doi: 10.1109/ACCAI53970.2022.9752656.

[3] I. Tsmots, O. Skorokhoda, and V. Rabyk, "Hardware implementation of sigmoid activation functions using fpga," in 2019 IEEE 15th International Conference on the Experience of Designing and Application of CAD Systems (CADSM), 2019, pp. 34–38, doi: 10.1109/CADSM.2019.8779253

[4] R. Pogiri, S. Ari and K. K. Mahapatra, "Design and FPGA Implementation of the LUT based Sigmoid Function for DNN Applications" 2022 IEEE International Symposium on Smart Electronic Systems (iSES), Warangal, India, 2022, pp. 410-413, doi: 10.1109/iSES54909.2022.00090.

[5] Z. Qin, Y. Qiu, H. Sun, Z. Lu, Z. Wang, Q. Shen, and H. Pan, "A novel approximation methodology and its efficient vlsi implementation for the sigmoid function," IEEE Transactions on Circuits and Systems II: Express Briefs, vol. 67, no. 12, pp. 3422–3426, 2020, doi: 10.1109/TCSII.2020.2999458

[6] S. Ngah, R. Bakar, A. Embong, and S. Razali, "Two-steps implementation of sigmoid function for artificial neural network in field programmable gate array," vol. 11, pp. 4882–4888, 04 2016

[7] B. K. Pandit and A. Banerjee, "VLSI Architecture of Sigmoid Activation Function for Rapid Prototyping of Machine Learning Applications," 2021 IEEE International Symposium on Smart Electronic Systems (iSES), Jaipur, India, 2021, pp. 117-122, doi: 10.1109/iSES52644.2021.00036.

[8] A. Vaisnav, S. Ashok, S. Vinaykumar and R. Thilagavathy, "FPGA Implementation and Comparison of Sigmoid and Hyperbolic Tangent Activation Functions in an Artificial Neural Network," 2022 International Conference on Electrical, Computer and Energy Technologies (ICECET), Prague, Czech Republic, 2022, pp. 1-4, doi: 10.1109/ICECET55527.2022.9873085.

[9] S. Dutt, S. Nandi, and G. Trivedi, "A comparative survey of approximate adders" in 2016 26th International Conference Radioelektronika (RADIOELEKTRON-IKA), 2016, pp. 61–65, doi: 10.1109/RADIOELEK.2016.7477392

[10] Sampath Kumar, Minakshi Poonia, Rahul Kumar, Gaurav Sharma, and Somesh Kumar, "Design and Implementation of Low Power, High-Speed Configurable Approximation 8-Bit Booth Multiplier" Journal of Circuits, Systems and Computers VOL. 31, NO. 17, 2022.

[11] P. Balasubramanian and D. Maskell, "Hardware efficient approximate adder design," in TENCON 2018 - 2018 IEEE Region 10 Conference, 2018, pp. 08060810, doi: 10.1109/TENCON.2018.8650127

[12] Pedro Aquino Silva and Cristina Meinhardt, "Energy-Efficient Design of Approximated Full Adders" 020 27th IEEE International Conference on Electronics, Circuits and Systems (ICECS).

Influence of Environmental Conditions on the Performance of Solar Power Generation Systems: Analysis of Light Intensity, Temperature, and Humidity

Muchlishah Muchlishah
Electrical Engineering
Politeknik Negeri Jakarta
Depok, Indonesia
muchlishah@elektro.pnj.ac.id

Dezetty Monika
Electrical Engineering
Politeknik Negeri Jakarta
Depok, Indonesia
dezetty.monika@elektro.pnj.ac.id

Fatahula Fatahula
Electrical Engineering
Politeknik Negeri Jakarta
Depok, Indonesia
fatahula@elektro.pnj.ac.id

Bharata Sena Indra Permana
Electrical Engineering
Politeknik Negeri Jakarta
Depok, Indonesia
bharata.senaindrapermana.te20@mhsw.pnj.ac.id

***Abstract*—This study examines how light intensity, temperature, and humidity affect the performance of the Solar Power Plant (PLTS) system. The solar power system utilized in this study is furnished with an Internet of Things (IoT)-based device which enables real-time monitoring via the Blynk application. Data from BH1750 light intensity sensor, DHT22 temperature, and humidity sensor, as well as PZEM-017 measurement module, was examined to assess the connection between environmental factors and the effectiveness and electricity production of the solar energy facility. The findings reveal that the brightness level is positively correlated with power output, whereas temperature and humidity negatively impact system efficiency. An increase in temperature results in a reduction in the energy conversion efficiency of photovoltaic cells, while high humidity can speed up the degradation of solar panel materials. This study offers valuable insights for enhancing the design and functioning of solar power plants to boost their efficiency in different environmental settings, particularly in tropical areas like Indonesia.**

***Index Terms*—Solar power plant, light intensity, temperature, humidity, IoT, Blynk.**

I. Introduction

The use of solar energy through solar power plants has been identified as a powerful answer to global energy and climate change concerns [1]. Solar PV uses photovoltaic cells to convert sunlight into electricity, resulting in a clean and renewable energy source. Solar power plants are increasingly being built in various parts of the world, including Indonesia. This is motivated by the desire to reduce dependency on fossil fuels and greenhouse gas emissions [2].

979-8-3315-1921-6/24/$31.00 ©2024 IEEE

However, solar power plants' efficiency greatly relies on the environmental conditions in their vicinity, such as light intensity, temperature, and humidity. Solar panels depend greatly on sunlight to produce electricity. A decrease in light intensity, due to factors like clouds or fog, results in lower power production from the solar system [3].

Furthermore, ambient temperature significantly influences the efficiency of solar power plants. While solar panels rely on sunlight for energy production, extremely high temperatures can diminish the energy conversion efficiency of photovoltaic cells. Research indicates that each 1°C rise in temperature results in a 0.5% drop in efficiency [4]. Although humidity has little direct effect on panel efficiency, it can accelerate the depreciation of solar panel materials and other components, especially in humid tropical conditions [5].

Environmental conditions can also increase the possibility of dust or dirt formation on the surface of solar panels, which can reduce the amount of light absorbed and lower overall system performance [6]. Given this, it is crucial to understand how those three environmental elements have an effect on the performance of sun energy plant life, mainly inside the context of tropical countries such as Indonesia. therefore, this look at pursuits to behaviour an in-depth analysis of the results of mild intensity, temperature, and humidity at the efficiency and energy output of sun electricity plants. The consequences of this observe are anticipated to provide useful insights for optimizing the layout and operation of solar electricity flora to make them more efficient under numerous environmental situations.

II. Research Method

This studies aims to research the influence of environmental conditions on the overall performance of the solar strength Plant (PLTS) system, focusing at the variables of mild intensity, temperature, and humidity. in this studies, the PLTS system is developed using diverse components which can be interconnected and monitored in actual-time through IoT-based totally gadgets controlled the usage of the Blynk software.

Latest studies on IoT-enabled photovoltaic systems have highlighted the significance of actual-time environmental tracking for optimizing sun panel performance. technologies integrating IoT sensors permit for continuous records series, which aids in right away identifying performance deviations because of environmental elements. This examine builds on those findings through using IoT-based monitoring to capture statistics on mild depth, temperature, and humidity, thereby imparting a nuanced knowledge of environmental impacts on sun panel overall performance.

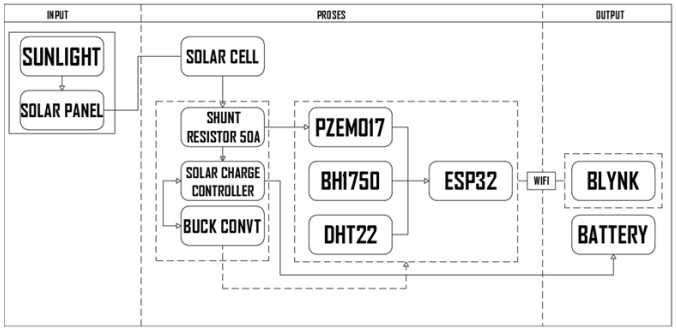

Fig. 1. Block Diagram

Figure 1 is a block diagram of the environmental situation monitoring device and the overall performance of sun panels, the following is an explanation of the block diagram, solar panels are used as the primary component to transform sun power into energy. The current generated by the solar panel is measured using a 50A shunt resistor, while the solar charge controller is used to regulate the flow of electrical power from the solar panel to the battery. The energy stored in the battery is then regulated again by the buck converter to match the needs of the load to be used. To measure various environmental parameters, a BH1750 sensor is used for light intensity, a DHT22 sensor for temperature and humidity, and a PZEM-017 module to measure voltage, current, power, and energy produced by the solar panels. All the data from these sensors is collected and processed by the ESP32 microcontroller, which then sends the data in real-time to the Blynk app over a WiFi network.

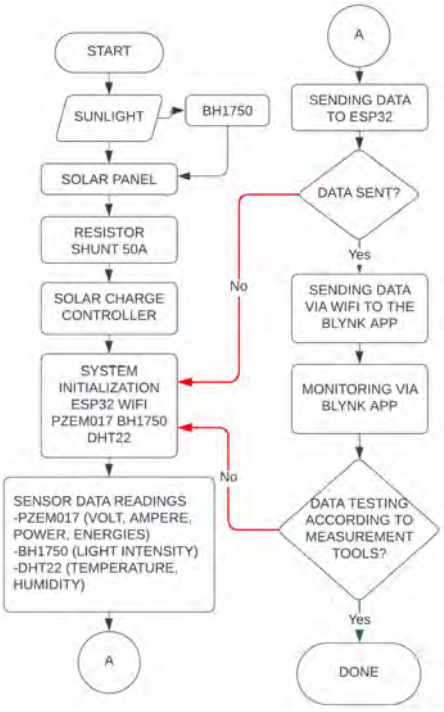

Fig. 2. Flowchart

In Figure 2 is a flowchart of the following research. The data collection process begins with setting up the solar panel in an optimal location to receive sunlight. The BH1750 sensor is positioned to measure the light intensity, whilst the DHT22 sensor measures the temperature and humidity around the panel. The PZEM-017 module measures the electric parameters generated with the aid of the solar system. Data from those three sensors is sent to the ESP32 microcontroller, which serves as the control center and sends data to the Blynk app. The Blynk app enables real-time monitoring of the solar power plant's performance and makes it easy to collect data for further analysis.

An analysis of the data was conducted to assess how variations in light intensity, temperature, and humidity impact the power output of the solar farm system. Data collected from the Blynk app was analyzed to establish the correlation between environmental conditions and the solar farm's performance. Tests were carried out to confirm the precision of the data collected from the system, through a comparison with results from reference measuring tools. If there are discrepancies found, the system will recalibrate to ensure accurate data is generated.

In this study, monocrystalline 50wp photovoltaic modules were used because of their specific response characteristics under different light intensity, temperature, and humidity levels. By detailing the types of cells used, we aim to provide insights into how distinct technologies may adapt or degrade under environmental stressors. This detail will support comparisons with other photovoltaic technologies and provide a clearer understanding of their behavior in real-world applications.

III. Result and Discussion

The following are the results of test data and analysis of the influence of environmental conditions on the performance of the solar power generation system (PLTS)

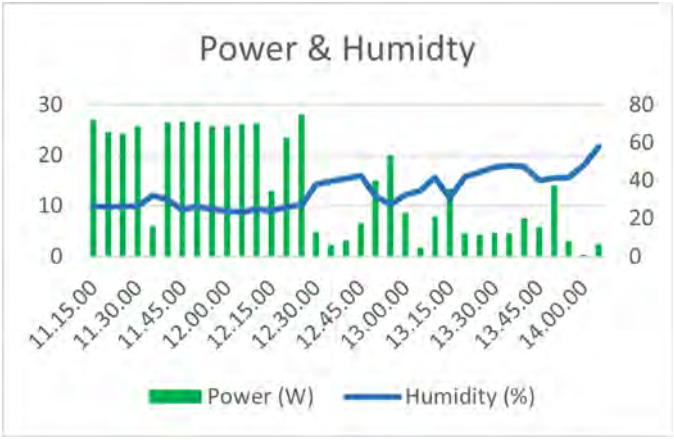

Fig. 3. corelation between power and humidity

From the check consequences shown in determine 3, we can see that air humidity has an effect at the overall performance of the solar strength Plant gadget. Over a time period, because the humidity will increase, there's a variant within the electricity generated. Humidity can affect the performance of sun panels via two essential mechanisms. first of all, high humidity ranges can cause condensation or fog at the floor of the sun panel, lowering the transmission of sunlight getting into the photovoltaic cellular [7]. This leads to a lower in the electricity generated due to the decreased variety of photons accomplishing the sun cells. Secondly, high humidity could have a cooling effect on solar panels, that may without a doubt improve power conversion efficiency. beneath perfect conditions, sun panels operate extra effectively at decrease temperatures. research by Goswami [8] aid those findings, in which they discovered that an increase in humidity can decrease the efficiency of solar panels due to a lower inside the intensity of mild received. but, humidity also can have a positive effect by way of preventing immoderate temperature upward thrust in the panels, thus maintaining efficiency optimized. As such, the impact of humidity on solar PV performance is complicated and relies upon on the general environmental situations.

While the short-term effects of humidity on photovoltaic performance are discussed, it is critical to examine the long-term consequences of excessive humidity exposure. Prolonged exposure to moisture can hasten material deterioration, especially in encapsulants and connectors. This deterioration not only reduces efficiency but may also increase the frequency of maintenance required in humid environments, reducing the operating lifespan of solar power systems. Future research might further investigate material robustness in these conditions to properly handle maintenance problems.

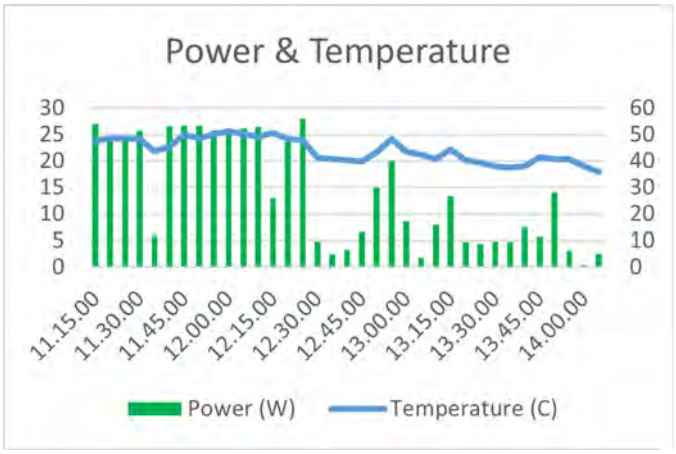

Fig. 4. corelation between power and temperature

Figure 4 depicts the link between temperature and electricity generated by the PV system. There is a definite negative association between temperature and output power: as the temperature rises, the power generated decreases. This is owing to the characteristics of the semiconductor materials used in solar cells. At greater temperatures, thermal motion in the semiconductor material increases, resulting in higher internal resistance and lower photovoltaic conversion efficiency. Furthermore, high temperatures can alter the voltage and current properties of solar cells, resulting in a drop in output power [9]. Research performed by way of Mehmood [10] suggests that each 1°C growth in temperature above the usual temperature (25°C) can reason a decrease in electricity performance of as much as 0.5%. This shows how important temperature management is for solar panels to maintain optimal performance. In conditions where temperature cannot be controlled, such as in locations with high solar intensity, the use of cooling systems or materials that have low temperature coefficients can be an effective solution to minimize power loss due to high temperatures.

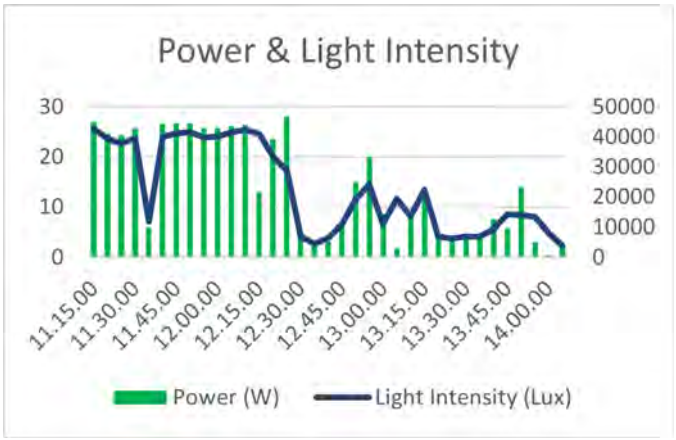

Fig. 5. corelation between power and light intensity

One of the key factors influencing solar panel performance is light intensity. Greater light intensity indicates that the solar

cell can convert more photons into electrical energy, increasing power generation. Photons from sunlight are absorbed by semiconductor materials, which then excite electrons to produce an electric current. Research studies by Dezfuli [11] and Laurent [12] have demonstrated that boosting light intensity can significantly enhance the power production of a solar PV system, particularly on sunny days with direct sunlight. However, in tropical regions during the peak summer season, if the light intensity is too high, the efficiency might decrease because the temperature rises along with the light intensity. As a end result, it's miles important to install sun panels with the correct tilt and orientation, moreover, choosing materials with excessive efficiency for the duration of a extensive range of the mild spectrum is vital for reinforcing mild absorption and boosting strength conversion.

IV. Conclusion

This research successfully demonstrates that environmental conditions have a significant influence on the performance of solar PV systems. Variations in light intensity, temperature, and humidity were shown to affect the efficiency and power output of the solar PV system. The following are the main points of the research conclusions:

- Light Intensity: The power generated by a solar farm is highly dependent on the light intensity. Higher light intensities create more electricity. Excessive light intensity can raise panel temperature and reduce system efficiency.
- Temperature: Temperature is negatively correlated with power output. As temperature rises, solar panels lose efficiency due to increased internal resistance in the semiconductor material. Maintaining optimal solar farm performance requires effective temperature management.
- Humidity: Humidity has a direct and indirect influence on solar power plant performance. High humidity levels might cause condensation on panel surfaces, reducing light transmission and power output. In favorable conditions, high humidity can help cool panels and improve power conversion efficiency.

Overall, this research provides important insights for more efficient solar power plant design and operation, especially under diverse environmental conditions such as in the tropics. Optimizing solar power plants requires dealing with moderate intensity, temperature, and humidity to provide maximum overall performance.

References

[1] I. Renewable and E. Agency, "Global Energy Transformation: A Roadmap to 2050, Executive Summary," *2018*.

[2] D. Gielen, F. Boshell, D. Saygin, M. D. Bazilian, N. Wagner, and R. Gorini, "The role of renewable energy in the global energy transformation," *Energy Strateg. Rev.*, vol. 24, no. June 2018, pp. 38–50, 2019, doi: 10.1016/j.esr.2019.01.006.

[3] H. L. Y. S. C. T. C. H. L. Z. A. Hove, "Toward the Development of an Empirical Model of Air Pollution Impact on Solar PV Output for Industry Use," vol. 13, 2023, doi: 10.1109/JPHOTOV.2023.3317636.

[4] R. Madurai Elavarasan et al., "Pathways toward high-efficiency solar photovoltaic thermal management for electrical, thermal and combined generation applications: A critical review," *Energy Convers. Manag.*, vol. 255, no. December 2021, p. 115278, 2022, doi: 10.1016/j.enconman.2022.115278.

[5] A. A. Sher, N. Ahmad, M. Sattar, U. Ghafoor, and U. H. Shah, "Effect of Various Dusts and Humidity on the Performance of Renewable Energy Modules," *Energies*, vol. 16, no. 13, 2023, doi: 10.3390/en16134857.

[6] M. R. Maghami, H. Hizam, C. Gomes, M. A. Radzi, M. I. Rezadad, and S. Hajighorbani, "Power loss due to soiling on solar panel: A review," *Renew. Sustain. Energy Rev.*, vol. 59, pp. 1307–1316, 2016, doi: 10.1016/j.rser.2016.01.044.

[7] Y. Gao, M. Xue, H. Tian, F. Guo, Y. Jin, and B. Wang, "Investigating the Impact of Humidity on Potential-Induced Degradation (PID) in Photovoltaic Modules with Ash Accumulation," *IEICE Electron. Express*, vol. 21, no. 16, pp. 1–6, 2024, doi: 10.1587/elex.21.20240357.

[8] A. Goswami, "Effect of Humidity on the Generation Capacity of Floating Solar Photovoltaic System," *Jordan J. Electr. Eng.*, vol. 9, no. 1, pp. 31–41, 2023, doi: 10.5455/jjee.204-1667584023.

[9] R. J. Mustafa, M. R. Gomaa, M. Al-Dhaifallah, and H. Rezk, "Environmental impacts on the performance of solar photovoltaic systems," *Sustain.*, vol. 12, no. 2, pp. 1–17, 2020, doi: 10.3390/su12020608.

[10] U. Mehmood, A. Al-Ahmed, F. A. Al-Sulaiman, M. I. Malik, F. Shehzad, and A. U. H. Khan, "Effect of temperature on the photovoltaic performance and stability of solid-state dye-sensitized solar cells: A review," *Renew. Sustain. Energy Rev.*, vol. 79, no. March 2016, pp. 946–959, 2017, doi: 10.1016/j.rser.2017.05.114.

[11] Z. Li, J. Yang, and P. A. N. Dezfuli, "Study on the Influence of Light Intensity on the Performance of Solar Cell," *Int. J. Photoenergy*, vol. 2021, 2021, doi: 10.1155/2021/6648739.

[12] W. Tercha, S. A. Tadjer, F. Chekired, and L. Canale, "Machine Learning-Based Forecasting of Temperature and Solar Irradiance for Photovoltaic Systems," *Energies,*, vol. 17, no. 5, 2024, doi: 10.3390/en17051124.

Analysis of the Effect of Analog Switches on the Digital Signal Oscilloscope Circuit

Arbai Yusuf
Division of Research and Collaborations
CTECH Labs Edwar Technology Co
Tangerang, Indonesia
Department of Electrical Engineering
Academy of Technology Bogor
Bogor, Indonesia
arbai@c-techlabs.com

Wahyu Widada
Structural Strength Technology Research Center
National Research and Innovation Agency
Jakarta, Indonesia
wahy016@brin.go.id

Warsito Purwo Taruno
Division of Research and Collaborations
CTECH Labs Edwar Technology Co
Tangerang, Indonesia
wsito@c-techlabs.com

Imamul Muttakin
Department of Electrical Engineering
Universitas Sultan Ageng Tirtayasa
Cilegon, Indonesia
ORCID 0000-0002-8409-4942

***Abstract*—Digital oscilloscopes sold in the market usually have limited functions. For other measurement purposes such as electrical properties, there is still a need to use additional equipment such as impedance analyzers and vector network analyzers. We designed a digital signal oscilloscope for special purposes, which can be used to measure, record, and display signals, as well as measure electrical properties such as inductance, capacitance, resistance, and impedance. Inside the digital signal oscilloscope, there is a switch circuit network that has the function of forwarding the input signal to the signal conditioning circuit. This network switch has stray capacitance and resistance that can affect signal measurements. This paper explains the effect of the network switch on signal measurement. The method used is to create an equivalent circuit model and create a mathematical model, then simulate them using MATLAB or Python. The simulation results show that the switch in the off state still produces a current of about 0.015A which indicates that there is still impedance even though the switch is off.**

***Index Terms*—Digital Signal Oscilloscope, Analog Switches, Data Acquisition, Signal Measurements, Impedance Measurements**

I. Introduction

A digital signal oscilloscope is an electronic device used to measure, record, and analyze signals. This oscilloscope converts the electrical signal of the object being measured into a visual, namely a graph that shows the signal changing against time [1]. The functions of the oscilloscope are very broad including measuring various types of electrical signals such as AC and DC signals, and visualizing signals into graphs displayed on a screen with two vertical and horizontal axes [2] [3]. In addition, it can also be used for signal analysis and diagnostics such as for signal characterization, frequency, amplitude, distortion, and noise [4] [5] [6].

Digital oscilloscopes available on the market typically have limited functionalities, as previously mentioned. For additional measurement needs, such as analyzing electrical mass properties, other equipment like impedance analyzers and vector network analyzers are used [7] [8]. At our laboratory at C-Tech Labs, we developed a specialized digital signal oscilloscope capable of measuring, recording, and displaying signals, as well as assessing electrical properties such as inductance, resistance, impedance, and capacitance as described in Fig. 1 (top). It has one output channel as a signal generator that can produce frequencies of 1Hz - 10MHz with an amplitude of 10Vpp. In addition, it also has two input channels with vertical scale gain values of volts per div from 0.01x - 50x and horizontal scale time per div up to 175µs.

The digital signal oscilloscope will measure the signal through the BNC (Bayonet Neill-Concelman) connector channel, then the signal is passed to the signal conditioning circuit through the network switch circuit as described in Fig. 1 (bottom). BNC connectors are quick-connect/disconnect mini radio frequency connectors used for coaxial cables. It is designed to maintain the same characteristic impedance of the cable, with 50 ohm and 75 ohm types being made. This switching network is a series of analog switches that resemble the letter ”T” because it is called the T-switch [9] [10]. The function of this analog switch is to connect the signal from the BNC connector to the signal conditioning circuit where this switch can be configured in four modes, namely on, off, ground, and floating modes.

979-8-3315-1921-6/24/$31.00 ©2024 IEEE

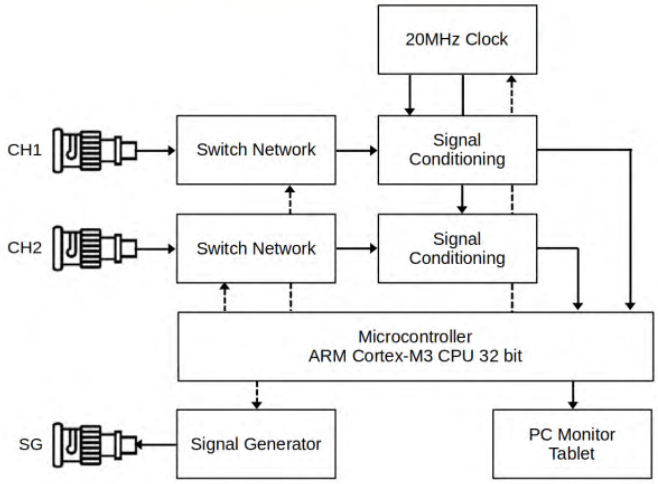

Fig. 1. Digital signal oscilloscope for special purpose

This analog switch is made of semiconductor materials which when the switch is ”on” or ”off” will have stray capacitance and resistance values. In general, this value can affect the impedance of the system and can also affect the performance of the signal entering the signal conditioning circuit, and can also affect the measurement. For this reason, this paper will explain the effect of analog switches on signal measurements in a digital signal oscilloscope. The analog network switch will be converted into an equivalent circuit model and mathematical model [11], then simulated using Matlab or Python to determine how much stray impedance value can affect the measurement signal.

II. Network Switch Configuration

As explained earlier the network switch in this design is the main entrance of the signal from the BNC connector to the signal conditioning circuit. In general, the block diagram of the digital signal oscilloscope is described in Fig. 1 (bottom), which consists of several block diagrams such as a network switch, signal conditioning circuit, signal generator, clock source, 32-bit microcontroller, and tablet PC monitor. The designed oscilloscope uses 3 ports, 2 input signal ports and 1 output signal port as a signal generator. In general, digital oscilloscopes on the market have 2 to 4 input signal ports and one output signal port. A configuration switch is required to connect and disconnect signals from the BNC connector for processing in multiple modes.

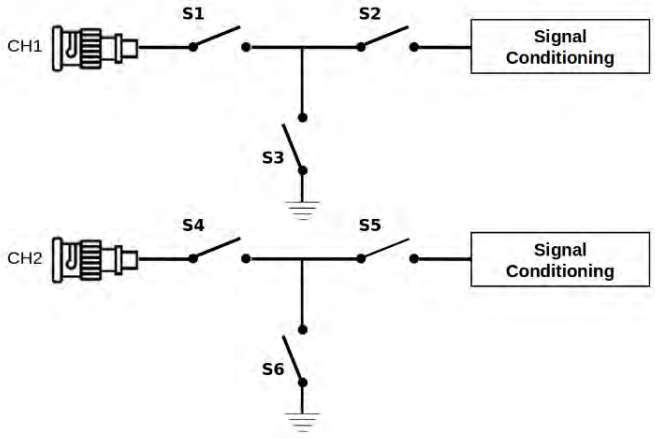

Fig. 2. Switch configuration on a digital signal oscilloscope

The switch configuration shown in Fig. 2 resembles the letter “T” hence it is called a T-switch, which can be configured in four modes namely on, off, ground, and floating. So far, we have designed network switches using Complementary Metal Oxide Semiconductor Integrated Circuit (CMOS IC) DG470 made by Vishay Siliconix. The chip is an SPDT (single pole dual tap) type, which has one common connection pin and two connection pins, namely NO (normally open) and NC (normally closed). The chip specifications are; supply voltage of 44 volts, analog signal range of ± 15 volts, low “on” resistance of 3.6 ohms, “off” capacitance of 85 pF, “on” capacitance of 125 pF, time on 200 ns, and time off 135 ns [12] as shown in Table I. These specifications will be used as a consideration in designing the network switch. Analysis of the switch equivalent circuit is very important, this analysis is intended to analyze and predict the impedance value of the switch, which impedance greatly affects the signal measurement results.

TABLE I
Parameter Analog Switch DG470

Cson	120 pF
Csoff	85 pF
Cg	37 pF
Rson	3.6 ohm

The T-switch configuration can be enabled into four modes namely: on mode, off mode, ground mode, and floating mode. In “on” mode, switches S1, S2, S4, and S5 are closed while

switches S3 and S6 are open, in this mode the signal from the BNC connector can be forwarded to the signal conditioning circuit. In "off" mode, switches S1, S2, S4, and S5 are open while switches S3, and S6 are closed, in this mode the input signal is not forwarded to the circuit of signal conditioning but will be connected to the ground. In ground mode, switches S2, S3, S5, and S6 are closed while switches S1 and S4 are open, in this mode the signal conditioning circuit will be connected to the ground. Usually, this mode is used to calibrate the tool so that the signal voltage goes to zero volts. While in floating mode, all switches S1, S2, S3, S4, S5, and S6 are open so that the signal conditioning circuit is not connected to the input signal or to ground however in a high impedance state.

III. Mathematical Model of Network Switch

Fig. 3 shows the equivalent circuit of the network switch for one channel. Each CMOS switch has an equivalent circuit with series capacitance (Cs), series resistance (Rs), and capacitance to ground (Cg) components. These components will change in value when the switch is "on" or "off" as shown in Table I, and will also change in value with the frequency used.

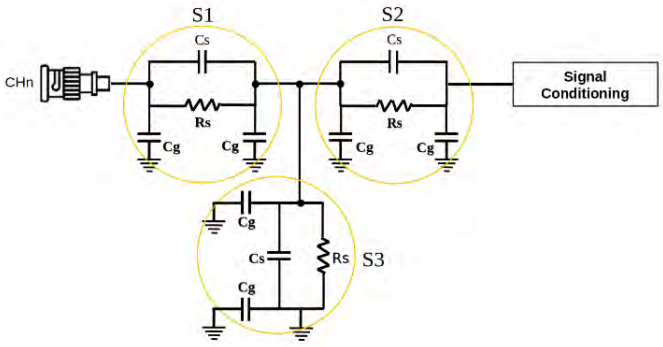

Fig. 3. Equivalent circuit of network switch on each channel

The next step is to analyze the switch when it is "on" and the switch when it is "off" as shown in Fig. 4. For switch "on", Fig. 4(a) shows the signal from the BNC connector connected to the signal conditioning circuit (S1 and S2 "on", S3 "off"). In this mode, the on-resistance on S1 and S2 is so small that it can forward the signal. While the off resistance on S3 will be very large so that only Coff is used, one terminal is also connected to the ground so that only one Cg is active. Therefore, the point between S1, S2 and, S3 will be connected in parallel with Cg and Csoff. The equivalent circuit is identical to a low-pass filter circuit, and if calculated, the maximum working frequency of 353 MHz will be obtained. Usually, signal measurements use frequencies between 1Hz - 10 MHz and are still within tolerance limits. Likewise for the OFF switch as shown in Fig. 4(b), with the same analysis for CS3 "on", the point between S1, S2, and S3 will be connected in parallel with Cg, Cson, and Rson. Meanwhile, S1 and S2 "off" have a very large off resistance so that only Csoff and Cg are retrieved.

The mathematical model when the switch is "on" is shown in Fig. 5 where Fig. 5(a) shows the model in the form of

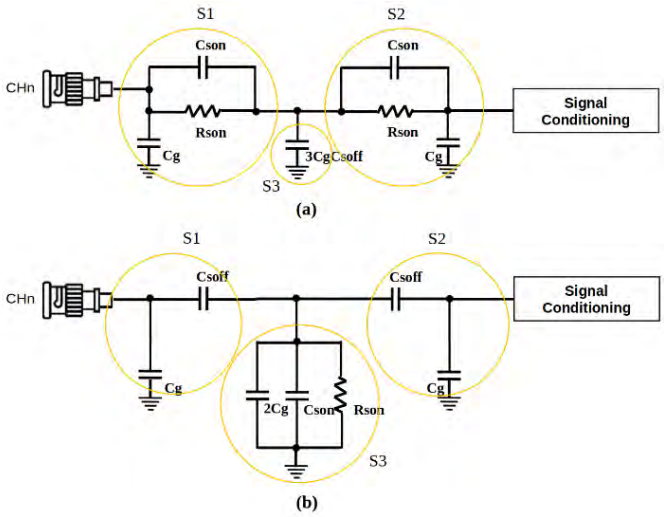

Fig. 4. Equivalent circuit for (a) switch "on" and (b) switch "off"

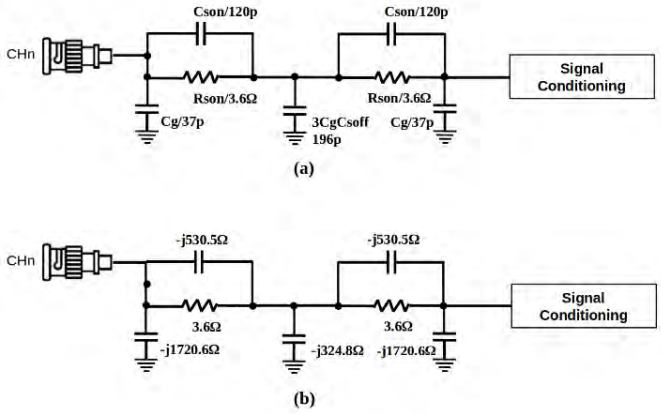

Fig. 5. Mathematical model for switch "on"; (a) in capacitance value; (b) in complex number value

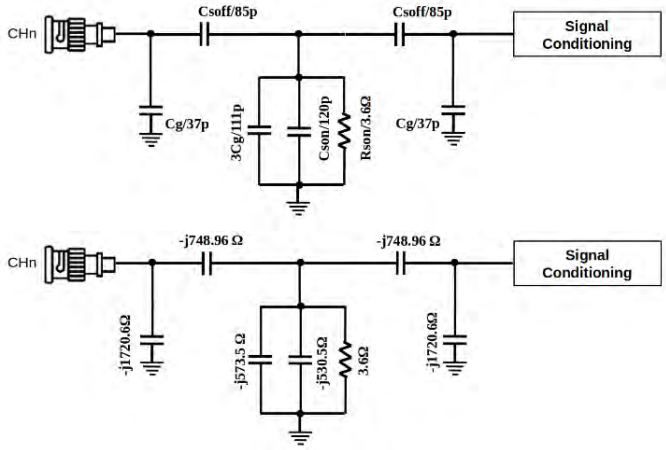

Fig. 6. Mathematical model for the "off" switch; (a) in capacitance values; (b) in complex number values

capacitance values, while Fig. 5(b) shows the model in the form of complex number values. Based on the datasheet in Table I, for S1 and S2 in the "on" position will be 120pF and 3.6 Ohm on resistance, while S3 in the "off" position is 196pF with infinite off resistance. The circuit approach is then made in the form of complex number equations. The same applies when the switch is in the "off" mode as shown in Fig. 6. The mathematical model of the switch in the "on" and "off" modes is shown in Table II.

TABLE II
MATHEMATICAL MODEL OF NETWORK SWITCH IN "ON" AND "OFF" MODE

Parameter	Switch "on"	Switch "off"
Z_R	3.6Ω	3.6Ω
Z_{CON}	$-j530.5\Omega$	$-j530.5\Omega$
$Z_{Cg} = Z_1 = Z_5$	$-j1720.6\Omega$	$-j1720.6\Omega$
$Z_2 = Z_4$	$3.599 - j0.024\Omega$	$-j748.96\Omega$
$Z_{CT} = Z_3$	$-j324.8\Omega$	$3.599 - j0.047\Omega$
Z_{tot}	$2.716 - j235.786\Omega$	$1.747 - j521.85\Omega$

IV. RESULT AND ANALYSIS

To make it easier to analyze the equivalent circuit of the network switch against the effect of measurement, the circuit is made in the form of an impedance circuit as shown in Fig. 7. The impedances in Z1 and Z5 refer to the capacitance Cg, while the impedances Z2 and Z4 are referring to switches S1 and S2, while the impedance Z3 is referring to switch S3. Then the impedance of each component can be calculated using the equations in the mathematical model as shown in Table II. Furthermore, by using Kirchoff's Law, the current equation in each loop can be found as follows:

TABLE III
THE CURRENT EQUATION FOR EACH LOOP

	$i = i_1 + i_2$
	$i_2 = i_3 + i_4$
Loop 1	$V_A = i_1 Z_1$
Loop 2	$V_A = i_2 Z_2 + i_3 Z_3$
Loop 3	$i_3 Z_3 = i_4 Z_4 + i_4 Z_5$

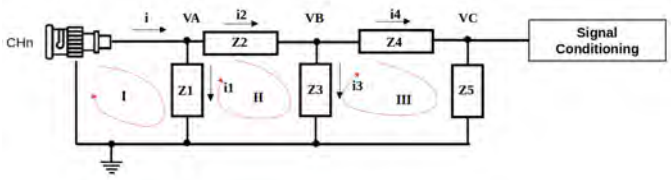

Fig. 7. Simplification of network switch circuit

We input the impedance value in the mathematical model in Table II into the current equation in Table III. The first thing to do is to find the current value of each branch as shown in Table IV. Then find the voltage value of each point as shown in Table V.

The current and voltage in the table above are in the form of complex numbers and can also be written in a polar form

TABLE IV
THE CURRENT ON EACH BRANCH FOR "ON" AND "OFF" SWITCHES

Current	Switch "on"	Switch "off"
i	$4.84 \times 10^{-4} + j0.042$ $0.042\angle 89.34°$	$10^{-4} + j0.0192$ $0.0192\angle 89.8°$
i_1	$j5.81 \times 10^{-3}$ $5.81 \times 10^{-3}\angle 90°$	$j5.81 \times 10^{-3}$ $5.81 \times 10^{-3}\angle 90°$
i_2	$4.84 \times 10^{-4} + j0.036$ $0.036\angle 89.23°$	$10^{-4} + j0.0134$ $0.0134\angle 89.72°$
i_3	$4 \times 10^{-4} + j0.03$ $0.0312\angle 89.26°$	$10^{-4} + j0.0134$ $0.0134\angle 89.64°$
i_4	$8.7 \times 10^{-5} + j0.0058$ $0.0058\angle 89.14°$	-1.95×10^{-5} $+j3.76 \times 10^{-7}$ $1.95 \times 10^{-5}\angle 178.89°$

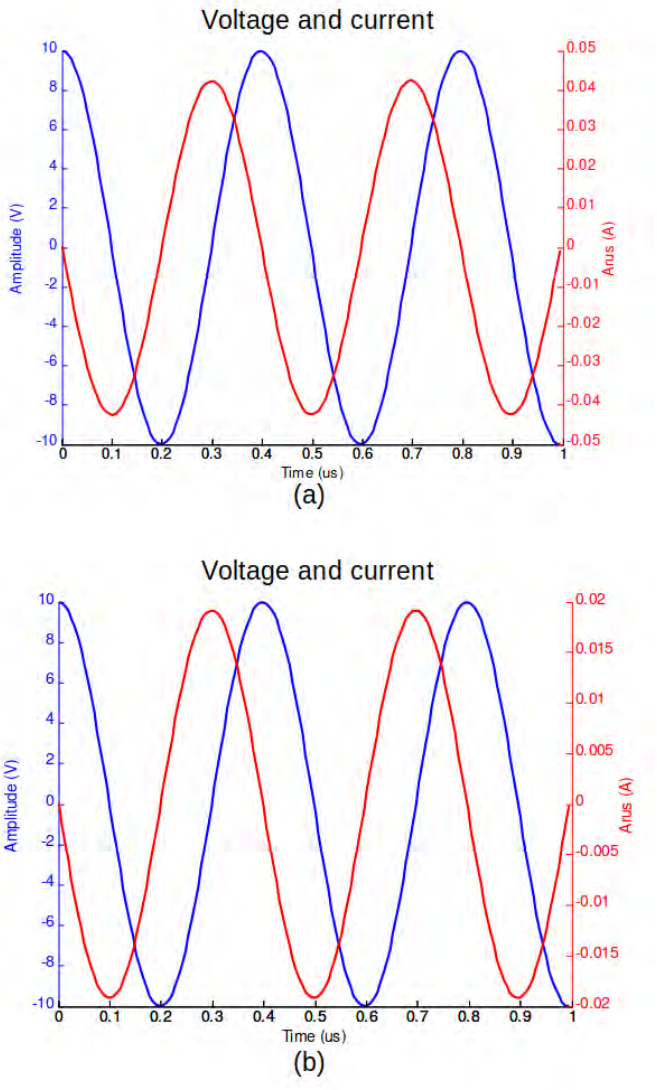

Fig. 8. Voltage and current at position VB; (a) Switch "on"; (b) Switch "off"

TABLE V
THE VOLTAGE ON EACH BRANCH FOR "ON" AND "OFF" SWITCHES

Voltage	Switch "on"	Switch "off"
V_A	$10\,\mathrm{V}$	$10\,\mathrm{V}$
V_B	$10.07\angle -0.74^\circ$ $10.07\cos(\omega t - 0.74^\circ)$	$0.048\angle 88.89^\circ$ $0.048\cos(\omega t + 88.89^\circ)$
V_C	$9.98\angle -0.86^\circ$ $9.98\cos(\omega t - 0.86^\circ)$	$0.0335\angle 88.89^\circ$ $0.0335\cos(\omega t + 88.89^\circ)$

containing certain angles. Based on these values, it is then simulated using Matlab to produce a sine waveform. The voltage in "VA" input is given a sine voltage with a value of 10Vpp so that using Kirchoff's law will get the voltage and current values for each point. This paper only shows the waveform voltage at point "VB" as shown in Fig. 8.

The signal in Fig. 8 is a simulated signal using Matlab that displays the voltage and current waves at point VB. Fig. 8(a) is a sine signal on the "on" mode switch which produces a maximum current of 0.04A. Fig. 8(b) is a sine signal on switch mode "off" which produces a current of 0.015A. By looking at the graph in Fig. 8, it can be concluded that when the switch is off there is still current flowing into the signal conditioning circuit, which can result in attenuation of the measurement signal. Analyzing the equivalent circuit of the switch is crucial, as this analysis helps in evaluating and predicting the switch's impedance, which significantly impacts the accuracy of signal measurement results.

V. CONCLUSION

By analyzing the equivalent circuit of the network switch in the "on" and "off" positions, the approximate value of the impedance and stray capacitance in the circuit can be determined. At certain frequencies, current can flow into the system even though the switch is in the "off" state. This current can cause attenuation in the signal measurement, and decrease the signal-to-noise ratio.

REFERENCES

[1] J. Czech, *Oscilloscope Measuring Technique: Principles and Applications of Modern Cathode Ray Oscilloscopes*. Springer, 2013.

[2] K. Johnson and D. Maliniak, "Oscilloscope probes for power electronics: Be sure to choose the right probe for accurate measurements," *IEEE Power Electronics Magazine*, vol. 5, no. 1, pp. 37–44, 2018.

[3] W. Jiang and F. Yuan, "Design of oscilloscope based on virtual instrument technique," in *2009 2nd International Conference on Power Electronics and Intelligent Transportation System (PEITS)*, IEEE, 2009, pp. 284–287.

[4] W. Huang *et al.*, "Design of portable high-speed oscilloscope analyzer for multifunctional integrated signal testing," *Measurement*, vol. 209, p. 112490, 2023.

[5] L. Xiaoling and Y. Xing, "Study on enhancing features of digital oscilloscope to measure the period of weak FM signal," in *2009 International Conference on Environmental Science and Information Application Technology*, IEEE, 2009, pp. 15–18.

[6] S. K. Pal, A. Kumar, and K. Kumawat, "Design and VLSI implementation of a digital oscilloscope," in *2012 Fourth International Conference on Computational Intelligence and Communication Networks*, IEEE, 2012, pp. 473–476.

[7] L. A. Buscaglia, J. P. Carmo, and O. N. Oliveira, "Simple-Z: a low-cost portable impedance analyzer," *IEEE Sens J*, 2023.

[8] D. F. Williams, J. C. M. Wang, and U. Arz, "An optimal vector-network-analyzer calibration algorithm," *IEEE Trans Microw Theory Tech*, vol. 51, no. 12, pp. 2391–2401, 2003.

[9] D. Sudiana, A. S. Tamsir, I. Muttakin, W. Widada, and W. P. Taruno, "Switch configuration effect on stray capacitance in electrical capacitance volume tomography hardware," *TELKOMNIKA (Telecommunication Computing Electronics and Control)*, vol. 14, no. 2, pp. 456–463, 2016.

[10] A. Yusuf, W. Widada and W. P. Taruno, "Determine of the Time Constant of Capacitance Applied to Electrical Capacitance Tomography," in *2022 International Conference on Informatics Electrical and Electronics (ICIEE)*, IEEE, 2022, pp. 1–6.

[11] D. Laschov and M. Margaliot, "Mathematical modeling of the lambda switch: A fuzzy logic approach," *J Theor Biol*, vol. 260, no. 4, pp. 475–489, 2009.

[12] A. Yusuf, I. Muttakin, A. Rudin, W. Widada, and W. P. Taruno, "Single signal conditioning multi electrode for ECVT data acquisition system," in *TENCON 2014-2014 IEEE Region 10 Conference*, IEEE, 2014, pp. 1–6.

Thrust Force Analysis and Simulation of Duct Wind Turbine Blade

Munnik Haryanti
Department of Electrical Engineering
Universitas Indonesia
Depok, Indonesia
munnik.haryanti21@ui.ac.id

Feri Yusivar
Department of Electrical Engineering
Universitas Indonesia
Depok, Indonesia
yusivar@ui.ac.id

Abdul Halim
Department of Electrical Engineering
Universitas Indonesia
Depok, Indonesia
a.halimr@ui.ac.id

***Abstract*—The venturi duct on a duct wind turbine is the fastest-flowing duct and has the highest thrust force of all ducts. As the wind passes through the turbine rotor, it moves the rotor blades, generating a thrust force that is transmitted to the structure of the turbine. The thrust force generated can affect the overall performance of the wind turbine including affecting the structural stability and efficiency of energy conversion from wind to electricity. This paper will discuss the influence of thrust force on the design of duct wind turbines. Based on the simulation results, the wind flow velocity at the inlet and collector section increases to about 4m/s and will increase sharply at the venturi duct to 9m/s. The thrust-force generated by the venturi duct is the largest among the other ducts which based on the simulation obtained about 1.5N and is still within the limits of the structure used.**

***Index Terms*—Thrust Force, Duct Wind Turbine, Blade, Ansys Fluent**

I. Introduction

A Ducted Wind Turbine is a type of wind turbine equipped with a duct that surrounds the turbine rotor [1], [2]. This duct is designed to direct and accelerate the airflow entering the rotor, to increase the efficiency of the turbine in generating electrical energy. The duct surrounding the rotor serves to collect and accelerate the airflow before it reaches the rotor blades. By accelerating the airflow, these ducts increase the relative wind speed hitting the blades, which in turn increases the power generated. Ducted wind turbines are designed to increase efficiency compared to conventional wind turbines (without ducts) [3], [4]. This efficiency can increase because the ducts help concentrate the airflow, allowing more kinetic energy to be extracted by the rotor.

Ducts can also help reduce the turbulence of the wind entering the rotor, which can result in more stable operation and reduced wear and tear on mechanical components. Ducted wind turbines tend to be more compact than conventional wind turbines, which makes them suitable for use in urban environments or places with limited space. However, due to their more complex design, they can be more expensive to manufacture and operate. Ducted wind turbines are often used in specialized applications where high efficiency or customization to specific environmental conditions is essential, such as in regions with low wind speeds or near tall buildings in cities [5], [6].

979-8-3315-1921-6/24/$31.00 ©2024 IEEE

Air flowing through the venturi duct will generate a thrust force, which is the force applied by the airflow to the turbine rotor and duct as the air moves through it [7]. As the wind passes through the turbine rotor, it moves the rotor blades, generating a thrust force that is passed on to the turbine structure. In ducted wind turbines, the ducts are designed to increase the velocity of the airflow passing through the rotor, thereby increasing the efficiency of the turbine. However, the duct also affects the thrust force distribution, as it directs and accelerates the airflow. This thrust force must be accounted for in the structural design of the wind turbine. Too much thrust force can cause excessive stress on the turbine, which can affect its stability and safety. The resulting thrust force can affect the overall performance of the wind turbine. Proper design of the rotor and duct is essential to optimize the thrust force to produce maximum energy with minimal mechanical losses. Hence thrust force is one of the important aspects in the design and operation of wind turbines, especially in ducted turbines, as it affects the structural stability and efficiency of energy conversion from wind to electricity.

For this reason, this paper will explain, analyze, and simulate the effect of thrust force on wind turbine duct design. Design and simulation using Ansys Fluent, then from the simulation results will be obtained the thrust force value at each point in the venturi duct. This thrust force will be used as a reference in designing the structure of the duct wind turbine and in reference design of the blade on the rotor.

II. Duct Wind Turbine

The duct wind turbine is divided into three main parts: the converging section, the venturi channel (throat), and the diverging section. The converging section is a curved entrance for liquid or air. Due to the shape is curved, the air flow starts to converge. According to the continuity equation, if the cross-sectional area decreases, the velocity of the liquid increases. According to Bernoulli's equation, if the velocity increases, the pressure must decrease. Then the second section is the venturi channel section (throat), where this section has a smaller shape than the inlet and outlet. The air flow enters the constant diameter section. Since the diameter is constant, the velocity and pressure in this channel do not change. Therefore, this is the right place to put the rotor. Then the third section

is the diverging section, which serves to recover the pressure at the flow rate. The angle of the diverging section is shorter than the converging section, making the length of the diverging section relatively longer than the converging section. This is done to reduce turbulence at the end of the channel.

Description of Fig. 2 as follows:
a1 = cross-sectional area of the inlet pipe
d1 = inlet pipe diameter
v1 = velocity at the inlet
p1 = pressure at the inlet pipe
a2 = cross-sectional area of the throat
d2 = throat diameter
v2 = velocity in the throat
p2 = pressure at the throat

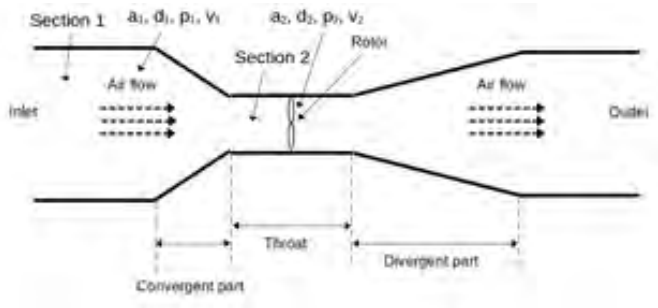

Fig. 1. Duct wind turbine block diagram.

The equation to calculate the airflow velocity in the venturi duct is using Bernoulli's Law, where the velocity increases as the pressure decreases [8], [9]. The Bernoulli equation used in sections (1) and (2) is as follows:

$$P_1 + \frac{1}{2}\rho v_1^2 + \rho g h_1 = P_2 + \frac{1}{2}\rho v_2^2 + \rho g h_2 \tag{1}$$

where ρ is the density of the liquid/air in the tube (kg/m³), g is the acceleration due to gravity (m/s²), h_1 (m) is the height of the tube at the inlet, and h_2 (m) is the height of the tube at the throat. Since the geometry of the tube is horizontal, the tube heights at the inlet and throat are the same ($h_1 = h_2$), so the equation simplifies to:

$$P_1 + \frac{1}{2}\rho v_1^2 = P_2 + \frac{1}{2}\rho v_2^2 \tag{2}$$

According to Bernoulli's equation, if the velocity increases, the pressure must decrease. The mass of air flowing at speed v (m/s) through a cross-section with area A (m^2) is expressed by the air mass flow rate $\dot{m}$ (m dot) with the following equation:

$$\dot{m} = \rho A v \tag{3}$$

m dot is the mass of air/liquid in a tube with a given cross-sectional area (kg). In the venturi effect, the air mass and density at the inlet and venturi channels are the same so the equation can be simplified which is referred to as the continuity equation. Based on the continuity equation, if the cross-sectional area decreases, the velocity of the liquid increases.

$$A_1 v_1 = A_2 v_2 \tag{4}$$

Kinetic energy or energy of motion is the energy present in an object due to its movement. The kinetic energy of an object is defined as the effort required to move an object of a certain mass from rest to a certain speed. The kinetic energy of an object is equal to the sum of the effort required to express its velocity and rotation, starting from rest. The kinetic energy in the venturi effect shown can be expressed by the following equation:

$$E_k = \frac{1}{2}\rho A v^3 \tag{5}$$

Where ρ is the density of the liquid/air in the tube (kg/s), A is the cross-sectional area (m), and v is the air/liquid flow velocity (m/s). Thus, using this method, the wind speed can be increased by 2-5x, and the turbine output power can be increased by 5-6x [1] - [3].

III. Simulation Trust Force Using Ansys Fluent

The wind turbine duct design is L-shaped with the vertical section consisting of the inlet/input duct and collecting duct, while the horizontal section consists of the directional duct, venturi duct, and exhaust duct as shown in 2. The design is made in three-dimensional form with a diameter of 24 cm, a total vertical length of about 100 cm, and a horizontal length of about 100 cm. The venturi channel diameter was made one-third of the tube diameter to produce optimum flow velocity as analyzed in the previous chapter [10]. To simulate the thrust

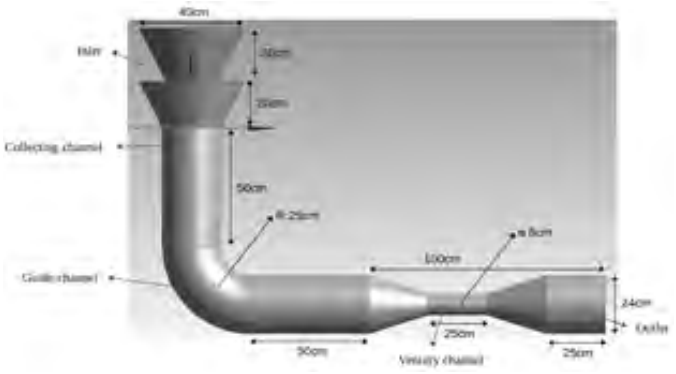

Fig. 2. Geometry of wind turbine duct in 3D.

force, a blade is placed in the venturi channel as shown in 3. This simulation uses Ansys Fluent 2023R3 software. The method used is to flow air from the inlet channel at a speed of 3m/s, then observe changes in velocity and pressure at each channel in the wind turbine duct. The velocity and pressure flowing inside the wind turbine duct will generate thrust force, where the highest thrust force is inside the venturi duct.

IV. Result and Analysis

The wind turbine duct design was simulated using a wind tunnel measuring 70x70x70 cm as shown in 4. Wind tunnel simulation is used to simulate the wind flow through the wind turbine duct. From the shape of the wind flow, it can be known and calculated the wind speed passing through the venturi channel can also be known as the pressure and turbulence that may occur around the turbine duct area. Air enters through the wind tunnel inlet channel on the left side and will flow to the right then hit the wind turbine duct and then be discharged to the outlet. The air velocity setting on the inlet channel is 3 m/s. Table 1 below shows the information system used in the venturi tube simulation. Ansys application used is Fluent type with three-dimensional geometry settings (3d) double precision, CPU used Intel core i5-2500 MHz with Windows operating system. The material properties of this simulation can be seen in Table 2 where the flow material used is air and a tube body is aluminum.

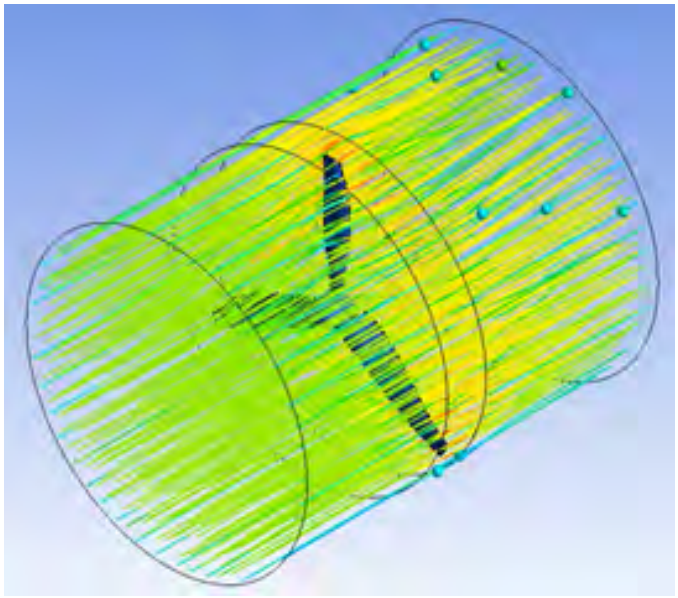

Fig. 3. Blade placement on the venturi channel.

TABLE I
System Information

Parameter	Details
Application	Fluent
Settings	3D, double precision, pressure-based, laminar
Version	22.2.0-10212
Source Revision	61a5bc1c97
CPU	Intel(R) Core (TM) i5-2500
OS	Windows

The speed simulation of the wind turbine duct is shown in 5 the wind flow speed in the wind tunnel is 3m/s. Based on the figure, can be seen that wind flow enters through the inlet channel then flows through the collecting and directing channels, then enters the venturi channel and exits through the outlet channel to be discharged. According to the figure can be

TABLE II
Material Properties

Udara	
Density	2719 kg/m^3
Cp (Specific Heat)	1006.43 J/(kg K)
Thermal Conductivity	0.0242 W/ (m K)
Viscosity	1.7894e-05 kg/ (ms)
Molecular Weight	28.966 kg/kmol
Alumunium	
Density	2719 kg/m^3
Cp (Specific Heat)	871 J/(kg K)
Thermal Conductivity	202.4 W/(m K)

seen that wind flow speed at the inlet and collector increases to about 4m/s and will increase sharply in the venturi channel up to 9m/s which is marked in red.

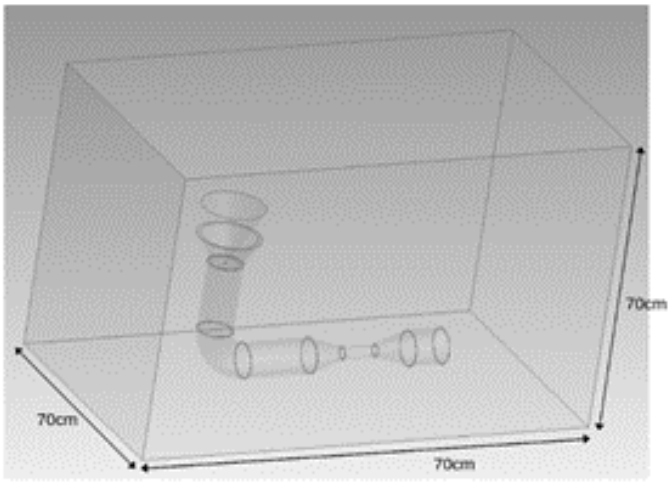

Fig. 4. Geometry of the duct wind turbine inside the wind tunnel.

Fig. 5. Velocity magnitude in ventury duct.

Then to simulate the airflow and thrust force conditions in the venturi channel, a blade with a total of three blades is placed as shown in 6. In 6, only the venturi channel section is shown where the airflow velocity is set at 3m/s. This is just to test how the airflow and thrust-force conditions in the

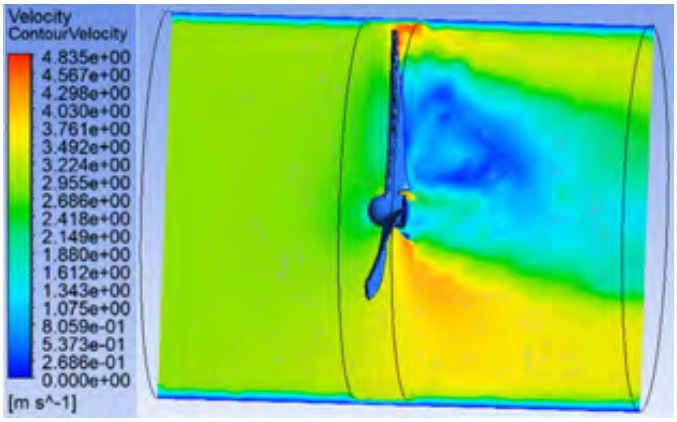

Fig. 6. Simulation results of the velocity contour inside the venturi using a blade.

duct. Based on the figure, it can be noted that the airflow and pressure will change when passing through a blade. The green color on the left side of the blade is faster while the blue color on the right side of the blade is lower, so with this difference in speed and pressure, a thrust force will be generated on this channel.

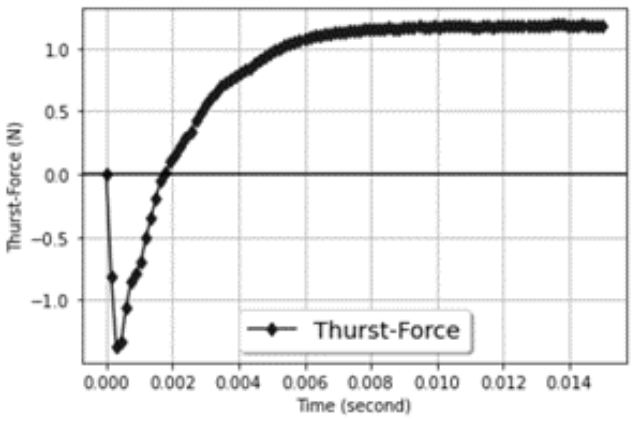

Fig. 7. Thrust force in venturi duct.

The thrust force generated by the venturi channel is the largest among the other channels because it has the highest wind speed. The thrust force generated from this simulation is about 1.5N as shown in 7, where this is the thrust force graph at the start of wind flow t=0 to t=0.015 seconds. When the wind starts to move (t=0) there is no thrust force on the channel which is characterized by a graph value of 0 to minus, then after a few milliseconds, the thrust force starts to appear which is characterized by an increase in the number on the graph. This thrust force is relatively small because the simulated dimensional structure is also small, only 8 cm in diameter. Thrust force is very important to accounted for in the design of the wind turbine duct structure.

V. Conclusion

The wind turbine duct has an L-shaped design, with the vertical section containing the inlet and collecting ducts, and the horizontal section comprising the directional, venturi, and exhaust ducts. The three-dimensional model has a diameter of 24 cm, with both vertical and horizontal sections measuring approximately 100 cm in length. A wind turbine duct has been designed and simulated to determine the thrust force strength of the venturi duct. The design of the wind turbine duct structure for simulation is small, only a few cm due to the license limitations of Ansys Fluent. The results of the simulation show that the thrust-force value is still within the tolerance limit of the structure used. Simulation results show that wind velocity rises from 4 m/s at the inlet to 9 m/s in the venturi duct, where the thrust force reaches approximately 1.5 N, remaining within structural limits. This research is the initial stage and will be further developed regarding the design analysis of the inlet, outlet, angle changes in the venturi tube, and will also make an initial prototype to determine the actual thrust strength.

References

[1] D. Allaei and Y. Andreopoulos, “INVELOX: Description of a new concept in wind power and its performance evaluation,” Energy, vol. 69, pp. 336–344, 2014.
[2] T. R. Reddy, C. I. Priyadarsini, and M. Krishna, “Guide vane height effect on performance of sheer wind turbine,” Journal of Xi’an University of Architecture & Technology, pp. 482–489, 2021.
[3] T. A. Khamlaj and M. P. Rumpfkeil, “Analysis and optimization of ducted wind turbines,” Energy, vol. 162, pp. 1234–1252, 2018.
[4] M. Li, A. Bussonnière, M. Bronson, Z. Xu, and Q. Liu, “Study of Venturi tube geometry on the hydrodynamic cavitation for the generation of microbubbles,” Miner Eng, vol. 132, pp. 268–274, 2019.
[5] N. Goudarzi, W. D. Zhu, and H. Bahari, “Wind energy conversion: the potential of a novel ducted turbine for residential and commercial applications,” in ASME international mechanical engineering congress and exposition, American Society of Mechanical Engineers, 2013, p. V04BT04A042.
[6] M. Rivarolo, A. Freda, and A. Traverso, “Test campaign and application of a small-scale ducted wind turbine with analysis of yaw angle influence,” Appl Energy, vol. 279, p. 115850, 2020.
[7] R. Bontempo and M. Manna, “Effects of the duct thrust on the performance of ducted wind turbines,” Energy, vol. 99, pp. 274–287, 2016.
[8] E. R. Marciotto, “Classic Bernoulli’s principle derivation and its working hypotheses,” Phys Educ, vol. 51, no. 4, p. 045005, 2016.
[9] B. E. Faulkner and F. M. Ytreberg, “Understanding Bernoulli’s principle through simulations,” Am J Phys, vol. 79, no. 2, pp. 214–216, 2011.
[10] M. Haryanti and F. Yusivar, “Simulation and Analysis of Venturi Tubes for Use in Duct Wind Turbine Power Plants,” in 2023 3rd International Conference on Electronic and Electrical Engineering and Intelligent System (ICE3IS), IEEE, 2023, pp. 282–287.

Utilization of River Flow as A Portable Microhydro Power Plant Using Open Flume Propeller Turbine

Ibrahim Nawawi
Electrical Engineering
Universitas Tidar
Magelang, Indonesia
ibrahim_nw@untidar.ac.id

Andriyatna Agung Kurniawan
Electrical Engineering
Universitas Tidar
Magelang, Indonesia
andriyatna@untidar.ac.id

Bagus Fatkhurrozi
Electrical Engineering
Universitas Tidar
Magelang, Indonesia
bagusf@untidar.ac.id

Rheza Ari Wibowo
Electrical Engineering
Universitas Tidar
Magelang, Indonesia
rhezaari@untidar.ac.id

Denny Haryanto Sinaga
Electrical Engineering
Universitas Negeri Medan
Medan, Indonesia
denny.sinaga@unimed.ac.id

***Abstract*—Utilization of river flow or water flow as a Portable Micro Hydro Power Plant with a weight that can be lifted by one person will make it easier to get electricity in remote areas where electricity is not yet available. This research is the second year of research that utilizes the results of the first year of research which produces data for calculating water discharge, water fall height and water discharge. However, due to the Covid-19 pandemic, the location chosen for this research is the Prego River with the following data: river flow velocity 1.11 m/s, river cross-sectional area 0.84 m2, water discharge value of 0.939 m3/s, the height of the waterfall is 0.5 m – 1 m. The purpose of this research is to plan and determine an open flume propeller turbine, choose the right generator so that it can generate an alternating voltage of 220 volts with a minimum power of 100 watts and construct turbines and generators with an overall weight of 15 kg. The method used in this research is the experimental method. This experimental method includes identification of requirements, design, manufacture, and testing. The results obtained from this study are Portable Micro Hydro Power Plant can produce a voltage of 15.6 VAC – 224 VAC at 154 rpm – 1.502 rpm, the power generated reaches 350 watts and the overall weight of the turbine and generator construction is 15.5 kg.**

***Index Terms*—generator, turbine, propeller, open flume.**

I. Introduction

Water resources are resources in the form of water that are useful for the survival of living things on earth. One of the uses of water for humans includes use in agriculture, home industry, recreation and environmental activities. Humans need water not only for daily activities. , but the use of water that requires water all the time, one of which is hydroelectric power plants or micro hydro power plants.

One of the biggest potential sources of new and renewable energy in Indonesia is water. The potential energy that can be produced by hydroelectric power plants reaches 65,764 MW, while only 17.4% can be utilized . The biggest obstacle to NRE is the very high investment cost, poorly trained human resources, system lengthy regulations and also inaccessible locations. One effort that can be made to utilize the existing energy potential at a low cost is the use of portable power plants [2].

979-8-3315-1921-6/24/$31.00 ©2024 IEEE

Research on the manufacture of portable hydroelectric power plants using a spiral shape turbine type [3]. This study resulted in the value of product efficiency reaching 90%.

In 2017 Indonesia was ranked as the fifth country with the highest level of electricity consumption in ASEAN, which is around 880 kWh per capita, even though the government is targeting that by 2025 Indonesia's electricity consumption level will reach 1,500 kWh per capita [4].

Judging from the type of power plant used, about 87% is dominated by the use of fossil fuels, namely coal and oil which will actually run out in the next few years [1]. Meanwhile, new and renewable energy (EBT) cannot be utilized optimally [5].

A portable power plant as an equipment used to generate electrical energy by connecting an electric generator with propulsion and then the equipment is packaged simply [6].

Several problems indicate that the current portable hydroelectric power plant cannot be used effectively and efficiently and endangers its users [7].

Research on hydroelectric power plants by utilizing slow water currents. This research focuses on the development of the turbine type used, the generator type, and the development cost. A portable hydroelectric power plant using a cross-flow water turbine. The results of this study found that the product they developed had an efficiency value of up to 70% [8].

A pico-hydro power plant using an open flume propeller turbine is a generator that utilizes a low-headed river flow as its driving force. Piko hydro using an open flume propeller turbine

does not require stock pipes and construction of a power house. The open flume propeller turbine is a reaction turbine that operates at a low head of less than 6 meters. The open flume propeller turbine has a simple construction and a relatively low price.

Paying attention to the research data in the first year, especially the Prego river, namely the flow velocity of 1.118 m/s, the results of the calculation of the water discharge 0.939 m3/s, the water fall height is very low, namely 0.5-1 m, the type of turbine that is suitable for the data on the progo river is a propeller turbine. With this data, researchers will implement it in the form of hardware, namely the design of a portable PLTMH that is lightweight and can be moved or carried by one person. The turbine used is an open flume propeller turbine and the generator used is a 220 VAC generator. This research was carried out in 5 (five) stages of activity, namely (1) inventory of needs, (2) calculation and design, (3) manufacture, (4) testing and (5) analysis of test results. The result that is expected to be achieved from this research is a portable PLTMH prototype that can produce 100 watts of power with an overall weight of less than 15 kg.

II. Literature Review

Research on the manufacture of a portable power plant using experiments on polymer electrolytemembrane fuel cell (PEMFC) [9]. in the experiment, the PEMFC reaction was able to produce energy of 0.9 V at a temperature of 65º C. The best performance obtained from this experiment was a power of 647 W at a temperature of 65º C and in 50 A.

A portable hydroelectric power plant using a cross-flow water turbine (CFWT) which was applied to a micro hydro power plant (PLTMH) [8]. From this study it was concluded that there are eight advantages of using CFWT, namely no current is needed to start the CFWT performance, this type of turbine is also able to work efficiently in the long term, no water evaporation process, optimizes the performance of turbine parts, does not require routine maintenance, simple design, this type of turbine is able to remove waste carried by water currents, and the last is that it can be used in small water currents.

A study was also conducted by Aprillianto et al (2013) using a hydro coil type turbine. From the experimental results, it is found that the rotation speed of this turbine reaches 965 rpm if there is no load while the rotation speed is constant at 500 rpm if a load is given. From the experiment, it is also known that the product developed has an efficiency level of up to 92.93%.

A micro hydro power plant (PLTMH) [10]. From this study, it was found that the product made was able to be used to supply electricity to the nearest village and for street lighting with an output power of 0.2 kW.

A portable hydroelectric power plant by utilizing weak water current energy. The results of this study indicate that there are several alternative options for turbines, and generators that can be chosen to assemble a portable hydroelectric power plant. This research also considers the cost aspect of product manufacturing.

A portable power plant by utilizing the chemical reaction of a micro directethanol fuel cell (Micro-DEFC) [11]. The results of this study found that the reaction was able to produce electrical energy of 0.9 mV.

III. Research Methods

Research sites or locations have experienced a reduction, not all research locations in the first year can be continued for testing turbines and generators as MHP this happens due to the Covid-19 Pandemic conditions starting April - September which have not been completed. The place or location chosen for research in this second year is the Progo river which is in the Magelang Regency area. Meanwhile, the data processing of the measurement results is carried out in the Electronics laboratory, Department of Electrical Engineering, Faculty of Engineering, Tidar University.

The Progo River has a watershed area of 2380 km2 with a river length of 140 km. The Progo River passes from the part of Central Java that disgorges on Mount Sindoro and passes through the Provinces of Central Java and the Special Region of Yogyakarta. Apart from the main upstream source of the Progo River, namely Mount Sindoro, it also comes from Mount Merapi, Mount Menoreh, Mount Merbabu and Mount Sumbing. 75% of the Progo watershed is in the Special Region of Yogyakarta Province. This research was conducted in Sidorejo village, Bandongan sub-district, Magelang regency

This research was carried out in stages, the stages carried out can be seen in Figure 1.

The turbine design on the PLTMH prototype functions to convert water into kinetic energy, where the turbine is made of iron. To design this turbine, the first step to analyze is turbine planning, In planning the turbine must pay attention to the water discharge $Q = V \cdot A$, where Q (m^3/s), V = velocity of water flow (m/s), A = cross-sectional area of the pipe (m^2). Turbine power output $P = \rho \cdot g \cdot Q \cdot h \cdot \eta_t$; Where P = turbine power (HP); density of water (kg/m^3); g = gravity (m/s^2); h = height of the falling water in meters (m); Q water discharge (m^3/s); and η_t = Efficiency of water turbine (84%- 94%).

Turbine specific speed:

$$n_s = n\frac{\sqrt{P}}{H_e^{\frac{5}{4}}} \tag{1}$$

with ns=specific speed(rpm); n= runner rotational speed (rpm); P = turbine power (HP); He=Effective water fall height (m).

Calculating the diameter of the Travel Blade (D):

$$D = \sqrt{\frac{4Q}{\pi C_x \left[1 - \left(\frac{d_h}{D}\right)^2\right]}} \tag{2}$$

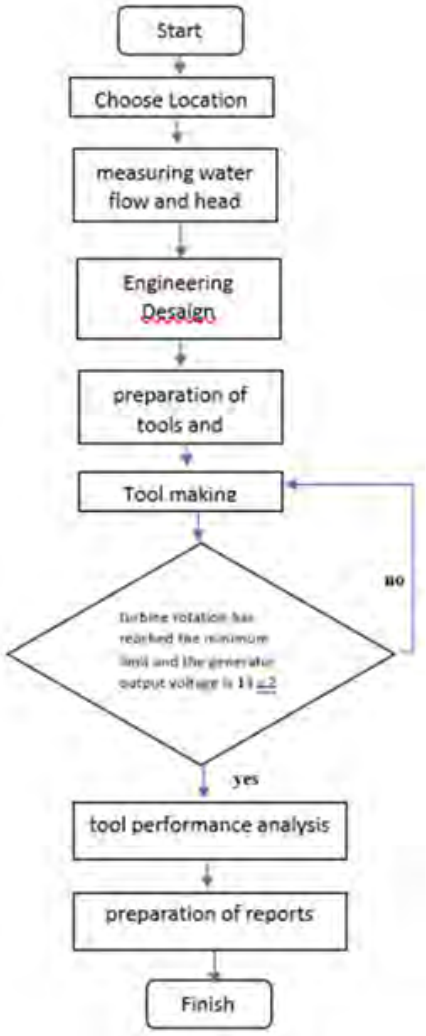

Fig. 1. Research Flowchart..

Calculating the Distance Between the blades:

$$S_i = \frac{\pi D \left(\frac{d_h}{D}\right)}{Z} \tag{3}$$

and calculate the Steering Blades:

$$Z = -\frac{1}{4}\sqrt{D} + 4 \tag{4}$$

Equipment and Measuring Tools used One unit of Turbine Propeller complete with generator, analog and digital multimeter, digital tachometer, 100 watt lamp, 350 watt electric iron, electric drill.

IV. Result and Discussion

The water discharge Q obtained is 0.93 m^3/s, with a turbine power output of 5.22 HP. The turbine specific speed is $n_s = 8.151\,\mathrm{rpm}$. The diameter of the blade is 5 cm, and the distance between the blades is 2.5 cm. The number of guide vanes 9.

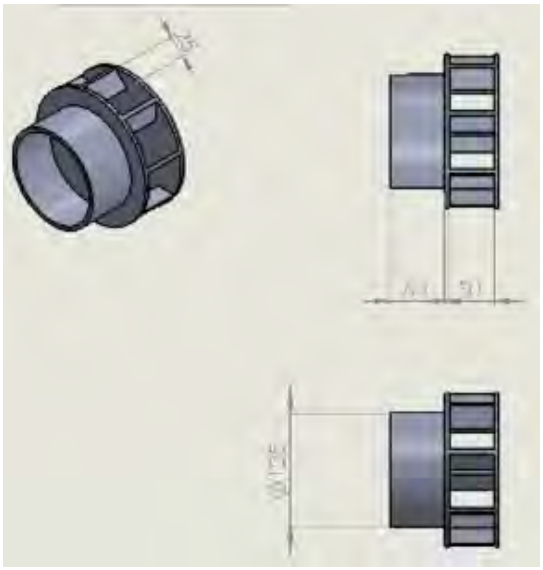

Fig. 2. Steering Blade

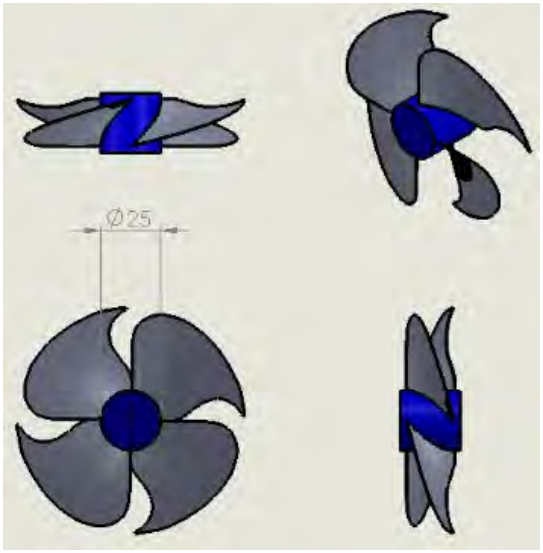

Fig. 3. Turbine vane.

Measurement of turbine speed and voltage generated by the generator includes 3 conditions, namely:

1. Measurement of turbine speed and generator voltage at no-load conditions;
2. Measurement of turbine speed and generator voltage with a load condition of incandescent lamps with a power of 100 watts;

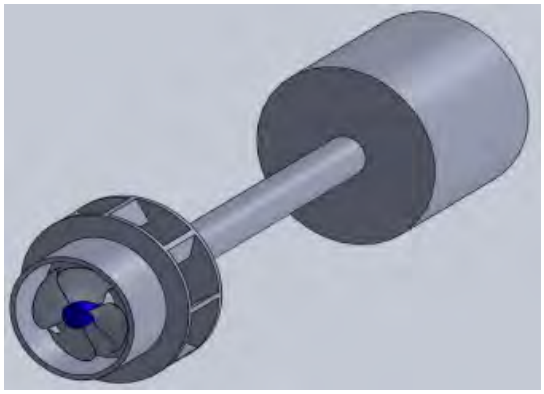

Fig. 4. Turbine and generator house

3. Measurement of turbine speed and generator voltage with a load condition of an electric iron with a power of 350 watts. The graph of the measurement results is shown in Figure 5, Figure 6, Figure 7, and Figure 8.

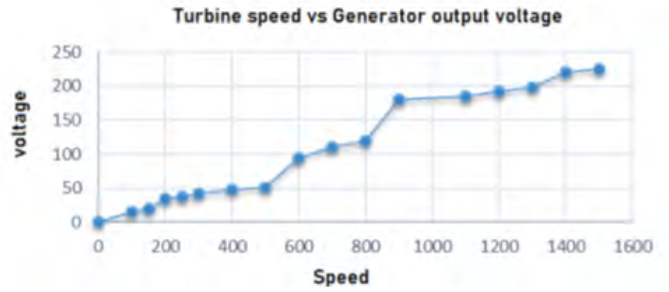

Fig. 5. Turbin speed vs Generator Output Voltage

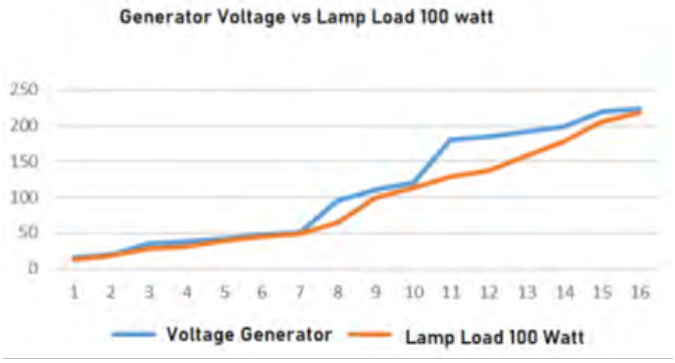

Fig. 6. Turbin speed vs Generator Output Voltage

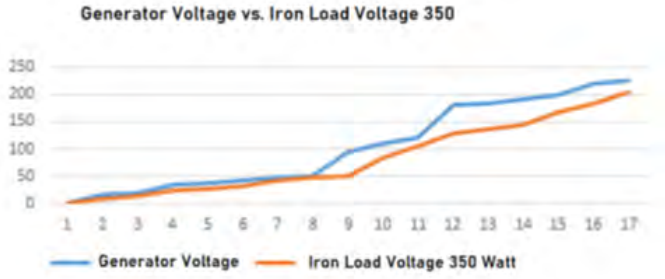

Fig. 7. Turbin speed vs Generator Output Voltage

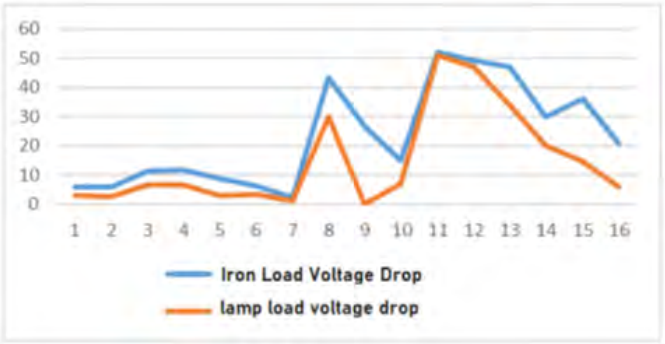

Fig. 8. Turbin speed vs Generator Output Voltage

V. Conclusion

The results of river flow measurements and water discharge calculations in the Progo rivers in the context of utilizing river flows as Portable Micro Hydro Power Plants, it can be concluded that the measurement of the Progo river flow velocity is 1.12 m/s; The measurement of the cross-sectional area of the Progo river is 0.84 m2; The calculation of the water discharge of the Progo river is 0.93 m3/s; The result of calculating turbine power (Pt) is 5.22 HP; The generator output voltage of 224 VAC is obtained at 1500 rpm; The average voltage drop with a 100 watt incandescent lamp is 14.8 VAC; The average voltage drop with a 350 watt electric iron load is 14.8 VAC; The overall weight of the open flume turbine and generator is 15.50 kg.

Acknowledgment

I would like to express my sincere gratitude to all those who have contributed to the successful completion of this research article.

First and foremost, I would like to thank my dean faculty, Gito Sugianto, for their invaluable guidance, support, and expertise throughout the course of this project. Their constructive feedback and encouragement have been crucial to the development of this work.

REFERENCES

[1] BPPT, "Outlook Energi Indonesia 2016," Jakarta: Badan Pengkaji dan Penerapan Teknologi. BPPT. 2017. Outlook Energi Indonesia 2017. Jakarta : Badan Pengkaji dan Penerapan Teknologi.

[2] T. Shantika and M. Ridwan, "Perancangan Prototipe Pikohidro Portable 200 Watt," *Seminar Nasional XII Rekayasa dan Aplikasi Teknik Mesin di Industri*, pp. 39-48, 2013.

[3] A. Apprilianto, Indarto, and Prajitno, "Design of Prototype Hydro Coil Turbine Applied as Micro Hydro Solution," *ASEAN Journal of System Engineering*, vol. 1, no. 2, pp. 72-76, 2013.

[4] T. T. Gultom, "Pemenuhan Sumber Tenaga Listrik di Indonesia," *Jurnal Ilmiah Research Sains*, vol. 3, no. 1, pp. 130-138, 2017.

[5] KESDM, "Statistik Ketenagalistrikan Tahun 2015," Jakarta: Kementrian Energi dan Sumber Daya Mineral, 2015.

[6] M. L. V. Balansay, M. R. Q. Añonuevo, R. M. Cuenca, and R. V. Garbin, "Enggang: Portable Hybrid Powered Water Filtration Device," *Asia Pacific Journal of Multidisciplinary Research*, vol. 3, no. 3, pp. 136-140, 2015.

[7] "Enggang: Portable Hybrid Powered Water Filtration Device," *Asia Pacific Journal of Multidisciplinary Research*, vol. 3, no. 3, pp. 136-140, 2015.

[8] S. U. Patel and P. N. Pakale, "Study on Power Generation Using Cross Flow Water Turbine in Micro Hydro Power Plant," *International Journal of Research in Engineering and Technology*, vol. 4, no. 5, pp. 1-4, 2015.

[9] Y. Devrim, H. Devrim, and I. Eoglu, "Development of 500 W PEM Fuel Cell Stack for Portable Power Generators," *International Journal of Hydrogen Energy*, vol. 40, pp. 7707-7719, 2015.

[10] K. P. Huparikar and G. R. Naik, "Development of Prototype Turbine Model for Ultra-low Head Hydro Power Potential in Western Maharashtra," *Journal of Mechanical and Civil Engineering*, vol. 12, no. 6, pp. 14-20, 2015.

[11] P. Saisirirat and B. Joommanee, "Study on the Performance of the Micro Direct Ethanol Fuel Cell (Micro-DEFC) for Applying with the Portable Electronic Devices," *Energy Procedia*, vol. 138, pp. 187-192, 2017.

Design and Development of An Automatic Energy Buffer System and Hybrid Energy Storage on PV System Using Supercapacitors

Rocky Alfanz
Electrical Engineering Dept.
Universitas Sultan Ageng Tirtayasa
Cilegon, Indonesia
rocky.alfanz@untirta.ac.id

Adi Nugraha
Electrical Engineering Dept.
Universitas Sultan Ageng Tirtayasa
Cilegon, Indonesia
adi.n@untirta.ac.id

Muhamad Otong
Electrical Engineering Dept.
Universitas Sultan Ageng Tirtayasa
Cilegon, Indonesia
muhamad.otong@untirta.ac.id

Muhammad Fadhill Haekal
Electrical Engineering Dept.
Universitas Sultan Ageng Tirtayasa
Cilegon, Indonesia
3332190075@untirta.ac.id

Wahyuni Martiningsih
Electrical Engineering Dept.
Universitas Sultan Ageng Tirtayasa
Cilegon, Indonesia
y_martiningsih@untirta.ac.id

Muhammad Firman Fauzy
Electrical Engineering Dept.
Universitas Sultan Ageng Tirtayasa
Cilegon, Indonesia
ffauzy1395@gmail.com

***Abstract*—This research, conducted at the Faculty of Engineering, Universitas Sultan Ageng Tirtayasa, Cilegon, examines local weather conditions and the characteristics of voltage and current during charging and discharging phases, alongside an evaluation of off-grid PV system effectiveness. To enhance the competitiveness of the renewable energy sector, this study develops a hybrid energy storage system (HESS) that improves power quality by incorporating energy buffering in electrical storage. The aim is to deepen understanding of renewable energy technology and strengthen analytical capabilities in renewable energy systems. The constructed system integrates supercapacitor technology within the HESS, enabling it to supply initial power to induction loads and manage inrush currents effectively. During discharge, the HESS reliably stores power from PV systems under various weather conditions, achieving full charge 2 minutes faster than conventional systems. As the system discharges, supercapacitor voltage drops from 16 V while battery voltage remains stable at 12.5 V with an average current of 2.5 A. Additionally, the system handles inrush currents during motor startup, using a supercapacitor buffering period of 1.8 minutes.**

***Index Terms*—Renewable Energy Off-grid PV; Hybrid Storage System; PV systems; Lead Acid Battery; Supercapasitor**

I. Introduction

The Indonesian government targets a renewable energy mix of 23% by 2025 [1] and 31% by 2050 [2], [3]. This initiative is reinforced by regulations from the Ministry of Energy and Mineral Resources (ESDM) aimed at reducing emissions, with hopes that Indonesia can contribute more rapidly to global net-zero emissions [4]. As of 2020, Indonesia's primary renewable energy mix had reached only 11.31% [5]. In the National Energy Master Plan (RUEN), the government is committed to increasing the use of renewable energy [6].

The global issue of fossil fuel scarcity has spurred the development of various alternative energy sources, one of which is Solar Power Generation (PLTS), known for its readily available electricity production as sunlight is accessible year-round [7]. Solar energy consists of two components: heat and light. Both components can be converted into electrical energy. In conventional PLTS processes, solar panels are used to convert light into electricity, a process known as Photovoltaic [8].

979-8-3315-1921-6/24/$31.00 ©2024 IEEE

Batteries typically involve an electrochemical process that includes ion transfer between two electrodes by passing electrical current in opposing polarities through an external circuit. This process includes the insertion/diffusion of ions in the electrolyte solution from the cathode to the anode and vice versa [9]. The current magnitude in electrical systems is significantly influenced by the power requirements of the system. In electric machines with inductive loads, high current is drawn for power consumption, a phenomenon known as inrush current in inductive loads [10]., [11]., where this high current is used to generate an electromagnetic field in the system. Once the electromagnetic field stabilizes, creating a back electromagnetic field [12]., the current gradually decreases over time until a steady-state condition is reached.

Initially, electric machines with inductive loads require a large current, reaching 5 to 7 times the steady-state current level [13]. This condition can cause a voltage drop in the power storage system. One approach to addressing this issue is designing a Hybrid Energy Storage System (HESS), which combines two types of electrical energy storage systems [14], [15].

II. Method

The system design consists of an electrical energy source, utilizing PV system modules that direct power to a solar charge controller to manage the hybrid battery system charging. A

12V relay component acts as a catalyst for the boost converter to the induction load, protecting the storage system from excess electrical power output below the battery's state of charge (SOC). This battery system includes an SMT127 lead-acid battery and a Green Cap EDLC supercapacitor with a rating of 2.7 volts and 500 farads, with six supercapacitor units connected in series to achieve 16.2 volts. Both battery systems are connected in a parallel circuit. The power output of the hybrid storage system is then connected to a boost converter module to stabilize the output voltage to 12 volts DC.

A. Charging Process

The charging process, which is the primary focus of this research, aims fundamentally to improve the quality of power delivered to electrical loads, particularly inductive loads. The system used in this study has been designed with a hybrid battery technology that combines a supercapacitor and a 12-volt lead-acid battery as the energy storage system. At the initial stage of the charging process, electrical power generated by the solar panels is directed to a solar charge controller as a control method. The electrical power is then routed to the hybrid energy storage system, where it is split into two storage paths.

First, for the supercapacitor component, the incoming electrical power is boosted in voltage using a boost converter to reach 16V. This step aims to increase the supercapacitor's storage capacity and ensure improved power quality. Second, for the lead-acid battery component, a boost converter is not required, though the battery's voltage is carefully monitored throughout the charging process. The battery voltage is gradually increased to reach 12.7V, which is essential for maintaining balance within the energy storage system and preventing overcharging that could damage the battery. This process is a critical part of efforts to enhance the efficiency and power quality provided by the hybrid energy storage system, ultimately benefiting the support of reliable and sustainable electricity needs. The charge process of the buffer system is illustrated in Fig. 1.

Based on Fig. 1, the data obtained from the charging process in the hybrid system provides a detailed illustration of how the charging is carried out. This charging process was initiated at 10 a.m. and continued for a period of 15 minutes to enable thorough monitoring and accurate analysis.

B. Discharging Process

The data obtained from the discharge process in the system provides significant insights into understanding the behavior of the energy storage system during the energy release phase. In this discharge process, a DC motor is used as an inductive electrical load.

The result from this research have the potential to improve the design and operation of energy storage systems in various applications, including renewable energy use and efficient energy management. In the initial phase of the hybrid system process, the power required by the inductive load is supplied exclusively by the supercapacitor component, which has an

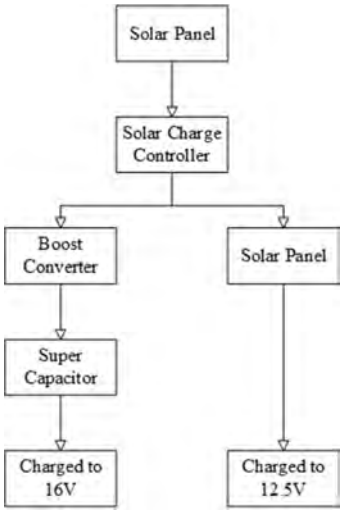

Fig. 1: Buffering system charging process

initial voltage of 16 volts. The supercapacitor is chosen as the primary power source in this initial stage due to its ability to supply power quickly and responsively. However, over time and use, the supercapacitor voltage decreases, eventually dropping to approximately 12.5 volts.

To maintain a consistent power supply, the hybrid system employs an intelligent approach by distributing the load power in parallel between the battery and the supercapacitor system.This configuration allows both components to simultaneously contribute to the load power supply. The battery system plays a role in sustaining a stable power supply when the supercapacitor's voltage has significantly dropped. This design aims to optimize the use of available resources and ensure that the inductive load continuously receives adequate power. The discharge process of the buffer system is illustrated in Fig. 2.

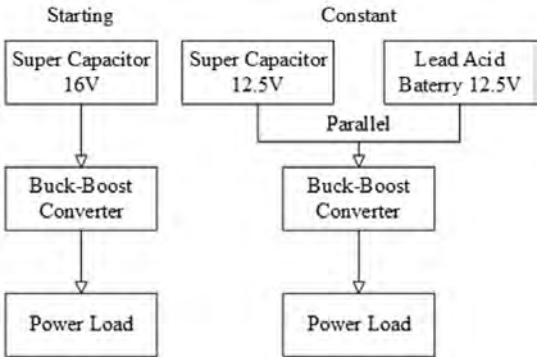

Fig. 2: Buffering system Discharging process

In the initial phase of the experiment, the starting voltage available from the supercapacitor was 16 volts. However, this voltage proved to be too high for the inductive load components used in the system. As is well known, inductive loads require an input voltage that aligns with their specifications to function effectively. Therefore, measures need to be taken to address the discrepancy between the voltage available from

the supercapacitor and the voltage required by the inductive load.

To resolve this issue, a Buck-Boost converter system is used, which is integrated before the input to the inductive load system. The primary function of the Buck-Boost converter is to adjust the input voltage from the supercapacitor to a more appropriate level, specifically 12 volts. This converter plays a crucial role in stabilizing the power supplied to the inductive load, ensuring that the load operates under optimal conditions and within the specified voltage requirements.

C. Supercapacitor Component Calculation

To determine the specifications for the number and configuration of supercapacitors, calculations were performed based on the specifications of the lead-acid battery used.

To determine the total capacitance of the supercapacitors required for the system design, (1) was used.

$$C_{\mathrm{Eq}} = \frac{I \cdot t}{U} \tag{1}$$

Based on the calculation results using (1), the total capacitance value obtained for the supercapacitors is $\geq 17.5F$.

After determining the required capacitance, the number of supercapacitors in the series array needed for the research system was calculated using (2).

$$C_{\mathrm{S}} = \frac{U}{U_{\mathrm{SC}}} \tag{2}$$

The calculation using (2) resulted in a required number of supercapacitors in the series array of approximately 5.111, which was rounded up to 6 units.

Once the required capacitance and number of supercapacitors were determined, the required capacitance of each supercapacitor for the research system was calculated using (3).

$$C_{\mathrm{SC}} = \frac{C_{\mathrm{Eq}}}{N_{\mathrm{S}}} \tag{3}$$

The result from (3) indicates that the capacitance of each supercapacitor is approximately 2.916 F.

Finally, after determining the required capacitance for each supercapacitor, the number of supercapacitors needed in the parallel array for the research system was calculated using (4).

$$N_{\mathrm{P}} = \frac{I}{I_{\mathrm{SC}}} \tag{4}$$

The result from (4) indicates that the required number of parallel arrays is 0.227, which is less than 1, meaning no additional parallel arrays are needed.

In this study, a Green Cap EDLC(DB) supercapacitor of 2.7 V 500 F is used, which has a larger capacitance value. As a result, the duration of the supercapacitor buffer is extended. Therefore, the capacitance value of the capacitors in the series array was recalculated using (5).

$$C_{\mathrm{SE}} = \frac{I}{\frac{I}{C_1} + \frac{I}{C_n} + \ldots} \tag{5}$$

Based on the calculation results using (5), the capacitance value for 6 Green Cap EDLC(DB) 2.7 V 500 F supercapacitors arranged in series is 83.33 F. Additionally, using the derivation from (1), (6) is obtained, which can be used to determine the buffering time.

$$t = \frac{C_{\mathrm{EQ}} \cdot \Delta U}{I} \tag{6}$$

Based on the calculation results using (6), the buffering time in the system is obtained as 97.21 seconds or 1.6 minutes.

D. Testing Method

Fig. 3 shows the methods used in system testing. The testing methods are conducted to obtain data analysis from the Hybrid Energy Storage System

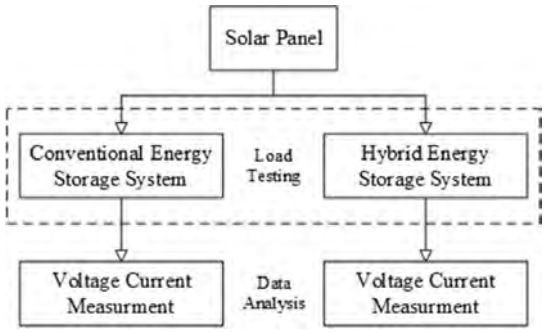

Fig. 3: Buffering system charging process

In the testing, an electrical machine with inductive load characteristics was used, tested under two system conditions: with and without the Hybrid Energy Storage System. The data obtained from the testing include the inrush current flowing through the system and the voltage drop that occurs when both systems are subjected to an inductive load. These two types of data will be used for comparison to determine the results of the research.

III. Result and Discussion

A. Irradiance and Temperature

The following are the recorded data on solar irradiance and temperature during the data collection conditions for analysis. The summarized solar irradiance data can be seen in Fig. 4, and the summarized temperature data can be seen in Fig. 5.

In Fig. 4, on the first day, the irradiation level measured was 794 W/m², indicating a high level of energy from the sun, which likely contributed to the warm temperatures. By the second day, this value decreased to 669 W/m², suggesting a reduction in solar energy reaching the surface. On the third day, the irradiation level dropped further to 397 W/m², indicating significantly less solar energy and potentially contributing to the cooler temperatures observed.

In Fig. 5, on the first day, the maximum temperature reached 31°C, indicating a relatively warm day. By the second day, the temperature slightly decreased, with the highest reading being 29°C, showing a small drop in warmth. On the third day, there was a more noticeable decline in temperature, as the maximum

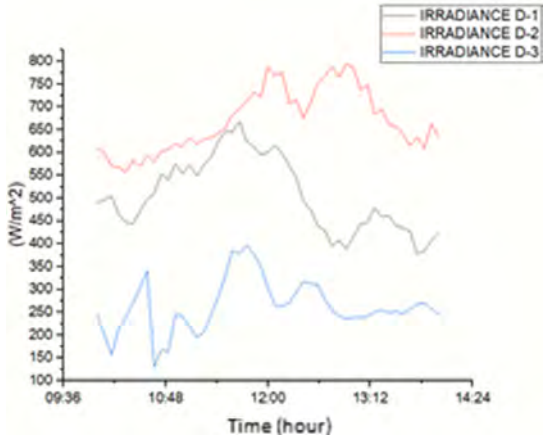

Fig. 4: System environmental irradiance graph

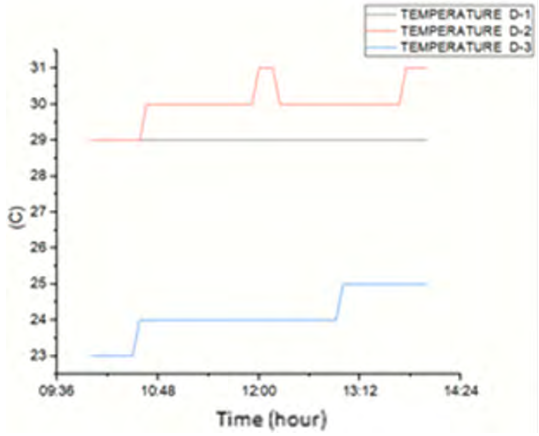

Fig. 5: System environmental temperature graph

reached only 25°C, suggesting a cooler day compared to the previous two.

B. Charging the System

This charging process is carried out to obtain voltage and current data for the supercapacitor and battery system. The charging process in the system is conducted over a 4-hour period using PV system research equipment at the Faculty of Engineering, Universitas Sultan Ageng Tirtayasa, Cilegon location. This process takes environmental conditions into account, with testing conducted over three different days under three different weather conditions: clear weather on day 1, cloudy weather on day 2, and rainy weather on day 3. The supercapacitor charging result can be seen in Fig. 6.

Fig. 6(a), displaying the charging voltage of the HESS supercapacitor, shows that all charging voltages yield almost identical results. This suggests a consistent charging pattern across different tests, indicating that the supercapacitor's performance is stable and predictable regardless of minor variations in charging conditions. The uniformity in the voltage curves highlights the efficiency and reliability of the supercapacitor's design in managing electrical energy storage.

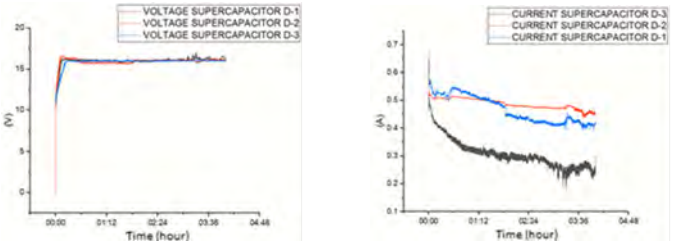

(a) (b)

Fig. 6: Charging HESS Supercapacitor; (a) Voltage; (b) Current

In Fig. 6(b), displaying the charging current of the HESS supercapacitor, the voltage on Day 1 appears unstable with varying amplitudes, indicating fluctuations during the charging process. On Day 2, the voltage shows much more stability, with consistent amplitudes suggesting a smoother and more controlled charging experience. By Day 3, the voltage becomes unstable again, but the amplitude is significantly lower, indicating less severe fluctuations compared to Day 1. This variation across days highlights differences in the charging behavior under different conditions.

In the HESS system, in addition to the supercapacitor, the lead-acid battery is also charged using the PV system. The lead-acid battery charging can be seen in Fig. 7.

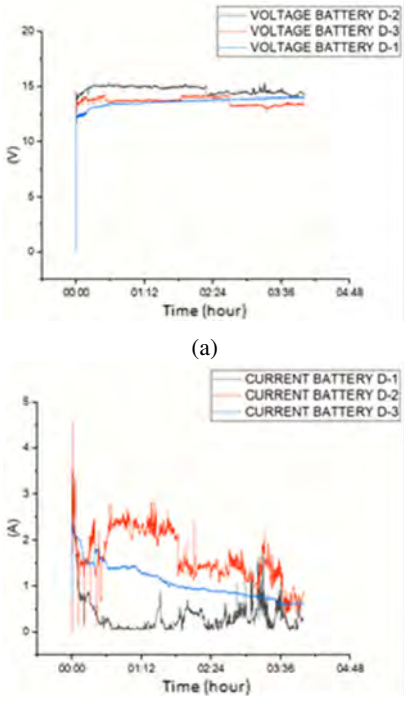

(a)

(b)

Fig. 7: Charging HESS Battery; (a) Voltage; (b) Current

In Fig. 7(a), illustrating the charging voltage of the HESS battery, Day 1 shows a very stable voltage, indicating a smooth charging process without significant fluctuations. On Day 2,

the voltage becomes unstable with much higher amplitude, suggesting significant fluctuations and possibly indicating issues with the charging conditions. By Day 3, while the voltage remains unstable, the amplitude is noticeably lower, pointing to less severe fluctuations than on Day 2. This variation highlights the changing stability of the battery's charging performance over the three days.

In Fig. 7(b), displaying the charging current of the HESS battery, Day 1 demonstrates a stable voltage, indicating a smooth and consistent charging process with minimal fluctuations. On Day 2, the voltage becomes unstable with much higher amplitude, suggesting significant variations and possible issues affecting the charging conditions. By Day 3, although the voltage remains unstable, the amplitude is considerably lower, indicating less severe fluctuations than observed on Day 2. This variation reflects the differences in charging stability and behavior across the three days.

In this study, the HESS system will be compared with a conventional system that does not use a supercapacitor, with direct charging from the PV system to the lead-acid battery. The conventional lead-acid battery charging can be seen in Fig. 8.

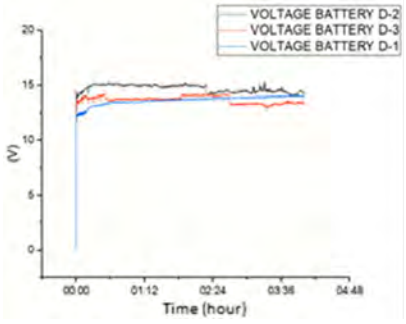

(a)

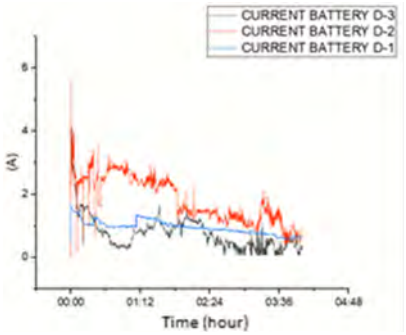

(b)

Fig. 8: Charging Conventional Battery; (a) Voltage; (b) Current

In Fig. 8(a), depicting the charging voltage of a conventional battery system, Day 1 shows a very stable voltage, indicating a smooth and consistent charging process. On Day 2, the voltage becomes unstable with varying amplitudes, suggesting fluctuations that might affect charging efficiency. By Day 3, the voltage remains unstable, but the amplitude is significantly lower, indicating less severe fluctuations compared to Day 2. This pattern illustrates the changing stability and behavior of the battery system over the three days.

In Fig. 8(b), showing the charging current of a conventional battery system, Day 1 displays a very stable voltage, indicating a smooth and consistent charging process. On Day 2, the voltage becomes unstable with varying amplitudes, suggesting fluctuations that could impact the charging efficiency. By Day 3, the voltage remains unstable, but the amplitude is significantly lower, indicating less severe fluctuations than on Day 2. This pattern highlights the variations in stability and charging behavior over the three days.

C. Discharging the System

The discharging process was carried out on both energy storage systems. This discharging process is carried out using an induction load of a 12V DC electric motor. At this stage, the energy storage system is tested in terms of its capacity to release energy that has been accumulated during the previous charging process. The induction load of a 12V DC electric motor is applied as an external load that allows current to flow out of the storage system, generating the power provided to the motor.

In the discharge testing, experiments were conducted using both the HESS system and the conventional method. These tests measured the current and voltage discharged from both methods over a period of 3 days. The current and voltage discharged on the first day using the HESS system can be seen in Fig. 9, while the conventional method can be seen in Fig. 10.

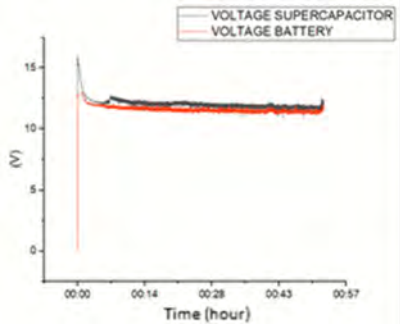

(a)

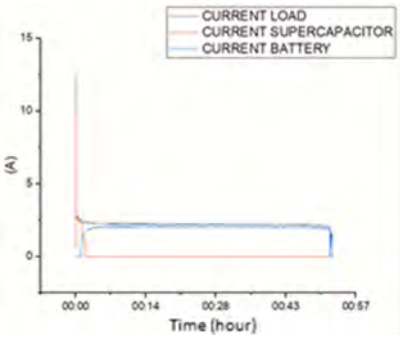

(b)

Fig. 9: Discharging HESS System Day-1; (a) Voltage; (b) Current

In Fig. 9(a), the discharging voltage graph for the HESS system on Day 1 shows that the discharging process is completed at 0:51:56. This relatively efficient discharge duration could be attributed to optimal external conditions, such as a stable temperature that allows the system to operate at its best performance. The consistent and relatively short discharge time suggests that the system was functioning under favorable conditions with minimal impact from external forces.

In Fig. 9(b), the discharging current graph for the HESS system on Day 1 shows a maximum current (Imax) of 11.384 A. This value indicates the peak current delivered during the discharging process under the conditions present on that day. The relatively stable and moderate current suggests that the system was operating under conditions that did not significantly affect its performance, possibly due to stable external factors like temperature

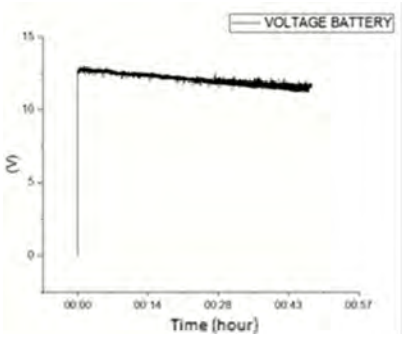

(a)

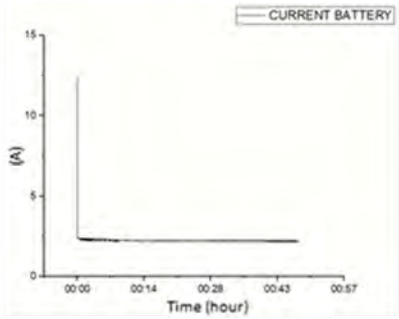

(b)

Fig. 10: Discharging Conventional Battery Day-1; (a) Voltage; (b) Current

In Fig. 10(a), the discharging voltage graph for the conventional battery system on Day 1 shows that the discharging process is completed at 0:47:08. This duration indicates that the battery discharged efficiently within this timeframe under stable conditions. The relatively short discharge time suggests that external factors, such as temperature, were favorable, allowing the battery to maintain its performance with minimal fluctuations.

In Fig. 10(b), the discharging current graph for the conventional battery system on Day 1 shows a maximum current (Imax) of 12.534 A. This value indicates a strong discharge performance with a high current output. The relatively stable and high peak current suggests that the battery operated under favorable conditions, likely with stable temperatures and minimal external disruptions, which allowed it to deliver efficient performance.

The second day of discharge testing using the HESS system can be seen in Fig. 11, and the conventional method can be seen in Fig. 12.

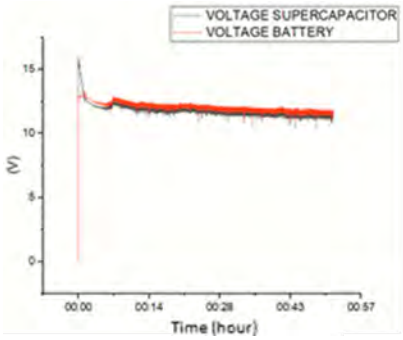

(a)

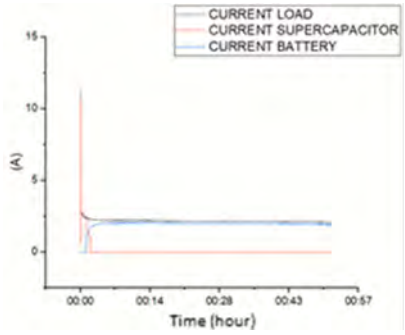

(b)

Fig. 11: Discharging HESS System Day-2; (a) Voltage; (b) Current

In Fig. 11(a), the discharging time extends to 0:52:46, indicating a slight increase compared to Day 1. This minor change could be caused by external factors such as fluctuations in temperature. If the temperature increased or decreased, it might have affected the battery's performance and efficiency, leading to a longer discharge time. Variations in temperature can influence the internal resistance and chemical processes within the battery, impacting its discharge characteristics.

In Fig. 11(b), the maximum current increases to 12.434 A. This rise in current could be influenced by external factors such as a change in temperature. If the temperature increased, it might have led to a reduction in internal resistance of the battery, allowing it to deliver a higher current. Alternatively, other external conditions could have contributed to this increased current. The higher peak current suggests that the system experienced different operational conditions compared to Day 1.

In Fig. 12(a), the discharging time extends to 0:47:57, showing a slight increase compared to Day 1. This minor extension in discharge duration could be attributed to external factors such as temperature variations. A slight change in temperature might have impacted the battery's efficiency, leading to a

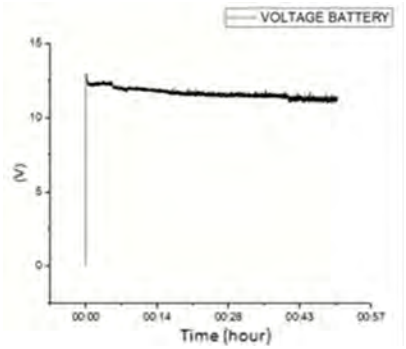

(a)

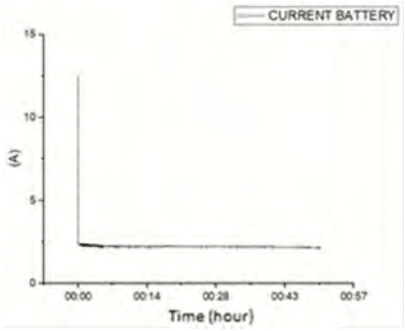

(b)

Fig. 12: Discharging Conventional Battery Day-2; (a) Voltage; (b) Current

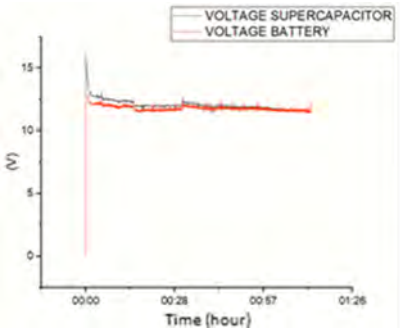

(a)

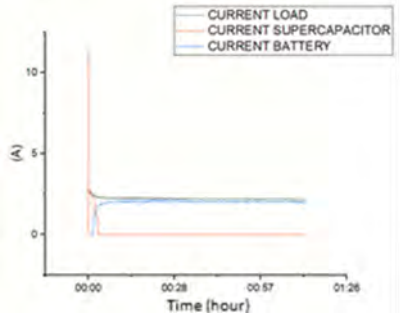

(b)

Fig. 13: Discharging HESS System Day-3; (a) Voltage; (b) Current

marginally longer discharge time. The small increase suggests that while conditions may have changed slightly, the battery's performance remained relatively stable.

In Fig. 12(b), the maximum current increases slightly to 12.690 A. This slight increase could be due to external factors such as a rise in temperature. An increase in temperature can reduce the battery's internal resistance, potentially allowing it to discharge more current. The higher peak current observed indicates improved performance or optimal operating conditions on this day compared to Day 1.

The third day of discharge testing using the HESS system can be seen in Fig. 13, and the conventional method can be seen in Fig. 14.

In Fig. 13(a), the discharging time significantly lengthens to 1:12:56. This considerable increase in duration suggests a more pronounced effect from external factors. If there were significant temperature fluctuations or if the temperature was more extreme, it could have substantially affected the battery's discharge efficiency. Extreme temperatures can alter the battery's internal resistance and performance, resulting in a longer discharge time as the system struggles to maintain optimal operation under less favorable conditions.

In Fig. 13(b), the maximum current decreases slightly to 11.349 A. This drop, while still relatively close to Day 1's value, may be indicative of less favorable conditions compared to Day 2. If the temperature or other external factors fluctuated again, it could have impacted the system's ability to deliver as high a current as on the previous day. This decrease in peak current suggests a return to conditions more similar to those on Day 1, but still reflecting some variability in performance.

In Fig. 14(a), the discharging time significantly lengthens to 1:06:39. This considerable increase in duration suggests a more pronounced effect from external factors. If there were significant fluctuations in temperature or other external conditions, it could have adversely affected the battery's discharge efficiency. The longer discharge time indicates that the battery faced challenges in maintaining optimal performance under less favorable conditions.

In Fig. 14(b), the maximum current decreases to 10.411 A. This notable drop in peak current may be the result of less favorable external conditions, such as a decrease in temperature or other environmental changes affecting battery performance. The lower current suggests that the battery experienced increased internal resistance or operational challenges, resulting in reduced discharge capability.

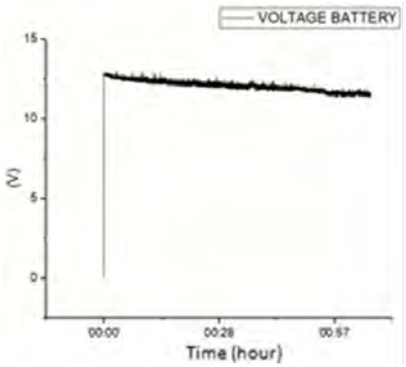

(a)

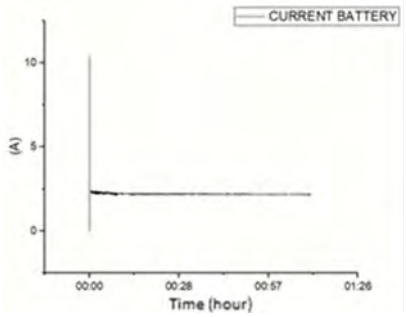

(b)

Fig. 14: Discharging Conventional Battery Day-3; (a) Voltage; (b) Current

IV. Conclusion

The following are the conclusions from the research data that have been carried out with the hybrid system was able to reliably receive PV systems power in sunny, cloudy and rainy weather tests, with the system fully charged an average of 2 minutes faster than conventional storage systems. When discharging, in hybrids the supercapacitor voltage drops from 16 V and the battery remains 12.5 V, the average current is 2.5 A, in conventional systems the battery voltage decreases from 12.5 V, the average current is 2.5 A. In the discharging process, the hybrid system effectively handles an average inrush current of 11.3 A for 1 second when starting the motor, with an average buffer period given by the supercapacitor for 1.8 minutes.

References

[1] A. Taufiqurrahman and J. Windarta, "Overview Potensi dan Perkembangan Pemanfaatan Energi Air di Indonesia," *Jurnal Energi Baru dan Terbarukan*, vol. 1, no. 3, pp. 124–132, Oct. 2020, doi: 10.14710/jebt.2020.10036.

[2] Ruslan, "Status Pemanfaatan Energi Baru Terbarukan dan Opsi Nuklir Dalam Bauran Energi Nasional," *Jurnal Pengembangan Energi Nuklir*, vol. 23, no. 1, pp. 39–49, 2021.

[3] P. Ahluriza and U. Harmoko, "Analisis Pemanfaatan Tidak Langsung Potensi Energi Panas Bumi di Indonesia," *Jurnal Energi Baru dan Terbarukan*, vol. 2, no. 1, pp. 53–59, Mar. 2021, doi: 10.14710/jebt.2021.11075.

[4] H. L. van Soest, M. G. J. den Elzen, and D. P. van Vuuren, "Net-zero emission targets for major emitting countries consistent with the Paris Agreement," *Nat Commun*, vol. 12, no. 1, Dec. 2021, doi: 10.1038/s41467-021-22294-x.

[5] A. E. Setyono and B. F. T. Kiono, "Dari Energi Fosil Menuju Energi Terbarukan: Potret Kondisi Minyak dan Gas Bumi Indonesia Tahun 2020 – 2050," *Jurnal Energi Baru dan Terbarukan*, vol. 2, no. 3, pp. 154–162, Oct. 2021, doi: 10.14710/jebt.2021.11157.

[6] G. A. Widyaningsih, "Ulasan Peraturan Peraturan Presiden nomor 22 Tahun 2017 tentang Rencana Umum Energi Nasional," *Jurnal Hukum Lingkungan Indonesia*, vol. 4, no. 1, pp. 139–152, Dec. 2017, doi: 10.38011/jhli.v4i1.53.

[7] J. S. Setyono, F. H. Mardiansjah, and M. F. K. Astuti, "Potensi Pengembangan Energi Baru dan Terbarukan di Kota Semarang," *Jurnal Riptek*, vol. 13, no. 2, pp. 177–186, Dec. 2019, [Online]. Available: http://riptek.semarangkota.go.id

[8] A. S. Joshi, I. Dincer, and B. V. Reddy, "Thermodynamic assessment of photovoltaic systems," *Solar Energy*, vol. 83, no. 8, pp. 1139–1149, Aug. 2009, doi: 10.1016/j.solener.2009.01.011.

[9] W. Liu, T. Placke, and K. T. Chau, "Overview of batteries and battery management for electric vehicles," *Energy Reports*, vol. 8, pp. 4058–4084, Nov. 2022, doi: 10.1016/j.egyr.2022.03.016.

[10] Y. Varetsky and M. Gajdzica, "Study of Short Circuit and Inrush Current Impact on the Current-Limiting Reactor Operation in an Industrial Grid," *Energies (Basel)*, vol. 16, no. 2, Jan. 2023, doi: 10.3390/en16020811.

[11] I. B. Hermawan, M. Ashari, and D. C. Riawan, "PV Farm Ancillary Function for Voltage Sag Mitigation Caused by Inrush Current of an Induction Motor," *International Journal of Intelligent Engineering and Systems*, vol. 15, no. 6, pp. 325–336, Dec. 2022, doi: 10.22266/ijies2022.1231.31.

[12] A. Navarro-Navarro, J. E. Ruiz-Sarrio, V. Biot-Monterde, J. A. Antonino-Daviu, V. Becker, and S. Urschel, "Application of Transient Analysis Techniques to Fault Diagnosis in Low- and Medium-Power Synchronous Machines," *Machines*, vol. 11, no. 2, Feb. 2023, doi: 10.3390/machines11020288.

[13] A. Dani and D. Erivianto, "Studi Perbandingan Arus Start Motor Induksi Sistem Pengasutan Dol Dan Star Delta Menggunakan Automation Studio," *Jurnal Indonesia Sosial Teknologi*, vol. 4, no. 4, pp. 413–422, Apr. 2023, doi: 10.59141/jist.v4i4.602.

[14] S. Hajiaghasi, A. Salemnia, and M. Hamzeh, "Hybrid energy storage system for microgrids applications: A review," *J Energy Storage*, vol. 21, pp. 543–570, Feb. 2019, doi: 10.1016/j.est.2018.12.017.

[15] Y. Sahri et al., "Energy management system for hybrid PV/wind/battery/fuel cell in microgrid-based hydrogen and economical hybrid battery/super capacitor energy storage," *Energies (Basel)*, vol. 14, no. 18, Sep. 2021, doi: 10.3390/en14185722.

Application of Genetic Algorithm for School Timetable Scheduling

Angelina Sylviani Budiarto
Faculty of Information Technology and Design
Primakara University
Bali, Indonesia
angelinabudiarto4@gmail.com

Ni Made Satvika Iswari
Faculty of Information Technology and Design
Primakara University
Bali, Indonesia
iswari@primakara.ac.id

Eddy Muntina Dharma
Faculty of Information Technology and Design
Primakara University
Bali, Indonesia
eddy@primakara.ac.id

***Abstract*—The school schedule is a crucial aspect of managing the teaching and learning activities at school. Its creation requires significant time and effort, especially if done manually. SMPK Santo Yoseph Denpasar is one such school that still uses a manual approach for scheduling, which can take approximately two weeks. This manual scheduling process poses challenges, particularly in meeting the distribution of class hours and adhering to the school's constraints. The issues in allocating the required weekly hour for each subject and for each class. Due to this issue, there can be up to 7 subjects in a single day, as most subject are allocated only 1 hour per session. A genetic algorithm is one of the best solutions for addressing scheduling issues. This study employs an applied research method, directly applying scientific knowledge to the problem at hand. The implementation of the genetic algorithm in this study begins with generating an initial population using subjects, class hours, days, and classes that was created to distribute teaching hours. It is followed by calculating the fitness value selection adjusted to the school's constraints, as well as crossover and mutation processes. The research results show that the genetic algorithm model used is capable of meeting the distribution of class hours with four specified constraints, as the number of subjects could be reduced to 4-5 subjects per day and, through an evolutionary process of 100 generations, can achieve and maintain the highest fitness value, which 0.0880 out of 1.**

***Index Terms*—genetic algorithm, scheduling**

I. Introduction

In any activity, such as school learning, a schedule is essential as it serves as a guide for the participants [1]. The school schedule supports the teaching and learning process by organizing and allocating resources, time, and available facilities [2] [3].. The teaching and learning process undergoes changes every academic year, which may be influenced by factors such as the addition or reduction of teachers, the number of classes, or changes in educational policies that require adjustments. These factors demand attention and focus during the scheduling process at schools [4]. Kemudian berurutan disitasi

Creating a school schedule is crucial and requires time, effort, and precision [5]. A good schedule must meet and consider several factors, such as the teachers assigned to subjects, classrooms, subjects, and other constraints [6]. to avoid overlapping schedules. Additionally, the correlation between scheduling components must be considered, such as the spacing of lesson hours for the same subject or adjusting class hours to the curriculum, among many other potential correlations during the scheduling process.

In schools that still use manual scheduling methods, it can be challenging to meet the correlations or constraints between components, which may lead to problems. Common issues in manually creating schedules include the allocation of resources, class hours, and classroom assignments [2].

To address the challenges of manual scheduling, computational and mathematical approaches can offer effective solutions, such as using algorithms. An algorithm is a set of instructions used to meet certain criteria and make decisions [7].

Several algorithms can be applied to scheduling problems, such as *Ant Colony Optimization, Genetic Algorithm, Particle Swarm,* dan *Steepest Ascent Hill Climbing*. To compare the performance of algorithms suitable for scheduling, reference can be made to previous studies, as shown in Table I.

TABLE I: SCHEDULING RESULTS

Scheduling Results		
Research Title	**Author**	**Research Results**
Performance Comparison of Genetic Algorithm and Ant Colony Optimization in Course Scheduling Optimization	Ahmad (2016)	The best performance of the genetic algorithm is achieved with a time of 21.6 seconds, while ant colony optimization takes 69.11 seconds.
Study of Optimization Algorithms for Course Scheduling	H. Tri (2020)	In a comparison of the genetic algorithm (GA), ant colony optimization (ACO), and particle swarm optimization (PSO), GA outperforms in obtaining optimal solutions, achieving a fitness value of 1, and having faster execution speed.
Comparison of Genetic Algorithm and Steepest Ascent Hill Climbing Algorithm for Course Scheduling Optimization	Ardiya (2022)	The results show that the genetic algorithm can produce a conflict-free schedule, although it requires a longer running time.

Based on the results of previous research in Table I, it can

979-8-3315-1921-6/24/$31.00 ©2024 IEEE

be concluded that the genetic algorithm has superior potential compared to other algorithms, both in terms of computational time and the best fitness value to produce optimal scheduling solutions.

SMPK Santo Yoseph is one educational institution where the scheduling process is still done manually, without the use of computational guidelines or calculations, and takes approximately two weeks. This manual process leads to high complexity and difficulty, particularly in ensuring and meeting the distribution of class hours that must be fulfilled within a week for each class.

Given the issues mentioned above, this research will focus on determining the appropriate distribution of class hours and the formulation of a fitness value that can be used to meet these constraints using the genetic algorithm.

II. Theoretical Review

A. Genetic Algorithm

The genetic algorithm is a technique for finding solutions using the principle of natural selection (biology), where individuals with better characteristics can survive and evolve [11] [3]. The genetic algorithm uses a chromosome representation of the problem at hand and applies the concepts of genetic selection, such as mutation, selection, and recombination, to obtain the best solution based on related rules [12] [13].

B. Steps of Genetic Algorithm

1) Initialization Population : The initial population is created by initializing or encoding the problem to be solved. Table II and Table III is showing how initialization for subject and day codes.

TABLE II: EXAMPLE OF SUBJECT CODING

Subject Code	Subject
BIND	Bahasa Indonesia
MTK	Matematika
IPA	IPA

TABLE III: EXAMPLE OF DAY CODING

Day Code	Day
1	Monday
2	Tuesday
3	Wednesday

Each encoded unit is called a gene, which is then randomly combined to form chromosomes. A collection of chromosomes forms an individual, and these individuals make up a population that represents the desired solution [14], as shown in the example in Figure 1.

2) Fitness Value Selection : The fitness value is calculated based on the number of violations or penalties associated with the problem faced by each chromosome. The fitness value serves as a reference to achieve the best score or fitness for that chromosome.

Fitness Calculation Formula :

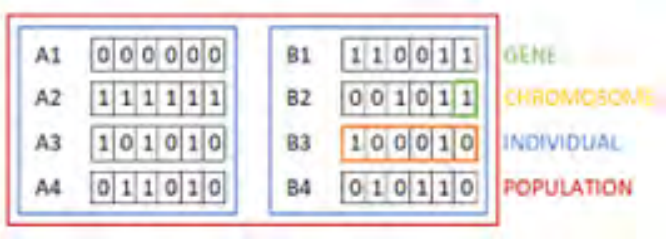

Fig. 1: Population Structure

$$F = \frac{1}{1 + \sum penalty} \tag{1}$$

The fitness value is then selected to be used as a parent in the next process using the elitism selection method, which involves choosing the parent based on the highest value to be carried forward to the next process [5].

3) Crossover : Crossover is a method of cutting parts of selected parent individuals from the selection results and then crossing them with other parent parts (as illustrated in Figure 2) to produce offspring that can increase diversity within a population [16] [17].

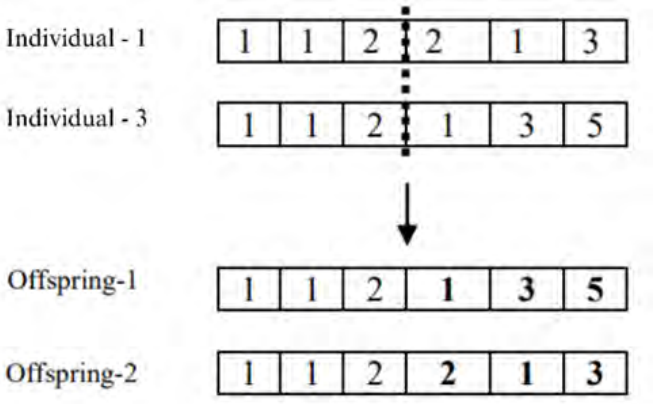

Fig. 2: Example of Crossover Process

4) Mutation : Mutation is the process of replacing genes that are deemed less suitable with genes that meet the criteria of the desired solution, as illustrated in Figure 3. This aims to produce chromosomes with better quality [18]

5) Stopping Criteria : The stopping criteria process occurs when the iteration and the desired results are close to or optimal for what is intended to be achieved.

III. Research Method

The method used in this study is applied research. Applied research involves applying theory and scientific knowledge with the goal of solving real-world problems and providing solutions [19], specifically testing whether the genetic algorithm is effective in solving the manually performed scheduling process.

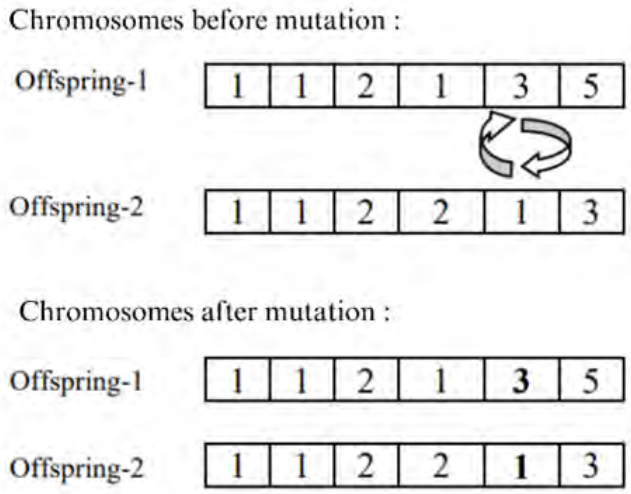

Fig. 3: Example of Mutation Process

There are several stages in applied research, explained as follows :

1) Problem Identification : This stage involves a deeper investigation into the issues faced by SMPK Santo Yoseph Denpasar in the scheduling process by conducting interviews with the scheduling team. The issue encountered is the difficulty in distributing class hours according to the applicable curriculum rules. Due to this difficulty, the number of subjects in a single day can reach up to seven.

2) Data Collection : This stage involves gathering the necessary data to solve the identified problem. The data collected includes the class schedule for the 2023/2024 academic year at SMPK Santo Yoseph Denpasar.

3) Data Analysis : This stage involves processing and analyzing the collected data. From the schedule data, data processing and validation are carried out regarding the number of subjects and class hours required for each subject.

4) Model Implementation and Evaluation : In this stage, the process involves integrating the existing model into the problem scope to be solved and assessing the model's performance. Based on the analyzed data, the genetic algorithm is applied, starting with the representation of the required solution, the formulation of the fitness value in line with the problem, crossover and mutation to generate population diversity, and determining the stopping criteria to achieve the best scheduling results.

IV. Implementation and Result

The data used in this study is the class schedule data from SMPK Santo Yoseph Denpasar for the 2023/2024 academic year. From this data, several pieces of information and criteria used in the schedule creation were obtained as follows :

- There are 28 classes.
- 9 class periods/day, except on the 5th day, with 7 class periods/day.
- 5 school days (Monday-Friday) each week.
- Allocation of class periods for each subject per week is shown on Table IV:

TABLE IV: WEEKLY SUBJECT HOURS

Subject	Weekly Hours (WH)
Bahasa Indonesia	6 WH
Matematika	5 WH
IPA	5 WH
Bahasa Inggris	4 WH
IPS	4 WH
PKN	3 WH
Informatika	3 WH
Seni Budaya	3 WH
PJOK	3 WH
Agama	2 WH
Bahasa Bali	2 WH
Bahasa Jepang	2 WH
BK	1 WH

Next is the formation of the initial population, initialized to consist of 28 individuals, each representing a class. Each individual contains 5 chromosomes representing the school days. Each chromosome contains genes representing subjects and 9 class periods.

TABLE V: SUBJECT HOURS CODING

Subject	Weekly Hours (WH)
Bahasa Indonesia	BIND1, BIND2, BIND3
Matematika	MTK1, MTK2, MTK3
IPA	IPA1, IPA2, IPA3
Bahasa Inggris	BING1, BING2
IPS	IPS1, IPS2
PKN	PKN1, PKN2
Informatika	IF1, IF2
Seni Budaya	SB1, SB2
PJOK	PJOK
Agama	AGAMA
Bahasa Bali	BBALI
Bahasa Jepang	BJPG
BK	BK
Jam kosong	E

The coding of class periods is done by dividing the required 2 class periods for each subject per week for each class as shown in Table V. For example, the Indonesian language subject requires 6 class periods, which are divided into 3 meetings per class, with each meeting having 2 class periods. The code for the Empty Class Period ('E') is used to balance the number of genes, as in genetic algorithms, the number of genes in a chromosome must be the same. For the other types of coding, refer to Table VI for the day codes and Table VII for class codes.

TABLE VI: LEARNING DAYS CODING

Day	Code
Monday	Day 1
Tuesday	Day 2
Wednesday	Day 3
Thursday	Day 4
Friday	Day 5

Figure 4 shows an example of the generated population:

TABLE VII: CLASS CODING

Day	Code
VII A	Class 1
VII B	Class 2
VIII C	Class 3
...	...
IX I	Class 28

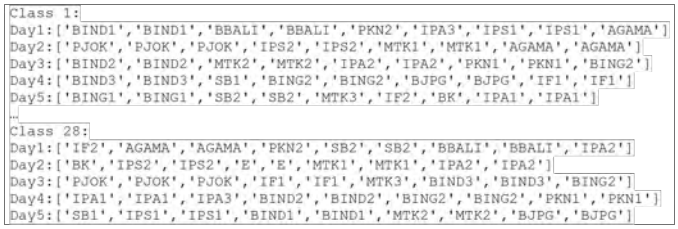

Fig. 4: Example of Mutation Process

The population used in this research is 10. From the 10 formed populations, the fitness value will be calculated using 4 formulas representing the applied penalties. The first formula is used to calculate the actual occurrence of the subject from the population generation:

$$count_fitness = \frac{1}{1+\sum |desired_counts[subject] - actual_counts[subject]|} \quad (2)$$

Abbreviations:
count_fitness = Counts the occurrence of a subject.
desired_counts = The desired number of class periods for that subject code.
actual_counts = The number of class periods generated from the initial population generation.

The second formula is used to calculate a penalty if the same subject code appears on the same day but with non-consecutive class periods, as it is considered ineffective if a subject is taught on the same day with non-consecutive periods.

$$distant_fitness = \frac{1}{1+distant_penalty} \quad (3)$$

Abbreviations:
distant_fitness = Measures the distance between subjects on the same day.
distant_penalty = Penalty for non-consecutive periods of the same subject.

The third formula is used to penalize subjects that appear more than 3 times because, according to the subject distribution, the maximum occurrence is 3 times.

$$over_count_fitness = \frac{1}{1+over_count_penalty} \quad (4)$$

Abbreviations:
over_counts_fitness = Counts subjects that appear more than 3 time.
over_count_penalty = Penalty for excessive subject occurrences.

The last formula is used to penalize if the Empty Class Period code ('E') does not appear in the 8th and 9th periods of the fifth chromosome in each individual (5th day, 8th & 9th periods). From these four calculations, the fitness formula becomes:

$$F = \frac{count_fitness + distant_fitness + over_count_fitness + e_fitness}{4} \quad (5)$$

The fitness value calculation results for the 10 populations are as follows in Figure 5:

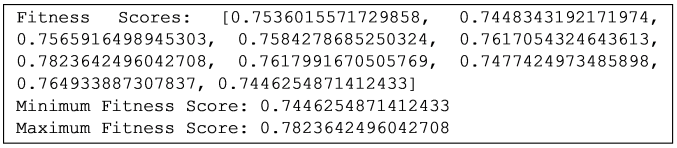

Fig. 5: Fitness Value Calculation Results for 10 Populations

Next, the fitness values will be selected using the elitism method to choose parents by taking half of the initial population and the selected parents index as in Figure 6.

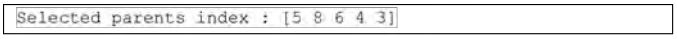

Fig. 6: Selected Parents

The next process is crossover as shown in Figure 7, using the one-point crossover method, selecting a random cut point. The offspring generated are 6 populations, which will be used as the new population for the mutation process.

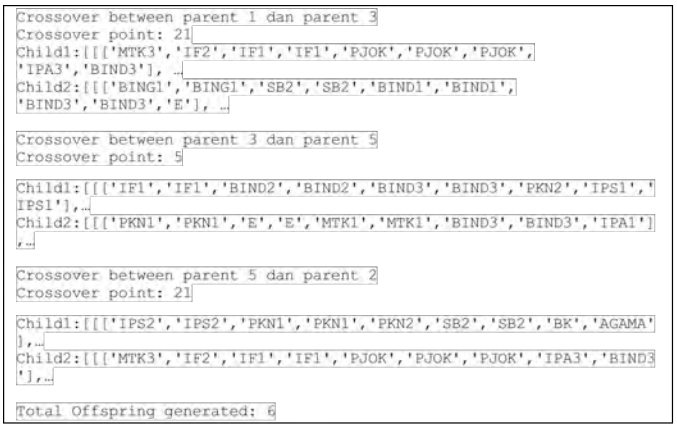

Fig. 7: Crossover Process

The new population from the crossover results is then subjected to mutation using a mutation rate of 0.01 or 1% to maintain the stability of the individual structure. The mutation is performed by swapping genes in individuals that still have insufficient or excessive class periods and swapping if the Empty Class Period ('E') is not in the 5th chromosome (5th day) 8th & 9th genes (8th & 9th periods). The mutation results as shown in Figure 8, by swapping the 5th day subject to 'E'.

After the mutation process, the next step is the evolution process carried out over 100 generations. This evolution process repeats all the stages of the genetic algorithm, starting

```
Population 1
Class 1:
['SB1','AGAMA','AGAMA','IPS1','IPS1','IPA1','IPA1','IF1','IF1']
['BK','MTK1','MTK1','IPA3','BIND1','BIND1','IPS2','BIND2','BING2']
['IPA2','IPA2','BJPG','BJPG','BING1','BING1','PKN2','BIND3','BIND3']
['SB2','SB2','BBALI','BBALI','MTK2','MTK2','PKN1','PKN1','IF2']
['BING2','BING2','PJOK','PJOK','PJOK','MTK3','IPS2','E','E']
...
Population 6
Class 1:
['BING2','BING2','IF2','BIND2','BIND2','SB2','SB2','IPA1','IPA1']
['SB1','BIND3','BIND3','PKN2','MTK3','IPS2','MTK2','IPS1','IPS1']
['BK','PJOK','PJOK','PJOK','MTK1','MTK1','BJPG','BJPG','IPA3']
['IF1','IF1','BIND1','BIND1','BING1','BING1','AGAMA','AGAMA','IPS2']
['BBALI','BBALI','PKN1','PKN1','IPA2','IPA2','IPS2','E','E']
```

Fig. 8: Crossover Process

from the initial population (population resulting from the mutation), fitness value selection, crossover, and mutation according to the desired number of generations. The fitness value results from 100 generations are as follows in Figure 9.

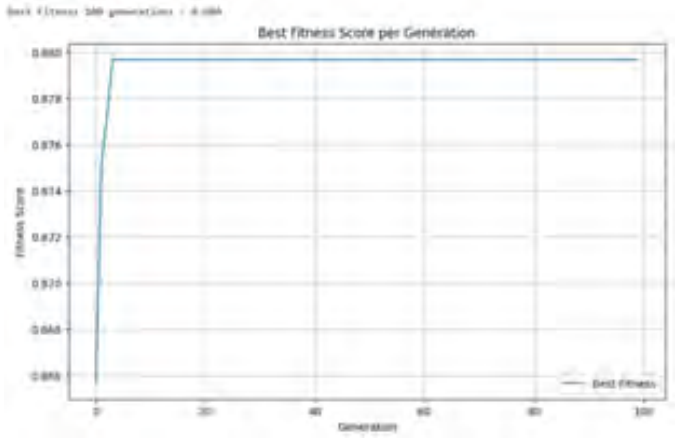

Fig. 9: Fitness Value per Generation

The best fitness value obtained from 100 generations is 0.880, with the best scheduling result shown in Figure 10. The best scheduling results in Figure 10 also shown that number of subjects per day could be reduced.

```
Best Schedule:
Class 1:
['SB1','AGAMA','AGAMA','IPS1','IPS1','IPA1','IPA1','IF1','IF1']
['BK','MTK1','MTK1','IPA3','BIND1','BIND1','IPS2','BIND2','BING2']
['IPA2','IPA2','BJPG','BJPG','BING1','BING1','PKN2','BIND3','BIND3']
['SB2','SB2','BBALI','BBALI','MTK2','MTK2','PKN1','PKN1','IF2']
['BING2','BING2','PJOK','PJOK','PJOK','MTK3','IPS2','E','E']
...
Class 28:
['BK','PKN1','PKN1','SB2','SB2','IPS1','IPS1','BING2','BING2']
['BIND1','BIND1','BJPG','BJPG','MTK3','PKN2','BBALI','BBALI','IPS2']
['IPA1','IPA1','MTK1','MTK1','PJOK','PJOK','PJOK','BING1','BING1']
['SB1','IPA3','BIND3','BIND3','AGAMA','AGAMA','MTK2','MTK2','IF1']
['IPS2','IPS2','BIND2','BIND2','IF2','IPA2','IPA2','E','E']
```

Fig. 10: Best Schedule Results

To facilitate viewing the occurrence of class periods compared to the desired class periods, the visual comparison can be made as in Figure 11:

The distribution of class periods obtained from this research is determined by dividing the total class periods required in one week by 2 class periods to determine the number of meetings per week in one class. Thus, in one meeting, the

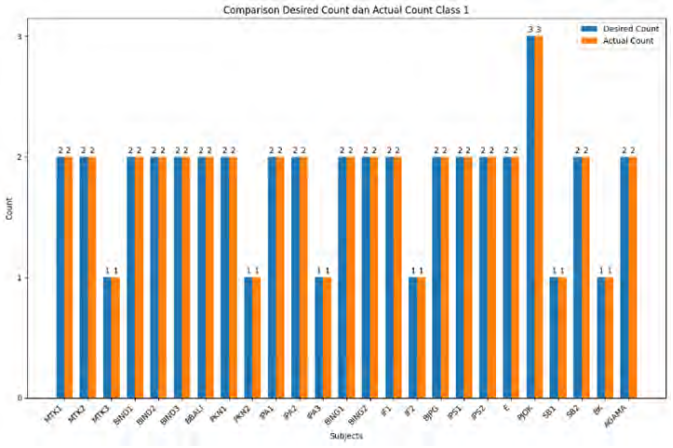

Fig. 11: Comparation of Subject Occurrences

subject is scheduled for a maximum of 2 class periods, in accordance with the school's policy that a single subject should not exceed 2 class periods on the same day. The only exception is for Physical Education (PJOK), which must be scheduled for 3 consecutive class periods, since the school requires, the Physical Education (PJOK) lessons to be scheduled for 3 hour per week and only allows 1 session per week for each class, the lesson cannot be split into the multiple time slots and must be scheduled as a continuous 3 hour in a row.

For example, the Indonesian language subject requires 6 class periods per week for one class, so the class will have 3 meetings on different days within the week, each consisting of 2 class periods. Another example is the Mathematics subject, which requires 5 class periods per week for one class, resulting in 3 meetings on different days: two meetings with 2 class periods each, and one meeting with 1 class period. A detailed breakdown can be seen in the Table VIII below:

TABLE VIII: WEEKLY SUBJECT HOURS

Subject	Weekly Hours (WH)	Group & Code of Lesson Hour Distribution
Bahasa Indonesia	6 WH	BIND1 (2 WH), BIND2 (2 WH), BIND3 (2 WH)
Matematika	5 WH	MTK1 (2 WH), MTK2 (2 WH), MTK3 (1 WH)
IPA	5 WH	IPA1 (2 WH), IPA2 (2 WH), IPA3 (1 WH)
Bahasa Inggris	4 WH	BING1 (2 WH), BING2 (2 WH)
IPS	4 WH	IPS1 (2 WH), IPS2 (2 WH)
PKN	3 WH	PKN1 (2 WH), PKN2 (1 WH)
Informatika	3 WH	IF1 (2 WH), IF2 (1 WH)
Seni Budaya	3 WH	SB1 (2 WH), SB2 (1 WH)
PJOK	3 WH	PJOK (3 WH)
Agama	2 WH	AGAMA (2 WH)
Bahasa Bali	2 WH	BBALI (2 WH)
Bahasa Jepang	2 WH	BWHG (2 WH)
BK	1 WH	BK (1 WH)

V. Conclusion

Based on the application of the genetic algorithm for scheduling using the class schedule data from SMPK Santo

Yoseph Denpasar for the 2023/2024 academic year, the following conclusions were:

The fitness value formula used in this research is divided into four parts: calculating the difference between the actual occurrences and the predefined occurrences according to the class period distribution; penalizing the same subject if it appears with a gap of more than one period on the same day; penalizing subjects that appear more than three times in any class; and penalizing if an empty class period occurs anywhere other than the 8th and 9th periods on the 5th day.

Based on the above, it can be concluded that the genetic algorithm is proven to be capable of scheduling with a focus on the distribution of class periods within a week for each class. The final schedule produced after 100 generations achieved a fitness value of 0.880 out of 1. The fitness value increased with each generation and did not decrease, indicating that the evolution process in this research was effective in improving the fitness value.

Based on the results and conclusions outlined, the following suggestions can be made: future research could explore scheduling using a genetic algorithm with different representations, fitness value formulas, crossover methods, and mutations, tailored to the specific scheduling challenges and constraints encountered.

REFERENCES

[1] A. Aris Widodo and M. Nur Cholis, "Optimasi Penyusunan Jadwal Guru Model Moving Class dengan Algoritma Genetika," *JOINTECS) J. Inf. Technol. Comput. Sci.,* vol. 3, no. 1, 2018, doi: 10.31328/jo.

[2] A. A. S, M. Assidiq, and A. A. Qashlim, "Sistem Informasi Penjadwalan Mata Pelajara Berbasis Web Menggunakan Metode Algoritma Genetika Pada Smkn 6 Majene," *J. Peqguruang Conf. Ser.,* vol. 3, no. 2, p. 861, 2021, doi: 10.35329/jp.v3i2.2235.

[3] D. Hermawanto, "Algoritma Genetika dan Contoh Aplikasinya," pp. 1–10, 2007.

[4] Amalia Yunia Rahmawati, "No Title No Title No Title," vol. 8, no. July, pp. 1–23, 2020.

[5] D. R. Anamisa, S. Kom, M. Kom, D. Jurusan, T. Multimedia, and D. J. Teknik, "Implementasi Alokasi Jadwal Mata Pelajaran SMU menggunakan Algoritma Semut," *J. Ilm. NERO*, vol. 1, no. 1, pp. 33–41, 2014.

[6] N. I. Kurniati, A. Rahmatulloh, and D. Rahmawati, "Perbandingan Performa Algoritma Koloni Semut Dengan Algoritma Genetika – Tabu Search Dalam Penjadwalan Kuliah," *Comput. Eng. Sci. Syst. J.,* vol. 4, no. 1, p. 17, 2019, doi: 10.24114/cess.v4i1.11387.

[7] M. S. Iswari, A. Suryadibrata, and N. D. Rucci, "Workshop Algoritma dan Pemrograman untuk Peserta Didik SMAS Katolik Cor Jesu Malang," pp. 55–61, 2022.

[8] I. A. Ashari, "Perbandingan Performansi Algoritma Genetika dan Algoritma Ant Colony Optimization dalam Optimasi Penjadwalan Mata Kuliah," *Repos. Univ. Negeri Semarang*, pp. 1–80, 2016, [Online]. Available: https://lib.unnes.ac.id/28048/1/4611412015.pdf

[9] T. Handayani, D. H. Fudholi, and S. Rani, "Kajian Algoritma Optimasi Penjadwalan Mata Kuliah," Petir, vol. 13, no. 2, pp. 212–222, 2020, doi: 10.33322/petir.v13i2.1027.

[10] L. P. S. Ardiyani, "Perbandingan Algoritma Genetika dengan Algoritma Steepest Ascent Hill Climbing untuk Optimasi Penjadwalan Kuliah," *J. Nas. Pendidik. Tek. Inform.,* vol. 11, no. 1, p. 63, 2022, doi: 10.23887/janapati.v11i1.43172.

[11] T. Handoyo, A. K. Rachmawati, and E. Prasetyo, "Sistem Penjadwalan Mata Pelajaran di SMA Muhammadiyah 1," vol. 11, no. 1, pp. 14–19, 2015.

[12] A. Nugroho, W. Priatna, and I. Romli, "Implementasi Algoritma Genetika Untuk Optimasi Penjadwalan Mata Kuliah," *J. Teknol. dan Ilmu Komput. Prima,* vol. 1, no. 2, pp. 35–41, 2018, doi: 10.34012/jutikomp.v1i2.238.

[13] R. (2021). P. P. A. G. U. P. A. P. M. P. (Doctoral dissertation, U. I. N. S. U. Ananda, *Penerapan Algoritma Genetika Untuk.* 2021.

[14] U. Bhayangkara, J. Raya, F. Ilmu, and K. Prodi, "3 1,2,3".

[15] Q. E. Muftikhali, A. Y. F. D. Yudhistira, A. Kusumawati, and S. Hidayat, "Optimasi Algoritma Genetika Dalam Menentukan Rute Optimal Topologi Cincin Pada Wide Area Network," *Inform. Mulawarman J. Ilm. Ilmu Komput.,* vol. 13, no. 1, p. 43, 2018, doi: 10.30872/jim.v13i1.1007.

[16] H. Ardiansyah and M. B. S. Junianto, "Penerapan Algoritma Genetika untuk Penjadwalan Mata Pelajaran," *J. Media Inform. Budidarma*, vol. 6, no. 1, p. 329, 2022, doi: 10.30865/mib.v6i1.3418.

[17] D. Wahyuningsih and E. Helmud, "Penerapan Algoritma Genetika Untuk Optimasi Penjadwalan pada MTS Negeri 1 Pangkalpinang," *J. Sisfokom (Sistem Inf. dan Komputer)*, vol. 9, no. 3, pp. 435–441, 2020, doi: 10.32736/sisfokom.v9i3.994.

[18] E. D. M.Kom., "Performance Algoritma Genetika (Ga) Pada Penjadwalan Mata Pelajaran," *InfoTekJar (Jurnal Nas. Inform. dan Teknol. Jaringan),* vol. 1, no. 1, pp. 56–60, 2016, doi: 10.30743/infotekjar.v1i1.42.

[19] I. Machali, *Metode Penelitian Kuantitatif*, no. April. 2021. [Online]. Available: https://digilib.uin-suka.ac.id/id/eprint/50344/1/Metode Penelitian Kuantitatif %28Panduan Praktis Merencanakan%2C Melaksa.pdf

Attendance Detection System Using Bluetooth Low Energy Based on ESP32 with Realtime Monitoring Through Website

Yusri Alfiyya
Dept. Electronic Engineering
Faculty of Engineering
Universitas Negeri Jakarta
Jakarta, Indonesia
alfiyyayusri@gmail.com

Aodah Diamah
Dept. Electronic Engineering
Faculty of Engineering
Universitas Negeri Jakarta
Jakarta, Indonesia
adiamah@unj.ac.id

Efri Sandi
Dept. Electronic Engineering
Faculty of Engineering
Universitas Negeri Jakarta
Jakarta, Indonesia
efri.sandi@unj.ac.id

***Abstract*—Manual attendance recording is susceptible to issues like data manipulation and human error. In such systems, employees fill out attendance sheets or books, and managers oversee their accuracy. To address these problems, there have been numerous proposed systems to automate the attendance detection systems that are based on biometric devices, RFID cards, face recognition, mobile applications among other technologies. Moreover, using fingerprint for attendance system will make a long queue and the hygiene cannot be guaranteed. In this study, we developed an automatic and contactless attendance detection utilizing Bluetooth Low Energy (BLE) features with the ESP32 to create an iBeacon. In addition to facilitate real-time attendance recording and monitoring, we are using a website with Message Queuing Telemetry Transport (MQTT) as standard messaging protocol for the Internet of Things (IoT). The system includes two types of devices: the first type is a beacon, carried by each individual and equipped with an AS608 optical fingerprint sensor for biometric authentication, and the second type receives and reads broadcast messages from the beacon, sending them to a web server using XAMPP localhost. Test results indicate that the system can detect individual employee presence up to 4 meters and display the attendance detection result through a website.**

***Index Terms*—Attendance Detection, Bluetooth Low Energy (BLE), ESP32, iBeacon, Fingerprint, MQTT, XAMPP**

I. Introduction

To report on the development of a company accurately, recording employee attendance is essential as it provides valid evidence of their presence. This can be done manually using paper-based methods, which require ongoing human supervision, or with attendance recording machines such as smart cards, fingerprints, smartphones, and facial recognition. However, manual methods are prone to issues like data manipulation and human error. According to Joshi et al. [1] , manual systems are time-consuming and challenging to monitor. They are not only require paper but also additional staff to verify the attendance and timings of employees, leading to overhead costs for organizations. Therefore, by taking advantage of technology, it is possible to decrease all complexity of manual attendance system with automatic attendance system such as using biometric devices, RFID cards, face recognition, mobile applications, etc [2]–[5]

979-8-3315-1921-6/24/$31.00 ©2024 IEEE

Automatic attendance system based on biometric fingerprint [2] is he most dependable technique for biometric recognition algorithms based on attendance systems is fingerprint recognition, which consists of sensing, feature extraction, and matching modules [6]. However using fingerprint as main attendance detection requires to put each finger in the same fingerprint sensor, so the hygiene cannot be guaranteed. Moreover it is requires queuing in a straight line so crowded queuing is inevitable.

Currently, automatic attendance detection system using energy-efficient Bluetooth-enabled device communication has been developed. Bluetooth technology was designed to facilitate short-distance connections between mobile devices and computers, standardized by the IEEE 802.15 working group as part of the Wireless Personal Area Network (WPAN) standard [7]. According to Townsend et al. [8], the Bluetooth 4.0 Core Specification includes Bluetooth Low Energy (BLE), also known as Bluetooth Smart. Although BLE might seem like a smaller, optimized version of classic Bluetooth, they have distinct histories and design goals. In this research, BLE is used because it is a component of iBeacon. A device that implements iBeacon functionality broadcasts BLE advertising packets with the following four values included with proximity UUID (universally unique identifier) parameters and major and minor RSSI values, can be functioning similarly to fingerprints and cards for identifying individuals nearby. Pušnik et al. [9], note that BLE is starting to replace RFID and Wi-Fi-based systems for indoor positioning by offering a fully wireless, autonomous hardware solution. The ESP32 supports both classic Bluetooth and BLE [10].

Communication between devices using BLE can be used for automatic employee attendance detection tool. The client device detects attendance through a nearby live server device and it's allows to implement contactless attendance detection

mechanism. Prafanto et al. [11], conducted research showing that BLE, an iBeacon component, can detect the presence of individuals, effectively replacing fingerprints and RFID cards. Individual presence is identified using the Bluetooth Device Address (BD_ADDR) of a registered smartwatch or gadget within the ESP32, based on the Receive Signal Strength Indicator (RSSI) value range programmed into the ESP32. However, this research does not fit the purpose that used to be because recently, smart watches on the market are using a random address on it Bluetooth address type. Moreover, the Bluetooth address cannot be registered anymore in the ESP32 because the address will change many times. Mangroliya et al. [12], also explored the use of BLE on ESP32 for electronic attendance, implementing two types of devices: BLE ID Cards as electronic ID cards and BLE scanners to locate these cards within a certain range. Their system can detect attendance by extracting student names and roll numbers that linked to the UUID (universally unique identifier) and sending this information to a database. The disadvantage of this research is lack of security such as the electronic card might use by other that is not authorized or entrusted to someone else. Lapointe et al. [13], developed a prototype using BLE and Raspberry Pi Zero W to track and identify people in multi-occupant settings, dividing the system into data management, real-time BLE RSSI-based positioning, and associating BLE devices with motion detection using passive infrared (PIR) sensors. Data from binary motion detection by PIR sensors and BLE packet advertisements received by Raspberry Pi Zero W are transmitted to a central computing unit for data collection and processing. In this research, BLE combined with PIR sensor able to identify person with two conditions like tracking device needs to detect motion and BLE RSSI in wearable BLE device.

This paper offers the following ways to improve utilize of Bluetooth low energy in attendance detection as follows:

- To confirm that iBeacon component can be used to identifying person like fingerprint or ID's card.
- Our research provides attendance detection system with portable fingerprint device and allow person to mark their attendance contactless and in place with random positions within a 4-meter range limit.
- The Internet of Things (IoT) has enabled direct integration of the physical world with computer-based systems via sensors and the internet, improving accuracy, efficiency, and economic value while reducing human involvement [14]. IoT connects various hardware through the internet to collect data in real-time, automatically filter and process it, and then send the data to and from the cloud. Implementing IoT in this research, we designed a website as an interface to store and process attendance data and display its real-time attendance data from the ESP32 and the data also can be downloaded to be used in preparing the report.

II. Design and Method

The automatic attendance detection was designed utilizing the following components: the ESP32 microcontroller, HC-SR501 PIR module, AS608 optical fingerprint sensor, I2C LCD, 18650 Li-Ion battery, TP4056 charging module, MT3068 DC to DC step-up converter module, XAMPP localhost, and the MQTT message protocol using the NodeJS library.

In this study, we use two types of devices, both leveraging Bluetooth Low Energy features supported by the ESP32 to create an iBeacon. The first type is a beacon device owned by each individual, equipped with an AS608 optical fingerprint sensor for biometric authentication, functioning as a BLE ID device. The second type is a scanning device that receives and reads broadcast messages from the beacon and sends them to the web server using XAMPP localhost with MQTT as the message protocol. This procedure allows the results of employee attendance detection to be displayed on a website. The block diagrams of the BLE ID device and the scanning device are shown in Fig. 1 and Fig. 2

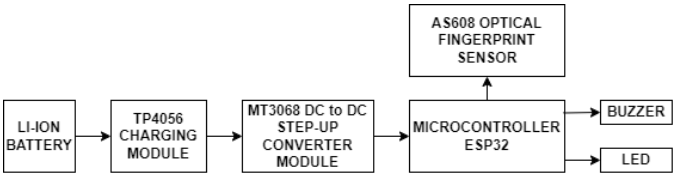

Fig. 1: Block Diagram of BLE ID Device

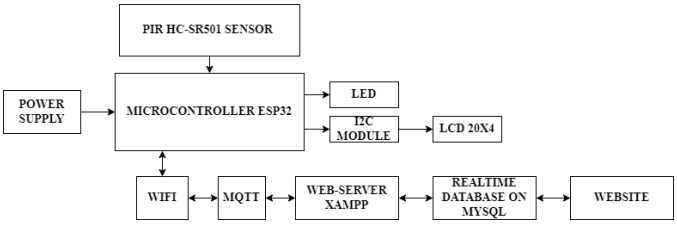

Fig. 2: Block Diagram of Scanning Device

For the system to detect attendance, individuals with registered fingerprints on their BLE ID devices must be within the detection range of the PIR sensor. When a registered fingerprint is matched, the BLE ID device begins advertising its packet, enabling communication with the scanning device. In this process, the advertising packet acts as the person's identity and broadcasts a message that the scanning device must detect. This allows attendance information to be stored in the cloud. The operation of the BLE ID device and Scanning Device is illustrated in Fig. 3 and Fig.4

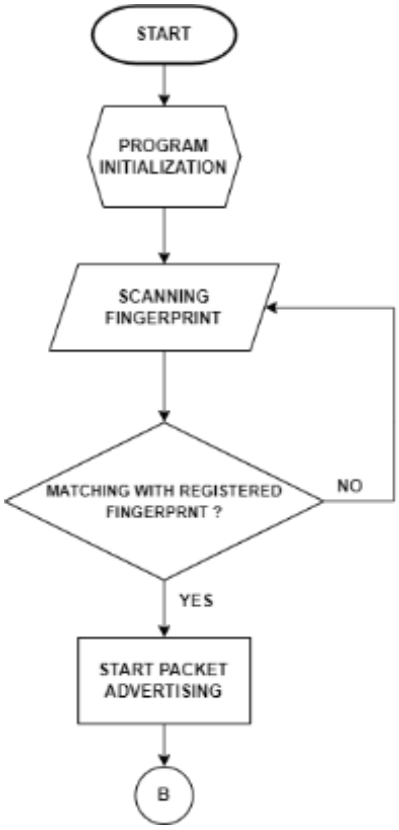

Fig. 3: Flowchart of BLE ID Device

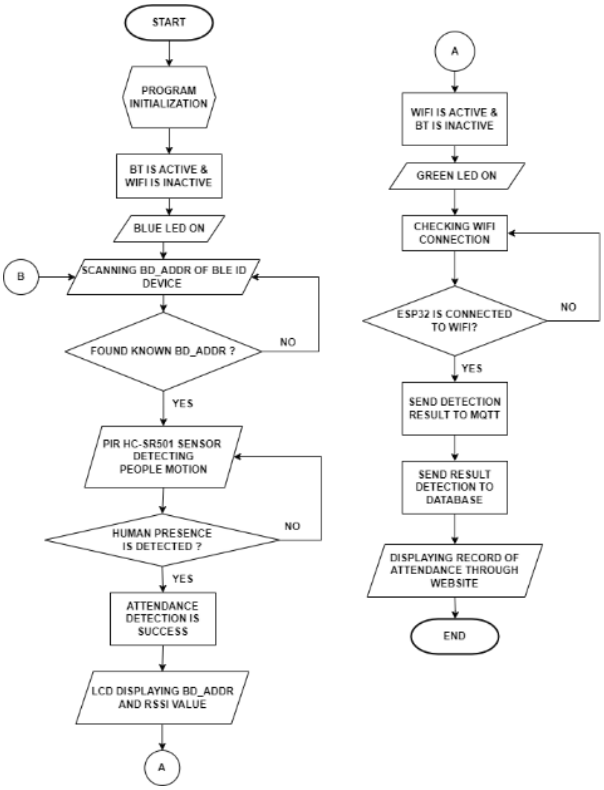

Fig. 4: Flowchart of Scanning Device

III. Experimental Results and Discussion

The testing of the scanner device was conducted to assess its ability to scan and detect the registered BD_ADDR of the beacon within the maximum detection range of the PIR sensor. The scanning device was programmed to receive advertising packets from the BLE ID device, with the received signal strength indicator (RSSI) set to -83 dBm. This value was chosen based on the HC-SR501 PIR sensor datasheet, which specifies a maximum detection range of 6 meters. Manual calculations were used to adjust the RSSI detection range to match the 6-meter range of the HC-SR501 PIR sensor, resulting in the use of -83 dBm, equivalent to a distance of 5.99 meters. The equation for determining the distance from the RSSI value [14], as in:

$$d = 10^{\frac{\text{RSSI}+55}{-36}} \quad (1)$$

The test results of the scanning device are shown in TABLE I.

TABLE I: THE TEST RESULTS OF THE SCANNING DEVICE

Real Distance of Object (m)	Readable RSSI value displayed on LCD I2C 20x4 (dBm)	Distance Estimation Result by Manual Calculation (m)	Individuals Detected by PIR Sensor	
			Yes	**No**
0.5	-56	1.0660	✓	
1	-57	1.1364	✓	
2	-67	2.1344	✓	
3	-76	3.83		✓
4	-65	1.8957	✓	
5	-79	4.6415		✓
6	-81	5.2749		✓

The results of the Scanner Device Testing at a Range of -83 dBm can be seen that the level of RSSI detection value reaches -81 dBm. The whole system can only detect the presence of employees with active BLE ID devices up to a distance of 4 meters from the real object. Comparing to the previous research conducted by Prafanto et.al [11] which sets the cutoff limit at -100 dBm can detect person until 45m while ours at -83 dBm can only detect person until 4m. This difference is due to the addition of individual detection conditions using a PIR motion sensor, which PIR motion sensor sensor can only detect the motion of people around it within a range of 6 meters. In the tests that have been carried out, the detection of RSSI values by the scanning device of the BLE ID device shows the accuracy of detection at a distance of 1 meter. The difference between the read RSSI value and the one calculated manually can be caused by environmental conditions, the direction of the device antenna and other physical obstacles. The graph of the difference between the real object distance and the estimated distance of the calculation results against the RSSI detection value is shown in Fig. 5.

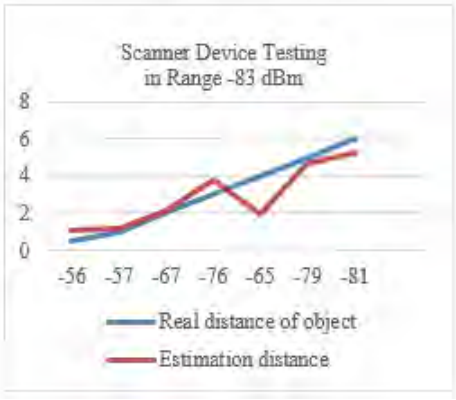

Fig. 5: Graph of the difference between the real object distance and the estimated distance of the calculation results against the RSSI detection value

The scanning device is shown in Fig. 6.

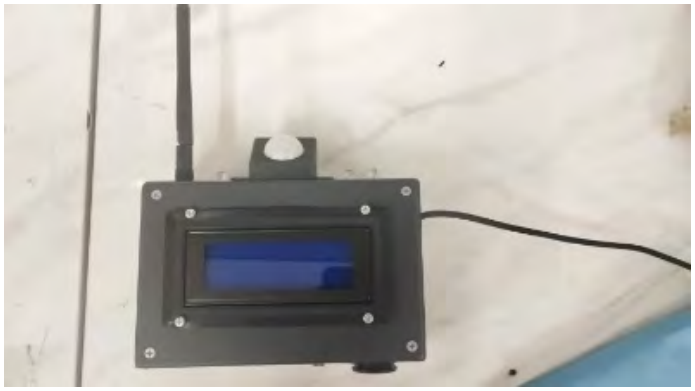

(a)

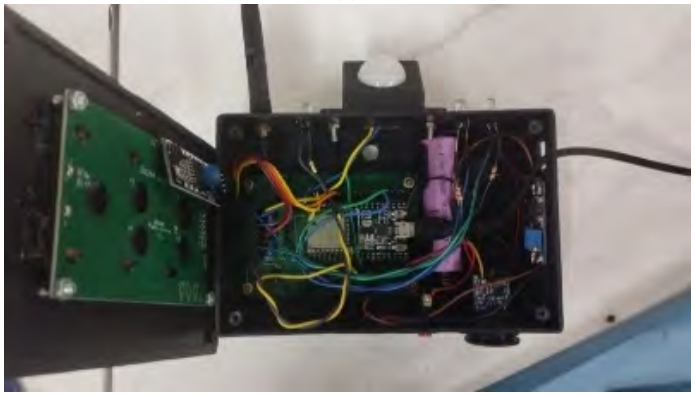

(b)

Fig. 6: The Scanning Device

As for the BLE ID device, we had 6 BLE ID devices for testing. For each one, a unique fingerprint is registered to activate the BLE ID then able to communicate with the scanning device as explained before in the design and method. Each BLE ID device can only be used by individuals whose fingerprints are registered in the AS608 optical fingerprint memory's device. Therefore all the BLE ID devices were tested to see if only the registered fingerprint can enable the BLE ID to advertise its advertising packet so that they can be found and communicated to the scanning device. The results of testing the BLE ID devices are shown in TABLE II - TABLE. VII.

TABLE II: RESULT OF TESTING BLE ID 1

Finger-prints	Enrolled Fingerprints		Voltage Value Read by Multimeter (Vdc)		Start BLE Data Advertising	
	Yes	No	Buzzer	LED	Yes	No
Employee 1	✓		0 V	3.19 V	✓	
Employee 2		✓	3 V	0 V		✓
Employee 3		✓	3 V	0 V		✓
Employee 4		✓	3.1 V	0 V		✓
Employee 5		✓	3 V	0 V		✓
Employee 6		✓	3 V	0 V		✓

TABLE III: RESULT OF TESTING BLE ID 2

Finger-prints	Enrolled Fingerprints		Voltage Value Read by Multimeter (Vdc)		Start BLE Data Advertising	
	Yes	No	Buzzer	LED	Yes	No
Employee 1		✓	2.98 V	0 V		✓
Employee 2	✓		0 V	3.17 V	✓	
Employee 3		✓	2.98 V	0 V		✓
Employee 4		✓	2.98 V	0 V		✓
Employee 5		✓	2.98 V	0 V		✓
Employee 6		✓	2.98 V	0 V		✓

TABLE IV: RESULT OF TESTING BLE ID 3

Finger-prints	Enrolled Fingerprints		Voltage Value Read by Multimeter (Vdc)		Start BLE Data Advertising	
	Yes	No	Buzzer	LED	Yes	No
Employee 1		✓	2.98 V	0 V		✓
Employee 2		✓	2.98 V	0 V		✓
Employee 3	✓		0 V	3.18 V	✓	
Employee 4		✓	2.98 V	0 V		✓
Employee 5		✓	2.98 V	0 V		✓
Employee 6		✓	2.98 V	0 V		✓

TABLE V: RESULT OF TESTING BLE ID 4

Finger-prints	Enrolled Fingerprints		Voltage Value Read by Multimeter (Vdc)		Start BLE Data Advertising	
	Yes	No	Buzzer	LED	Yes	No
Employee 1		✓	2.73 V	0 V		✓
Employee 2		✓	2.73 V	0 V		✓
Employee 3		✓	2.73 V	0 V		✓
Employee 4	✓		0 V	3.22 V	✓	
Employee 5		✓	2.73 V	0 V		✓
Employee 6		✓	2.73 V	0 V		✓

TABLE II - TABLE VII shows that each BLE ID device can only be used by individual employees based on the fingerprint registered in the memory of the BLE ID device. In addition, the results of BLE ID Testing are fully able to complement the

TABLE VI: RESULT OF TESTING BLE ID 5

Finger-prints	Enrolled Fingerprints		Voltage Value Read by Multimeter (Vdc)		Start BLE Data Advertising	
	Yes	No	Buzzer	LED	Yes	No
Employee 1		✓	2.98 V	0 V		✓
Employee 2		✓	2.98 V	0 V		✓
Employee 3		✓	2.98 V	0 V		✓
Employee 4		✓	2.98 V	0 V		✓
Employee 5	✓		0 V	3.18 V	✓	
Employee 6		✓	2.98 V	0 V		✓

TABLE VII: RESULT OF TESTING BLE ID 6

Finger-prints	Enrolled Fingerprints		Voltage Value Read by Multimeter (Vdc)		Start BLE Data Advertising	
	Yes	No	Buzzer	LED	Yes	No
Employee 1		✓	3 V	0 V		✓
Employee 2		✓	3 V	0 V		✓
Employee 3		✓	3 V	0 V		✓
Employee 4		✓	3 V	0 V		✓
Employee 5		✓	3 V	0 V		✓
Employee 6	✓		0 V	3,19 V	✓	

lack of functionality on its security in the research conducted by Mangroliya et.al [12]. The buzzer and led outputs can function according to the commands set on the program so that individuals can ensure that their devices can start advertising Bluetooth packets to be detected by the scanner device.

The BLE ID device is shown in Fig. 7

Fig. 7: The BLE ID Device

Website testing is done to find out whether the hardware has been integrated with the website properly or not by displaying information about the registered person's attendance based on name, device address, and attendance time. The results of the website testing are shown in Fig. 8 – Fig. 13.

The overall testing, calculation, and measuring results show that the system functions as intended in detection attendance. It ensures that only registered fingerprints can activate the BLE ID device and detects attendance only for known (BD_ADDR) that can be identified by the scanning device.

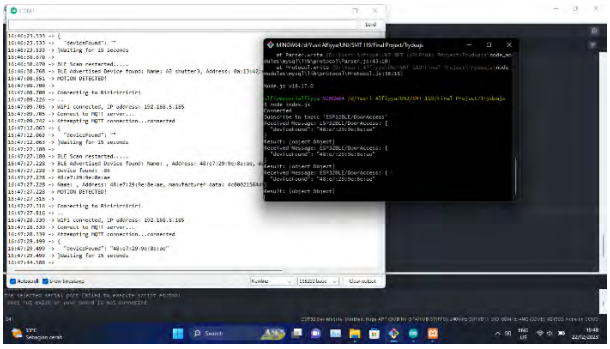

Fig. 8: System Connected with MQTT

Fig. 9: Dashboard Page

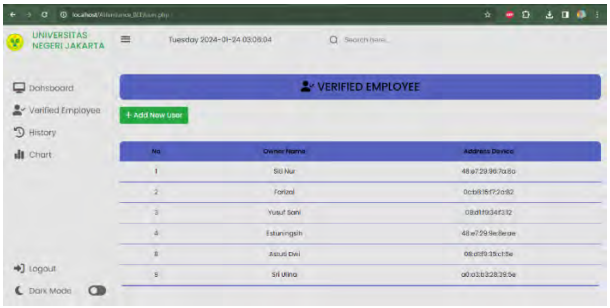

Fig. 10: Verified Employee Page

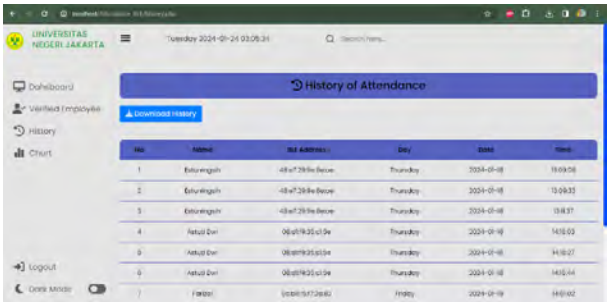

Fig. 11: History Page

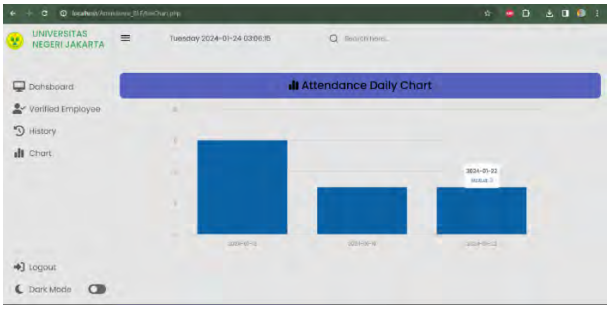

Fig. 12: Chart Page

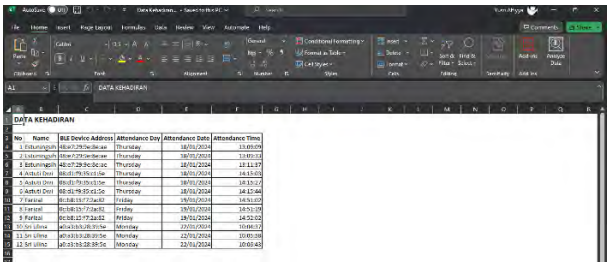

Fig. 13: Result of Download Attendance Data Log from Website

IV. Conclusion

The employee attendance detection system is designed using the ESP32 microcontroller as the main control system. Utilizing the Bluetooth Low Energy feature on the ESP32, the system can detect individual presence and recognize employees/system users based on scanned advertising packets matched in the program. The HC-SR501 PIR sensor is incorporated to detect the motion of individual employees within a detection range of up to 4 meters. It is prove that attendance detection can be done contactless. As for the detection angle of 120 degrees in PIR motion sensor does not requires person to mark their attendance in a straight line to the receiver. The AS608 fingerprint sensor handles biometric authentication, identifying and verifying the owner of the BLE ID device to validate whether the advertising packet should be started, allowing the BLE address to be detected and recorded as a form of employee presence.

Test results indicate that the system can detect individual employee attendance up to 4 meters. The integrated 20x4 LCD with I2C module serves as an output, providing employees with detection status. Additionally, website testing confirms that the implementation of the website as an Internet of Things (IoT) interface, using MQTT as a standard messaging protocol, functions effectively to monitor the employee attendance detection system.

Although an indoor environment can be a good testing ground to show ability Bluetooth range detect, our research did not include testing in an outdoor environment or with many Bluetooth signal sources (like a crowded entry point building) where these effects are amplified. Moreover, this research did not provide web monitoring for employee to make sure their detection attendance is actually sent to the cloud. This evaluation can be part of an extension of this work.

References

[1] J. A. Dargham, A. Chekima, E. G. Moung, H. T. Wong, and S. K. Chung, "Estimating the Number of Cameras Required for a Given Classroom for Face-based Smart Attendance System," *2020 IEEE 2nd International Conference on Artificial Intelligence in Engineering and Technology (IICAIET)*, 2020, pp. 1–5. doi: 10.1109/IICAIET49801.2020.9257817.

[2] B. Swain, J. Halder, S. Sahany, P. P. Nayak, and S. Bhuyan, "Automated Wireless Biometric Fingerprint Based Student Attendance System," *2021 1st Odisha International Conference on Electrical Power Engineering, Communication and Computing Technology (ODICON)*, 2021, pp. 1–7. doi: 10.1109/ODICON50556.2021.9428983.

[3] U. Koppikar, S. Hiremath, A. Shiralkar, A. Rajoor, and V. P. Baligar, "IoT based Smart Attendance Monitoring System using RFID," *2019 1st International Conference on Advances in Information Technology (ICAIT)*, 2019, pp. 193–197. doi: 10.1109/ICAIT47043.2019.8987263.

[4] N. Palanivel, S. Aswinkumar, and J. Balaji, "Automated Attendance Systems Using Face Recognition by K-Means Algorithms," *2019 IEEE International Conference on System, Computation, Automation and Networking (ICSCAN)*, 2019, pp. 1–8. doi:10.1109/ICSCAN.2019.8878790.

[5] A. Dankar and P. P. Kundapur, "Automated Mobile Attendance System (AMAS)," *2019 International Conference on Advances in Computing, Communication and Control (ICAC3)*, 2019, pp. 1–6. doi: 10.1109/ICAC347590.2019.9036787.

[6] V. D. Nguyen, H. Van Khoa, T. N. Kieu, and E. N. Huh, "Internet of Things-Based Intelligent Attendance System: Framework, Practice Implementation, and Application," *Electronics (Switzerland)*, vol. 11, no. 19, Oct. 2022, doi: 10.3390/electronics11193151.

[7] M. Usama, *Building Bluetooth Low Energy Systems*. Packt Publishing, 2017.

[8] K. Townsend, C. Cufí, Akiba, and R. Davidson, *Getting Started with Bluetooth Low Energy: Tools and Techniques for Low-Power Networking*. O'Reilly Media, 2014.

[9] M. Pušnik, M. Galun, and B. Šumak, "Improved Bluetooth Low Energy Sensor Detection for Indoor Localization Services," *Sensors (Switzerland)*, vol. 20, no. 8, 2020, doi: 10.3390/s20082336.

[10] Espressif Systems, "ESP32 Bluetooth Architecture," 2019.

[11] A. Prafanto, E. Budiman, P. P. Widagdo, G. M. Putra, and R. Wardhana, "Pendeteksi Kehadiran Menggunakan ESP32 untuk Sistem Pengunci Pintu Otomatis," *Jurnal Teknologi Terapan (JTT)*, vol. 7, no. 1, p. 37, 2021, doi: 10.31884/jtt.v7i1.318.

[12] V. Mangroliya, P. Singh, and S. Ram, "Contactless E-Attendance for Organization," vol. 32, no. 04, pp. 1247–1251, 2022.

[13] P. Lapointe, K. Chapron, K. Bouchard, and S. Gaboury, "A New Device to Track and Identify People in a Multi-Residents Context," *Procedia Computer Science*, Elsevier B.V., 2020, pp. 403–410. doi: 10.1016/j.procs.2020.03.082.

[14] M. Ivanić and I. Mezei, "Distance Estimation Based on RSSI Improvements of Orientation Aware Nodes," *2018 Zooming Innovation in Consumer Technologies Conference (ZINC)*, 2018, pp. 140–143. doi: 10.1109/ZINC.2018.8448660.

Overview of Pumped Storage Hydropower Systems and Their Potential Utilization in Indonesia

Tyas Kartika Sari
Electrical Engineering Department
Universitas Trisakti
Jakarta, Indonesia
tyas.kartika@trisakti.ac.id

Fariz Maulana Rizanulhaq
Research Center for Energy Conversion and Conservation
National Research and Innovation Agency
Jakarta, Indonesia
fari012@brin.go.id

Dianing Novita Nurmala Putri
Electrical Engineering Department
Universitas Trisakti
Jakarta, Indonesia

Chairul Gagarin Irianto
Electrical Engineering Department
Universitas Trisakti
Jakarta, Indonesia

Maulasukma Widjaja
Electrical Engineering Department
Universitas Trisakti
Jakarta, Indonesia

***Abstract*—The increasing demand of sustainable energy sources as well as intermitten of power generation from renewable energy sources, energy storage system will become the most important system to ensure grid stability and reliability. Indonesia has abundant of renewable energy sources, i.e solar energy, wind energy, geothermal energy and hydro energy. Recently renewable energy harnessing in Indonesia is encouraged to meet energy mix target 23% in 2025 and replace fossil energy. Based on Indonesia Outlook Energy Book, in 2023 the total capacity of power generation in Indonesia is about 83,8 GW, almost 50% still use coal energy meanwhile RES in energy mix around 15%. Indonesia has commited on paris agreement which is related to climate change problem solving in order to reduce green house gas emission. Indonesia also has target towards net zero emission in 2050. Therefore, renewable energy harnessing must be boosted. The abundance of renewable energy sources made Indonesia use renewable energy for the future energy particularly in power generation. One of the problems in renewable energy sources (RES) for power generation is intermittent, hence the energy storage systems are needed to secure the electricity supply as well as grid stability and reliability. Indonesia has potential to develop pumped storage hydropower because of Indonesian location in the mountain and hill. Nowdays Indonesia first pumped storage hydropower system still builds in Upper Cisokan. Therefore, the study of energy storage systems is needed for sustainable energy sources in the future. This paper aims to analyze the principle and technology of Pumped Storage Hydropower (PSH), evaluate the potential as well as the simple simulation of harnessing PSH system in Indonesia.**

***Index Terms*—power generation, renewable energy, storage system, intermittent, PSH**

I. Introduction

The use of RES to replace fossil energy in power generation will be the future trend of the power industry. Nowdays, power generation installed capacity in Indonesia is dominated by fossil energy as shown in Fig. 1 power generation installed capacity in Indonesia 2013 - 2022. Power generation installed capacity in Indonesia is about 83,8 GW, almost 50% still uses coal energy, 25% uses gas meanwhile only 15% uses renewable energy sources.

979-8-3315-1921-6/24/$31.00 ©2024 IEEE

Fig. 1. Overview of the measurement device setup.

Practically Indonesia has abundant solar energy potential based on Indonesia Energy Outlook Report 2023 [1]. The potentiaal of RES in Indonesia is shown in Table 1 below.

The worldwide energy sector is undergoing substantial changes as societies shift to more sustainable and low emission energy systems.The change is driven by growing awareness of increasing climate change mitigation, reducing fossil energy and energy security [2]. The growth of renewable energy such as solar and wind becomes the center of transition energy. However, these energy sources are intermittent because of dependence on nature. Therefore, providing sustainable in electricity energy and stability grid electricity become more challenging, hence energy storage system development is needed particulary for large scale capacity in power generation [3], [4]. In public transportation, it can be used battery for energy storage system, but for power generation needed large scale capacity energy storage system. PSH system will become the best choice since the mature technology of PSH system compared to other energy storage technologies.

TABLE I
RES POTENTIAL IN INDONESIA AND POWER GENERATION INSTALLED CAPACITY FROM RES

RES	Potential Total (GW)	Installed Capacity (GW)	% of Installed Capacity
Ocean	63	-	-
Geothermal	23	2.4	10.3%
Bioenergy	57	3.1	5.4%
Wind	155	0.2	0.1%
Hydro	95	6.7	7%
Solar	3.294	0.3	0.01%
Total	**3.687**	**12.6**	**0.3%**

This paper proposes PSH system harnessing as well as its development in Indonesia. Meanwhile this paper reviews literature study of the technology of pumped storage hydropower, the detail study about comparisons with other storage technologies such as battery or hydrogen will be discussed later. The following diagram for literature study can be shown in Fig. 2 below. From Fig.2 below, it can be explained how the literature study method in this research.

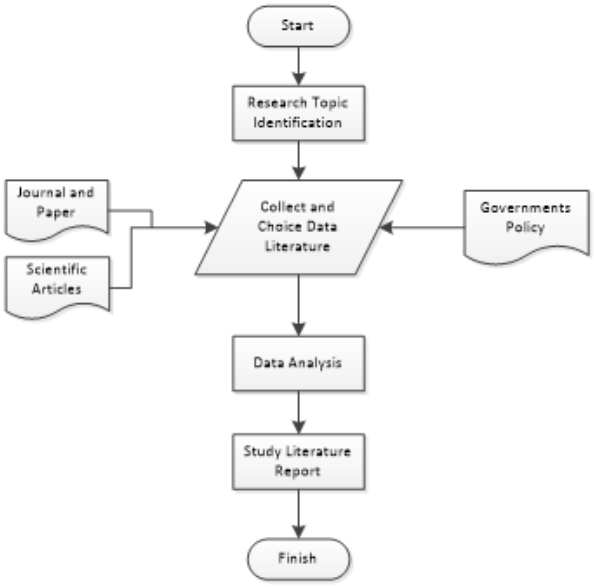

Fig. 2. Literature Study Flow Diagram.

In the future study will be focused on economic analysis of pumped storage hydropower especially in Indonesia and also detailed simulation about the operation of the system is needed.

Based on the paper which will be discussed below, there are describe about worldwide hydropower growth in over the world, type of energy storage system and how the integration of pumped storage hydropower incorporate with other RES, meanwhile the simulation for dynamic system will need to be detailed in future study.

II. WORLDWIDE HYDROPOWER GROWTH

In 2022, global hydropower capacity reached 1.330 GW and generate a total of 4.370 TWh of electricity energy. However, hydropower install capacity in Indonesia is relatively small, just only 6,7 GW. Fig. 3 Worldwide Hydropower Installed Capacity describes that China have a biggest hydropower install capacity in the world with 370,2 GW.

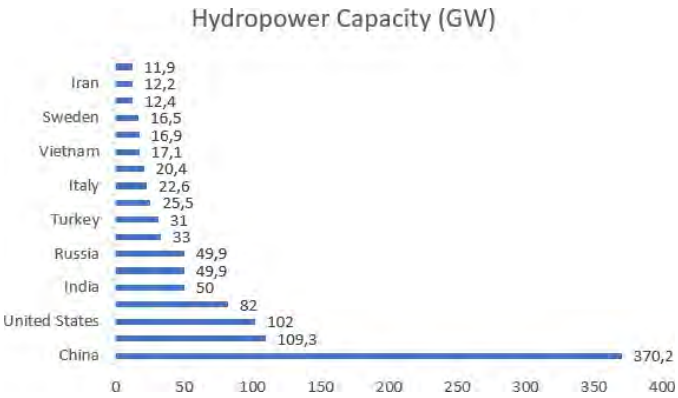

Fig. 3. Worldwide Hydropower Installed Capacity

In the end of 2020, several countries have finished hydropower construction project with the biggest hydropower installed capacity in China 12,7 GW, meanwhile Indonesia succeeded increasing hydropower installed capacity 236 MW.

Indonesia has a small hydropower installed capacity of 6,7 GW. For comparison, the global hydropower installed capacity reached 1.330 GW. From Table 1 above, Indonesia has relatively small renewable energy potential from ocean, geothermal, bioenergy, wind and hydro, however Indonesia has vast solar energy potential of 3.294 GW [5]. In the future Indonesia will rely mostly on solar energy for its sustainable energy needs. Therefore, Indonesia will need substantial energy storage systems for overnight and longer periods [6], [7].

Pumped storage hydropower system (PSH), in recent years, have represented 99% of the electricity storage capacity in the world, which makes them the most used mechanical energy storage systems. This paper also presents that Indonesia has huge potential for low cost off river PSH with low environmental and social impact, furthermore as a future renewable energy power generation from solar energy Indonesia need them to ensure the stability of electricity grid [8], [9].

III. ENERGY STORAGE SYSTEM TECHNOLOGIES

Energy storage systems can be classified into five major categories : mechanical systems, thermal system, chemical, electrochemical system and electrical storage technologies. Fig. 4 describes Energy Storage System Classification [10].

From Fig. 4, the PSH system was classified into mechanical storage systems. PSH stores excess electrical energy by harnessing the potential energy store in water. The growing need for energy storage systems globally will become a trend in the future since the power production from renewable energy is intermitten thus it needs reliable and mature energy storage systems. Hence, currently many countries focus on energy storage research and how a comparison of batteries and PSH system as energy storage systems with the integration of

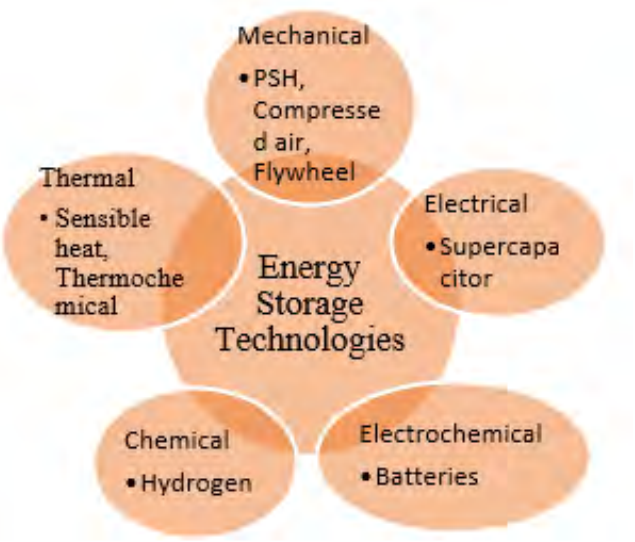

Fig. 4. Energy Storage Systems Classification

wind and solar PV energy sources, which are the major trend technologies in the renewable energy sector [11].

In recent years, there are ten countries which have constructed energy storage systems on pumped storage hydropower is the largest constructed as described in Fig. 5 Ten Countries with Large Energy Storage System. China was the country which have either the largest energy storage system capacity in the world or pumped storage hydropower system. Fig. 6 describes worldwide pumped storage hydropower installed capacity 2016 – 2023 [12].

Hydropower has the largest contribution among all RES. The increasing demand of energy and the transition toward clean energy have proposed new challenges, such as increased energy efficiency and storage. Energy storage systems are a critical area of research, which is required for integration of renewable energies [13].

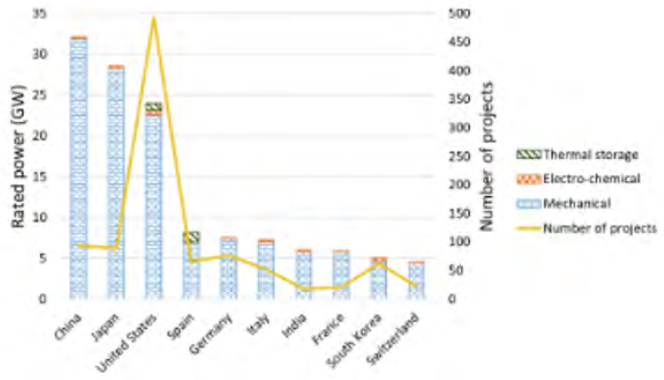

Fig. 5. Ten Countries with Large Energy Storage System

IV. Pumped Storage Hydropower

Pumped storage hydropower system (PSH) stock surplus electrical energy by utilizing the potential energy stored in water. Fig. 7 describes principle of pumped storage Pumped storage hydropower system (PSH) stock surplus electrical energy by utilizing the potential energy stored in water. Fig. 7 describes principle of pumped storage hydropower system, energy surplus from the system stored in water, in which excess energy is utilized to transfer water from lower artificial lakes to higher ones. Meanwhile, when electricity demand rises, water from higher artificial lakes is pumped through turbines connected to generators to generate electricity, effectively operating as a hydropower plant. Energy stored in Pumped Storage Hydropower (PSH) can be quickly released during periods of high demand, converting it into electrical energy [14]. PSH has the potential for balancing demand and supply from renewable energy power generation, levelling other generating units and ensuring security and reliability electricity grid.

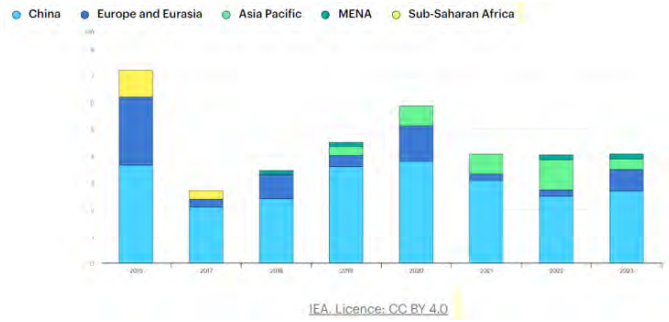

Fig. 6. Worldwide Pumped Storage Hydropower Installed Capacity 2016 - 2023

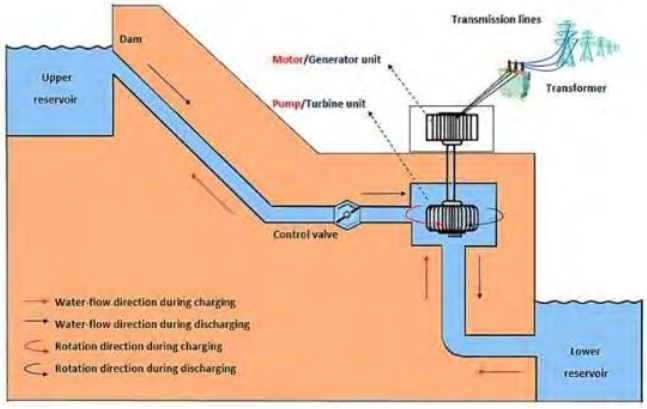

Fig. 7. Principle of Pumped Storage Hydropower

A. Characteristic of PSH Systems and Used of PSH

In recent years, numerous detailed studies have been conducted on energy storage systems, most of them concludes that PSH systems have seen wide opportunity for implementation because PSH systems have some advantages characteristics, including large scale capacity on storage systems and power capabilities, long term energy storage systems potential as well as operational efficiency [15].

PSH systems highlight technical characteristics which make them appropriate for the huge storage energy systems when there is surplus from renewable energy sources (RES). Nowdays PSH systems contribute to peak electricity generation, grid stability and ancillary services. They also aid in integrating variable renewable energy (VRE) by storing surplus energy produced during periods of low demand [16]. PSH systems have power capacity ranges from 10 to 4000 MW, level of technology readiness of 11/11 based on the International Energy Agency (IEA) guides as well as providing flexibility in system design. The duration of discharge for PSH system at rated power ranges between 1 to over 24 hours, with storage durations spanning hours to days. PSH systems have an efficiency of 70 – 85% and maintain effective energy storage. With the minimal reaction time, PSH systems adapt to fluctuating energy demands.

The technical characteristics of PSH systems listed below:

- Energy Storage
- Grid Stability
- Integration of VRE (Variable Renewable Energy)
- Load Balancing
- Low Environmental Impact and Long Lifespan

B. Integrated PSH systems with RES

Although renewable energy sources environmentally friendly but there are intermittent. This feature becomes a challenge for ensuring reliable power supply and grid stability, crucial aspects for delivering energy storage systems to end users [17].

Solar energy exhibits lower intermittency than wind energy due to fluctuations wind velocity as meteorological factors. This variability will impact directly on renewable energy power generation and consequently also impact the stability of the power grid [18]. Grid stability is crucial problem as growing rapidly renewable energy power generation. Fig.8 describes Curtailment Energy from Solar PV Energy.

The curtailment energy of solar PV caused by no integration with energy storage system, over supply and limited transmission grid on the dispatch electricity energy to other location which have peak load at the same time. As the more renewable energy connected on grid, the more over supply risk if there are no compatible energy storage systems. Consequently, the risk in curtailment on PV and wind energy actually no need but it will happen. Fig. 9 describes an example on curtailment PV and wind energy [19], [20].

V. Pumped Storage Hydropower Potential in Indonesia

Indonesia has set target net zero emission (NZE) by 2050 as Paris agreement related with climate change. If Indonesia depend on fossil energy continuously to supply electricity energy, it is difficult to reach the target NZE in 2050. Currently, the largest renewable energy power generation uses in Indonesia is solar PV energy.

In recent years, the Indonesian government has revised its estimates for renewable energy potential to 3.687 GW, with

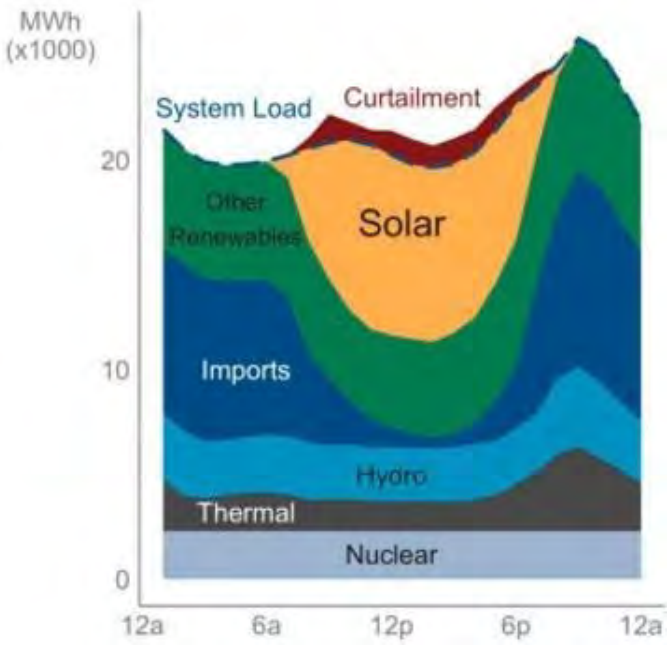

Fig. 8. Solar PV Energy Curtailment

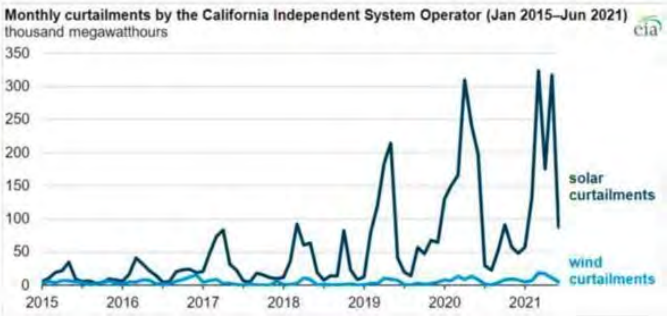

Fig. 9. Solar PV Energy Curtailment

3.294 GW from solar PV energy and 394 GW from wind, hydro, geothermal, ocean energy and bioenergy combined.

Power generation installed capacity in Indonesia is 75 GW, whereas potential solar PV energy total 3.294 GW. Thus, in the future renewable energy power generation will supply electricity energy needs. Indonesia, as the sole large tropical archipelago, has weather data indicating that it could potentially generate 180.000 TWh per year of solar electricity from its maritime regions over a period of 40 years. Therefore, Indonesia will need large scale energy storage systems for overnight and longer period to store excess energy from RES and integration VRE into energy storage systems. Nowdays Indonesia starts construct PSH system project in Upper Ciocan for the pilot energy storage systems project. In recent years underlining PSH systems and batteries is the leading technology of energy storage system for electrical energy. Pumped Storage Hydropower (PSH) makes up approximately 95% of global storage capacity and 99% of global storage energy. It is a well-established and widely deployed technology known for

its cost-effectiveness. The working fluid used in PSH, water, is much more abundant compared to the chemicals used in batteries.

Battery storage encompasses applications for homes, utilities and electric vehicles (EVs). The future deployment of EV batteries is expected to exceed that of home and utility batteries. Presently, the Pumped Storage Hydropower (PSH) system is more cost-effective than batteries for applications requiring overnight and longer-term storage. In the future, the cost of battery storage is expected to decrease, although there is significant uncertainty regarding future prices. If V2G (Vehicle to Grid) technology gains prominence, EV batteries could play a significant role in meeting future storage needs.

This is due to the scale of battery storage potential within an EV fleet is considerable and the cost of these batteries is largely offset by their primary purpose, which is mobility.

Indonesia has potential off river PSH system based on pumped hydro energy storage atlas was undertaken by The University of National Australian. Fig. 10 describes potential 150 GWh Greenfield off river pumped storage hydropower (PSH) sites in Indonesia.

Potential of PSH in Indonesia Based on Greenfield Data According to the global greenfield atlas, Indonesia has identified a total of 26.000 off-river PSH sites, with a combined energy storage capacity of 800 TWh. Currently, Indonesia has no PSH system caused by fossil energy still dominate in the harnessing of power generation. However, this is about changing. Indonesia has included 4000 MW off river PSH system in RUPTL or National Electricity Development Plan document. Table 2 below describes planning of PSH system in Indonesia.

Fig. 10. Potential of PSH in Indonesia Based on Greenfield Data

According to the global greenfield atlas, Indonesia has identified a total of 26.000 off-river PSH sites, with a combined energy storage capacity of 800 TWh. Currently, Indonesia has no PSH system caused by fossil energy still dominate in the harnessing of power generation. However, this is about changing.

Indonesia has included 4000 MW off river PSH system in RUPTL or National Electricity Development Plan document. Table 2 below describes planning of PSH system in Indonesia.

The electricity company state Indonesia (Perusahaan Listrik Negara) / PLN plan to develop 4 x 250 MW PSH systems in Sumatera, which are expected connect to grid PLN in 2029 – 2032.

TABLE II
PLANNING OF PSH SYSTEM IN INDONESIA

Location of PSH	Capacity (MW)	Operation Target
PSH Upper Cisokan, West Java	1,000	2025
PSH Avengeing, West Java	943	2028
PSH Grindle, East Java	1,000	2030

In the next chapter, it will estimate how many energies storage system which are required in 2050 as net zero emission (NZE) program from government. Underlining, in 2050 power generation in Indonesia will be covered by renewable energy from solar PV energy and wind energy. Indonesia located in Khalistan area so Indonesia has tropes season, the sun will radiate continuously over the year. Thus, seasonal energy storage system is not really needed because Indonesia don't have summer and winter season. This paper proposes PSH system should be used for weekly energy storage system for balancing over night and day period. It is estimated energy storage system requirement to sustain 100% renewable energy power generation in the country which have low latitudes as Indonesia also located, is shown in Table III estimation energy storage system in some country and Annual Demand (TWh).

TABLE III
ESTIMATION ENERGY STORAGE SYSTEM IN SOME COUNTRY

Author	Blakers et) al., (2017)	Lu et al., (2021)	Lu et al., (2021)	Cheng et al., (2021)
Studied country	Australia	Australia	Southeast Asia	Japan
Scope of Study	Electricity	Energy	Electricity	Electricity
Annual Demand (TWh)	205	393	7524	896

Country	Energy Storage (GWh)-min/max	Estimated required storage (day)
Australia	407 - 574	0.7 - 1.0
Australia	321 - 2049	0.9 - 1.3
Southeast Asia	15,506 - 44,707	0.8 - 2.2
Japan	2069 - 13,750	0.8 - 5.6

By following the rule of thumb of this one-day storage system, Indonesia, which is carbon-free, prosperous and has a developed industry, by 2050 will consume 9,000 TWh of renewable electricity per year. This amount was obtained with the assumption that currently electrical energy consumption in Indonesia is 300 TWh per year. If it is assumed that the annual increase in electrical energy consumption is 300 TWh, then in 2050 or 30 years from now, the estimated electrical energy consumption will increase 30 times greater. from this year or around 9000 TWh. This assumption is based on the upper limit calculation and assumes population growth of 335 million. Assuming this data, energy storage of 25 TWh (75 kWh per person) and a power storage capacity of 1000 GW are needed.

A. PSH System Operation Mode

1) Open Loop Pumped Storage Hydropower: According to the Department of Energy in USA, Open Loop PSH is defined as a system that is continuously connected to natural water flow. Open loop PHS systems involve the movement of significant volumes of water between upper and lower reservoirs. This primary advantage lies in leveraging existing water resources and infrastructure, minimizing the requirement for extensive land use and construction. However, these systems can pose environmental challenges, affecting water quality, aquatic habitats and local ecosystems. Moreover, their operation depends on water availability and may be impacted by seasonal fluctuations and droughts. When the lower artificial lakes are an existing dam, the power plant can be situated downstream, eliminating the need for excavation.

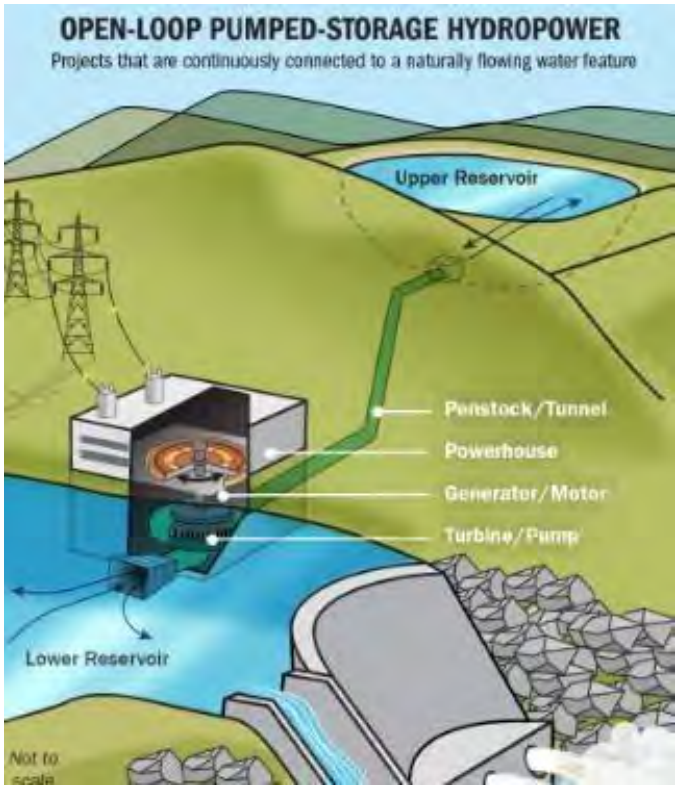

Fig. 11. Open Loop Pumped Storage Hydropower

2) Closed Loop Pumped Storage Hydropower: According to the USA's Department of Energy definition, a closed-loop PSH "is not constantly linked to a naturally flowing water feature. Thus, typically, a closed-loop PHS system includes upper and lower reservoirs located away from major water sources, with limited water input. However, the term continuous is crucial in this definition since some PSH projects are classified as closed systems despite initially using water from natural flowing surface water features to fill their reservoirs and periodically replace losses from evaporation and seepage. Closed-loop systems cause less environmental disruption than open-loop systems by reducing water consumption and avoiding disruption to natural water bodies. Additionally, these systems can also be situated in regions where open loop systems may not be viable due to limited water resources. However, closed-loop systems necessitate significant upfront investment in reservoir construction and water supply, potentially reducing their cost- effectiveness compared to open-loop systems. This system can be utilized in small artificial lakes filled by rainfall or water transported from various locations.

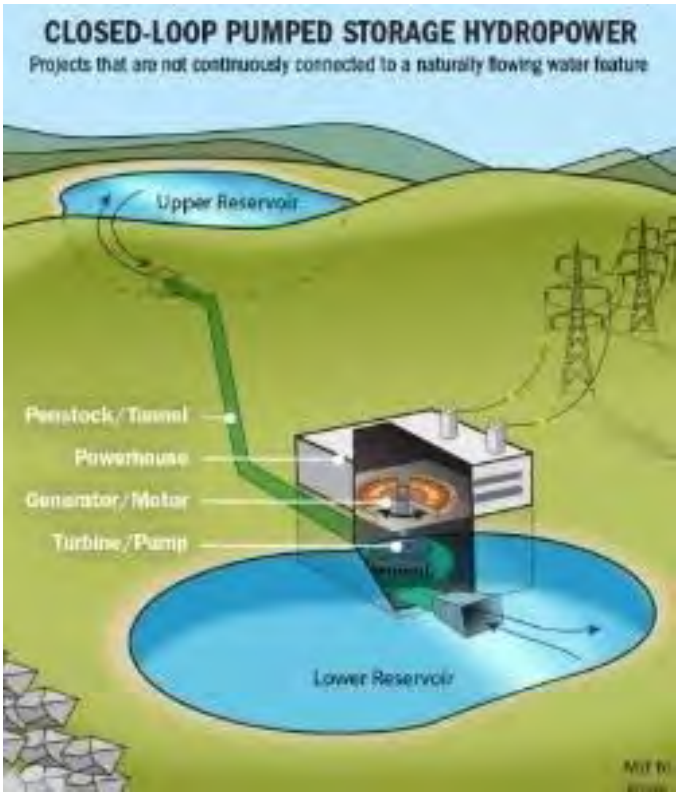

Fig. 12. Closed Loop Pumped Storage Hydropower

VI. Conclusions

The temporary conclusion that can be obtained from this literature review is that in short, PSH (Pumped Storage Hydropower) systems provide a range of distinct benefits that gain importance a renewable energy sources are adopted more widely. Through offering essential services such as frequency regulation, voltage support, load shifting and enhancing system resilience, PSH systems bolster the stability and dependability of today's electrical grid. Its fast response time, flexibility and ability to seamlessly integrate with renewable energy sources make it a critical part in the energy system of the future. Meanwhile, the future study is needed for more detail simulation with actual data in Indonesia, how the harnessing and efficiency of this system must be clarified with the actual condition in Indonesia.

References

[1] Dewan Energi Nasional, "OUTLOOK ENERGI INDONESIA 2023," DKI Jakarta, 2023.

[2] P. C. Nikolaos, F. Marios, and K. Dimitris, "A Review of Pumped Hydro Storage Systems," *Energies*, vol. 16, no. 11. MDPI, Jun. 01, 2023. doi: 10.3390/en16114516.
[3] C. Ringler, A. Bhaduri, and R. Lawford, "The nexus across water, energy, land and food (WELF): potential for improved resource use efficiency?" *Environmental Sustainability*, vol. 5, no. 6, pp. 617–624, Dec. 2013, Accessed: Apr. 20, 2024. [Online]. Available: https://doi.org/10.1016/j.cosust.2013.11.002
[4] D. Griggs et al., "Sustainable development goals for people and planet," 2013. [Online]. Available: www.cbd.int/sp/
[5] H. D. Puspitarini, F. Tumiwa, M. Citraningrum, P. Simamora, and D. Arinaldo, "Beyond 443 GW. Indonesia's infinite renewable energy potential," 2021.
[6] H. Ardiansyah, "Hydropower Technology: Potential, Challenges, and the Future," in *Indonesia Post-Pandemic Outlook: Strategy towards Net-Zero Emissions by 2060 from the Renewables and Carbon-Neutral Energy Perspectives*, Penerbit BRIN, 2022. doi: 10.55981/brin.562.c6.
[7] A. Taufiqurrahman and J. Windarta, "Overview Potensi dan Perkembangan Pemanfaatan Energi Air di Indonesia," *Jurnal Energi Baru dan Terbarukan*, vol. 1, no. 3, pp. 124–132, Oct. 2020, doi: 10.14710/jebt.2020.10036.
[8] D. F. Silalahi, A. Blakers, B. Lu, and C. Cheng, "Indonesia's Vast Off-River Pumped Hydro Energy Storage Potential," *Energies (Basel)*, vol. 15, no. 9, May 2022, doi: 10.3390/en15093457.
[9] M. Stocks, C. Cheng, A. Blakers, and B. Lu, "Towards 100% renewable electricity for Indonesia: the role for solar and pumped hydro storage." [Online]. Available: https://www.energy-
[10] T. M. Letcher, "Storing Energy," Amsterdam, 2022.
[11] A. T. Kabo-Bah, F. A. Diawuo, and E. O. Antwai, "Pumped Hydro Energy Storage for Hybrid Systems," London, 2023.
[12] International Hydropower Association, "2021 hydropower status report," 2021.
[13] S. Kimura and S. Ichimura, "Present status of pumped hydro storage operations to mitigate renewable energy fluctuations in Japan," *Global Energy Interconnection*, vol. 2, pp. 423–428, Oct. 2019, doi: 10.1016/j.gloei.2019.
[14] I. Energy Agency, "Technology Roadmap Energy storage." [Online]. Available: www.iea.org
[15] H. Muhammad Bintang et al., "The Levelized Cost of Electricity and Levelized Cost of Storage in Indonesia A 2023's Update on The Levelized Cost of Electricity and Levelized Cost of Storage in Indonesia."
[16] P. Balducci, K. Mongird, and M. Weimar, "Understanding the Value of Energy Storage for Power System Reliability and Resilience Applications," doi: 10.1007/s40518-021-00183-7/Published.
[17] F. Arnesen et al., "Flexible hydropower providing value to renewable energy integration Contributors."
[18] E. O'Shaughnessy, J. R. Cruce, and K. Xu, "Too much of a good thing? Global trends in the curtailment of solar PV," *Solar Energy*, vol. 208, pp. 1068–1077, Sep. 2020, doi: 10.1016/j.solener.2020.08.075.
[19] D. Al. Katsaprakakis, N. Papadakis, D. G. Christakis, and A. Zervos, "On the wind power rejection in the islands of Crete and Rhodes," *Wind Energy*, vol. 10, no. 5, pp. 415–434, Sep. 2007, doi: https://doi.org/10.1002/we.229.
[20] W. He, M. King, X. Luo, M. Dooner, D. Li, and J. Wang, "Technologies and economics of electric energy storages in power systems: Review and perspective," *Advances in Applied Energy*, vol. 4. Elsevier Ltd, Nov. 19, 2021. doi: 10.1016/j.adapen.2021.100060.

Development Of A Deep Learning Model For Classification Of Eye Conditions Using Cascading Techniques

Ajib Setyo Arifin
Department of Electrical Engineering
Faculty of Engineering, Universitas Indonesia
Depok, Indonesia
ajib.sa@ui.ac.id

Rayhan Ameriazandy
Department of Electrical Engineering
Faculty of Engineering, Universitas Indonesia
Depok, Indonesia
rayhan.ameriazandy@ui.ac.id

***Abstract*—Blinking is a physiological function that involves the rapid, involuntary closure of the eyelids. This action serves a critical role in maintaining ocular health by facilitating the removal of debris and moisturizing the eyes. Additionally, the frequency and pattern of blinking can be indicative of an individual's level of fatigue, making blink detection a valuable tool in fatigue assessment. In this study, we propose an eye blink classification system utilizing Convolutional Neural Networks (CNNs), specifically leveraging the Cascading MobileNet architecture, including MobileNet and MobileNetV2 models, for training and testing. These models are employed to detect eye states with a focus on accurately identifying blink occurrences. The experimental results demonstrate that the proposed model effectively classifies eye conditions and successfully detects blinks, which can serve as an indicator of fatigue with 96% accuracy, 15% better than that the existing result.**

***Keywords*—Eye blink, MobileNet, MobileNetV2, classification, accuracy**

I. Introduction

Traffic accidents rank among the leading global causes of mortality. According to a report published by the World Health Organization (WHO) on February 7, 2020 [1], it is estimated that 1.35 million individuals lose their lives annually as a result of injuries sustained in traffic collisions. Such incidents are also a primary cause of death among individuals aged 5 to 29 years. Furthermore, traffic accidents contribute to approximately 3% of the Gross Domestic Product (GDP) in many nations. A variety of factors contribute to the occurrence of traffic accidents, including speeding, failure to use recommended safety gear, poor road conditions, vehicle malfunctions, absence of immediate medical attention for accident victims, driving under the influence of alcohol, and driver fatigue or drowsiness. While most of these factors can be mitigated through responsible driving practices, the risk of drowsiness remains significant for all drivers. This condition poses a serious danger not only to the driver but also to others on the road.

Drowsiness during driving can be attributed to multiple factors, including fatigue, monotony during long drives, and loss of focus on the vehicle. Based on the degree of fatigue, driver drowsiness can be detected through three principal methods: (1) Physiological signals, which are assessed by monitoring oxygen levels in brain and muscle cells [2] [3]; (2) Vehicle behavior, which is determined by variations in steering movements, lane position, speed, acceleration, and braking patterns; and (3) Facial expressions, which involve monitoring the driver's facial behaviors, such as yawning and blinking frequency. Among these methods, facial expression analysis is the most accessible and straightforward for data collection and analysis, as it only requires monitoring the driver's face.

Blinking is an involuntary physiological process that involves the rapid closing of the eyelids, primarily to cleanse the eyes by removing debris and maintaining moisture. The frequency of blinking typically increases in response to complex visual stimuli or during mentally demanding tasks.

Previous studies have explored methods for detecting drowsiness in drivers. For instance, W. Deng developed a method called DriCare, which detects fatigue based on yawning, blinking, and the degree of eye closure [4]. A. Islam also conducted research on drowsiness detection by calculating blink frequency using facial landmark detection (FLD) and the eye aspect ratio (EAR) [5]. Additionally, P. Vishesh et al. [6] investigated eye classification using the MobileNetV2 architecture and the Closed Eyes in the Wild (CEW) dataset. However, despite numerous studies on this subject, none have utilized cascading techniques.

In the present study, we propose the use of a cascading technique aimed at improving classification accuracy. The Cascading MobileNet design integrates two neural networks, MobileNetV2 and MobileNet, which concurrently process the same image input to increase the depth of the deep learning model, while maintaining a smaller network size compared to other neural networks. The deep learning model developed in this study is intended for real-time drowsiness detection in drivers. The primary focus of this research is to enhance the accuracy and precision of previous models by improving the

979-8-3315-1921-6/24/$31.00 ©2024 IEEE

deep learning architecture.

II. Literature Study

Numerous studies have been conducted worldwide with similar goals but employing different methodologies to detect driver drowsiness. One such method uses pulse rate and yawning frequency to identify fatigue, achieving accuracies of 90.3%, 94.4%, and 93.7%, respectively [7]. Another notable approach is DriCare, which detects fatigue by monitoring yawning, blinking, and the degree of eye closure, yielding an accuracy of 92% [4]. Eye blink detection, specifically, has become a key parameter in drowsiness detection. By utilizing facial landmark detection (FLD) and the eye aspect ratio (EAR), systems can effectively detect blinking patterns, with eye closure duration serving as the primary indicator of drowsiness. This method has reported an accuracy of 92.7% [5]. Additionally, techniques that combine multiple features have been developed, such as integrating driver characteristics with the YOLOv3 CNN model to detect facial regions in challenging driving conditions. Using the dlib toolkit, EFu (Evolving Fuzzy Neural Network) and MFU (Mask Field Utilization) evaluate the driver's eye and mouth conditions, achieving a detection accuracy of 95.1% [8].

While many facial features such as yawning, head movements, and blinking can be extracted and used to detect drowsiness, creating a system that accurately and consistently detects all these features remains a challenge. A comprehensive review of existing techniques found that support vector machines (SVM) are the most commonly used; however, convolutional neural networks (CNNs) have outperformed other methods in terms of accuracy [9]. Research by Pothuraju Vishesh et al. utilized CNN with the MobileNetV2 architecture, in combination with the Closed Eyes in the Wild (CEW) dataset, achieving an accuracy of 81% [6]. Despite the advancements in drowsiness detection systems, a significant challenge is the diversity of datasets used by different researchers, which makes direct comparisons difficult. Moreover, the datasets often originate from controlled environments and may not perform well in real-world scenarios. In this proposed research, the Closed Eyes in the Wild dataset, selected by Xiaoyang Tan from Nanjing University of Aeronautics and Astronautics [10] and previously used by Pothuraju Vishesh et al. [6], will be employed. The objective of this study is to enhance prediction accuracy through the development of a more robust detection model.

III. Cascading Architecture

The eye blink detection model is developed using two CNN, MobileNet and MobileNetV2, which are integrated via the concatenate function. This allows the two networks to operate in tandem, ensuring cohesive performance in accordance with the specified objectives. The architectural layout of the model is depicted in Figure 1.

As illustrated in Figure 1, the input dimensions are (224, 224, 3), where 224 represents the height and width of the image, and 3 refers to the number of channels, corresponding

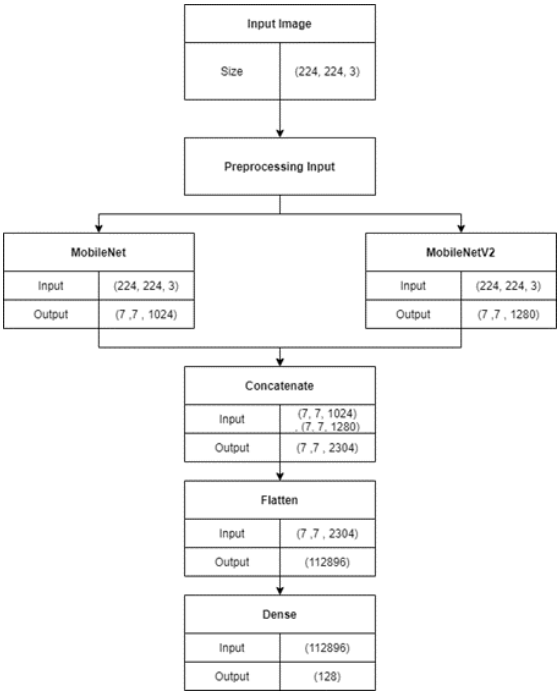

Fig. 1. Cascading architecture model using MobileNet and MobileNetV2.

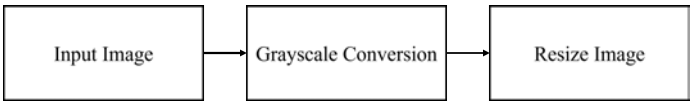

Fig. 2. Preprocessing image.

to the Red, Green dan Blue (RGB) color space used in the dataset. Prior to entering the pretrained model, the image input undergoes a preprocessing stage, as shown in Figure 2.

Figure 2 demonstrates that the RGB input image is converted into grayscale to facilitate processing by the neural network. Additionally, the image is resized from its original dimensions of 100×100 pixels to 224×224 pixels to meet the input size requirements of MobileNet and MobileNetV2, both of which necessitate an image input dimension of 224×224 pixels. Once preprocessing is complete, the image is fed into the pretrained model, which is implemented using the Keras library. Both the MobileNet and MobileNetV2 networks accept the same input size of (224, 224, 3). After processing, MobileNet generates an output of size (7, 7, 1024), and MobileNetV2 produces an output of size (7, 7, 1280). These outputs are then combined using the concatenate function from the Keras library. The concatenate function is employed to merge two or more neural networks, thereby increasing the number of features that the model can recognize by leveraging outputs from different networks. As shown in Figure 1, the output from the concatenation process is (7, 7, 2304), which represents the sum of the channels from MobileNet and MobileNetV2.

The output from the concatenate function is then passed through a flatten layer, which transforms the matrix input from

$A \times B$ into a $B \times 1$ vector, enabling it to be processed by the dense layer. The dense layer, which serves as the final classification layer, outputs 128 units. The overall architecture of the Cascading MobileNet consists of 27 layers.

IV. Dataset and Experimental Setup

The dataset used in this reserach is the Closed Eyes in The Wild (CEW) Dataset, created by Xiaoyang Tan from Nanjing University of Aeronautics and Astronautics [10]. The dataset consists of two folders containing a total of 2,425 images, with 1,232 images of faces with open eyes and 1,193 images of faces with closed eyes. The images in this dataset have dimensions of 100x100 pixels and are in RGB color format.

We conducted five testing scenarios, which involved varying the proportions of data used for training and validation. These five scenarios were used to observe the variation in results caused by different splits of the dataset for training and validation, ensuring the study remained unbiased. In the first scenario, 90% of the dataset images were allocated for training and 10% for validation. In the second scenario, 80% of the images were used for training and 20% for validation. In the third scenario, the split was 70% for training and 30% for validation, while the fourth scenario allocated 60% for training and 40% for validation. Finally, the fifth scenario split the data evenly, with 50% of the images for training and 50% for validation. After training the model for each scenario, data was collected based on evaluation metrics, including accuracy, precision, recall, and F1-score.

V. Result and Analysis

The results of this thesis testing are accuracy, precision, recall, and F1-Score. These testing results were obtained after the model completed training and validation according to the predefined scenarios. The following are the test results for the classification of two classes: open eyes and closed eyes.

A. Accuracy

Accuracy The accuracy evaluation in this study is divided into two categories: training accuracy and validation accuracy. Training accuracy refers to how well the model classifies data within the training set, while validation accuracy indicates the model's performance in predicting unseen data from the validation set. Validation accuracy is crucial in preventing overfitting, as it assesses the model's ability to generalize from the training data to new inputs. In this study, accuracy refers to the percentage of correctly classified eye states (open or closed) out of the total dataset. Higher accuracy indicates that the model is able to learn and classify fine-grained pixel-level details accurately. The comparison of accuracy results is summarized in Table 1. From Table 1, it is evident that the overall accuracy of the Cascading Architecture model exceeds 91% across all scenarios. The highest training accuracy, 97.79%, was achieved in the fifth validation scenario, while the lowest accuracy was observed in the first scenario. Validation accuracy ranged between 91.23% and 96.18%. The average difference between training and validation accuracy, at 2.9%, suggests that overfitting is not present. In the fifth scenario, the validation accuracy exceeded the training accuracy. This result is likely due to the smaller size of the validation dataset, which made it easier for the model to achieve higher accuracy during validation compared to the more complex training phase. Ideally, this discrepancy should be minimized, as the model is more familiar with the training data, while the validation data serves to test its generalization to new, unseen inputs.

TABLE I
Result of Accuracy

Scenario	Training	Validation
1^{st}	96.18%	97.12%
2^{nd}	97.27%	94.23%
3^{th}	97.23%	94.5%
4^{th}	97.54%	94.43%
5^{th}	97.79%	91.23%
Mean	97.2%	94.3%

TABLE II
Result of Precision

Scenario	Closed Eye	Open Eye	Average
1^{st}	97%	97%	97%
2^{nd}	97%	92%	94.5%
3^{th}	96%	93%	94.5%
4^{th}	95%	94%	94.5%
5^{th}	97%	87%	92%

B. Precision

Precision measures the proportion of human faces that were correctly predicted in relation to their true eye state, whether open or closed. This metric is essential to assess whether the high accuracy observed in the study is unbiased. The precision values for the Cascading Architecture model are provided in Table 2. As shown in Table 2, nearly all precision values exceed 90%, with the exception of the fifth scenario for open eyes, which yielded a precision of 87%. The highest precision, 97%, was achieved in the first scenario for both open and closed eyes, as well as in the second and fifth scenarios for closed eyes. These results demonstrate the model's capacity to accurately detect the eye region in facial images, with precision consistently above 90%.

C. Recall

Recall reflects the proportion of correctly predicted eye states relative to the total number of true positive instances

TABLE III
Result of Recall

Scenario	Closed Eye	Open Eye	Average
1^{st}	97%	98%	97.5%
2^{nd}	91%	97%	94%
3^{th}	92%	96%	94%
4^{th}	94%	95%	94.5%
5^{th}	85%	98%	91.5%

TABLE IV
RESULT OF F1-SCORE

Scenario	Closed Eye	Open Eye	Average
1^{st}	97%	97%	97%
2^{nd}	94%	94%	94%
3^{th}	94%	95%	94.5%
4^{th}	94%	95%	94.5%
5^{th}	91%	92%	91.5%

TABLE V
COMPARISON WITH PREVIOUS RESEARCH

Model	Number of Epoch	Accuracy
MobileNetV2 [6]	5	81%
Proposed Model	5	96%

in the dataset. For instance, to calculate recall for closed eyes, one would determine how many instances of closed eyes were correctly identified compared to the total number of actual closed-eye instances in the dataset. Table 3 illustrates that the recall values for the model are consistently above 90%, with the exception of the fifth scenario for closed eyes, which yielded a recall of 85%. The highest recall, 98%, was achieved in the first and fifth scenarios for open eyes. With an average recall above 90%, the proposed model demonstrates a strong ability to distinguish between different eye states.

D. F1-Score

The F1-Score represents the harmonic mean of precision and recall, providing a comprehensive evaluation of the model's performance in both detecting the eye region and classifying its state. As shown in Table 4, all F1-Score values exceed 90%, with the highest score of 97% in the second scenario, and the lowest score of 91% in the fifth scenario for closed eyes. These findings suggest that the proposed model effectively identifies the eye region and accurately classifies its condition as either open or closed.

E. Comparison with Previous Research

The performance of our proposed model is also compared with previous research using the same dataset [6]. The comparison results can be seen in Table 5. In the previous study, only the accuracy metric was used with the first scenario and five epochs. Under these settings, the proposed model achieved a higher accuracy of 96%, which is 15% better than the previous study. The cascading architecture model performed better as it is capable of recognizing a greater number of features.

VI. CONCLUSION

The indicator of fatigue while driving can be detected by the frequency of eye blinks. To detect the number of blinks, a system is required to detect the condition of the eyes, whether open or closed. The eye condition detection system must be able to accurately classify the state of the eyes. In this study, a classification method for eye condition detection using deep learning based on a cascading architecture with MobileNet is proposed. The proposed cascading architecture has been tested with four metrics: accuracy, precision, recall, and F1-score. Additionally, the proposed model has an accuracy performance of 96%, which is 15% better than the previous study.

ACKNOWLEDGMENT

This work was supported by the Universitas Indonesia under Grant LK NKB-2582/UN2.F4.D/PPM.00.00/2023.

REFERENCES

[1] "Road traffic injuries - penelusuran google," 12 2013. [Online]. Available: https://www.who.int/news-room/fact-sheets/detail/road-traffic-injuries

[2] Z. Mardi, S. N. Ashtiani, and M. Mikaili, "Eeg-based drowsiness detection for safe driving using chaotic features and statistical tests," *Journal of Medical Signals and Sensors*, vol. 1, p. 130, 5 2011. [Online]. Available: /pmc/articles/PMC3342623/ /pmc/articles/PMC3342623/?report=abstract https://www.ncbi.nlm.nih.gov/pmc/articles/PMC3342623/

[3] M. Patel, S. K. Lal, D. Kavanagh, and P. Rossiter, "Applying neural network analysis on heart rate variability data to assess driver fatigue," *Expert Systems with Applications*, vol. 38, pp. 7235–7242, 6 2011.

[4] W. Deng and R. Wu, "Real-time driver-drowsiness detection system using facial features," *IEEE Access*, vol. 7, pp. 118 727–118 738, 8 2019.

[5] A. Islam, N. Rahaman, and M. A. R. Ahad, "A study on tiredness assessment by using eye blink detection," *Jurnal Kejuruteraan*, vol. 31, pp. 209–214, 10 2019.

[6] P. Vishesh, P. Vishesh, R. S, S. Jankatti, and R. V, "Eye blink detection using cnn to detect drowsiness level in drivers for road safety," *Indonesian Journal of Electrical Engineering and Computer Science*, vol. 22, pp. 222–231, 4 2021. [Online]. Available: https://ijeecs.iaescore.com/index.php/IJEECS/article/view/24413

[7] C. Zhang, X. Wu, X. Zheng, and S. Yu, "Driver drowsiness detection using multi-channel second order blind identifications," *IEEE Access*, vol. 7, pp. 11 829–11 843, 1 2019.

[8] K. Li, Y. Gong, and Z. Ren, "A fatigue driving detection algorithm based on facial multi-feature fusion," *IEEE Access*, vol. 8, pp. 101 244–101 259, 6 2020.

[9] A. A. Jordan, A. Pegatoquet, A. Castagnetti, J. Raybaut, and P. L. Coz, "Deep learning for eye blink detection implemented at the edge," *IEEE Embedded Systems Letters*, vol. 13, pp. 130–133, 9 2021.

[10] F. Song, X. Tan, X. Liu, and S. Chen, "Eyes closeness detection from still images with multi-scale histograms of principal oriented gradients," *Pattern Recognition*, vol. 47, pp. 2825–2838, 9 2014.

Machine Learning Model Based on Universal Sentence Encoder and TensorFlow for Matching Algorithm on Collabolio Collaborative Platfrom

Teguh Firmansyah
Dept. of Electrical Engineering
Universitas Sultan Ageng Tirtayasa
Cilegon, Indonesia
teguhfirmansyah@untirta.ac.id

Amelia Nur Safitri
Dept. of Electrical Engineering
Universitas Sultan Ageng Tirtayasa
Cilegon, Indonesia
liaameng6@gmail.com

Dina Estiningtyas Lufianawati
Dept. of Electrical Engineering
Universitas Sultan Ageng Tirtayasa
Cilegon, Indonesia
dina.lufianawati@untirta.ac.id

Irma Saraswati
Dept. of Electrical Engineering
Universitas Sultan Ageng Tirtayasa
Cilegon, Indonesia
irma.saraswati@untirta.ac.id

***Abstract*—Currently, the unemployment rate in Indonesia is increasing. Then, the open unemployment rate reached 7.07% in February 2021. The use of technology contributes to high unemployment among graduates who lack soft skills. There is a wide gap between job vacancies and the skills of new graduates, so a more complex job matching process is needed. This study proposes the Collabolio system. Collabolio uses Universal Sentence Encoder (USE) and Tensorflow Recommenders (TFRS) to match users' job skills and interests, enabling collaboration between individuals and project ideas. The Universal Sentence Encoder generates similarity scores between items in the dataset, while Tensorflow Recommenders is used to build a recommendation system model that addresses cold-start and unsupervised learning issues. Using USE and TFRS in Collabolio results in a good prediction with an overall loss of 5.50. In the future, it is hoped that the use of USE and Tensorflow can be further optimized for various purposes.**

***Index Terms*—USE, TFRS, Recommendation System**

I. Introduction

Unemployment in Indonesia has increased since the COVID-19 pandemic hit in early 2020. According to data from the Central Statistics Agency (BPS) in February 2021, the open unemployment rate in Indonesia was 7.07%, up from 5.50% in August 2020 [1]. The increase in unemployment is primarily due to the decline in economic activity caused by the pandemic. Many companies experienced difficulties and had to implement layoffs or reduce working hours. People's lifestyles have started to shift towards being predominantly online, which is happening due to technological developments [2]. The increased use of technology in daily life has brought both positive and negative impacts, including rising unemployment rates, especially among university graduates who lack soft skills such as teamwork and collaboration. Therefore, the use of matching algorithms is absolutely necessary to obtain better job choices. Several interesting studies were proposed.

979-8-3315-1921-6/24/$31.00 ©2024 IEEE

In the study [3], the Universal Sentence Encoder (USE) method is proposed to produce multi-label classification of news. In the first stage, the title of the news will be grouped into several classifications. Then, several methods are proposed starting from multi-nominal NB, logistic regression and SVC to obtain the most precise classification results.

The next research was proposed by D. Sheth [4], in this research the USE algorithm was used to search and classify employee performance. This classification is useful for improving employee performance. In addition, the use of semantic-search is also very useful in terms of search accuracy. In addition, in the study [5], the use of USE was combined with the label powerset (LP) technique on several models. The results of the study showed that the proposed algorithm had an accuracy value of 89

The use of the USE algorithm for document ranking was proposed by [6]. Specifically, a combination of USE and SentenceBERT was used. Performance testing was carried out with MAPm F-measure and NDCG values. The test results showed that the proposal had an accuracy above 90

In addition to the use of the USE algorithm, the use of Tensorflow is also quite often done. In research [7], the use of the tensorflow algorithm was proposed to search for book recommendations. The results showed that the use of tensorflow was able to provide accurate responses quickly. In the study [8], the use of hybrid tensorflow is proposed to search for portable document formatted. The proposed system gives users the freedom to search for data in PDF files. Some of the data that can be searched is in the form of meta data and then matched with its recommendations. The results show that the use of tensorflow is quite good

and produces precise performance. In general, the USE and Tensorflow algorithms have various advantages and can be applied to various conditions [9-14].

This study proposes the Collabolio system. Collabolio uses Universal Sentence Encoder (USE) and Tensorflow Recommenders (TFRS) to match users' job skills and interests, enabling collaboration between individuals and project ideas. The Universal Sentence Encoder generates similarity scores between items in the dataset, while Tensorflow Recommenders is used to build a recommendation system model that addresses cold-start and unsupervised learning issues.

II. USE ENCODER AND TENSORFLOW MATCHIN

The proposed USE algorithm stages include data input, preprocessing, use of the USE model, search for top similar results. Then continued with ID input. If the ID input is successful, it will be directed to the search for similar users.

A. Word Embedding

Word embedding is a vector representation used to represent words in natural language processing or NLP. Essentially, word embedding is used to convert words into numerical forms that can be understood by machine learning models. In word embedding, each word is represented by a multidimensional numerical vector. This occurs because each dimension in the vector represents a certain feature or aspect.

B. USE and TFRS

In this study, the methodology used involves the development of a machine learning model using Universal Sentence Encoder (USE) and TensorFlow Recommendation (TFRS) to improve accuracy in the recommendation system. The following is a research flow diagram using the USE method, which can be seen in Figure 1.

The following is a research flow chart using the TFRS method can be seen in Figure 2. In detail, it includes input data preprocessing, use of the TRFS model, split data, 80% train and 20% test data, then application measurement and use of the recommendation model [15-22].

III. MACHINE LEARNING MODEL BASED ON UNIVERSAL SENTENCE ENCODER AND TENSORFLOW FOR MATCHING ALGORITHM ON COLLABOLIO COLLABORATIVE PLATFROM

A. Universal Sentence Encoder (USE) Result

In the process of creating a top user dictionary that will contain every top user who has a high similarity to the current user. The dictionary will have two keys "user id" and "score" which represent user ID and user similarity score. The use of for and zip() loops to combine the list of user id and the list of similarity scores into one object facilitates the process of iterating simultaneously. The user data dictionary creation will be added to the most similar users data list using the append() method. This will bring up the top users who are most similar to the current user. The final result obtained is a dictionary

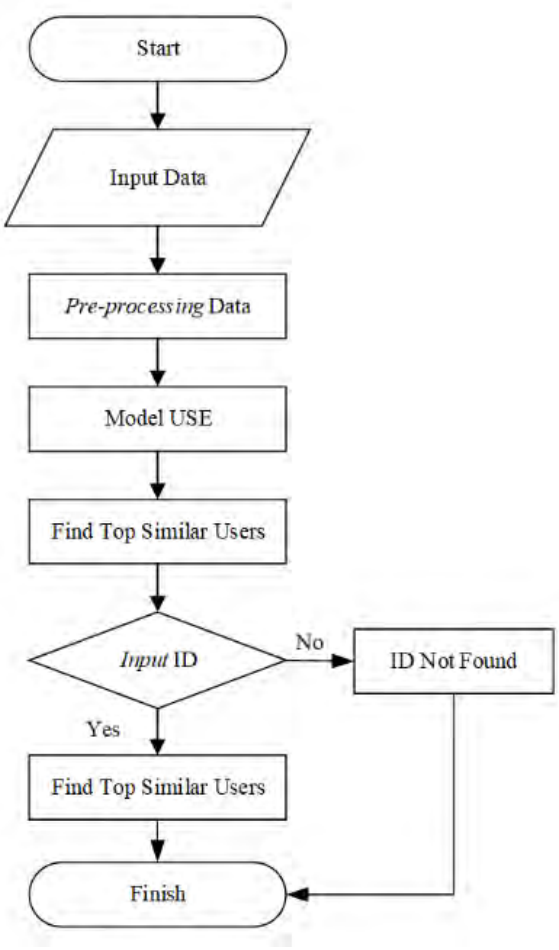

Fig. 1. USE research flow diagram.

list containing user id and similarity score which can be seen as follows.

Similar score results are in a certain range of values such as 0 and 1. Similar score values close to 1 indicate a high level of similarity and vice versa if the value is close to 0 indicates a low level of similarity. Similar score can indicate the quality of representation generated by the embed model. If the similar score between users has a high value, it indicates that the embed model is successful in capturing similarities or interrelationships between users. However, if the similar score is low, it indicates that the embed model needs to be improved.

B. Tensorflow Recommendation Result

This process uses the Factorized Top K matrix to evaluate the model and recommendation performance based on item ranking. The JobLensModel class combines the user model, job model, and tasks from tfrs.tasks.Retrieval to retrieve relevant items. The compute loss method calculates the loss value of the model. The model is trained with a random seed and uses Adagrad with a learning rate of 0.1 for convergence efficiency. The training data is randomized and divided into batches of 8192, with caching to speed up the process. Training is performed for 10 epochs, during which the model

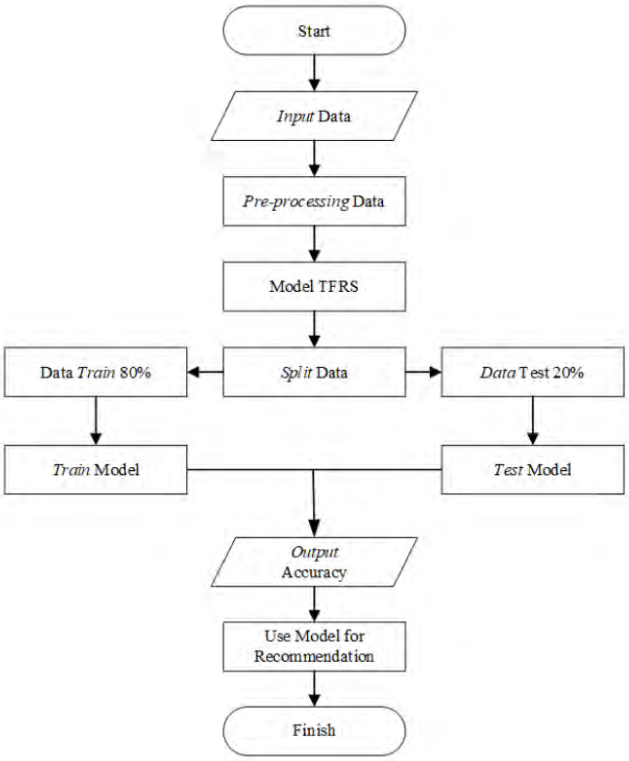

Fig. 2. TFRS research flowchart

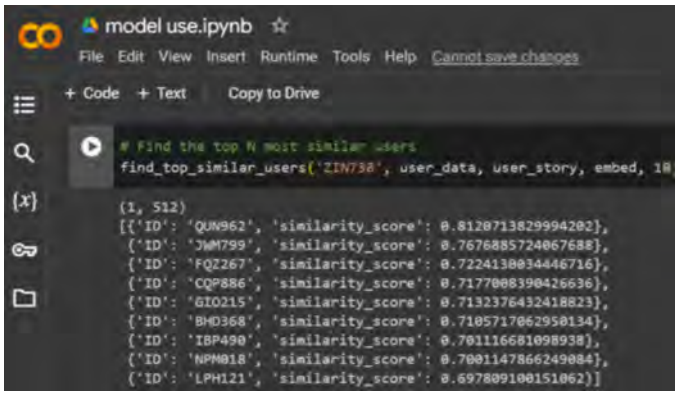

Fig. 3. USE result.

is updated based on the loss value. Test data is used to monitor the model and prevent overfitting, with evaluation resulting in matrices such as loss and top-k. The recommendation results can be seen in Figure 4.

This research shows the results of the accuracy and loss matrix measured during model evaluation. Loss function result is 5.559291839599609. Total loss is a matrix that measures the extent to which the model prediction is from the actual value. The lower the total loss value, the better the model in producing accurate predictions, and vice versa. In this study, the total loss value obtained was 5.50. So it can be said that the model made shows a fairly good prediction level reviewing the small loss results, as shown in Table 1.

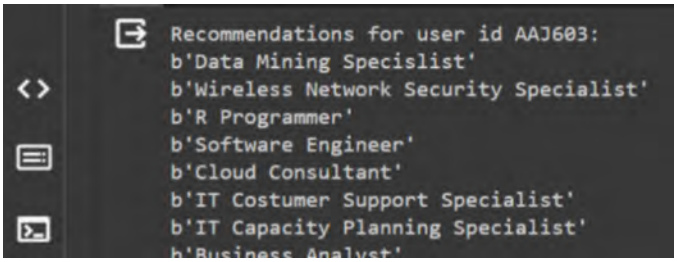

Fig. 4. TFRS result

TABLE I
RESEARCH COMPARISON RESULT

Characteristics	Universal Sentence Encoder (USE)	TensorFlow Recommendation (TFRS)
Dataset	Jobs Interest and Skills	Jobs Interest and Skills
Evaluation Metric	Similar Score	Loss Function
Platform Dataset	Firebase	Google Colab file (.csv)
Recommendation	User ID	Jobs

Based on the results of the research that has been carried out previously, the following conclusions have been obtained as follows. Recommendation results using USE in the form of user IDs that have the same background as other users. Meanwhile, the Tensorflow Recommendation (TFRS) method can produce job recommendations that are suitable for users according to their expertise.

The Universal Sentence Encoder (USE) method generates a similar score or similarity score between items contained in the dataset. A similar score value close to 1 indicates a high level of similarity and vice versa if the value approaches 0 indicates a low level of similarity. The Tensorflow Recommendation (TFRS) method uses a loss function to see a matrix that measures how good the machine learning model is. The resulting total loss is 5.50. The USE method and TFRS method improve accuracy in this study through effective representation of the USE model, use of similar score, adjustment of the learning rate in the TFRS model, and use of appropriate datasets stored using efficient platforms such as Firebase and Google Colab.

IV. CONCLUSION

The Universal Sentence Encoder (USE) encodes sentences into embedding vectors using natural language processing (NLP). With USE, recommendations are based on user IDs with similar backgrounds. Meanwhile, TensorFlow Recommendation (TFRS) generates job recommendations aligned with users' skills. Both methods in this study use a dataset with two parameters: job interest and skills. USE computes a similarity score between items, where values closer to 1 indicate high similarity, and those near 0 indicate low similarity. TFRS, using a loss function to evaluate model performance, resulted in a total loss of 5.504, indicating good prediction accuracy due to the small loss value. Both USE and TFRS rely on TensorFlow's efficient framework to enhance model performance, achieving better accuracy through USE's effective representation and similarity scoring.

ACKNOWLEDGMENT

This paper was supported by LPPM Universitas Sultan Ageng Tirtayasa and DRTP Kemdikbudristek

REFERENCES

[1] B. P. Statistics, "February 2020: Open Unemployment Rate (TPT) of 4.99 percent," May 2020.0.

[2] F. Rokhim, "Factors influencing unemployment in Indonesia," Journal of Scientific Research, Education, and Technology (JSRET), vol. 2, no. 1, pp. 122–131, 2023.

[3] Y. Li, C. Xu, J. Cai and Y. Xia, "Multi-label Classification of News Topics Based on Universal Sentence Encoder," 2024 5th International Conference on Electronic Communication and Artificial Intelligence (ICECAI), Shenzhen, China, 2024, pp. 419-422, doi: 10.1109/ICECAI62591.2024.10675181.

[4] D. Sheth, A. R. Gupta and L. D'Mello, "Using Universal Sentence Encoder for Semantic Search of Employee Data," 2021 International Conference on Computational Intelligence and Computing Applications (ICCICA), Nagpur, India, 2021, pp. 1-4, doi: 10.1109/ICCICA52458.2021.9697114.

[5] N. Kumar, S. Kumar, A. Dev and S. Naorem, "Leveraging Universal Sentence Encoder to Predict Movie Genre," 2021 7th International Conference on Advanced Computing and Communication Systems (ICACCS), Coimbatore, India, 2021, pp. 1013-1018, doi: 10.1109/ICACCS51430.2021.9441685.

[6] V. Gupta, A. Dixit and S. Sethi, "A Comparative Analysis of Sentence Embedding Techniques for Document Ranking," in Journal of Web Engineering, vol. 21, no. 7, pp. 2149-2185, October 2022, doi: 10.13052/jwe1540-9589.2177.

[7] A. Anandaraj, P. Yeshwanth Ram, K. Sri Ram Kumar, M. Revanth and R. Praveen, "Book Recommendation System with TensorFlow," 2021 7th International Conference on Advanced Computing and Communication Systems (ICACCS), Coimbatore, India, 2021, pp. 1665-1669, doi: 10.1109/ICACCS51430.2021.9441927.

[8] G. Goyal and S. Dhingra, "Hybrid tensorflow based portable document formatted recommender system," 2017 International Conference on I-SMAC (IoT in Social, Mobile, Analytics and Cloud) (I-SMAC), Palladam, India, 2017, pp. 357-363, doi: 10.1109/I-SMAC.2017.8058371.

[9] I. K. Loukia Karanikola, "A Fuzzy Logic Approach for Reasoning under Uncertainty and Vagueness - A," in 2016 2nd International Conference on Information Management (ICIM), London, UK, 2016.

[10] Y. Y. e. a. Cer Daniel, "Universal Sentence Encoder," arXiv, 2018.

[11] A. M. Fattoh, "Semantic Sentiment Classification for COVID-19 Tweets Using," Hindawari, 2022.

[12] Y. C. D. A. A. G. M. L. J. C. N. K. R. Yang, "Multilingual Universal Sentence Encoder for Semantic Retrieval," arXiv , 2019.

[13] N. . G. I. Reimers, "Sentence Embeddings using Siamese BERT-Networks," in Conference on Empirical Methods in Natural Language Processing and the 9th International Joint Conference on Natural Language Processing (EMNLP-IJCNLP), 2019.

[14] T. M. Pratama, "Classification Model of Prospective New Students for Undergraduate Study Program Recommendation System Based on Machine Learning," Information Technology and Computer Science (JTIIK), vol. 9, 2022.

[15] S. Tambunan, "Comparison of Classification with Machine Learning Approach to Identify Hoax Tweets on Social Media Twitter," Journal of Informatics Education and Research (JEPIN), vol. 7, 2021.

[16] C. Mar'i, "Professional Recommendation System Based on Big Five Personality Dimensions Using Tsukamoto Fuzzy Inference System," Journal of Information Technology and Computer Science (JTIIK), vol. 6, 2019.

[17] Y. Nafea, "On Recommendation of Learning Object using Felder-Silverman Learning Style Model," IEEE TRANSACTIONS and JOURNALS, vol. 4, 2016.

[18] M. X. Althbiti, "Adderessing Data Sparsity in Collaborative Filtering Based Recommender System Using Clustering and Artficial Neural Network," IEEE Computing and Communication Workshop and Conference, 2021.

[19] S, Slamet "Yoga Recommendation System for the Mental Well-Being of Students using Machine Learning," in International Conference on Electronics, Communication and Aerospace Technology, Coimbatore, India, 2022.

[20] M. Tiwari, "Crop Recommendation using Machine Learning and Plant Disease Identification using CNN and Transfer-Learning Approach," in IEEE Conference on Interdisciplinary Approaches in Technology and Management for Social Innovation (IATMSI), Gwalior, India, 2022.

[21] R. Kumar, R. M and P. R, "Book Recommendation System with Tensorflow," in International Conference on Advanced Computing Communication System (ICACCS), Coimbatore, India, 2021.

[22] B. I. e. a. Bahri, "Implementation of Food Recommendation System on EatAja Application Using Collaborative Filtering Algorithm," MULTINETICS, vol. 7, 2021.

Mitigating Voltage Rise on Low-Voltage Distribution Networks with High Solar Photovoltaic Penetration: A Review

Mustafa Abo Alwaz
Dept. of Electrical Engineering
Universiti Putra Malaysia
Dept. of Artitecture Engineering
Almuthana University
Almuthana,Iraq
Mustafa.Hussein@mu.edu.iq

Jasronita Jasni
Dept. of Electrical Engineering
Universiti Putra Malaysia
Kuala Lumpur, Malaysia
Jas@upm.edu.my

Raghad Wahab
Dept. of Electrical Engineering
Kerbala University
Karbala, Iraq
raghad.w@uokerbala.edu.iq

Lubna Mueen
Dept. of Computer technology
Imam Ja'afar Al-Sadiq University
Lubnaaljanabi95@gmail.com

Mohd Amran Mohd Radzi
Dept. of Electrical Engineering
Universiti Putra Malaysia
Kuala Lumpur, Malaysia
amranmr@upm.edu.my

Norhafiz Azis
Dept. of Electrical Engineering
Universiti Putra Malaysia
Kuala Lumpur, Malaysia
Norhafiz@upm.edu.my

***Abstract*—The integration of photovoltaic (PV) systems into distribution networks poses challenges related to voltage rise, a critical concern for network stability and equipment performance. This research investigates the techniques for mitigating the voltage rise on distribution networks with high PV penetration. However, the intermittent nature of PV systems and their increasing penetration into distribution networks necessitate innovative control strategies to address voltage rise. Three primary mitigation methods are explored: Energy Storage Systems (ESSs), active power curtailment, and reactive power control. ESSs store surplus energy during periods of high PV generation and release it during peak load demand, contributing to voltage stability. Active power curtailment reduces PV generation during high sun irradiance and low power demand periods. Reactive power control manages voltage by adjusting the injection of reactive power into the network. Various research studies and proposed techniques are reviewed to evaluate their effectiveness in mitigating voltage rise. The advantages and limitations of each approach are compared, considering factors such as network losses, equipment stress, and system reliability. The review emphasizes the significance of reactive power control techniques in mitigating voltage rise during high PV penetration in distribution networks. The paper highlights the need for advanced control strategies to manage voltage rise effectively and maintain network stability in the presence of PV systems. It presents a comparison of techniques, enabling decision-makers and researchers to select appropriate methods based on their specific network requirements and operational goals. The findings underscore the importance of reactive power control techniques in addressing voltage rise challenges.**

***Index Terms*—Photovoltaic (PV), Reactive power control, Energy storage system, Voltage rise**

I. Introduction

Energy serves as a crucial element for industries, agriculture, and people's everyday lives. With the world population increasing and daily electricity consumption growing, the demand for energy is surging. Traditional power plants, dependent on fossil fuels for generating electricity, pose significant environmental threats by emitting CO2 and NOX through fossil fuel combustion. Additionally, the Unequal distribution of fossil fuel reserves forces some nations to depend on imports, negatively impacting their economies [1].

In response to these challenges, the adoption of photovoltaic cells (PVs) has seen remarkable growth over the past decade [2]. The International Energy Agency (IEA) forecasts solar energy to become a predominant energy source by 2050, contributing around 11% to global power generation [3] [4]. The IEA also predicts that PV systems, as distributed generators (DGs), will attain global penetration levels exceeding 50% This shift is exemplified by China's transition from coal-dependent electricity generation to renewable sources, such as solar energy, elevating its PV-based electricity production from under 20 TWh in 2012 to over 160 TWh in 2018. The United States and Australia have also significantly enhanced their electricity generation reliability through PV systems, witnessing increases from 2.08 TWh and 0.29 TWh to 97.12 TWh and 12 TWh respectively by 2018, as shown in Figure 1.

The rising integration of photovoltaic (PV) systems into low voltage distribution networks brings various technical challenges concerning frequency, power, current, and voltage [6] [7]. Among these, voltage rise is a critical issue during PV system integration into distribution networks. Voltage rise, an increase in voltage levels due to high PV penetration, occurs when the power generated by PV systems surpasses the power consumed by local loads, leading to excessive voltage. This can impact the performance and longevity of electri-

979-8-3315-1921-6/24/$31.00 ©2024 IEEE

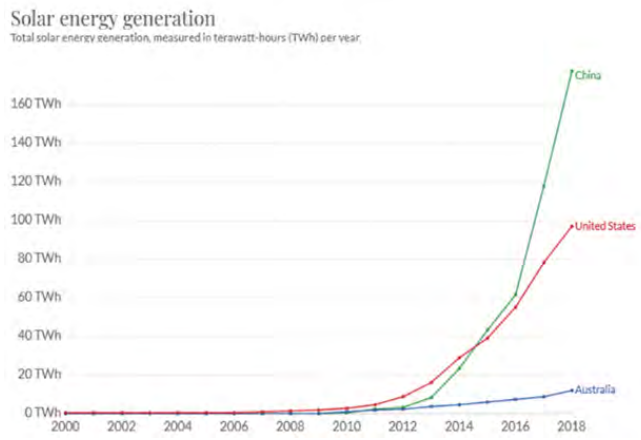

Fig. 1. Power generation through PV (2000–2018) [5].

cal equipment like transformers, switchgear, and appliances, potentially causing damage due to heightened stress levels. Addressing these challenges requires extensive research and the development of advanced control systems, especially to mitigate voltage rise. Research efforts have focused on various strategies to tackle this issue, including energy storage systems (ESSs), active power curtailment, and reactive power control [8].

Energy Storage Systems (ESS) primarily store excess energy, which is later distributed into the network during peak power demands. Active power curtailment techniques, such as smart inverters, manage PV output power, easing the integration effects into distribution networks. Reactive power control inverters are used to adjust reactive power levels. Additionally, devices like static synchronous compensators, on-load tap chargers (OLCTs), and step voltage regulators are implemented to regulate voltage and mitigate the impacts of PVs on distribution networks.

This study offers an overview of ESS and reactive power control techniques, examining their benefits and limitations. It also reviews previous research to understand the evolution of these methods in addressing voltage rise on distribution networks. A comparative analysis of different voltage rise mitigation techniques highlights their strengths and weaknesses, showing that reactive power control is particularly effective in managing voltage rise during high PV penetration.

II. Voltage Rise Mitigation Techniques

A. Energy Storage System (ESS) technique to mitigate voltage rise.

Voltage rise is directly proportional to solar PV production, especially during mid-day when solar irradiance is at its peak and the load demand is lower. To prevent such events, the high production rate should be reduced, or the surplus energy consumed. Energy Storage Systems (ESSs) are commonly used to address this issue by storing surplus energy during periods of high irradiance and feeding it back to the network during periods of high load demand. Various types of ESSs are available, including pumped hydro storage, supercapacitors, flywheels, and compressed energy storage. Among them, battery ESSs are the preferred choice for integrated PV systems [9]. Different types of batteries, such as high-temperature, lithium-ion, lead-acid, conventional, flow batteries, and nickel-cadmium, are utilized. The discharging and charging processes can be calculated using Equations (1) and (2) [10].

$$E(t + \Delta t) = E(t) + \Delta t \cdot P_c \cdot \eta_c \tag{1}$$

$$E(t + \Delta t) = E(t) - \Delta t \cdot P_d \cdot \eta_d \tag{2}$$

In this context, d and c stand for the efficiencies during discharge and charging, correspondingly. E represents the stored energy, while t indicates the duration the battery requires to store energy E. Additionally, Pd and Pc denote the powers involved in discharging and charging, respectively.

A study by Zillmann et al. focused on voltage regulation in distribution networks, exploring the impact of various Energy Storage System (ESS) strategies. They identified potential limitations in ESS strategies, notably increased capital and operational costs [11]. Tewari et al. proposed a coordinated control strategy for On-Load Tap Changers (OLTC) and Battery Energy Storage Systems (BESS) to enhance voltage regulation in distribution networks with high solar PV penetration. This strategy optimizes the use of OLTC and BESS to reduce voltage deviations and enhance system performance, though it requires a communication network, adding complexity and potential vulnerabilities [12].

X. Liu et al. discussed the utility of ESSs with step voltage regulation and OLTCs, aiming to reduce operational stress on OLTCs but introducing complexities in system design and maintenance [13]. Sugihara et al. proposed using ESSs on the customer side to alleviate voltage rise on networks with high PV penetration, facing challenges such as limited space and end-user resistance [14]. Y. Yang et al. presented an approach for battery sizing in distribution networks that considers battery lifespan, balancing cost, and operational effectiveness. However, this approach is influenced by uncertainties in battery degradation and technology standards [15].

C. Xie et al. introduced a sophisticated sizing approach for ESS within smart microgrids experiencing significant PV integration. Their method integrates a virtual energy storage system alongside a risk component. Although comprehensive, this strategy presents challenges in both modeling and computational complexity [16]. Babacan et al. used a Genetic Algorithm for multi-objective optimization of battery allocation in distribution systems, enhancing battery allocation but with computational complexity issues [17]. Marra et al. proposed various energy storage concepts for voltage regulation in networks with high PV penetration, facing deployment challenges due to regulatory and policy hurdles [18]. Xie et al. proposed a Model Predictive Control algorithm to regulate voltage in distribution networks with high PV penetration, facing challenges with computational burden in real-time scenarios [19].

Marra et al. explored the use of electric vehicles to reduce voltage rise on networks with high PV penetration, facing infrastructure development and standardization challenges [20].Zeraati et al. developed a consensus algorithm for coordinating energy storage-based electric vehicles and active power curtailment, but it may face challenges in diverse stakeholder scenarios [21].

B. Reactive Power Control

Reactive power control techniques are essential for mitigating voltage rise on distribution networks with high photovoltaic (PV) penetration. These techniques leverage inverters for their capacity to absorb or inject reactive power. There are two primary methods for reactive power control to mitigate voltage rise:

1) Active power-dependent reactive power control, which includes:
   a) Fixed Power Factor (FPF) control.
   b) Variable Power Factor (PF(P)) control.
2) Voltage-dependent reactive power control (Q(V)).

The Fixed Power Factor (FPF) control technique is a common method for regulating reactive power. In this technique, reactive power injection is directly proportional to active power generation to maintain a constant power factor. Equation (3) calculates the reference value for reactive power in this approach. Figure 2 illustrates the FPF technique, showing that during periods of low solar irradiance, the reactive power injection is minimal in comparison to active power generation. Conversely, at peak PV generation, the generator produces the maximum possible reactive power (Qlim). However, during periods of low active power injection, the risk of voltage rise is significantly reduced. This means that the injection of reactive power control could lead to unnecessary losses, a limitation that should be considered when employing this technique.

$$Q_{\text{ref}} = \frac{\sqrt{1 - \text{PF}_{\text{ref}}^2}}{\text{PF}_{\text{ref}}} \cdot P \tag{3}$$

To overcome this limitation, a technique known as variable power factor (PF(P)) reactive power control has been developed. This method adjusts the power factor in response to the active power output of the PV system. The PF reference in this approach is determined using Equation (4). Figure 3 illustrates the variable PF reactive power technique graphically, showing that when the PV system's active power injection is low, the PF reference is 1, signifying no reactive power injection. As the PV system's active power injection increases, the PF reference gradually decreases, eventually reaching a predefined limit (PFlim) at the maximum PV active power output.

However, both the FPF and variable PF techniques, which base reactive power injection on PV active power output, overlook variations in load demand. Therefore, during periods of high PV generation coinciding with high load demand, the risk of voltage rise is negligible. Despite this, these techniques result in maximum reactive power injection, thereby increasing energy losses. While effective in providing voltage regulation, these methods can lead to higher network losses, a significant drawback highlighted by [8].

$$\text{PF} = \begin{cases} 1, & P < P_1 \\ \frac{\text{PF}_{\text{lim}} - 1}{P_1 - P_2}(P - P_1), & P_1 \le P \le P_2 \\ \text{PF}_{\text{lim}}, & P_2 < P \end{cases} \tag{4}$$

The Q(V) technique is a reactive power control method that is directly proportional to the voltage on the point of the common coupling. The reactive power reference in this technique is determined using equation (5). However, it's important to note that the effectiveness of this technique is also influenced by the PV system's location within the network. The Q(V) technique demonstrates a high level of accuracy and effectiveness in locations where voltage sensitivity to active and reactive power is significant, and vice versa [22]. Figure 4 provides an illustration of the Q(V) approach illustrating the correlation between reactive power and the voltage of the distribution network using a segmented linear curve.

$$Q_{\text{ref}} = \begin{cases} Q_{\text{lim}}, & V < V_{\text{min}} \\ \frac{Q_{\text{lim}}}{(V_{\text{min}} - V_{\text{dp min}})}(V - V_{\text{min}}), & V_{\text{min}} \le V < V_{\text{dp min}} \\ 0, & V_{\text{dp min}} \le V < V_{\text{dp max}} \\ \frac{Q_{\text{lim}}}{(V_{\text{dp max}} - V_{\text{max}})}(V - V_{\text{dp max}}), & V_{\text{dp max}} \le V < V_{\text{max}} \\ -Q_{\text{lim}}, & V_{\text{max}} \le V \end{cases} \tag{5}$$

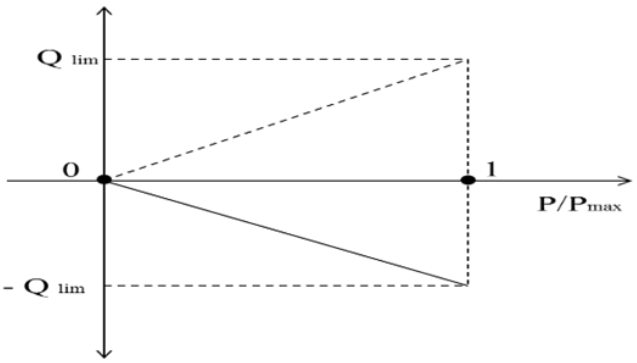

Fig. 2. Curve of FPF control

Yan et al. modified the IEEE 13-bus system with different PV penetrations to demonstrate voltage stability problems, suggesting the use of inverters for reactive power support to mitigate these issues [23]. Almeida et al. compared four reactive power control techniques in terms of grid reinforcement requirements, losses, and costs. This comparative analysis provides valuable insights, but its applicability to specific distribution network scenarios may vary [24].

Demirok et al. pointed out the limitations of traditional reactive power control techniques and concluded that end customers experience increased efficiency as the distance between the inverter and the customer decreases [25]. Bletterie et al. investigated the performance and effectiveness of various reactive power approaches in terms of network

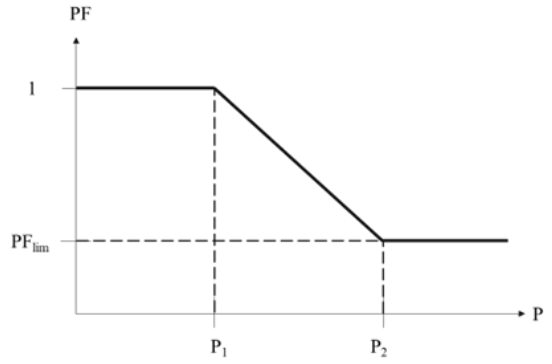

Fig. 3. graph of PF(P) reactive control

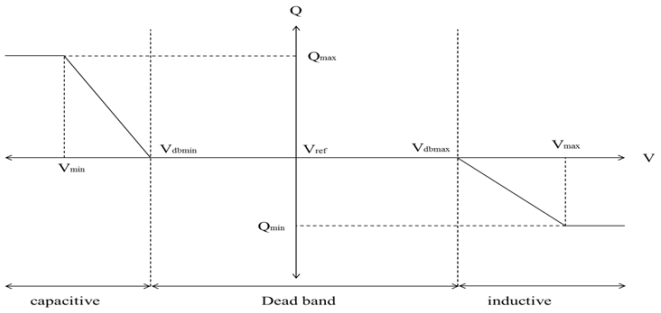

Fig. 4. Curve of Q(V) reactive power control

losses, additional reactive power flows, and effectiveness in mitigating voltage rise. However, the practical implementation of these approaches may face challenges related to system compatibility and coordination [26].Kim and Song proposed a hybrid reactive power control approach using the weighted sum of the PF(P) and Q(V) methods. Reactive power reference is determined based on the active power output of Distributed Generators (DGs). When the active power output is high, the PF(P) control dominates, while when the active power output is low, the Q(V) control dominates to minimize distribution network losses. However, this approach may face challenges in scenarios with highly dynamic load profiles and high DG outputs [27].

Ca et al. developed a local reactive power control approach with four modes to mitigate the effects of high PV penetration on Low Voltage Distribution Networks, such as voltage fluctuation, undervoltage, overvoltage, high losses, and low power factor. They also proposed a PF(P) reactive power control approach that considers the active and reactive powers of the load, preventing insufficient reactive power injection and reducing distribution network losses and voltage fluctuation. However, the local reactive power control approach may face challenges in terms of scalability and adaptability to changing network conditions [28]. Kabiri et al. proposed a combined strategy involving the use of an electronic tap changer in the transformer of a distribution feeder to provide voltage regulation functionality. PV systems were used at each feeder bus for local reactive power control to minimize losses. Despite its effectiveness, the integration of electronic tap changers may introduce additional costs and maintenance requirements [29].

Hu et al. proposed a novel method for mitigating voltage fluctuations due to high PV penetrations. This method coordinates the operation of on-load tap changers (OLTCs), capacitor banks (CBs), reactive power control, and active power curtailment using a two-level approach: a mixed integer nonlinear programming (MINP) model based on model predictive control (MPC) for planning and a leader–follower consensus algorithm (LFCA) for real-time control. However, the proposed control involves sophisticated mathematical modeling and requires robust communication systems for effective coordination [30]. Hashemi et al. presented an approach based on voltage sensitivity to assess the effect of local reactive power control on the capacity of energy storage units. This approach can model different levels of PV penetration and load conditions and determine the required energy storage capacity for preventing overvoltage based on customer location. However, the deployment of energy storage units may face challenges such as limited space availability and cost considerations. The study confirmed that reactive power control can reduce the required energy storage capacity by approximately 30%. However, the reduction in energy storage capacity may compromise the system's ability to handle unexpected fluctuations in PV output [31].

Emarati et al. introduced a two-level voltage control method for managing over-voltage issues in distribution networks with high photovoltaic (PV) penetration. The first level involves day-ahead scheduling of battery energy storage systems and on-load tap changer (OLTC) adjustments, while the second level employs reactive power compensation through PV inverters for fine-tuning voltage profiles. The strategy aims to enhance voltage stability by integrating battery storage and inverter capabilities. A potential drawback of this approach is the reliance on accurate forecasting for day-ahead scheduling introduces uncertainty, potentially affecting the system's effectiveness in dynamically varying conditions [32]. Adetokun et al. developed a reactive power-voltage in Q(V) form-based framework to evaluate voltage instability sensitivities in power systems with increasing renewable energy penetration. It introduces two sensitivity indices: the Critical Voltage Sensitivity Index (CVSI) and the Critical Reactive Power Sensitivity Index (CQSI). These indices measure the impact of renewable energy penetration on the critical voltage level and reactive power loss intolerance of power system buses. On the other side, a potential drawback of this technique is its reliance on detailed and accurate modeling of the power system, which can be complex and time-consuming. Additionally, the effectiveness of the indices in different types of power systems and under varying conditions may require extensive validation [33].

Takayama et al. presented a novel voltage control approach based on reactive power control using a PV inverter with reinforcement learning, eliminating the need for information exchange between inverters. However, the implementation of reinforcement learning may require extensive computational

resources and may face challenges in scenarios with dynamic network conditions [34]. Howlader et al. conducted an experimental analysis of the Volt/Var control's capacity to regulate voltage, revealing that the injection of reactive power increases when reactive power absorption in the distribution network decreases [35]. Ghasemi et al. presented an adaptive droop-based algorithm for controlling reactive and active powers in a grid integrated with PV, aiming to reduce losses, increase grid capacity, and prevent overvoltage. The algorithm was tested on a modified IEEE 33-bus system through computer simulation. However, the adaptive nature of the algorithm may introduce challenges in terms of stability and predictability [36].

Hasheminamin et al. proposed a single-point reactive power control method to avoid reverse power flow in distribution networks and employed mathematical analysis to determine the reactive power support. However, the reliance on mathematical analysis may require precise network models, and deviations from the assumed conditions may impact the accuracy of the proposed control method [37]. Bernal et al. proposed a fuzzy logic-based reactive power control technique for voltage regulation in grids with high PV penetration. While fuzzy logic-based control provides flexibility, the robustness of the control system may be affected by uncertainties in the network and load conditions [38]. Bedawy et al. introduced a multi-agent reactive power control system using a reactive power index that considers each DG's ability to inject or absorb reactive power as a control agent. This approach facilitates coordination between different voltage regulation devices and DGs, resulting in better voltage regulation of the distribution network. However, the coordination of multiple agents may introduce challenges related to communication delays and synchronization [39].

The paper by Arshad and Lehtonen discusses a multi-level voltage control strategy for distribution networks with high photovoltaic penetration. It integrates Flicker Control, Local Voltage Control, and Coordinated Voltage Control using PV inverters. While effective in optimizing inverter set points and reducing curtailment and losses, the strategy faces challenges like potential communication latency and reliance on specific inverter capabilities, requiring precise coordination under dynamic network conditions [40]. I. Kim and Harley introduced a method for voltage regulation through a Volt/Var-control approach, using the positive-sequence sensitivity impedance matrix with power-factor constraints. This method was validated in the IEEE 34-bus test feeder and is aimed at maintaining bus voltage within specific ranges [41].

1) Active Power Curtailment Technique: Active power curtailment is utilized to mitigate voltage rise in distribution networks with high photovoltaic (PV) penetration. This method reduces the active power output of PV systems during high solar generation periods to maintain acceptable voltage levels within the network. The PV system limits its active power injection into the grid, thus controlling excess generation that could cause voltage rise. The technique adjusts the amount of active power injected by the PV system based on the voltage at the common coupling point. Figure 5 illustrates that there is no curtailment of PV active power injection when the network voltage is below the threshold. However, as the network voltage exceeds this threshold, the PV active power injection decreases with increasing voltage, stopping completely when the voltage reaches the maximum allowable limit. Despite its effectiveness, this technique is not favored by renewable source owners due to the associated active power losses [42]. Tonkoski et al. proposed coordinated active power curtailment to prevent voltage rise on a Canadian distribution network, tested over a 12-hour period. This approach's limitation is the lack of long-term performance data and its efficacy in diverse weather conditions [43]. Ku et al. suggested a hybrid approach combining active power curtailment and reactive power compensation to mitigate voltage rise during load exchange in low voltage systems, which could be less effective in systems with fluctuating load demands [44]. Ghosh et al. proposed droop-based reactive power compensation with active power curtailment based on short-term PV power generation forecasting using the Kalman filter theory. The major drawback here is the reliance on accurate short-term forecasting, which can be challenging in unpredictable weather conditions [45]. Verma et al. presented a novel technique to mitigate voltage rise on distribution networks using a de-rating technique on the DC-DC converter to curtail the PV active power injection into the distribution network. However, this might lead to reduced efficiency and increased wear on the converters [46]. Conti et al. introduced active power curtailment based on on/off control depending on the node voltage. A drawback of this method is its potential for abrupt changes in power output, which can stress the electrical grid [47]. Finally, practical results of distribution networks with high PV penetration improved by active power curtailment were presented, but these studies may lack scalability and adaptability to different types of grid infrastructures [48] [49].

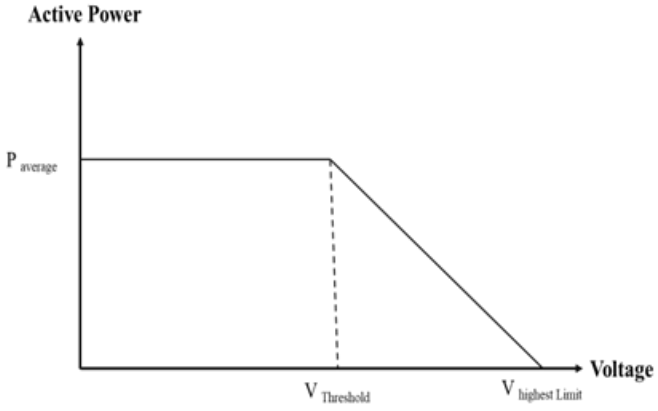

Fig. 5. Typical graph of active power curtailment

III. Discussion

In this study of voltage rise mitigation on low voltage distribution networks with high photovoltaic (PV) penetration, we explore several strategies, including Energy Storage

Systems (ESSs), active power curtailment, and reactive power control. While ESSs offer a buffer to manage excess energy, their high costs and spatial demands make them less feasible. Active power curtailment, though effective in reducing excess generation, leads to underutilization of PV resources. Among these, reactive power control emerges as the most promising technique. It adeptly manages voltage levels without significantly impacting power production. Despite its complexity, ongoing advancements in control algorithms and system compatibility make reactive power control a preferred solution for addressing voltage rise issues on PV-rich networks. This method's ability to adapt to dynamic network conditions while maintaining efficient operation positions it as a key player in future renewable energy integration. Table I provides a comparison among four categories of techniques for mitigating voltage rise

TABLE I
COMPARISON OF VOLTAGE REGULATION METHODS

Characteristics	Typical voltage regulation approaches	ESS	Reactive Power control	Active power curtailment
Effect on power factor	No effect	No effect	Decrease	No effect
Efficiency	Low	High	High	High
Losses in system	Less	Low	High	Low
Responsiveness	Slow	Fast	Extremely Fast	Extremely Fast
Cost	High	High	Higher than active Power	Low
Losses in renewable energy	No effect	Low	Less than Active power	High

IV. CONCLUSION

The article explores challenges in conventional fossil fuel power plants and the rising energy demand. PV systems have gained traction as an alternative. It emphasizes PV's growing use in low voltage distribution networks and the key issue of voltage rise. Three main strategies to counter this issue are discussed: energy storage systems (ESSs), active power curtailment, and reactive power control. ESSs are vital for mitigating voltage rise by storing surplus energy during peak solar exposure and releasing it during high demand. Battery ESSs are preferred for integrated PV systems. Combining ESSs with tools like step voltage regulators and on-load tap changers is also considered. Reactive power control techniques employ inverters to absorb or inject reactive power. They fall into three categories: fixed power factor control, voltage-dependent reactive power control, and power factor linked to injected active power. The article references various studies on PV integration's effects and mitigation techniques. It offers an overview of ESS and reactive power control techniques, discussing their pros and cons and comparing their effectiveness in mitigating voltage rise in distribution networks. In summary, the article underscores the importance of managing voltage rise in high PV penetration distribution networks, presenting diverse mitigation strategies. ESSs and reactive power control are identified as pivotal solutions. The article is structured around sections on high PV penetration impacts, voltage rise mitigation, and comparative analysis.

ACKNOWLEDGMENT

The author would like to acknowledge the assistance of artificial intelligence tools which were instrumental in proofreading and correcting grammatical errors in this manuscript. This technology provided valuable support in ensuring the linguistic accuracy of the content presented.

REFERENCES

[1] T. M. L. Wigley, "Could reducing fossil-fuel emissions cause global warming?" *Nature*, vol. 349, no. 6309, pp. 503–506, 1991, doi: 10.1038/349503a0.

[2] M. Hosenuzzaman, N. A. Rahim, J. Selvaraj, M. Hasanuzzaman, A. B. M. A. Malek, and A. Nahar, "Global prospects, progress, policies, and environmental impact of solar photovoltaic power generation," *Renewable and Sustainable Energy Reviews*, vol. 41, pp. 284–297, Jan. 2015, doi: 10.1016/J.RSER.2014.08.046.

[3] F. Diner, "The analysis on photovoltaic electricity generation status, potential and policies of the leading countries in solar energy," *Renewable and Sustainable Energy Reviews*, vol. 15, no. 1, pp. 713–720, Jan. 2011, doi: 10.1016/J.RSER.2010.09.026.

[4] S. M. Moosavian, N. A. Rahim, J. Selvaraj, and K. H. Solangi, "Energy policy to promote photovoltaic generation," *Renewable and Sustainable Energy Reviews*, vol. 25, pp. 44–58, Sep. 2013, doi: 10.1016/J.RSER.2013.03.030.

[5] "Photovoltaic solar power – the reliable future energy source – Analysis - IEA," Accessed: Dec. 25, 2023. [Online]. Available: https://www.iea.org/articles/photovoltaic-solar-power-the-reliable-future-energy-source

[6] E. J. Coster, J. M. A. Myrzik, B. Kruimer, and W. L. Kling, "Integration issues of distributed generation in distribution grids," *Proceedings of the IEEE*, vol. 99, no. 1, pp. 28–39, Jan. 2011, doi: 10.1109/JPROC.2010.2052776.

[7] D. G. Infield and M. Thomson, "Network power-flow analysis for a high penetration of distributed generation," *2006 IEEE Power Engineering Society General Meeting*, PES, 2006, doi: 10.1109/PES.2006.1709489.

[8] S. Shivashankar, S. Mekhilef, H. Mokhlis, and M. Karimi, "Mitigating methods of power fluctuation of photovoltaic (PV) sources – A review," *Renewable and Sustainable Energy Reviews*, vol. 59, pp. 1170–1184, Jun. 2016, doi: 10.1016/J.RSER.2016.01.059.

[9] C. A. S. Rangel, L. Canha, M. Sperandio, and R. Severiano, "Methodology for ESS-type selection and optimal energy management in distribution system with DG considering reverse flow limitations and cost penalties," *IET Generation, Transmission and Distribution*, vol. 12, no. 5, pp. 1164–1170, 2018, doi: 10.1049/iet-gtd.2017.1027.

[10] C. M. Shepherd, "Design of Primary and Secondary Cells," *J Electrochem Soc*, vol. 112, no. 7, p. 657, 1965, doi: 10.1149/1.2423659.

[11] M. Zillmann, R. Yan, and T. K. Saha, "Regulation of distribution network voltage using dispersed battery storage systems: A case study of a rural network," *2011 IEEE Power and Energy Society General Meeting*, 2011, doi: 10.1109/PES.2011.6039094.

[12] T. Tewari, A. Mohapatra, and S. Anand, "Coordinated control of OLTC and energy storage for voltage regulation in distribution network with high PV penetration," *IEEE Trans Sustain Energy*, vol. 12, no. 1, pp. 262–272, Jan. 2021, doi: 10.1109/TSTE.2020.2991017.

[13] X. Liu, A. Aichhorn, L. Liu, and H. Li, "Coordinated control of distributed energy storage system with tap changer transformers for voltage rise mitigation under high photovoltaic penetration," *IEEE Trans Smart Grid*, vol. 3, no. 2, pp. 897–906, 2012, doi: 10.1109/TSG.2011.2177501.

[14] H. Sugihara, K. Yokoyama, O. Saeki, K. Tsuji, and T. Funaki, "Economic and efficient voltage management using customer-owned energy storage systems in a distribution network with high penetration of photovoltaic systems," *IEEE Transactions on Power Systems*, vol. 28, no. 1, pp. 102–111, 2013, doi: 10.1109/TPWRS.2012.2196529.

[15] Y. Yang, H. Li, A. Aichhorn, J. Zheng, and M. Greenleaf, "Sizing strategy of distributed battery storage system with high penetration of photovoltaic for voltage regulation and peak load shaving," *IEEE Trans Smart Grid*, vol. 5, no. 2, pp. 982–991, 2014, doi: 10.1109/TSG.2013.2282504.

[16] C. Xie, D. Wang, C. S. Lai, R. Wu, X. Wu, and L. L. Lai, "Optimal sizing of battery energy storage system in smart microgrid considering virtual energy storage system and high photovoltaic penetration," *J Clean Prod*, vol. 281, Jan. 2021, doi: 10.1016/j.jclepro.2020.125308.

[17] O. Babacan, W. Torre, and J. Kleissl, "Optimal allocation of battery energy storage systems in distribution networks considering high PV penetration," *IEEE Power and Energy Society General Meeting*, vol. 2016-Novem, pp. 1–5, 2016, doi: 10.1109/PESGM.2016.7741191.

[18] F. Marra, Y. T. Fawzy, T. Bulo, and B. Blažič, "Energy storage options for voltage support in low-voltage grids with high penetration of photovoltaic," *IEEE PES Innovative Smart Grid Technologies Conference Europe*, pp. 1–7, 2012, doi: 10.1109/ISGTEurope.2012.6465690.

[19] C. Xie, D. Wang, C. S. Lai, R. Wu, X. Wu, and L. L. Lai, "Optimal sizing of battery energy storage system in smart microgrid considering virtual energy storage system and high photovoltaic penetration," *J Clean Prod*, vol. 281, Jan. 2021, doi: 10.1016/j.jclepro.2020.125308.

[20] F. Marra et al., "EV charging facilities and their application in LV feeders with photovoltaics," *IEEE Trans Smart Grid*, vol. 4, no. 3, pp. 1533–1540, 2013, doi: 10.1109/TSG.2013.2271489.

[21] M. Zeraati, M. E. Hamedani Golshan, and J. M. Guerrero, "A Consensus-Based Cooperative Control of PEV Battery and PV Active Power Curtailment for Voltage Regulation in Distribution Networks," *IEEE Trans Smart Grid*, vol. 10, no. 1, pp. 670–680, 2019, doi: 10.1109/TSG.2017.2749623.

[22] S. Shivashankar, S. Mekhilef, H. Mokhlis, and M. Karimi, "Mitigating methods of power fluctuation of photovoltaic (PV) sources - A review," *Renewable and Sustainable Energy Reviews*, vol. 59, pp. 1170–1184, 2016, doi: 10.1016/j.rser.2016.01.059.

[23] R. Yan and T. K. Saha, "Investigation of voltage stability for residential customers due to high photovoltaic.

[24] D. Almeida, J. Pasupuleti, and J. Ekanayake, "Comparison of Reactive Power Control Techniques for Solar PV Inverters to Mitigate Voltage Rise in Low-Voltage Grids," *Electronics*, vol. 10, no. 13, p. 1569, Jun. 2021, doi: 10.3390/ELECTRONICS10131569.

[25] E. Demirok, P. C. González, K. H. B. Frederiksen, D. Sera, P. Rodriguez, and R. Teodorescu, "Local reactive power control methods for overvoltage prevention of distributed solar inverters in low-voltage grids," *IEEE J Photovolt*, vol. 1, no. 2, pp. 174–182, 2011, doi: 10.1109/JPHOTOV.2011.2174821.

[26] B. Bletterie, S. Kadam, R. Bolgaryn, and A. Zegers, "Voltage Control with PV Inverters in Low Voltage Networks-In Depth Analysis of Different Concepts and Parameterization Criteria," *IEEE Transactions on Power Systems*, vol. 32, no. 1, pp. 177–185, 2017, doi: 10.1109/TPWRS.2016.2554099.

[27] S. Bin Kim and S. H. Song, "A hybrid reactive power control method of distributed generation to mitigate voltage rise in low-voltage grid," *Energies (Basel)*, vol. 13, no. 8, Apr. 2020, doi: 10.3390/en13082078.

[28] Y. Ca, W. Tang, L. Li, B. Zhang, L. Zhan, and Y. Wang, "Multi-mode adaptive local reactive power control method based on pv inverters in low voltage distribution networks," *IET Generation, Transmission and Distribution*, vol. 14, no. 4, pp. 542–551, 2020, doi: 10.1049/iet-gtd.2018.6955.

[29] R. Kabiri, D. G. Holmes, B. P. McGrath, and L. G. Meegahapola, "LV Grid Voltage Regulation Using Transformer Electronic Tap Changing, with PV Inverter Reactive Power Injection," *IEEE J Emerg Sel Top Power Electron*, vol. 3, no. 4, pp. 1182–1192, 2015, doi: 10.1109/JESTPE.2015.2443839.

[30] R. Hu et al., "Coordinated active and reactive power control for distribution networks with high penetrations of photovoltaic systems," *Solar Energy*, vol. 231, pp. 809–827, Jan. 2022, doi: 10.1016/j.solener.2021.12.025.

[31] S. Hashemi, J. Ostergaard, and G. Yang, "Effect of reactive power management of PV inverters on need for energy storage," *Conference Record of the IEEE Photovoltaic Specialists Conference*, pp. 2304–2308, 2013, doi: 10.1109/PVSC.2013.6744938.

[32] M. Emarati, M. Barani, H. Farahmand, J. Aghaei, and P. C. del Granado, "A two-level over-voltage control strategy in distribution networks with high PV penetration," *International Journal of Electrical Power Energy Systems*, vol. 130, p. 106763, Sep. 2021, doi: 10.1016/J.IJEPES.2021.106763.

[33] B. B. Adetokun, J. O. Ojo, and C. M. Muriithi, "Reactive Power-Voltage-Based Voltage Instability Sensitivity Indices for Power Grid with Increasing Renewable Energy Penetration," *IEEE Access*, vol. 8, pp. 85401–85410, 2020, doi: 10.1109/ACCESS.2020.2992194.

[34] S. Takayama and A. Ishigame, "Autonomous Decentralized Control of Distribution Network Voltage using Reinforcement Learning," *IFAC-PapersOnLine*, vol. 51, no. 28, pp. 209–214, 2018, doi: 10.1016/j.ifacol.2018.11.703.

[35] A. M. Howlader, S. Sadoyama, L. R. Roose, and S. Sepasi, "Distributed voltage regulation using Volt-Var controls of a smart PV inverter in a smart grid: An experimental study," *Renew Energy*, vol. 127, pp. 145–157, 2018, doi: 10.1016/j.renene.2018.04.058.

[36] M. A. Ghasemi and M. Parniani, "Prevention of distribution network overvoltage by adaptive droop-based active and reactive power control of PV systems," *Electric Power Systems Research*, vol. 133, pp. 313–327, 2016, doi: 10.1016/j.epsr.2015.12.030.

[37] M. Hasheminamin, V. G. Agelidis, A. Ahmadi, P. Siano, and R. Teodorescu, "Single-point reactive power control method on voltage rise mitigation in residential networks with high PV penetration," *Renew Energy*, vol. 119, pp. 504–512, Apr. 2018, doi: 10.1016/J.RENENE.2017.12.029.

[38] E. Bernal A., M. Bueno-López, and F. Salazar-Caceres, "Fuzzy-Based Reactive Power Control for Smart PV Inverters in LV Distribution Systems," *IFAC-PapersOnLine*, vol. 50, no. 1, pp. 7705–7710, Jul. 2017, doi: 10.1016/J.IFACOL.2017.08.1147.

[39] A. Bedawy and N. Yorino, "Reactive Power Control of DGs for Distribution Network Voltage Regulation Using Multi-Agent System," *IFAC-PapersOnLine*, vol. 51, no. 28, pp. 528–533, 2018, doi: 10.1016/j.ifacol.2018.11.757.

[40] A. Arshad and M. Lehtonen, "A comprehensive voltage control strategy with voltage flicker compensation for highly PV penetrated distribution networks," *Electric Power Systems Research*, vol. 172, pp. 105–113, Jul. 2019, doi: 10.1016/J.EPSR.2019.02.019.

[41] I. Kim and R. G. Harley, "Examination of the effect of the reactive power control of photovoltaic systems on electric power grids and the development of a voltage-regulation method that considers feeder impedance sensitivity," *Electric Power Systems Research*, vol. 180, Mar. 2020, doi: 10.1016/j.epsr.2019.106130.

[42] H. T. Yang, Y. T. Chen, J. T. Liao, and C. T. Yang, "Over-voltage mitigation control strategies for distribution system with high PV penetration," in *2015 18th International Conference on Intelligent System Application to Power Systems, ISAP 2015*, Institute of Electrical and Electronics Engineers Inc., Nov. 2015. doi: 10.1109/ISAP.2015.7325529.

[43] R. Tonkoski, L. A. C. Lopes, and T. H. M. El-Fouly, "Coordinated active power curtailment of grid connected PV inverters for overvoltage prevention," *IEEE Trans Sustain Energy*, vol. 2, no. 2, pp. 139–147, Apr. 2011, doi: 10.1109/TSTE.2010.2098483.

[44] T. T. Ku, C. H. Lin, C. S. Chen, C. T. Hsu, W. L. Hsieh, and S. C. Hsieh, "Coordination of PV Inverters to Mitigate Voltage Violation for Load Transfer between Distribution Feeders with High Penetration of PV Installation," *IEEE Trans Ind Appl*, vol. 52, no. 2, pp. 1167–1174, Mar. 2016, doi: 10.

[45] A. G. Madureira, M. G. de Freitas, and L. A. C. Lopes, "Reactive Power Control for Low-Voltage PV Inverters to Mitigate Overvoltage," *IEEE Transactions on Power Systems*, vol. 28, no. 2, pp. 1895–1903, May 2013, doi: 10.1109/TPWRS.2012.2233413.

[46] A. Z. Sahraei, S. K. M. T. R. Goudarzi, and M. K. Sheikh-El-Eslami, "Smart reactive power control of photovoltaic inverters in distribution networks for voltage regulation," *Energy*, vol. 188, p. 116006, Jan. 2020, doi: 10.1016/J.ENERGY.2019.116006.

[47] J. C. R. Pereira, M. P. M. Rodrigues, and L. A. P. de Albuquerque, "Optimal Control of Voltage and Reactive Power in PV Inverters for Voltage Stability Improvement," *Energy Reports*, vol. 5, pp. 479–486, Apr. 2019, doi: 10.1016/j.egyr.2019.02.002.

[48] M. Liu, Y. Liu, and L. Luan, "Reactive power control of photovoltaic inverters based on voltage optimization in distribution systems,"

IEEE Access, vol. 7, pp. 133700–133708, 2019, doi: 10.1109/ACCESS.2019.2944647.

[49] S. Bolognani, M. B. L. R. Di Benedetto, F. D. Paola, and A. M. Storti, "Voltage Control in Distribution Networks With High Penetration of Distributed Generation: An Overview of Voltage Control Techniques," *IEEE Transactions on Smart Grid*, vol. 8, no. 5, pp. 2193–2202, Sep. 2017, doi: 10.1109/TSG.2017.2679538.

Detection and Mitigation of Distributed Denial of Service (DDoS) Attacks on Software Defined Networks (SDNs) Using Multilayer Perceptron (MLP)

Rian Fahrizal
Department of Electrical Engineering
Universitas Sultan Ageng Tirtayasa
Cilegon, Indonesia
rian.fahrzal@untirta.ac.id

Ivan Munandar
Department of Electrical Engineering
Universitas Sultan Ageng Tirtayasa
Cilegon, Indonesia
rfrianef2@gmail.com

Fadil Muhammad
Department of Electrical Engineering
Universitas Sultan Ageng Tirtayasa
Cilegon, Indonesia
fadil.muhammad@untirta.ac.id

***Abstract*—Distributed Denial of Service (DDoS) attacks on Software Defined Networks (SDNs) have become a growing threat, resulting in serious disruptions to service availability and infrastructure reliability. Currently, the most common DDoS attack detection technique used on both traditional and SDN networks is the statistic-based detection method, but this method has a weakness in detecting new or unprecedented attacks. This can be overcome by using deep learning methods that are able to handle non-linear, heterogeneous, and high-dimensional data, which are often found in network traffic data. This research develops a DDoS attack detection and mitigation system on SDN network traffic using the Multilayer Perceptron (MLP) algorithm. The tests conducted show that the DDoS attack detection and mitigation system developed in this study has an accuracy level of 71.17%. This system has proven to be effective in detecting DDoS attacks. Post-mitigation network performance analysis shows a significant improvement in performance compared to pre-mitigation conditions. Previously, bottlenecks were identified in the tissues. However, after mitigation, the network can return to optimal functioning.**

***Index Terms*—Distributed Denial of Service (DDoS), Deep Learning (DL), Software Defined Network (SDN), Multilayer Perceptron (MLP), detection, mitigation.**

I. Introduction

Rapid advances in networks and information technology have made it possible for seamless connections to store and communicate information on a large scale [1]. One of the most dominant major attacks leading to denial of service to users is Distributed Denial of Service (DDoS) [2], [3]. A DDoS attack is a type of cyber-attack that aims to attack computer infrastructure by flooding servers with excessive internet traffic [4]. DDoS attacks can be carried out by using many computers infected by malware or by using a botnet network consisting of thousands of computers so that the server becomes overloaded and cannot process requests from legitimate users [5].

In Cisco's annual internet report, 2018–2023, it shows that the trend of DDoS attacks from 2018 to 7.09 million to 2023 is expected to increase by 15.4 million [6]. Attackers typically exploit vulnerabilities in data transport, networking, and application-layer protocols such as Transmission Control Protocol (TCP), User Datagram Protocol (UDP), and Internet Control Message Protocol (ICMP) [7].

Software-Defined Networks (SDN) are a type of computer network that separates the control plane from the data, making it possible to be a solution in protecting against DDoS attacks with more flexible and adaptive controls [8]. The advantages of SDN involve several crucial aspects, such as flexibility, efficiency, and scalability [9]. Over the past few years, SDN has proven to be able to generate effective defenses against various types of network-based DDoS attacks [10].

Currently, the most commonly used DDoS attack detection technique on SDN networks is the statistics-based detection method, but this method has a weakness in detecting new or unprecedented attacks [11]. The research conducted by [12] using statistics-based DDoS detection methods has several drawbacks. One of its main drawbacks is its poor performance on very large DDoS attacks.

This study proposes a deep learning-based method for detecting DDoS attacks in the SDN environment. A multilayer perceptron (MLP) model is used to study normal network traffic patterns and identify anomalies that indicate DDoS attacks. The MLP was selected based on its ability to handle complex and non-linear relationships in network traffic data, potentially providing better performance than traditional machine learning techniques.

The main contributions of this paper are:

1) A new MLP-based approach to DDoS attack detection in SDN environments.
2) A comprehensive evaluation of the proposed method using a dataset of DDoS attacks generated through simulations on an SDN network environment that includes different types of DDoS attacks, such as ICMP Flood, UDP Flood, and TCP-SYN Flood.

979-8-3315-1921-6/24/$31.00 ©2024 IEEE

3) Comparative analysis of network performance before and after the implementation of the proposed detection and mitigation system. This analysis includes Quality of Service (QoS) metrics such as throughput, delay, packet loss, and resource utilization.

II. Related Works

Recent research in the field of network security shows that Distributed Denial of Service (DDoS) attacks are the most frequent threats to Internet of Things (IoT) networks and devices. One approach that has shown high effectiveness is the use of ResNet18 transfer learning, which is able to achieve 99.9% accuracy in detecting DoS and DDoS attacks, as well as 87% in classifying specific attack types such as SYN flood, UDP flood, and NTP Amplification [4].

In the context of Software Defined Networks (SDNs), a comparison of various DDoS attack classification mechanisms shows that machine learning methods consistently outperform other approaches [13]. Statistical and threshold methods, while faster and requiring less data, are often less accurate at detecting complex attacks.

Further research explores the efficiency of deep learning algorithms in detecting abnormal activity such as DDoS. The Convolutional Neural Network (CNN) showed excellent performance, achieving 99% accuracy when tested using standard datasets such as NSL-KDD. CNN has managed to outperform classical algorithms such as Decision Tree, Support Vector Machine (SVM), K-Nearest Neighbors (K-NN), and conventional Neural Network (NN). This advantage of CNN shows the great potential of deep learning algorithms in improving network security [14].

In addition to CNNs, the study [15] also shows the advantages of Multi-Layer Perceptron (MLP) in dealing with non-linear and complex problems that are often encountered in intrusion detection. MLP shows better performance compared to algorithms such as CNN, Long Short-Term Memory (LSTM), and Stacked Auto-encoder (SAE) in the context of cyber-attack detection, especially brute-force SSH attacks on SDN networks. These findings extend the application of MLPs in various areas of network security.

Innovations in sampling techniques have also contributed significantly to the effectiveness of DDoS attack detection. The use of sFlow and adaptive polling sampling in SDN environments, combined with deep learning models such as Stacked Autoencoders (SAE), has been proven to reduce network load while maintaining high detection accuracy [16]. The sFlow-based approach shows very promising results, with the True Positive rate reaching 95% and the False Positive rate being less than 4%.

III. Proposed Methodology

The methodology of this research aims to design a Multi-Layer Perceptron (MLP) algorithm as a DDoS attack detection system and utilize Software-Defined Network (SDN) as the main component in the development of the research system.

The DDoS attack detection system on SDN networks using the MLP algorithm consists of two main stages, namely learning and detection. In the learning stage, datasets containing normal network flow and DDoS data are collected and used to train MLP algorithms in recognizing network data patterns. The resulting model is then stored on the SDN controller. In the detection stage, real-time data from the operating SDN network is classified using a model that has been built. If a DDoS attack is detected, the SDN controller will mitigate and provide a warning to the network administrator.

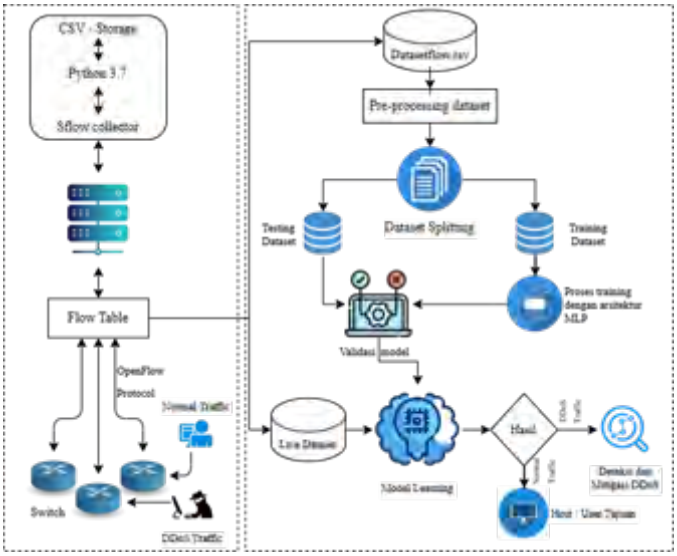

Fig. 1. System Planning

A. Software Defined Network (SDN) Topology Design

This network simulation environment is created inside, the Ubuntu 22.4 operating system which acts as a platform that provides infrastructure and resources to run the simulation. The following is a network configuration table used in the study.

TABLE I
Software Defined Network Configuration

Component	Configuration Details
Topology	5 Switches are connected linearly, each connected to 3 hosts, a total of 15 hosts.
Switches	• **s1:** Connected to h1, h2, h3, s2 • **s2:** Connected to h4, h5, h6, s1, s3 • **s3:** Connected to h7, h8, h9, s2, s4 • **s4:** Connected to h10, h11, h12, s3, s5 • **s5:** Connected to h13, h14, h15, s4
Hosts	h1 to h15, each with a unique IP address and MAC, is connected to the switch in order.
Controller	• **IP:** 127.0.0.1 • **Port:** 6653 • **Protocol:** OpenFlow 1.3
Monitoring	sFlow & Wireshark: Used for network monitoring

B. Data Acquisition and Pre-processing

1) Data Acquisition

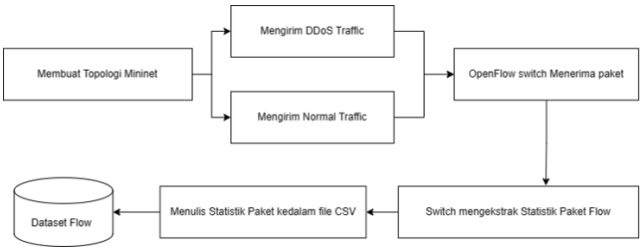

Fig. 2. Block diagram of dataset creation

The process of creating a dataset on an SDN network includes: creating a network topology with Mininet, sending normal and DDoS data packets, receiving packets by openflow switch, extracting flow statistics, and storing data in CSV format. The resulting dataset consists of 21 parameters that describe the data flow in the OpenFlow network.

TABLE II
NETWORK PARAMETERS

Features on datasets		
Timestamp	tp_dst	idle_timeout
datapath_id	ip_proto	hard_timeout
flow_id	icmp_code	Flags
ip_src	icmp_type	packet_count
tp_src	flow_duration_sec	packet_count_per_nsecond
ip_dst	flow_duration_nsec	packet_count_per_second
byte_count	byte_count_per_second	byte_count_per_nsecond

2) Data pre-processing

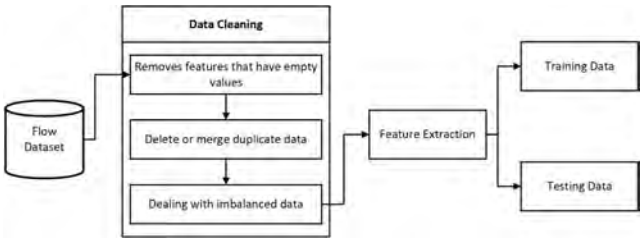

Fig. 3. Data Pre-processing Flows

SDN traffic dataset pre-processing consists of data cleaning, feature transformation, and feature selection using Recursive Feature Elimination (RFE). Categorical features are encoded with one-hot encoding, and the dataset is divided into training data (80%) and test data (20%), followed by standardization. The result is a clean and balanced dataset.

C. Perceptron Multilayer Algorithm Design (MLP)

D. Quality of Service (QoS) Analysis

QoS analysis is carried out using the TIPHON standard to measure network quality. The parameters used to conduct QoS analysis are throughput, delay, jitter, and packet loss. Here is a table showing the TIPHON standard categories for these parameters.

TABLE III
MLP ARCHITECTURE

Models	Hyperparameters
MLP	Layer : 2 layers (256 and 128 neurons) Activation : relu L2 Regulation : 0.0001 Random state : 42 Solver : Adam Learning rate : 0.001

TABLE IV
TIPHON STANDARD

QoS Parameters	Very Good	Good	Keep	Bad
Throughput	¿ 2.1 Mbps	1200 kbps – 2.1 Mbps	700 – 1200 kbps	338 – 700 kbps
Delay	¡ 150 ms	150 – 300 ms	300 – 450 ms	¿ 450 ms
Jitter	0 ms	0 – 75 ms	75 – 125 ms	125 – 225 ms
Packet Loss	0 – 2%	3 – 14%	12 – 24%	¿ 25%

IV. RESULT AND DISCUSSION

A. Network Topology and Simulation Setup

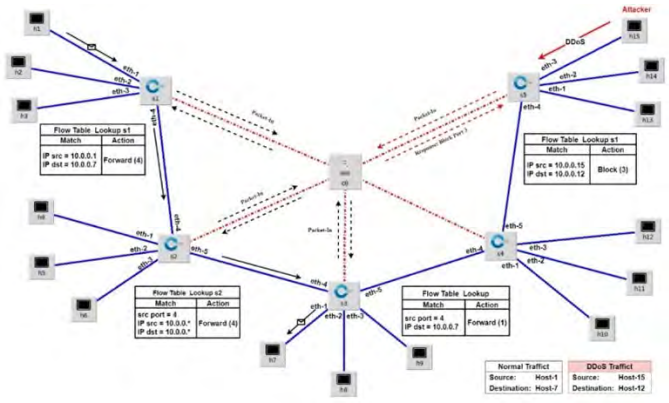

Fig. 4. Linear Topology

Figure 4 shows the topology simulation of the SDN network used in this study. There are three main components in the formation of an SDN network, namely hosts, OVS Switches, and controllers. The switch in this study functions as a data traffic regulator and flow rule maker using the Ryu controller. This topology allows for multiple paths between hosts, which increases network redundancy and resiliency.

B. Dataset Generation and Preprocessing

Figure 5 provides a clear visualization of the composition of the dataset collected before the pre-processing process. The graph illustrates a comparison between the number of packets categorized as DDoS traffic, which reaches 1.7 million packets, and normal traffic, which amounts to 9 thousand

packets. Next, the pre-processing stage was carried out, where the amount of data had been balanced to 50% for each category.

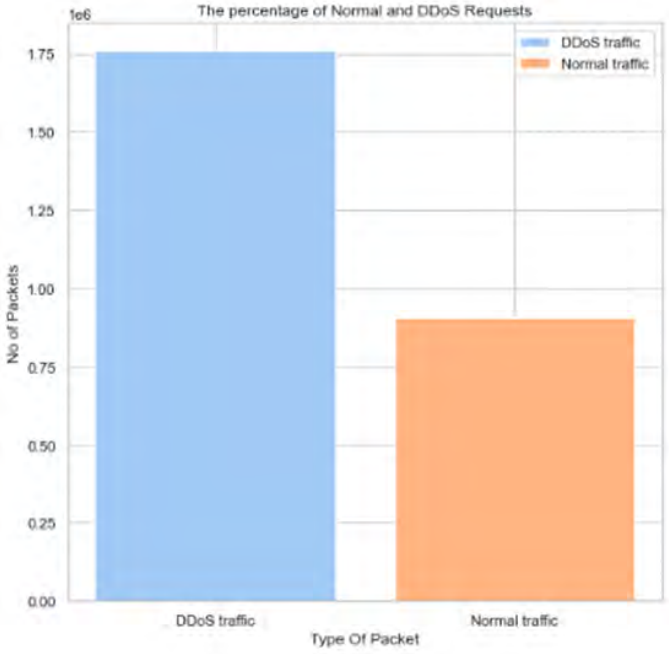

Fig. 5. Distribution of Packet Count on Datasets

C. Effectiveness of Model Training

	precision	recall	f1-score	support
0	1.00	0.15	0.26	226596
1	0.70	1.00	0.82	440285
accuracy			0.71	666881
macro avg	0.85	0.58	0.54	666881
weighted avg	0.80	0.71	0.63	666881

Fig. 6. Model Training Results Report

MLP models that have demonstrated performance vary between non-DDoS (class 0) and DDoS (class 1) classes. For the non-DDoS class, the model has a perfect precision of 1.00, but the recall is only 0.15, indicating that the model often fails to identify normal traffic, with 85% of non-DDoS cases missing. In contrast, for the DDoS class, the model has a perfect recall of 1.00, but the precision is only 0.70, which indicates the presence of false alerts on normal traffic. The overall accuracy of the model is 71%, and while it looks moderate, the perfect recall for the DDoS class shows that the model is very effective at detecting DDoS attacks, although it can still be improved to reduce false alerts on non-DDoS traffic.

The model successfully detected 34,373 DDoS attack cases correctly as attacks (True Positives/TP), while 440,251 normal

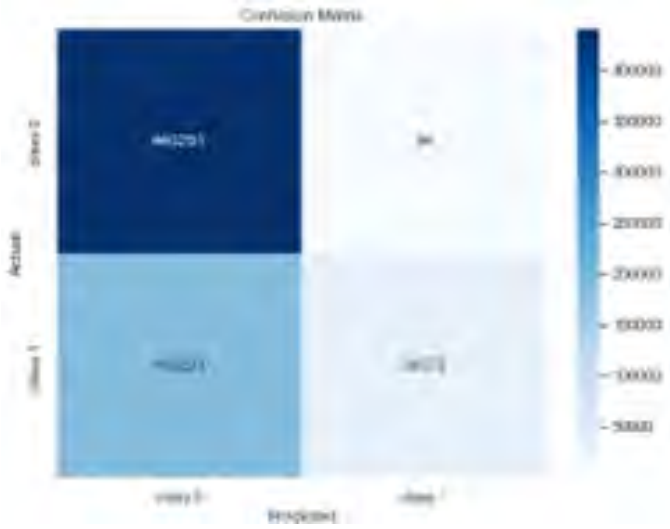

Fig. 7. Confusion Matrix

traffic cases were correctly classified as non-attacks (True Negatives/TN). However, there were 34 cases of normal traffic that were incorrectly classified as attacks (False Positives/FP). In addition, the model failed to detect 192,223 cases of attacks, which were incorrectly classified as normal traffic (False Negatives/FN).

D. Network Performance Analysis

1) **Jitter Measurement**

- Normal Traffic Conditions. Jitter measurements on normal traffic show a very low value of 0.026 ms, which is categorized as ”very good” according to the TIPHON standard (below 75 ms). This reflects optimal network performance without significant interference.

TABLE V
JITTER ON NORMAL TRAFFIC NETWORK

Normal Traffic	Jitter (ms)
Jitter at Normal Conditions (ms)	0.026

- During DDoS Attacks. During a DDoS attack, jitter cannot be measured due to Request Time Out (RTO) due to network instability caused by packet flooding. However, after mitigation was implemented, the jitter decreased significantly, close to normal conditions. In ICMP flood attacks, the jitter drops to 0.011 ms, the UDP flood to 0.013 ms, and the TCP SYN flood to 0.007 ms, all of which fall into the ”very good” category according to the TIPHON standard. Mitigation mechanisms have proven to be effective in restoring network stability.

2) **Delay Analysis**

- Normal Traffic Conditions. On normal traffic, the network latency is low and stable with an average of 0.28 ms, which is categorized as ”very good”

TABLE VI
JITTER DURING ATTACKS AND AFTER MITIGATION

Types of DDoS Traffic	**Jitter During DDoS Occurrence (ms)**	**Jitter After Mitigation (ms)**
ICMP flood	RTO	0.011
UDP flood	RTO	0.013
TCP SYN flood	RTO	0.007

according to the TIPHON standard, reflecting a healthy network without significant disruption.

TABLE VII
DELAY DURING DDOS ATTACKS

Normal Traffic Delay			
Min	Avg	Max	mdev
0.052 ms	0.280 ms	8.492 ms	1.1 ms

- Impact of DDoS Attacks. During a DDoS attack, delay measurements cannot be performed due to network congestion that causes many ICMP Echo Request packets to go unresponsive, resulting in RTOs. This indicates severe congestion and network instability.

TABLE VIII
DELAY DURING DDOS ATTACKS

Types of DDoS Traffic	**During DDoS Occurrence (ms)**			
	Min	**Avg**	**Max**	**mdev**
ICMP flood	RTO	RTO	RTO	RTO
UDP flood	RTO	RTO	RTO	RTO
TCP SYN flood	RTO	RTO	RTO	RTO

- Effectiveness of Mitigation Strategies. After mitigation, the delay experienced significant improvement. In ICMP flood attacks, the average delay reaches 0.242 ms with a standard deviation of 1.162 ms, which is still in the ”very good” category according to the TIPHON standard. Post-mitigation UDP flood attacks recorded an average delay of 0.4 ms with a standard deviation of 2,322 ms, also categorized as ”very good” despite a slight spike. In TCP SYN flood attacks, despite the increase in maximum values, the average delay remained in the ”very good” category as per the TIPHON standard, indicating improved network stability after mitigation.

TABLE IX
DELAY AFTER DDOS ATTACKS

Types of DDoS Traffic	**After Mitigation (ms)**			
	Min	Avg	Max	mdev
ICMP flood	0.028	0.242	8.717	1.162
UDP flood	0.037	0.4	20.409	2.322
TCP SYN flood	0.04	0.375	17.544	2.045

3) Throughput Evaluation

- Normal Network Capacity. On normal traffic, 6.24 Gbps of data is successfully transferred in 10 seconds with a bandwidth of 5.36 Gbps, which meets the ”very good” category based on the TIPHON standard. This indicates optimal network performance.

TABLE X
NETWORK THROUGHPUT ON NORMAL TRAFFIC

Normal Traffic Throughtput		
Interval	Transfer	Bandwitch
0-10 s	6.24 Gbps	5.36 Gbps

- Throughput Degradation During Attacks. When a DDoS attack occurs, the throughput cannot be measured due to network communication disruptions caused by overload, indicating a decrease in data transmission efficiency.

TABLE XI
THROUGHPUT DURING A DDOS ATTACK

Types of DDoS Traffic	**Interval**	**During DDoS Occurs (GBYTS)**	
		Transfer	**Bandwidth**
ICMP flood	0-10 s	RTO	RTO
UDP flood	0-10 s	RTO	RTO
TCP SYN flood	0-10 s	RTO	RTO

- Recovery After Mitigation. Once mitigation is implemented, there is a significant improvement in all types of attacks. In ICMP flood, data transfer reaches 3.75 Gbytes with a bandwidth of 3.21 Gbps, while in UDP flood, transfer reaches 3.61 Gbytes with a bandwidth of 3.09 Gbps. For TCP SYN flood, transfer reaches 4.06 Gbytes with a bandwidth of 3.49 Gbps. These results show that mitigation is effective in reducing the impact of the attack and restoring network performance to a near-optimal condition, still meeting the ”very good” category based on the TIPHON standard.

TABLE XII
THROUGHPUT AFTER MITIGATION

Types of DDoS Traffic	**Interval**	**During DDoS Occurs (GBYTS)**	
		Transfer	**Bandwidth**
ICMP flood	0-10 s	3.75	3.21
UDP flood	0-10 s	3.61	3.09
TCP SYN flood	0-10 s	4.06	3.49

4) Packet Loss Assessment

- Normal Operating Conditions. In normal traffic, there is no packet loss during 100 packet shipments, which indicates optimal network conditions with stable and efficient performance. According to the

TIPHON standard, this value is in the ”very good” category with packet loss below 1%.

TABLE XIII
PACKET LOSS IN NORMAL TRAFFIC

Packet Loss Normal Traffic	
Number of Packages	packet loss (%)
100	0

- Packet Loss During DDoS Events. When a DDoS attack occurs without mitigation, packet loss reaches 100%, indicating a total disruption to the network.

TABLE XIV
PACKET LOSS DURING DDOS ATTACKS

Types of Data Traffic	**Number of Packages**	**As long as DDoS occurs**
		packet loss (%)
ICMP flood	100	100
UDP flood		100
TCP SYN flood		100

- Mitigation Effectiveness on Packet Loss Reduction. After mitigation, packet loss decreased significantly: to 39% in ICMP flood attacks, 35% in UDP flood attacks, and 49% in TCP SYN flood attacks. Although it is still in the ”poor” category according to the TIPHON standard, it shows that mitigation has succeeded in reducing the impact of attacks and significantly improving network stability and efficiency.

TABLE XV
PACKET LOSS AFTER MITIGATION

Types of Data Traffic	**Number of Packages**	**As long as DDoS occurs**
		packet loss (%)
ICMP flood	100	39
UDP flood		35
TCP SYN flood		49

E. Resource Utilization

1) **Normal Operating Conditions** Under normal conditions, the system shows high efficiency with stable CPU and memory usage. The CPU Process is only 0.3%, the CPU System is 12.5%, and the memory usage is 39.1%, indicating that the network is able to handle traffic without overloading.

TABLE XVI
RESOURCE UTILIZATION ON NORMAL TRAFFIC

Normal Traffic Resource (%)		
System CPU	Memory Usage	CPU Process
12.5	39.1	0.3

2) **During Attacks** DDoS attacks such as ICMP Flood, UDP Flood, and TCP SYN Flood caused a significant spike in resource usage. ICMP Flood increases CPU usage by 99.2% and memory to 52%. UDP Flood causes the CPU to reach 100% and the memory to go up to 59.8%, while TCP SYN Flood boosts the CPU to 100% with 55.9% memory. This results in a decrease in system performance.

TABLE XVII
RESOURCE UTILIZATION DURING DDOS ATTACKS

Types of DDoS Traffic	**Resources During DDoS Occurrence (%)**		
	System CPU	Memory Usage	CPU Process
ICMP flood	99.2	52	1.9
UDP flood	100	59.8	3.37
TCP SYN flood	100	55.9	0.58

3) **Post-Mitigation** After mitigation was implemented, there was a significant decrease in resource usage: ICMP Flood decreased to 74.7% CPU and 8.56% memory, UDP Flood to 53.6% CPU and 51.2% memory, and TCP SYN Flood to 48.8% CPU and 39.6% memory. Although some specific processes are experiencing increased CPU usage, this is related to monitoring and blocking activities for mitigation. Overall, mitigation has proven to be effective in restoring system performance and efficiency close to normal conditions, demonstrating the importance of appropriate mitigation strategies to maintain network stability and performance in the face of DDoS attacks.

TABLE XVIII
RESOURCE UTILIZATION AFTER MITIGATION

Types of DDoS Traffic	**Resources After Mitigation**		
	System CPU	Memory Usage	CPU Process
ICMP flood	74.7	8.56	11.1
UDP flood	53.6	51.2	0.39
TCP SYN flood	48.8	39.6	0.37

V. CONCLUSION

Distributed Denial of Service (DDoS) attacks remain a significant threat to the security of modern networks, including Software-Defined Networking (SDN) infrastructure. This study proposes an innovative approach using the Multilayer Perceptron (MLP) model for the detection and classification of DDoS attacks on SDN networks, achieving an accuracy of 71.17%. The methodology developed involves the preparation of a comprehensive dataset of 2 million data packets, which are flattened to avoid bias, as well as model optimization using the RandomSearchCV algorithm.

The results of the experiment show that the mitigation measures implemented have succeeded in significantly reducing the impact of DDoS attacks. Analysis of post-mitigation network metrics showed substantial improvements, with jitter,

delay, throughput, and resource utilization returning to the "good" to "very good" categories according to the TIPHON standard. Although packet loss still needs further optimization, the overall improvement in network performance demonstrates the effectiveness of the mitigation strategies implemented.

In conclusion, the integration of the MLP model with effective mitigation techniques offers a promising approach in improving the resilience of SDN networks to DDoS attacks. This research not only contributes to a deeper understanding of the application of deep learning in network security, but also paves the way for the development of more sophisticated attack detection and mitigation systems in the future. With the ability to adapt to evolving attack patterns, this approach has significant potential to improve the security and reliability of modern network infrastructure.

REFERENCES

[1] P. A and S. S, "DDOS Attack detection in telecommunication network using machine learning," *Journal of Ubiquitous Computing and Communication Technologies*, vol. 01, no. 01, pp. 33–44, Sep. 2019, doi: 10.36548/jucct.2019.1.004.

[2] F. J. Abdullayeva, "Distributed denial of service attack detection in E-government cloud via data clustering," *Array,* vol. 15, Sep. 2022, doi: 10.1016/j.array.2022.100229.

[3] P. Khuphiran, P. Leelaprute, P. Uthayopas, K. Ichikawa, and W. Watanakeesuntorn, "Performance Comparison of Machine Learning Models for DDoS Attacks Detection," in *2018 22nd International Computer Science and Engineering Conference (ICSEC)*, IEEE, Nov. 2018, pp. 1–4. doi: 10.1109/ICSEC.2018.8712757.

[4] F. Hussain, S. G. Abbas, M. Husnain, U. U. Fayyaz, F. Shahzad, and G. A. Shah, "IoT DoS and DDoS Attack Detection using ResNet," in *Proceedings - 2020 23rd IEEE International Multi-Topic Conference, INMIC 2020*, Institute of Electrical and Electronics Engineers Inc., Nov. 2020. doi: 10.1109/INMIC50486.2020.9318216

[5] B. A. Khalaf, S. A. Mostafa, A. Mustapha, M. A. Mohammed, and W. M. Abduallah, "Comprehensive review of artificial intelligence and statistical approaches in distributed denial of service attack and defense methods," IEEE *Access*, vol. 7, pp. 51691–51713, 2019, doi: 10.1109/ACCESS.2019.2908998.

[6] "Cisco Annual Internet Report - Cisco Annual Internet Report (2018–2023) White Paper - Cisco." Accessed: Mar. 30, 2023. [Online]. Available: https://www.cisco.com/c/en/us/solutions/collateral/executive-perspectives/annual-internet-report/white-paper-c11-741490.html

[7] H. S. Obaid and E. H. Abeed, "Abeed,-DoS and DDoS Attacks at OSI Layers," *International Journal of Multidisciplinary Research and Publications Hadeel S. Obaid and Esamaddin H*, vol. 2, no. 8, pp. 1–9, 2020.

[8] B. Nugraha and R. N. Murthy, "Deep Learning-based Slow DDoS Attack Detection in SDN-based Networks," in *2020 IEEE Conference on Network Function Virtualization and Software Defined Networks, NFV-SDN 2020 - Proceedings*, Institute of Electrical and Electronics Engineers Inc., Nov. 2020, pp. 51–56. doi: 10.1109/NFV-SDN50289.2020.9289894.

[9] S. Saraswat, V. Agarwal, H. P. Gupta, R. Mishra, A. Gupta, and T. Dutta, "Challenges and solutions in Software Defined Networking: A survey," *Journal of Network and Computer Applications*, vol. 141, pp. 23–58, Sep. 2019, doi: 10.1016/j.jnca.2019.04.020.

[10] P. Karthika and K. Arockiasamy, "Simulation of SDN in mininet and detection of DDoS attack using machine learning," *Bulletin of Electrical Engineering and Informatics*, vol. 12, no. 3, pp. 1797–1805, Jun. 2023, doi: 10.11591/eei.v12i3.5232.

[11] F. Hussain, S. G. Abbas, M. Husnain, U. U. Fayyaz, F. Shahzad, and G. A. Shah, "IoT DoS and DDoS Attack Detection using ResNet," in *Proceedings - 2020 23rd IEEE International Multi-Topic Conference, INMIC 2020*, Institute of Electrical and Electronics Engineers Inc., Nov. 2020. doi: 10.1109/INMIC50486.2020.9318216.

[12] H. Majed, H. N. Noura, O. Salman, M. Malli, and A. Chehab, "Efficient and secure statistical DDoS detection scheme," in *ICETE 2020 - Proceedings of the 17th International Joint Conference on e-Business and Telecommunications*, SciTePress, 2020, pp. 153–161. doi: 10.5220/0009873801530161

[13] Y. Wood et al., "Towards DDoS detection mechanisms in Software-Defined Networking," Sep. 15, 2021, *Academic Press*. doi: 10.1016/j.jnca.2021.103156.

[14] A. R. Shaaban, E. Abd-Elwanis, and M. Hussein, "DDoS attack detection and classification via Convolutional Neural Network (CNN)," in *2019 Ninth International Conference on Intelligent Computing and Information Systems (ICICIS)*, IEEE, Dec. 2019, pp. 233–238. doi: 10.1109/ICICIS46948.2019.9014826.

[15] Institute of Electrical and Electronics Engineers, 2020 IEEE International Conference on Communications Workshops (ICC) : proceedings : Dublin, Ireland, 7-11 June 2020. 2020.

[16] R. M. A. Ujjan, Z. Pervez, K. Dahal, A. K. Bashir, R. Mumtaz, and J. González, "Towards sFlow and adaptive polling sampling for deep learning based DDoS detection in SDN," *Future Generation Computer Systems*, vol. 111, pp. 763–779, Oct. 2020, doi: 10.1016/j.future.2019.10.015.

Kalman Filter For Radon based Earthquake Early Detection

Wahyu Sukestyastama Putra
Department of Electrical Engineering and Information Technology
Universitas Gadjah Mada
Yogyakarta, Indonesia
Faculty of Computer Science
Universitas AMIKOM Yogyakarta
Yogyakarta, Indonesia
wahyu.sie14@mail.ugm.ac.id
ORCID: 0000-0002-5631-0767

Sunarno
Department of Nuclear Engineering and Physics Engineering
Universitas Gadjah Mada
Yogyakarta, Indonesia
sunarno@ugm.ac.id

I Wayan Mustika
Department of Electrical Engineering and Information Technology
Universitas Gadjah Mada
Yogyakarta, Indonesia
wmustika@ugm.ac.id

***Abstract*—Radon measurement for earthquake prediction is challenging due to environmental noise and sensor limitations. Factors such as temperature, humidity, and soil moisture cause fluctuations in radon levels, making distinguishing seismic-related changes from normal variations difficult. In addition, sensor limitations, such as sensor resolution, can reduce the ability of early warning systems to detect precursor signals. In this study, we designed an early earthquake detection method using the Kalman Filter on radon gas concentration data collected using an ion chamber sensor at a sampling interval of 1 minute. The Kalman Filter was applied to overcome the uncertainties in sensor measurements and the radon-earthquake phenomenon. The differences between the filter predictions and the raw sensor data indicate the presence of external factors, possibly earthquake precursors. In all six analyzed events, radon anomalies were effectively captured through the difference of squares, indicating the potential of the method as an early warning system for seismic activity. The proposed method detected radon anomalies 1 to 19 days before an earthquake.**

***Index Terms*—Earthquake Prediction, Radon, Kalman Filter**

I. Introduction

Radon is a potential precursor for early detection of earthquakes [1], [2]. Radon measurements for earthquake prediction pose a challenge in overcoming the measurement uncertainty. Sensor accuracy affects this uncertainty. Natural factors, such as temperature, humidity, barometric pressure, and soil moisture, can also affect the accuracy of radon measurements. The ability of the system to distinguish between changes in radon concentration that can indicate an impending earthquake and changes in radon concentration caused by the environment can improve the reliability of the early earthquake detection system.

Previous research has developed methods for detecting radar anomalies before earthquakes. The methods are KNN [3], SVM [3], [4], boosted tree [3], bagged CART (Classification and Regression Trees) [3], Multiple Linear Regression (MLR) [5], Artificial Neural Networks (ANN) [4], [5], Decision Trees (DT) [5], Boxplot [6] and LSTM [4]. However, these methods do not consider the measurement uncertainty problem. To improve the reliability of earthquake prediction, methods such as temporal and spatial averaging and anomaly detection algorithms are essential for isolating meaningful patterns from background noise. Without these approaches, detection of radon anomalies linked to seismic events remains highly uncertain.

One of the key advantages of the Kalman filter in environmental sensing is its ability to handle noisy data from various sensors. Kalman filter is adept at managing the complexities of environmental datasets, which often include thousands of observations per time-step and exhibit irregular characteristics [7]. This capability is particularly beneficial in applications such as atmospheric boundary layer monitoring, where the filter can effectively track parameters based on LiDAR returns [8]. The extended Kalman filter (EKF) is especially useful in these scenarios because it can accommodate the non-linear system dynamics that are common in environmental processes [9]. A transistor-based analog Kalman filter circuit, enabling continuous processing of sensor data, has been developed to reduce power consumption and latency in sensor fusion tasks [10].

This study contributes to the early detection of earthquakes based on radon precursors by using the Kalman filter method. This paper consists of five sections. The introduction provides the background of the problem, while the related works section discusses the progress in radon-based earthquake prediction and application of the Kalman filter. The proposed method section explains the Kalman Filter, early detection method, and data-collection process. The results and discussion section presents the simulation results of the proposed method along with an analysis of the research findings. The final section, the conclusion, explains the research findings, limitations, and future work in radon-based earthquake early detection

979-8-3315-1921-6/24/$31.00 ©2024 IEEE

research.

II. Related Works

A primary challenge in using radon for earthquake prediction is the uncertainty in radon measurements. Studies indicate that radon levels fluctuate significantly due to environmental factors such as temperature, humidity, and atmospheric pressure [11]. This uncertainty complicates interpreting radon anomalies as seismic precursors. Although the correlation between recurrent radon anomalies and local earthquake magnitudes has been established, the relationship remains complex and requires further investigation to be fully understood [12]. Thus, robust statistical models are needed to distinguish between normal fluctuations and significant precursor signals.

Geological and hydrological factors significantly impact radon emissions, which arise from uranium decay in Earth's crust and are influenced by geological stress and microcracks in rocks [13], [14]. The spatial and temporal resolutions of radon monitoring challenge effective earthquake prediction. Continuous monitoring is crucial to detect transient radon anomalies preceding seismic events [15]. Continuous atmospheric radon monitoring helps evaluate earthquake risk in densely populated areas [16]. However, deploying monitoring stations and collecting high-resolution data are resource-intensive and logistically challenging.

The Kalman filter has become crucial for earthquake prediction, improving seismic forecasts through state estimation and data assimilation. It addresses multiple facets of seismic data processing, real-time location estimation, and the integration of diverse sensor inputs. Kalman filters are primarily used in real-time earthquake event localization [17]. The Kalman filter's recursive nature allows continuous updates of location estimates with new data, improving prediction reliability. The Kalman filter has been successfully used for seismic data deconvolution, enhancing signal clarity and accuracy [18]. This is crucial for earthquake prediction, as clearer data aids in better understanding and modeling seismic events.

Several studies have shown the benefits of the Kalman filter in earthquake prediction. Although it has been widely applied in earthquake research, its primary use is to reduce noise in seismic signals, not to manage uncertainty in precursor-based predictions. In several studies, radon-based earthquake predictions have not considered the uncertainty aspect in measurements. The Kalman Filter can be considered for earthquake precursor signal prediction, especially radon gas, based on these conditions.

III. Proposed Method

A. Kalman Filter

The Kalman filter consists of two steps: prediction and update [19]. The Kalman Filter consists of 5 equations written in the Eq.1 to Eq.5. The system is predicted based on the previous state and the dynamic state model in the prediction step. The state prediction is expressed as

$$\hat{x}_{k|k-1} = F_k \hat{x}_{k-1|k-1}. \tag{1}$$

$\hat{x}_{k|k-1}$ represents the predicted state at time k, based on the information available up to time $k-1$. The state transition matrix F_k describes the evolution of the state from time $k-1$ to time k. In this study, a 1-dimensional Kalman Filter was used. Thus, the F_k value can be expressed as 1. The prediction of the error covariance is calculated as

$$P_{k|k-1} = P_{k-1|k-1} + Q_k. \tag{2}$$

In this equation, the predicted error covariance $P_{k|k-1}$ is computed using updated error covariance from the previous time step $P_{k-1|k-1}$. Matrix Q_k represents the uncertainty in the system model.

The second step of the Kalman Filter involves updating the predicted state using measurement data. The Kalman Gain was calculated to determine the optimal weighting between the prediction and measurement. The Kalman Gain is expressed as

$$K_k = P_{k|k-1} H_k^\top (H_k P_{k|k-1} H_k^\top + R_k)^{-1}. \tag{3}$$

In this equation, the Kalman Gain K_k determines the weight given to the measurement compared to the prediction. Measurement matrix H_k relates the measurements to the system state, whereas R_k represents the measurement error covariance.

Once the Kalman Gain is computed, the state is updated as follows:

$$\hat{x}_{k|k} = \hat{x}_{k|k-1} + K_k(z_k - H_k \hat{x}_{k|k-1}), \tag{4}$$

where $\hat{x}_{k|k}$ is the updated state estimate computed by adding the weighted measurement residual to the predicted state. The actual measurement at time k, denoted by z_k, is compared with the predicted measurement $H_k \hat{x}_{k|k-1}$.

Finally, the error covariance is updated to reflect the remaining uncertainty after incorporating the measurement written as

$$P_{k|k} = (I - K_k H_k) P_{k|k-1}. \tag{5}$$

This equation updates the error covariance $P_{k|k}$, thereby reducing uncertainty based on the measurement.The identity matrix I is used to ensure that the updated covariance maintains its appropriate form.

The Kalman Filter begins by determining the number of iterations based on the length of the measured data. Each iteration corresponds to a time step, in which the filter processes a new measurement. The sizes of the arrays used in the filter, such as the state estimates, error variances, and Kalman Gain, were set according to the number of iterations. This ensured that there was sufficient space to store the calculated values for each time step.

Next, the mean of the measurement data was calculated to serve as a baseline for further computation. This mean value provides a reference point for estimating the uncertainties and setting the initial values for the filter parameters. The uncertainty was initialized as 10% of the mean measurement value to determine the measurement noise. This uncertainty

is used to quantify the potential error or uncertainty in the measurement process.

The first state estimate is initialized using the first measurement in the dataset. Because no prior knowledge exists in the first time step, the filter assumes that the initial state estimate is equal to the first measured value. In addition, the initial error variance was set to 1.0, indicating a starting point of uncertainty regarding the accuracy of the first estimate.

Measurement noise variance was then determined by squaring the previously derived uncertainty. This variance represents the expected noise in the measurement process, and reflects the extent to which the filter should be placed in the measurements. Finally, the process noise variance is initialized to account for any potential fluctuations or uncertainties in the system model. It was set to a small value, specifically, 1% of the mean measurement, to account for minor process variations during each time step.

B. Radon Earthquake Precursor Detection

An algorithm based on radon precursors was designed for early earthquake detection. Kalman filter is used to remove noise signals in radon measurement. The results generated by the Kalman Filter were compared with actual radon measurements. If a significant difference is found between the values predicted and measured by the sensor, then the deviation is potentially identified as a precursor to a radon-based earthquake. The Kalman Filter considers measurement noise and process noise in the prediction model to overcome uncertainty. The method proposed in this study is illustrated in Fig.1.

Fig.1 illustrates the earthquake precursor anomaly detector using the Kalman filter. The system was designed to process and update the measurements to detect potential earthquake precursors. After the state estimation was updated through the update stage of the Kalman Filter, it was fed into the anomaly detector. Anomaly detectors calculate the difference between the estimated radon value and the measured state. This condition can indicate impending seismic activity if a significant difference is found.

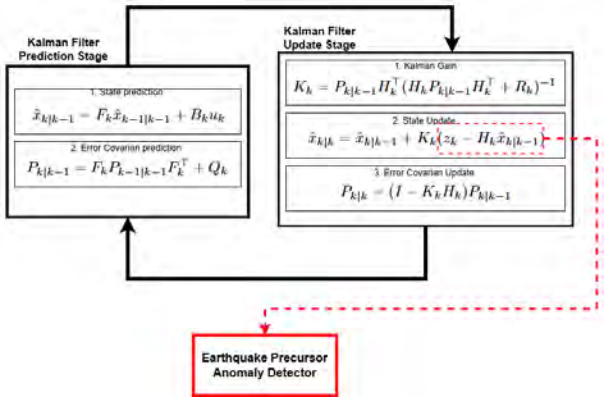

Fig. 1. Kalman Filter based Radon precursor earthquake prediction

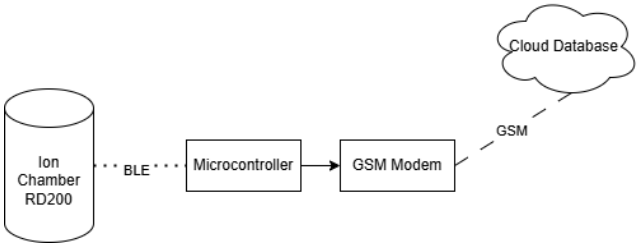

Fig. 2. Data Aquicition System

C. Data Collection

An ion chamber sensor (RD200) was installed in the Special Region of Yogyakarta Province (latitude -7.7531627 S, longitude 110.4215244 E) in the central part of Java Island for radon data collection. The data were read every minute using the ESP32 microcontroller with BLE communication. The measurement data were sent to a Cloud Database using a GSM network. The radon data-acquisition scheme used in this study is shown in Fig.2.

This study also used historical earthquake data accessed from *earthquake.usgs.gov*. The selected earthquake data complied with the earthquake preparation zone criteria set by Dobrovolsky in [5]. According to Dobrovolsky, the radius of the earthquake preparation zone, R is defined as

$$R = 10^{0.43M}. \tag{6}$$

where R is the radius of the preparation zone in kilometers and M is the earthquake magnitude. This equation was used to determine the affected area surrounding the epicenter, where precursory signals, such as radon gas anomalies, are likely to occur. The earthquakes eligible for analysis based on the earthquake preparation zone criteria are summarized in Table 1.

Table 1 provides information regarding the six significant earthquakes in 2023, with details regarding their time of occurrence, geographic coordinates (latitude and longitude), depth in kilometers, and magnitude. The first earthquake was recorded on January 9, 2023, with a magnitude of 5.3 and

TABLE I
EARTHQUAKE DATA USED IN THIS WORK

No	Time (UTC)	Latitude	Longitude	Depth (km)	Magnitude
1	2023-01-09 12:26:33.947	-8.8299	111.1757	67.859	5.3
2	2023-04-14 09:55:45.220	-6.0413	112.0478	597	7
3	2023-06-07 17:04:55.412	-8.8517	110.7921	18	5.6
4	2023-06-30 12:57:42.414	-8.6478	110.0229	76.421	5.9
5	2023-07-23 12:33:29.354	-8.6271	111.1186	96.623	5.1
6	2023-08-28 19:55:30.875	-6.7888	116.5211	500	7.1

depth of 67.859 km, followed by an event on April 14, 2023, with a magnitude of 5.7 and depth of 597 km. On June 6, 2023, another earthquake with a magnitude of 5.6 and a shallow depth of 18.905 km was documented. A larger earthquake was observed on July 17, 2023, with a magnitude of 5.9 and a depth of 76.421 km; shortly thereafter, on July 23, 2023, a smaller event with a magnitude of 5.1 and a depth of 96.623 km was recorded. The last earthquakes were noted on August 28, 2023, with a magnitude of 7.1 and a depth of 500 km. These events were selected for analysis based on adherence to specific criteria, emphasizing their importance in this study.

IV. Result and Discussion

The proposed method was designed to address the issues of measurement and process uncertainty in earthquake prediction. The method was simulated using radon gas measurement data to assess its effectiveness in managing uncertainties and improving the prediction accuracy. The simulation results are presented in Figures 3, 4, 5, 6, 7 and 8.

Fig.3 shows the radon concentration data related to the 5.3 M earthquake that occurred on January 9, 2023. Radon measurements were compared with the results generated by the Kalman filter and the 7-day moving average in the first plot. The radon measurements showed significant fluctuations on December 27, December 29, January 5-6, and January 8, 2023. The black star indicates an earthquake that occurred on January 9, 2023. The second plot shows the squared differences between the raw radon measurements and Kalman filtered results. The figure shows fluctuations in the differences on December 27, December 29, January 5, and January 8, with the most significant differences occurring on January 6, 2023. Some of these fluctuations occurred up to the day before the earthquake, indicating potential precursors to the seismic event.

In the fig. 3, it can be seen that the proposed detection method assumes that the fluctuations on December 30, 2022-January 1, 2023, can be predicted by the Kalman filter so that the earthquake precursors that can be used are fluctuations on December 27, 2022, December 29, 2022, January 5-6, 2023 and January 8, 2023. The proposed method shows that before the earthquake, precursor signs were found 1-12 days before the earthquake occurred.

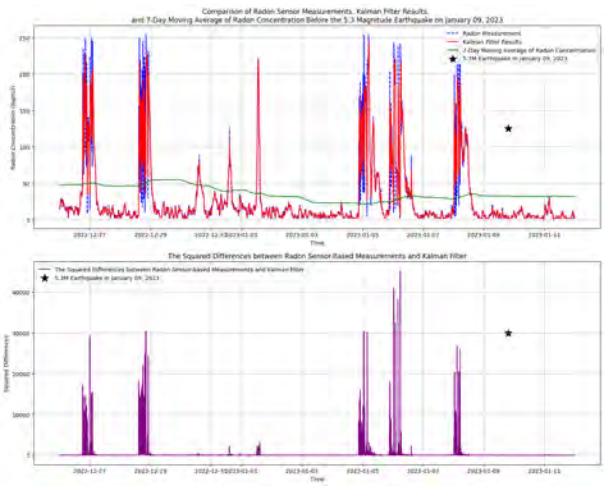

Fig. 3. Comparison between radon Sensor Measurement and Kalman Filter before January 09, 2023 Earthquake

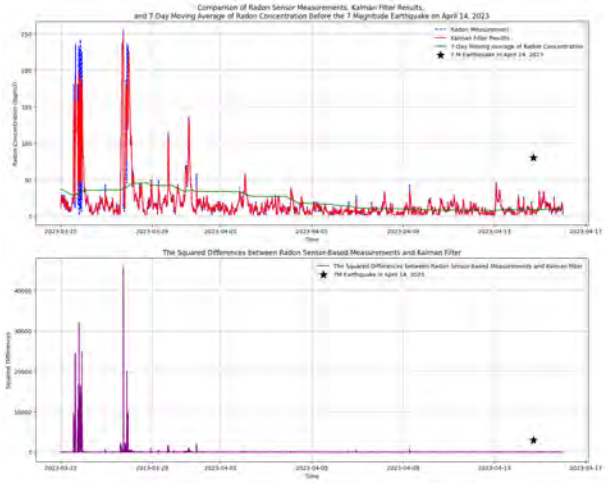

Fig. 4. Comparison between radon Sensor Measurement and Kalman Filter before April 14, 2023 Earthquake

Fig.4 shows the radon concentration before the 7.0 M earthquake on April 14 2023. The first plot in Fig.4 shows the results of the radon sensor measurements, Kalman filter results, and a 7-day moving average. Radon measurements show fluctuations before March 26 2023, and March 28 2023, before the April 14 2023, earthquake. The second plot shows the squared difference between the radon measurements and Kalman filter results. This plot also shows fluctuations on March 26 and 28. The proposed method shows that the Kalman filter can predict small fluctuations on March 29-31, 2023, so the earthquake precursors that can be used are fluctuations on March 26, 2023, and March 28, 2023. The proposed method shows that before the earthquake, precursor signs were found 18-19 days before the earthquake occurred.

Figure 5 shows the radon concentration before the 5.6M earthquake on June 7, 2023. The first plot shows the fluctuation of radon concentration on May 26, 2023, May 29, 2023, and June 1, 2023. The second plot shows the square difference between the radon measurements and the Kalman filter results. The plot shows a significant difference between the radon measurements and the Kalman Filter results on June 1, 2023. The proposed method shows that the fluctuations on May 28, 2023, and May 30, 2023, can be predicted by the Kalman filter, so the earthquake precursor that can be used is the fluctuation on June 1. With the proposed method, it can be seen that precursor signs were found 5 days before the earthquake occurred.

Figure 6 shows the radon concentration before the 5.9M earthquake on June 30, 2023. The first plot shows the fluctuation of radon concentration on June 17-20, 2023 and June

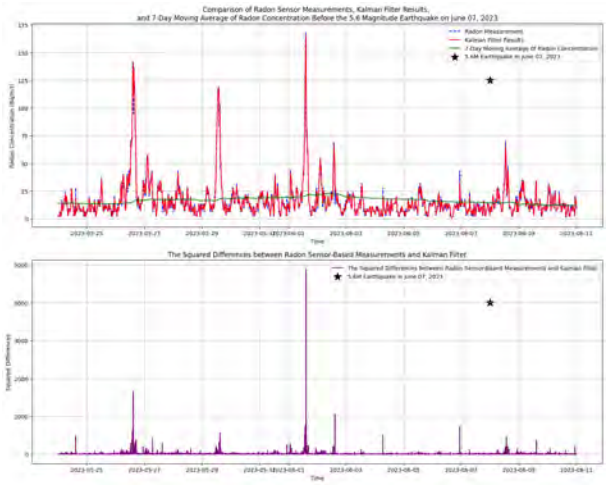

Fig. 5. Comparison between radon Sensor Measurement and Kalman Filter before June 07, 2023 Earthquake

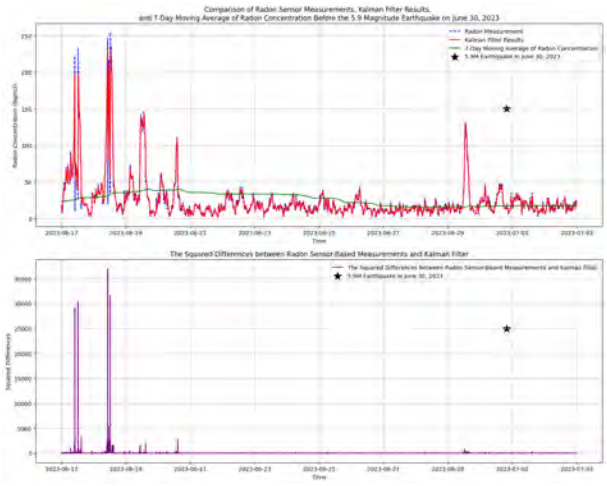

Fig. 6. Comparison between radon Sensor Measurement and Kalman Filter before June 30, 2023 Earthquake

29, 2023. The second plot shows the square of the difference between radon measurements and the Kalman filter results. The plot shows a significant difference between the radon measurements and the Kalman Filter on June 17, 2023 and June 18, 2023. The proposed method shows that the fluctuations on June 19-20, 2023, and June 30, 2023, can be predicted by the Kalman filter, so the earthquake precursor that can be used is the fluctuation on June 17-18. With the proposed method, it can be seen that precursor signs were found 12-13 days before the earthquake occurred.

Figure 7 shows the radon concentration before the 5.1M earthquake on July 23, 2023. The first plot shows fluctuations in radon concentration on July 9-15, 2023, July 18-19, 2023 and July 22, 2023. The second plot shows the square of the difference between radon measurements and the Kalman filter results. The plot shows a significant difference between the radon measurements and the Kalman Filter results on July 22, 2023. The proposed method shows that the fluctuations

Fig. 7. Comparison between radon Sensor Measurement and Kalman Filter before July 23, 2023 Earthquake

on July 9-15, 2023, July 18-19, 2023 and July 22, 2023, can be predicted better than the fluctuation on July 22. So, the earthquake precursor that can be used is the fluctuation on July 22. With the proposed method, it can be seen that precursor signs were found 1 day before the earthquake occurred.

Figure 8 shows the radon concentration before the 7.1M earthquake on August 28, 2023. The first plot shows the fluctuation of radon concentration on August 19, 2023, and August 24-28, 2023. The second plot shows the square difference between the radon measurements and the Kalman filter results. The plot shows a significant difference between the radon measurements and the Kalman Filter results on August 24-25, 2023. The proposed method shows that the fluctuations on August 15-28, 2023, can be predicted except for fluctuation on August 24-25, 2023. So, the earthquake precursor that can be used is the fluctuation on August 24-25, 2023. With the proposed method, it can be seen that precursor signs were

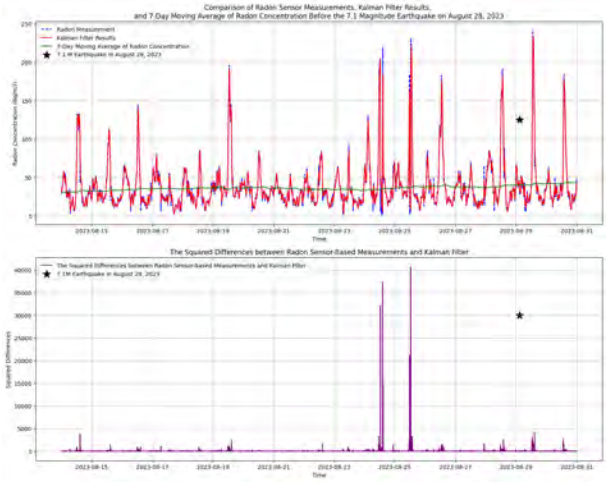

Fig. 8. Comparison between radon Sensor Measurement and Kalman Filter before August 28, 2023 Earthquake

found 3-4 days before the earthquake occurred.

The proposed method, utilizing a Kalman filter to address the measurement and process uncertainty, was applied to radon concentration data in the lead up to six significant earthquakes. The analysis consistently showed that radon sensor measurements displayed fluctuations before each seismic event, with notable peaks identified days or hours before earthquakes. The squared differences between the raw sensor data and Kalman filter predictions revealed significant discrepancies, often occurring just before the seismic activity, indicating potential precursors.

Across all six events, radon anomalies were observed through squared differences, suggesting that the Kalman filter successfully captured deviations in the data that could be linked to earthquake precursors. When processed using this method, the results showed that radon-based signals could provide useful early warning indicators of upcoming seismic activity. This approach demonstrated the potential of integrating radon measurements with Kalman filtering techniques to enhance earthquake prediction models.

However, this method still has limitations. This method cannot distinguish between real and fake earthquake precursor signals. In Figure 3, there are two groups of anomalies, namely those that occurred on December 27, 29, 2022 and January 5, 6, and 9, 2023. There is a time difference of 6 days between both precursor groups, so it is still being determined whether the first precursor group is related to the January 9, 2023 earthquake or other factors. In the next study, other detection features besides radon concentration need to be added to improve predictions. Efforts can be made to use historical data to predict the estimated time of the earthquake. In addition, sensor calibration must also be considered to ensure no changes in sensor characteristics over a long period.

V. Conclusion

The Kalman filter was applied to address uncertainties in sensor measurements and the radon-earthquake phenomenon by smoothing the data and reducing noise, thereby improving the reliability of radon concentration readings. Discrepancies between the filter predictions and raw sensor data suggest the presence of external factors, likely earthquake precursors. In all six analyzed events, radon anomalies were effectively captured through squared differences, demonstrating the potential of the method as an early warning system for seismic activity. The proposed method detected precursors 1–19 days before earthquakes, and future work will focus on predicting specific earthquake parameters, such as magnitude, time, and location, to enhance mitigation efforts. Other detection features besides radon concentration should be added to improve predictions.

References

[1] Nury Morales-Simfors & R. Wyss & J. Bundschuh,"Recent progress in radon-based monitoring as seismic and volcanic precursor: A critical review", Critical Reviews in Environmental Science and Technology, vol.50, p.979-1012, 2020.

[2] T.O. Pratama, Sunarno, A.B. Wijatna, E. Haryono,"Earthquake magnitude prediction in Indonesia using a supervised method based on cloud radon data ", International Journal of Reconfigurable and Embedded Systems (IJRES), vol.13, no.03, p.577-585, 2024.

[3] A. A. Mir et al., "Anomalies Prediction in Radon Time Series for Earthquake Likelihood Using Machine Learning-Based Ensemble Model," IEEE Access, vol. 10, pp. 37984–37999, 2022.

[4] A. Muhammad, F. Külahcı, and S. Birel, "Investigating radon and TEC anomalies relative to earthquakes via AI models," Journal of Atmospheric and Solar-Terrestrial Physics, vol. 245, p. 106037, Apr. 2023.

[5] T. Haider et al., "Identification of radon anomalies induced by earthquake activity using intelligent systems," Journal of Geochemical Exploration, vol. 222, p. 106709, Mar. 2021.

[6] A. D. K. Tareen, M. S. A. Nadeem, K. J. Kearfott, K. Abbas, M. A. Khawaja, and M. Rafique, "Descriptive analysis and earthquake prediction using boxplot interpretation of soil radon time series data," Applied Radiation and Isotopes, vol. 154, p. 108861, Dec. 2019.

[7] J. Rougier, A. Brady, J. Bamber, S. Chuter, S. Royston, B. Vishwakarmaet al., "The scope of the kalman filter for spatio-temporal applications in environmental science", Environmetrics, vol. 34, no. 1, 2022.

[8] D. Lange, J. Tiana-Alsina, U. Saeed, S. Tomás, & F. Rocadenbosch, "Atmospheric boundary layer height monitoring using a kalman filter and backscatter lidar returns", Ieee Transactions on Geoscience and Remote Sensing, vol. 52, no. 8, p. 4717-4728, 2014.

[9] J. Pak, S. Yoo, M. Lim, & M. Song, "Weighted average extended fir filter bank to manage the horizon size in nonlinear fir filtering", International Journal of Control Automation and Systems, vol. 13, no. 1, p. 138-145, 2014.

[10] S. Rehman, M. Khan, H. Kim, & S. Kim, "Analog–digital hybrid computing with sns2 memtransistor for low-powered sensor fusion", Nature Communications, vol. 13, no. 1, 2022.

[11] V. Walia, H. Virk, T. Yang, S. Mahajan, M. Walia, & B. Bajwa, "Earthquake prediction studies using radon as a precursor in n-w himalayas, india: a case study", Terrestrial Atmospheric and Oceanic Sciences, vol. 16, no. 4, p. 775, 2005.

[12] T. Kuo, C. Su, C. Liu, C. Lin, C. Chang, & C. Chiang, "Correlating recurrent radon precursors with local earthquake magnitude and crust strain near the chihshang fault of eastern taiwan", Natural Hazards, vol. 59, no. 2, p. 861-869, 2011.

[13] Y. Han, T. Kuo, K. Fan, C. Chiang, & Y. Lee, "Radon distribution in groundwater of taiwan", Hydrogeology Journal, vol. 14, no. 1-2, p. 173-179, 2004.

[14] Y. Omori, H. Nagahama, Y. Yasuoka, & J. Muto, "Radon degassing triggered by tidal loading before an earthquake", Scientific Reports, vol. 11, no. 1, 2021.

[15] P. Dutta, M. Naskar, & O. Mishra, "Test of strain behavior model with radon anomaly in seismogenic area: a bayesian melding approach", International Journal of Geosciences, vol. 03, no. 01, p. 126-132, 2012.

[16] J. Muto, Y. Yasuoka, N. Miura, D. Iwata, H. Nagahama, M. Hiranoet al., "Preseismic atmospheric radon anomaly associated with 2018 northern osaka earthquake", Scientific Reports, vol. 11, no. 1, 2021.

[17] Y. Chen, H. Zhang, & D. Eaton, "Real-time earthquake location based on the kalman filter formulation", Geophysical Research Letters, vol. 47, no. 11, 2020.

[18] X. Deng, Z. Zhang, & D. Yang, "Seismic data deconvolution using kalman filter based on a new system model", Geophysics, vol. 81, no. 1, p. V31-V42, 2016.

[19] G. Bishop and G. Welch, "An introduction to the kalman filter," Proc of SIGGRAPH, Course, vol. 8, no. 27599–23175, p. 41, 2001.

Real-Time Motorcyclist Helmet Detection using YOLOv8 on Edge Device

Fadil Muhammad
Department of Electrical Engineering
Universitas Sultan Ageng Tirtayasa
Cilegon, Banten

Ismail Bintang
Department of Electrical Engineering
Universitas Sultan Ageng Tirtayasa
Cilegon, Banten

Rian Fahrizal
Department of Electrical Engineering
Universitas Sultan Ageng Tirtayasa
Cilegon, Banten

Ceri Ahendyarti
Department of Electrical Engineering
Universitas Sultan Ageng Tirtayasa
Cilegon, Banten

Romi Wiryadinata
Department of Electrical Engineering
Universitas Sultan Ageng Tirtayasa
Cilegon, Banten

Imamul Muttakin
Department of Electrical Engineering
Universitas Sultan Ageng Tirtayasa
Cilegon, Banten
imamul@untirta.ac.id
ORCID 0000-0002-8409-4942

***Abstract*—In Indonesia, ubiquitous motorcycling poses highly risk accident without the proper safety equipment. This circumstance is exacerbated by the typical lack of compliance in wearing a helmet which is crucial for riding safety. The research develops helmet detection technology for motorcyclists based on deep learning implemented on edge device in real-time. The You Only Look Once (YOLO) model has a high helmet detection capability in live testing, with an F1 score of 91.1% for the 'Helmet' class, 81.7% for the 'Rider' class, and 33.0% for the 'No Helmet' class. Computational analysis shows an average CPU usage of 78.0%, average RAM usage of 77.4%, component temperatures ranging from 33°C to 65°C, total average power consumption of 6.5 W, varying GPU usage (from 0.1% to 99%), and an average frames per second (FPS) of 11. This system is capable of being implemented as an artificial intelligence of things framework in the smart city infrastructure.**

***Index Terms*—helmet detection, YOLO, Jetson Nano, AIoT, Smart City.**

I. Introduction

The use of helmets while riding motorcycles is vital for ensuring safety. In addition, Helmets provide head protection and can reduce the risk of head injuries by up to 69% and the likelihood of fatalities by up to 42% [1]. In Indonesia, the Traffic and Road Transport Law No. 22 of 2009 mandates that helmets must comply with national safety standards. However, enforcing helmet compliance among riders continues to be a significant challenge. As a result, developing an automated helmet detection system is crucial to strengthen regulations and improve overall safety [2].

A recent approach to enhance helmet compliance among motorcyclists is the use of technology, such as Electronic Traffic Law Enforcement (E-TLE). E-TLE is a system that leverages technology to automatically monitor and penalize traffic violations. E-TLE usually using Closed Circuit Television (CCTV) cameras to capture images of violations, which are processed by the system to detect these infractions [3].

979-8-3315-1921-6/24/$31.00 ©2024 IEEE

In the E-TLE system, deep learning technology is integrated into CCTV systems to identify objects in both images and video footage. Object detection is a fundamental task in computer vision, with various applications such as facial recognition, autonomous driving, and surveillance [4]. Some of the widely used object detection techniques include Region-Based Convolutional Neural Networks (R-CNN), Faster R-CNN, Single-Shot Detector (SSD), and You Only Look Once (YOLO) [5]. This research adopts YOLO because it offers high-precision object detection in real-time, making it ideal for helmet detection where quick response is essential.

Application of CNN models like YOLO and the Jetson Nano platform for data processing has been proposed by many researchers. Research reported in [6] developed a motorcycle helmet violation detection system, utilizing YOLO for motorcycle detection, GoogleNet for helmet violation classification, and the Kristan method for object tracking. Furthermore, this study introduced a low-cost yet high-performance CPU-GPU system architecture that can handle multiple camera streams simultaneously. This research proposed low-cost CPU-GPU system that can detect 97% of helmet violations with a 15% false alarm rate.

Additional studies covered mask detection systems using Jetson Nano and TensorFlow. In addition, MobileNetV2 was utilized for computer vision. The system resulted an average accuracy of 99.48% in detecting users either not wearing masks or wearing them incorrectly, and 99.12% in detecting users who correctly wore masks [7]. Further research explored the application of computer vision and deep learning to detect camels on highways to prevented vehicle-camel collisions, which pose a serious issue in Saudi Arabia and other regions. This research compared five object detection algorithms: CenterNet, EfficientDet, Faster R-CNN, SSD, and YOLOv8, using a custom dataset comprising 250 camel images in different scenarios. The evaluation was conducted based on mean aver-

age precision (mAP) and mean average recall (AR) at different intersections over a combined threshold. The findings indicate that YOLOv8 is the most accurate and efficient algorithm, with CenterNet following closely behind [8].

Moreover, another study introduced the use of YOLOv5 and ensemble learning techniques to detect automatically and classify motorcyclists and their passengers based on helmet usage. The model achieved a high mean average precision (mAP) score of 0.526 on test data, successfully identifying most classes despite variations in video lighting and weather conditions. However, the model was not applicable for real-time use due to challenges such as the effects of the operating devices, changed in lighting conditions, detected obstacles, and distinguished of diversity of motorcycles and helmets. These factors might impact the model's effectiveness and reliability in practical, real-world applications [9]. This research aimed to enhance the accuracy, effectiveness, and efficiency of helmet detection using technologies such as the YOLOv8 model.

Therefore, this study are expected to contribute to the development of E-TLE by improving the accuracy and reliability of helmet detection, thereby assisting law enforcement in minimizing ticketing errors. Furthermore, this research is anticipated to raise public awareness about the importance of adhering to driving regulations and using appropriate safety equipment, particularly helmets, to foster a safer driving environment [10].

II. Research Methodology

In this research, a helmet detection system is implemented using Convolutional Neural Network (CNN) methodology. The YOLOv8 model is used, which is a sophisticated object detection model enhanced for both speed and accuracy relative to earlier YOLO versions. The system is designed for real-time detection, utilizing the Jetson Nano platform for model processing and a webcam for data input.

A. Data Acquisition and Data Preprocessing

During the data acquisition phase, choosing the right location, timing, and recording methods is critical. High-quality data acquisition is a fundamental step in the development of a helmet detection system. This phase includes collecting relevant images or videos and ensuring precise annotations, which will be utilized to train and evaluate the YOLOv8 model. The data were independently collected as video footage using a Logitech C270 webcam and subsequently converted into image frames during the data pre-processing phase. The categories used in this research were 'Rider' for motorcyclists, 'Helmet' for those wearing helmets, and 'No Helmet' for those not wearing helmets. Videos for the 'Helmet' and 'Rider' classes are captured on the Cilegon highway from the Cilegon pedestrian overpass, a site was selected for its high volume of helmet-wearing motorcyclists. On the other hand, data for the 'No Helmet' class are gathered from areas with significant foot traffic, like crowded public spaces, to ensure a diverse dataset. For this research, data collection took place at the Phinisi Pedestrian and Bicycle Bridge (JPOS) and Martha Tiahahu Literacy Park.

Data pre-processing aims to develop a dataset for training the YOLOv8 model. The dataset was divided into three segments: training, validation, and testing, all sourced from the previously recorded videos. These videos are processed to pre-processing involving three different steps. In this stage, the successfully extracted frames are stored in .jpg format. Out of 8 training videos, 7922 frames were extracted, annotated with the relevant classes, and subsequently reduced to 3513 frames due to their relevance. The remaining frames, considered less relevant, were then horizontally augmented using the augmentations library to produce a total of 7026 frames.

B. Dataset Training

The dataset training process begins with preparing the previously created dataset. For training the helmet violation detection model, this study employs the smallest version of the YOLOv8 architecture, namely YOLOv8n.

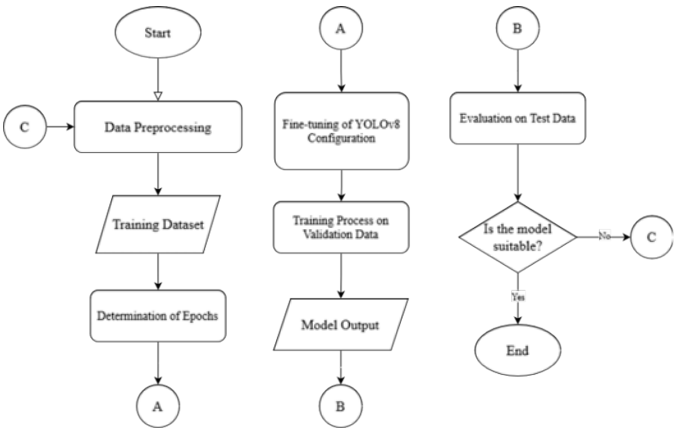

Fig. 1. Dataset Training

Fig. 1 illustrates that the model training process is carried out with the assistance of Google Colab, ClearML, and the PyTorch library. The result of this training was a detection model that will be employed in the testing phase. In this phase, the model would be assessed using new data from the test set. It is essential that the test data have similar characteristics to the training data to ensure that the testing results are valid.

TABLE I
HYPERPARAMETER CONFIGURATION

Hyperparameter	Selected Value
Epochs	50
HSV-Hue augmentation	0.01
HSV-Saturation augmentation	0.5
HSV-Value augmentation	0.0
Translate	0.0
Degrees	0.0
Scale	0.1
Flip Left-Right	0.0
Flip Up-Down	0.0
Mosaic	0.0

Table I presents the best hyperparameter configuration for the custom YOLOv8 model after several experiments and fine-tuning. The configurations listed in the table reflect the changes made, while those not listed were set to their default values. In addition, reducing the additional augmentation values or setting them to zero resulted in a better-performing model compared to using higher augmentation values or the default YOLOv8 settings.

C. Detection System Design

This process aims to develop a helmet violation detection system based on the YOLOv8 model that has been created. Fig. 2 illustrates the overall system procedure during testing. The custom model was integrated with ByteTrack. Integrating ByteTrack with the trained YOLOv8 model enhances the helmet detection system's efficiency by minimizing the required cropping. The system would detect helmet users with a green bounding box, while violators are marked with a red bounding box. Additionally, a snapshot of the violators, in the form of image files, is taken and saved into a folder designated for violators.

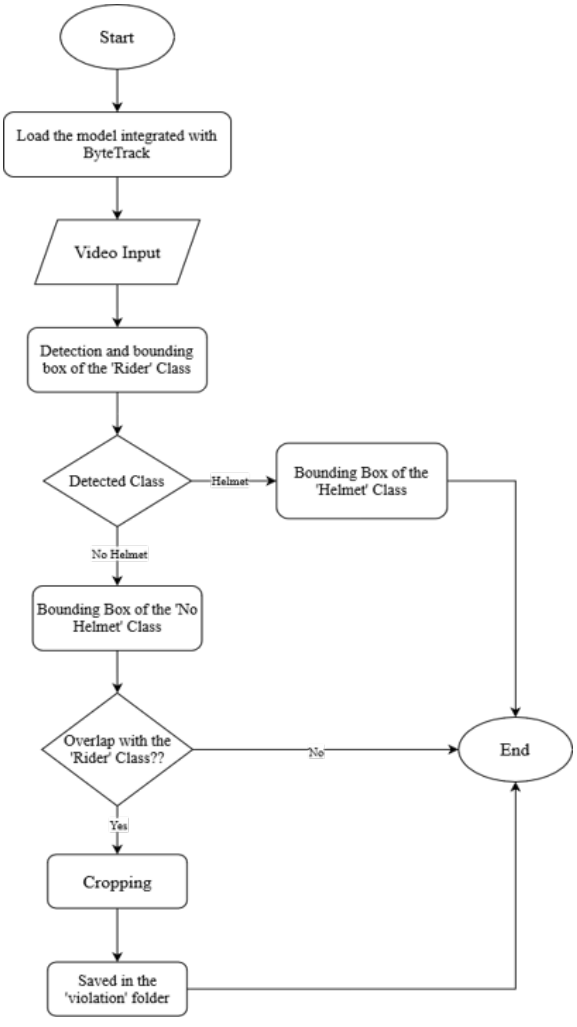

Fig. 2. Helmet Detection System

D. Deployment System

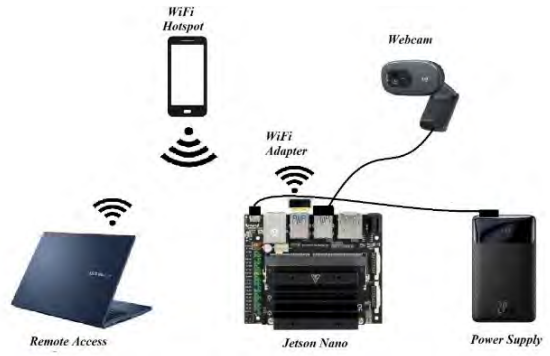

Fig. 3. Helmet Detection System

In the scheme shown in Fig. 3, the Jetson Nano was powered by a power bank and connected to a WiFi hotspot generated by a smartphone. Furthermore, a laptop will connect to the same hotspot. Once both devices were connected to the WiFi network, the Graphical User Interface (GUI) of the Jetson Nano can be accessed via remote desktop connection or Secure Shell (SSH) access. From this point, the real-time detection system will be initiated through the laptop.

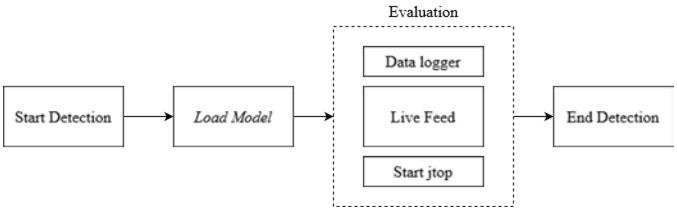

Fig. 4. System Testing Arrangement

Fig. 4 shows the performance testing process of the system. When initiating the system and starting the live feed, 'jtop' was initially shown to track device statistics and assess the Jetson Nano's performance during the live feed. The system also includes a data logger that records data in .txt format for subsequent evaluation of the Jetson Nano.

III. Result and Discussion

A. Training Model Analysis

Fig. 5 shows that the confusion matrix representing the model's performance in classification. The model accurately classified 'Rider' 776 times out of 864 annotations and 'Helmet' 778 times out of 899 annotations, indicating high true positive rates for these two classes. However, 'No Helmet' was correctly identified only 45 times out of 117 annotations, which is lower compared to the other two classes. The 'background' class, representing non-object areas detected by the YOLOv8 model, correlates with false negatives and false positives to provide a more comprehensive view. Detection errors occurred as follows:

1) The 'Rider' class was predicted as 'background' 88 times.

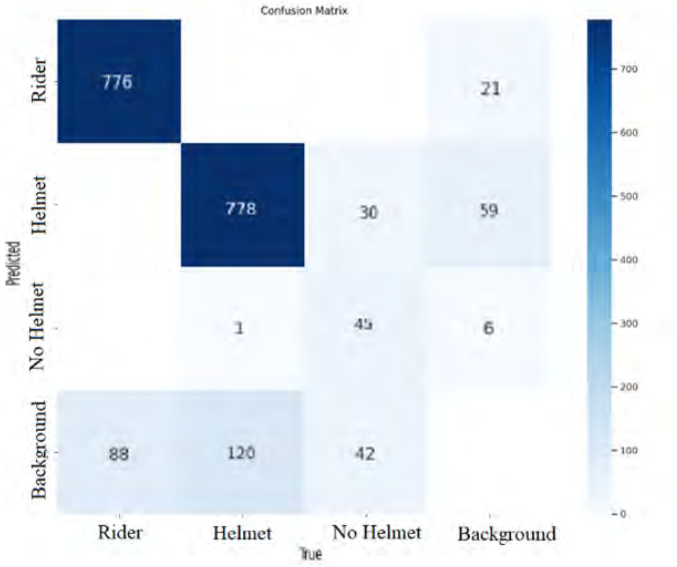

Fig. 5. Training Model Confusion Matrix

2) The 'Helmet' class was predicted as 'No Helmet' once and 'background' 120 times.
3) The 'No Helmet' class was predicted as 'Helmet' 30 times and 'background' 42 times.

In addition, the model often classified 'background' as object classes, including 6 instances for 'Rider,' 59 for 'Helmet,' and 21 for 'No Helmet.' The confusion matrix analysis provided insights into these classification challenges.

TABLE II
TRAINING MODEL METRIC EVALUATION RESULTS

Class	Precision	Recall	mAP50	mAP50–95	F1–score
All Classes	85.9%	87.9%	90.4%	50.5%	86.8%
Rider	95.6%	93.8%	97.7%	68.0%	94.5%
Helmet	81.3%	91.5%	92.7%	46.2%	85.9%
No Helmet	80.6%	78.3%	80.7%	37.3%	79.4%

Table II presents the evaluation results for YOLOv8, indicating a precision of 85.9% and a recall of 87.9%. The low mAP50-95 score highlights difficulties in object detection at high Intersection over Union (IoU) values. The detection performance for 'Rider' is satisfactory, with high scores in precision, recall, mAP50, mAP50-95, and F1-score. For 'Helmet,' although recall is high, precision is lower, resulting in more false positives at elevated IoU levels. The 'No Helmet' detection showed balanced performance but faced challenges at high IoU thresholds. These issues were likely due to complex object shapes, varying lighting conditions, environmental obstructions, and a potentially unrepresentative or imbalanced training dataset.

Fig. 6 presents the precision-recall curves, which demonstrate the balance between precision and recall at different threshold levels for the three classes and overall performance. The 'Rider' class has the highest Average Precision (AP)

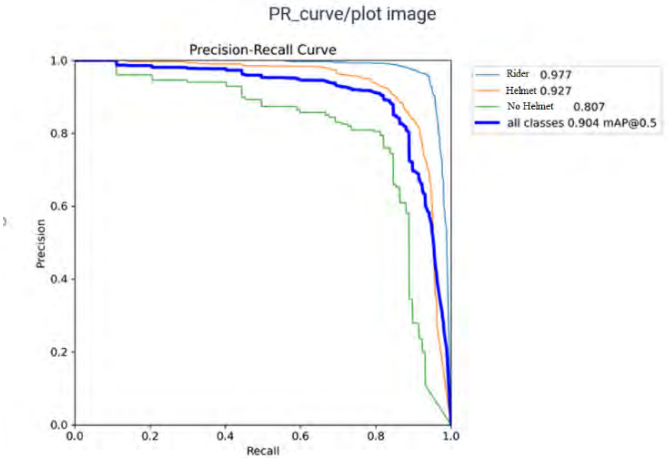

Fig. 6. Training Model Precision-Recall Curve

of 0.977, followed by 'Helmet' at 0.927, and 'No Helmet' at 0.807, with an overall mean Average Precision (mAP) of 0.904 at an IoU of 0.5. The curves reveal high precision with low recall, indicating effective identification of easily detected positive cases by the model. However, as recall increased, precision decreased, reflecting difficulties in accurately detecting all positive cases. The Area Under the Curve (AUC) assessed the model's capability to distinguish between classes, with a curve closer to the top-right corner signifying better model performance.

B. Testing Model on Video Analysis

At this stage, the trained model proceeds to testing by integrating it with the ByteTrack tracking algorithm and analyzing its performance on video data. The evaluation parameters were consistent with those applied previously.

TABLE III
MODEL PREDICTION AND EVALUATION RESULTS ON MORNING TESTING VIDEO

Class	Actual	Predictions			Precision	Recall	F_1 –score
		TP	FP	FN			
Rider	350	350	12	0	96.7%	100%	98.3%
Helmet	443	443	48	0	90.2%	100%	94.9%
NoHelmet	30	24	10	6	70.6%	80%	75%

Table III displays the prediction and evaluation results of the model under morning lighting conditions. The 'Rider' class exhibits the highest precision at 96.7%. Both the 'Rider' and 'Helmet' classes achieve perfect recall values of 100.0%, while the 'No Helmet' class has a recall of 80.0%. The highest harmonic mean between precision and recall was found in the 'Rider' class, at 98.3%. Despite the model's accuracy for 'Rider' and 'Helmet', there were instances of false positives involving non-actual objects and backgrounds, as well as incorrect predictions for other classes. The 'No Helmet' class suffers from both false positives and false negatives, impacting the evaluation scores.

TABLE IV
MODEL PREDICTION AND EVALUATION RESULTS ON DAYTIME TESTING VIDEO

Class	Actual	Predictions			Precision	Recall	F_1 –score
		TP	FP	FN			
Rider	381	381	24	0	94.1%	100%	96.9%
Helmet	481	480	44	1	91.6%	99.8%	95.5%
NoHelmet	19	13	25	6	34.2%	68.4%	45.6%

Table IV outlines the model's prediction and evaluation results for midday lighting conditions. The 'Rider' and 'Helmet' classes achieved high precision, while the 'No Helmet' class had a lower precision of 34.2%. Both the 'Rider' and 'Helmet' classes reached perfect recall, with the 'Rider' class achieving nearly perfect performance and the 'Helmet' class almost reaching 100%. However, the 'No Helmet' class had a lower recall of 68.4%. The 'Rider' class showed the highest f1-score of 96.9%, whereas the 'No Helmet' class only reaches 45.6%. Prediction errors for 'No Helmet' include false positives with non-actual objects and background and misclassifications of other classes. Furthermore, some 'No Helmet' violations were missed or resulted in false negatives, affecting the overall evaluation of this class.

TABLE V
MODEL PREDICTION AND EVALUATION RESULTS ON EVENING TESTING VIDEO

Class	Actual	Predictions			Precision	Recall	F_1 –score
		TP	FP	FN			
Rider	610	607	5	3	99.2%	99.5%	99.4%
Helmet	728	721	53	7	93.2%	99.0%	96.0%
NoHelmet	16	11	23	5	32.4%	68.8%	44.0%

Table V presents the evaluation results of the model under evening lighting conditions. The 'Rider' and 'Helmet' classes exhibit high precision, with values of 99.2% and 93.2%, respectively, whereas the 'No Helmet' class shows a very low precision of just 32.4%. Both 'Rider' and 'Helmet' classes also demonstrate good recall, but the 'No Helmet' class had a low recall of 68.8%. The f1-score, representing the harmonic mean of precision and recall, was highest for the 'Rider' class at 99.5%, while it is significantly lower for the 'No Helmet' class, at 44.0%.

The prediction errors for the 'No Helmet' class were attributed to false positives related to non-relevant objects and background, along with incorrect predictions in other classes. Moreover, some instances across the three classes were either missed or incorrectly classified as false negatives, impacting the overall performance assessment. This indicates a need to refine the model's ability to differentiate the 'No Helmet' class to reduce detection errors and improve overall model effectiveness.

C. Jetson Nano Live Feed Analysis

At this stage, the developed model and system were tested in a real-world setting using the Jetson Nano. This testing aimed to assess the system's ability to detect objects in real-time across three different lighting conditions: morning, midday, and evening, over a 25-minute period. Evaluation metrics such as precision, recall, and f1-score were analyzed, like previous evaluations. Additionally, the system's performance on the Jetson Nano were reviewed, focusing on resource usage including CPU, RAM, and GPU. This thorough analysis helps to gain a comprehensive understanding of the system's performance and highlights areas that might require further enhancement.

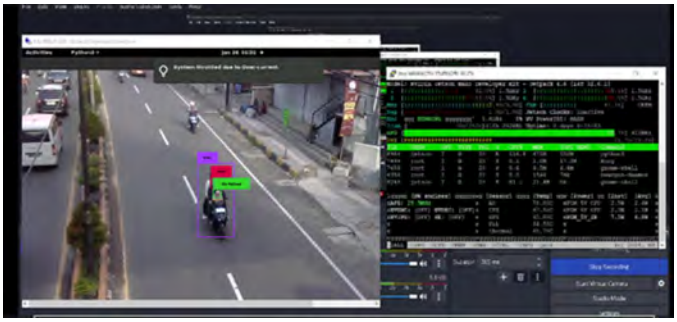

Fig. 7. Real-time Helmet Detection System Interface using Jetson Nano

Fig. 7 illustrates the GUI of the helmet detection system being operated on a laptop through remote access applications like PuTTY. On the right side, there was a jtop window used to assess performance and analyze resource usage on the Jetson Nano during the operation of the helmet detection system. This evaluation includes an analysis of the Jetson Nano's performance with a focus on monitoring CPU usage (CPU1 to CPU4), RAM, GPU, component temperature, thermal power, and total power consumption during system operation.

The key factors affecting the real-time performance of the helmet detection system were the model performance and the computational demands. The average performance for each class was calculated from the model obtained under different lighting conditions.

TABLE VI
OVERALL TESTING RESULTS

Class	Precision $\tilde{x}$	Recall $\tilde{x}$	F1–score $\tilde{x}$
Rider	99.7%	74.5%	81.7%
Helmet	98.9%	85.9%	91.1%
NoHelmet	31.0%	47.8%	33.0%
All Classes $\tilde{x}$	76.5%	69.4%	68.6%

Table VI shows in the helmet detection system testing cases, the 'Helmet' class had a higher f1-score compared to other classes. The class with the lowest performance was 'No Helmet'. This indicates that the model had difficulty distinguishing the 'No Helmet' class from other classes, particularly from the 'Helmet' class. The low performance of the 'No Helmet' class affects the overall evaluation of the model,

resulting in a relatively low f1-score of 68.6%. This was due to a high number of false positives and false negatives.

Fig. 8. False Positive Cases in Live Feed

Fig. 8 shows various instances of false positives encountered during live testing. Motorcyclists without helmets were frequently identified as 'Helmet' class, especially when approaching the camera or moving out of sight, leading to inconsistent detection results. The 'No Helmet' class often includes false positives with pedestrians, who were not the intended targets of the helmet detection system. In the 'Rider' class, motorcyclists traveling in the wrong direction or on different lanes were occasionally detected, although this was rare. This problem was due to the camera's excessively wide angle, covering irrelevant areas. Further challenges include differentiating between headgear like hats, scarves, and helmets, as well as detecting bicycles and other non-motorized vehicles. Roadway artifacts also affect detection for 'Helmet' and 'No Helmet' classes, which was likely caused by lighting conditions and a less representative dataset.

Fig. 9. False Negative Cases in Live Feed

Fig. 9 displays several instances of false negatives observed during live testing, particularly for the 'Rider' and 'No Helmet' classes. During daytime testing, bounding box detection was frequently missed across all three classes. In the evening, the 'Rider' class was more often overlooked due to dim lighting and the illumination of motorcycle lights, which results in blurring when objects move quickly. High light intensity during the day and the rapid movement of riders also contribute to false negatives. Utilizing ByteTrack to minimize redundancy or excessive duplication in the cropped motorcyclist detection results has demonstrated substantial efficiency and effectiveness, despite some minor errors that could be due to the model itself.

Fig. 10 shows the 'violation' folder, which includes cropped images without the tracking system. It was evident that there were numerous duplicate images of the same objects, especially when the 'No Helmet' class overlaps with the 'Rider' class, leading to a total of 218 images in one folder.

Fig. 10. Cropping Results without Tracking System

Fig. 11. Cropping Results with Tracking System

Fig. 11 displays the 'violation' folder with cropped images processed using the integrated tracking system. The duplication of images of the same object has been notably reduced, particularly when the 'No Helmet' class overlaps with the 'Rider' class, leading to only 25 images within one folder.

The performance of the Jetson Nano system may be impacted by computational demands, especially in edge computing scenarios. Discrepancies between the calculated FPS and the actual display on the screen were frequently observed, particularly during remote access testing. This could be attributed to latency and bandwidth issues due to the back-and-forth data exchange between the Jetson Nano and the remote device. The processing of live feeds and the AI model also put a load on the components, raising temperatures and potentially causing thermal throttling, especially in high-temperature environments. Furthermore, the 'System throttled due to over-current' notification may appear if high-power USB devices were used, surpassing the system's electrical handling capacity.

IV. Conclusion

The motorcycle helmet detection system, utilizing deep learning with the YOLOv8 model, has been successfully deployed in real-time with the Jetson Nano on roadway. This system also performs automatic cropping images of offenders not wearing helmets. During testing, the model achieved an F1-score of 91.1% for helmet detection, 81.7% for rider detection, and 33.0% for detecting offenders without helmets. In terms of system performance on morning, midday and evening over 25 minutes, average CPU usage was 78.0%, average RAM usage was 77.4%, device temperature ranged from 33°C to 65°C, average power consumption was 6.5 W, and average FPS was 11, although GPU usage is fluctuated between 0.1% and 99%.

ACKNOWLEDGMENT

The authors would like to thank members of the Applied Electromagnetics Laboratory FT UNTIRTA for their help in experiments. We acknowledge the use of Gemini [11] to refine the title wording of this paper.

REFERENCES

[1] M. Tabary et al., "The effectiveness of different types of motorcycle helmets – A scoping review," *Accid Anal Prev*, vol. 154, May 2021, doi: 10.1016/j.aap.2021.106065.

[2] Y. O. Susilo, T. B. Joewono, and U. Vandebona, "Reasons underlying behaviour of motorcyclists disregarding traffic regulations in urban areas of Indonesia," *Accid Anal Prev*, vol. 75, pp. 272–284, Feb. 2015, doi: 10.1016/J.AAP.2014.12.016.

[3] D. Yu, A. A. Dewi, S. N. Wijaya, and A. A. S. Gunawan, "Utilization Big Data and GPS to Help E-TLE System in the Cities of Indonesia," *Proceedings of 2021 1st International Conference on Computer Science and Artificial Intelligence*, ICCSAI 2021, pp. 236–242, 2021, doi: 10.1109/ICCSAI53272.2021.9609741.

[4] J. Chai, H. Zeng, A. Li, and E. W. T. Ngai, "Deep learning in computer vision: A critical review of emerging techniques and application scenarios," *Machine Learning with Applications*, vol. 6, pp. 1–13, 2021, doi: 10.24433/CO.0411648.v1.

[5] S. Srivastava, A. V. Divekar, C. Anilkumar, I. Naik, V. Kulkarni, and V. Pattabiraman, "Comparative analysis of deep learning image detection algorithms," *J Big Data*, vol. 8, no. 1, Dec. 2021, doi: 10.1186/s40537-021-00434-w.

[6] A. Chairat, M. N. Dailey, and D. Raj, "Low Cost, High Performance Automatic Motorcycle Helmet Violation Detection," in *2020 IEEE Winter Conference on Applications of Computer Vision (WACV)*, 2020, pp. 3560–3568. doi: 10.1109/WACV45572.2020.9093538.

[7] M. Luqman Bukhori and E. E. Prasetiyo, "Jetson Nano-Based Mask Detection System with TensorFlow Deep Learning Framework," *Jurnal Nasional Teknik Elektro dan Teknologi Informasi*, vol. 12, no. 1, pp. 15–21, 2022, doi: 10.22146/jnteti.v12i1.5472.

[8] K. Al-Nujaidi, G. Al-Habib, and A. Al-Odhieb, "Spot-the-Camel: Computer Vision for Safer Roads," *International Journal of Artificial Intelligence & Applications*, vol. 14, no. 2, pp. 1–10, Mar. 2023, doi: 10.5121/ijaia.2023.14201.

[9] G. Agorku et al., "Real-Time Helmet Violation Detection Using YOLOv5 and Ensemble Learning," *arXiv e-prints*, Apr. 2023, doi: 10.48550/arXiv.2304.09246.

[10] M. Fahri, A. Natua Siregar, and A. Hakim, "Utility on ETLE and Trust on ETLE As a Booster of Social Order and Habit through Traffic Compliance and Awareness based on Information Technology," *J Theor Appl Inf Technol*, vol. 28, p. 2022, 2022, [Online]. Available: www.jatit.org.

[11] Gemini. Google AI. Accessed: Sep. 27, 2024. [Online]. Available: https://gemini.google.com/

Stock Buy/Sell Prediction Based on Technical Analysis and News Sentiment Using Deep Learning

Arya Yudhi Wijaya
Department of Informatics
Institut Teknologi Sepuluh Nopember
Surabaya, Indonesia
arya@if.its.ac.id

Dini Adni Navastara
Department of Informatics
Institut Teknologi Sepuluh Nopember
Surabaya, Indonesia
dini_navastara@its.ac.id

Ichlasul Hasanat
Department of Informatics
Institut Teknologi Sepuluh Nopember
Surabaya, Indonesia
ichlasulhasanat14@gmail.com

***Abstract*—The stock market is a compelling arena for investors and researchers. Its movement is influenced by various global factors, including public information, social conditions, macroeconomic policies, and the political climate of a nation. Given the multitude of factors, news regarding stocks can serve as a significant criterion in the decision-making process for buying or selling stocks. This study employs pretrained transformer models, including FinBERT, FinancialBERT, and FinBERT-tone, to evaluate sentiment in stock news. Technical stock indicator features, including Moving Average, Moving Average Convergence Divergence (MACD), Bollinger Bands, and Relative Strength Index (RSI), are utilized to enhance the model. The two datasets are subsequently merged by modifying the index, and the training procedure is executed utilizing deep learning and ensemble learning techniques in the format of a Voting Classifier. These methods pertain to four categories of Recurrent Neural Network (RNN) architectures: Long Short-Term Memory (LSTM), Bidirectional Long Short-Term Memory (Bi-LSTM), Gated Recurrent Unit (GRU), and Bidirectional Gated Recurrent Unit (Bi-GRU). The Voting Classifier model employs comprehensive deep learning techniques, leveraging all technical indicator features and sentiment labels to achieve optimal accuracy when evaluated on BBRI stock, targeting a 50-day period, with four classification labels and a 30-day sliding window. The accuracy achieved with this strategy was 94.22%**

***Index Terms*—Stock Prediction, LSTM, GRU, Voting, Technical Indicators, Sentiment Analysis, Deep Learning**

I. Introduction

Stocks are the most recognized financial market instrument to date. The fluctuation of stock prices is affected by public information, social conditions, macroeconomic policies, and the political climate of a nation, among other factors.

With the growing interest in Natural Language Processing (NLP), there is an increasing awareness of stock news sentiment analysis and its applications in stock market strategies among both academics and practitioners. Numerous studies indicate that financial news serves as a crucial information source for investors, who adjust their trading actions based on their sentiment towards the news, subsequently influencing stock market movements [2]. Nonetheless, relying solely on news sentiment analysis is insufficient for decision-making. Consequently, incorporating additional features, such as technical indicators, into historical stock data can enhance the precision of stock investment decision-making.

979-8-3315-1921-6/24/$31.00 ©2024 IEEE

The progression of computing technology has led to numerous approaches for developing predictive systems available in the market. The preliminary techniques established typically rely on template matching within trading charts, as exemplified by [3]. In a review of articles on predictive systems, [4] noted that classifiers can be effectively utilized to forecast financial data. A classifier is a system that generates output labels for predicted input data. In addition to stock trading data, news or issues pertaining to technical or non-technical aspects of a stock, group of stocks, or industrial sector can also influence stock price fluctuations. In addition to technical analysis, an analysis of news sentiment is also required. The study [5] aimed to analyze news through text mining techniques to forecast daily stock fluctuations, subsequently [6] examined news sentiment utilizing the Naïve Bayes and K-Nearest Neighbor (K-NN) classifiers, and [7] employed Support Vector Machine (SVM) for analysis. The most recent technique for news sentiment analysis employs deep learning methods, specifically Convolutional Neural Networks (CNN), Long Short-Term Memory (LSTM), or a CNN-LSTM hybrid, which enhances performance [8], [9].

Based on this, [10] combines stock price data series information and news sentiment analysis for stock price prediction with Naïve Bayes and SVM. While the latest [11] performs price prediction with stock price data series input and optimized NN-based sentiment analysis, and [12] uses the deep learning concept (LSTM). Recently, [13] fused it with the sentiment of news headlines scored with FinBERT. The prediction results are used for predicting the price one day ahead with LSTM. Because it is only one day ahead, the accuracy is not very good and it does not provide an alternative for holding over several days ahead.

The addition of news sentiment analysis adds accuracy to price predictions, but [10]- [12] all do not display the buy, sell, or hold predictions needed by investors. Therefore, this study will conduct stock buy and sell predictions based on historical data and news sentiment analysis using deep learning, which has proven to be good for data series. Stock news data is collected from the CNBC Indonesia, Bisnis, and Kontan websites, while historical stock data will be collected

from Yahoo Finance.

By using this method, it is expected that the prediction model can provide a comprehensive understanding of the dynamics of stock market movements. It is also expected that this study can help provide an overview of stock buy/sell predictions and can be used as a strong reference in considering decisions in the future stock investment process.

II. Literature Review

A. Stock Technical Indicators

Technical indicators are a series of data points generated from the use of a formula on certain stock price data [14]. Technical indicators use stock prices as input for their calculations and usually the closing price of a stock is used in a trade. The types of technical indicators used in this study can be seen in Table I, where Ct is the closing price, DIFF: EMA(12)t - EMA(26)t, EMA is exponential moving average, α smoothing factor: 2/1 + k, k is time period of k day exponential moving average, MAn: n-day Moving Average, Upt means the upward price change, Dwt means the downward price change at time t.

TABLE I
SELECTED TECHNICAL INDICATORS AND THEIR FORMULAS

indicators	Formulas
n-day Moving Average	$\frac{C_t + C_{t-1} + \cdots + C_{t-n}}{n}$
Exponential Moving Average (EMA)	$EMA(k)_{t-1} + \alpha \times (C_t - EMA(k)_{t-1})$
Moving Average Convergence Divergence (MACD)	$MACD(n)_{t-1} + 2/n + 1 \times (DIFF_t - MACD(n)_{t-1})$
Bollinger Bands	$MA_n \pm 2\sqrt{\frac{\sum_{i=1}^{n}(C_t - MA_n)^2}{\sum_{i=1}^{n} C_t}}$
Relative Strength Index (RSI)	$\frac{100^n - 100}{1 + \left(\frac{\sum_{i=1}^{n} UP_{t-1}/n}{\sum_{i=1}^{n} DW_{t-1}/n}\right)}$

B. Sentiment Analysis

Sentiment analysis is a technique or method used to identify how a sentiment is expressed using text and how that sentiment can be categorized as positive or negative sentiment [15].

Text mining is the process of exploring and analyzing large amounts of unstructured text data with the help of software that can identify concepts, patterns, topics, keywords, and other attributes in the data [16].

Preprocessingor preprocessing is the process of preparing and transforming data that is useful for better output [17]. This process consists of several stages, such as case folding, translation, tokenization, stopword filtering, and lemmatization or stemming [18].

- *Folding case* is a process where all letters in a document are changed to lowercase.
- *Translation* is a language translation process that uses a translator's dictionary.
- *Tokenization* is the process of breaking down sentences into specific groups of words.
- *Filtering Stopwords* is the stage of removing important words from the token results.
- *Lemmatization* is the removal of word inflection to its original form.

C. Transformer Models

Model transformer, provides substantial solutions to long-standing problems faced in sequence manipulation, breaking the norm at an astonishing rate in the NLP research space [19].

BERT is a deep bidirectional model that has been pre-trained on a plain, unlabeled text corpus (such as Wikipedia and a book corpus) to obtain statistical property representations of the English language [20].

FinBERT is a model developed by Araci.trained using a dropout probability of 0.1, a warm-up proportion of 0.2, 64 maximum sequence lengths, 2e-5 learning rate, 64 mini batch sizes, and 6 epochs. Financial sentiment prediction training is done by adding a dense layer after the last hidden state of the token [21].

The Financial BERT model is a Hazourli brainchild model that is pre-trained using the financial corpus of Reuters, Bloomberg News, EDGAR database, transcripts of earnings calls between companies, analysts, investors, and the media. This model was trained for 23 days using standard BERT optimization parameters, namely using AdamWeight decay as the optimizer, 5e-5 learning rate, 32 batch size, 0.1 dropout rate, and 512 maximum sequence lengths [22].

The FinBERT-tone model is a brainchild of Yang et.al. which is trained using corporate reports from 10K & 10Q, earnings call transcripts, and analysis reports. This model is initiated from the original BERT-Base uncased/cased model, which is then pre-trained using a financial corpus of 250 thousand iterations at a lower learning rate of 2e-5 [23].

D. Pseudolabeling for Model Fine-tuning

Pseudolabeling is the process of generating labels for unlabeled data based on predictions from a previously trained model, effectively using the model's own inference to augment the training data. Formula $\hat{y}_i = \arg\max P(y_i \mid x_i; \theta)$ describes the pseudolabeling algorithm with is the pseudolabel for the i-th data point, is the input, and $P(y_i \mid x_i; \theta)y_i x_i$ is the probability of the label given the input as predicted by the model with parameters θ [24].

The pseudolabeling process carried out in this study involves a fine-tuning method of the pre-trained model to be used. Fine-tuning of the pre-trained model is carried out so that the model can be more generalized with the dataset to be trained [25].

E. Stock Buy/Sell Prediction

Before carrying out the stock buy/sell prediction process, several stages need to be carried out first, namely the process of dividing the dataset, normalizing the data, and training the dataset.

Split datasetis the process of dividing the data composition into two, namely training data and testing data. After

separating the dataset, data normalization is carried out using the Standard Scaler function. Standard Scaler receives dataset information and adjusts it in each component and will scale it in such a way that its distribution is around 0, with a standard deviation of 1 [18].

Deep Learningis one of the developments of Machine Learning which consists of a high-level abstraction modeling algorithm on data using a set of non-linear transformation functions which are arranged in layers and in depth [26].

LSTM (Long Short-Term Memory) designed by Hochreiter and Schmidhuber, is able to overcome the limitations of RNN by using hidden layer units known as memory cells [27].

Bidirectional Long Short Term Memory(Bi-LSTM) consists of two different LSTM hidden layers with the same output in opposite directions. With this architecture, both past and future information are exploited in the output layer [27].

GRU (Gated Recurrent Unit) is a simple variant of LSTM which has two gates, the first is the update gate which consists of an input gate, a forget gate, and a reset gate [27].

Bidirectional Gated Recurrent Unit(Bi-GRU) is a sequence processing model based on two GRUs. Where one takes input in the forward direction, while the other takes it backward, thereby helping the model in producing more reliable decisions [28].

The ensemble approach is done by combining the outputs of various base classifiers to improve the performance of the system. Most systems use a homogeneous ensemble approach by combining the same base classifiers with different hyperparameters [29].

F. Recursive Feature Elimination with Cross-Validation (RFECV) and Principal Component Analysis (PCA)

Recursive Feature Elimination with Cross-Validation (RFECV) is an algorithm that functions to remove redundant features and has little impact on prediction results. The main objective of the RFECV algorithm is to select the best features from a number of attributes through automatic cross-validation [30].

Principal Component Analysis (PCA) is a statistical method that uses orthogonal transformations to turn features that might be related into a set of features that are not related in any way. These features are called principle components. It's important to know that PCA is affected by how big the original features were [31]. It creates new extracted vectors that are orthogonal basis sets that are not related to each other.

III. Methodology

The proposed system design can be seen in Fig. 1 The stages include collecting stock news data and historical stock data, data preprocessing, model finetuning, sentiment analysis for news data, technical indicator calculations, buying/selling strategy planning for historical data, merging the two data, model training, and evaluation at the final stage.

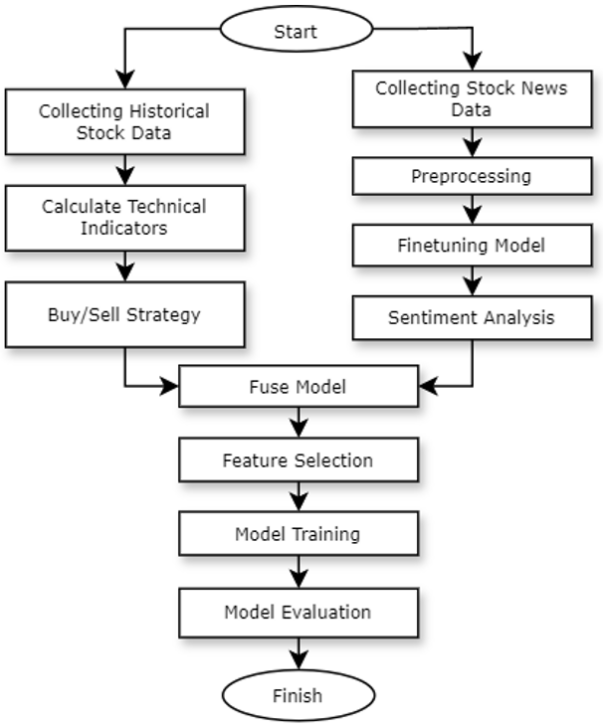

Fig. 1. The proposed system design, stock buy/sell prediction based on technical analysis indicators and news sentiment using deep learning

A. Data collection

The dataset used for the prediction process is divided into two sectors, namely the financial sector and the basic materials sector. Each stock will take data from the past 5 years starting from September 2018 to September 2023.

B. Preprocessing Historical Data and Stock News

After obtaining historical stock data, the buy/sell target labeling process is initiated based on the daily difference and the chosen investment strategy, which includes daily target variations and threshold percentages for buy/sell decisions. This strategy uses four labels: strong sell, weak sell, weak buy, and strong buy, based on the thresholds set in the experimental scenario. For technical analysis, indicators such as 200-day EMA & SMA, MACD, Bollinger Bands, and RSI are calculated using the 'ta-lib' library. Furthermore, the preprocessing stage for sentiment analysis on news titles includes translation using Deep Translate, case folding, tokenization, stopword removal, and lemmatization or stemming with the help of the NLTK library.

C. Stock News Sentiment Analysis

The training process to obtain news headline sentiment is carried out using preprocessed data and the pre-trained FinBERT model from Hugging Face Transformer. Training begins by creating a pipeline that inputs the model and its type, receives preprocessed data, and produces two outputs: predicted labels and confidence scores.

After obtaining sentiment data from BBRI stock news, it is continued by comparing and determining the best pre-trained model when combined with historical data. This process involves fine-tuning using specific news headlines and hyperparameter tuning to optimize the model. Finally, pseudolabeling is performed with all data and parameters that have been set, repeating the fine-tuning process until the majority of the data is labeled, with the initial data being the ground truth.

D. Model Merger

The sentiment data contained a significant amount of news information in a single day prior to the data merging process. This is due to the inconsistency in the number of news items appearing each day, which can result in multiple news items appearing in a single day or none at all. To address this issue, the author created a program that calculates the mode of the most labels on a given day to represent sentiment. To further strengthen sentiment's influence on the model training process, the author added one more label containing the sum of all sentiments in one day.

Then, using historical data, you can combine the data. However, before combining, ensure that the index of both data sets follows the same format, specifically the date format. After the combining process, set the NaN value in the sentiment label to 0 to signify a day without any stock news.

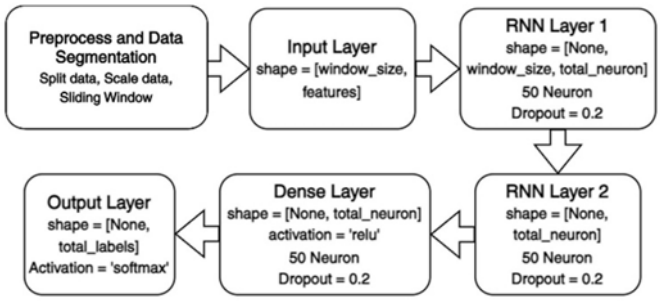

Fig. 2. Neural Network Structure for All Model

E. Model Training Using Deep Learning

There are many built-in features in a deep learning model that can tell you when to buy or sell stocks. These include stock values (open, high, low, close, and volume), technical indicators (EMA, SMA, Bollinger Bands, MACD, and RSI), and news sentiment values (total sentiment and majority sentiment) with the label "Action" made from historical data. This model has several layers that were set up in the testing scenario, and the last layer is activated by softmax. A loss function called "categorical-crossentropy," an optimizer based on the testing scenario, and accuracy as the metric are used to build the model. In all tests, this model's structure stays the same, with the same number of layers and neurons, as shown in Fig. 2.

IV. Experiment and Discussion

In order to obtain good evaluation results, testing will be carried out using several scenarios which will then be compared and analyzed simultaneously at the end of the research.

A. Experiment I, News Sentiment Labeling Analysis

The analysis of the accuracy of news sentiment labeling was carried out by comparing the models (FinBERT, FinancialBERT, and FinBERT-tone), hyperparameter tuning (max length = [16, 32, 64, 128], length size = [8, 16, 32, 64], and learning rate = [1e-4, 1e-5, 1e-6]), and comparison of pseudolabeling methods. The test results can be seen in Table II

Table II shows that the FinBERT-tone model, which was selected as the best model out of the three tested models, successfully provided accurate stock sentiment predictions with a high level of confidence using optimization parameters of max length = 32, batch size = 16, and learning rate = 1e-5.

In the pseudolabeling trials, it showed more accurate sentiment predictions compared to other scenarios, which is likely due to the gradual use of pseudolabeling, compared to scenarios that classify a large amount of data at once, causing bias in the results.

TABLE II
News Sentiment Labeling Analysis Experiment Results

Parameter	Best Method	Metric	Value (%)
News Data	Translation (Without Stemming)	Accuracy	58.80
Pre-trained Model	FinBERT-tone	Average Confidence Level	99.00
	Max Length = 32	Validation	52.95
Hyper-parameter Tuning	Batch Size = 16	Loss	31.47
	Learning Rate = 1e-5	Validation	52.95
Pseudo-labeling	Per-stock	Average Confidence Level	99.48

B. Experiment II, Stock Buy/Sell Strategy

TABLE III
Experimental Results of Stock Buy/Sell Strategy

Parameter	Best Method	Metric	Value (%)
Target Day (2 labels)	50 days	Accuracy	84.00
Classification Labels	4 Label	Accuracy	74.03
Threshold	14 %	Accuracy	77.93

The Stock Buy/Sell Strategy is carried out by comparing the target days (1, 5, 20, 50), the stock buy/sell prediction label strategy (sell/buy, sell/hold/buy, and sell/sell weak/buy weak/buy), and the threshold (11%, 12%, 13%, 14%). The results of the stock buy/sell strategy trial can be seen in Table III

Table III identifies the best method of stock buy/sell prediction using a 50-day target with four prediction labels and a threshold of 13%, although a more detailed evaluation shows that four labels do not always produce the best evaluation compared to other scenarios. However, four labels were chosen to provide deeper insight to decision makers, allowing for more precise identification of the right time to buy or sell,

as opposed to fewer labels that may limit effective decision-making capabilities.

The buy/sell criteria using 4 labels can be seen in Table IV, where the lower and upper thresholds are the limits for strong/weak predictions. The pseudolabeling analysis shows a comparison of evaluation values based on threshold percentage scenarios, with an estimated stock movement range of 11%-14%, providing insight into the influence of thresholds in predicting BBRI stock movements.

TABLE IV
BUY/SELL LABELING CRITERIA WITH 4 LABELS

Label Requirements	Label
Lower Threshold $>$ Target	Sell
Lower Threshold $\leq$ Target $<$ Close Price	Sell (Weak)
Upper Threshold $\geq$ Target $\geq$ Close Price	Buy (Weak)
Upper Threshold $<$ Target	Buy

C. Experiment III, Comparison of Stock Prediction Performance

Comparison of Stock Prediction Performance is done by measuring the performance of LSTM, Bi-LSTM, GRU, Bi-GRU, and Voting methods. The test results can be seen in Table V, with the highest accuracy of 94.22% with voting of all models.

TABLE V
BUY/SELL LABELING CRITERIA WITH 4 LABELS

Model	Precision (%)	Recall (%)	F1-score (%)	Accuracy (%)
LSTM	91.50	91.11	91.06	91.11
Bi-LSTM	91.23	91.11	91.13	91.11
GRU	89.24	88.44	88.35	88.44
Bi-GRU	90.43	90.22	09.017	90.22
Voting (All Models)	**94.24**	**94.22**	**94.22**	**94.22**

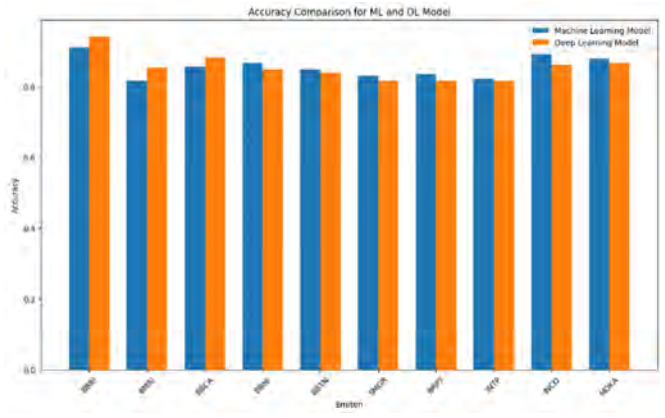

Fig. 3. Comparison of Accuracy between Deep Learning Models and Machine Learning Models on 10 Stocks.

D. Trial IV, Comparison of Prediction Performance with Deep Learning with Machine Learning

We conducted a comparison of prediction performance between deep learning and machine learning on 10 stocks, using deep learning as the voting method for LSTM, Bi-LSTM, GRU, and Bi-GRU. Machine learning utilizes the Random Forest, AdaBoost, XGBoost, SVM, and K-NN methods for voting. Fig. 3 displays the test results.BBRI, BMRI, and BBCA are the three stocks where the deep learning method significantly outperforms the machine learning method. On 7 stocks, specifically BBNI, BBTN, SMGR, BRPT, INTP, INCO, and MDKA, the machine learning method slightly outperforms the deep learning method. Therefore, we can conclude that neither method is better than the other

V. CONCLUSION

The study's trials and discussions yielded the best evaluation results using a 30-day sliding window and the Voting Classifier method with all model estimators. This method significantly improved accuracy using previously obtained sentiment labels and all technical indicator features, reaching 94.22%. These results conclude that the Voting Classifier method, utilizing all models, performs well on data with relatively high complexity. However, for data with low complexity, models such as Bi-LSTM and Bi-GRU are able to produce better accuracy compared to LSTM, GRU, and ensemble methods.

REFERENCES

[1] Pradhypta, IC, Iskandar, D., & Tarumingkeng, RC (2018). Analysis of factors affecting the composite stock price index on the Indonesia Stock Exchange, J. Manaj. Bisnis Kompetensi, vol. 133, no. 1, pp. 43–56.

[2] Loughran, T. & McDonald, B.. (2016). Textual Analysis in Accounting and Finance: A Survey, J. Account. Res., vol. 54, no. 4, pp. 1187–1230.

[3] Leigh, W., Frohlich, C.J., Hornik, S., Purvis, R.L., & Roberts, T.L. (2008). Trading with a stock chart heuristic. IEEE Transactions on Systems, Man, and Cybernetics Part A: Systems and Humans, 38(1), 93–104.

[4] Kao, L. J., Chiu, C. C., Lu, C. J., & Yang, J. L. (2013). Integration of nonlinear independent component analysis and support vector regression for stock price forecasting. Neurocomputing, 99, 534–542.

[5] Dang, M., & Duong, D. (2016). Improvement methods for stock market prediction using financial news articles. NICS 2016 - Proceedings of the 2016 3rd National Foundation for Science and Technology Development Conference on Information and Computer Science, 125–129.

[6] Khedr, A.E., Salama, S.E., & Yaseen, N. (2017). Predicting stock market behavior using data mining techniques and news sentiment analysis. International Journal of Intelligent Systems and Applications, 9(7), 22–30.

[7] Ren, R., Wu, D. D., & Wu, D. D. (2019). Forecasting stock market movement direction using sentiment analysis and support vector machine. IEEE Systems Journal, 13(1), 760–770.

[8] Rehman, A.U., Malik, A.K., Raza, B., & Ali, W. (2019). A Hybrid CNN-LSTM Model for Improving Accuracy of Movie Reviews Sentiment Analysis. Multimedia Tools and Applications, 78(18), 26597–26613

[9] Kim, H., & Jeong, Y.S. (2019). Sentiment classification using Convolutional Neural Networks. Applied Sciences (Switzerland), 9(11).

[10] V. Sharma, R. Khemnar, R. Kumari and B.R. Mohan, "Time Series with Sentiment Analysis for Stock Price Prediction," 2019 2nd International Conference on Intelligent Communication and Computational Techniques (ICCT), Jaipur, India, 2019, pp. 178-181, doi: 10.1109/ICCT46177.2019.8969060.

[11] BL, S. and BR, S. (2023), "Combined deep learning classifiers for stock market prediction: integrating stock price and news sentiments", Kybernetes, Vol. 52 No. 3, pp. 748-773.https://doi.org/10.1108/K-06-2021-0457

[12] AS Rajpurohit, H. Mhaske, PS Gaikwad, SP Ahirrao and NB Dhamale, "Data Preprocessing for Stock Price Prediction Using LSTM and Sentiment Analysis," 2023 6th International Conference on Information Systems and Computer Networks (ISCON), Mathura, India, 2023, pp. 1-6, doi: 10.1109/ISCON57294.2023.10112026.

[13] Chen, P., Boukouvalas, Z. & Corizzo, R. A.(2024), “deep fusion model for stock market prediction with news headlines and time series data”, Neural Comput & Applic. https://doi.org/10.1007/s00521-024-10303-1
[14] Ong, E. (2011) Technical Analysis for Mega Profit. Jakarta: Mega Options.
[15] Nasukawa, T. & Yi, J., (2003). Sentiment Analysis: Capturing Favorability Using Natural Language Processing. In Proceedings of the 2nd International Conference on Knowledge Capture. pp. 70–77.
[16] Runimeirati, Muis, A., & Muhammad, F. (2023). Text Mining Training Using Python Programming Language, Makassar: Megarezky University Makassar, 1.
[17] Jamshed, H., Khan, MSA, Khurram, M., Inayatullah, S., & Athar, S. (2019). Data Preprocessing: A preliminary step for web data mining. 3C Tecnología Glosas de Innovación Applications a La Pyme, May. https://doi.org/10.17993/3ctecno.2019. special issue 2. 206-221.
[18] Afrianto, N. (2022). Stock Prediction with Bidirectional LSTM and Sentiment Analysis, Yogyakarta: Faculty of Industrial Technology, Islamic University of Indonesia, 18-19.
[19] Acheampong, F.A., Mensah, H.N., Chen, W. (2021). Transformer models for text-based emotion detection: a review of BERT-based approaches. Artificial Intelligence Review, (), –. doi:10.1007/s10462-021-09958-2.
[20] Sidogi, T. Mbuvha, R., Marwala, T. (2021). Stock Price Prediction Using Sentiment Analysis. IEEE International Conference on Systems, Man, and Cybernetics (SMC), Melbourne, Australia. doi: 10.1109/SMC52423.2021.9659283.
[21] Araci, D. (2019) Finbert: Financial sentiment analysis with pre-trained language models, Faculty of Science, University of Amsterdam. arXiv preprint arXiv:1908.10063.
[22] Hazourli, A. R. (2022). FinancialBERT - A Pretrained Language Model for Financial Text Mining. DOI:10.13140/RG.2.2.34032.12803.
[23] Yang, Y., UY, MCS, Huang, A. (2020). FinBERT: A Pretrained Language Model for Financial Communications. School of Business and Management, Hong Kong University of Science and Technology. arXiv:2006.08097v2.
[24] Xu, J., Jiang, Y., Yuan, B., Li, S., & Song, T. (2023). Automated Scoring of Clinical Patient Notes using Advanced NLP and Pseudo Labeling. International Conference on Artificial Intelligence and Computer Appl. DOI: 10.1109/ICAICA58456.2023.10405427.
[25] Mohammadi, S. & Chapon, M. (2020). Investigating the Performance of Fine-tuned Text Classification Models Based-on Bert. Search-ForeSight. DOI: 10.1109/HPCC-SmartCity-DSS50907.2020.00162.
[26] Cholissodin, I., Sutrisno, Soebroto, AA, Hasanah, U., & Febiola, YI (2020). AI, MACHINE LEARNING DEEP LEARNING (Theory Implementation), Faculty of Computer Science, Brawijaya University, Malang.
[27] Shahid, F., Zameer, A., Muneeb, M. (2020). Predictions for COVID-19 with deep learning models of LSTM, GRU and Bi-LSTM. Chaos, Solitons & Fractals, 140(), 110212–. doi:10.1016/j.chaos.2020.110212.
[28] Billah, MM & Das, S. (2021). Analysis and Prediction Gold Price using CNN and Bi-GRU based Neural Network Model. Department of Computer Science and Engineering Khulna University of Engineering & Technology. Khulna-9203, Bangladesh. DOI: 10.1109/ICCIT54785.2021.9689880.
[29] Soumya, S., Pramod, K.V. (2023). An Enhanced Approach for Sentiment Analysis of Malayalam Text using Ensemble Deep Learning Models. 4th IEEE Global Conference for Advancement in Technology (GCAT), Bangalore, India. doi: 10.1109/GCAT59970.2023.10353435.
[30] Mustaqim, AZ, Adi, S., Pristyanro, Y. & Astuti, Y. (2021). The Effect of Recursive Feature Elimination with Cross-Validation (RFECV) Feature Selection Algorithm toward Classifier Performance on Credit Card Fraud Detection. Amikom University Yogyakarta. Yogyakarta, Indonesia. DOI: 10.1109/ICAICST53116.2021.9497842.
[31] Rehman, A., Khan, A., Ali, M.A., Khan, M.U., Khan, SU & Ali, L. (2020). Performance Analysis of PCA, Sparse PCA, Kernel PCA and Incremental PCA Algorithms for Heart Failure Prediction. Istanbul, Turkey. DOI: 10.1109/ICECCE49384.2020.9179199.

The Performance of Vacant Parking Spaces Detection Using YOLOv5

Anan Nugroho
Dept. of Electrical Engineering
Universitas Negeri Semarang
Semarang, Indonesia
anannugroho@mail.unnes.ac.id

Muhammad Fathurrahman
Dept. of Electrical Engineering
Universitas Negeri Semarang
Semarang, Indonesia
071203fathur@students.unnes.ac.id

Zidan Vieri Wijaya
Dept. of Electrical Engineering
Universitas Negeri Semarang
Semarang, Indonesia
zidanvieri@students.unnes.ac.id

***Abstract*—Parking challenges are increasingly significant in urban areas, particularly in nations with high numbers of private vehicles, such as Indonesia. Conventional parking systems often struggle to effectively identify available spaces, leading to wasted time, congestion, and environmental issues. This study addresses these challenges by implementing YOLOv5, a deep learning-based object detection model, to improve the efficiency and accuracy of vacant parking space detection. The proposed system processes video input from parking areas to detect vehicle presence and determine the occupancy status of designated parking spaces. A dataset of 3,843 images was compiled for model training and testing, encompassing diverse conditions to enhance detection robustness. The model's performance was tested on two video samples recorded under different environmental conditions, achieving a high accuracy rate of 96.4% in detecting vacant and occupied spaces. These results underscore the potential of YOLOv5 for optimizing parking management, reducing the limitations of traditional systems, and providing a scalable solution for smart city infrastructure.**

***Index Terms*—Smart Parking, YOLOv5, Object Detection, Parking Management**

I. Introduction

Parking issues represent one of the primary challenges in major cities, especially in areas with a high volume of private vehicles [1]. According to BPS (Nation Statistics Agency) ,in Indonesia, the number of private vehicles, particularly cars, reached 17,168,862 units in 2022, with an annual growth rate of 2.6% [2]. This situation adds to the complexity of parking problems, which not only inconvenience vehicle users but also contribute to increased traffic congestion, air pollution, and economic burdens [3]. Another significant impact is the wastage of time and energy, along with a rise in public frustration. The conventional parking systems, which typically rely on parking attendants and the availability of spaces, often fail to consider optimal parking capacity [4]. This leads to drivers encountering difficulties in finding available parking spaces [5]. The inability to determine parking availability forces drivers to circle the area or even leave if no spaces are found [6]. Yet, parking areas are critical facilities that must be provided in public spaces to ensure smooth mobility [7]. As the development of Industry 5.0 progresses, the implementation of smart technologies becomes increasingly essential in addressing complex parking issues. One emerging solution is the smart parking system, which enables remote monitoring and provides real-time information on parking availability [8]. This technology aims to enhance user efficiency and effectiveness in finding parking spaces [9].

979-8-3315-1921-6/24/$31.00 ©2024 IEEE

Several methods in smart parking systems have been developed to detect parking availability. Pulungan et al. (2022) developed an automated parking system based on Arduino microcontrollers and infrared sensors to detect vehicle presence in parking slots. This system automatically operates the entrance and exit gates, and displays parking slot availability information via an LCD monitor. Additionally, LED indicators at each parking slot make it easier for users to determine whether a slot is occupied or vacant, thus saving time and enhancing efficiency [10]. The study improved the traditional background difference method for parking space detection by integrating the Local Binary Pattern (LBP) operator to address environmental changes and interference from pedestrians. The system uses the OpenCV library in Python to process images, extracting texture features and calculating image similarity using perceptual hashing (pHash) and Hamming distance. This enhanced approach reduces the impact of lighting changes and pedestrian interference, ensuring accurate identification of parking spaces. Available spaces are detected by comparing the similarity between the current image and the background, marking spaces as vacant or occupied based on threshold values. Available parking spaces are marked in green, while occupied spaces are marked in red. This method enhances parking management, particularly in dynamic environments [11].

However, further evaluation is necessary due to several limitations in existing studies on smart parking systems, such as the suboptimal effectiveness of sensors in detecting vehicles [12], and the potential for errors in detection that may misidentify non-vehicle objects as cars [13]. In this context, advancements in deep learning-based image processing present a promising approach for accurate vacant parking space detection, offering a pathway to overcome these challenges. Previous research on vehicle detection in smart parking systems has utilized various methods. The use of Convolutional Neural Networks (CNNs) with custom datasets has achieved a satisfactory accuracy rate of 86% for detecting vehicle presence in parking spaces with a custom dataset 5,800 images [14]. Other studies have reported an accuracy of 90% in vehicle detection by employing CNN-based models with a custom dataset 8,336 images [15]. Additionally, the application of You Only Look Once version 3 (YOLOv3) with a custom dataset of 4,900 images demonstrated an accuracy of 94.7% in detecting vacant parking space [16]. Despite these promising results, these studies often require extensive datasets, which may be inefficient in practical applications. YOLOv5 addresses this limitation through the use of mosaic data augmentation during the training phase, which allows the model to learn

effectively even with limited data [17]. By utilizing smaller image sizes during training, YOLOv5 has proven superior in detecting small objects, making it well-suited for large-scale monitoring of construction areas due to its high accuracy and faster detection speed compared to other YOLO versions [18].

Therefore, this study proposes the use of the YOLOv5 method to improve accuracy and efficiency in detecting parking space availability. YOLOv5, a single-stage deep learning model, is known for its stable detection and accuracy, which makes it an ideal choice for real-time applications in smart parking systems, addressing both detection reliability.

II. Related Work

Object detection is an innovative technology with great potential, especially when integrated with hardware such as CCTV to maximize its functionality [19]. This technology plays an important role in various sectors, including security, transportation, and industry. Success in object detection is crucial to ensuring safety as well as improving efficiency in surveillance systems. One of the leading algorithms that is currently the top choice in object detection is YOLO. YOLO offers advantages in various fields thanks to its ease-of-use, high accuracy, and advanced technology [20]. In recent years, rapid advances in surveillance technology, particularly through the use of computer vision-based YOLO, have contributed significantly to the development of object detection systems [21] . Zhang et al (2022) [22] conducted research using an improved YOLOv5 algorithm for real-time vehicle detection in various traffic scenarios. By utilizing a multi-type vehicle dataset collected under different conditions and employing the Flip-Mosaic data enhancement algorithm, they were able to improve the detection accuracy of small and occluded vehicle targets [22]. The experimental results demonstrated that their method significantly reduced the false detection rate, achieving more accurate and reliable vehicle detection across multiple traffic environments. Another study by Zhou et al. (2023) [23] focused on detecting small targets using drones, comparing various types of YOLO across different scales. The results demonstrated improved accuracy compared to higher versions. Also, Sukkar et al. (2021) [24] proposed a pedestrian detection system leveraging the YOLOv5 algorithm, which was trained with a custom dataset focusing on pedestrian age classification. By incorporating data augmentation techniques, the system demonstrated improved accuracy in detecting pedestrians across different age groups. The implementation achieved real-time performance with a detection rate of 25 frames per second (fps), underscoring its potential for applications in autonomous driving and Advanced Driver Assistance Systems (ADAS). In these studies, the feasibility of adopting YOLO for detecting parking slot availability is evident.

While these studies demonstrate YOLOv5's adaptability in real-time detection, they do not fully address the unique challenges of detecting vacant parking spaces, such as potential interference from non-vehicle objects and the need for high spatial precision. Additionally, existing parking detection models often require extensive datasets, which can be impractical for applications with limited data. Recent innovations, such as YOLOv5's mosaic data augmentation, allow more effective training with smaller datasets and improved accuracy in smaller-object detection [15], [18].

This study leverages YOLOv5, which introduces mosaic data augmentation, allowing effective training on smaller datasets. This approach not only mitigates the limitations of data requirements but also enhances YOLOv5's ability to detect smaller objects and improve detection speed and accuracy in real-time, bridging critical gaps left by previous methods in achieving scalable, efficient parking management solutions.

III. Method

The selection of the YOLO architecture is based on its high accuracy and real-time detection capabilities, making it a highly effective object detection method. YOLOv5, in particular, has been shown to offer a more stable performance compared to its earlier and later versions [15]. In prior studies, using the COCO2017 dataset, YOLOv5 achieved an Average Precision (AP) of 55.8%, outperforming YOLOv4 with an AP of 43.5% and even YOLOv6, which reached only 52.5% [20]. This performance advantage further underscores YOLOv5's suitability for practical applications requiring robust detection accuracy [15].

A. Yolo Architecture

Yolo Architectureon a single-pass detection approach, which enables the network to identify multiple objects within an image or video in real-time. By processing the input in one go, YOLO offers a highly efficient object detection system. The network divides the input image into an SxS grid, where each grid cell is responsible for predicting the presence of objects whose center falls within that cell. The prediction for each object includes a bounding box and a confidence score, reflecting the probability that the object is present within that area. Each bounding box consists of five elements: the x and y coordinates (indicating the box's center relative to the grid cell), the width (w) and height (h), and the confidence score C [20].

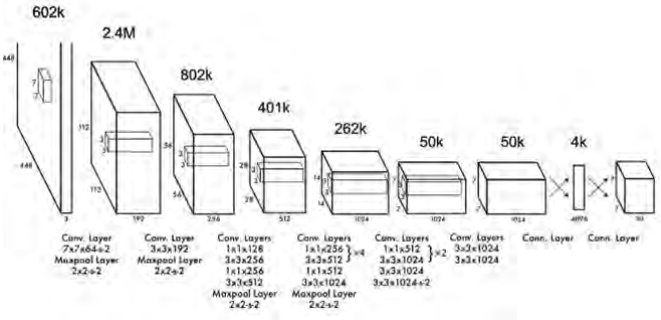

Fig. 1. Yolo Architecture

The YOLO architecture, as depicted in Figure 1, accepts images as input and resizes them to 448 x 448 pixels while maintaining the aspect ratio through padding. Once resized, the image is processed through a CNN. The model comprises 24 convolutional layers, 4 max-pooling layers, followed by 2 fully connected layers. To reduce the number of parameters, YOLO employs 1 x 1 convolution layers followed by 3 x 3 convolution layers [20]. The 24 convolutional layers demonstrate specific kernel and filter values for each layer; however, the precise values of these filters during the training process are not explicitly detailed as they are treated as a black box within the YOLO algorithm. The final output of this network is a prediction tensor in the form of feature map with dimensions of $7 \times 7 \times 30$ as shown in Figure 2.

In this final output, 7×7 refers to the grid size that divides the image into 49 individual grid cells, and 30 refers to the number of values predicted per cell. Each grid cell is responsible for predicting 2 bounding boxes, each with 5 parameters: the center coordinates (b_x, b_y), the width (b_w), and the height (b_h) of the bounding box. In addition, each

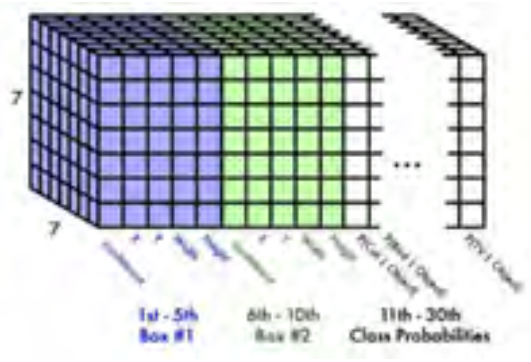

Fig. 2. Feature map yolo

bounding box predicts a confidence score (P_c) representing the likelihood that an object exists within that box. The remaining values in the prediction tensor represent the class probabilities (C) for a total of 20 object classes in the original YOLO model [20].

After completing the feature map process, YOLO identifies each grid cell using four values in the equation as represented in Figure 3.

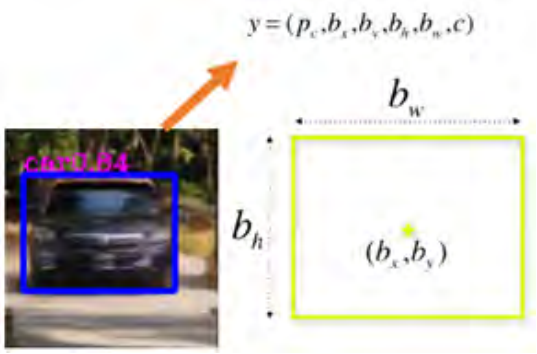

Fig. 3. Example Bounding-box YOLO

B. Dataset Collection

Data collection is obtained from various car shape references, with datasets taken from Roboflow Universe which provides datasets, as well as images and videos obtained from the internet and the results of independent shooting. The process of taking pictures and videos independently is carried out with various viewpoints, car types, and vehicle conditions. The collected datasets will be manually labeled with car objects. Roboflow, a platform that facilitates data collection and labeling, allows each car object to be properly annotated with bounding boxes [26]. The total dataset used amounted to 3,843 images. Some examples of the dataset are illustrated in Figure 4.

C. System design

The system workflow can be observed in Figure 5, beginning with the labeling process on the input image. The user marks the parking spaces using pickle, which subsequently stores the coordinates of the labeled parking areas. Next, using the same captured image, YOLOv5 will receive video input from the parking area. YOLOv5 detects the presence of vehicles and integrates this detection with the labeled parking

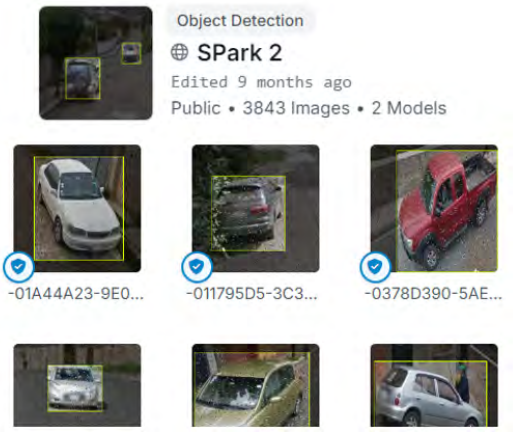

Fig. 4. Collection of research datasets

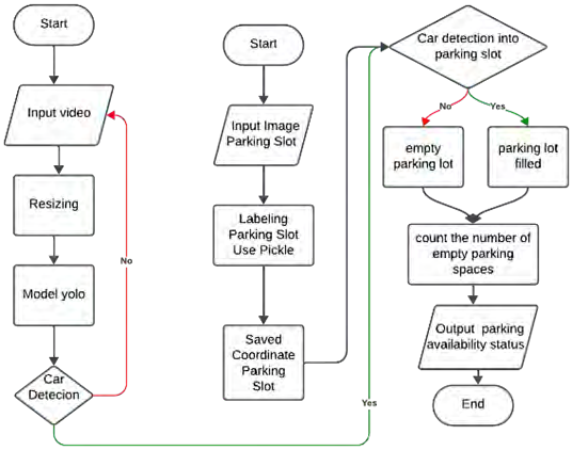

Fig. 5. Proposed framework workflow

spaces. A parking space is marked as occupied when a vehicle is detected within the labeled area. Conversely, if no vehicle is detected, the space is considered vacant. Based on these detection results, the system calculates parking availability from the total number of available spaces.

D. Perfomance Metric

Accuracy is the primary performance metric used to evaluate the detection of parking slot availability in this study. It provides an overall measure of how well the detection model correctly identifies both occupied and available parking slots. Accuracy is calculated based on the proportion of true positive (TP), true negative (TN), false positive (FP), and false negative (FN) indexs, with detailed scenario descriptions as provided in Table I.

The accuracy metric gives a balanced understanding of the model's overall performance by considering both correct and incorrect detections. It is calculated using equation (1).

$$\text{Accuracy} = \frac{TP + TN}{TP + TN + FP + FN} \tag{1}$$

TABLE I
MEASUREMENT SCENARIOS

Measurement	Quantity
True Positive (TP):	A parking slot is correctly detected as available.
True Negative (TN):	A parking slot is correctly detected as occupied.
False Positive (FP):	A parking slot is incorrectly detected as available, but it is actually occupied.
False Negative (FN):	A parking slot is incorrectly detected as occupied, but it is actually available.

This metric helps assess the model's ability to handle both positive and negative detections, ensuring that the system performs well in real-time parking availability scenarios.

E. Training Data

In this study, data training was conducted to develop model weights for human detection. The YOLOv5 algorithm, implemented with PyTorch on Google Colaboratory, was used for training. The process ran for five hours, using a 640x640 pixel image size to enhance detail in vehicle detection and a batch size of 64 to expedite training by processing multiple images simultaneously. Over 300 epochs, the model was refined to identify complex data patterns, focusing solely on detecting vehicles as a single object class. Upon completion, the YOLOv5 model produced a .onnx file for vehicle detection in the system. The training yielded a precision of 96.2%, recall of 97.1%, mAP50 of 97%, and mAP50-95 of 72.0%. Precision reflects the model's accuracy in detecting vehicles without false positives, while recall indicates its ability to capture all present vehicles. mAP50 and mAP50-95 provide accuracy across various IoU thresholds, assessing model robustness under different conditions [27]. These metrics underscore YOLOv5's strong performance in vehicle detection, as illustrated in Figure 6.

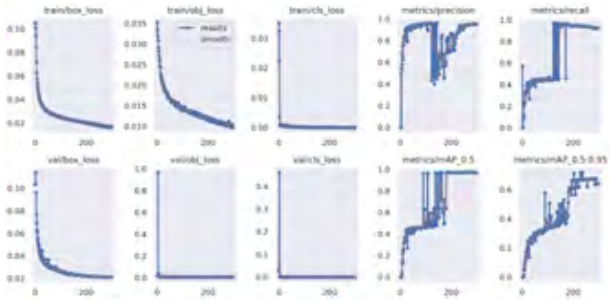

Fig. 6. YOLOv5 Training Results

It is noteworthy that while multiple indices are employed during training to optimize different aspects of model performance, testing focuses solely on accuracy as a measure of the model's generalization to new, unseen data.

F. Experimental Setup

The experimental setup for this study utilized a combination of hardware and software to implement and evaluate the parking detection system. The hardware consisted of the following:

1) ASUS TUF GAMING A15 Laptop with the following specifications:
   a) Processor: AMD Ryzen 7 6800H with Radeon Graphics 3.20 GHz
   b) Graphics: NVIDIA® GeForce RTX™ 3060 Laptop GPU, 1752MHz* at 140W (1702MHz Boost Clock +50MHz OC, 115W +25W Dynamic Boost)
   c) RAM: 16 GB
   d) Storage: 512 GB
   e) OS: Windows 10 Home
2) Camera CCTV Hikvision 1080P DS-2CD1021-I 2MP
3) 15-meter long USB 2.0 Male to Female cable
4) Software used:
   a) Visual Studio Code
   b) Google Colab Colaboratory
   c) Python 3.11.9
   d) OpenCV 4.10.0

In this study, testing was conducted using two sample videos, each with a duration of 1 minute and 45 seconds, representing a parking lot under two distinct conditions: Video 1 featured a camera positioned at a distance of less than 15 meters, while Video 2 had a closer setup at under 3 meters.

These videos were processed using Python code that applies the YOLOv5 model, pre-trained on a dataset previously collected for this purpose. The model outputs detection results with bounding boxes marking identified vehicles, and each video is analyzed by capturing two frames per second for subsequent evaluation.

IV. RESULT AND DISCUSSIONS

This research is experimental, testing two videos under different conditions, including cloudy and clear weather, varying angles, different types of vehicles, and distinct locations. The first video has a duration of 1 minute with a total of 8 parking slots, which will be divided into 102 frames. The second video lasts 45 seconds with a total of 5 parking slots, resulting in 75 frames. These videos will focus on detecting parked vehicles.

Fig. 7. Video detection result 1

Fig. 8. Video detection result 2

Figures 6 and 7 show several detected objects, highlighted with light blue bounding boxes, along with their classifications and confidence levels for each detection. The videos display the number of detected cars and the availability status of parking slots. Video 1 demonstrates detection with a distant camera view, while Video 2 captures a closer perspective, allowing for performance testing of YOLOv5 in detecting parking availability from both distances. Detection is confirmed when a car's bounding box enters a designated parking slot, changing the slot's indicator to red to denote occupancy.

Conversely, when no car is detected within a slot, the indicator reverts to green, signifying an available space.

The results from Video 1 and Video 2 are shown in Table II and Table III, respectively.

TABLE II
MEASUREMENT SCENARIOS VIDEO 1

Measurement	Quantity
True Positive (TP):	242
True Negative (TN):	536
False Positive (FP):	0
False Negative (FN):	38

TABLE III
MEASUREMENT SCENARIOS VIDEO 2

Measurement	Quantity
True Positive (TP):	78
True Negative (TN):	292
False Positive (FP):	0
False Negative (FN):	5

From Tables I and II, the results of Video 1 and Video 2 in detecting the absence of parking spaces resulted in accuracy Using the accuracy calculation formula, the accuracy value is obtained:

Video 1:

$$\text{Accuracy} = \frac{242 + 536}{242 + 536 + 0 + 38} = \frac{778}{816} = 0.953 \quad (2)$$

Video 2:

$$\text{Accuracy} = \frac{78 + 292}{78 + 292 + 0 + 5} = \frac{370}{375} = 0.986 \quad (3)$$

Based on the evaluation results indicate that Video 1, which involves a more distant camera view, achieved an accuracy of 0.953. This is slightly lower than the 0.986 accuracy obtained for Video 2, which represents detection at a closer range. These differences in accuracy are influenced by various factors, including the field of view, potential obstructions, and the overall reach of the camera. The closer proximity of Video 2 likely provides enhanced detail, improving detection accuracy.

However, the high accuracy values from both videos demonstrate the robustness of YOLOv5 in detecting parking availability even from a distance. This suggests the system's potential for real-world application in parking facilities, where effective detection across varied camera placements is essential. A summary of these detection results for Video 1 and Video 2 is provided in Table IV.

TABLE IV
TOTAL MEASUREMENT SCENARIOS

Measurement	Quantity
True Positive (TP):	320
True Negative (TN):	828
False Positive (FP):	0
False Negative (FN):	43

From Tables I and II, the results can be combined, and the total true positive (TP), true negative (TN), false positive (FP), and false negative (FN) can be seen in Table III. By using the accuracy calculation formula, the accuracy value is obtained:

$$\text{Accuracy} = \frac{320 + 828}{320 + 828 + 0 + 43} = \frac{1148}{1191} = 0.964 \quad (4)$$

rall accuracy of 0.964 in detecting available parking slots in both Video 1 and Video 2, indicating strong performance. While this accuracy does not reach a perfect 100%, several factors contribute to the limitation, including partial obstructions of vehicles, suboptimal camera quality, greater object distances, and variable weather conditions across the videos. Nevertheless, the performance achieved in this study surpasses previous object detection methods. For instance, a study utilizing the RCNN method for vehicle detection reported an accuracy of 90.65% in identifying cars [28].

Another study focusing on autonomous vehicle detection on roads with CNN achieved an accuracy of 94.3% under optimal sunny conditions [29]. In further research on vehicle categorization using the earlier YOLO version, YOLOv4, the highest accuracy attained was 93% [30]. Given its superior accuracy, YOLOv5 demonstrates significant potential for real-time parking availability monitoring applications, establishing it as a more effective choice for this purpose [31].

Despite these challenges, the system achieves a relatively high accuracy, demonstrating its effectiveness in detecting parking availability. This system shows promise for real-world application in CCTV-equipped parking facilities, where it could streamline the parking process by helping drivers locate available slots more quickly, either through hardware integration or mobile applications. This would reduce search time and enhance overall parking efficiency. Furthermore, these findings open avenues for future research focused on improving detection accuracy through advanced image processing techniques and more robust models. Although the test video does not encompass all possible real-world scenarios, it provides a solid foundation for future research aimed at expanding coverage and enhancing detection accuracy across varied conditions.

V. CONCLUSION

This research demonstrates the effectiveness of YOLOv5 in detecting vacant parking spaces with high accuracy. Through experimentation on two different video samples, the system achieved an overall accuracy of 96.4%, with consistent detection of both available and occupied parking slots. The application of YOLOv5 allowed for real-time detection, handling various weather conditions, angles, vehicle types, and locations, highlighting the versatility and robustness of the model. However, when implemented on different hardware platforms, such as lower-spec embedded systems or devices with limited processing power, the performance may degrade, particularly in terms of detection speed and accuracy. Additionally, video angles that are significantly tilted or skewed can reduce the precision of detection, as YOLOv5 may struggle to accurately interpret object boundaries and positions in such conditions. Future work may focus on optimizing the system for these challenges and integrating it with broader smart city initiatives.

ACKNOWLEDGMENT

The authors gratefully acknowledge funding from Institute of Research and Community Service (LPPM) of Universitas Negeri Semarang (UNNES) under grant number 155.26.2/UN37/PPK.10/2024. This research was also supported by the Artificial Intelligence, Robotics & Internet of Things Laboratory (AIRIoT Lab) at the Digital Center of Universitas Negeri Semarang, whose invaluable resources and support were essential in completing this work. We hope that the outcomes of this research contribute meaningfully to the advancement of science and technology.

REFERENCES

[1] Ibrahim and Hossam El-Din, "Car Parking Problem in Urban Areas: Causes and Solutions," 1st International Conference on Towards a Better Quality of Life, pp. 1–13, 2017.

[2] I. Sefriyadi, I. G. A. Andani, A. Raditya, P. F. Belgiawan, and N. A. Windasari, "Private car ownership in Indonesia: Affecting factors and policy strategies," *Transp Res Interdiscip Perspect*, vol. 19, p. 100796.

[3] R. Elavarasi and P. K. Senthilkumar, "Smart Car Parking," *Indian J Sci Technol*, vol. 10, no. 9, pp. 1–4, Feb. 2017, doi: 10.17485/ijst/2017/v10i9/111018.

[4] T. Singh, R. Rathore, K. Gupta, E. Vijay, and R. Harikrishnan, "Artificial Intelligence-Enabled Smart Parking System," 2024, pp. 419–436. doi: 10.1007/978-981-99-8661-331.

[5] J. Parmar, P. Das, and S. M. Dave, "Study on demand and characteristics of parking system in urban areas: A review," *Journal of Traffic and Transportation Engineering (English Edition)*, vol. 7, no. 1, pp. 111–124, Feb. 2020, doi: 10.1016/j.jtte.2019.09.003.

[6] A. Kurek and E. Macioszek, "Drivers' Subjective Assessment of the Ease of Finding a Vacant Parking Space in an Area Equipped with Vehicle Detection Devices," *Sensors*, vol. 22, no. 18, p. 6734, Sep. 2022, doi: 10.3390/s22186734.

[7] S. Biswas, S. Chandra, and I. Ghosh, "Effects of On-Street Parking in Urban Context: A Critical Review," *Transportation in Developing Economies*, vol. 3, no. 1, p. 10, Apr. 2017, doi: 10.1007/s40890-017-0040-2.

[8] A. Raj and S. D. Shetty, "Smart parking systems technologies, tools, and challenges for implementing in a smart city environment: a survey based on IoT & ML perspective," *International Journal of Machine Learning and Cybernetics*, vol. 15, no. 7, pp. 2673–2694, Jul. 2024, doi: 10.1007/s13042-023-02056-5.

[9] T. Rijwani et al., "Industry 5.0: a review of emerging trends and transformative technologies in the next industrial revolution," *International Journal on Interactive Design and Manufacturing (IJIDeM)*, Jun. 2024, doi: 10.1007/s12008-024-01943-7.

[10] K. Kumar, V. Singh, L. Raja, and S. N. Bhagirath, "A Review of Parking Slot Types and their Detection Techniques for Smart Cities," *Smart Cities*, vol. 6, no. 5, pp. 2639–2660, Oct. 2023, doi: 10.3390/smartcities6050119.

[11] Y. Li, H. Mao, W. Yang, S. Guo, and X. Zhang, "Research on Parking Space Status Recognition Method Based on Computer Vision," *Sustainability*, vol. 15, no. 1, p. 107, Dec. 2022, doi: 10.3390/su15010107.

[12] C. Biyik et al., "Smart Parking Systems: Reviewing the Literature, Architecture and Ways Forward," *Smart Cities*, vol. 4, no. 2, pp. 623–642, Apr. 2021, doi: 10.3390/smartcities4020032.

[13] A. A. Musa, S. I. Malami, F. Alanazi, W. Ounaies, M. Alshammari, and S. I. Haruna, "Sustainable Traffic Management for Smart Cities Using Internet-of-Things-Oriented Intelligent Transportation Systems (ITS): Challenges and Recommendations," *Sustainability*, vol. 15, no. 13, p. 9859, Jun. 2023, doi: 10.3390/su15139859.

[14] M.-C. Wu and M.-C. Yeh, "Early Detection of Vacant Parking Spaces Using Dashcam Videos," *Proceedings of the AAAI Conference on Artificial Intelligence*, vol. 33, no. 01, pp. 9613–9618, Jul. 2019, doi: 10.1609/aaai.v33i01.33019613.

[15] K. Gkolias and E. I. Vlahogianni, "Convolutional Neural Networks for On-Street Parking Space Detection in Urban Networks," *IEEE Transactions on Intelligent Transportation Systems*, vol. 20, no. 12, pp. 4318–4327, Dec. 2019, doi: 10.1109/TITS.2018.2882439.

[16] W. Li, L. Cao, L. Yan, J. Liao, and Z. Wang, "Vacant parking slot detection and tracking during driving and parking with a standalone around view monitor," *Proceedings of the Institution of Mechanical Engineers, Part D: Journal of Automobile Engineering*, vol. 235, no. 6, pp. 1539–1551, May 2021, doi: 10.1177/0954407020980869.

[17] U. Sirisha, S. P. Praveen, P. N. Srinivasu, P. Barsocchi, and A. K. Bhoi, "Statistical Analysis of Design Aspects of Various YOLO-Based Deep Learning Models for Object Detection," *International Journal of Computational Intelligence Systems*, vol. 16, no. 1, p. 126, Aug. 2023, doi: 10.1007/s44196-023-00302-w.

[18] M. Park, D. Q. Tran, J. Bak, and S. Park, "Small and overlapping worker detection at construction sites," *Autom Constr*, vol. 151, p. 104856, Jul. 2023, doi: 10.1016/j.autcon.2023.104856.

[19] J. Kaur and W. Singh, "Tools, techniques, datasets and application areas for object detection in an image: a review," *Multimed Tools Appl*, vol. 81, no. 27, pp. 38297–38351, Nov. 2022, doi: 10.1007/s11042-022-13153-y.

[20] J. Terven, D.-M. Córdova-Esparza, and J.-A. Romero-González, "A Comprehensive Review of YOLO Architectures in Computer Vision: From YOLOv1 to YOLOv8 and YOLO-NAS," *Mach Learn Knowl Extr*, vol. 5, no. 4, pp. 1680–1716, Nov. 2023, doi: 10.3390/make5040083.

[21] C.-Y. Wang and H.-Y. Liao, "YOLOv1 to YOLOv10: The fastest and most accurate real-time object detection systems," 2024 IEEE Conference on Computer Vision and Pattern Recognition (CVPR), Aug. 2024.

[22] Y. Zhang, Z. Guo, J. Wu, Y. Tian, H. Tang, and X. Guo, "Real-Time Vehicle Detection Based on Improved YOLO v5," *Sustainability*, vol. 14, no. 19, p. 12274, Sep. 2022, doi: 10.3390/su141912274.

[23] J. Zhou, T. Su, K. Li, and J. Dai, "Small Target-YOLOv5: Enhancing the Algorithm for Small Object Detection in Drone Aerial Imagery Based on YOLOv5," *Sensors*, vol. 1, p. 134, Dec. 2023, doi: 10.3390/s24010134.

[24] M. Sukkar, D. Kumar, and J. Sindha, "Real-Time Pedestrians Detection by YOLOv5," in *2021 12th International Conference on Computing Communication and Networking Technologies (ICCCNT)*, IEEE, Jul. 2021, pp. 01–06, doi: 10.1109/ICCCNT51525.2021.9579808.

[25] J. Redmon, S. Divvala, R. Girshick, and A. Farhadi, "You Only Look Once: Unified, Real-Time Object Detection," in *2016 IEEE Conference on Computer Vision and Pattern Recognition (CVPR)*, IEEE, Jun. 2016, pp. 779–788, doi: 10.1109/CVPR.2016.91.

[26] F. Ciaglia, F. Zuppichini, P. Guerrie, M. McQuade, and J. Solawetz, "Roboflow 100: A Rich, Multi-Domain Object Detection Benchmark," arXiv preprint arXiv:2211.13523, pp. 1–12, 2022.

[27] R. Padilla, S. Netto, and E. Silva, "A Survey on Performance Metrics for Object-Detection Algorithms," in *2020 International Conference on Systems, Signals and Image Processing (IWSSIP)*, IEEE, 2020.

[28] X. Wang, W. Zhang, X. Wu, L. Xiao, Y. Qian, and Z. Fang, "Real-time vehicle type classification with deep convolutional neural networks," *J. Real Time Image Process.*, vol. 16, no. 1, pp. 5–14, Feb. 2019, doi: 10.1007/s11554-017-0712-5.

[29] I. A. Tarmizi and A. A. Aziz, "Vehicle Detection Using Convolutional Neural Network for Autonomous Vehicles," in *2018 International Conference on Intelligent and Advanced System (ICIAS)*, IEEE, Aug. 2018, pp. 1–5, doi: 10.1109/ICIAS.2018.8540563.

[30] J. Kim, J.-Y. Sung, and S. Park, "Comparison of Faster-RCNN, YOLO, and SSD for Real-Time Vehicle Type Recognition," in *2020 IEEE International Conference on Consumer Electronics - Asia (ICCE-Asia)*, IEEE, Nov. 2020, pp. 1–4, doi: 10.1109/ICCE-Asia49877.2020.9277040.

[31] V. S and V. M. Bhuvanesh, "Real Time Theft Detection Using YOLOv5 Object Detection Model," in *2023 3rd International Conference on Innovative Sustainable Computational Technologies (CISCT)*, IEEE, Sep. 2023, pp. 1–5, doi: 10.1109/CISCT57197.2023.10351223.

Design of Lightning Strike Danger Zone Detection System Using the Rolling Sphere Method Integrated with Smartphones

Adi Nugraha
Department of Electrical Engineering
Universitas Sultan Ageng Tirtayasa
Cilegon, Indonesia
adi.n@untirta.ac.id

Felycia
Department of Electrical Engineering
Universitas Sultan Ageng Tirtayasa
Cilegon, Indonesia
felycia@untirta.ac.id

***Abstract*—Buildings on the campus of the Faculty of Engineering Untirta have the potential to reflect or experience direct lightning strikes during storms, which can endanger pedestrians in open areas. Unfortunately, until now there has been no danger warning in the open area, so pedestrians are not prepared to face unexpected situations, especially when it rains accompanied by lightning. Direct lightning strikes are one of the most risky hydrometeorological events. The impact can damage various objects and threaten human life. With a large open area on campus, the threat of lightning strikes can occur at any time, especially during the rainy season. Therefore, this study aims to design and apply a lightning strike danger zone detection device in the campus area of the Faculty of Engineering Untirta, which is located in Cilegon. This tool is designed to provide early warning through smartphone notifications, so pedestrians can be more aware of potential dangers. The research stage includes analyzing the open area of the campus using the Rolling Sphere method, which is used to identify vulnerable points affected by lightning strikes. After that, area plotting is carried out based on the results of the analysis. The next step is to create a detection tool that functions to identify the danger zone of a direct lightning strike, which is then integrated with smartphone notifications. With this tool, it is hoped that pedestrian safety on the campus of the Faculty of Engineering Untirta can be better maintained, especially in bad weather conditions.**

***Index Terms*—ligthing, detector lighting, lightning strike zone, rolling sphere, Petir phenomenon**

I. Introduction

Lightning is a discharge event that occurs between clouds, within clouds or between clouds and ground [1]. In the cloud there is a positive charge and a negative charge, so when these charges meet each other there will be an explosion / lightning. In general, lightning is one of the sources of electromagnetic interference that can damage electrical equipment. In addition to damaging electrical equipment, lightning can also be dangerous to human safety. In the case of lightning striking the human body, lightning usually strikes the surface of the body [2].

There are six lightning mechanisms when striking the human body, including direct lightning strikes, contact voltage, strikes from the side of buildings, step voltage, upward streamers, and explosion effects. The lightning strike mechanism is very dangerous and can cause casualties. The skin contains a lot of fluids and the nature of very short electrical pulses encourages current to flow throughout the surface of the body. The effects of lightning strikes on the body can damage the eardrum and bruise the internal organs, as well as too strong light that can cause cataracts [3].

In general, cases of direct lightning strikes that hit humans and usually occur in open areas [4]. For example, a recent case that an elderly person who is 70 years old was directly hit by lightning while working in a field about 1 kilometer away from his home [5]. So that open areas are quite dangerous areas for humans because they have the potential to be struck by lightning directly. Especially if the open area is an area that is often passed through for certain activities.

In theory, an object or tall building is a medium of direct lightning strike. So that with tall objects such as buildings, towers and so on, lightning will easily discharge these objects. In addition, with the analysis of the rolling sphere, there are several areas that will be the area of the lightning strike fall point directly and also affect the surrounding area. So that when there are tall objects or tall buildings in a large area, the potential for lightning strikes to the area is very high [6].

The campus of the Faculty of Engineering, Sultan Ageng Tirtayasa University (UNTIRTA) which is located in the city of Cilegon is a campus that has a fairly tall building of about 5 floors. In addition, there is a building object that has a considerable distance from other buildings, namely the canteen building. In addition, there is a rock climbing tower object that is quite tall when compared to a canteen building. In the canteen building, the open area is quite large and the distance between the canteen and the campus building is quite far so that the area is not safe from direct lightning strikes.

The potential for direct hits and bounces from buildings during thunderstorms can endanger pedestrians in the open area of the Faculty of Engineering Untirta campus. So far, there has been no danger warning in the open area so that pedestrians in the area are not prepared if unwanted things

979-8-3315-1921-6/24/$31.00 ©2024 IEEE

happen, especially when there is rain and lightning. Therefore, pedestrians who are residents of the technical campus need to be warned not to be in the direct lightning strike zone when a lightning storm occurs.

In this study, the researcher wanted to create a device that could provide warnings to pedestrians who were in or passing through the red zone area of lightning strikes directly. Not all areas have red zones. So that with the tool made by the researcher, pedestrians who are in the campus area of the faculty of engineering can be ranked to immediately stay away from the area when entering the red zone of the lightning strike directly. This direct lightning strike red zone detection tool is designed to be integrated with the user's mobile phone. Therefore, when pedestrians are in the red zone of a direct lightning strike, the user's mobile phone will receive a warning notification to immediately stay away from the area and go to the green zone in the surrounding area.

II. Study Literature

A. Lightning Potential

Research on lightning disturbances was carried out at the UNTIRTA engineering campus located on Jl. Jenderal Sudirman Km 3, Kotabumi, Purwakarta District, Cilegon City, Banten.

Fig. 1. Research location

In this area, if you look at the lightning strike map according to BMKG in August 2022 (rainy season), the intensity of lightning strikes is quite high and reaches more than 60 thousand lightning strikes directly. Shown by the following Fig 1.

B. The Process of Lightning Occurrence

There is a process and requires several conditions for a lightning cloud to form. Some of them are as follows.

1) Up-Draft

Updraft is the process of the air rising upwards and forming a cloud. This is due to soil surface warming or orthographic properties. The more areas that have water and the longer the heating lasts from the sun, the greater the lightning clouds can

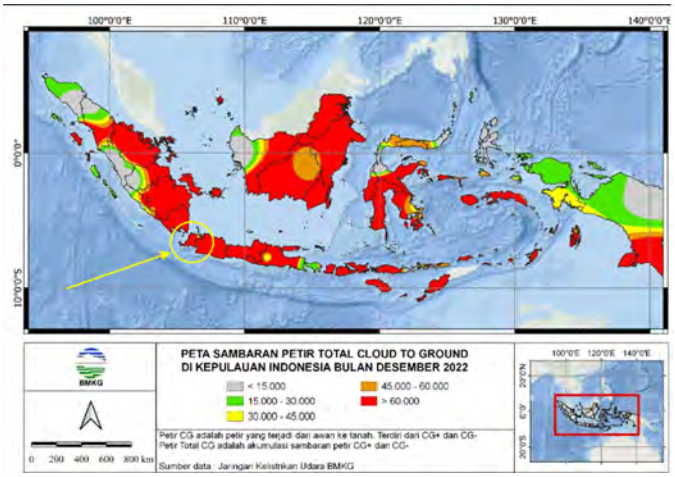

Fig. 2. Map of lightning strikes in Indonesia

form.

2) Aerosol

An aerosol is a particle that floats in the air freely and is hygroscopic (absorbs water). Usually aerosols are produced from sea salt or industrial particles/pollutants that rise with the up-draft. Due to its water-absorbing properties, the water vapor produced from the updraft will be collected easily into water droplets.

3) Humidity

Humid air is one of the conditions for producing lightning. Because with enough air humidity, water can turn into ice granules. From this friction of ice, static electricity is formed. Indonesia is an area that has a large enough forest, so the air in Indonesia has enough moisture to be able to produce thundercloudsAll margins, column widths, line spaces, and text fonts are prescribed; please do not alter them. You may note peculiarities. For example, the head margin in this template measures proportionately more than is customary. This measurement and others are deliberate, using specifications that anticipate your paper as one part of the entire proceedings, and not as an independent document. Please do not revise any of the current designations.

C. Rolling Sphere Method

The Rolling Sphere method is a lightning protection method that imagines a sphere with a certain radius (S) rolling over and around a building structure. When this sphere touches the structure, that point is considered a vulnerable area for lightning strikes and should be protected by an air termination conductor. The sphere's radius (S) depends on the lightning current magnitude, and lightning within this radius has an equal chance of striking the building. This method considers parameters such as strike distance, peak current distribution, and protective area to ensure optimal lightning protection [6].

III. METHOD

A. Design of Lighting Hazard Zone

The design of the Lightning Hazard Zone Detection Tool is shown by the following flow diagram.

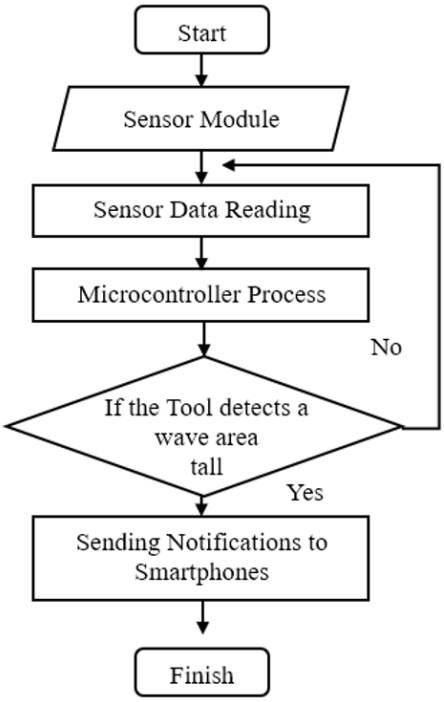

Fig. 3. Flow Chart

The design of the tool was carried out after obtaining the results of the analysis of the open area in the FT building using the Rolling sphere method. The data was then measured with a measuring tool and plotted manually. So that the points of the danger zone of direct lightning strikes are obtained. The data is then recorded and stored for data integration on the microcontroller. The design of the lightning strike detection device was carried out by combining several electronic components with GPS sensors NEO6MV2 to read the results of previous measurements.

The data read by the sensor is then processed on the microcontroller and if the sensor reads the previous plotting results . The plotting area is initiated into a program so that when the sensor reads the category of the direct lightning strike danger zone, the tool will send a notification in the form of a warning message to the smartphone in the form of an invitation to leave the area immediately. If the sensor does not read the previous plotting results, the tool will not send any warning.

B. Research Steps

The steps of this research are as follows.

1) Creating a rolling sphere from peak lightning currents.
2) Forming a rolling ball that is installed on the building.
3) Mark which areas are affected by the line of the rolling ball.
4) Mark the affected area with the GPS sensor
5) Saves an area and gives commands to the tool to identify that it is a direct lightning strike point.

IV. DISCUSSION

A. Sketch of the Faculty of Engineering Building (FT)

The first process carried out in this study is to select a sample of the building to be used as a point for the lightning strike area directly. The sample of the building chosen for this study is the dean's building of FT Untirta. One of the reasons is because among the FT buildings, one of the buildings that has the highest potential to be struck by lightning is the FT dean's building.

In making a sketch of the FT building, a simple sketch is carried out with the actual size so that the image has a scale reference. With this scale, the design or sketch of the FT building area can be calculated in various sizes. With this scale, it will then be easier to calculate the lightning strike area with the rolling sphere method. The sketch of the building is as follows.

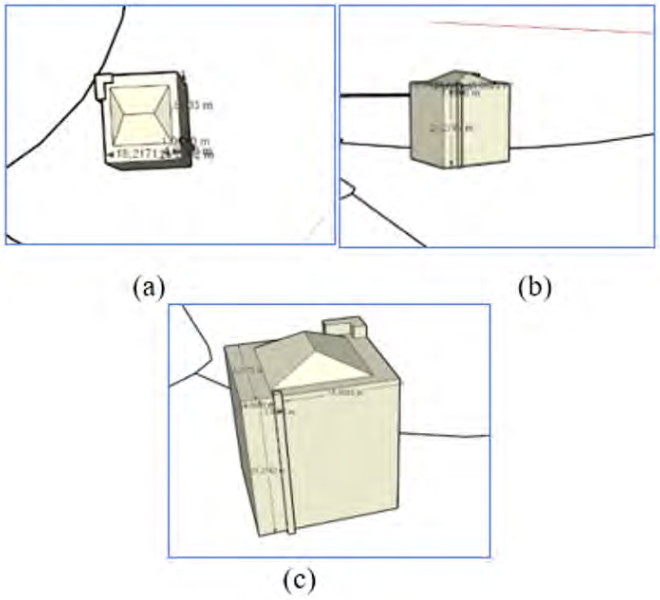

Fig. 4. Gedung FT UNTIRTA: (a) Top view; (b) Side view; (c) Front Side View

B. Lightning strike area modeling

Modeling the lightning strike area directly using corel draw software. With this software we can determine the size clearly and precisely. In addition, the size setting on each corel draw shape makes it easier to make visualizations of the lightning strike area with the rolling sphere method.

C. Tool design process

a) Tool drawing design

The tool design process begins with making a drawing design from the tool to be made. From the results of calculations

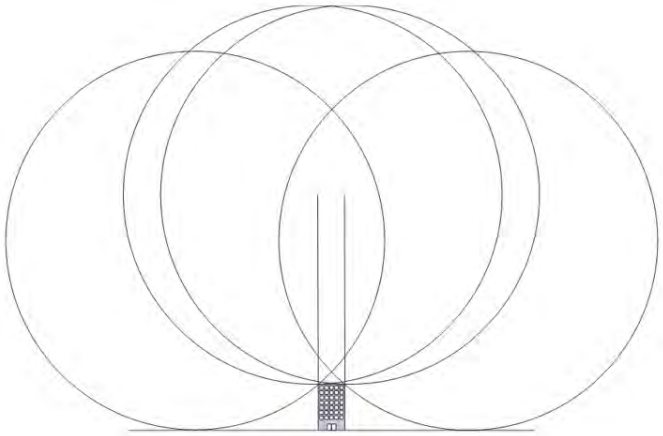

Fig. 5. Lightning strike area

and considerations both aesthetically and philosophically, the lightning detector that is formed to resemble a rocket is drawn first on the sketch software. This design process was carried out for one month. This is because in the process of designing the drawing of the tool, various things are considered in detail. These forms of consideration include adjustments to the dimensions of the module, the size of the microcontroller, the ease of obtaining materials, the aesthetics of the tools, and so on.

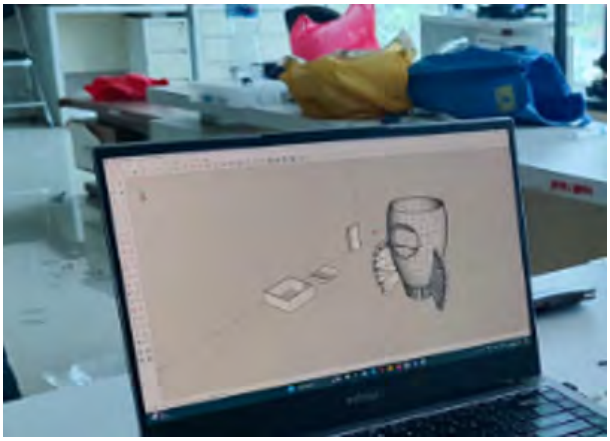

Fig. 6. The process of creating a tool drawing design

b) Lightning Detector Tool Assembly

Once the tool case is finished molding, the next step is to assemble the electronic components to be made into a lightning detector tool. Multiple components are assembled in such a way that the equipment can form a single system that can read are lightning strikes according to a predetermined design. In this assembly process, it is necessary to pay attention to the size of several things, including the lightning strike area calculated using the rolling sphere method, the image scale, and the lightning strike area that will be used as a test area of the tool.

By determining some of the parameters mentioned earlier, the tool is assembled and adjusted to the case that has been made. The placement of components must be adjusted to the position or part of the case that has been adjusted. That way, the case will contain all the necessary components and the lightning detector function for the lightning strike area can be instantly splasheda.

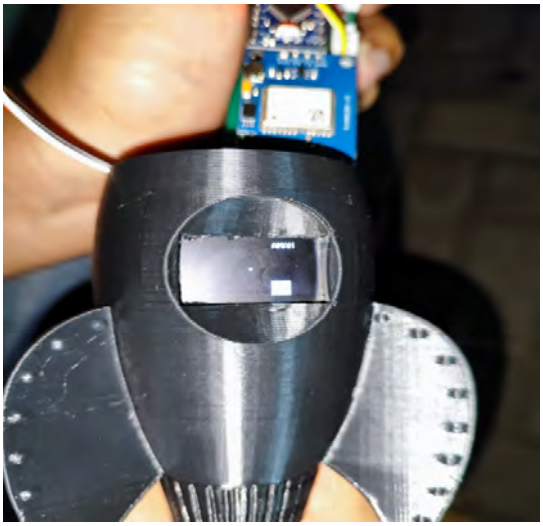

Fig. 7. Electronic component assembly

c) Tool manufacturing

The tool that has been drawn in detail is then designed to be made using a 3D printer. There are several preparations before the tool is printed using a printer, including making sure that the drawing has the right details. In addition, the dimensions of several electronic components that will be included in the results of the 3D printer printing are carried out. After checking the electronic components in accordance with the dimensions of the tool to be made using 3D Printing, the process of printing the tool design is carried out. This printing process takes up to 6 hours.

Fig. 8. Tool case printing process

V. Conclusion

The open area that is categorized as a red zone or an area that has the potential to be directly hit by a crate which is analyzed using the rolling sphere method in the FT building is 300 meters away from the reference point of the FT deanate building. The use of current values in the category of lightning current values in the campus area of the faculty of engineering as a reference in determining the calculation of the analysis of the red zone of direct lightning strikes with the rolling sphere method is 40K. The manufacture of a direct lightning strike red zone detector integrated with a smartphone as a warning to users when entering the red zone in the open area of the UNTIRTA faculty of engineering campus is designed to be limited to the trial stage.

Acknowledgment

Thank you to LPPM Sultan Ageng Tirtayasa University.

References

[1] A. Nugraha and R. Zoro, "Sistem Proteksi Petir Pada Sistem Tegangan Rendah Dan Peralatan Elektronik Di Gardu Induk Tegangan Tinggi," Institut Teknologi Bandung, 2021.

[2] R. van Ruler, T. Eikendal, F. O. Kooij, and E. C. T. H. Tan, "A Shocking Injury: A Clinical Review Of Lightning Injuries Highlighting Pitfalls And A Treatment Protocol," Injury, vol. 53, no. 10, pp. 3070–3077, 2022, doi: 10.1016/j.injury.2022.08.024.

[3] R. Blumenthal, "Lightning and the Forensic Pathologist," Acad. Forensic Pathol., vol. 8, no. 1, pp. 98–111, 2018, doi: 10.23907/2018.007.

[4] K. Ariga, M. Mursyidah, and H. Husaini, "Penentuan Zona Petir Wilayah Aceh Menggunakan Model Warna HSV," J. Teknol. Rekayasa, vol. 1, no. 1, pp. 20–24, 2017.

[5] R. Bintang, "Lansia di Aceh Jaya Meninggal Disambar Petir Saat Tanam Padi, Begini Kronologi versi Masyarakat," tribunnews.com, 2023. https://aceh.tribunnews.com/2023/09/21/lansia-di-aceh-jaya-meninggal-disambar-petir-saat- tanam-padi-begini-kronologi-versi-masyarakat. (accessed Sep. 24, 2023).

[6] I. B. Sulistiawati, M. Z. S. Shaufi, and I. M. Wartana, "Penggunaan Metode Rolling Sphere untuk Pengamanan Jaringan 150 kV dari Sambaran Petir Langsung," J. JEETech, vol. 4, no. 1, pp. 20–29, 2023, doi: 10.32492/jeetech.v4i1.4104.

Author Index